JAEA-Conf 2006-003

JP0650411

Proceedings of 2005 JAEA-KAERI Joint Seminar on Advanced Irradiation and PIE Technologies

November 16-18, 2005
JAEA Oarai R&D Center, Japan

JAEA KAERI

May 2006

Japan Atomic Energy Agency

Photographs in JAEA-KAERI Joint Seminar

November 16-18, 2005, at Oarai Research and Development Center of JAEA in Japan

Commemorative photography

Korean participants with the mayor of the Oarai Town before the opening ceremony.

Participants on the FBR Cycle International R&D Center building (F-Cerveaux).

Photographs in the meeting room

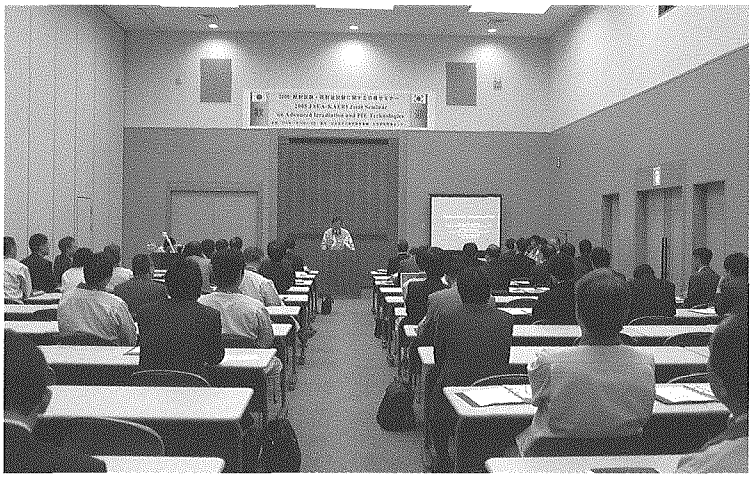

Opening address by Director General of the Oarai Research & Development Center in JAEA.

Presentation on the irradiation technology.

After the closing ceremony.

Courtesy call and technical tour

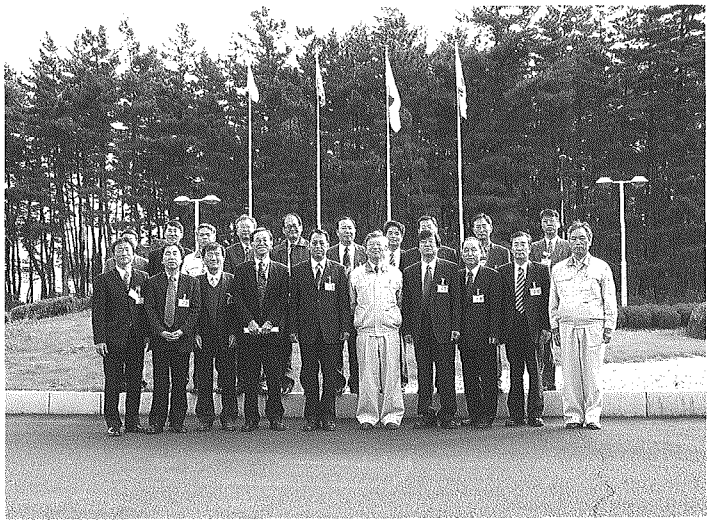

Courtesy call on Director General of the Oarai Research & Development Center in JAEA.

In front of JMTR Hot Laboratory.

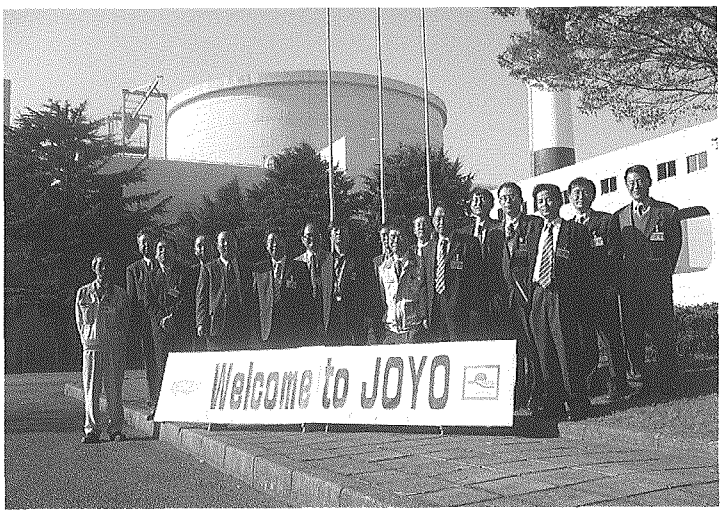

In front of JOYO.

Opening ceremony

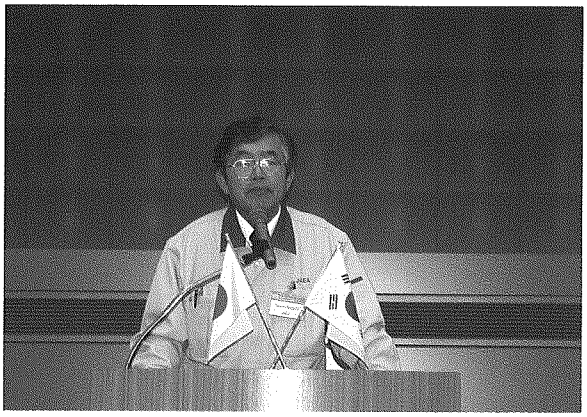

Opening address by Dr. Takashi Nagata.
(Director General, Oarai R&D Center in JAEA)

Opening address by Dr. Kwon-Pyo Hong.
(Director, Nuclear Fuel Cycle
Examination Division in KAERI)

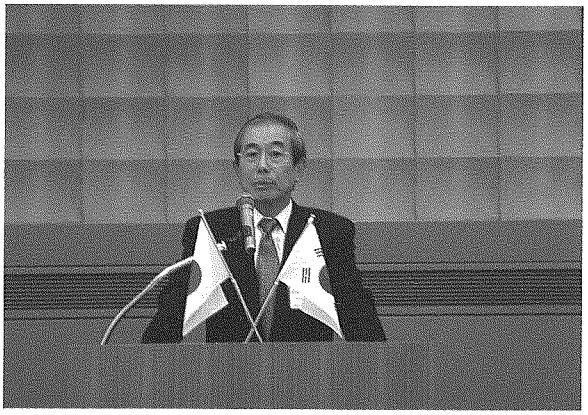

Welcome speech by Mr. Takaaki Kotani.
(Mayor, Oarai Town)

Closing ceremony

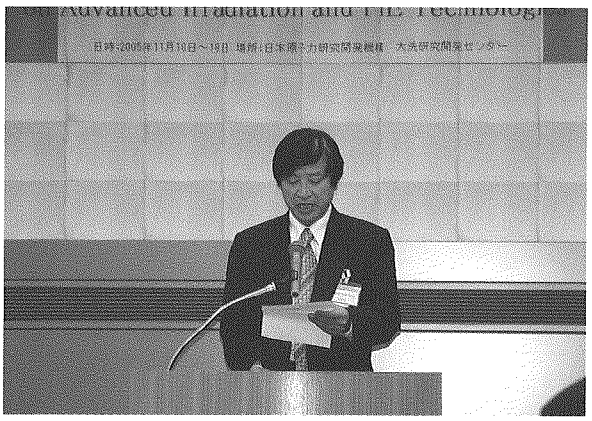

Closing address by Dr. Young Hwan Kang.
(Principal Researcher, HANARO Utilization
Technology Development Division in KAERI)

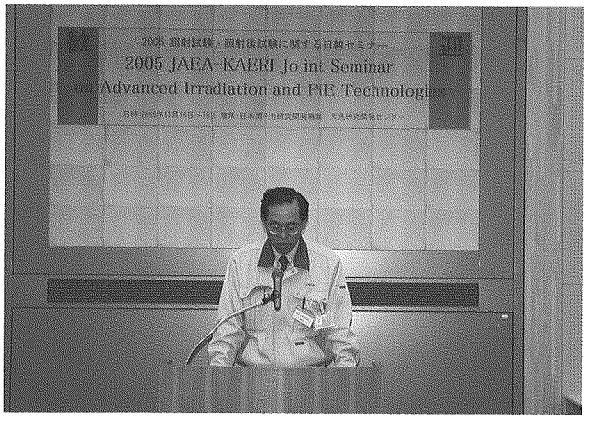

Closing address by Mr. Teruo Nakajima.
(Deputy Director General, Oarai R&D Center in JAEA)

Presentation by participants

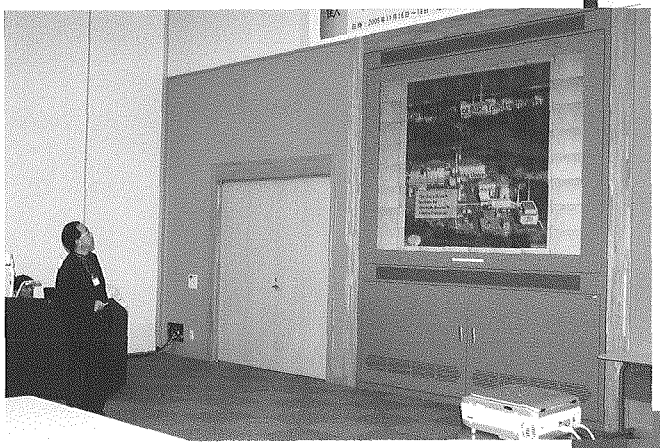

Presentations.

Reception etc.

Welcome party.

Before the opening ceremony.

Reception.

After lunch time.

JAEA-Conf 2006 - 003

Proceedings of 2005 JAEA-KAERI Joint Seminar on Advanced Irradiation and PIE Technologies

November 16-18, 2005, Oarai Research and Development Center, JAEA, Japan

Department of JMTR and Technology Development Department

Oarai Research and Development Center
Japan Atomic Energy Agency
Oarai-machi, Higashiibaraki-gun, Ibaraki-ken

(Received February 17, 2006)

Under the Arrangement for the Implementation of Cooperative Research Program in the Field of Peaceful Uses of Nuclear Energy between the Japan Atomic Energy Agency (JAEA) and the Korea Atomic Energy Research Institute (KAERI), the 2005 JAEA-KAERI Joint Seminar on Advanced Irradiation and PIE (post-irradiation examination) Technologies has been held November 16-18, 2005, at the Oarai Research and Development Center. This seminar was organized by the Department of JMTR and the Technology Development Department in JAEA with the cooperation of the related sections in JAEA. As another point, it was our first time to have the seminar combined with two fields on the irradiation and PIE technologies. In this seminar, participants had an aggressive discussion about not only the current status and future prospect on the technological development of the high-performance tests required in each field but also the status on the technological development of the advanced tests like the re-irradiation test and the in-pile test accomplished by the cooperation of both fields' technologies. Furthermore, participants from both countries were able to deepen a friendship through this seminar.

In this seminar, total participants of over 100 were joined from JAEA, KAERI, Hanyang University, Chungnam National University, Kyung Hee University, Oarai Branch of Institute for Materials Research (IMR) of Tohoku University, Nippon Nuclear Fuel Development Co., Ltd., Nuclear Development Corporation and others. The technical development and experimental data on the irradiation test and PIE were aggressively discussed in this seminar. Contributed presentations were 35 in three sessions; Current status and future program on irradiation test and PIE (10 presentations), Development of irradiation and PIE technologies (15 presentations) and Evaluation of irradiation and PIE data (10 presentations). Development of instrumented capsule technologies for HANARO irradiation, current PIE activities in each hot laboratory of both countries, development of

irradiation capsules in JMTR for the Irradiation Assisted Stress Corrosion Cracking (IASCC) study, development of irradiation and PIE techniques for the safety research on the high burnup fuel, utilization plan of JOYO and development of MOX fuel containing americium have been widely noticed as topic items on irradiation and PIE technologies.

This proceedings is containing papers presented in the 2005 JAEA-KAERI Joint Seminar. It also indicates the current status of the aggressive information exchange activity on two fields of irradiation test and PIE technologies between JAEA and KAERI under the Arrangement for the Implementation of Cooperative Research Program mentioned above.

Keywords; Irradiation Technology, PIE Technology, JMTR, JOYO, HANARO, JRR-3, JRR-4, Hot Laboratory, IASCC, High Burnup Fuel

JAEA-Conf 2006 - 003

2005 照射試験・照射後試験技術に関する日韓セミナー　論文集

2005年11月16日～18日、大洗研究開発センター、大洗町

日本原子力研究開発機構
大洗研究開発センター
材料試験炉部・技術開発部

(2006年 2月17日 受理)

材料試験炉部及び技術開発部は、日本原子力研究開発機構（原子力機構）と韓国原子力研究所（韓国原研）が結んでいる「原子力の平和利用分野における研究協力実施取決め」に基づき、関係各所の協力の下に、大洗研究開発センターにおいて、「2005照射試験・照射後試験技術に関する日韓セミナー」を2005年11月16日～18日に開催した。特に今回のセミナーは、照射試験技術と照射後試験技術の二つの分野について初めて合同で開催したものであり、各々の分野で要求される高性能試験の技術開発の現状と展望についてはもちろんのこと、両分野の技術の融合、協調によってはじめて可能となる再照射試験や放射化試料の照射下試験など、先端的試験の技術開発の状況についても活発な討論を進めることとなった。更に、両国の参加者が今回のセミナーを通して友好的な関係を深めることができた。

本セミナーでは、原子力機構と韓国原研の他、日本の東北大学金属材料研究所、日本核燃料開発株式会社及びニュークリア・デベロップメント株式会社、韓国の漢陽工科大学、忠南大学及び慶熙大学等から総勢100余名の参加者を得て、照射試験及び照射後試験技術に係わる情報交換が精力的に行われた。

３つのセッションに分かれた講演は、照射試験及び照射後試験の現状と将来展望に関する報告10件、照射試験及び照射後試験に係わる技術開発に関する報告15件、照射試験データ及び照射後試験データの評価・解析に関する報告10件の計35件であり、HANAROにおける計装型照射キャプセルの開発、日韓両国の照射後試験施設における試験や技術開発の現状、軽水炉構造材料のIASCC研究のためのJMTRにおける照射キャプセル開発、高燃焼度燃料の安全性研究に係る照射試験・照射後試験技術の開発、常陽の利用計画、アメリシウム混合MOX燃料の開発等、最新の研究や技術開発に関する報告が行われた。

本報告書は、この日韓セミナーで発表された論文を収録したものであり、上記の研究協力実施取決めの下で、照射試験技術及び照射後試験技術の二つの分野に関する情報交換が活発に行われていることを示すものである。

大洗研究開発センター：〒311-1393 茨城県東茨城郡大洗町成田町4002

This is a blank page.

Foreword

The Arrangement of the Implementation of Cooperative Research Program in the Field of Peaceful Uses of Nuclear was renewed between the Japan Atomic Energy Agency (JAEA) and the Korea Atomic Energy Research Institute (KAERI) to continue the mutual information exchange on several kinds of items of nuclear safety and other related fields when JAEA was born on October 1, 2005, as a new research and development organization by a consolidation between the Japan Atomic Energy Research Institute (JAERI) and the Japan Nuclear Cycle Development Institute (JNC).

Before the consolidation, under the arrangement between JAERI and KAERI the mutual exchange of technical information and mutual visits of both specialists and scientists had been periodically carried out on the field of the post-irradiation examination (PIE) and the irradiation test activities since 1985 and 1989, respectively. To summarize the results of mutual information exchange on the PIE activities, the 1st, 2nd, 3rd and 4th JAERI-KAERI Joint Seminars on the PIE Technology were organized by JAERI in November 1992, KAERI in September 1995, JAERI in March 1999 and KAERI in October 2002, respectively. On the irradiation test activities, the 1st JAERI-KAERI Joint Seminar on the Irradiation Technology was organized by KAERI in October 2002.

The 2005 JAEA-KAERI Joint Seminar on Advanced Irradiation and PIE Technologies was held at the Oarai Research and Development Center of JAEA on November 16-18, 2005 under the auspices of the Oarai Research and Development Center of JAEA. It was the first time to have a seminar on both two fields of the irradiation technology and PIE technology simultaneously.

Over 100 participants were joined in this seminar from JAEA, KAERI, Hanyang University, Chungnam National University, Kyung Hee University, Oarai Branch of Institute for Materials Research (IMR) of Tohoku University, Nippon Nuclear Fuel Development Co., Ltd., Nuclear Development Corporation and others. 35 presentations were carried out for two days in the following three sessions; Current status and future program on irradiation test and PIE (10 presentations), Development of irradiation and PIE technologies (15 presentations) and Evaluation of irradiation and PIE data (10 presentations). The technical development and experimental data on both the irradiation test and PIE were aggressively discussed in this seminar.

At the seminar, it was confirmed that key issues were to continue the mutual information exchange and the international collaboration and furthermore to grasp the perspectives of next generation's irradiation and PIE technologies. All the participants made an agreement to meet again in the next joint seminar which will be held three years later in Korea.

This is a blank page.

Contents

目　　次

Opening Address

by
Takashi Nagata
Director General, Oarai Research and Development Center
Japan Atomic Energy Agency

Good morning Ladies and gentlemen.

It's a great pleasure for me to make welcome speech for '2005 JAEA-KAERI Joint Seminar on Advanced Irradiation and PIE Technologies', here at Oarai Research and Development Center of JAEA.

Under the arrangement for the implementation of 'Cooperative Research Program between JAERI and KAERI', we have successfully achieved effective and valuable information exchange through the past seminars held in the field of the irradiation technology and the PIE technology respectively, since the first seminar held at Oarai JAERI in 1992, and this is our first time to have the seminar on both two fields simultaneously.

As you know, both in Japan and in Korea, nuclear power plays an important and inevitable role to secure the national energy supply, and to keep our natural environment as well. There it should be pointed out that the irradiation and the associated PIE compose one of the essential base technologies to utilize this nuclear energy.

The Japan Atomic Energy Agency, JAEA, was born just this October 1st as a new and unique research & development organization by a consolidation between the Japan Atomic Energy Research Institute, JAERI, and the Japan Nuclear Fuel Cycle Development Institute, JNC. I believe that this seminar, held only one-and-half months later after the start of JAEA, will extend the way for further tight and close cooperative relationship between JAEA and KAERI.

In this seminar, we have as many as about 70 participants from KAERI, Chungnam National University, Kyunghee University, Hanyang University, of Korea, and from Tohoku University, Nippon Nuclear Fuel Development Company, Nuclear Development Corporation and JAEA of Japan. 35 presentations are going to be presented. I believe that eager discussions will be made, and this joint seminar will provide a good and fruitful opportunity for all the participants to exchange information and to establish valuable personal relationship for future cooperation.

Thank you for your attention.

Opening Address

by
Kwon-Pyo Hong
Director, Nuclear Fuel Cycle Examination Division
Korea Atomic Energy Research Institute

It is my great pleasure to have this opportunity to make opening address for "2005 JAEA-KAERI Joint Seminar on Advanced Irradiation and PIE Technologies" being held in this Oarai R&D Center.

First of all, I would like to express my sincere appreciation to Dr. Nagata, director general of JAEA Oarai R&D Center, for his help on this Joint Seminar, and also I would like to extend my appreciation to Mr. Nakajima and Dr. Wada and their staffs for their efforts in organizing this joint seminar.

As nuclear energy seems to be a unique and practical energy source for the future energy crisis, advancement of nuclear technology is inevitable both in Korea and Japan. In this sense, Irradiation and PIE technologies will be more important than ever because they are essential to development of nuclear technology.

At the past seminars held at KAERI and JAERI, we had exchanged a lot of technical information and experiences on PIE technologies. At this time, however, the Joint Seminar has been expanded to the field of Irradiation Technology. This combined seminar of two fields would be expected to be more effective and synergistic. It is my sincere desire that this seminar will contribute greatly to improvement of PIE and Irradiation technology of both countries through exchanging broad technical experiences, new ideas, and relevant information.

As a representative of the participants from Korea, I would like to express that it is our great pleasure to participate this seminar and to share our long-time friendship with all of you, and again I want to express my appreciation to all staffs for preparation of this seminar.

Thank you very much.

歓迎のご挨拶

大洗町長
小谷　隆亮

みなさま、ようこそ大洗町にお越し下さいました。私、大洗町町長の　小谷　隆亮と申します。

２００５照射試験・照射後試験技術に関する日韓セミナーが、ここ大洗町で開催されますことは、地元にとりましてとても喜ばしいことであります。

また、両セミナーが共同開催されますのは、このセミナーが初めてと伺い、一層の期待を寄せるところです。

ＪＭＴＲにつきましては、原子炉の研究開発にかかる燃料、材料の照射試験に供するとともにさまざまな原子力の研究開発と利用に大きな貢献をしていただいております。

本日開催されます国際会議において、専門家の皆さまによる最新技術の情報や、これからの技術開発の動向について多くの議論がなされ、日韓両国、更には世界的にも、よりすばらしい研究開発に繋がることを祈念申し上げます。

会場のみなさま、町内にはさまざまな観光スポットがあります。ぜひ、お立ち寄りください。お待ち申しております。

Welcome Message
(English translation)

by
Takaaki Kotani
Mayor
Oarai Town

Good Morning, Ladies and gentlemen, my name is Takaaki Kotani, mayor of Oarai town. I am pleased to welcome all of the participants to Oarai.

It is a great pleasure for us to open "2005 JAEA-KAERI Joint Seminar on Advanced Irradiation and Post Irradiation Examination Technologies" here in Oarai.

I heard that effective information exchange have been continued through the past 4 seminars, and I expect that their activities will be further in progress by cooperating works.

As you all know, the Japan Materials Testing Reactor of JAEA has made a contribution to the irradiation examinations of nuclear fuels, materials, and various research and development on nuclear technologies.

In this seminar, I hope active discussions on the latest nuclear technologies will be made among the participants. And I expect that this joint seminar will establish good personal relationship for future cooperation relationship between Korea and Japan.

Finally, I would like to conclude my greeting speech with hopes that you will enjoy the stay in Oarai. Please visit our wonderful sight seeing spots.

Thank you very much for your attention.

Session 1

Current Status and Future Program on Irradiation Test and PIE

Chairs:

【1.1 ~ 1.6】

Kwon Pyo Hong (KAERI) and Toshimitsu Ishii (JAEA)

【1.7 ~ 1.10】

Duck Kee Min (KAERI) and Tatsuo Shikama (Tohoku Univ.)

This is a blank page.

1.1 STATUS OF THE MATERIAL CAPSULE IRRADIATION AND THE DEVELOPMENT OF THE NEW CAPSULE TECHNOLOGY IN HANARO

Kee-Nam Choo, Young-Hwan Kang, Myoung-Hwan Choi, Man-Soon Cho and Bong-Goo Kim

HANARO Utilization Technology Development Division
Korea Atomic Energy Research Institute
150 Deokjin-dong, Yuseong-gu, Daejeon 305-353, Korea

ABSTRACT

A material capsule system including a main capsule, fixing, control, cutting, and transport systems was developed for an irradiation test of non-fissile materials in HANARO. 14 irradiation capsules (12 instrumented and 2 non-instrumented capsules) have been designed, fabricated and successfully irradiated in the HANARO CT and IR test holes since 1995. The capsules were mainly designed for an irradiation of the RPV (Reactor Pressure Vessel), reactor core materials, and Zr-based alloys. Most capsules were made for KAERI material research projects, but 5 capsules were made as a part of national projects for the promotion of the HANARO utilization for universities. Based on the accumulated irradiation experience and the user's sophisticated requirements, development of new instrumented capsule technologies for a more precise control of the irradiation temperature and fluence of a specimen irrespective of the reactor operation has been performed in HANARO.

INTRODUCTION

Various irradiation facilities such as the rabbit(small non-instrumented capsule) irradiation facilities, the loop facilities, and the capsule irradiation facilities for irradiation tests of nuclear materials, fuels, and radioisotope products have been developed at HANARO(High flux Advanced Neutron Application Reactor) [1]. Extensive efforts have been made to establish design, manufacturing, and irradiation technology for a capsule and capsule related systems, which should be compatible with HANARO's characteristics [2,3]. 5,600 specimens from 32 domestic research institutes, 2 nuclear industry companies and 67

universities, have been irradiated in HANARO for 53,000 hours using the irradiation capsule system since 1995 [4]. The capsule related systems including the capsule temperature controlling system, supporting system and cutting system were also developed. The rabbit irradiation systems in the HTS(Hydraulic Transfer System) and IP(Irradiation Position) holes that were originally designed for RI Production can be used for the irradiation of small sized specimens in a lower neutron flux condition than a capsule system. The main activities of the capsule development and utilization programs are focused on an in-reactor material test, new and advanced fuel research and development, safety-related research and development for nuclear reactor(commercial and next-generation) materials and components, and a basic irradiation research for universities.

In an irradiation test using a capsule, the temperature and fluence of a specimen are mainly dependent on the reactor operation conditions such as the reactor power mode and operation time. As a consequence, the irradiated specimen is subjected to a change of the temperature as well as of the neutron flux during a reactor power transient such as a start-up and a shut-down. A large difference in the defect structure has been reported to be caused by this transient irradiation from the mechanism of a defect structure development [5].

Therefore, the development of new capsule technology is required to overcome these limitations. In this paper, the irradiation experience and current status of the development of the capsule for controlling the temperature and fluence in HANARO are described.

CAPSULE IRRADIATION IN HANARO

HANARO Reactor

The High-flux Advanced Neutron Application Reactor (HANARO) is a multi-purposed research reactor located at KAERI, Korea. It was designed to provide a peak thermal flux of $5x10^{14}$ n/cm^2.sec at a 30MW maximum thermal power. The core features a combination of a light-water cooled/moderated inner core and a light-water cooled/heavy-water moderated outer core. The inner core has 28 fuel sites and 3 test sites. 3 test sites are in hexagonal shapes and used for capsules, FTL(Fuel Test Loop), and RI(Radioisotope) production. The outer core consists of 4 fuel sites and 4 test sites, which are embedded in the reflector tank. There are several vertical test holes such as CT, IR1, IR2(hexagonal type) and OR(cylindrical type) in the core of HANARO, and LH(Large Hole), HTS(Hydraulic Transfer System), NTD(Neutron Transmutation Doping) and IP(Irradiation Position) in the reflector region of the reactor for nuclear fuels/materials irradiation testing, RI production and Si-doping, as shown in **Fig. 1**. **Table 1** shows the characteristics of the reactor test holes for a fuel/material irradiation in HANARO.

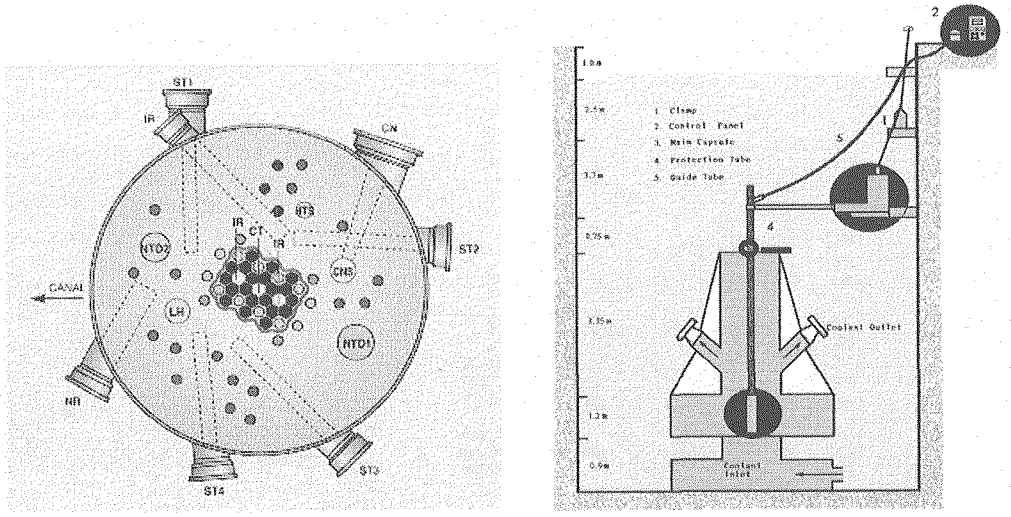

Fig. 1 Core configuration of the HANARO and a Schematic view of the HANARO capsule system.

Table 1 Characteristics of the test holes for a fuel/material irradiation in HANARO

Location	Hole		Inside Dia. (cm)	Neutron Flux (n/cm^2 . sec)		Remarks
	Name	No.		Fast Neutron (>0.82 Mev)	Thermal Neutron (<0.625 ev)	
Core	CT	1	7.44	2.10×10^{14}	4.39×10^{14}	Fuel/material test
	IR	2	7.44	1.95×10^{14}	3.93×10^{14}	Radioisotope production
	OR	4	6.00	2.23×10^{14}	3.36×10^{14}	
Reflector	LH	1	15.0	6.62×10^{11}	9.77×10^{13}	Fuel/material and others test
	HTS	1	10.0	9.44×10^{10}	47.97×10^{13}	
	IP	17	6.0	1.45×10^{9} - 2.20×10^{12}	2.40×10^{13} - 1.95×10^{14}	Radioisotope production

Irradiation Facilities

Among the irradiation facilities in HANARO, the capsule and rabbit systems have been used for the irradiation of nuclear materials. And the FTL will be installed in IR1 by 2008.

The rabbit(small non-instrumented capsule) was originally designed for isotope production, but it can be used for the irradiation test of a fuel and a material. **Fig. 2** shows the typical rabbit(20mm in diameter and 30mm in length) inserted in the HTS(Hydraulic Transfer System) hole. It is very useful for the numerous irradiation tests of small specimens at a low temperature(below 200°C) and neutron flux condition.

The instrumented and non-instrumented capsules have been developed at HANARO for new alloy and fuel developments and the life time estimation of nuclear power plants. For the

development of an instrumented capsule system, the capsule related systems such as a supporting, connecting, and controlling system were also developed as shown in **Fig. 1**. After a locking of the capsule in the test hole, the instrumented capsule is fixed by the chimney bracket and the robotic arm supporting systems. Two sets of cantilever type robotic arm systems for the CT and IR2 test holes were installed at the location of the platform level of the reactor that is 5.5 m in height from the bottom of the capsule, but the in-chimney bracket is temporarily installed on the top of the reactor chimney for a capsule irradiation test. At the Junction Box system, heaters and thermocouples can be easily connected and separated to/from the capsule controlling system before/after an irradiation test. The capsule temperature control system consists of three subsystems: a vacuum control system, a multi-stage heater control system, and a man-machine interface system. After an irradiation test, the main body of the instrumented capsule is cut off at the bottom of the protection tube with the cutting system and is transported to the IMEF(Irradiated Materials Examination Facility) by using a HANARO fuel cask.

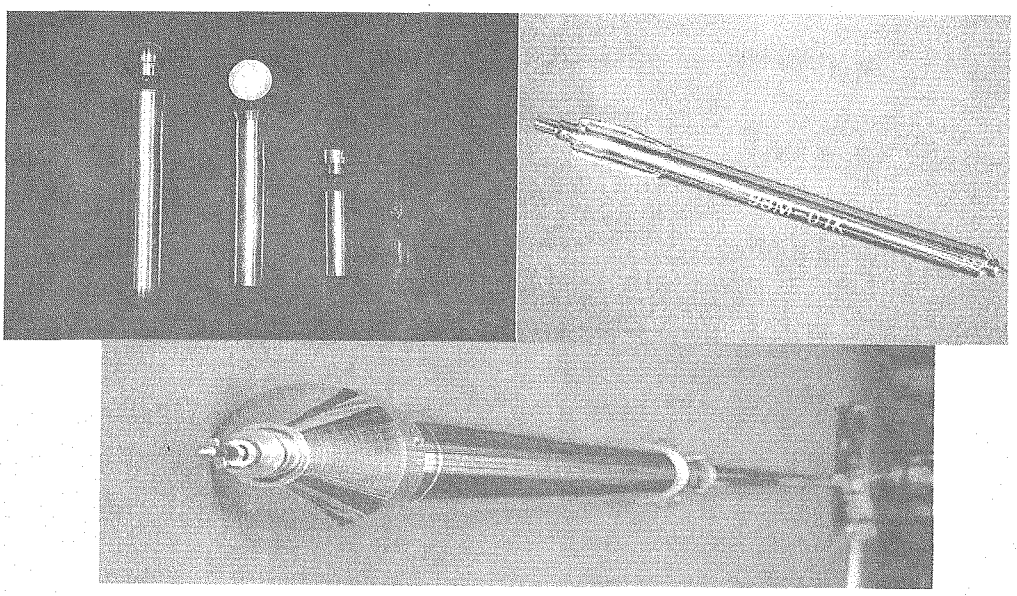

Fig. 2 Irradiation rabbit, non-instrumented capsule and an instrumented capsule.

Capsule Irradiation

12 instrumented capsules and 2 non-instrumented capsules have been successfully irradiated in the HANARO CT and IR test holes since 1995. The capsules were mainly designed for an irradiation of the RPV (Reactor Pressure Vessel), reactor core materials, and Zr-based alloys. Most capsules were made for KAERI material research projects, but 5 capsules were made as a part of national projects for the promotion of the HANARO utilization for universities. 5,600 specimens from 32 domestic research institutes, 2 nuclear industry companies and 67 universities, were irradiated in HANARO for 53,000 hours using capsule and rabbit irradiation systems.

Fig. 3 shows the increasing trends of the irradiation specimen and the time requested by users. Through this research, the nuclear characteristics of the HANARO capsules were also produced and stored in our database. The metallic material specimens were mainly irradiated at around 300℃ up to a fast neutron fluence of 1.3×10^{21}(n/cm^2) (E>1.0MeV).

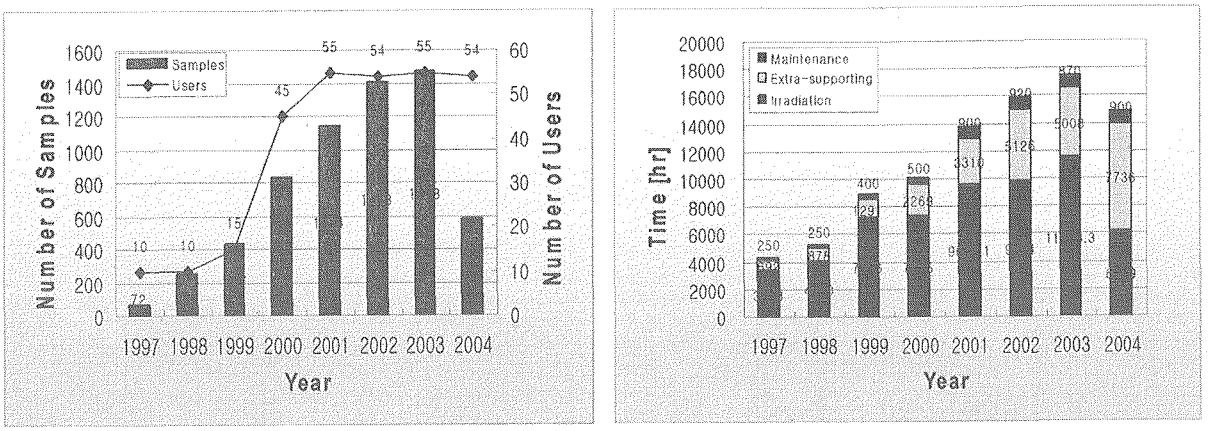

Fig. 3 Annual trends of HANARO users, samples, irradiation times.

New Capsule Technology

(1) Development of a Temp. Control Capsule

The irradiation temperature of the specimen is determined by the micro-heater output and He gas pressure of the gap in the capsule as well as the neutron flux of the capsule itself. However, during a reactor power transient such as a start-up, the irradiated specimen is subjected to a change of the temperature as well as of the neutron flux. Such simultaneous changes of the temperature and neutron flux, both of which affect an irradiation damage of the material, which makes it difficult to elucidate the radiation damage mechanism. The results of previous researches clearly show that temperature changes during a reactor startup and shutdown affect the microstructures of the irradiated specimens [3,4]. To avoid such undesirable effects, the temperatures of the specimens during a reactor start-up and shut-down should be kept as uniform as possible with that of a specimen at a normal operation of a reactor. Thus it was required to keep a sample at a specified temperature by heating the sample using auxiliary devices before a reactor power increase in order to eliminate the effect of a temperature transient in the recent irradiation tests. **Fig. 4** shows a typical concept of a temperature control irradiation test in HANARO. The temperature control is done by an electric heater and by controlling the He gas pressure in the capsule. First temperature control capsule (03M-06U) irrespective of the reactor operation was designed, manufactured and irradiated in HANARO. The specimen temperature was successfully raised up to the target temperature of 300℃ before a reactor start-up.

(2) Development of a Fluence Control Capsule

For the required specific fluence of the specimens, the reactor operation period has been

controlled in HANARO. However it became difficult because of an increased number of reactor users and a stabilized reactor operation schedule. Therefore, short time irradiation tests such as RPV materials requiring only a 2 day-irradiation for a life time neutron fluence requires new capsule technology.

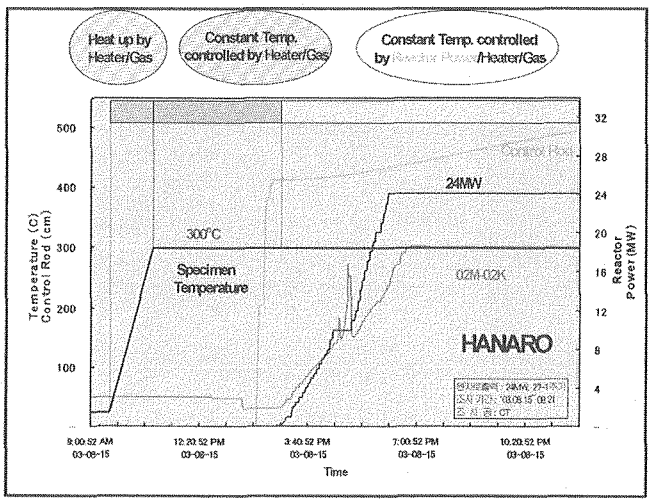

Fig. 4 Design concept of the temperature control irradiation capsule in HANARO.

Fig. 5 shows the conceptual design of the fluence control capsule. The system mainly consists of a main capsule, a protecting tube, a junction box, and a lifting device. Five subcapsules simulating square and round bar type specimens are accommodated in one stage of the capsule and each sub capsule can be taken out of the HANARO core during a reactor operation. The subcapsule could be lifted up by a pulling out mechanism using a steel wire. To take the subcapsule out of the reactor core, the length of the capsule would be twice as long as that of the conventional capsule. Moreover, the fluence control capsule will make it possible to irradiate specimens at different temperatures and with different fluences. With this one capsule, five different total fluences at five different temperatures can be ideally realized. Usually, one capsule realizes only one irradiation fluence at one temperature. Thus, it takes several years and an expensive irradiation cost for several capsules to carry out a systematic irradiation at different temperatures with different neutron fluences.

A mock-up capsule(04M-22K) was designed, manufactured and out-of-pile tested to confirm the capsule technology. The mock-up capsule consists of three main parts which are connected to each other: protection tube (5m), guide tube (9.5m) and the capsule main body. The main body including five subcapsules and instruments is a cylindrical shape tube of 60mm in diameter and was designed to be the same length as a conventional capsule. Specimens will be inserted in these subcapsules or to replace these subcapsules. The main body has 4 stages with independent micro-electric heaters and contains 12 thermocouples. The electric heaters were coiled on the outer surfaces of the aluminum block. A gap between

the aluminum block and a outer tube provides an appropriate heat removal rate for a temperature control. The gap is filled with helium gas.

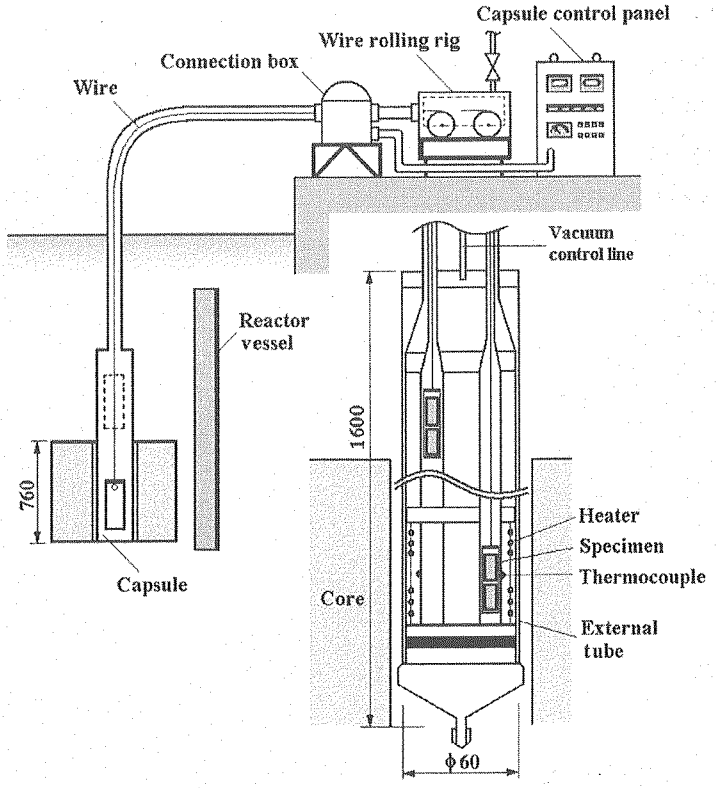

Fig. 5 Schematic diagram of the fluence control capsule.

To compare the easiness of moving for different designs, two transfer tubes were installed in the capsule, being thermally bonded by an aluminum block. Heaters, thermocouples, and specimen lifting wires are connected to a capsule temperature controlling system through a guide tube and a junction box system. The mock-up capsule was successfully tested under air environment at room temperature and a temperature of 300℃. Although the subcapsules having a transfer tube showed a better mobility, all of the subcapsules were easily lifted up by this pulling out mechanism using a piano steel wire.

Through parametric out-of-pile tests, an optimal design of the fluence control capsule could be suggested. However, several technical and safety analyses should be performed to apply this capsule in HANARO. The length of the outer tube should be determined according to the HANARO reactor characteristics and some manufacturing techniques should be improved. Finally the safety of the capsule should be strictly examined for an irradiation in the reactor.

CONCLUSIONS

A material capsule system was developed for an irradiation test of non fissile materials in HANARO. 14 irradiation capsules (12 instrumented and 2 non-instrumented capsules) containing 5,600 specimens from 101 users have been irradiated in HANARO since 1995. It provides us with very useful information for designing and evaluating nuclear materials. Based on the accumulated irradiation experience and the user's sophisticated requirements, development of new instrumented capsule technologies for a more precise control of the irradiation temperature and fluence of a specimen irrespective of the reactor operation has been performed in HANARO. These technologies will also be effectively applied to the researches for various test variables.

ACKNOWLEDGEMENT

This study was supported by Korea Science and Engineering Foundation (KOSEF) and Ministry of Science & Technology (MOST), Korean government, through its National Nuclear Technology Program.

REFERENCES

(1) KAERI, HANARO Summarized Report, KAERI, KAERI/PR-001/97 (1997).
(2) Y.H. Kang et als, A study on the development of instrumented capsule for the material irradiation test, KAERI Research Report, KAERI/RR-1760/96 (1997).
(3) Y.H. Kang et als, Safety analysis report (SAR) for the HANARO capsule and related systems, KAERI Technical Report, KAERI/TR-985/98 (1998).
(4) K.N. Choo et als, Irradiation experience and technology development of a material capsule, HANARO 2005 Symposium, 2005, Daejeon, Korea.
(5) M. Kiritani, "The Need for Improved Temperature Control during Reactor Irradiation," J. Nuclear Materials, 160, 135 (1988).
(6) F.A. Garner, et al., "Influence of details of reactor history on microstructural development during neutron irradiation," J. Nuclear Materials, 205, 206 (1993).

1.2 CURRENT STATUS OF IRRADIATION FACILITIES IN JRR-3 AND JRR-4

Naohiko Hori, Shigeru Wada, Fumio Sasajima and Tsuyoshi Kusunoki

Research Reactor Utilization Section
Department of Research Reactors and Tandem Accelerator
Nuclear Science Research Institute, Tokai Research and Development Center
Japan Atomic Energy Agency
2-4, Shirakata Shirane Tokai-mura, Naka-gun, Ibaraki-ken, 319-1195 Japan

ABSTRACT

The Department of Research Reactor has operated two research reactors, JRR-3 and JRR-4. These reactors were constructed in the Tokai Research Establishment. Many researchers and engineers use these joint-use facilities.

JRR-3 is a light water moderated and cooled, pool type research reactor using low-enriched silicide fuel. JRR-3's maximum thermal power is 20MW. JRR-3 has nine vertical irradiation holes for RI production, nuclear fuels and materials irradiation at reactor core area. JRR-3 has many kinds of irradiation holes in a heavy water tank around the reactor core. These are two hydraulic rabbit irradiation facilities, two pneumatic rabbit irradiation facilities, one activation analysis irradiation facilities, one uniform irradiation facility, one rotating irradiation facility and one capsule irradiation facility. JRR-3 has nine horizontal experimental holes, that are used by many kinds of neutron beam experimental facilities using these holes.

JRR-4 is a light water moderated and cooled, swimming pool type research reactor using low-enriched silicide fuel. JRR-4's maximum thermal power is 3.5MW. JRR-4 has five vertical irradiation tubes at reactor core area, three capsule irradiation facilities, one hydraulic rabbit irradiation facility, and one pneumatic rabbit irradiation facility. JRR-4 has a neutron beam hole, and it has used neutron beam experiments, irradiations for activation analysis and medical neutron irradiations.

KEYWORDS: JRR-3, JRR-4, Neutron Irradiation, Neutron Beam Experiment, Medical neutron irradiation

INTRODUCTION

We are thinking about many kinds of the utilization of the research reactors, activation analysis, production of radioisotopes, production of silicon semiconductors, medical irradiation, fuel and material irradiation, neutron beam experiments (neutron scattering experiment, neutron radiography, prompt gamma-ray analysis) and others (training course for reactor engineers, reactor engineering study, shielding experiment etc.).

Department of Research Reactor has operated two research reactors, JRR-3 and JRR-4. JRR is the abbreviation of Japan Research Reactor. These reactors were constructed in the Tokai Research Establishment. Many researchers and engineers use these joint-use facilities.

UTILIZATION OF JRR-3

Purpose of JRR-3

- Neutron Beam Experiments
    - Neutron scattering Experiment
    - Neutron Radiography
    - Prompt Gamma-ray Analysis
- Neutron Activation Analysis
- Production of Radioisotopes
- Production of Silicon Semiconductors
- Fuel and Material Irradiation
- etc.

Outline of JRR-3

JRR-3, the first Japanese designed and constructed reactor, had been utilized since 1962 by numerous researchers. Demands for higher performance and greater utilization to respond to various experiments had increased with the progress of nuclear science and technology. To keep pace with these demands, modification of JRR-3 was initiated in 1985.

Modified JRR-3 is a high-performance, multi-purpose research reactor, and attained first criticality in March 1990. With a maximum thermal power of 20 MW, it began operation in November of the same year. JRR-3 is a light water moderated and cooled, pool type research reactor using low-enriched silicide fuel (LEU: approximately 20% enriched uranium).

The reactor core is installed at the bottom of the reactor pool, which has the depth of 8.5 m, the internal diameter of 4.5 m, and the keyhole shaped horizontal cross section. A cylindrical reactor core is 60 cm in diameter and 75 cm in height. A heavy water tank, 200 cm in diameter and 160 cm in height, surrounds the reactor core.

Cold Neutron Source facility is installed in Heavy water tank at the horizontal hole 9C. In this Facility thermal neutrons pass through about -250 degrees Celsius liquid hydrogen. The resulting neutrons have reduced energy and are referred to as cold neutrons. Cold neutrons have a long wavelength in comparison to thermal neutrons and are useful to study the structures of giant molecules.

Utilization facilities include irradiation facilities for using vertical irradiation holes in the reactor core and the heavy water tank, and beam experimental facilities using horizontal experimental holes in the heavy water tank. Both cold and thermal neutrons can be utilized for beam experiments. Neutrons are guided to the experimental building from the horizontal experimental holes by the neutron guide tubes, which are rectangular glass tubes coated with a thin, vaporized nickel film. The variety of experimental devices installed on the ports of neutron guide tubes.

General view of the JRR-3's reactor room is shown in **Fig. 1**, and JRR-3 reactor core is shown in **Fig. 2**.

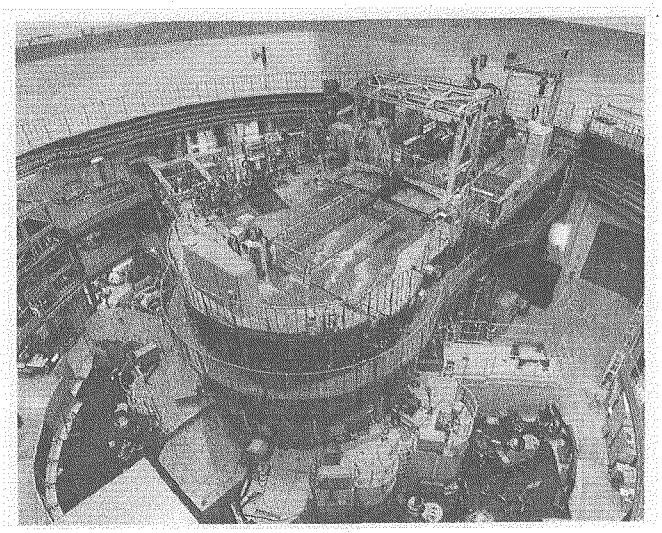

Fig.1 General View of the JRR-3's Reactor Room.

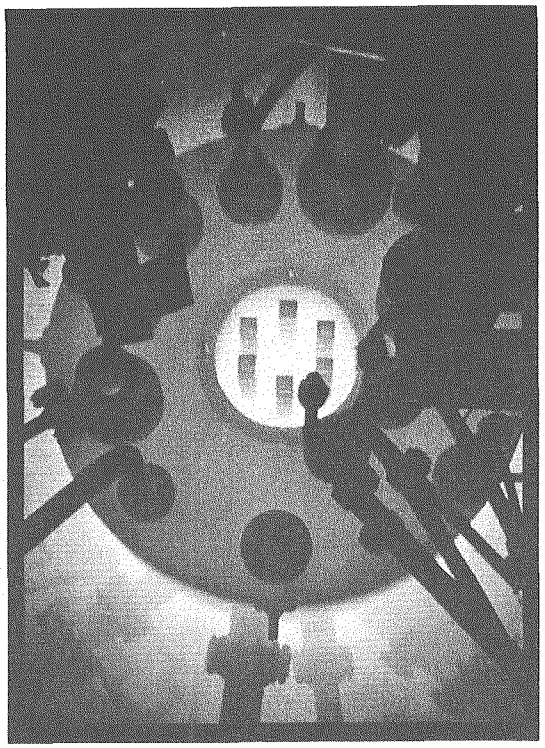

Fig.2 JRR-3 Reactor Core.

Irradiation facilities and horizontal experimental holes of JRR-3

Arrangement of experimental holes at JRR-3 is in the **Fig. 3**. Specification of JRR-3 irradiation facilities are shown in **Table 1**.

JRR-3 has nine vertical irradiation holes (VT-1, RG-1, -2, -3, -4, BR-1, -2, -3, and -4) at reactor core area. These are capsule irradiation facilities for long-term irradiation (a month - several years). Instrumented and non-instrumented capsules are used for long-term irradiation tests of fuels and materials. One type of instrumented capsules can control the

temperature of the specimen.

Irradiation tests together with post-irradiation examinations of fuels and materials contribute to the confirmation of their property change caused by neutron irradiation and to the research and development of fission and fusion nuclear reactor.

JRR-3 has many kinds of irradiation holes in the heavy water tank around the reactor core. These are two hydraulic rabbit irradiation facilities (HR-1 and -2), two pneumatic rabbit irradiation facilities (PN-1 and -2), one activation analysis irradiation facilities (PN-3), one uniform irradiation facility (SI-1: mainly using the production of semiconductors), one rotating irradiation facility (DR-1) and one capsule irradiation facility (SH-1). JRR-3 has nine horizontal experimental holes (1G, 2G, 3G, 4G, 5G, 6G, 7R, 8T and 9C), that are need for many kinds of neutron beam experimental facilities (neutron scattering experimental facilities, neutron radiography facilities , prompt gamma-ray analysis devices etc.).

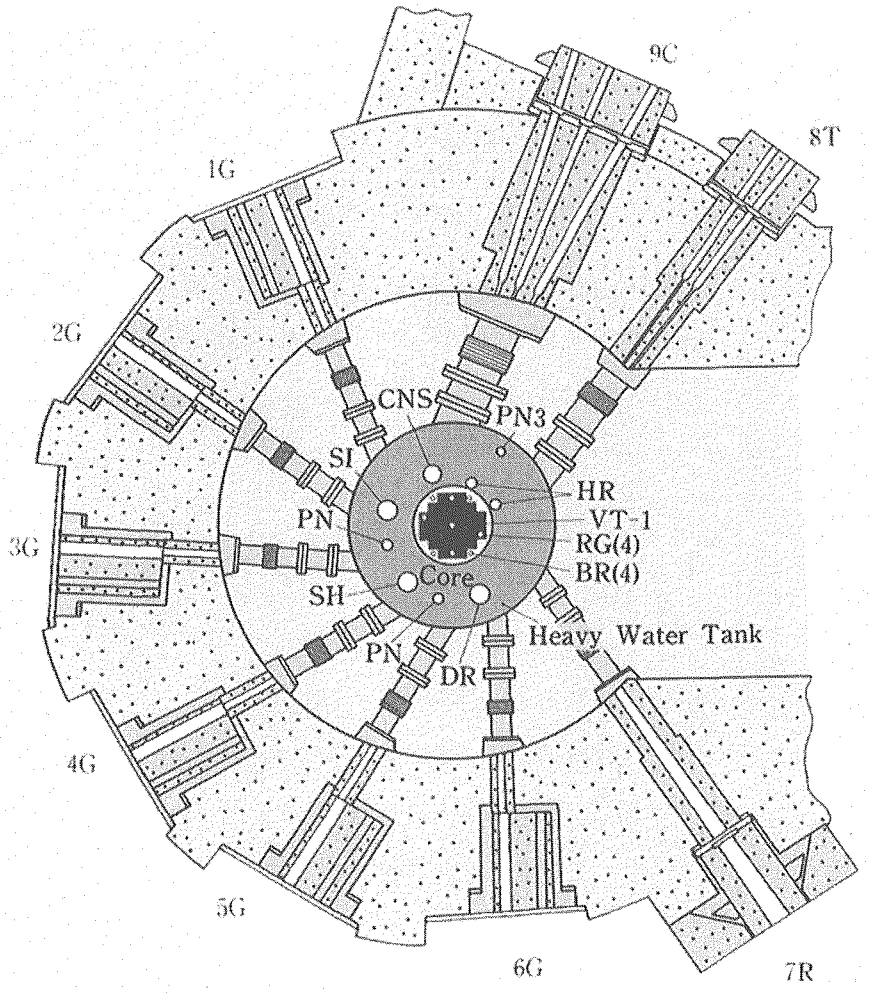

Fig. 3 Arrangement of experimental holes of JRR-3.

Table 1 Specification of JRR-3 irradiation facilities

Name	No.	Neutron Flux ($m^{-2}s^{-1}$)		Application
		Thermal	Fast	
Capsule Irradiation (VT)	1	3.0×10^{18}	2.0×10^{18}	Exposure Test RI Production
Capsule Irradiation (RG)	4	2.0×10^{18}	1.0×10^{18}	
Capsule Irradiation (BR)	4	2.0×10^{18}	1.0×10^{18}	
Hydraulic Rabbit (HR)	2	9.8×10^{17}	1.7×10^{16}	RI Production, NAA
Pneumatic Rabbit (PN)	2	5.2×10^{17}	1.2×10^{15}	RI Production, NAA
Activation Analysis (PN-3)	1	1.5×10^{17}	4.4×10^{13}	NAA
Uniform Irradiation (SI)	1	2.0×10^{17}	-	Silicon Doping,
Rotating Irradiation (DR)	1	3.0×10^{17}	-	Large Material Irradiation
Capsule Irradiation (SH)	1	4.0×10^{17}	-	Exposure Test RI Production
Horizontal Experimental Tube (1G – 6G, 7R, 8T, 9C)	9	1.2×10^{13} | 7.4×10^{13}	-	Neutron Scattering PGA, NRG

NAA: Neutron Activation Analysis

PGA: Prompt Gamma-ray Analysis

NRG: Neutron Radiography

UTILIZATION OF JRR-4

Purpose of JRR-4

- Neutron Activation Analysis
- Shielding Studies
- Nuclear Engineering Studies
- Irradiation Test
- Production of Radioisotopes
- Production of Silicon Semiconductors
- Education and Training
- Medical Irradiation
- Prompt Gamma-ray Analysis
- etc.

Outline of JRR-4

JRR-4 is the enriched uranium, light water moderate, coolant swimming pool type

reactor. Fuel elements' enrichment of U-235 is about 20 wt%. Fuel core material is uranium-silicon dispersion alloy(U3Si2-Al). The reactor core is composed of twenty fuel elements, seven Control Rods(Boron Stainless Steel) and is surrounded by reflector elements and tubes for irradiation experiments.

JRR-4's reactor core is shown in **Fig. 4**. And reactor core configuration of JRR-4 is shown in **Fig. 5**.

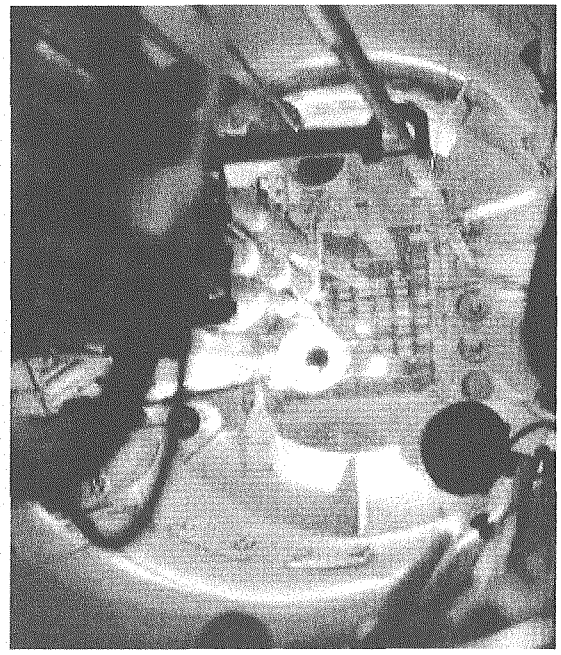

Fig. 4 JRR-4's Reactor core.

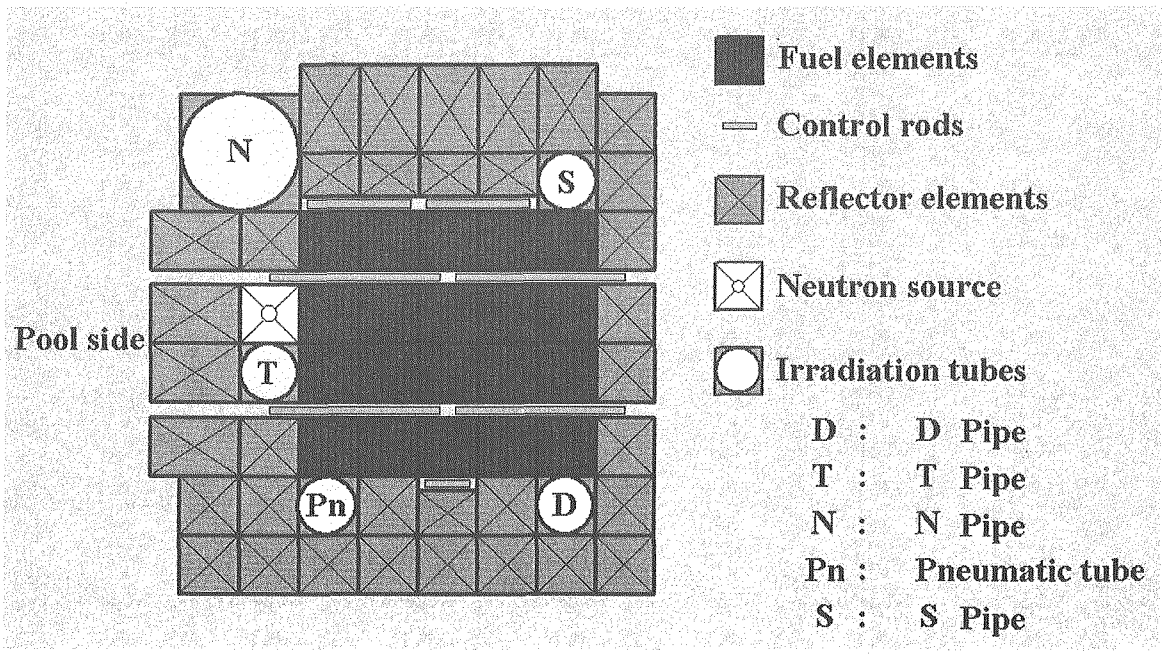

Fig. 5 Reactor core configuration of JRR-4.

Irradiation facilities of JRR-4

Specification of JRR-4 irradiation facilities are shown in **Table 2**. Medical neutron irradiation at neutron beam facility (NBF) is shown in **Fig. 6**.

JRR-4 has five vertical irradiation tubes at reactor core area, three capsule irradiation facilities (N pipe, S pipe, D pipe), one hydraulic rabbit irradiation facility (T pipe), and one pneumatic rabbit irradiation facility (Pn). JRR-4 has a neutron beam facility, and it has used neutron beam experiments, irradiations for activation analysis and medical neutron irradiations.

Table 2 Specification of JRR-4 irradiation facilities

Name	No.	Neutron Flux Thermal ($m^{-2}s^{-1}$)	Application
Capsule Irradiation Facilities (N, D, S)	3	$(1.5 - 4.3) \times 10^{17}$	Silicon Doping Material Irradiation
Hydraulic Rabbit (T)	1	5.3×10^{17}	RI Production
Pneumatic Rabbit (Pn)	1	3.2×10^{17}	NAA
Neutron Beam Facility	1	2.0×10^{13}	Medical Irradiation Neutron Beam Experiment

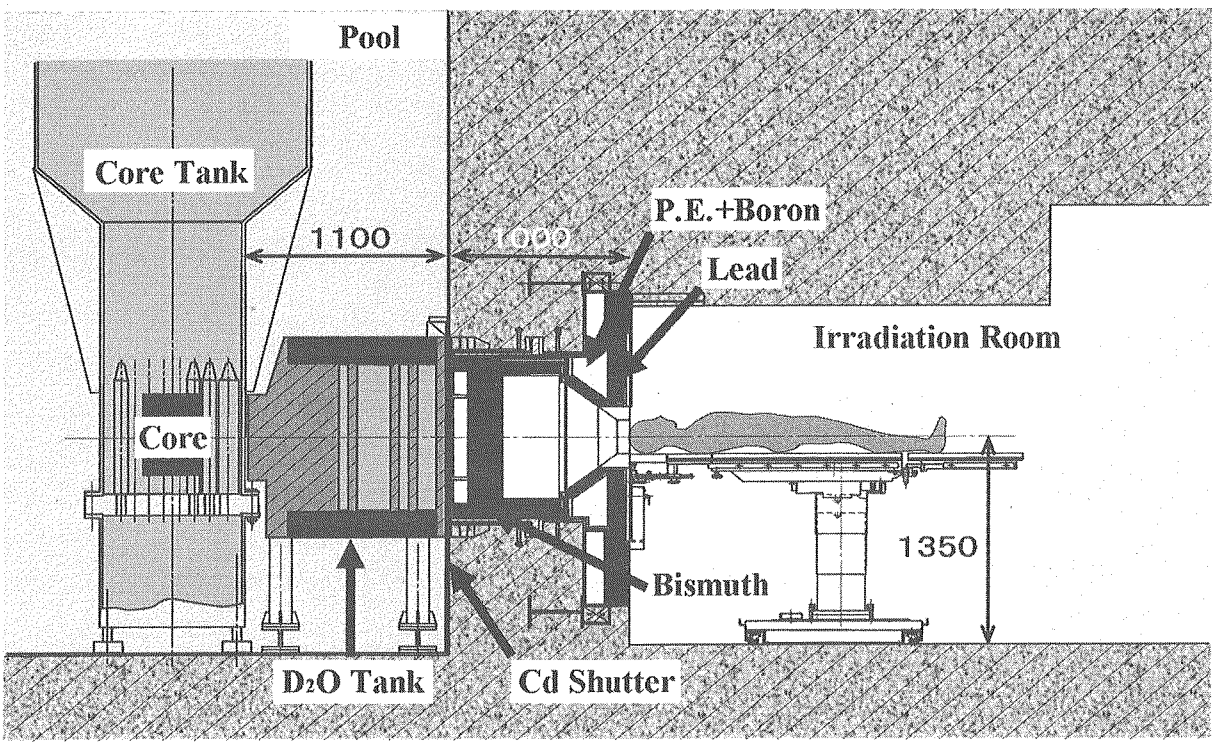

Fig. 6 Medical irradiation at neutron beam facility.

IRRADIATION CAPSULES

Polyethylene Capsules

Polyethylene capsules are mainly used for short-term irradiation in the pneumatic tube (PN) in JRR-3 and the hydraulic irradiation facility (T pipe) in JRR-4. The maximum irradiation time are 20 min. in the PN and 40 min. in the T pipe. (See **Fig. 7**.)

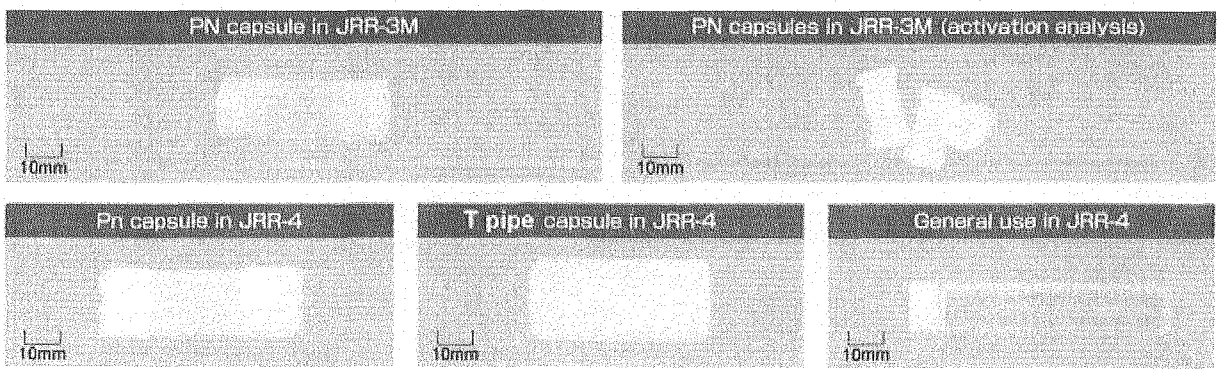

Fig. 7 Polyethylene Capsules.

Aluminum Capsules

Aluminum Capsules are mainly used for long-term irradiation in the HR in JRR-3 and hydraulic rabbit irradiation facility (T pipe) in JRR-4. (See **Fig. 8**)

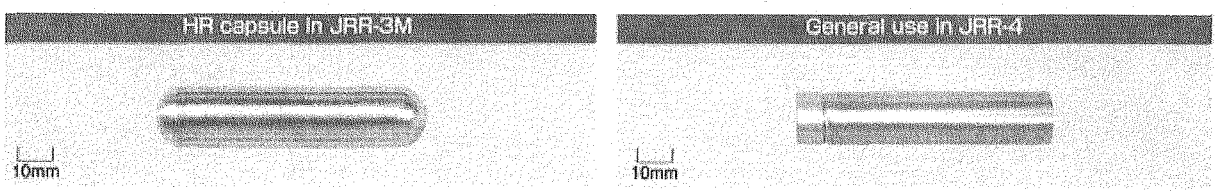

Fig. 8 Aluminum capsules.

STATUS OF UTILIZATION OF CAPSULES IRRADIATION

Status of utilization of capsule irradiation in 2004 is shown in **Fig. 9**. Irradiations for Neutron activation analysis are about 80%, Silicon Irradiations are about 10%.

JMTR will suspend operation for several years from spring in 2005. It is expected that the use of JRR-3 and JRR-4 increases by a part of the JMTR researchers using JRR-3 and JRR-4. We can make preparations for their irradiations and experiments.

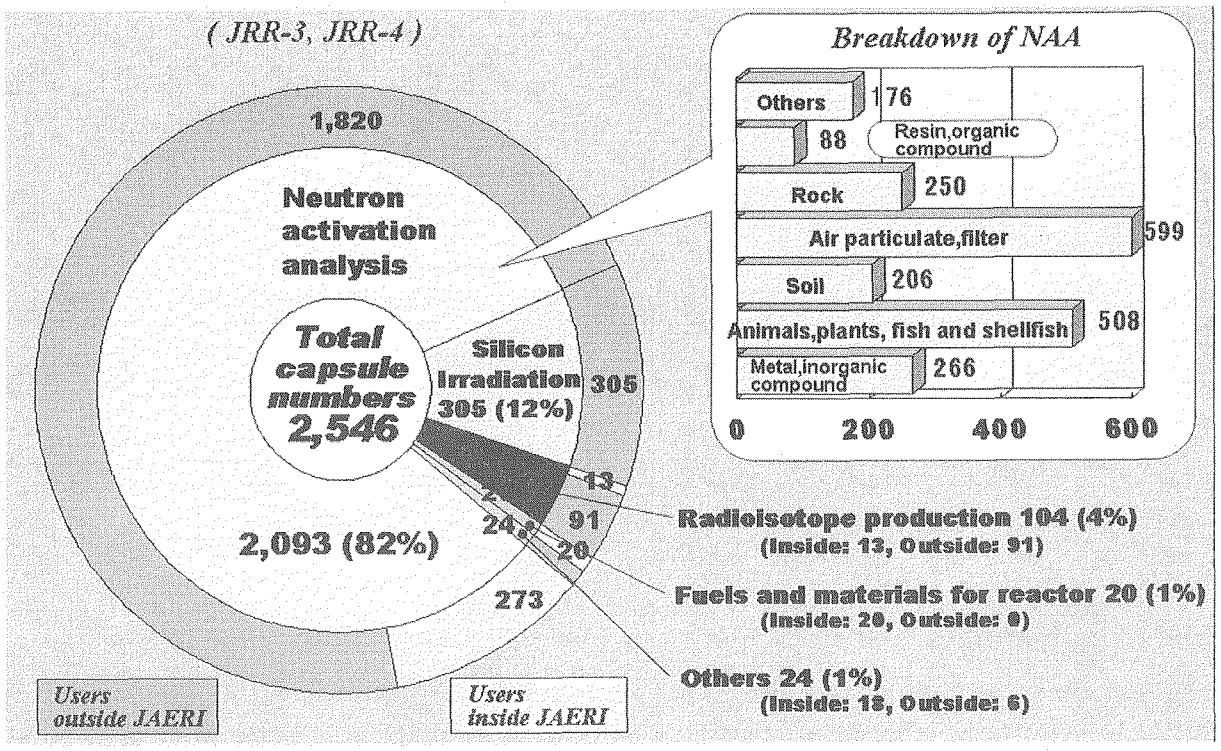

Fig. 9 Status of utilization of capsule irradiation in 2004.

REFERENCES

(1) Department of Research Reactor, Research Reactors Current status and their major roles (1999)

(2) Department of Research Reactor, Handbook for Utilization of Research Reactors 2nd Edition (1999)

1.3 INTRODUCTION OF THE EXPERIMENTAL FAST REACTOR JOYO

Ken-ichi Matsuba, Hirotaka Kawahara and Takafumi Aoyama

Fast Reactor Technology Section, Experimental Fast Reactor Department,
O-arai Research and Development Center, Japan Atomic Energy Agency,
4002 Narita, O-arai-machi, Higashi-Ibaraki-gun, Ibaraki-ken, 311-1393 Japan

ABSTRACT

The experimental fast reactor JOYO at O-arai Engineering Center of Japan Nuclear Cycle Development Institute is the first liquid metal cooled fast reactor in Japan. This paper describes the plant outline, experiences on the fast reactor technology and test results accumulated through twenty eight years successful operation of JOYO.

KEYWORDS: Experimental Fast Reactor, JOYO, MK-III core, Irradiation Test, Impurity Control, Fuel Failure Detection, Corrosion Product, Optical fiber Technology, Self-Actuated Shutdown System

INTRODUCTION

The experimental fast reactor JOYO at O-arai Engineering Center of Japan Nuclear Cycle Development Institute is the first liquid metal cooled fast reactor in Japan. JOYO achieved its initial criticality in April 1977 as the MK-I breeder core. From 1983 to 2000, JOYO was operated with the MK-II irradiation core to develop the fuels and materials for future fast reactors. Thirty-five duty cycle operations and thirteen special tests with the MK-II core were completed by June 2000 without any fuel pin failure or serious plant trouble. The reactor was upgraded to the MK-III high performance irradiation core to increase its irradiation capability, and the initial criticality with the MK-III core was attained in July 2003. This paper describes a review of the operational experiences obtained through twenty eight years successful operation of JOYO.

PLANT DESCRIPTION

JOYO is a sodium cooled fast reactor which uses plutonium and uranium mixed oxide (MOX) fuel. The main core parameters of JOYO are shown in **Table 1**, in which MK-III core is compared with MK-I and MK-II core. The active core is cylindrical and 80cm in diameter and 50cm in height. It is a conventional two-region core in which the contents of the fissile materials differ. The driver fuel is MOX with ~18% enriched uranium. The fissile plutonium content [(^{239}Pu+^{241}Pu)/(U+Pu)] is ~16% in the inner core and ~21% in the outer core. The core region is surrounded by a radial reflector region of stainless steel. The shielding subassemblies with B_4C (Boron Carbide) are loaded in the outer two rows of the reactor grid.

As a result, fast neutron flux in the MK-III core was up to 1.3 times higher than in the MK-II core, with 140MW (thermal) reactor power and 420W/cm (450W/cm at the overpower condition) maximum linear heat rate in the fuel pins. Also, the space of irradiation test field with a high neutron flux is twice than that of the MK-II core. This was achieved by relocating two control rods and expanding the fuel region (number of fuel assemblies increased from 67 to 85). JOYO core configuration is shown in **Fig. 1**.

The JOYO cooling system has two primary sodium loops, two secondary loops and an auxiliary cooling system. The auxiliary system consisting of primary and secondary loops is used for decay heat removal in case the main cooling system is not available. Approximately 200 tons of sodium is used for the cooling systems in JOYO. In the MK-III core, sodium enters the core at 350 degree-C at a flow rate of 1350 t/h per loop, and exits the reactor vessel at 500 degree-C thorough 500 mm diameter piping. The maximum outlet temperature of the fuel assemblies is about 550 degree-C. An intermediate heat exchanger (IHX) separates radioactive sodium in the primary system from non-radioactive sodium in the secondary system. Secondary sodium loops transport the reactor heat from the IHX to the air-cooled dump heat exchangers (DHXs). Two DHXs were installed in each secondary loop. All the generated heat is removed by these DHXs, because JOYO has no steam generator. JOYO cooling system diagram is shown in **Fig. 2**.

OPERATION HISTORY

The operation history of JOYO is shown in **Fig. 3**. JOYO achieved its initial criticality in April 1977 as a breeder core (MK-I core). After the low-power test and the power ascension test, JOYO initially operated two 50-MW(thermal) and six 75-MW(thermal) duty cycles with the MK-I core. In this period, there were about 260 reactor start-ups resulting from many kinds of tests, such as those dealing with reactor physics, reactor dynamics, power ascension and transients. Through this program, it was confirmed that the plant system satisfied the design objectives. In addition, the breeding

ratio was verified by post-irradiation examination (PIE) of the core and blanket fuels. The MK-I operation was completed at the end of 1981.

Later, core transformation work was carried out in which the MK-I core was replaced by the MK-II core. JOYO achieved initial criticality with MK-II core in 1982 and attained a maximum thermal output of 100 MW in 1983. Since then, 35 duty cycle operations and 13 special tests were completed by June 2000.

After the completion of the MK-II operation in 2000, the upgrading to MK-III core including modification of the cooling system was carried out to increase its irradiation capability, and MK-III rated-power operation started in 2004. At present, the net operation time of JOYO since its initial criticality reached over 65,000 hours and the heat generation reaches over 5,500GWh.

OPERATIONAL EXPERIENCES

Chemical Analysis of Sodium and Cover Gas

It is essential for steady and safe operation of a sodium cooled fast reactor to control the impurities in coolant and cover gas to prevent corrosion of reactor component materials and to reduce radiation dose by corrosion products (CPs). Therefore, impurity concentrations of both coolant sodium and cover gas argon were measured during the duty cycle operation and annual inspection period. The sodium impurity data include O_2, H_2, N_2, Cl, ^{3}H, metal elements and radioactive ^{110m}Ag, ^{22}Na, ^{137}Cs. The cover gas impurity data include O_2, N_2, CO, CO_2, H_2, CH_4, He, ^{3}H and radioactive xenon and krypton isotopes.

These data were measured by chemical analysis, gas chromatography, beta-ray scintillation and gamma-ray spectrometry. The sodium impurity concentrations were also measured by the sodium temperature of the plugging indicator. As an example, the trend of oxygen and hydrogen concentration in the primary sodium are shown in **Fig. 4**. The oxygen concentration in the primary sodium has been kept from 1 to 7 ppm below the upper control value of 10 ppm. The oxygen and hydrogen concentration were relatively high around the start of MK-II operation, because operating temperature of the cold trap was raised to prevent an increase in the pressure loss across the trap due to a sequential mesh arrangement. Since the cold trap was replaced by a new one with a parallel mesh arrangement in 1987, the oxygen and hydrogen concentration in the primary sodium have been kept stable and low with its constant operating temperature. The cause of an occasional increase of hydrogen concentration in the cover gas is likely dissociation of a small amount of alcohol that might be brought into the reactor vessel by fuel handling machines that are usually washed by alcohol [(1)].

Fuel Failure Simulation Test

(1) Objective of Fuel Failure Simulation Test

When a fuel failure occurs in a reactor, it is essential to detect quickly the event and identify the failed fuel subassembly in order to secure the operational reliability and to achieve high plant availability. It is also important to reduce the radiation exposure and the fission gas release to the environment. After the identification of failed fuel subassembly, the identified subassembly is discharged from the core to restart the reactor operation. In LMFBRs, several methods of fuel failure detection (FFD) and failed fuel detection and location (FFDL) were developed and equipped to reactors.

As JOYO has not yet experienced any natural fuel pin failure, three fuel failure simulation tests had been conducted in the JOYO MK-II core to evaluate the fission gas release behavior and to establish the plant operating procedure. In 2003, the core and cooling system were modified to the MK-III to increase the neutron flux density of the core [(2), (3)]. Accordingly the reactor thermal power was increased from 100 MWt to 140 MWt and maximum pin averaged burn-up of the driver fuel was increased from 75 GWd/t to 90 GWd/t. To accommodate the increased thermal power, the primary coolant flow rate and the temperature difference between reactor inlet and outlet were increased by 22 % and 20 degree-C, respectively. Corresponding to upgraded core and plant, performance of the FFD and FFDL systems and the plant operating procedure in case of fuel failure were confirmed.

(2) Outline of Fuel Failure Simulation Test

The schematic diagram of JOYO FFD and related system in connection with the fuel failure simulation test [(4)], along with test fuel assembly, is shown in **Fig. 5**. The FFD system consists of the delayed neutron monitoring system (FFD-DN) and the cover gas monitoring system. The FFD-DN is installed along the hot leg piping of each primary cooling system. Two kinds of neutron detectors, BF_3 proportional counter and boron lined B-10 counter, are used to measure the delayed neutrons emitted from their precursors such as ^{87}Br, ^{89}Br and ^{137}I. These nuclides are released from the failed fuel pins into sodium and transferred to the primary sodium. The cover gas monitoring system consists of two methods to measure the radioactivity of the argon cover gas in the primary cooling system. One is the cover gas precipitating system (Precipitator: FFD-CG) which detects ^{88}Rb and ^{138}Cs, the products by beta decay of ^{88}Kr and ^{138}Xe, released from the failed pins to the cover gas. The other is the on-line gamma-ray monitor (OLGM) which can identify the fission gas nuclides by means of gamma-ray spectrometry using germanium semiconductor detector.

The test fuel subassembly was loaded in the center position of JOYO MK-III core in November 2004 after the second duty operational cycle. Two test fuel pins each of which has an artificial slit filled with fusible alloy, and its sibling fuel pin without artificial slit were placed inside the test subassembly. The slit was 0.1 mm width $\times$ 1.0 mm length at

a gas plenum region through the cladding tube, and sealed with the fusible alloy melting about 300 degree-C. Therefore, the slit is opened to simulate the fuel failure when test fuel pin temperature exceeds 300 degree-C by nuclear heating.

(3) Test Results

The time history of the reactor power and FFD-CG signal are shown in **Fig. 6**. The sodium temperature was increased from 250 degree-C to 350 degree-C by nuclear heating about a few MWt. Then, the reactor power was increased step by step at 5 MWt interval. At each power step, the signal of neutron instrumentation system (NIS) and coolant inlet/outlet temperature were measured until the core and plant reached steady state. The subsequent power increase was allowed only if the FFD signal did not show the noticeable increase. The FFD-CG signal rose rapidly when the reactor power reached 120 MWt which corresponded to 86 % of the rated power of JOYO MK-III, and it exceeded the twice the background counting rate as shown in **Fig. 6**. The FFD-DN signal was varied proportion to the reactor power and did not show any increase beyond the background level, as it was predicted. In case of the fuel failure in plenum region, there was no direct contact of the MOX fuel and coolant sodium which enhanced the release of DN precursor into the sodium.

After the radioactivity in the cover gas was decreased by cover gas cleaning system (CGCS) operation and cover gas purge, the FFDL operation was initiated to identify the failed fuel subassembly. The sodium sipping method used in the FFDL system and measured result by the FFDL system are shown in **Fig. 7**. FFDL is mounted on the rotating plug and is addressed to the subassembly to be measured with the primary coolant flow rate of 75 % to 80 %. In this test, at first a reflector and a high burn-up fuel subassembly were measured for comparison, then the test fuel subassembly was measured. The gamma-ray counting rates obtained from radial reflector and high burn-up driver fuel subassembly were 1 cps, and the test subassembly was approximately 600 cps. Measured counting rate for another driver fuel subassembly conducted after the test subassembly was less than 2 cps. Therefore, the failed fuel was certainly identified by the sodium sipping FFDL system.

Through this test, plant operating procedure in case of fuel failure was confirmed, including fuel failure detection by FFD-CG system, identification of failed fuel by FFDL and the primary cover gas cleaning.

Measurement of Radioactive Corrosion Products

In order to reduce the radiation dose from activated sodium (long-lived ^{22}Na) during the periodical inspection and maintenance work for primary cooling system, all primary coolant sodium in the main circulating loops is drained into a storage tank. Under this condition, most personnel dose is due to gamma-ray from the corrosion products (CPs) deposited on inner surfaces of the primary main piping and components. Therefore, it is

important to evaluate gamma-ray dose rate distribution due to the CP deposits in the primary cooling system.

The amounts of CP deposits on the inner surfaces of the primary main piping have been measured at every periodical inspection. These measurements have been made at 4 locations, shown in **Fig. 8**, using a germanium solid-state detector system. The detector system was calibrated with a piping mock-up using two planer type standard gamma-ray sources, ^{54}Mn and ^{60}Co, so that the absolute amounts of CP deposits could be obtained from the measured gamma-ray spectra.

Gamma-ray dose rates from CP deposits have been also measured using calcium sulfate ($CaSO_4$) thermo-luminescence dosimeters (TLDs). The gamma-ray dose rate distribution near the piping is measured in detail at 93 locations at one-meter intervals along loop (A). At each location, four TLDs are placed every 90 degrees around the heat insulator cover. The geometrical conditions for these measurements are almost the same as those for the radioactive CP deposit mentioned above. The measured radiation data has been used to verify the CP behavior analysis code PSYCHE [5] which analyzes the distribution of CP in the primary cooling system.

In addition to TLDs, a Plastic Scintillation Fiber (PSF) has been applied to measurement of the dose rate distribution in the primary cooling system[6]. Block diagram of PSF measurement system, along with the measured gamma-ray dose rate profile of the A loop IHX, is shown in **Fig. 9**. Polystyrene was used as a scintillator which emits light in response to gamma-rays. The radiation source's location was determined with the time of flight method by measuring the time interval between the signals from two photo multipliers (PMT) at each end of PSF. As seen in **Fig. 9**, two peaks were observed in the position in which horizontal plates such as shroud seal ring and lower tube plate were installed. CPs are likely to be deposited at the corner of these plates due to stagnant sodium flow. Therefore, the measured two peaks indicate a large amount of CP deposits.

Comparing PSF results with a series of TLD point data, large differences were observed at these peaks before unfolding. However, by employing the unfolding method, the PSF data coincided with the TLD results. The use of PSF greatly reduced the cost of the gamma-ray dose rate distribution measurement.

Measurement test of temperature distribution using optical fiber technology

Optical fiber sensors have many advantages such as flexible configuration, noise resistance in electromagnetic fields, long-distance data transfer capability and so on. Therefore, it is very useful to apply optical fiber sensors for measurement of fast reactor plant states.

In order to evaluate the applicability of Raman Distributed Temperature Sensor (RDTS; one of the optical fiber sensors) for fast reactor plant instrumentation, temperature distribution measurement in the primary coolant loop has been carried out using RDTS. Measurement system using RDTS, along with measured temperature distribution, is shown

in **Fig. 10**. RDTS is based on the Raman scattering phenomena of the optical fiber, in which the intensity ratio of two kind of scattered light (stokes and anti-stokes) depends on the temperature of scattering points. Two optical fiber sensors were installed spirally around the outer surface of primary piping heat insulator.

The temperature distribution data in the primary cooling loop was obtained over 180 EFPDs of JOYO's operation. Under the high dose rate condition during nuclear plant operation, measurement errors due to radiation-induced transmission loss of optical fibers are not neglected. Therefore, calibration method using two thermocouples has been developed to reduce radiation-induced temperature errors.

Through this test, the radiation-induced temperature errors were successfully calibrated by thermocouple readings, and the temperature distribution on the piping was measured with the accuracy of approximately ±3 degree-C after calibration. It was also confirmed that the temperature distribution on the piping was caused by non-uniform settings of heat insulator.

Measurement of strain and vibration in the primary cooling loop has been also carried out using Fiber Bragg Grating (FGB) sensor. The principle of strain and vibration measurement using FBG sensor is based on the characteristic in which the wavelength of reflective light from FBG depends on applied strain. In the present, the durability of FBG sensors under fast reactor conditions and radiation-induced change of their measurement sensitivity are studied.

These optical technologies will be reflected on development of an innovative on-line structure monitoring system for fast reactor plants.

Demonstration Test of The Holding Stability of The Self-Actuated Shutdown System

Self-actuated shutdown system (SASS) with a Curie point electromagnet (CPEM) has been developed for use in a large scale fast breeder reactor (FBR) in order to establish the passive shutdown capability against anticipated transient without scram (ATWS) events. The basic characteristics of SASS have already been investigated by various out-of-pile tests. As the final stage of the development, the stability of SASS needs to be confirmed under the actual reactor-operational environment with high temperature, high neutron flux and flowing sodium in order to ensure the high plant availability factor. For this purpose, the demonstration test of holding stability using the reduced-scale experimental equipment of SASS was conducted through the JOYO MK-III 1st and 2nd operational cycles (for five months). The schematics of SASS experimental equipment is shown in **Fig. 11**.

As a result of the test, both the rod-holding stability and the rod-recovering functions of the driving system to re-connect and pull out the separated control rod were successfully confirmed. These results indicate that there is no essential problem for the practical use of SASS about its operational trouble involving the unexpected drop during reactor operation.

FUTURE PLANNING

The unitization plan of JOYO is shown in **Table 2.** Oxide dispersion strengthened ferritic steel (ODS), which is the most promising candidate for fuel cladding of future long-life fuel, will be irradiated with the MARICO and the core material irradiation rig (CMIR). Then, leading very high burn-up irradiation tests will be started, and some rigs will open the door of fuel breach to investigate fuel life limit design. Targeted to realize economical fuel, short-process MOX fuel pellets, vibratory compaction (vipac) MOX fuel, or metal fuel will be tested instead of conventional MOX fuel. The sodium bonded-type control rods with shroud tubes started which is irradiated to demonstrate their extremely long life.

In the transmutation area, which is aimed at reducing the environmental burden of long-lived radionuclides, MOX fuel with 5% americium added and with both neptunium and americium added will be irradiated in 2006. Then, testing of LLFP incineration such as ^{99}Tc and ^{129}I by using moderator such as beryllium and metal hydride will be started.

In the reactor engineering area, slow power transient testing, anticipated transient testing without scram (ATWS), and in-service inspection and repair (ISI&R) demonstrations are being considered.

SUMMARY

The successful operations of JOYO provide a wealth of experiences with core management, impurity control, reactor engineering tests and innovative instrumentation techniques. These experiences and accumulated data are to be used for the design of future fast reactors.

REFERENCES

(1) T. Aoyama et al., "Operational Experience and Upgrading Program of the Experimental Fast Reactor JOYO", Proc. IAEA Technical Mtg. Operational and Decommissioning Experience with Fast Reactors, Cadarache, France, March 2002, International Atomic Energy Agency (2002).

(2) H. Hara et. al., "JOYO MK-III, State-of-the-Art, FBR Irradiation Test Facility", Proceedings of 14th Pacific Basin Nuclear Conference, Honolulu, Hawaii, USA, March 21-25, 2004 (2004).

(3) Y. Maeda et. al., "DISTINGUISHED ACHIEVEMENTS OF A QUARTER-CENTURY OPERATION AND A PROMISING PROJECT NAMED MK-III IN JOYO", Nuclear Technology, Vol. 150, NT-4 03113 (2004).

(4) T. Aoyama et. al., "Introduction of Nuclear Instrumen- tations and Radiation Measurements in Experimental Fast Reactor JOYO (4th Edition)", PNC TN 9423 98-001, Power Reactor and Nuclear Fuel Development Corporation (1998).
(5) K. Iizawa et al., "Transport of Radioactive Corrosion Product in Primary Systems of a Sodium Cooled Fast Reactor", Proc. Material Behavior and Physical Chemistry in Liquid Metal Systems 2, Plenum Press, ISBN 0-306-45069-0, pp. 9-26 (1995).
(6) T. Aoyama et al., "Application of Optical Fiber for Radiation Measurement in Fast Reactor Primary Cooling System", Proc. 12th Pacific Basin Nuclear Conference, Seoul, Korea, Oct. 29 - Nov. 2, 2000, Vol. 2, pp. 1095-1105 (2000).

Table 1 Main Core Parameters of JOYO

Basic Specifications of JOYO

Items		MK-I	MK-II	MK-III
Reactor Thermal Output	MWt	50/75	100	140
Max. Number of Driver Fuel S/A		82	67	85
Max. Number of Test Fuel S/A		0	9	21
Core Diameter	cm	80	73	80
Core Height	cm	60	55	50
^{235}U Enrichment	wt%	~23	~18	~18
Pu Content Total	wt%	~18	<30	<30
Fissile	wt%	—	~20	~16/21*
Max. Linear Heat Rate	W/cm	320	400	420
Max. Neutron Flux Total	n/cm²•s	3.2×10^{15}	4.5×10^{15}	5.7×10^{15}
Fast (>0.1MeV)	n/cm²•s	2.2×10^{15}	3.2×10^{15}	4.0×10^{15}
Max. Burn-up (Pin Average)	GWd/t	42	75	90
Primary Coolant Flow Rate	t/h	2,200	2,200	2,700
Temperature (Inlet)	deg.C	370	370	350
Temperature(Outlet)	deg.C	435/470	500	500
Blanket/Reflector/Shielding		Blanket/SUS	SUS / SUS	SUS / B_4C

*) Inner/Outer Core

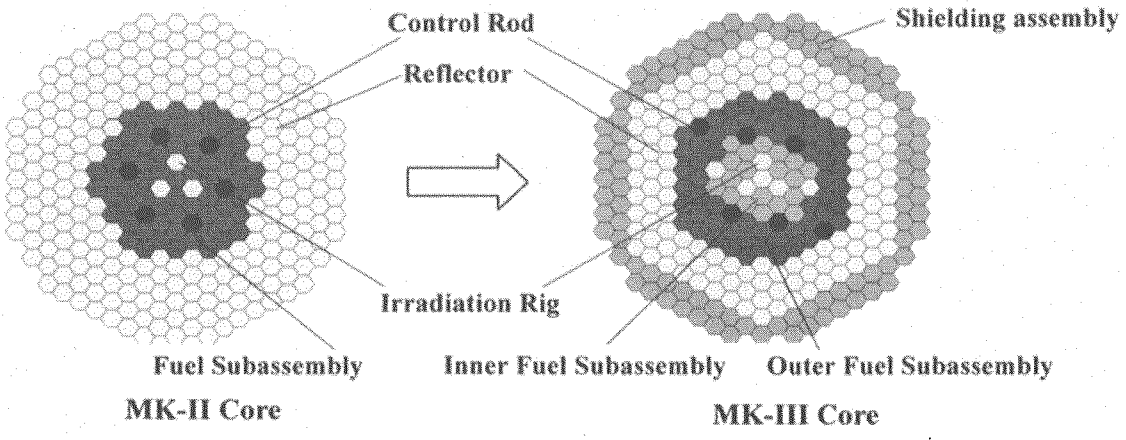

Fig. 1 JOYO Core Configuration.

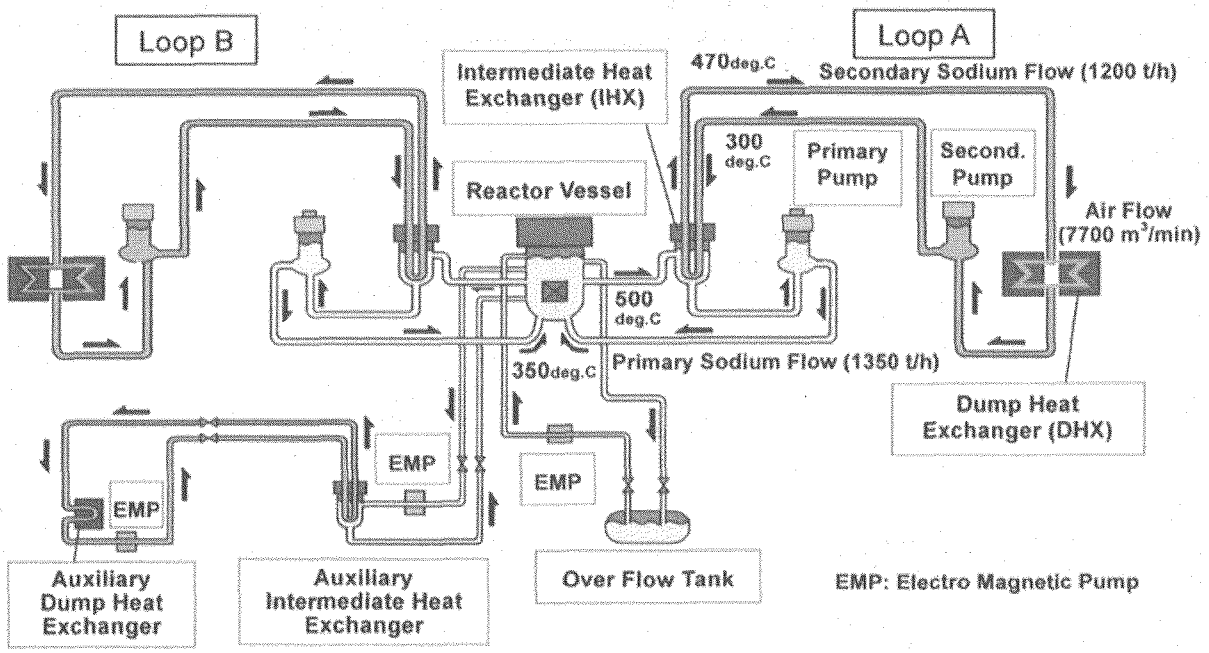

Fig. 2 JOYO Cooling System Diagram.

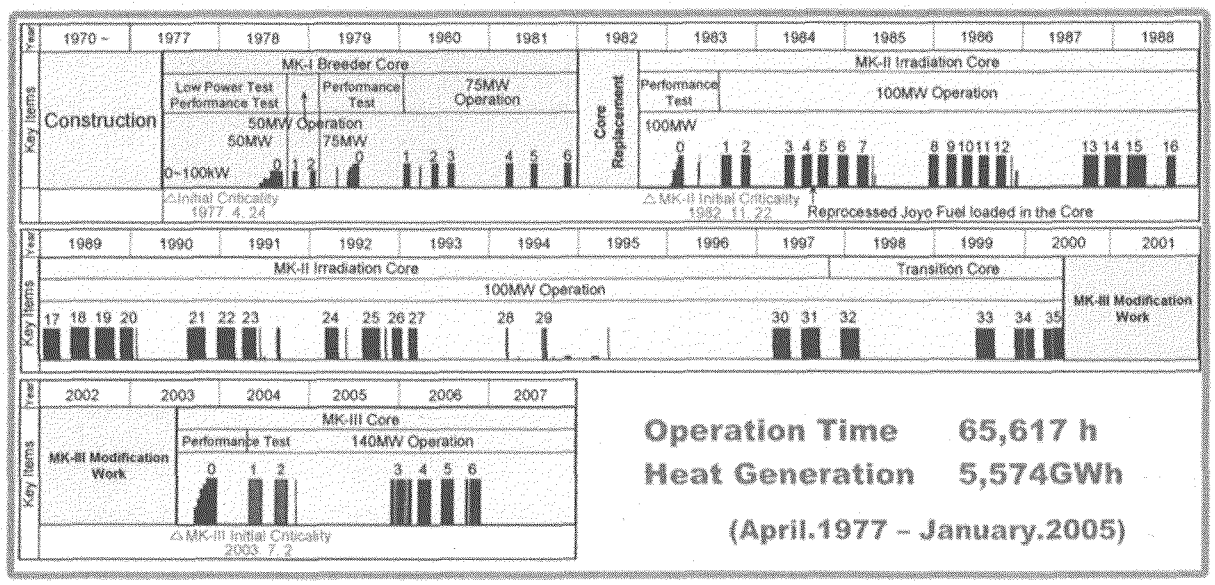

Fig. 3 Operation History of JOYO.

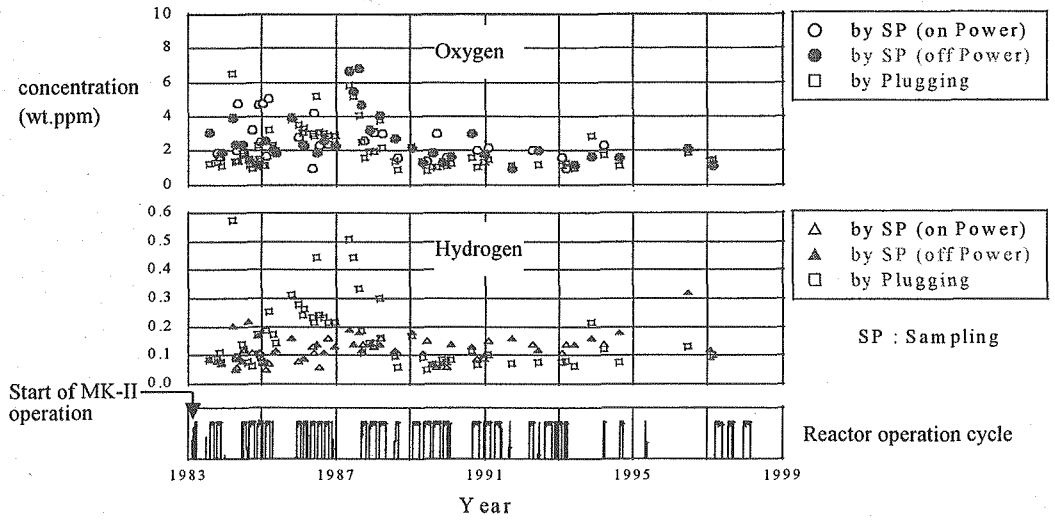

Fig. 4 Oxygen and Hydrogen Content in Primary Coolant Sodium.

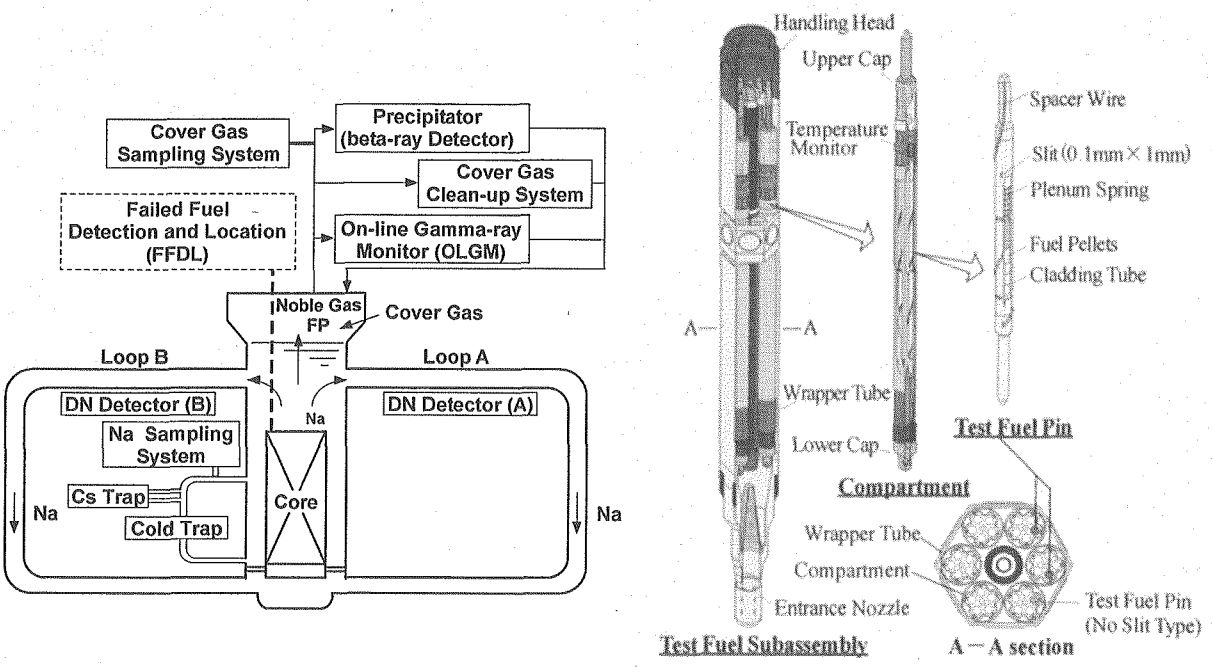

Fig. 5 Schematic Diagram of JOYO Fuel Failure Detection and Related System in Connection with the Fuel Failure Simulation Test.

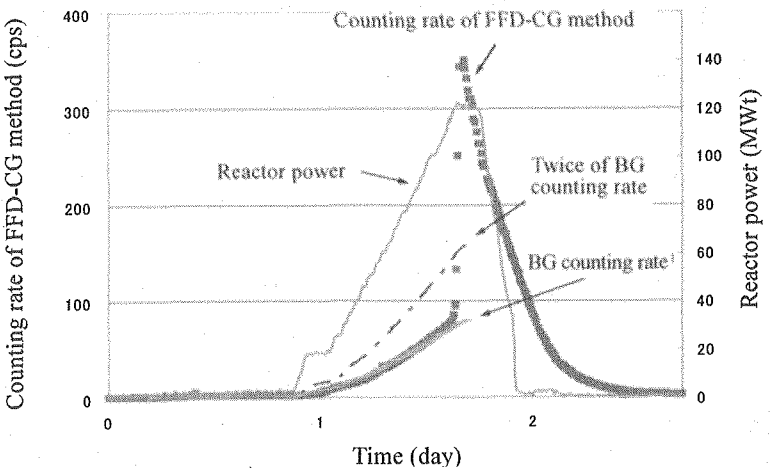

Fig. 6 Time History of reactor power and FFD-CG signal.

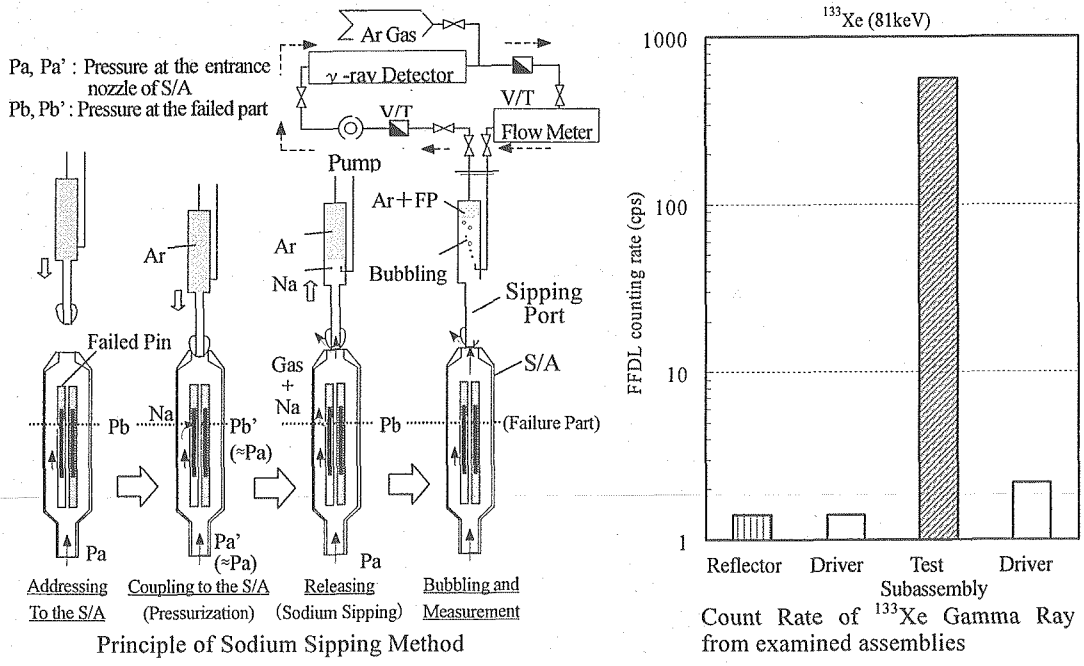

Fig. 7 Identification of failed fuel by FFDL system.

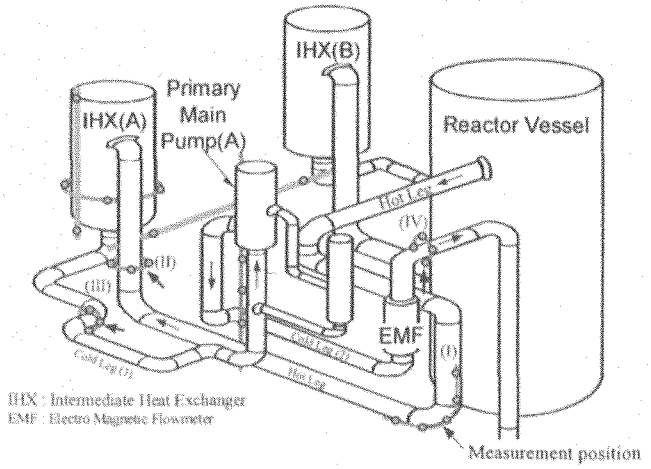

Fig. 8 Measurement Position of Radioactive Corrosion Products in Primary Cooling Loop.

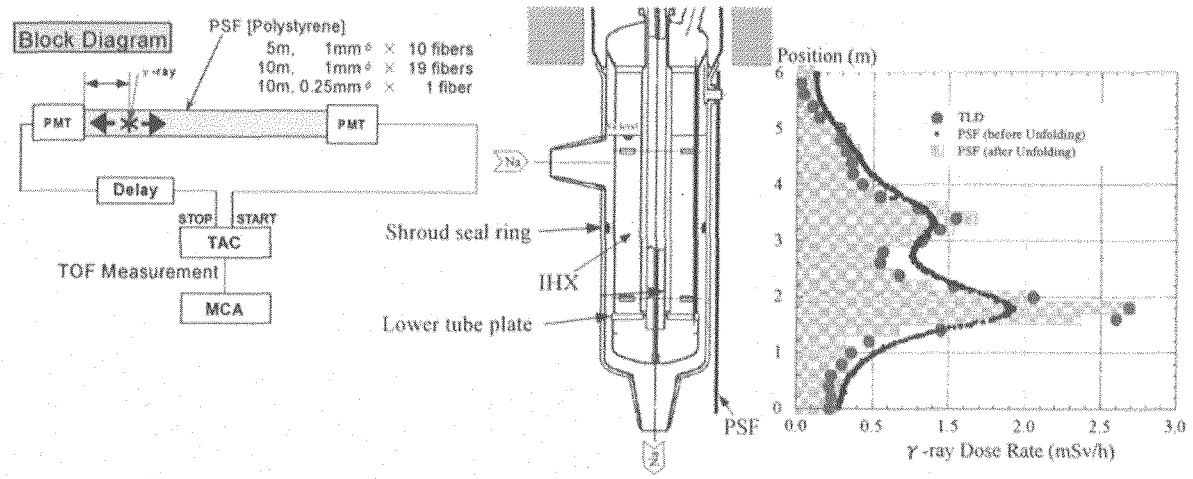

Fig. 9 Block Diagram of PSF Measurement System and Measured Gamma-Ray Dose Rate Profile of the A Loop IHX.

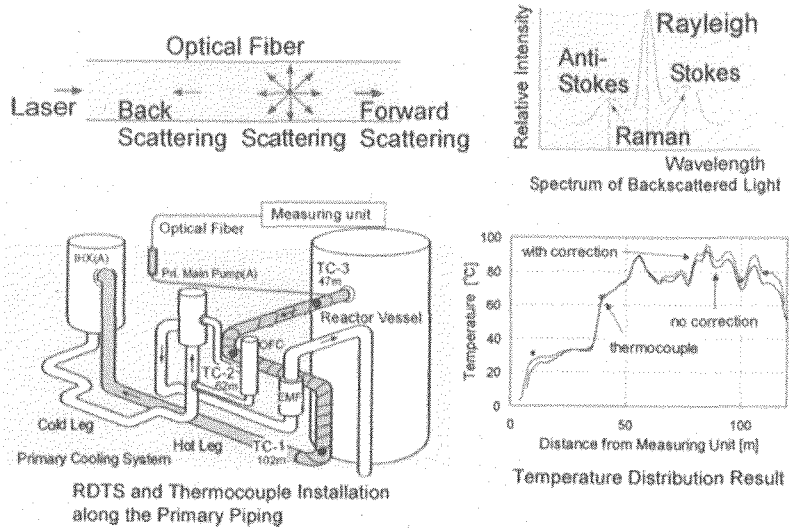

Fig. 10 Measurement of Temperature Distribution by RDTS.

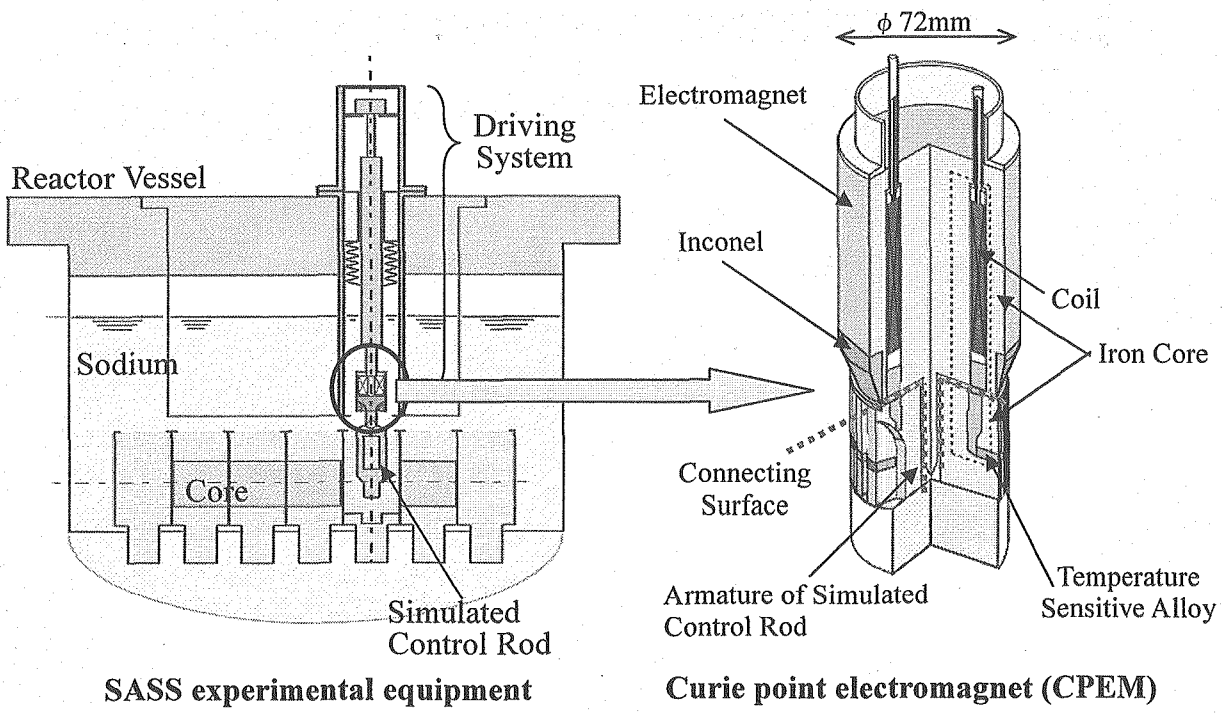

Fig. 11 Schematics of SASS Experimental Equipment.

Table 2 Utilization Plan of JOYO

JOYO Operation	JFY 2005	2010	2015
1. Fuel & Materials Tests			
(1) Development of High Burn-up Fuel using ODS Cladding			
・Material Irradiation Test (200-250 dpa)			
・Fuel Irradiation Test (250 GWd/t)			
(2) Development of Fuel Fabrication			
・Vipac/Short Process Fuel ・Metal/Nitride			
(3) Irradiation Test for Long Life Control Rod			
・Sodium Bond Type			
2. Irradiation Tests on MA and LLFP			
(1) Minor Actinide Added Fuel Irradiation Test			
(2) Long Life Fission Product Transmutation Test			
3. Test for FBR Safety			
(1) Self Actuated Shut Down System (SASS)			
(2) Fuel Transient Test			
(3) Demonstration Test for FFDL and ISI&R etc.			
(4) Demonstration Test for Anticipated Transients without Scram (ATWS)			

1.4 CURRENT STATUS OF NUCLEAR FUEL CYCLE EXAMINATION FACILITIES IN KAERI

Kwon Pyo Hong and Sung Won Park

Nuclear Fuel Cycle Examination Division
Korea Atomic Energy Research Institute
Duckjin-dong Yuseong-gu, Daejeon, Korea

ABSTRACT

The Nuclear Fuel Cycle Examination Facilities (NFCEF) in KAERI are composed of 5 nuclear facilities, which are the Irradiated Materials Examination Facility (IMEF), the Post Irradiation Examination Facility (PIEF), the Chemical Analysis Facility (CAF), the Radioactive Waste Treatment Facility (RWTF), and the Radioactive Waste Form Examination Facility (RWFEF). The main role of NFCEF is to supply the hot cell examination services or radioactive waste management services to the clients. The objects of examinations in NFCEF hot cells are nuclear fuels, nuclear materials, or radioactive wastes. A good reliability on the examination is a first current topic in NFCEF. The second subject of NFCEF is the safety insurance of the facilities. To assure the safety during operation, several programs are introduced.

KEWORDS: Nuclear Fuel Cycle, Post Irradiation Examination, PIE Facility, Nuclear Fuels

INTRODUCTION - NUCLEAR ENERGY IN KOREA

These days the importance of nuclear energy is increasing in Korea. At present 20 nuclear power plants (NPP), where 16 are PWRs, 4 are CANDUs, are under the operation in Korea. The first Korean NPP, Kori-1 started its operation in 1978, and the last NPP, Uljin-6 just started on June this year. The amount of electricity generation by nuclear energy is about 18 GW and it became to occupy about 40 % of the total electricity generation in Korea. According to the governmental plan, 8 more nuclear power reactors - all PWR types - will construct until 2015. Because Korea is a poor natural resources country, the expansion and promotion of nuclear energy is inevitable even though

anti-nuclear groups are also gradually strengthened.

One of current issue in nuclear industry field in Korea is to find a radioactive waste disposal site. On the experience of the past several failures in getting a disposal site, Korean government takes the reasonable procedure step by step. The final decision on the location of disposal site would be expected to be completed at the end of this year.

Meanwhile Nuclear energy research program in Korea is modified almost every year. Several main research projects, which are mostly focused on the development of new reactors, are setting up these days. One of them is a development of SFR (Sodium cooled Fast Reactor) among the Gen-IV reactors. KALIMER is the name of Korean SFR. The other one is a HTGR (High Temperature Gas cooled Reactor) for hydrogen production. And SMART (System-integrated Modular Advanced ReacTor), which is a small size reactor for the electricity production and the fresh water production from sea water, is also highly concentrating project.

NFCEF will play an important role on the above nuclear energy development in Korea.

According to this situation, NFCEF has set up a long term plan as **Fig. 1**.

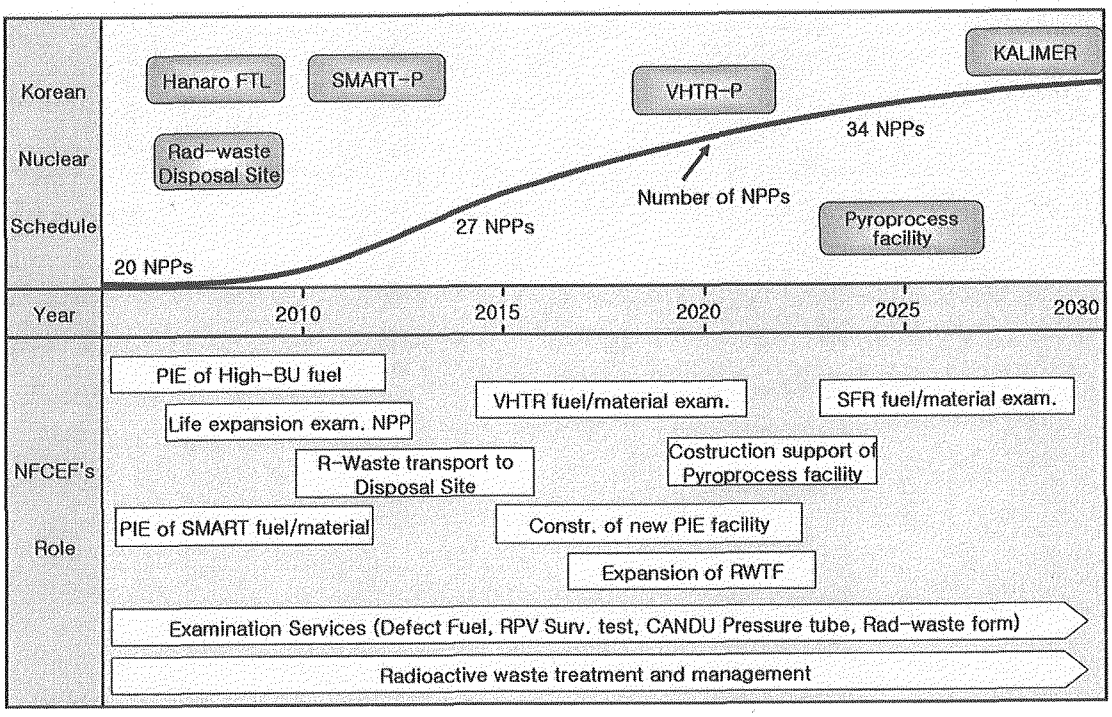

Fig. 1 Korea's nuclear plan and NFCEF's role.

CURRENT STATUS OF NFCEF

Outline of NFCEF

NFCEF hot cells have been used in PIE or integrity test of nuclear fuels, nuclear structural materials, and radioactive wastes since 1980s. The first facility, PIEF including CAF was finished its construction at the end of 1985 for the purpose of PIE of PWR irradiated fuels. The first full scale PIE object at PIEF was the spent fuel of Kori-1. RWTF was subsequently started its operation in 1990 to treat and manage the radioactive waste produced in KAERI.

Meanwhile IMEF and RWFEF were constructed in 1990s by domestic technology in order to complement some insufficient functions and strengthen the examination capabilities. So IMEF became to have additionally mechanical property examination functions, and RWFEF became to have the physical property examination functions of solidified wastes.

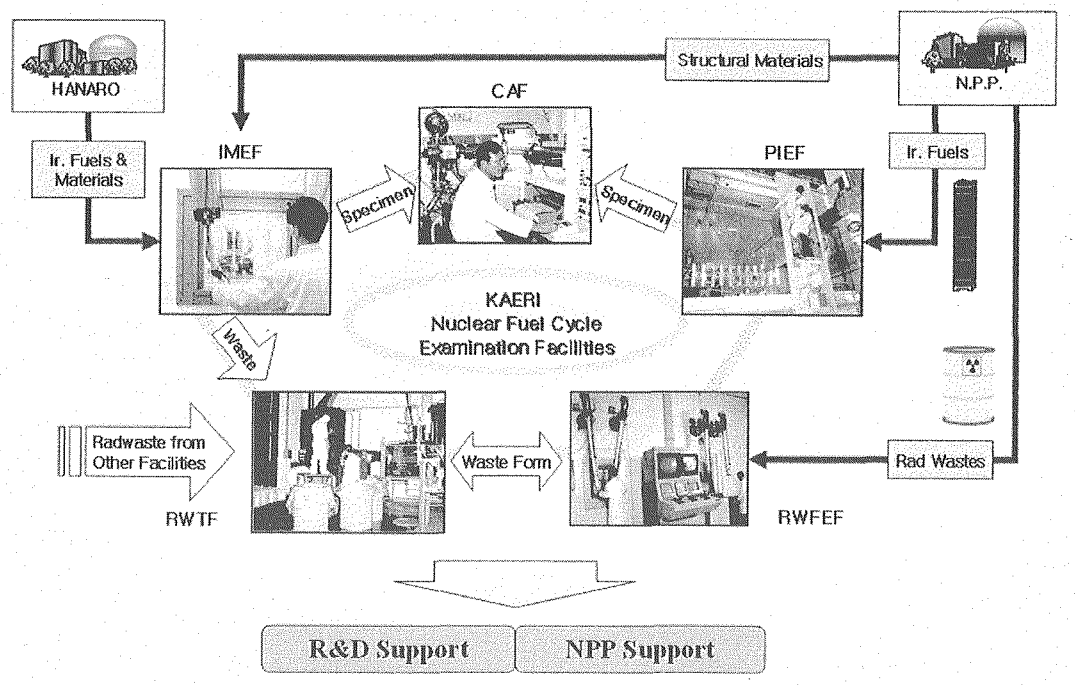

Fig. 2 Functions and organization system of NFCEF.

The number of regular staffs related in operation and maintenance of NFCEF is totally about 50. Besides these staffs, some health physics staffs and other supporting staffs are involved in NFCEF. Among the NFCEF, CAF belongs to Nuclear Chemical Research Division (NCRD). And others belong to Nuclear Fuel Cycle Examination Division (NFCED).

As shown in **Fig. 2**, from the research reactor HANARO, irradiated fuels or materials are transported to IMEF. After dismantling of irradiation assembly in HANARO pool, the irradiated fuels or materials are carried into IMEF hot cell by using of truck and crane. The maximum size of irradiated materials to be received in IMEF is limited to 1.5 m in length.

From a nuclear power plant, irradiated fuels, materials or radioactive wastes are transported into PIEF, IMEF or RWFEF respectively. For the transportation of irradiated fuels from NPP the KSC-1 transportation cask is used, which has the capacity of 1 PWR assembly.

In order to undergo chemical analysis, usually small specimens are transported from IMEF or PIEF into CAF. In that case the Padirac cask and its own adaptor are commonly used.

RWTF is a radioactive waste treatment facility. This facility is actually composed of 3 independent facilities, which are "General Treatment Facility(GTF)", "Solar Evaporation Facility(SEF)", and "Interim Storage Facility(ISF)". The functions of these sub-facilities are as follows.

A brief description of NFCEF is as **Table 1**.

Table 1 Specifications and Functions of NFCEF

Facility Name	Specifications	Function
IMEF (Irradiated Materials Examination Facility)	• Built in 1993 • 8 Hotcells and 1 Pool • 26 Working Stages	• Exam. of NPP Structural Materials • Exam. of Fuels and Materials Irradiated at HANARO
PIEF (Post Irradiated Examination Facility)	• Built in 1985 • 6 Hotcells and 3 Pools	• Exam. of NPP Irradiated Fuels • Performance Test of Hi-Burnup Fuel
CAF (Chemical Analysis Facility)	• Lab.-I (Inactive Lab.) - XPS, Mass Spec, etc. • Lab.-II (Active Lab.) - ICP, etc.	• Chemcal Analysis of Active Specimen • Develop. of Analysis Techniques
RWTF (Radioactive Waste Treatment Facility)	• Built in 1990 • Waste Treatment Facility • Low Level and Medium Level Solid Waste Storage • Solar Evaporation Facility	• Waste Treatment Processing - Liquid Waste Treatment - Solid Waste Treatment - Equipment Decontamination • Interim Storage of Radioactive Waste
RWFEF (Radioactive Waste Form Examination Facility)	• Built in 1992 • 1 Large Hotcell • Physical Property Exam. Eq.	• Evaluation of Integrity and Safety of Radwaste Form

Current Activities and Future Prospects of NFCEF

(1) Examination Services of Fuel, Materials, and Wastes

The main job of NFCEF is to supply the examination services to clients. The clients are KAERI's research groups, universities, or any other organizations related in nuclear industry. Some of recent examination services are as follows.

1) PIE of NPP Fuels and Development Fuels

Recently some high burn-up NPP fuels - Uljin NPP and Younggwang NPP - have been examined in PIEF. The recorded burn-up is sometimes up to more than 50 GWD/tU. The PIE results are reported to the client, KNFC(Korea Nuclear Fuel Fabrication Company) for fuel design feed back. Some examination results are as shown in **Fig. 3**.

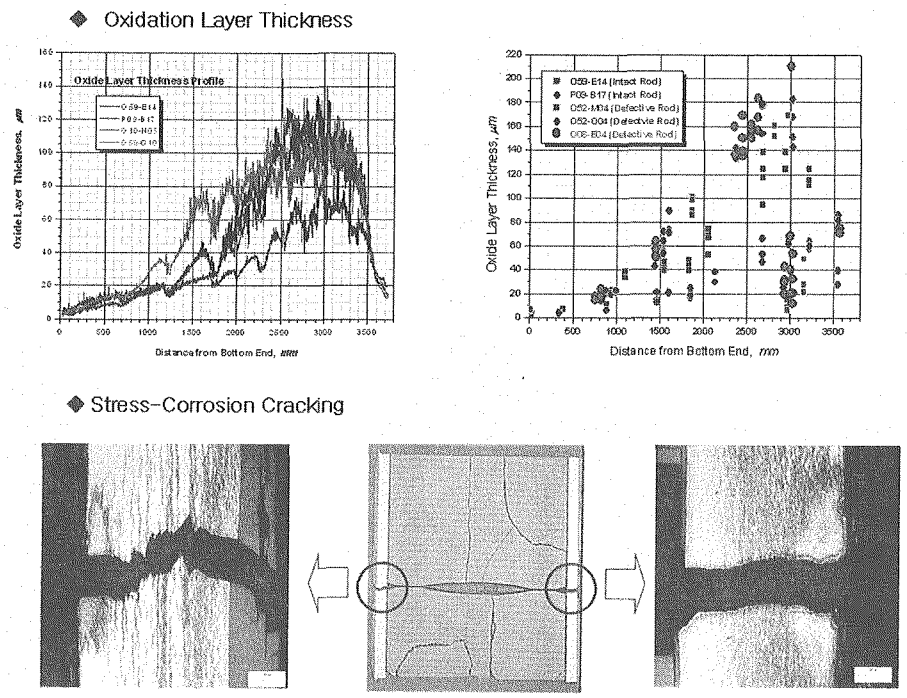

Fig. 3 PIE of high burn-up NPP fuel.

Mean while, several development fuels were examined in IMEF. Most of development fuels are irradiated in HANARO research reactor. A representative development fuel is SMART fuel. The SMART means the System-integrated Modular Advanced Reactor, which is a 330 MWth thermal reactor. As a precedent step SMART-P reactor which has 65 MWt power is under the development in KAERI. This pilot scale research reactor will be constructed until 2010. SMART fuel examination has been

executed since September in 2001.

Besides, there are several research fuels are examined in NFCEF hot cells, such as HANARO driving fuel, DUPIC fuel and so on.

2) Hot cell Examination of Structural Materials

Kori unit-1, the first NPP in Korea, was started its operation in 1978. Its design life time is 30 years. As the one of activities to extend its lifetime, a hot cell examination of the reactor vessel material is doing in IMEF.

Surveillance test is the one of steady job in IMEF. Two or three times of surveillance test is done in IMEF annually. Totally 29 times of surveillance tests have been done in IMEF since 1995.

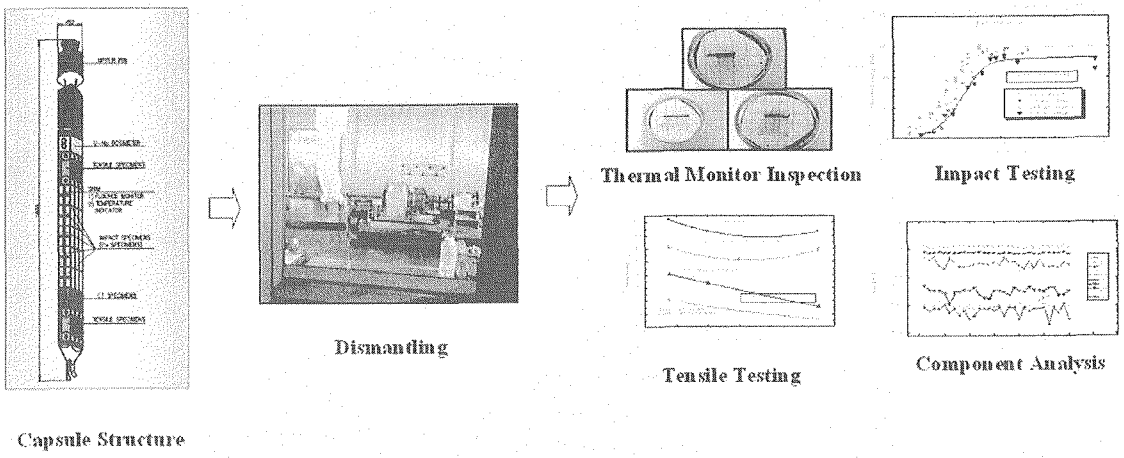

Fig. 4 Surveillance Test on PWR RPV.

3) Chemical Analysis

CAF is also busy in chemical analysis. The amount of chemical analysis services is about 6,000 times annually. The clients of chemical analysis are mostly KAERI researchers and the most frequent analysis service is the component analysis by ICP-AES/AA/IC/CHONS.

4) Radioactive Waste Form Examination

In RWFEF the physical and chemical characterization of radioactive waste form is executed as shown in **Fig. 5**. Recently the examination on the 44 waste drums from the NPPs has been finished in order to survey the characteristics of NPP's radioactive waste. This project was supported by KHNP (Korea Hydro Nuclear Power company).

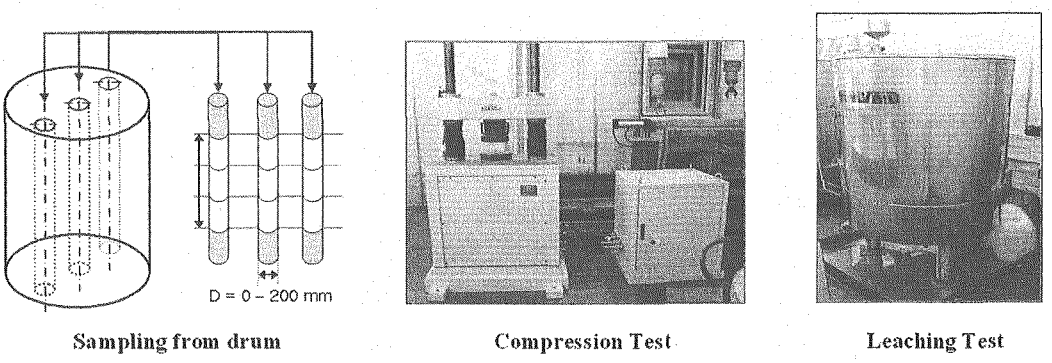

Fig. 5 Physical property test of radioactive waste form drum of NPP.

(2) Treatment and Management of Radioactive Waste

The main function of RWTF is the treatment of liquid waste and solid waste produced in KAERI. Liquid waste is solidified or solar-evaporated as **Fig. 7**. The annual amount of radioactive waste to be treated or to be stored is about 180 ton for liquid waste, and about 320 drums for solid waste. The total amount of storing solid waste is about 10,000 drums.

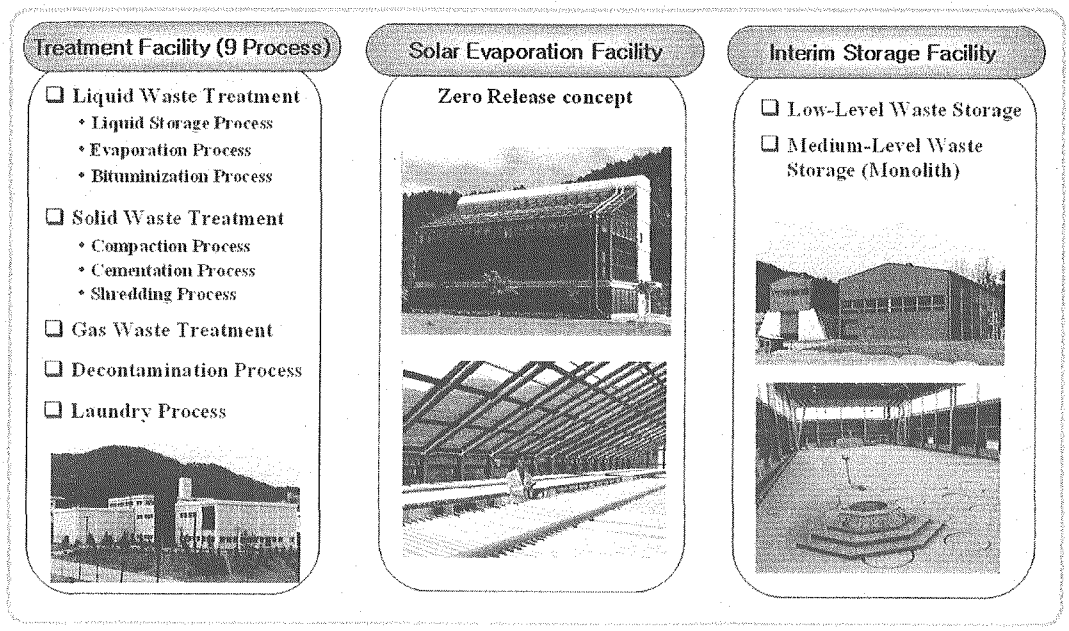

Fig. 6 Composition of Radioactive Treatment Facility.

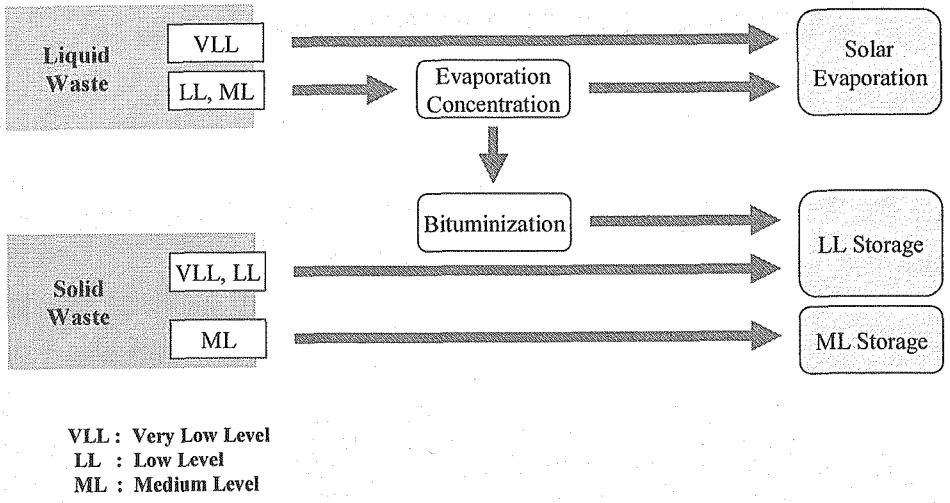

Fig. 7 Radioactive waste treatment process.

(3) Safety of NFCEF

The most important and most basic requirement in the operation and management of NFCEF is safety. To accomplish the safety requirement there are various activities in NFCEF. Some of these activities are as follows.

1) Nuclear Safety Mark Acquisition

Few years ago Korean government introduced nuclear safety mark system to decrease the nuclear accident and expand the safety culture. Periodically the Government awards this honorable mark to an excellent organization or techniques or products which is remarkably contributed in nuclear safety improvement.

NFCEF has been awarded the 9-th Korea Nuclear Safety Mark in January 2004. (2-nd prize in KAERI). The contributions on PIE services of NPP's fuels and materials and the long time safe operation history of NFCEF are considered.

2) The Safety Inspection Day Event

The first Tuesday of every month is designated as "the Safety Inspection Day" in Korea. On the day some special events take place as followings.

- Self inspection on the vulnerable point in safety,
- Safety instruction and encouragement to the staffs,
- Training and exercise against the accident.

This event is also originated from Korean government to expand the safety culture to the engaging persons in nuclear field.

1.5 CURRENT ACTIVITIES IN DEVELOPMENT OF PIE TECHNIQUES IN JMTR HOT LABORATORY

Toshimitsu Ishii [1], Masao Ohmi [2] and Michio Shimizu [2]

1: Irradiation Technology Section, Technology Development Department
2: JMTR Hot Laboratory Section, Department of JMTR
Oarai Research and Development Center, Japan Atomic Energy Agency
4002 Narita-cho, Oarai-machi, Higashi-Ibaraki-gun, Ibaraki-ken, 311-1393 Japan

Yoshiyuki Kaji [3] and Fumiyoshi Ueno [4]

3: Research Group for Corrosion Damage Mechanism, Nuclear Science and Engineering Directorate
4: Corrosion Resistant Materials Development Group, Nuclear Science and Energy Directorate
Japan Atomic Energy Agency
2-4 Shirakata Shirane, Tokai-mura, Naka-gun, Ibaraki-ken, 319-1195 Japan

ABSTRACT

A wide variety of post-irradiation examinations (PIEs) for research and development of nuclear fuels and materials to be utilized in nuclear field has been carried out since 1971 in three kinds of $\beta-\gamma$ hot cells; concrete, lead and steel cells in the JMTR Hot Laboratory (JMTR HL) associated with the Japan Materials Testing Reactor (JMTR). In addition to PIEs, the re-capsuling work including re-instrumentation was also conducted for the power ramping tests of the irradiated LWR fuels using Boiling Water Capsule (BOCA). Recently, new PIE techniques are required for the advanced irradiation studies.

In this paper, the irradiation assisted stress corrosion cracking (IASCC) growth test technique of irradiated in-core structural materials and the remote operation technique of the atomic force microscope (AFM) are described as JMTR HL's current activities in the development of new PIE techniques.

KEYWORDS: JMTR Hot Laboratory, Post-irradiation examination, IASCC, Crack growth test, AFM

INTRODUCTION

The Japan Materials Testing Reactor (JMTR) has been utilized for irradiation tests of nuclear fuels and structural materials, and for the radioisotope production since 1970[1]. The JMTR Hot Laboratory (JMTR HL) associated with JMTR was also put into service in 1971 to perform post-irradiation examinations (PIEs) of nuclear fuels for the light water reactor (LWR) and structural materials for LWR and a fusion reactor after the irradiation test in JMTR[1]. In recent several years, main PIE works of JMTR HL are for the safety research on the aged LWR and for the development of both high temperature gas cooled reactor and fusion reactor[2].

In this paper, the facilities of JMTR HL are described. Furthermore, JMTR HL's activities in the development of an irradiation assisted stress corrosion cracking (IASCC) growth test machine and a remote-controlled atomic force microscope (AFM) apparatus are also presented.

FACILITIES OF JMTR HL

A plane view of JMTR HL is shown in **Fig.1**. JMTR HL is located adjacent to JMTR. There are eight concrete cells, four microscope lead cells, seven lead cells and five steel cells for PIEs of irradiated fuels and materials in JMTR HL. These are $\beta - \gamma$ type hot cells. Six globe-boxes for handling tritium-containing materials can be used for the study on the fusion blanket. Since the No.1 concrete cell in JMTR HL is connected with the reactor by a canal pool, irradiated capsules including several kinds of specimens are easily transferred from JMTR to the No.1 concrete cell through the canal pool. Irradiated capsules are dismantled in the No.2 concrete cell to pull irradiated specimens out from them. PIEs that are tensile test, Charpy impact test, miniaturized specimen test, slow strain rate test, stress corrosion cracking test, fatigue test, fracture toughness test and creep test are mainly carried out in the lead and steel cells after the irradiated specimens are transferred from the No.2 concrete cell to both lead and steel cells. Furthermore, a scanning electron microscope (SEM) is installed in the lead cell to observe the fracture surface of the tested specimens.

CURRENT ACTIVITIES IN DEVELOPMENT OF PIE TECHNIQUES

Development of IASCC growth test technique of irradiated in-core structural materials

In 2000, Ministry of Economy, Trade and Industry (METI) has begun the project for IASCC technology development as a part of the more comprehensive program for technological development of countermeasures for aged of LWRs[3]. In the project for IASCC technological development, the basic essential data were planned to be prepared for

the maintenance standard and safety evaluation of core internals under a promotion of the Japan Nuclear Energy Safety Organization (JNES). Japan Atomic Energy Agency (JAEA) is engaged in the boiling water reactor (BWR) related testing and research program, which includes the neutron irradiation at JMTR and PIEs shared by industry and governmental organizations. In a part of the METI project aiming at IASCC of BWR, the objective is to evaluate IASCC initiation and propagation data necessary for making IASCC database satisfactory to contribute for preparing the maintenance standard against IASCC, which will be used for the assessment of timing and intervals of the inspections of core internals. In the IASCC project for BWR, core internal materials used for BWR, i.e. types 304, 304L and 316 stainless steels will be examined at hot laboratories after irradiation at JMTR up to four levels of neutron fluence of $5x10^{24}$, $1x10^{25}$, $3x10^{25}$ and $1x10^{26}$ n/m^2 (E>1 MeV) to assess dependency of IASCC behavior on the neutron fluence. Experimental data to be obtained through the PIEs are the crack propagation rate data, IASCC susceptibility data form slow strain rate testing (SSRT) in high temperature water, etc. The IASCC national project will be completed in FY2008.

In March 2004, a new IASCC test machine having two autoclaves for producing the test condition of high temperature water was installed in the No.6 concrete cell. Crack growth tests and SSRTs on irradiated steels, by using different test jigs, have been conducted in the machine. A photograph of the test machine installed in the hot cell is shown in **Fig. 2**. The maximum operational parameters for crack growth tests and SSRTs in a simulated BWR environment are as follows; load capacity: 10 kN, temperature: 573 K, pressure: 10 MPa, and flow rate: 30 little per hour. The 0.5T-CT type test specimens with 12.7, 6.4 or 5.6 mm in thickness can be applied to the IASCC growth test by this machine.

A schematic drawing of the circulating system of the high-temperature and high-purity test water is shown in **Fig.3**. The test water is circulated in the system by a main pump and a booster pump. The pressure in the system can be controlled by a pressure control valve. The temperature of the test water is controlled by band heaters set around the autoclave and pre-heaters set in the system. This machine also has heat exchangers to control the temperature of the test water economically. The dissolved oxygen concentration can be controlled within the range of 10ppb – 32ppm to simulate the BWR environment in the circulating system. Furthermore, the electrochemical potential (ECP) of the specimen is measured by using an external Ag/AgCl/0.1 M KCl reference electrode.

The crack growth length is measured by means of the DC potential drop method during the test. After the test, crack length is calibrated by optical observation of the fracture surface of the CT specimen.

Development of remote operation technique of AFM

A microscopic examination in the hot cell is a very important PIE item to investigate the mechanism of mechanical property change and to analyze the behavior of degradation in the nuclear fuels and structural materials after neutron irradiation tests. An optical

microscope, a shield type electron probe microanalyzer (EPMA) and a SEM that were modified as remote-controlled apparatuses have been already installed in JMTR HL for PIEs of irradiated specimens.

In 2004, the remote-controlled AFM apparatus was developed to perform nano-scopic examinations of irradiated specimens in the hot cell as a new examination technique. It was developed with former Research Group for Reactor Structural Materials of Tokai Establishment under the JAERI (Japan Atomic Energy Research Institute) – JNC (Japan Nuclear Cycle Development Institute) joint research program from 2003 to 2005[4, 5], which titled: A study on degradation of structural materials used under the irradiation environment in nuclear reactors. The purpose of this study is to develop the method for the damage evaluation and detection in earlier stage of progression process of the irradiation damage along the grain boundary. The observation of the electro-chemical corrosion behavior along the grain boundary of irradiated specimens by means of AFM that can observe the three-dimensional surface configuration in nano-scale is one of the effective PIE methods to evaluate the irradiation damage along the grain boundary[6].

A schematic drawing of the AFM apparatus is shown in **Fig.4**. The irradiated specimen is mounted in the acrylic tube and observed its surface. Scanning area of the AFM apparatus is from 500 x 500 nm^2 to 800 x 800 μm^2. The vertical resolution is 0.3nm in minimum. A detector that is about 6.5 x 4.5 x 1 mm^3 is called cantilever. Optical microscope is also equipped in the apparatus, the area of 500 x 400 μm^2 can be observed. A general procedure for setting the mounted specimen is as follows. The electro-chemical corrosion test of the mounted specimen is performed in the hot cell. The mounted specimen is put on the specimen stage of the AFM apparatus. It is observed by the optical microscope to find a location for the AFM scanning area. Finally, that location is scanned by the AFM.

The remote-controlled AFM apparatus was installed in the No.6 lead cell of JMTR HL as shown in **Fig.5**. The cantilever, which is the sensor tip of AFM, is too small to handle by the manipulator. Therefore, the development of a cantilever exchange system was essential to modify AFM to completely remote-controlled type. The exchange system has a cantilever handling arm and a cartridge stage. A new cantilever is put on a cartridge by manual and kept into the new cantilever storage box made of acrylic at outside of the cell. The box having ten cartridges with a new cantilever is carried into the hot cell before AFM observation. The cartridge having a new cantilever is put on the cartridge stage from the storage box by the manipulator. A cantilever handling arm approaches to the cantilever on the cartridge remotely. The arm removes the cantilever from the cartridge, and mounts the cantilever on the AFM head unit.

The AFM observation result of the high-purity type 304 model stainless steel[7] irradiated up to 1 dpa in JRR-3 is shown in **Fig.6**. A clear three-dimensional image of grains can be obtained by the remote-controlled AFM.

SUMMARY

For recent years, several kinds of PIE techniques have been developed to carry out IASCC growth tests of BWR's core internal materials and the AFM observation of irradiated specimens.

In March 2004, the new IASCC growth test machine having two autoclaves for producing the test condition of high-temperature and high-purity water was installed in the No.6 concrete cell in order to evaluate the IASCC growth rate under the BWR environmental conditions. IASCC growth tests of four irradiated CT specimens have already been finished until August 2005.

In 2005, AFM observation data on un-irradiated and irradiated specimens after the creep test have been obtained by using the remote-controlled AFM apparatus installed in the No.6 lead cell. In a future work of JMTR HL, this apparatus will be useful for nano-level evaluation of irradiation damages in structural materials used in nuclear power plants.

ACKNOWLEDGEMENTS

Authors would like to thank the colleagues in JMTR HL for their technical support in the development of these PIE techniques. They would also like to thank Dr. Tsukada and Dr. Nemoto of JAEA for their helpful advice on the development of the PIE techniques. Authors would like to acknowledge technical advice on the IASCC growth test technique from JNES and IRI (Institute of Research and Innovation).

REFERENCES

(1) Department of JMTR, "Annual Report of JMTR FY1997 [April 1, 1997-March 31, 1998]", JAERI-Review 99-005, (1999)

(2) Department of JMTR, "Annual Report of JMTR FY2002 [April 1, 2002-March 31, 2003]", JAERI-Review 2003-041, (2003), in Japanese

(3) Editorial Committee on Nuclear Safety Research Results, "Progress of nuclear safety research -2003", JAERI-Review 2004-010, (2004)

(4) T. Hoshiya, F. Ueno, et al., "JNC-JAERI United Research Report, A study on degradation of structural materials under irradiation environment in nuclear reactors", JNC TY9400 2004-026 & JAERI-Research 2004-016, (2004), in Japanese

(5) F. Ueno, Y. Nagae, et al., "JAERI-JNC United Research Report, A study on degradation of structural materials under irradiation environment in nuclear reactors", JAERI-Research 2005-023 & JNC TY9400 2005-013, , (2005), in Japanese

(6) Y. Nemoto, Y. Miwa, et al., "AFM evaluation of grain boundary corrosion behavior on ion irradiation stainless steel", Int. Symp. on Materials Chemistry in Nuclear Environment (Material Chemistry '02), March 13-15, 2002, Tsukuba, (JAERI-Conf 2003-001), pp.397-404
(7) T. Tsukada, et al., J. Nuclear Mater. 258-263 (1998) 1669.

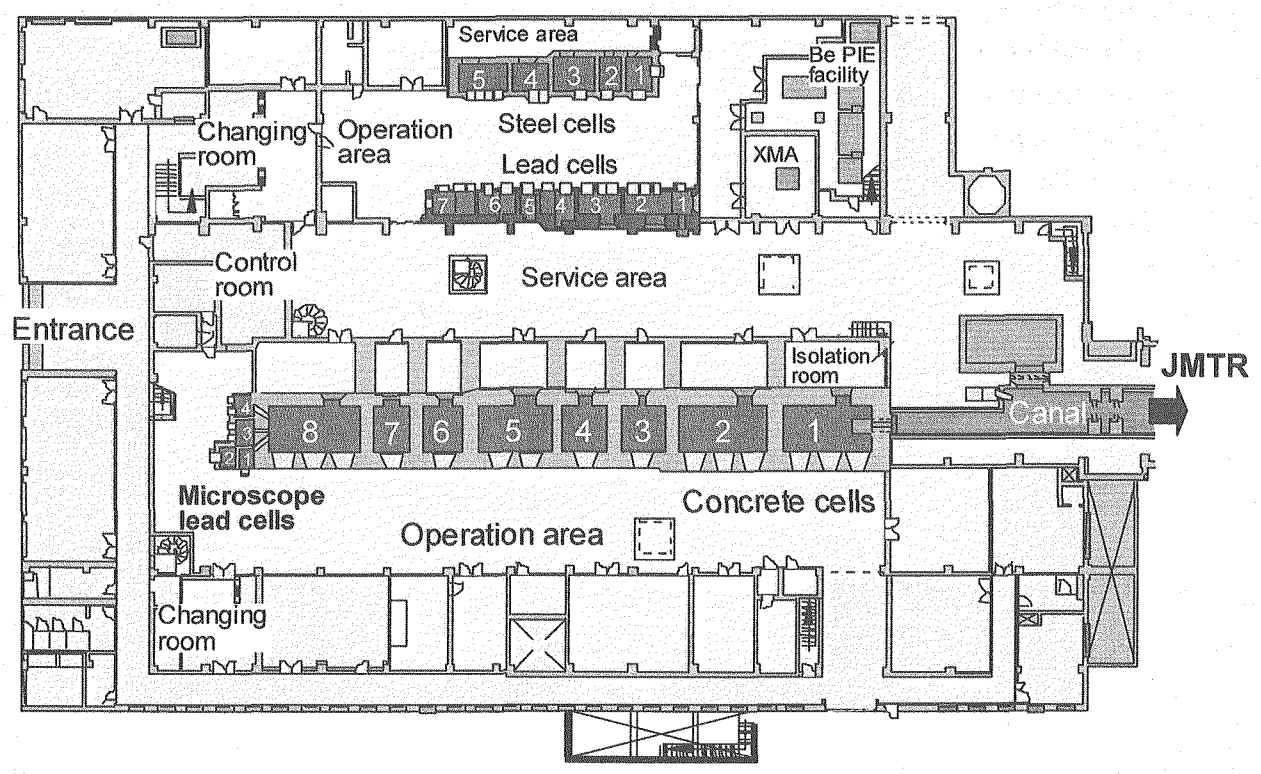

Fig.1 Plane view of JMTR hot laboratory.

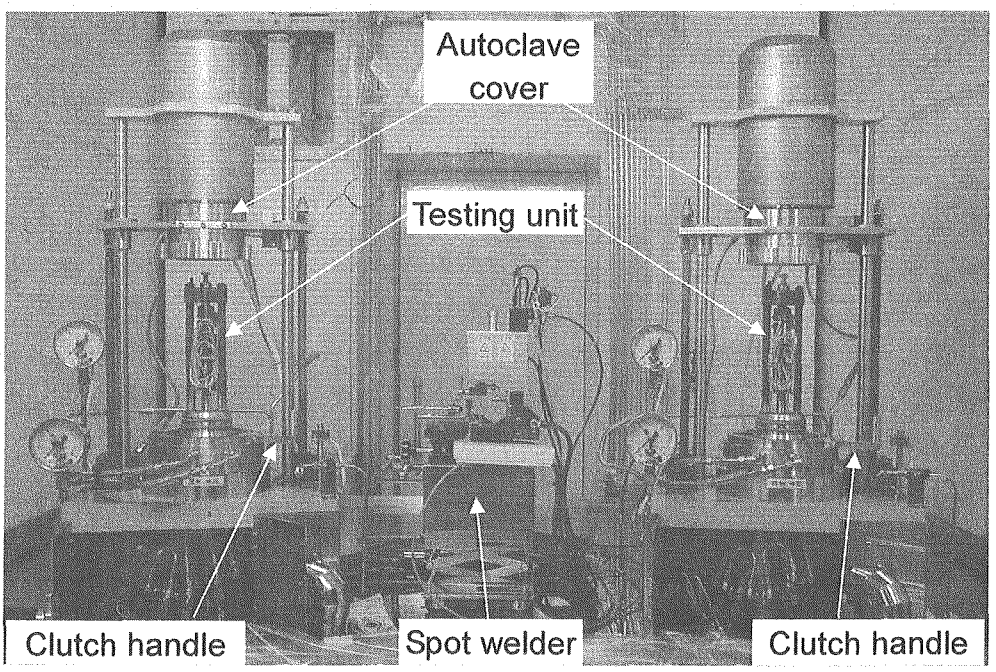

Fig.2 Photograph of IASCC growth test machine installed in hot cell.

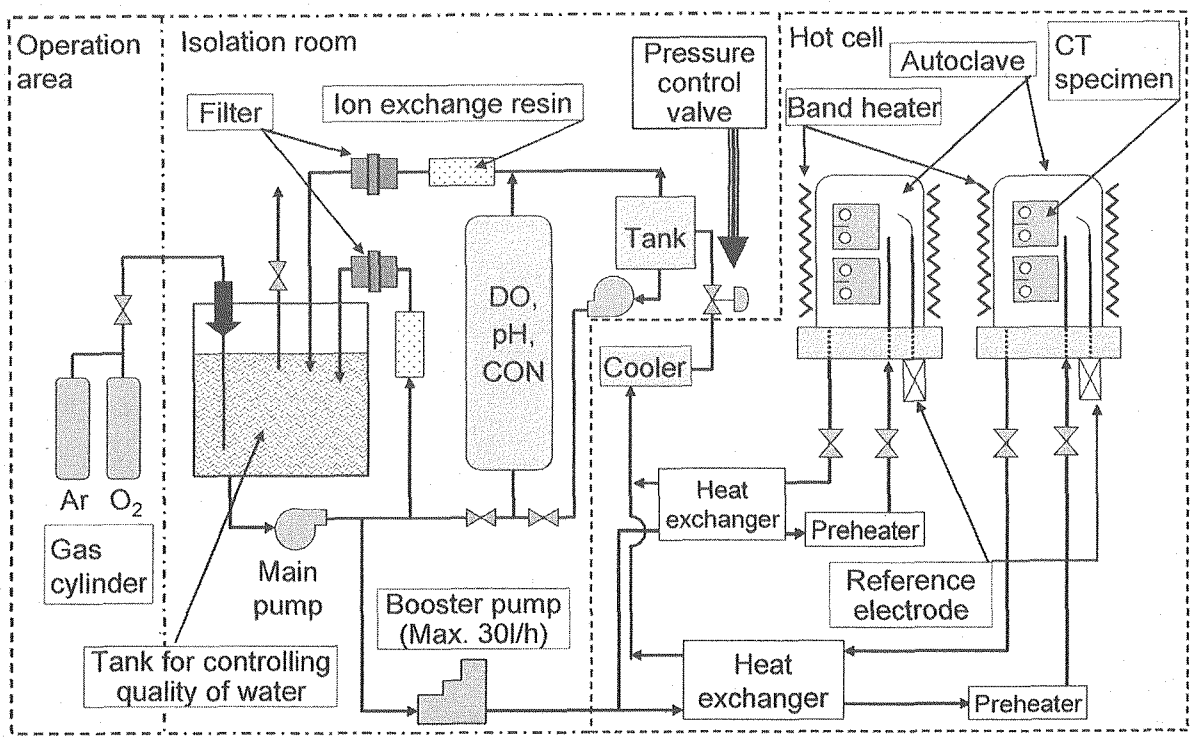

Fig.3 Schematic drawing of circulating system of high-temperature and high-purity water.

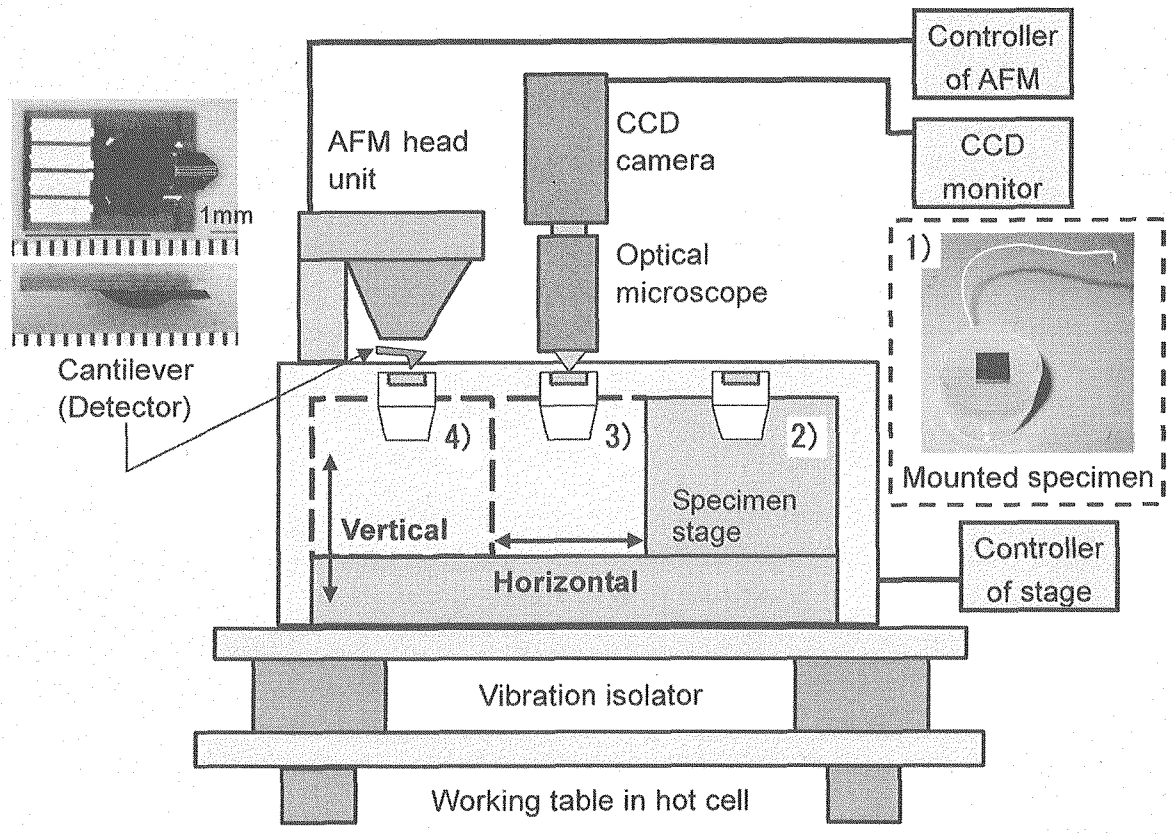

Fig.4 Schematic drawing of remote-controlled AFM.

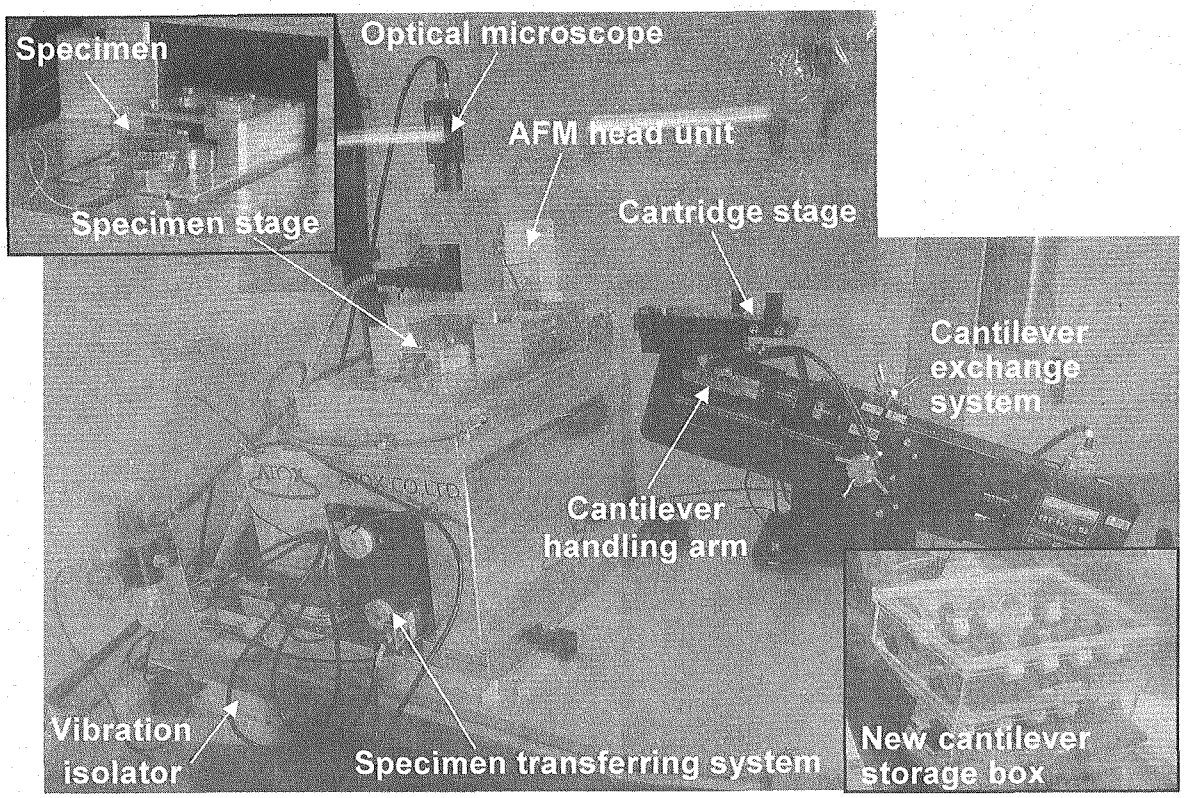

Fig.5 Photograph of remote-controlled AFM installed in hot cell.

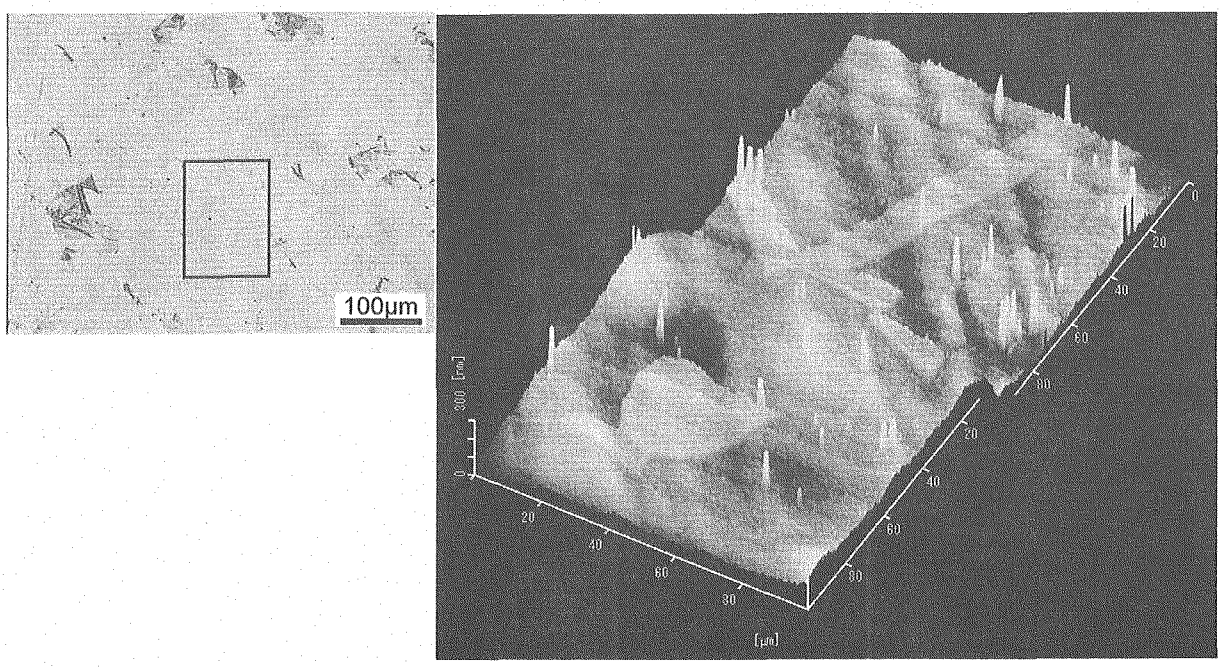

Fig.6 AFM observation result of model alloy irradiated up to 1 dpa in JRR-3.

JP0650417

1.6 PIE ACTIVITIES IN NFD HOT LABORATORY

Mitsuhiro Kodama, Mutsumi Hirai and Noriyuki Sakaguchi

Nippon Nuclear Fuel Development Co., Ltd.
2163 Narita-cho, Oarai-machi, Higashi-Ibaraki-gun, Ibaraki-ken, 311-1313 Japan

ABSTRACT

Nippon Nuclear Fuel Development Co., Ltd. (NFD) has been operating hot laboratory facility since 1977 for post-irradiation examinations (PIE) of boiling water reactor (BWR) fuels and structural materials. Various examination techniques have been developed to meet the research requirements. The BWR fuel design, which has been revised for step-by-step burnup extension, has been verified at each step through comprehensive PIEs. A large number of fuels and materials have been examined in various research and development programs. High burnup fuel pellets were extensively examined in terms of fission gas behavior and microstructural evolution. Mechanical properties of fuel cladding under increased fuel burnup were studied from a viewpoint of the hydrogen concentration. Reactor core structural materials have also been studied for plant life management and development of remedies.

KEYWORDS: BWR Fuel, High Burnup, Fission Gas Release, Rim Structure, Cladding, Mechanical Properties, Hydrogen Concentration, Structural Material, IASCC, Crack Growth Rate

INTRODUCTION

Nippon Nuclear Fuel Development Co., Ltd. (NFD), a joint venture of Hitachi LTD. and Toshiba Corp., has been operating hot laboratory facility since 1977 for extensive post-irradiation examinations (PIE) of boiling water reactor (BWR) fuels and structural materials. NFD hot laboratory has capability to accommodate full size commercial BWR fuel bundles. Comprehensive PIE programs have been carried out on many BWR fuel bundles [1-5] including failed fuel bundles [6] and MOX fuel bundles [7], as well as test fuel and material specimens irradiated in test reactors.

To meet the demands for detailed mechanistic understanding of fuel performance and material degradation, more precise microscopic and specific PIE techniques are required. Various examination techniques have been developed during the course of the PIE programs to meet the research requirements. This paper presents the overview of recent PIE activities in NFD hot laboratory.

OUTLINE OF THE NFD HOT LABORATRY

NFD hot laboratory consists of a storage pool, an inspection pool, six concrete cells, six steel shielded cells, two waste storage cells, and an isolation area. It has a capability to accommodate full size commercial BWR fuel bundles.

Standard PIE procedures include non-destructive examinations followed by destructive ones. A window is installed in the side wall of the inspection pool so that the fuel bundles can be observed directly. Non-destructive examinations on fuel bundle and fuel rods can be performed in the inspection pool and the monitoring cell. Concrete cells, shielded by heavy concrete, are used for destructive examinations such as metallography using optical microscope and scanning electron microscope (SEM). Steel shielded cells annexed to the concrete cells are used for the tests on relatively small specimens, such as mechanical and stress corrosion cracking testing.

Various kinds of microscopic equipment, including transmission electron microscope (TEM), field emission electron gun equipped TEM (FEG-TEM), FEG-SEM, electron probe micro-analyzer (EPMA), X-ray diffractometer (XRD), X-ray fluorescence spectrometer (XRF), and focused ion beam (FIB) are installed in precise measurement labs.

OVERVIEW OF PIE ACTIVITIES

PIEs on fuel pellets and FP behavior

There are many factors affecting the fission gas release (FGR) in oxide fuels at

normal, transient and accident conditions, out of which irradiation-induced microstructure change or rim structure formation has been recognized in the last 15 years as resulting from high burnup.

FGR rate of irradiated fuel rods can be measured by both destructive (puncture test) and non-destructive methods. The latter utilizes the measurement of ^{85}Kr gamma activity at the rod plenum. Some FGR data[8] are shown in **Fig. 1**. Fuel rod axial distribution of fission products (FPs) is measured by gamma scanning in a hot cell. Radial distributions in a fuel pellet cross section are examined with EPMA. A large amount of data has been accumulated in the fuel performance database to support development of a fuel performance analysis code which employs mechanistic models of FP gas behavior.

FGR behavior at rapid heating conditions of high burnup UO_2 fuels with developed rim structure has been examined using two different out-of-pile heating techniques with no restraint pressure[9]. A small specimen of irradiated fuel pellet was heated in the high temperature furnace and the released ^{85}Kr was measured by gamma activity. **Fig. 2** shows FGR results for the 60 and 86 GWd/t fuels at a heating rate of 90 °C/s. This rate roughly corresponds to that of power transient events in a BWR. A significant difference was found between the two fuels. The FGR process strongly depended on fuel burnup (extent of rim structure formation) and heating conditions (heating rate, terminal temperature). At higher heating rates above at least 90 °C/s, instantaneous FGRs, which originated from the occurrence of microcracks and fuel fragmentation induced by the overpressurization of rim bubbles, arose at higher temperatures above 700 °C, only for the high burnup fuels of 86 GWd/t with developed rim structure. Almost no FGR was found for non rim-structured fuels, even at the higher terminal temperatures of 1500 - 1800 °C.

PIEs on fuel cladding materials

Cladding waterside corrosion and associated hydrogen pickup are also important issues at high burnup. Oxide thicknesses of the cladding outer surface are measured non-destructively by eddy current method and destructively by metallography. Typical data of oxide thickness are shown **Fig. 3**[5]. Fuel rods of recent step III design showed a remarkable improvement in corrosion resistance.

Mechanical properties of fuel cladding tubes under increased fuel burnup is considered to be one of the controlling factors for the reduced failure enthalpy of simulated reactivity initiated accident (RIA) irradiation tests. Mechanical properties are strongly dependent on stress state in a specimen, so that tests should be conducted under a clearly defined stress state (e.g. circumferential uniaxial tension). As shown in **Fig. 4**, internal pressurization of tubes under the open end burst loading system was employed to meet this requirement and to obtain the basic mechanical properties[10]. Ultimate hoop strength and failure strain of the irradiated fuel cladding tubes versus fuel burnups and neutron fluences are plotted in **Fig. 5**. Strength increased with the increase of burnup except the specimen

with higher hydrogen concentration. The reason for the strength reduction of the specimen was due to the failure before plastic deformation. There seemed to be no strong dependence between failure strain and fuel burnups or neutron fluences. The same data on the strength and failure strain are plotted as a function of hydrogen concentration in **Fig. 6**. For the irradiated specimens, circumferential failure strain dropped sharply with the increase of hydrogen.

PIEs on structural materials

Irradiation assisted stress corrosion cracking (IASCC) is a recent concern in materials for nuclear in-reactor components of Light Water Reactor (LWR) [11-13]. It takes the form of intergranular stress corrosion cracking (IGSCC) and the critical fluence level has been reported to be about $5x10^{24}n/m^2$ (E>1MeV) in Type 304 stainless steels (SS) [11-13].

Slow strain rate tensile and crack growth rate tests have been performed on irradiated specimens obtained from commercial LWR core components under simulated LWR conditions [13-16]. Specimens were machined remotely by milling machine in a hot cell. The dependence of neutron fluence on IASCC susceptibility under BWR normal water conditions (NWC) is shown in **Fig. 7** [15]. IASCC susceptibility increases rapidly exceeding $1x10^{25}n/m^2$ (E>1MeV). **Fig. 8** shows the SCC growth rate acquired under NWC and the disposition curves of JSME NA1-2002 standard for sensitized SUS304 and for L-grade SS in NWC. All of the data are below the upper limit, $9.2x10^{-10}m/s$ [16]. Microstructures of irradiated stainless steels were examined utilizing FEG-TEM which enabled to analyze microscopic area with high resolution to investigate radiation induced defects and grain boundary segregation affecting the mechanical and corrosion behaviors such as IASCC [15-16].

SUMMRAY

The major interest of BWR fuel R&D is high burnup fuel performance. And the major interest of BWR structural material R&D is plant life management. To meet the demands for detailed mechanistic understanding fuel performance and material degradation, more precise microscopic and specific PIE techniques are required. Various examination techniques have been developed in NFD during the course of the PIE programs to meet the research requirements.

A large number of fuels and materials irradiated in commercial reactors as well as those in test reactors have been examined in various research and development programs. Detailed PIEs on fuel pellets, cladding materials, and core structural materials have been successfully carried out and significant amounts of data have been accumulated.

REFERENCES

(1) Y. Mishima and T. Aoki, Paper presented at IAEA International Symposium on Improvements in Water Reactor Fuel Technology and Utilization, IAEA-SM-288/58, Stockholm, Sept. 15-19 (1986).

(2) M. Oishi, Paper presented at IAEA Technical Committee Meeting on Fuel Performance at High Burnup for Water Reactors, Nykoping (1990).

(3) H. Ohara, et al., Proc. International Topical Meeting on Light Water Reactor Fuel Performance, West Palm Beach, April 17-21 (1994).

(4) H. Hayashi, et al., Proc. International Topical Meeting on Light Water Reactor Fuel Performance, Portland, May 2-6 (1997).

(5) H. Hayashi et al., Proc. International Topical Meeting on Light Water Reactor Fuel Performance, Park City, April 10-13 (2000).

(6) K. Ogata, et al., Proc. International Topical Meeting on Light Water Reactor Fuel Performance, West Palm Beach, April 17-21 (1994).

(7) M. Ichkawa, et al., J. At. Energy Soc. Japan, 39, 2 (1997) pp.93-111 (in Japanese).

(8) Y. Hirano, et al., Proc. 2005 Water Reactor Fuel Performance Meeting, Kyoto, Oct. 2-6 (2005).

(9) K. Une, S. Kashibe and A. Takagi, Proc. 2005 Water Reactor Fuel Performance Meeting, Kyoto, Oct. 2-6 (2005).

(10) M. Nakatsuka, et al., Proc. 2004 International Meeting on LWR Fuel Performance, Orlando, Sep. 19-22 (2004).

(11) W.L. Clarke and A.J. Jacobs, Proc. 1st International Symposium on Environmental Degradation of Materials in Nuclear Power System-Water Reactors, Myrtle Beach, August (1983) 451-461.

(12) P.L. Andresen, et al., Proc. 4th International Symposium on Environmental Degradation of Materials in Nuclear Power System-Water Reactors, Jekyll Island, August (1989) 83-121.

(13) M. Kodama, et al., Proc. 5th International Symposium on Environmental Degradation of Materials in Nuclear Power System-Water Reactors, Monterey, August (1991) 948-954.

(14) G. Furutani, et al., J. Nucl. Mater., 283, (2001) pp.179-186.

(15) K. Chatani, et al., Proc 12th International Conference on Environmental Degradation of Materials in Nuclear Power System-Water Reactors, Snow Bird, August (2005) to be published.

(16) S. Ooki, et al., Proc 12th International Conference on Environmental Degradation of Materials in Nuclear Power System-Water Reactors, Snow Bird, August (2005) to be published.

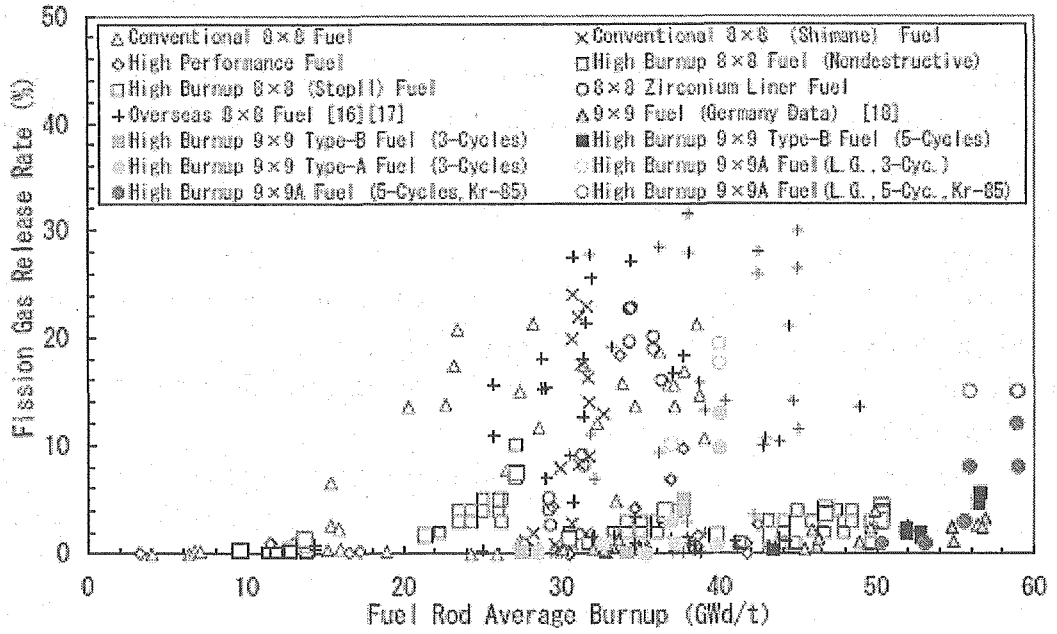

Fig. 1 Burnup dependence of FGR rate.

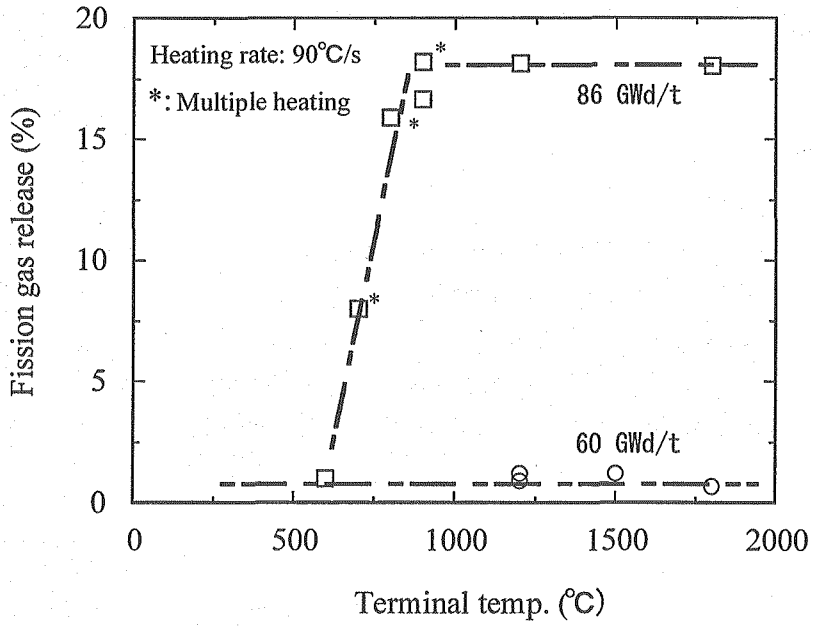

Fig. 2 Terminal temperature dependence of FGR at 90 °C/s.

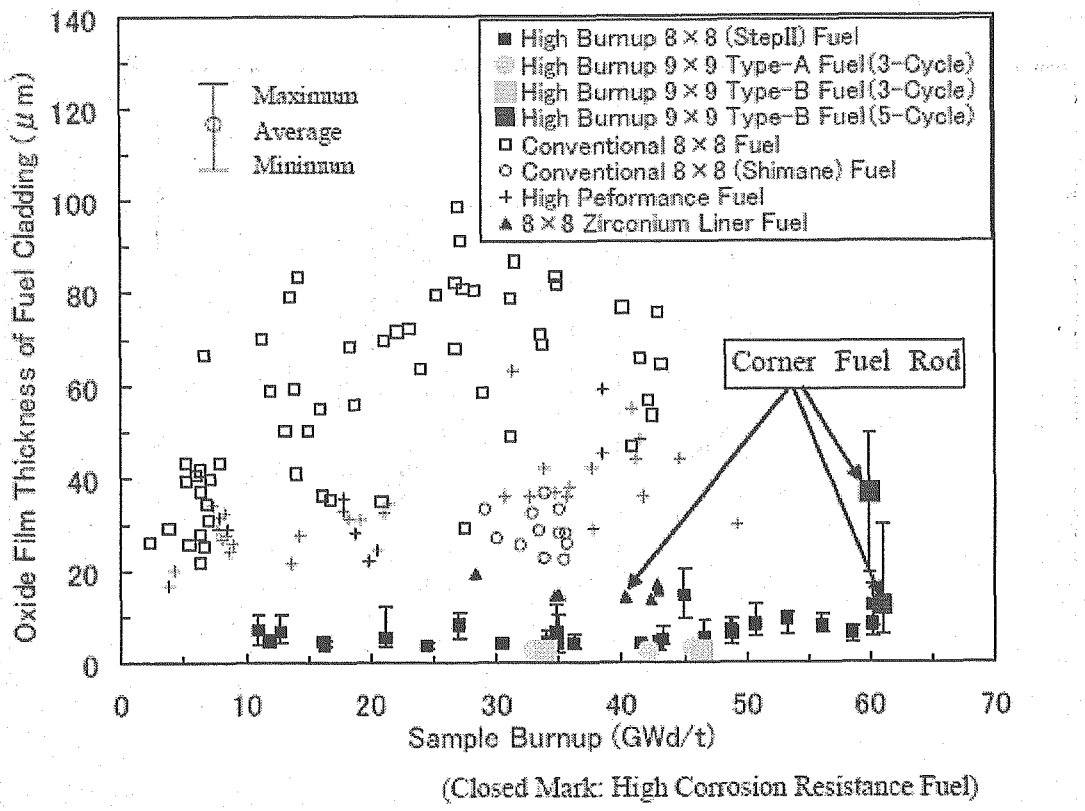

Fig. 3 Burnup dependence of oxide film thickness of fuel cladding irradiated in BWRs by metallography observation.

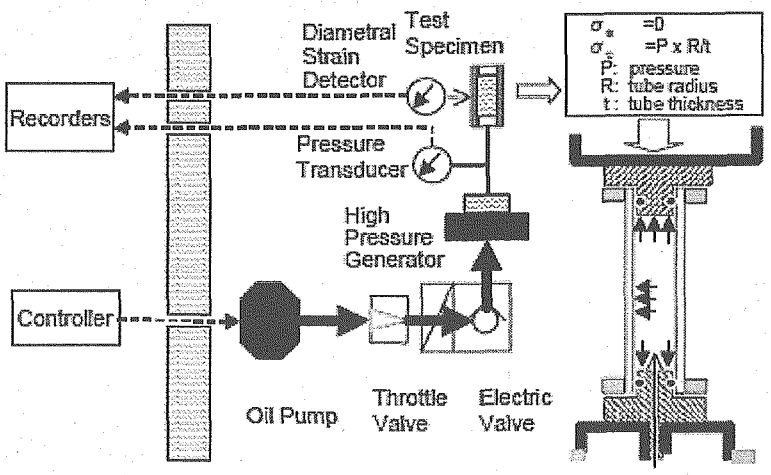

Fig. 4 Schematic diagram of testing assembly for the RIA simulated rapid internal pressurization.

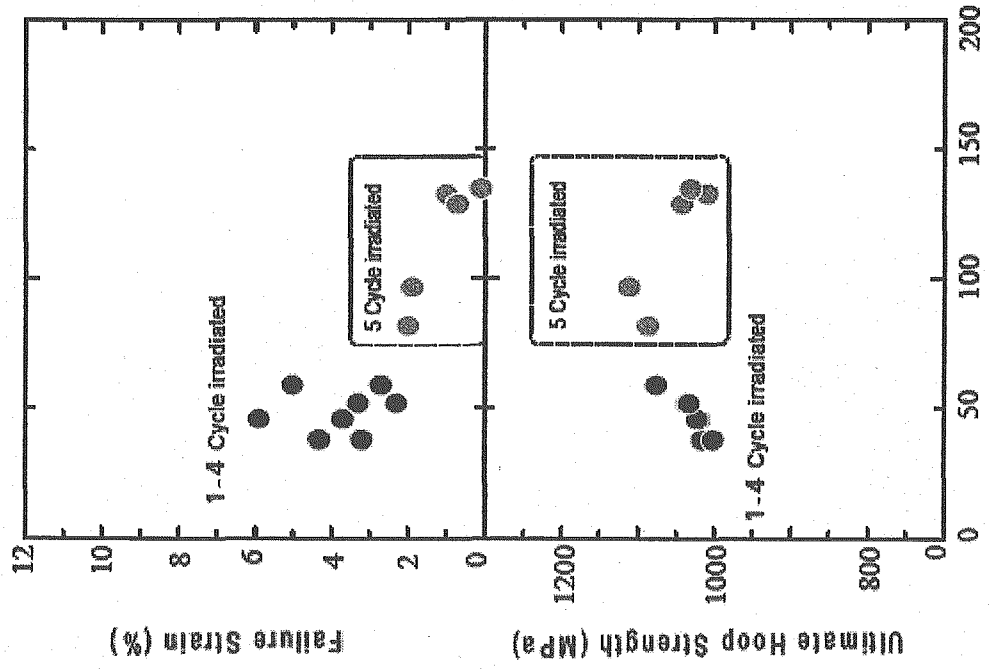

Fig. 6 Effect of hydrogen concentration on strength and failure strain of zirconium lined fuel cladding tubes irradiated in BWRs.

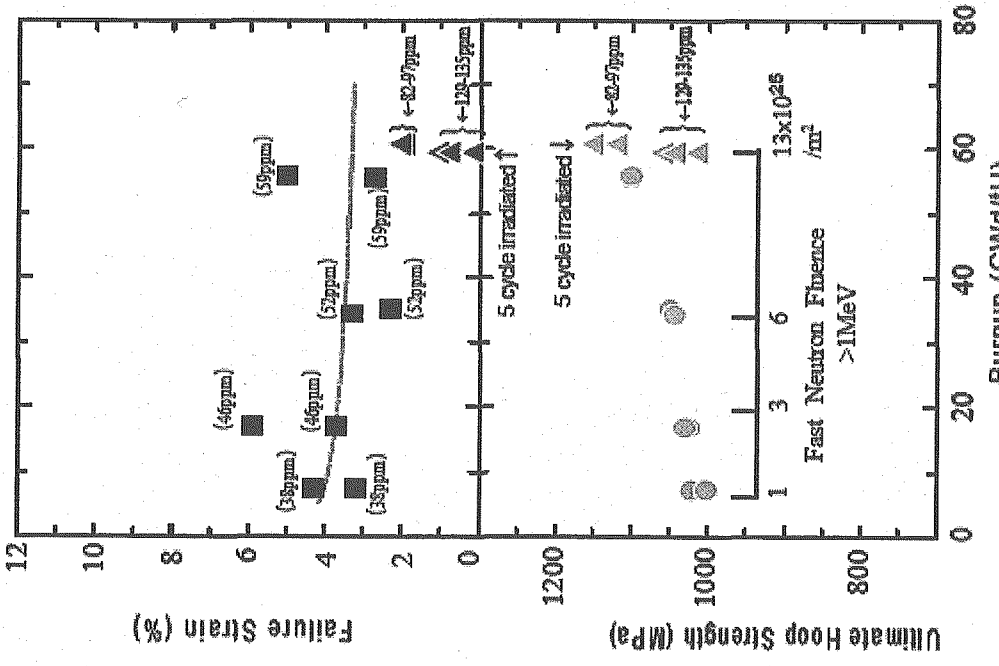

Fig. 5 Effect of fuel burnup on strength and failure strain of zirconium lined fuel cladding tubes irradiated in BWRs.

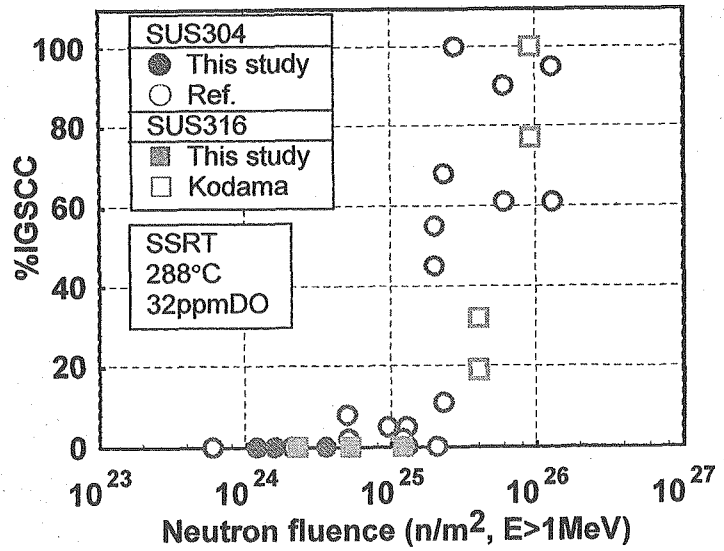

Fig. 7 Neutron fluence dependence of IASCC susceptibility (%IGSCC).

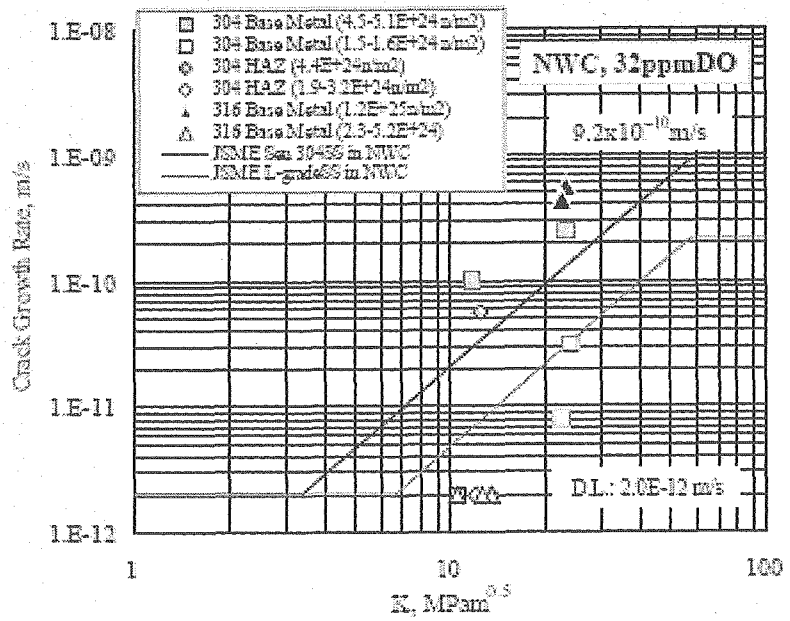

Fig. 8 Crack growth rate under NWC of irradiated 304SS and 316SS specimens prepared from used BWR core components.

1.7 THE OARAI BRANCH OF IMR, TOHOKU UNIVERSITY AS OPEN FACILITY FOR UNIVERSITY RESEARCHERS UTILIZING FISSION REACTORS

Tatsuo Shikama

Institute for Materials Research, Tohoku University
2-1-1 Katahira, Aobaku, Sendai, 980-8577 Japan
Tel. +81-22-215-2060, Fax. +81-22-215-2061, E-mail; shikama@imr.tohoku.ac.jp

ABSTRACT

For advanced future research activities utilizing fission reactors and hot laboratories, effective interlinks among fission reactors and hot laboratories are indispensable. Oarai Branch of Institute for Materials Research in Tohoku University has been playing an important role for supplying related tools for university researchers, in fission reactor irradiation and post irradiation examinations, under tight collaboration with JAERI and JNC. Now the Oarai Branch is planning to expand its collaborative functions, utilizing multi-reactors over the world and making effective interlinks among related hot laboratories in several institutions. The talk will give rough view of the present plan of the Oarai Branch, IMR, Tohoku University for tight and effective collaboration among institutions.

INTRODUCTION

The Oarai Branch (hereafter referred as the Oarai Branch) of Institute for Materials Research in Tohoku University was established in 1972 in the site of the JAERI-Oarai, to take care of university researchers, who were under the jurisdiction of the Ministry of Education, for their utilizing the Japan Materials Testing Reactor (JMTR) which belonged to the Science and technology Agency. At that time, the Japan Research Reactor 2 (JRR-2) was still working in JAERI-Tokai along with the initial JRR-3, for irradiation tests and studies of materials. Although the JRR-2 had some advantageous features for the materials irradiation, such as a hard neutron spectrum and high flux of high energy neutrons, its core was small and its ability to deal with sophisticated

irradiation, to which researchers in universities had increasing demands with progress of studies of radiation effects in materials, was limited. As a fission reactor whose mission was exclusively focused on the nuclear materials and fuels, the JMTR offered versatile features such as a temperature control by way of the change of a helium gas pressure in an instrumented rig and an ability of complicated instrumentations with its unique connecting box system.

University utilization of the JMTR started with simple irradiation of materials and fuels in a simple rig and with standard measures for post irradiation examinations (PIEs). Being conscious of the main mission for researches in universities, the Oarai Branch has focused its efforts on three major fields:

1. Control of irradiation conditions as precise as possible to make a fission rector irradiation be compatible with the advanced material science.
2. Providing appropriate measures of PIEs for studying radiation induced evolution of microstructures, which will be competent with the rapidly-advancing contemporary materials science.
3. In-situ studies of dynamic property changes of materials under a reactor irradiation.

Figure 1 schematically shows current major efforts of the Oarai Branch, with major research topics.

The unification of two Japanese major nuclear organizations, the Japan Atomic Energy Research Institute (JAERI) and Japan Nuclear fuel Cycle Development Corporation (JNC) into the new establishment of the Japan Atomic Energy Authority (JAEA) and the temporary stop of the JMTR operation are forcing the Oarai Branch to restructure its major roles in the utilization of fission reactors and its relationship with outer research organizations. However, the Oarai Branch was confident that its essential roles will not be altered by these drastic changes of the environment surrounding it. Rather, the Oarai Branch will keep its stance and proceed further to promote the materials science in the field of the nuclear technology, under the cooperation with the new organization, the JEAE.

Concerning terms 1 and 3 of the three major topics mentioned above, the Oarai Branch has accumulated experiences and developed needed technologies under close collaboration with the JAERI and the JNC. Some of the experiences and the technologies accumulated in the Oarai Branch have been applied in oversea reactors such as the HFIR (High Flux Isotope Reactor) of Oak Ridge National Laboratory in the USA, and now, it is planned for the Oarai Branch to extend its activity to other reactors than the JMTR, such as the JOYO, the sodium cooled high flux fast reactor, JRR-3 and oversee reactors such as the BR-2 (Belgium Reactor 2).

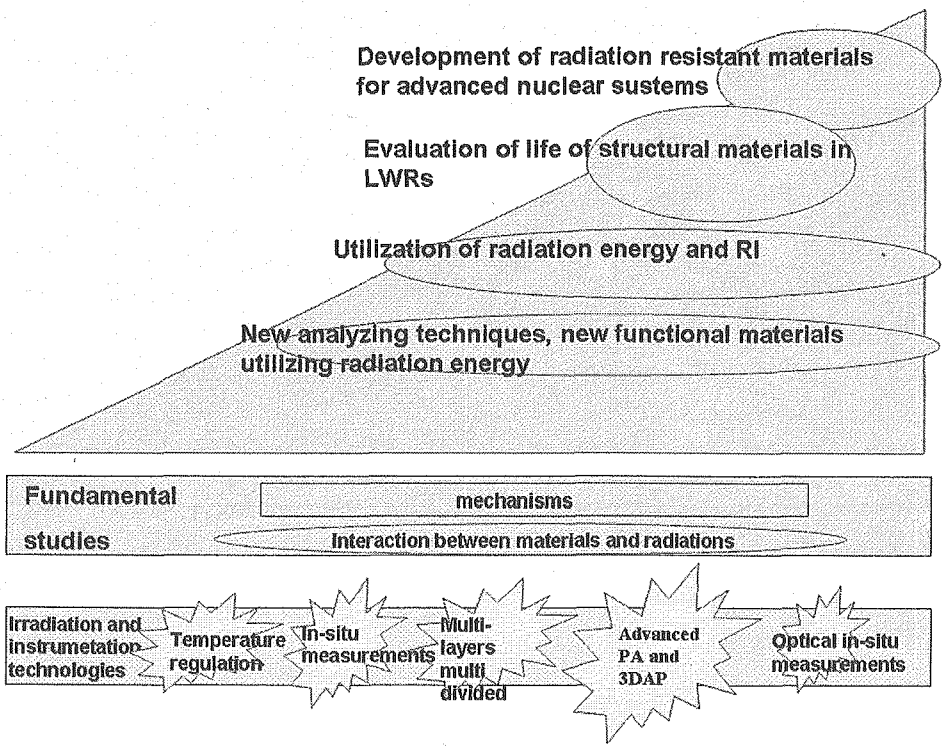

Figure 1 current major efforts of the Oarai Branch.

CONTROL OF IRRADIATION CONDITIONS IN FISSION REACTORS

It is not an easy work to control irradiation conditions in a fission reactor properly for a reliable study of radiation effects in materials and fuels. Among many parameters, the temperature is the most important (studies have been extensively carried out led by M.Kiritani). Especially, the temperature should be controlled being independent of the reactor power in the course of reactor-startup and -shutdown, when a reactor power and a nuclear heating rate change drastically. **Figure 2** shows an example of effects of temperature-history upon the radiation induced change of mechanical properties of a vanadium alloy, which was studied by T.Muroga under the Japan-USA collaboration in the HFIR. The irradiation rig used in the experiment and the examples of temperature control is shown in **Fig. 3**. An example of the precise temperature control realized in the JMTR is shown in **Fig. 4**.

Figure 5 shows the system proposed now for the installation in the to-be revised JMTR, for fundamental studies of radiation effects in nuclear materials (after H.Kawamura, Y.Matsui and T.Shikama). In a shroud type irradiation facility, the temperature, the environments such as variety of gases, oxygen-potential controlled

waters, etc, can be realized being not strictly restricted by the reactor-core regulation. With advanced temperature control technology, the irradiation temperature can be in the range of 10-1200K. With in-situ measuring technology, which will be described below, detailed behavior of nuclear materials can be studied under the irradiation.

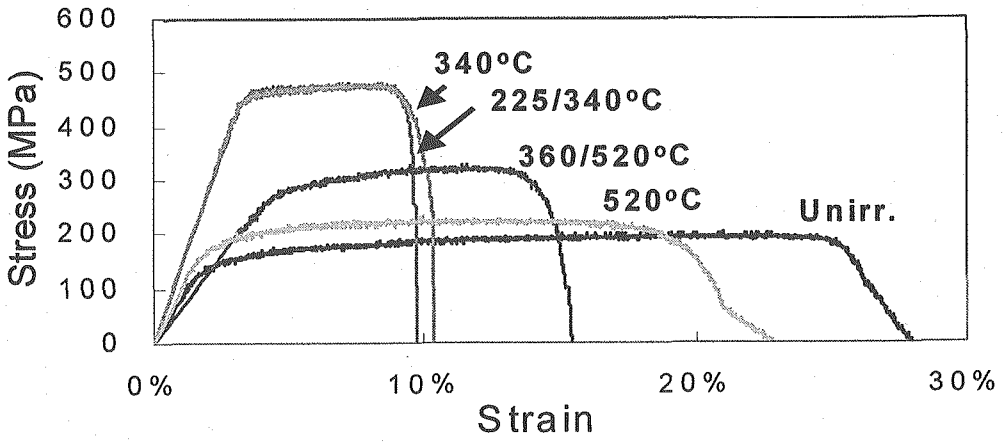

Figure 2 Tensile behavior of vanadium alloy after irradiation in HFIR with different temperature history (after T.Muroga).

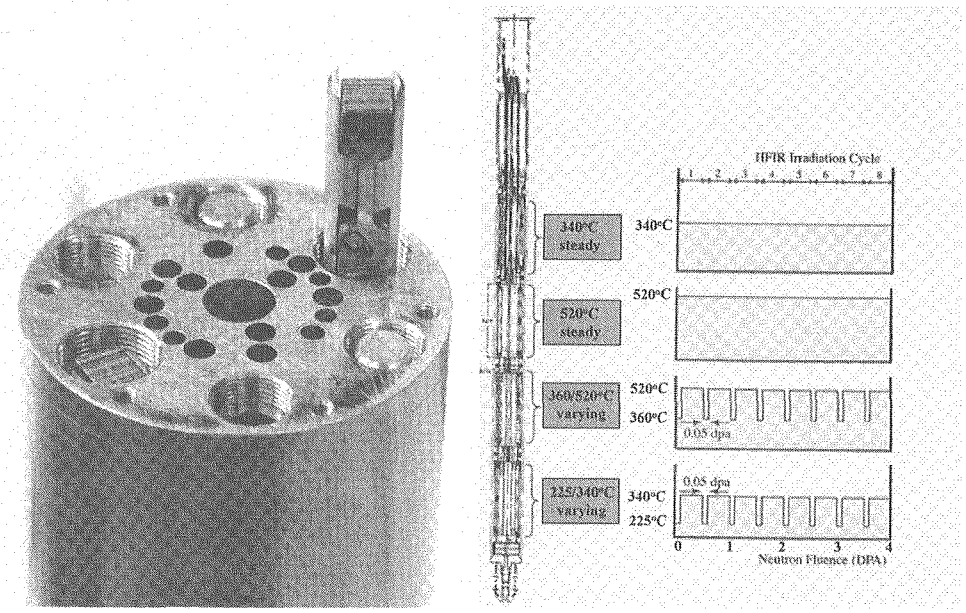

Figure 3 Subcapsule of the HFIR and its temperature history.

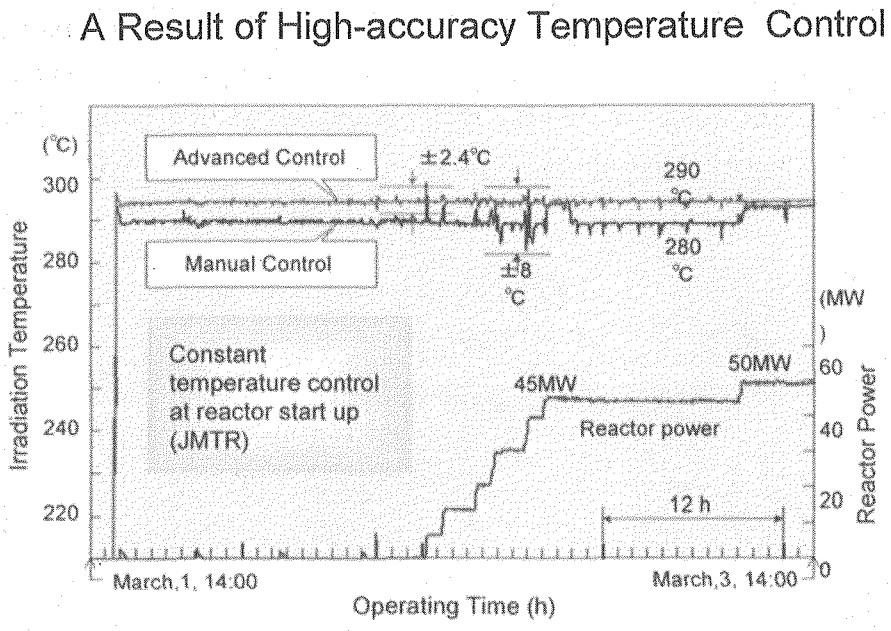

Figure 4 Example of temperature control in JMTR.

ADVANCED PIE INSTRUMENTS

An irradiated rig is disassembled in the JMTR hot cell, however, university irradiation-rig is usually multi-purposed and omnibus-style. So, many kinds of materials with a variety of configurations are accommodated in subcapsules in a rig. The subcapsules (**Figure 6**) are transferred to small hot cells (**Figure 7**) in the Oarai Branch. Specimens are sorted and distributed to many researchers for a variety of PIEs.

Two major activities can be pointed out for the PIEs in the Oarai Branch:

1. The miniature specimen technologies for mechanical tests.
2. The advanced analyzing systems for studying microstructure evolutions.

The first topic will be covered by H.Kurishita in the present symposium. As for the second topic, the Oarai Branch has the world-most advanced systems of the positron-annihilation measurements (**Figure 8** after M.Hasegawa and K.Nagai), which are most effective to study the fundamental processes of defects migrations and agglomerations in the process of radiation induced microstructural evolutions (**Figure 9** after M.Hasegawa and K.Nagai). With the newest three dimension atom probe field emission microscope (3D-AP), the Oarai Branch and its research group are now producing the world-top experimental results on the microstructural evolutions of ferritic steels of LWRs applications. Enjoying the present advantageous status, the Oarai Branch is planning to expand its ability to analyze microstructural evolutions of materials caused by reactor irradiations.

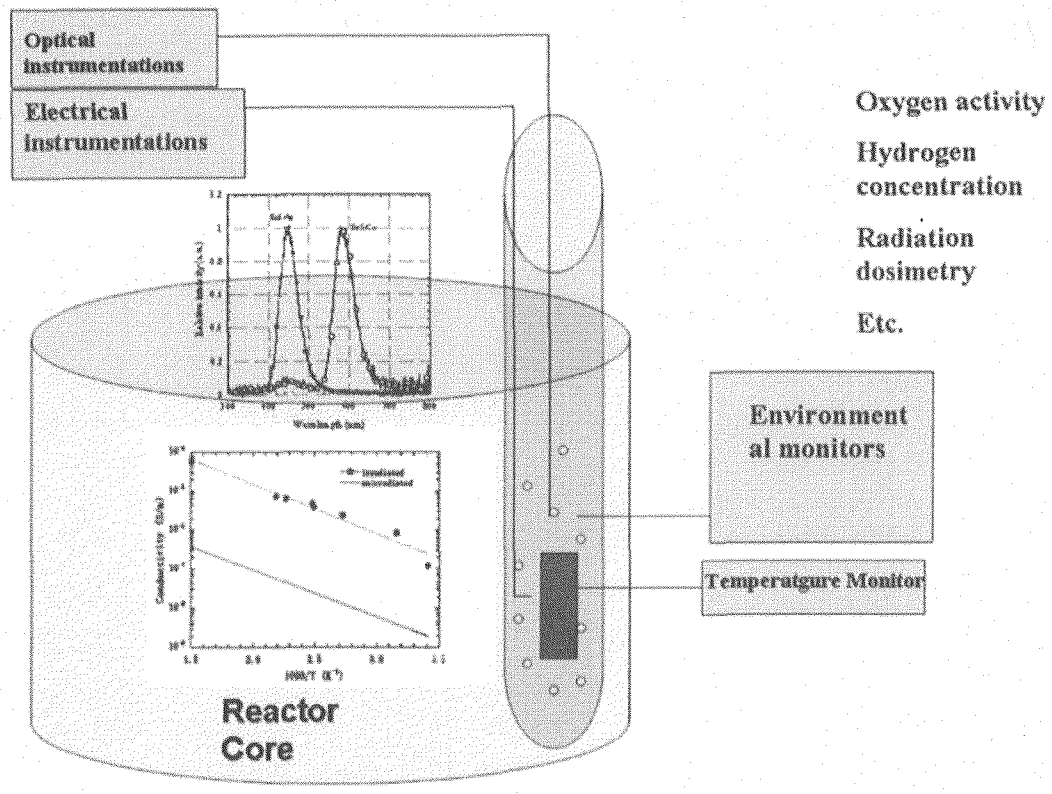

Figure5 Proposed multi purpose irradiation system in the JMTR.

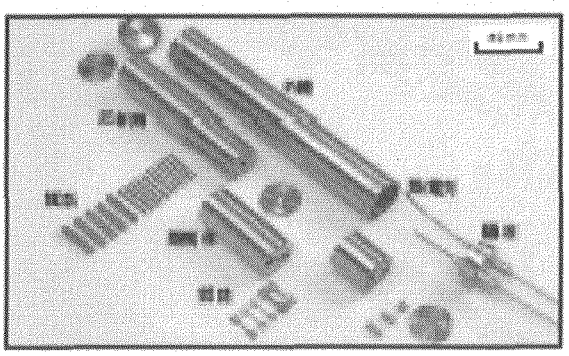

Figure 6 Subcapsules in the JMTR.

Figure 7 Hot cell in the Oarai Branch.

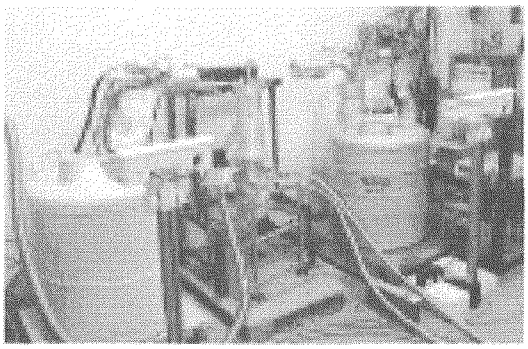

Figure 8 Positron Annihilation system.

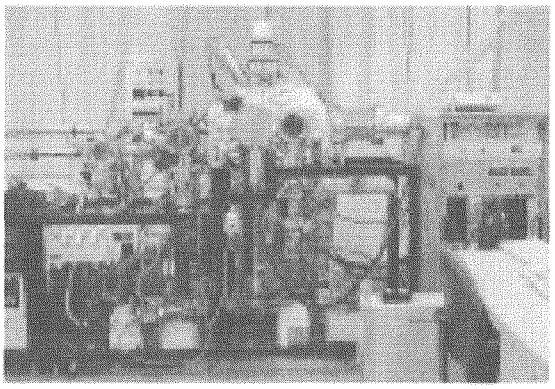

Figure 9 3D Atom Probe system.

IN-SITU STUDIES

Studying dynamic behavior of nuclear materials under the irradiation is becoming more and more important, however, it is not easy for the reactor irradiation. Having collaboration of the JAERI-JMTR, the Oarai Branch has being developing in-situ technologies to measure dynamic property changes of nuclear materials. **Figure 10** shows data of the radiation induced electrical conductivity of ceramic insulators, which were accumulated through reactor irradiations in the JMTR, and the HFIR, as well as other irradiations such as the gamma-ray irradiation, 14MeV fast neutron irradiation. Electrical conductivity of conductive materials can be also measured in the JMTR. The conductivity change of a electrically conductive gold meander was also measured under the JMTR irradiation. Hydrogen mobility in proton conductive ceramics was estimated by measuring proton conductivity under the JMTR irradiation as shown in **Fig. 5**. Some proton conductive ceramics show large proton conductivity under the JMTR irradiation, which is suggesting that the proton mobility is increased dynamically by the irradiation.

In the meantime, optical measurements can be done in the JMTR. **Figure 11** shows the transmitting behavior of the white light through radiation resistant silica-core optical fibers which are running through the core region of the JMTR. Some fibers show good radiation resistance and the white light came out of the optical fiber as the white light. Radiation induced luminescence in the JMTR core region can be measured with these radiation resistant optical fibers.

Establishment of in-situ technologies for electrical and optical measurements makes it possible to study dynamic behaviors of nuclear materials under the reactor irradiation.

For example, corrosion behavior of zircalloy alloy can be studied, by inspecting surface area optically (visual inspection of surfaces and measuring radioluminescence from oxide films), and by measuring electrical properties of oxide films (electrical

potential through the thickness of the oxide film, electrical conductivity of the oxide film which will be modified by the mobility of hydrogen). With the system proposed in **Fig. 5**, complicated instrumentations can be done and detailed behaviors of nuclear materials can be studied in-situ under the reactor irradiation. With the advanced technologies of the microstructural evolution in the PIEs mentioned above, the comprehensive understandings of behaviors of nuclear materials in the actual environments can be realized.

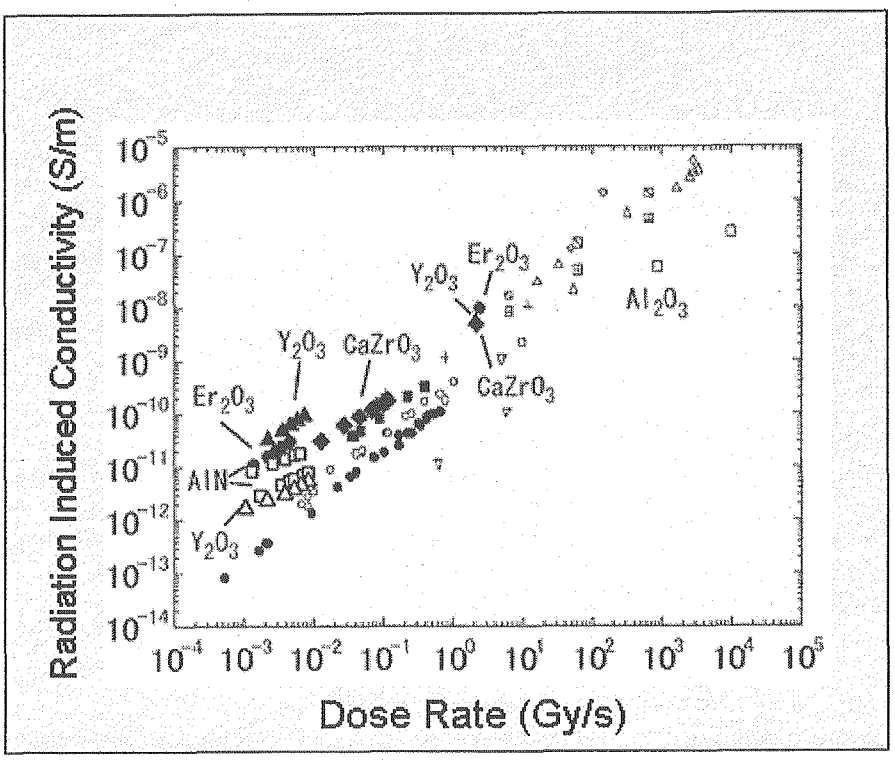

Figure 10 Radiation induced electrical conductivity of ceramic materials (after T.Tanaka).

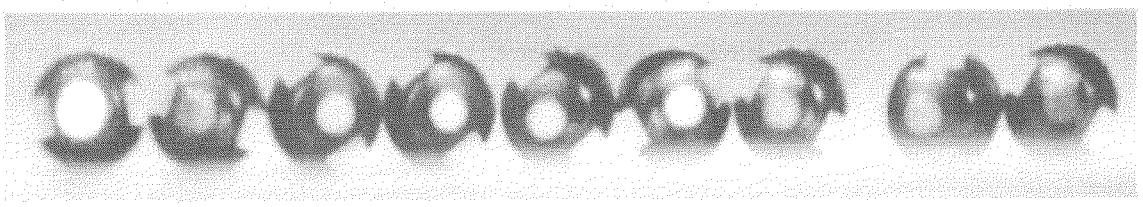

Figure 11 White lighted transmitted through radiation resistant optical fibers in the JMTR core while the JMTR is under operation with its full power.

FUTURE SCOPE FOR THE OARAI BRANCH

Drastic changes are taking place in environments surrounding the Oarai Branch, the unification of the two organizations into the new JEAE and the temporary stop of the JMTR. However, in the course of its operation for more than 30 years, the Oarai Branch has established its unique features as the interface between university researchers and the reactor utilization for the materials studies, under cooperation with the JAERI and the JNC. It had high potential for the material-science based analyzing technologies for the microstructural evolution in irradiated materials. Also, it played an important role to improve the irradiation technologies in reactors, including in-situ type measurements. A new framework will need to be established for the Oarai Branch to play appropriate roles in the new circumstances. One primitive proposal will be as shown in **Fig. 12**, which will promote further collaboration with JEAE and other organizations in the world.

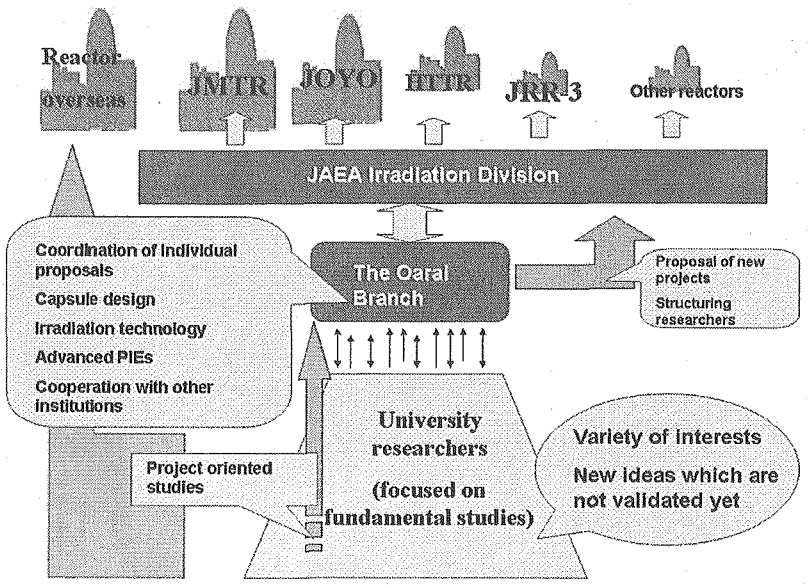

Figure 12 Proposed framework for the Oarai Branch.

ACKNOWLEDGEMENT

Future aspects of the Oarai Branch are extensively under discussions among concerned personals. The author would like to express his sincere gratitude to Prof. H.Matsui, Director of the Oarai Branch, IMR, Tohoku University, Prof. M.Hasegawa, Vice Director General of the Institute for Materials Research, Tohoku University, and Prof. Y.Shiokawa of the IMR, Tohoku University. He also would like to express his thanks to Dr. S.Shiozawa, previous Director General of the Oarai Research Establishment of the JAERI-Oarai, Dr. M.Niimi, Dr. H.Kawamura, Mr. Y.Matsui in the JAERI-Oarai, as well as Dr. M.Itoh, Vice Director General of the new JAEA-Oarai.

1.8 PIE RESULTS AND NEW TECHNIQUES APPLIED FOR 55GWd/t HIGH BURNUP FUEL OF PWR

Tomohiro Tsuda, Yoichiro Yamaguchi, Yasunari Shinohara, Mitsuteru Sugano, Yuji Kosaka and Yasuhiro Takeda

Nuclear Development Corporation, 622-12, Funaishikawa, Tokaimura, Ibaraki 319-1111, Japan

Takaaki Kitagawa

Mitsubishi Heavy Industries, LTD., 1-1-1 Wadasakicho, Hyogo-ku, Kobe 652-8585, Japan

ABSTRACT

Post-irradiation examinations (PIE) for 55GWd/t high burnup fuel which had been irradiated at a domestic PWR plant was conducted at the fuel hot laboratory of the Nuclear Development Corporation (NDC). In this PIE, such new techniques as the defueling method by drilling and clamping for axial tensile test were used in addition to existing techniques to confirm the integrity of 55GWd/t high burnup fuel. The superiority of improved corrosion-resistant claddings over currently used current Zircaloy-4 claddings in terms of corrosion-resistance was also confirmed. This paper describes the PIE results and the advanced PIE techniques.

KEYWORD : PWR, PIE, 55GWd/t, Defueling, Density measuring

INTRODUCTION

Japanese PWR utilities are planning to increase the burnup of fuel from 48 GWd/t to 55GWd/t for the purposes of improving the fuel cycle economy and reducing the amount of spent fuel. To make such an increase feasible, confirmation of the integrity of the fuel is necessary prior to the practical use of 55 GWd/t fuel. The present PIE was conducted at the fuel hot laboratory of NDC using 55 GWd/t fuel rods which had been spent for four cycles at a PWR plant in Japan.

In addition to confirming the integrity of conventional claddings and pellets, this PIE also

checked the improvement effects of improved corrosion-resistant claddings and large grain-size pellets designed to reduce the released amount of FP gas. This paper introduces the data of the PIE which was conducted to confirm the integrity of conventional claddings and pellets and the improvement effects of improved corrosion-resistant claddings and large grain-size pellets.

In this PIE, advanced PIE techniques such as ① the defueling method by drilling, ② the tube-shape axial tensile test and ③ the pellets density measurement method for high burnup fuels, had been applied in addition to conventional PIE items. This report explains these new techniques and their results.

PIE RESULT OF 55GWd/t BURNUP FUEL USING CONVENTIONAL TECHNIQUES

Fuel Rods

Table 1[(1)] shows the specifications of the fuel rods used in this PIE. The average burnup of a fuel assembly was 52 GWd/t and 13 fuel rods were removed from the assembly for their transportation to a hot laboratory. The assembly was the 17 x 17 type with advanced fuel materials. That is three types of the claddings: ① Zircaloy-4 claddings, which are currently in use, ② MDA and ③ ZIRLO^{TM} as improved corrosion-resistant claddings and three types of fuel pellets : ① pellets currently in use, ② large grain-size pellets aimed at reducing the released amount of FP gas and ③ pellets with added Gd_2O_3 at a rate of 10 wt% were contained.

PIE Results

(1) γ Scanning Measurement

The γ scanning measurement was conducted to confirm the burnup along the axial direction of the fuel rods and the migration of FP. **Fig. 1**[(1)] shows the measurement results of the γ ray intensity of Cs-137 along the axial direction. The observed γ ray intensity showed an almost flat pattern except at the grid section and the upper and lower ends, confirming almost even burning along the axial direction..

(2) Measurement of Dimensions

Fig. 2[(1)] shows the measurement results of the fuel rod length. The rod length changes was smaller with the improved corrosion-resistant claddings (MDA/ZIRLO^{TM}) than current Zircaloy-4 claddings, presumably because of the different alloy constituents of these claddings. Meanwhile, the fuel rods containing large grain-size pellets showed a largeer rod length changes, presumably because of the influence of PCMI.

(3) Measurement of FP Gas Release Rate

The puncture test was conducted to check the released amount of FP gas. **Fig. 3**[1] shows the test results compared with the overseas data. While the FP gas release rate increased with increased burnup, the measurement results this time were lower than the overseas data. The difference in the grain-size of pellets did not significantly affect the FP gas release rate.

(4) Cladding Oxide Film Thickness and Hydrogen Content

The oxide film thickness on the outer surface of the cladding was measured by the eddy current method to check any positive effect of the improved corrosion-resistant claddings. **Fig.4**[1] shows the measurement results for the peak oxide film thickness and the corresponding data of an earlier study. The results indicate a better corrosion-resistance performance of the improved corrosion-resistant claddings than current Zircaloy-4 claddings.

Fig. 5[1] shows the relationships between the measured hydrogen content and the oxide film thickness on claddings. In short, the hydrogen content of this study claddings was 400 ppm or lower.

(5) Cladding Mechanical Properties

The tensile test by using the dog-bone shape specimen was conducted at 385°C to identify the mechanical properties. **Fig. 6**[1] and **Fig. 7**[1] shows 0.2% yield strength and fracture elongation along with corresponding data of an earlier study. The results indicate that this study claddings have good mechanical properties perfomance in the high burnup region. The mechanical properties data of the improved corrosion-resistant claddings fall within the existing data range for the claddings currently in use.

PIE OF 55 GWd/t BURNUP FUEL USING NEW TECHNIQUES

Improvement of Defueling Method

In the PIE of 48 GWd/t burnup fuel, pellets were removed from the cut piece of fuel rod to prepare specimens for the mechanical properties test of the claddings while vibrating the carbide needle. With 55 GWd/t high burnup fuel, however, it was difficult to separate the pellets from the cut piece of fuel rod because of their bonding due to reaction. The method of drilling out the pellets was, therefore, used for the 55 GWd/t high burnup fuel. The appearance of the defueling device using the drilling method is shown in **Fig. 8** and the processing steps using this device are shown in **Fig. 9**.

It is possible to remove pellets without damaging the inner surface of the claddings through four steps with a different length and outer diameter of the drilling edge. Pellets can be extracted from a tube of up to 150 mm in length by means of reserving the tube so that drilling work can be conducted from both ends. Although the temperature of the claddings increases during drilling, it remains lower than 100°C, thereby causing no negative impacts on the mechanical properties. The remaining 0.5 mm thick pellets on the inner surface of the

cladding are dissolved by nitric acid.

The defueling device used was provided with the cover to prevent scattering of the pellet powder, substantially reducing the contamination inside the hot cell.

Improvement of Clamping Jig for Cladding Tensile Test

The axial tensile test for a tubular specimen of a cladding is conventionally conducted to establish the mechanical properties of claddings. However, the obtaining of elongation data is difficult because of the fracture within not gauge length(GL) section but at the wedge grip type chuck section. To solve this problem, the method to clamp the specimen was changed from the wedge type chuck to the collet type chuck for the present PIE as shown in **Fig. 10**. Because of the lack of precedence of this method, it was necessary to find a suitable clamping force to prevent any slippage of the tubular specimen. A hydrogen-absorbed non-irradiated specimen for the tube axial tensile test was used to check this suitable force and it was found that the necessary clamping force was approximately 240 N.m. A clamping jig with a structure of a combination of gears was manufactured to enable clamping work by remote control. **Fig. 11** shows the appearance of this jig. For the present PIE, this jig was used to clamp the specimen for the axial tensile test. The test results were that fracture took place within the GL of the tubular specimen and that the measured elongation data was reasonable results.

Examination of Density Measuring Method for High Burnup Fuel

To evaluate the densitication as well as swelling of fuel pellets due to irradiation the conventional method of density measurement is conventionally conducted using several pellet fragments extracted from the fuel rod. However, it was supposed that the collection of fuel fragments by the conventional method would be difficult in the case of high burnup fuel because of the bonding between the cladding and fuel pellet. There was also concern in regard to adverse impacts of the volume of the remaining layer of pellets on the inner surface of the claddings after defueling on the pellet density value. For this reason, the conventional method and a new method were carried out in present PIE for high burnup fuel and the both results were compared In the new method, the density of a cut piece (claddings and fuel pellets) and the density of the claddings after defueling are measured and then the pellet density is evaluated based on the above measured results. The specimen was produced by cutting the fuel rod by some 3mm in length. The weights were measured in air and in liquid based on the immersion method. **Fig. 12** shows the density measuring results based on the conventional and the new methods, which indicates good agreement between the both measurement results. Accordingly, it is confirmed that the results of the new measuring method should be valid as those of the conventional measuring method are.

CONCLUSIONS

The PIE was conducted at the fuel hot laboratory of the NDC to check the soundness of 55 GWd/t high burnup fuel and any effects of improved corrosion-resistant claddings and large grain-size pellets aimed at reducing the release of FP gas.

Apart from the accumulation of integrity data for 55 GWd/t fuel, the results confirmed the superior corrosion resistance of improved corrosion-resistant claddings compared to the current Zircaloy-4 claddings which are currently in use.

The present PIE established new techniques regarding defueling using a drilling edge, reliable axial tensile test method and density measuring and contributed to the soundness checking of 55 GWd/t high burnup fuel.

REFERENCES

(1) T. Kitagawa, T. Takahashi, Y. Shinohara, M. Sugano, Y. Kosaka, T. Sendo, "Post Irradiation Examination of fuel rods in 55GWd/t Lead Use Assembly", 2005 Water Reactor Fuel Performance meeting.

Table1 General specifications of fuel rods [1]

	Fuel rods in LUA *
Cladding	
Material	MDA
	ZIRLO
	Low Tin Zircaloy-4
Outer Diameter	9.50mm
Inner Diameter	8.36mm
Pellet	
Material	Current UO_2
	Large grain UO_2
	10wt%Gd_2O_3 doped UO_2
Diameter	8.19mm
Length	10mm
Density	95%T.D.
Enrichment	4.5wt%
	2.0wt%(10wt%Gd)
Fuel Rod	
Fuel Stack Length	3.6m
Length	3.9m
Fuel Assembly	
Type	17x17
Grid Material	Inconel

* : Lead Use Assembly

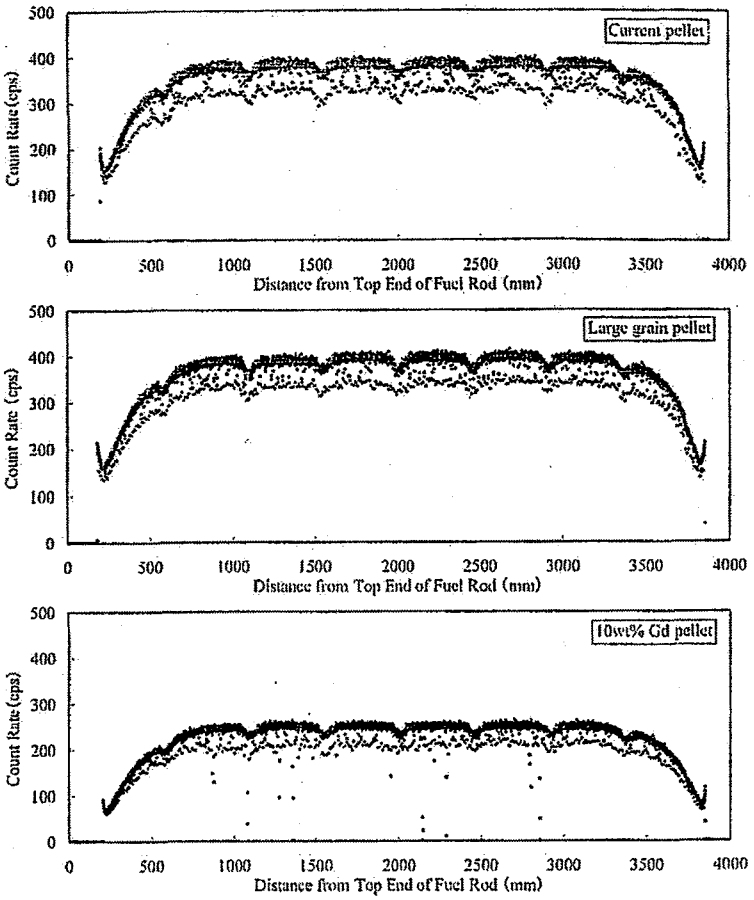

Fig.1 Axial Cs-137 gamma scanning trace[1].

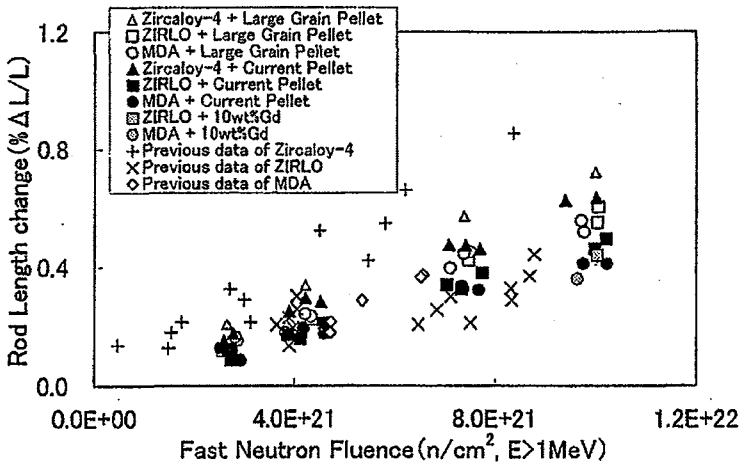

Fig.2 Relationship between Rod length change and fast neutron fluence[1].

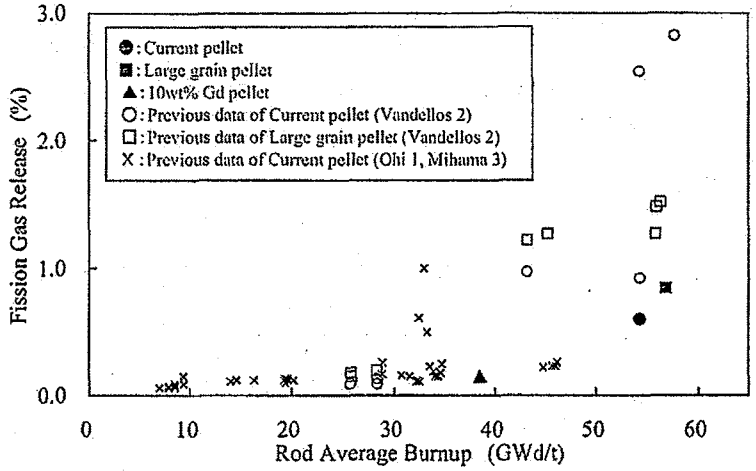

Fig.3 Comparison of fission gas release among the fuel pellet types[1].

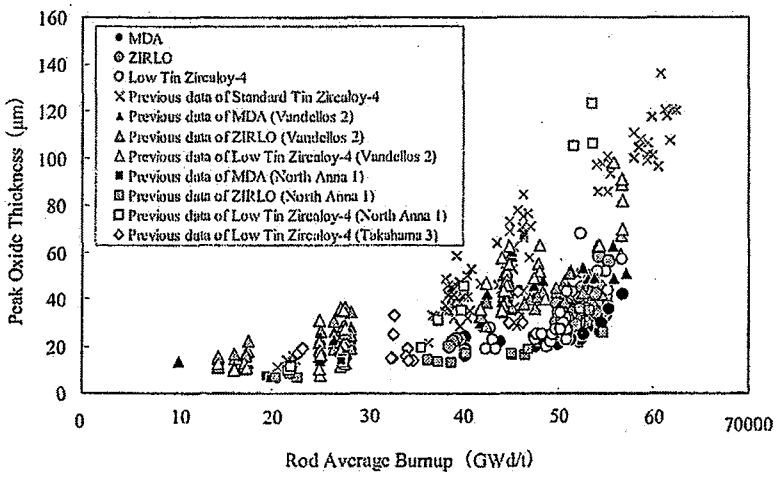

Fig.4 Measurement results of peak oxide thickness by ECT[1].

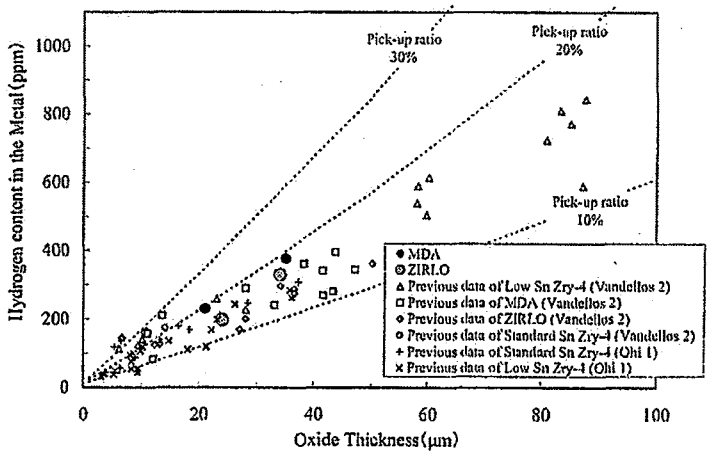

Fig.5 Relationship between oxide thickness and hydrogen content[1].

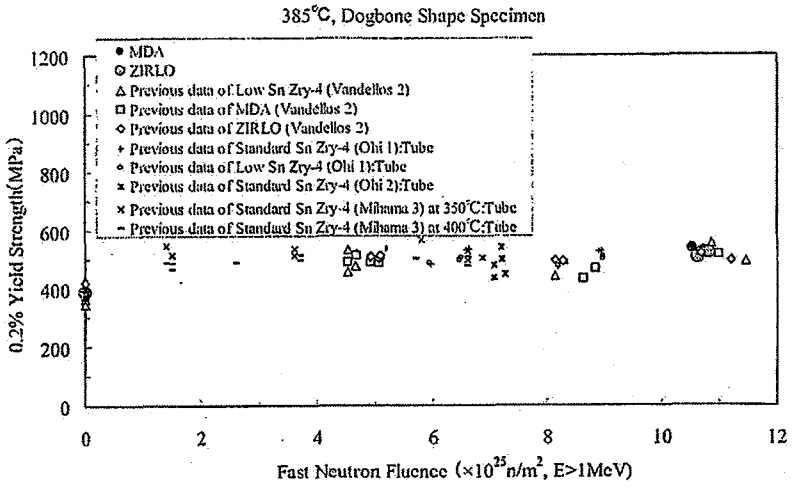

Fig.6 Relationship between fast neutron fluence and 0.2% yield strength of the cladding[1].

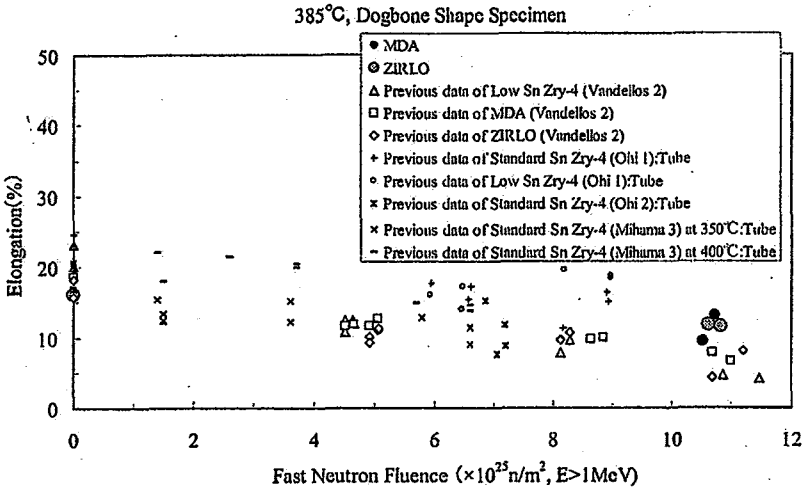

Fig.7 Relationship between fast neutron fluence and elongation[1].

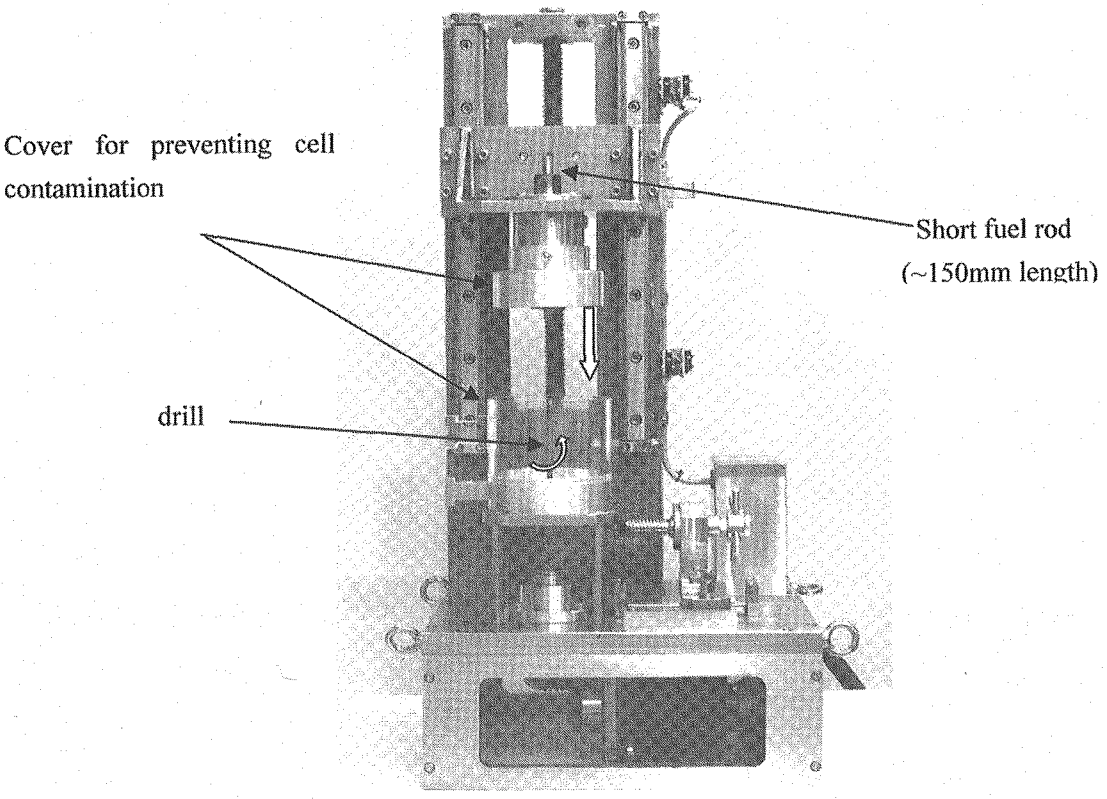

Fig.8 Appearance of the defueling device.

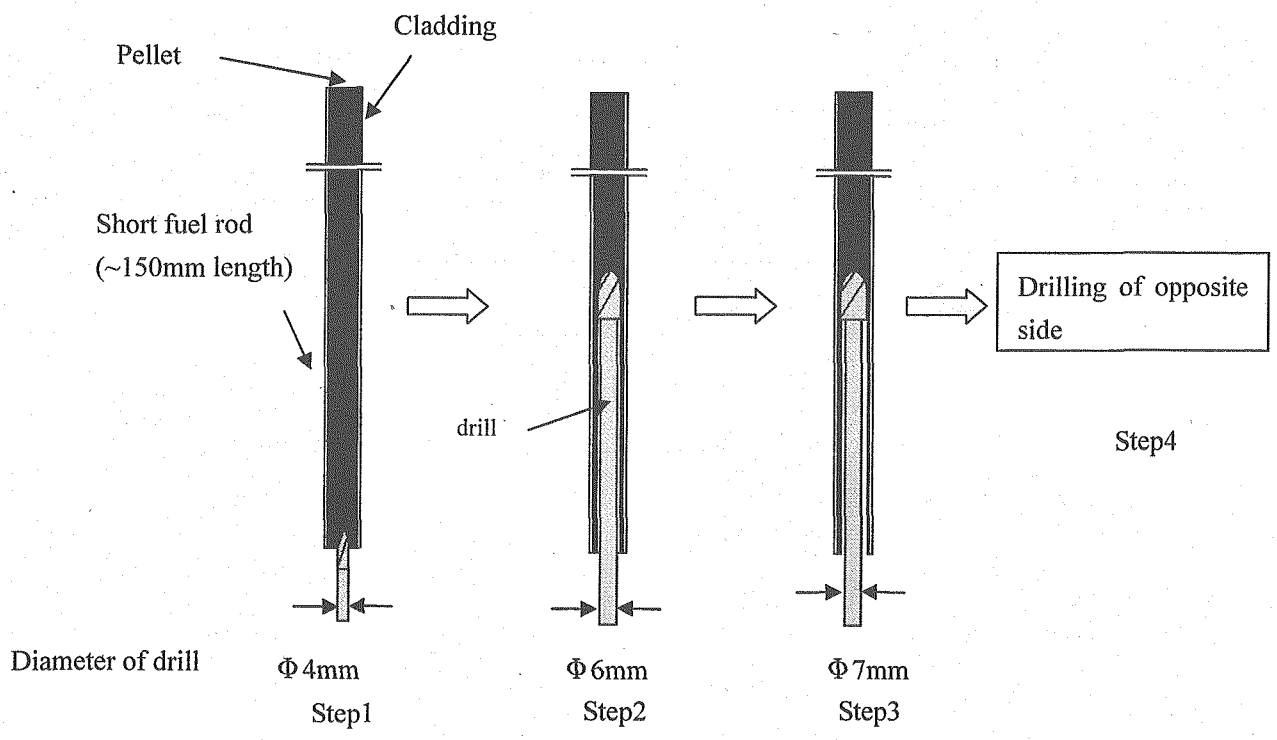

Fig.9 Drilling process.

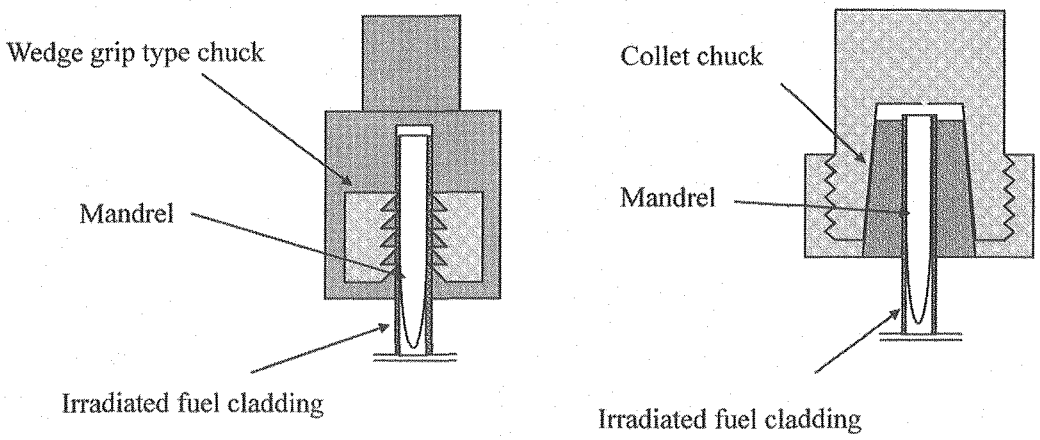

Fig.10 Clamping method.

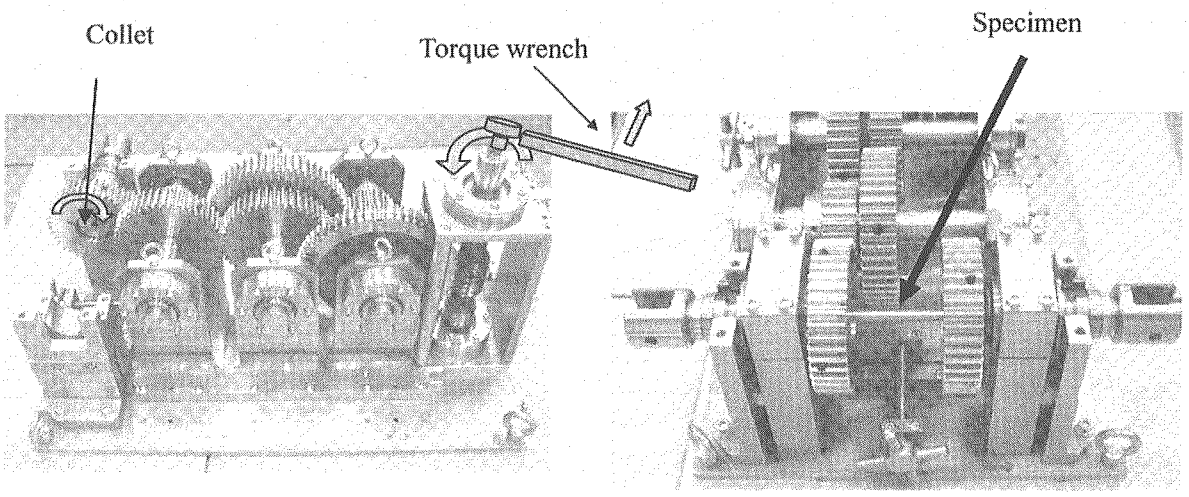

Fig.11 Appearance of clamping jig.

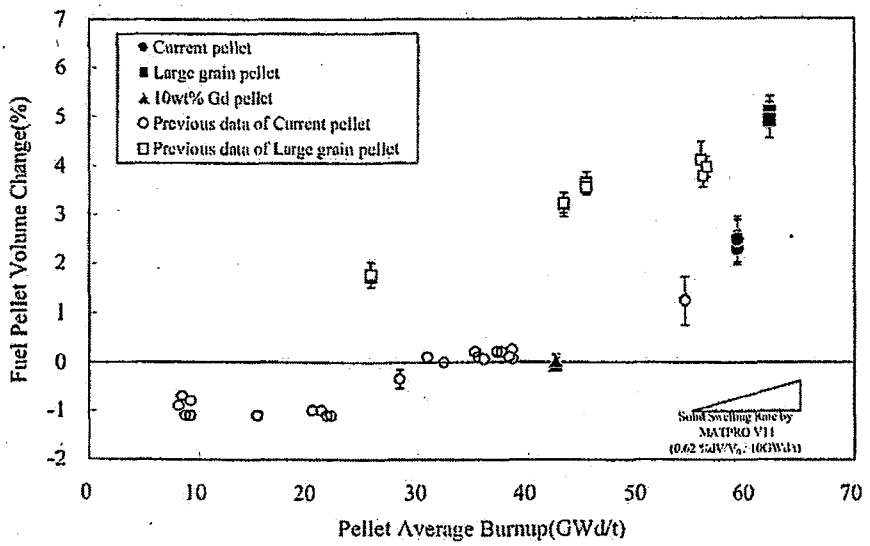

Fig.12 Fuel pellet volume change with burnup[1].

1.9 POST-IRRADIATION EXAMINATION OF HIGH BURNUP PWR FUEL

D.K. Min, Y.B. Chun, E.P. Lee, H.G. Lee, H.S. Seo, S.H. Eom and H.M. Kwon

Department of Nuclear Fuel Cycle Examination
Korea Atomic Energy Research Institute
P.O. Box 105, Yuseong, Daejeon 305-600, Korea

ABSTRACT

Since the first examination on 14x14 type PWR spent fuels in KAERI PIE facility, 1987, the comprehensive post-irradiation examination(PIE) on various type of PWR nuclear fuels with normal burnup, have been conducted to evaluate the performance and integrity at KAERI PIE facility. Recently, KAERI set up the PIE program for high burnup PWR fuels including the development of related some PIE techniques, and currently the most of the KAERI PIE works are focusing on the high burnup fuels to investigate the in-reactor performance behaviors at the high burnup region.

As a first phase of the high burnup PIE program, the comprehensive PIEs of the 12 high burnup PWR fuel rods with the advanced Zircaloy-4 clad fuels, which were irradiated at Y1 and U2 PWR nuclear power plants in Korea, were conducted, and the further PIEs of Zirlo clad high burnup fuels, including the newly developed fuels for advanced reactor by KNFC, will be continued in next decade.

This paper describes PIE facility description, the current PIE on the high burnup PWR fuels and some PIE results available up to now, and the future PIE plan for high burnup fuels.

KEYWORDS: High Burnup Fuel, Spent Nuclear Fuel, Post-Irradiation Examination

INTRODUCTION

Since the KAERI PIE facility (PIEF) was put into service in 1987, the comprehensive PIEs on various type of PWR spent fuels with normal burnup have been conducted. However, from the beginning of 1990s, the discharge burnup of PWR spent fuels in Korea had been gradually extended in order to reduce the amounts of spent fuels and increase the fuel efficiency and availability. At the end of 1990s, the high burnup fuel with long-term fuel

cycle was implemented in all of Korean PWRs.

As a part of surveillance program and the preparation of data base on in-core performance behaviors of high burnup fuel, the KAERI set up the PIE program on the high burnup fuels, which were irradiated at PWR nuclear power plants(NPPs) in Korea, including the development of some PIE technology, sponsored by national R&D program and Korea Nuclear Fuel Co (KNFC), which is Korean nuclear fuel vendor.

Currently, the most KAERI PIE works are focusing on the high burnup fuels to investigate the performance behaviors at the high burnup in detail.

FACILITY DESCRIPTION AND EXAMINATION TECHNIQUES

KAERI PIEF, which was originally designed for PWR spent fuels, consist of three pools for reception, storage and in-pool non-destructive examination (NDE), four concrete hot cells, two lead cells for the destructive examination (DE), and one steel cell for shielded scanning electron microscope [1].

PIE of PWR spent fuels includes in-pool NDE for the fuel assembly, hot cell NDE for the fuel rod and DE techniques for fuel specimen. **Fig. 1** shows the typical flow diagram of PIE on high burnup PWR spent fuels in KAERI.

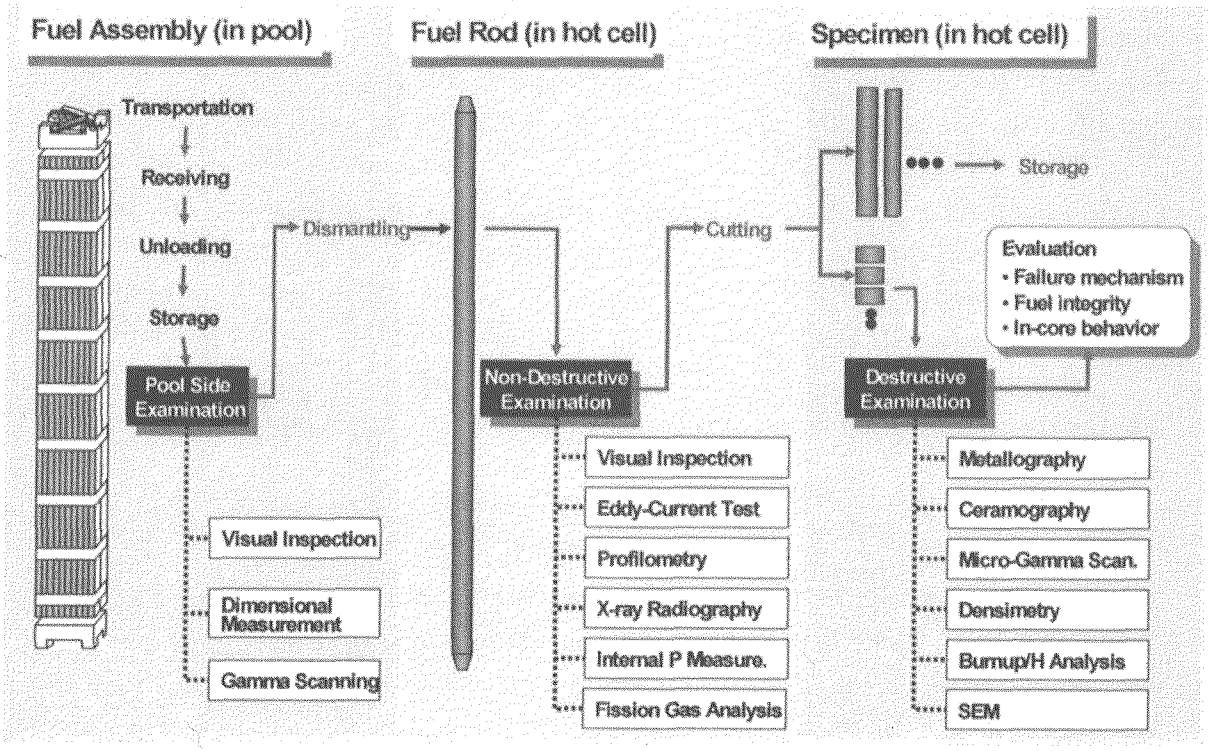

Fig. 1. Typical Flow Diagram of PIE on PWR Spent Fuel in KAERI PIEF.

PIE OF HIGH BURNUP FUEL

Development of PIE techniques

In order to evaluate the fuel performance and safety of the high burnup fuels, it is very important to get the detailed data on the clad corrosion behavior, fission gas release, and micro-structure property. For the PIE of high burnup fuels, KAERI developed the new PIE techniques and devices, such as the fission gas puncturing device, post-irradiation annealing device, shielded scanning electron microscope (SSEM), the oxide layer thickness measurement device by ECT probe, and the devices were installed in hot cells.

PIE of high burnup fuels

As a first phase of the high burnup PIE program, the comprehensive PIEs of 12 high burnup fuel rods (average burnup range of 48~57 GWd/tU), with the advanced Zircaloy-4 clad fuels (K-V5H type fuels), which were irradiated at Y1 and U2 (PWR NPPs in Korea), were conducted. The NDE items are gamma scanning, eddy current test, profilometry, oxide thickness measurement by ECT probe, fission gas and internal pressure measurement, and the DE items are metallo-/ceramo-graphy, densitometry, burnup/hydrogen analysis, SEM/EPMA, and post-irradiation annealing test. **Fig. 2** shows KAERI PIE experience and program of PWR fuels, and **Fig. 3~7** show some PIE results of high burnup fuels (K-V5H type fuels)[(1)].

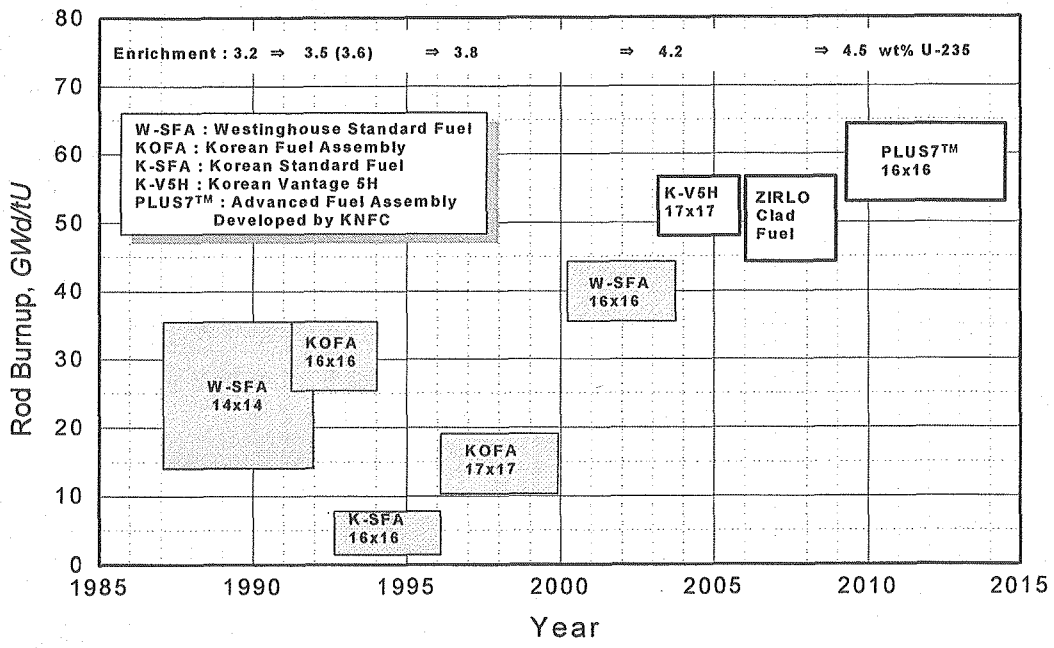

Fig. 2. KAERI PIE Experience and Program of PWR Fuels.

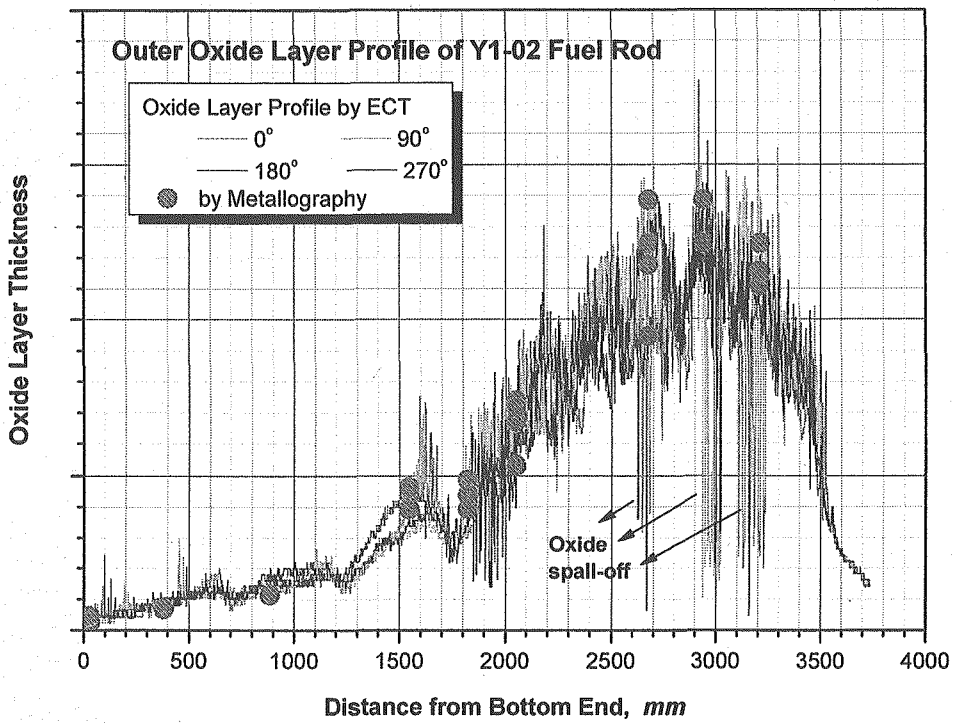

Fig. 3. Oxide Layer Profiles.

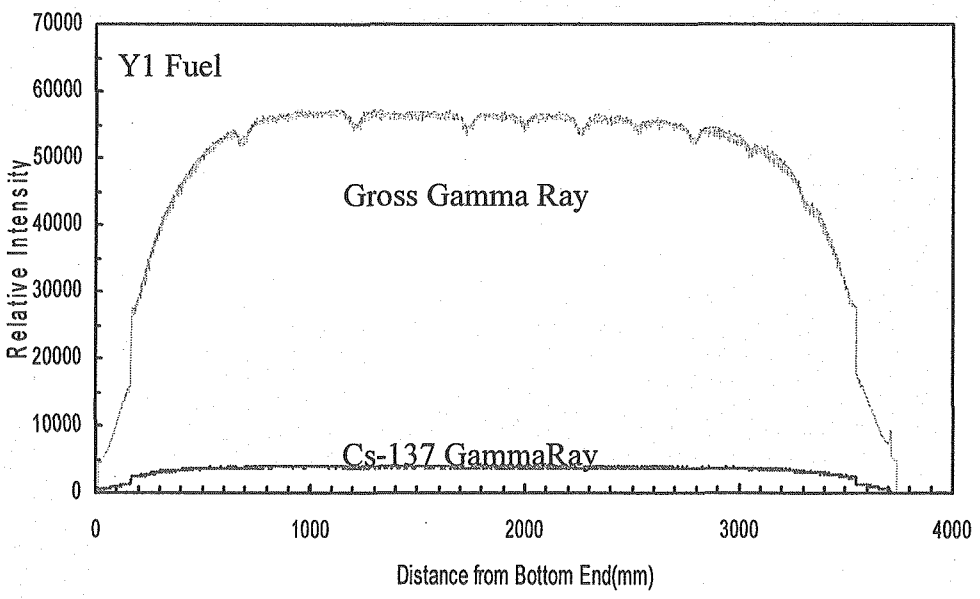

Fig. 4. Axial Gamma-Ray Profiles.

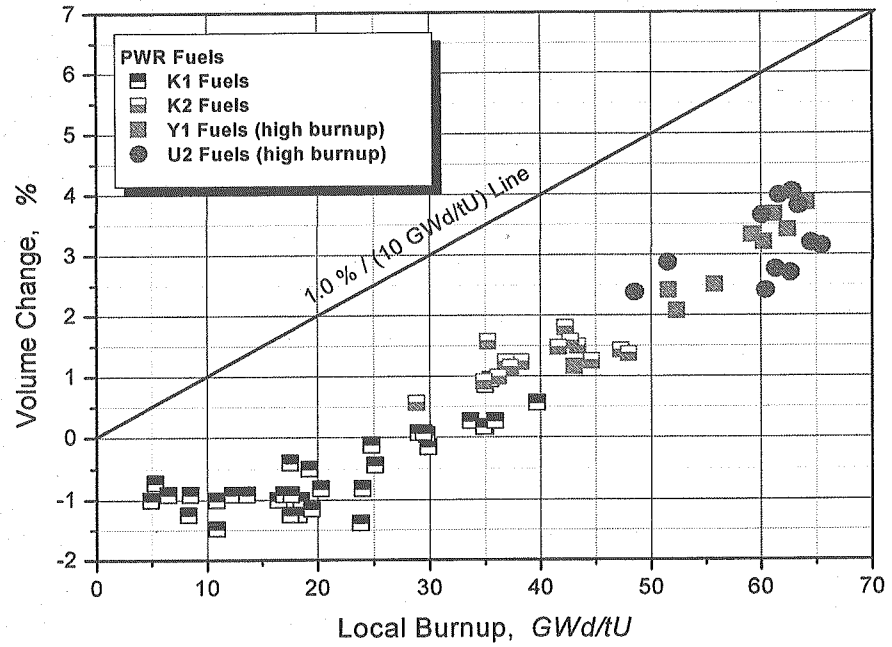

Fig. 5. Volume Change of UO_2 Pellet.

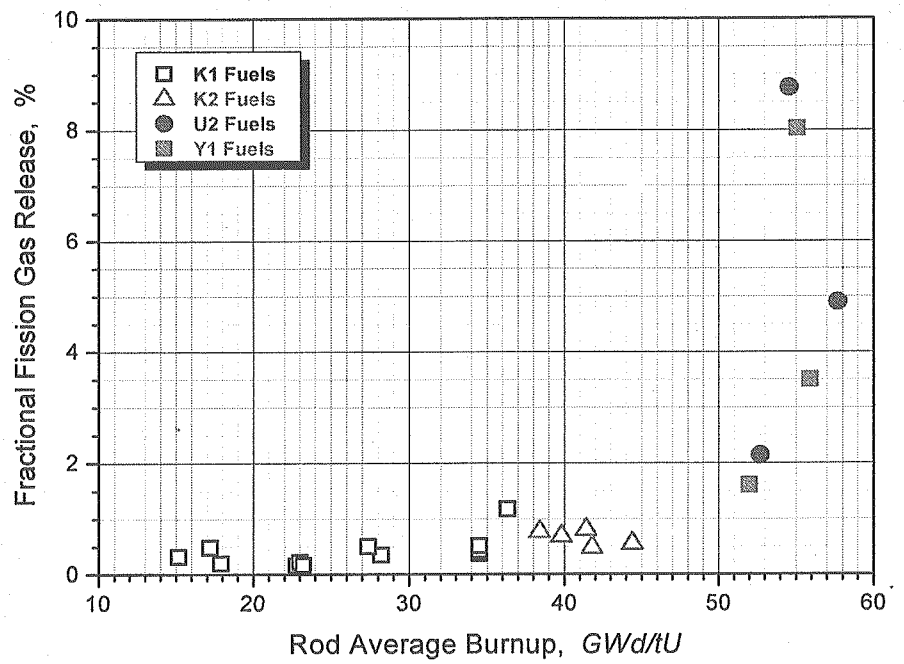

Fig. 6. Fractional Fission Gas Release.

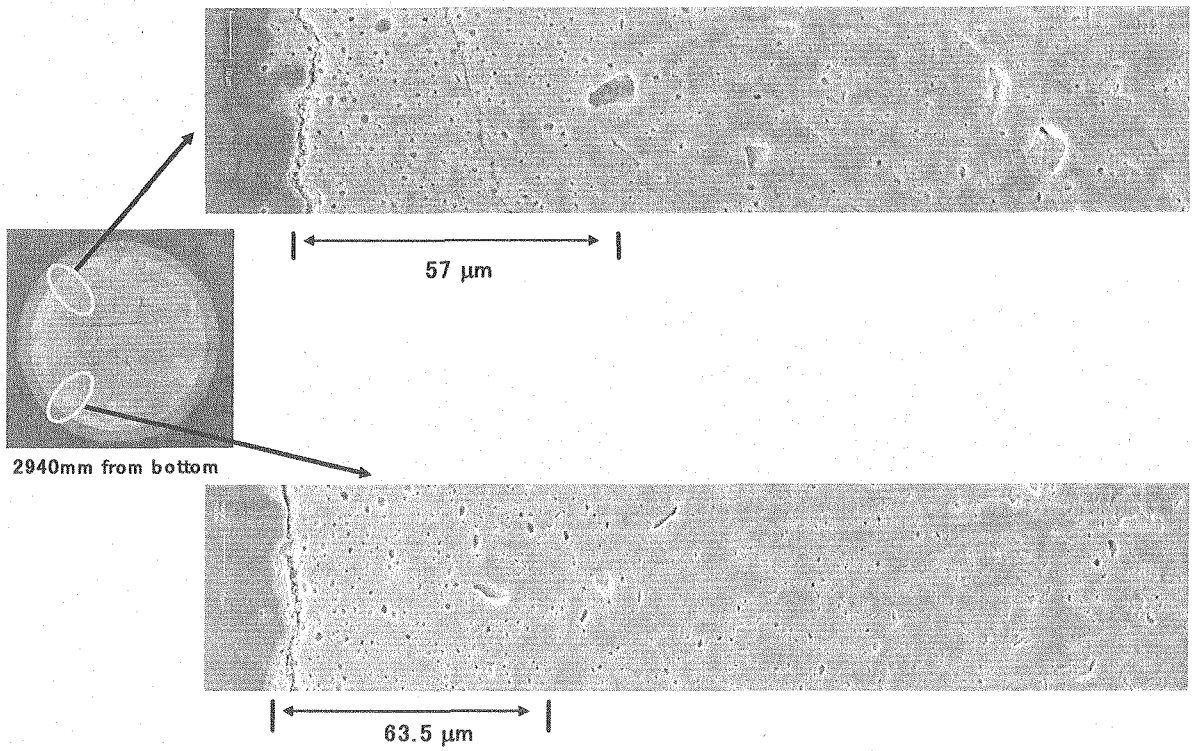

Fig. 7. SEM Images of Rim Region (unetched).

FUTURE PIE PLAN

PIEs on the Zirlo clad high burnup fuels will be carried out from the beginning of the next year, and PIEs on the PLUS7™ lead test assembly, which is irradiated at Korean NPP, are scheduled in near future [2].

REFERENCES

(1) E.K. Kim, "Activities on PIE of Nuclear Power Plant Fuels in KAERI" in the Proceedings of the 3rd JAERI-KAERI Joint Seminar on the PIE Technology, March 5-26, 1999, JAERI-Oarai, JAPAN, 10-16 (1999).

(2) K.T. Kim, "PLUS7™ Advanced Fuel Assembly Development Program for KSNPs and APR-1400" in the Proceedings of the 17th KAIF/KNS Annual Conference, April 17-19, 2002, Seoul, KOREA, 289-302 (2002).

1.10 RECENT CHEMISTRY WORK FOR THE BURNUP MEASUREMENT IN KAERI

Jong-Goo Kim, Kih-soo Joe, Jung-Suck Kim, Young-Shin Jeon, Byung-Chul Song and Sun-Ho Han

Korea Atomic Energy Research Institute, Nuclear Chemistry Research Division
150 Duckjindong, Yusung, Daejeon 305-353, Korea

ABSTRACT

Burnup data is considered to be the most basic one among all sorts of PIE data. This paper represents some chemistry works which KAERI-NCRD has performed recently for the burnup measurement of some irradiated nuclear fuels. The sample dissolution method using acids was studied for the burnup determination of irradiated U-Zr alloy fuel of SMART(System-integrated Modular Advance ReacTor). The burnup of U-Zr fuel was determined with regard to several burnup monitors ^{148}Nd, $^{145+146}$Nd, ^{137}Cs and the results were compared.

In the chemical burnup determination the reliability of chemical separation process of burnup monitor is an important point. The applicability of high performance liquid chromatography in the separation process was studied, which would give rapid and exact result compared to the conventional resin column method having been used in NCRD up to now. The column combination and elution condition in HPLC were found for the exact separation of U, Pu and ^{148}Nd as a burnup monitor.

KEYWORDS: Burnup determination, U-Zr alloy fuel, Liquid chromatography

INTRODUCTION

KAERI is developing a 330 MWt integrated reactor, SMART(System-integrated Modular Advanced ReacTor). The U-Zr alloy fuel for the SMART design with an enrichment of 8.1 w/o, which consists of 37.2 wt.% U-62.8 wt.% Zr was irradiated in High-flux Advanced Neutron Application Reactor(HANARO). And PIE for the fuel was carried out. For the chemical burnup measurement, the optimum acid condition for the complete dissolution of U-Zr alloy fuel was found. And the total burnup by using various

Nd and ^{137}Cs monitors for an irradiated U-Zr fuel was determined and compared.

It has been reported that the corrosion rate of Zr and Zr-based alloys in HNO_3 is very small because a very resistive layer of zirconium oxide prohibits a direct attack of the metal by an aggressive solution[1] and the U-Zr alloy fuel can be dissolved by applying a mixture of HF and HNO_3, NH_4NO_3 and H_2O_2, HF and KF, ethyl acetate-bromine, and HCl at 300-400^{O}C[2]. In this work, the dissolution kinematics of unirradiated U-Zr alloy were investigated regarding temperature difference and mixture ratios of HF/HNO_3.

As another chemistry work, the applicability of high performance liquid chromatography in the separation process of burnup measurement was studied, which would give rapid and exact result compared to the conventional resin column method having been used in KAERI up to now. A coupled column of reversed phase column using alpha-hydroxyisobutyric acid as an eluent used for the separation of U and Pu and cation exchange column prepared by coating 1-eiocosylsulfate for lanthanides was applied for the PWR spent nuclear fuel sample solutions.

DISSOLUTION AND CHEMICA BURNUP DETERMINATION OF IRRADIATED U-ZR ALLOY NUCLEAR FUEL

Dissolution rate measurement of unirradiated U-Zr fuel

The unirradiated U-Zr alloy samples(0.644 g) were vertically suspended in a 30 mL Teflon bottle which could be kept at the preset temperature in a water bath. The 10 mL HNO_3/HF mixtures of different concentrations were added, and the samples dipped for 10 minutes. The samples were removed and immediately rinsed with deionized water. After drying and weighing the samples then were put back into the same solution. The weight loss Δm(in g/cm^2) was determined for all the experiments.

Typical examples for such weight loss curves are given in **Figs.1-4**. The dependency of the dissolution rates on the HF concentrations in the solutions which contained U-Zr alloys is shown in **Fig. 1**. The overwhelming influence of the HF concentration on the dissolution kinematics is obvious. The weight loss rate(0.343) of the 3 M HNO_3-1 M HF at 150 min. on **Fig. 1** is similar to that(0.340) for the 3 M HNO_3-0.5 M HF, but the dissolution rate of the former is fast than that of the latter. In this experiment for the dissolution rate measurement, the pure U-Zr alloy without cladding(Zr-Nb) was used as samples, whereas the real irradiated U-Zr alloy fuel transferred for the dissolution at the hot laboratory includes the cladding and the Zr produced by fission. That is to say, the Zr portion in the real irradiated U-Zr fuel is some higher than that of the pure U-Zr alloy used in the preliminary experiments. It is therefore believed that the 3 M HNO_3-1 M HF is effective for a complete dissolution of the real irradiated fuel sample. In **Fig. 2** examples for the dependency of the weight loss curves on the HNO_3/HF mixture at different temperatures are shown. In **Fig. 3** examples for the dependency of the weight loss curve on the HNO_3/HF mixture at different

HNO_3 concentrations are shown. The overall weight loss as well as the reaction rate for the dissolution U-Zr alloys depends apparently on the HNO_3 and HF concentrations, and the temperature. Consequently, from the experimental results we chose the 3 M HNO_3-1 M HF mixture as the optimum dissolvent for a complete dissolution of all the irradiated U-Zr alloy fuel with a dissolution which continues for 8 hours.

Dissolution of irradiated U-Zr fuel

An irradiated U-Zr fuel sample(0.106 g) having been weighed exactly was placed into a 100 mL dissolution flask of the dissolution apparatus with a separatory funnel, and then 15 mL of 3 M HNO_3-1M HF without a catalyst was added dropwise, while applying a water cooling. The fuel sample was refluxed for more than 8 hours. The dissolved fuel solution was weighed and an aliquot was diluted with HNO_3(1+1) to give a ^{148}Nd concentration of about 200 ng per mL solution with the aid of an ORIGEN[3] calculation for the estimation of the nuclides content in the irradiated nuclear fuel. An aliquot of the diluted fuel solution was placed in a capped vial and transferred from the shielded facility into a glove box.

Comparison of burnup values by different method

Table 1 shows the total burnup values determined using several burnup monitors ^{148}Nd, $^{145+146}Nd$, ^{137}Cs. The total burnup value by the ^{137}Cs method was in the range of 12.2% relative difference with that by ^{148}Nd. The use of the fission product ^{148}Nd as a burnup monitor for nuclear fuel is generally accepted as a standard method since the issue of the ASTM method E 321-69[4]. The isotope ^{148}Nd was selected mainly because its fission yield is independent of the fissioning actinide, and because of its low thermal neutron capture cross section. The ^{137}Cs method(ASTM E 219-80) is based on the determination of U atom percent fission that has occurred in U fuel from analysis of the ^{137}Cs to U ratio after irradiation. The advantage of this method is its application to a dissolved fuel solution without chemical separations or elaborate preparations being necessary. However, the radioactive fission product, ^{137}Cs should be completely dissolved with the U to maintain the true ratio of the fission product ^{137}Cs to U. In addition, a quantitative analysis for the U concentration in a sample solution must be determined separately. The U determination in this work was carried out by IC-ICP-MS. The accuracy of this method is limited, not only by the experimental error of the ^{137}Cs and U, but also by the accuracy with which the fission yield and half life of ^{137}Cs known. A simplified assumption is made that the yield of ^{137}Cs from the thermal fission of ^{235}U is representative of all the fissions occurring in a nuclear fuel. The in-file decay corrections necessitate an accurate knowledge of the fuel power history. The another disadvantages of this method are found in the volatility of Cs and its precursors at fuel operating temperature, interference in counting from ^{134}Cs and ^{136}Cs, and some uncertainty in physical constants.

SEPARATION OF BURNUP MONITORS IN PWR SPENT FUEL SAMPLES BY LIQUID CHROMATOGRAPHY

Application to Synthetic solution

A stepwise gradient elution of the HiBA eluent concentration was attempted to separate the lanthanides, plutonium and uranium from a synthetic sample solution using a coupled column system as shown in **Table 2.** As a first step 0.025 M HiBA(pH 3.8) eluent flowed through both the reversed phase column and the cation exchange column in series for 6 min after an injection of the sample solution. At this step uranium and plutonium are adsorbed onto the reversed phase column and the lanthanides are retained on the cation exchange column after passing through the reversed phase column because the formed uranyl-HiBA complexes stay onto the reversed phase column during this time as shown in **Fig. 5** and the lanthanides don't make neutral complexes with HiBA at a low concentration of HiBA due to their lower stability constants[5]. As a second step 0.1 M HiBA only flowed through the cation exchange column for 19 min to separate the lanthanides individually as shown in **Fig. 6**. As for the third step 0.1 M HiBA containing 25% CH_3OH only flowed through the reversed phase column for 12 min to elute the plutonium(~ 29 min) and uranium(~ 31 min) adsorbed, and for 5 min additionally for the column washing. Finally, the eluent condition returned to the original state and was maintained for 20 min to make the system equilibrated. At this eluent condition, plutonium ions elute earlier than uranyl ions because the stability constant between PuO_2^{2+} and HiBA is higher than that between UO_2^{2+} and HiBA[6]. In **Fig. 7**, a good separation of Np, Nd, Pu and U was obtained with the retention times of 5.5 min, 14.7 min, 29.6 min and 31.1 min, respectively, from a synthetic sample solution which was prepared to be 0.12 μg /mL of Np, 0.1 ~ 0.6 μg /mL of lanthanides, 2.5 μg /mL of Pu and 250 μg /mL of U. The heavier lanthanides were not resolved individually because only an isocratic elution of 0.1M HiBA was applied in this system. However, this isocratic elution has no problem for the separation of Nd followed by the determination of ^{148}Nd by mass spectrometry for a burnup determination. In the case of the samples containing Am and Cm, these elements were reported to elute at the retention time ahead of UO_2^{2+} on the reversed phase column[7] and at the position of Eu and Gd ahead of Nd on the cation exchange column[8], respectively, using the HiBA eluent. Accordingly, based on the results studied until now the actinides such as Np, Am and Cm have been proved not to interfere for the separation of Nd, Pu and U from the spent fuel sample solutions by a coupled column liquid chromatography. A full procedure for the separations was finished within about 40 min of the running time. Especially, in this study the stepwise gradient elution was selected rather than a linear gradient elution because this elution technique gives a better reproducibility for the retention time of a burnup monitors even though the linear gradient elution shows a better resolution for an individual separation of the total lanthanides.

Application to PWR spent nuclear fuel sample

In **Fig. 8** the spent nuclear fuel sample solution was applied for the separation of Nd, Pu and U. The contents of ^{148}Nd, Pu and U were determined by an isotope dilution mass spectrometry after separation and collection. Especially, more attention was paid in this work to get rid of the memory effect caused by a high concentration of uranium matrix by flowing an excess amount of the eluent prior to another sample injection. Any chromatographic problem associated with an injection volume was not observed up to 1 mL of the sample solution in which uranium concentration was about 150 μg/mL. The amount of Nd(^{148}Nd), Pu and U separated were determined by mass spectrometry and the burnup was calculated using equation (3). Where, *BU* is the burnup(atom % fission), *N* is the atom number of the burnup monitor(^{148}Nd), *Y* is the fission yield of the burnup monitor(^{148}Nd) and *HE* is the atom

$$BU = \frac{(N/Y)100}{(HE + N/Y)} \quad \text{.....(3)}$$

number of the heavy elements(Pu and U). In **Table 3** the burnup data determined by this method is shown and the results showed a good agreement to within 1 % of a difference between this method and the conventional anion exchange method.

SUMMARY

The irradiated U-Zr alloy fuel can be dissolved in a mixed acid condition of 3 M HNO_3 and 1 M HF at 90^{O}C for 8 hours under a reflux. The burnup value by the Cs-137 method was in the range of 12.2% relative difference with that using ^{148}Nd as a fission monitor.

A coupled column liquid chromatography system was successfully applied for the separation of burnup monitors such as lanthanides and actinide elements in spent nuclear fuel sample solutions with a short separation time by a single injection of the sample solution. This separation method also showed a good reliability and much convenience when compared to a conventional anion exchange method for burnup determinations.

REFERENCES

(1) Z. Goncalves and H. Munzel, J. Nucl. Mater. 170 (1990) 261
(2) H. Sorantin, "Determination of Uranium and Plutonium in Nuclear Fuels", Kernchemie in Einzeldarstellungen; Vol. 5, Verlag Chemie, Germany (1975)
(3) S. G. Ro, J. M. Park, D. K. Min, P. I. Choi and H. S. Shin, *KAERI/PIED/note-001/87* (1987).
(4) American Society for Testing and Materials Standard Method E 321-69, (1969) 1045
(5) Martell, A. E.; Smith, R. M. Critical Stability Constants: Other Organic Ligands; Plenum Press, NY and London, Vol 3 (1979) 37
(6) Perrin, D. D. Stability Constants of Metal-Ion Complexes, Part B Organic Ligands; Pergamon Press: Oxford UK (1979) 188
(7) Elchuk, S.; Burns, K. I.; Cassidy, R. M.; Lucy, C. A. J. Chromatography 558(1991) 197-207
(8) Cornelius The Chemistry of the Transuranium Elements; Verlag Chemie GmbH, Germany Vol 3 (1971) 217-229

Table 1. Total Burnup in Atom % Fission Determined by Chemical Methods for an Irradiated Fuel Sample

Isotope	F_T(Atom % Fission)	Difference
Nd-148(C)	2.1720±0.0195	1.000
Nd-(145+146)	2.2389±0.0202	1.031
Nd-(143+144)	2.0817±0.0187	0.958
Nd-Total	2.1623±0.0195	0.995
Nd-148(NC)*	2.3597±0.0021	1,086
Cs-137	2.4375±0.1414	1.122

Total : 143+144+145+146+148+150

* calculated without correction for excess Nd-148 produced from capture on Nd-147

Table 2. Stepwise gradient elution for the separation of Pu, U and lanthanides from the spent nuclear fuel sample solution

Time(min)	Eluent	RPC	CEC
0-6	0.025M HiBA, pH 3.8	adsorption of Pu and U	adsorption of lanthanides
6-25	0.1 M HiBA, pH3.8	-	separation of lanthanides
25-37	0.1 M HiBA-25% CH_3OH, pH3.8	elution of Pu and U	-
37-42	0.1 M HiBA-25% CH_3OH, pH3.8	column washing	-

* RPC: reversed phase column(LC-18, 15cmx0.46cm, 5mm particle size),

**CEC: cation exchange column(1-eicosylsulfate coated onto LC-18)

Table 3. Burnup data for the spent nuclear fuel samples determined by coupled column liquid chromatography

Unit : MWD/MTU

Method Sample	Coupled Column System(A)	Anion Exchange Chromatography(B)	Difference 100(A-B)/B
J14E11(No 4)	35897.3±707	36200	- 0.8 %
J14E11(No 7)	36334.7	36200	+ 0.4 %
J14E11(No 9)	39037.1	39000	+ 0.1 %

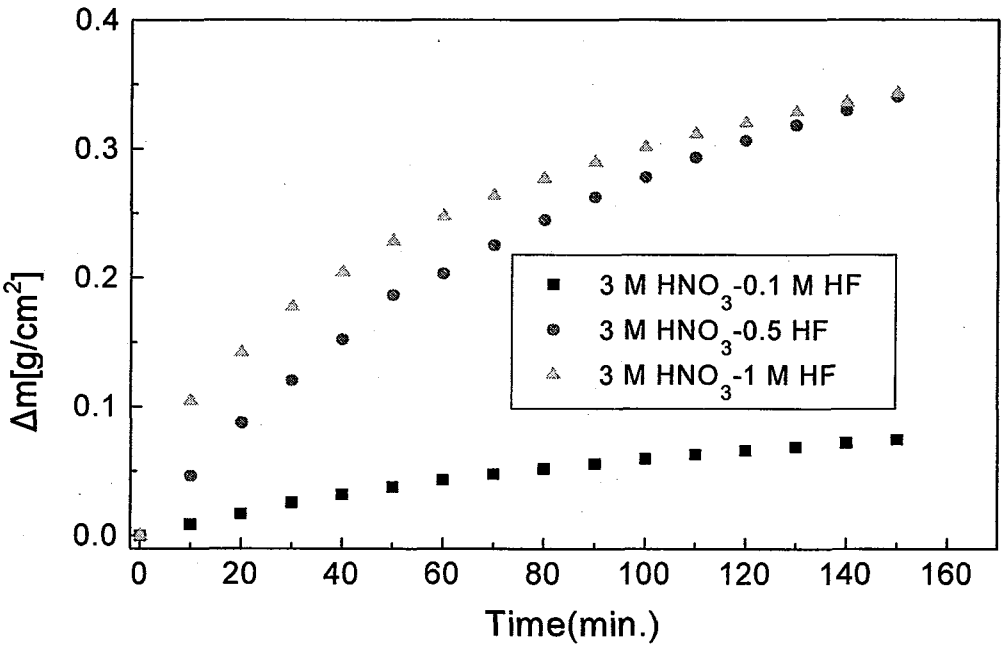

Fig. 1. Weight Loss Curves for the Reactions with Initial HF Concentrations of 0.1, 0.5 and 1 mol/L in 3 M HNO_3 at a Temperature of 30 ^{O}C.

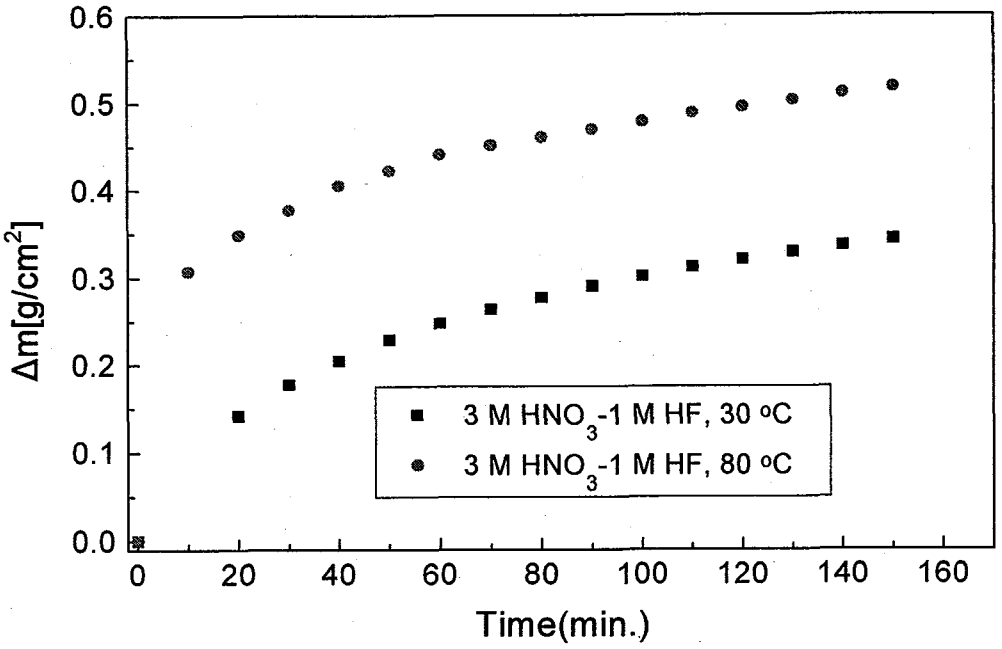

Fig. 2. Weight Loss Curves for the Reactions with Initial HF Concentration of 1.0 mol/L in 3 M HNO_3 at Different Temperatures of 30 ^{O}C and 80^{O} C.

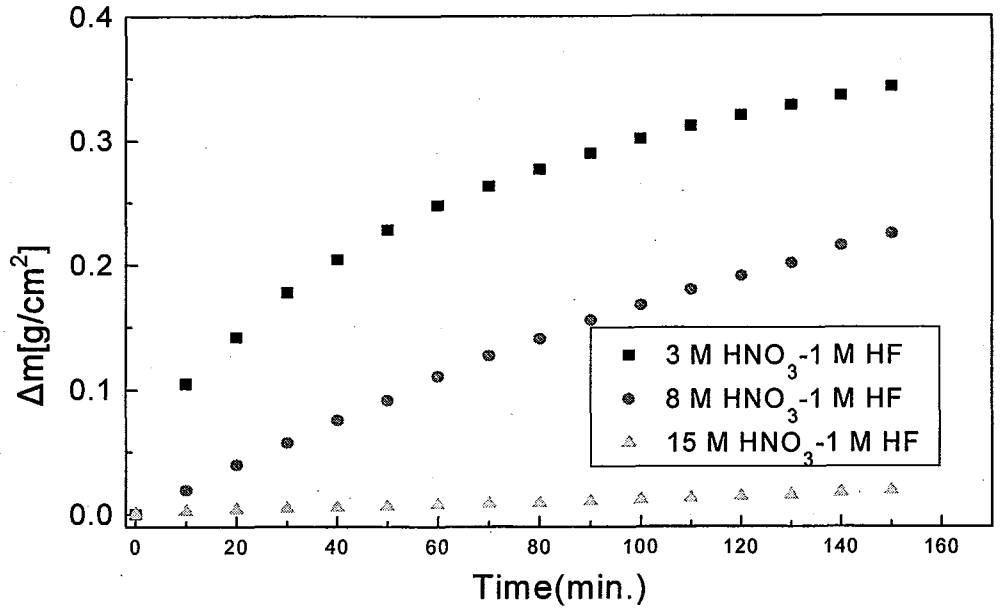

Fig. 3. Weight Loss Curves for the Reactions with Initial HF Concentration of 1.0 mol/L in 3 M, 8 M and 15 M HNO_3 at a Temperatures of 30 ^{O}C.

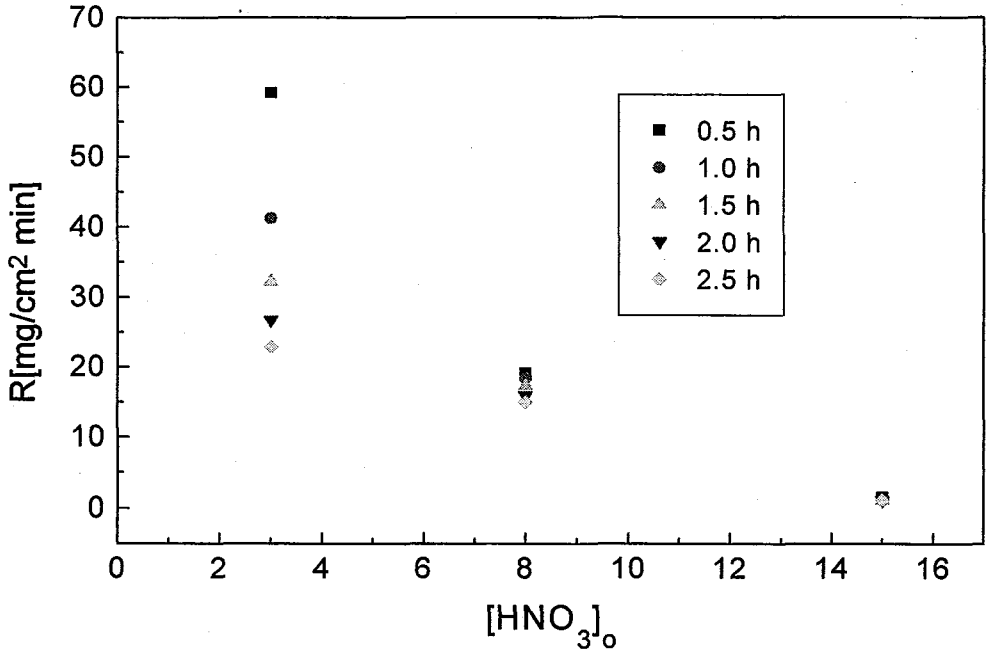

Fig. 4. Dependence of the Reaction Rate R for the Reactions with Initial HNO_3 Concentrations of 3, 8 and 15 mol/L in 1 M HF at a Temperature of 30 ^{o}C.

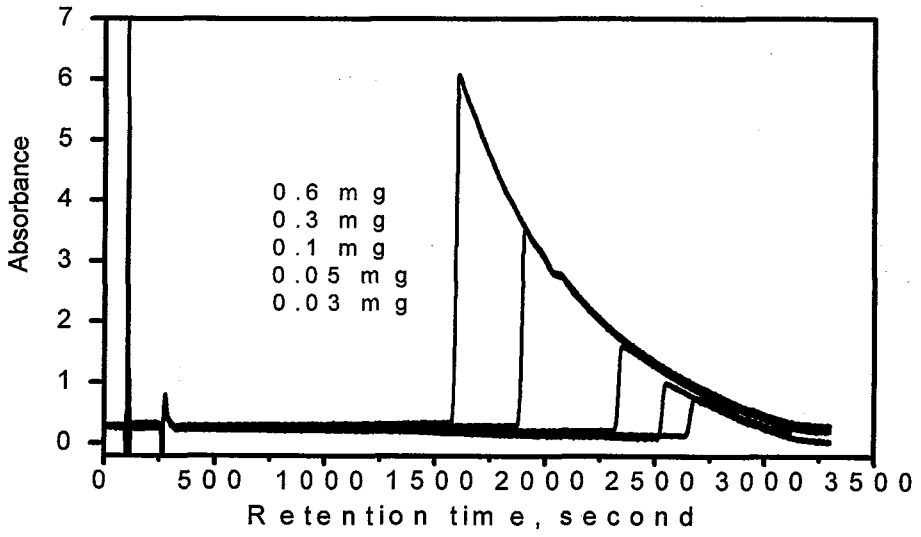

Fig. 5. An overlay of the chromatograms of uranium on the reversed phase column. column; LC-18(15cmx0.46cm, 5mm particle size), eluent; 0.025M HiBA, pH 3.8, flow rate; 1 mL/min., sample injected; 100 mL of U in 0.1M HiBA matrix at pH ~3, detection; 414nm.

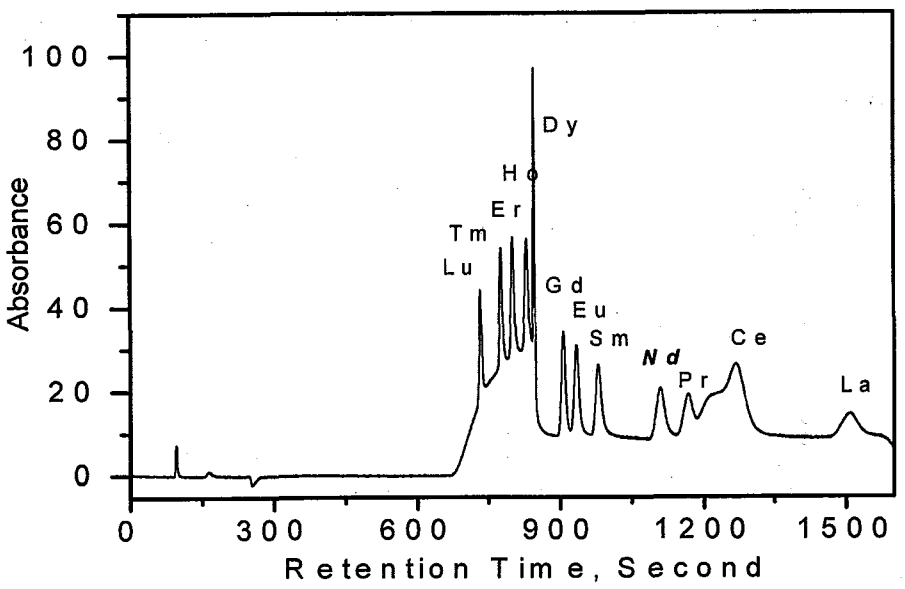

Fig. 6. Chromatogram of lanthanides separated by a stepwise gradient elution of HiBA eluent. Sample injected; 20 μL of 2 μg/mL each lanthanide, flow rate; 1 mL/min, gradient condition; same as in Table 2.

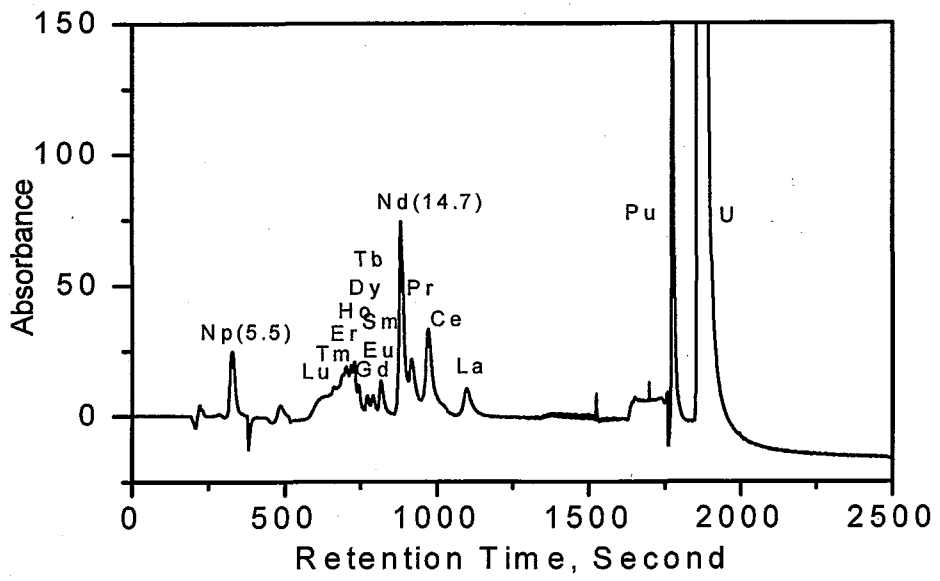

Fig. 7. Separation of Np, Pu, U and lanthanides in synthetic sample solution by stepwise gradient elution. Sample: U 250, Pu 2.5, Np 0.12, La 0.3, Ce 0.6, Pr 0.3, Nd 1, Sm 0.2 Eu 0.1, Gd 0.1, Tb 0.1, Dy 0.1, Ho 0.1, Er 0.1, Tm 0.1 and Lu 0.1 μg/mL,
gradient condition; same as in Table 1, sample injection; 100 μL,
flow rate; 1 mL/min., detection; 658 nm after post-column reaction with Arsenazo III.

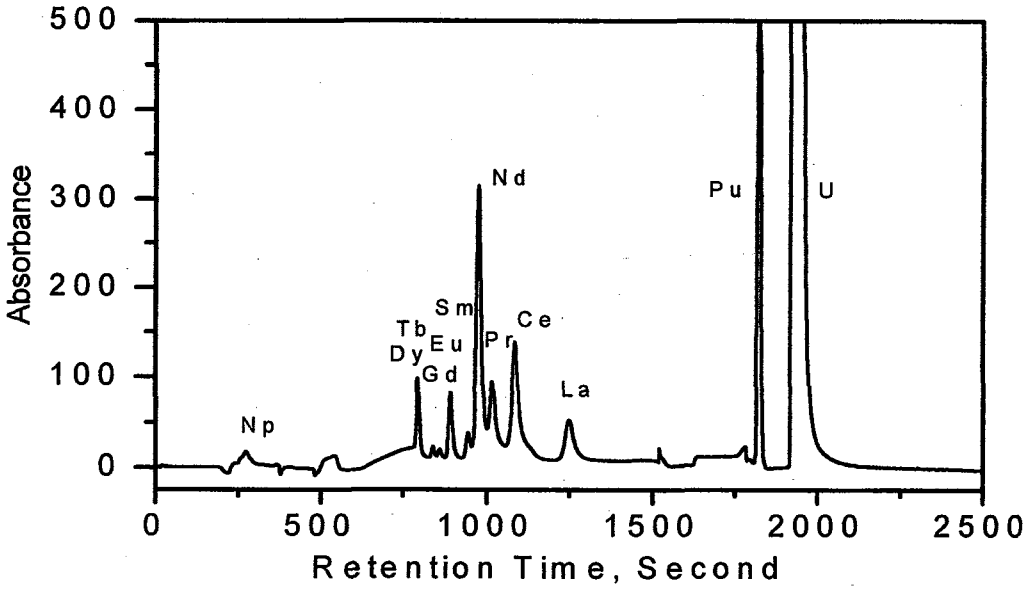

Fig. 8. Separation of Nd, Pu and U in the spent nuclear fuel sample solutions for burnup determination using coupled column liquid.
Elution condition; same as in Table 1.

Session 2

Development of Irradiation and PIE Technologies

Chairs:

【2.1 ~ 2.8】

Yong Bum Chun (KAERI) and Yoshinori Matsui (JAEA)

【2.9 ~ 2.15】

Young Hwan Kang (KAERI) and Hiroaki Kurishita (Tohoku Univ.)

This is a blank page.

JP0650422

2.1 DEVELOPMENT OF IN-PILE CAPSULE FOR IASCC STUDY AT JMTR

Yoshinori Matsui[1], Satoshi Hanawa[1], Hiroshi Ide[2], Masahiro Tobita[2], Jinsaku Hosokawa[2], Yuichi Onuma[2], Kazuo Kawamata[2], Yoshiharu Kanazawa[2], Shigemi Iwamatsu[2] and Jun-ichi Saito[2]

1: Technology Development Department
2: Department of JMTR
Oarai Research and Development Center, Japan Atomic Energy Agency
Oarai-Machi, Higashi-ibaraki-Gun, Ibaraki-Ken 311-1393 Japan

Hirokazu Ugachi and Takashi Tsukada

Nuclear Fuel and Materials Division
Nuclear Science and Engineering Directorate, Japan Atomic Energy Agency
Tokai-Mura, Naka-Gun, Ibaraki-Ken 319-1195 Japan

ABSTRACT

Irradiation assisted stress corrosion cracking (IASCC) caused by the simultaneous effects of radiation, stress and high temperature water environment is considered to be one of the critical concerns of in-core structural materials not only for light water reactors (LWRs) but also for water-cooled fusion reactors. In the research field of IASCC, post-irradiation examinations (PIEs) for irradiated materials have been mainly carried out, because there are many difficulties on SCC tests under neutron irradiation environment. Hence we have embarked on a development of the test techniques for performing the in-pile SCC tests.

In this paper, we describe the developed several in-pile test techniques and the current status of in-pile SCC tests at Japan Materials Testing Reactor (JMTR).

KEYWORDS: IASCC, crack growth test, crack initiation test, examinations under irradiation, capsule assembly, remote handling, remote welding, JMTR

INTRODUCTION

Irradiation assisted stress corrosion cracking (IASCC) occurs in the core under simultaneous effects of radiation, stress and high temperature water environment in water reactors. In general, IASCC can be reproduced on the materials irradiated over a certain threshold fluence level of fast neutron by the post-irradiation examinations (PIEs), therefore in-pile and out-of-pile SCC tests must be carried out in high temperature water using these irradiated materials with loading. In the research field of IASCC, PIEs for irradiated materials have been mainly carried out, because there are many difficulties on SCC tests under neutron irradiation. In-pile SCC test is important to investigate IASCC mechanism for actual core materials, but it is rarely carried out without IASCC study on OECD Halden reactor project.

For in-pile tests, a capsule assembly technique in the hot cell[*1] and a loading technique under irradiation are very important. The capsule assembly technique is indispensable both for inserting the irradiated specimens into the capsule and for welding the inner and outer tubes by remote handling with manipulators.

Therefore the design of the capsule to set irradiated specimens in the capsule must have the device to make capsule assembly easily and weld the joint parts of inner and outer tube by remote handling in hot cell[(1)]. Moreover, the loading equipment must be developed to carry out in-pile SCC tests (a crack growth test and a crack initiation test) for this study. And the equipment was checked to the control of the load examination at out-of-pile test. In addition, the pressure inside the capsule and the flow condition around specimens were checked using a mock-up capsule. These techniques for in-pile test were established in 3 years.

OUTLINE OF CAPSULE FOR IN-PILE SCC TEST

At JMTR, in-pile crack growth and crack initiation tests have to perform at irradiation holes which are comparable neutron flux for core structural materials of BWRs. The following technical subjects for these in-pile tests have to be confirmed to investigate the in-pile SCC study.

The contents are (1) capsule design, (2) geometry of test units for installing an irradiated specimen easily using remote handling, (3) estimation of irradiation temperature, (4) remote welding technique for the capsule assembly, (5) loading technique under irradiation, (6) monitoring technique for crack length and crack initiation, (7) measurement of flow rate (flow velocity) in capsule and so on.

The features of the capsule design are as follows: (1) Since the gamma heating rate of the irradiation hole is about 0.8 W/g (by type 316 stainless steel (SS)), the structure of irradiation capsule is adopted the double tube design of adiabatic layer between an

inner tube and an outer tube for prevention of radiation. (2) The test unit is adopted an open-type structure for installing irradiated specimen easily. And the design adopts a partition pipe system of capsule assembly. Water flows downstream outside of the partition pipe and turn up on a lower plug of the capsule, and then flows upstream around of the specimens. The concept of the capsule for in-pile test is shown in **Fig.1**. (3) Because of irradiation space, loading capacity and influence of irradiation for capsule components, a loading method using metal bellows is adopted.

Using SATCAP-C of heat calculation code[2),(3)], irradiation temperature was confirmed to be within the target temperature in the case that a vacuum pressure of adiabatic layer between outer and inner tubes was at 100 Pa. The calculation results of the irradiation temperature are shown in **Fig.2-1** and **Fig.2-2**. Techniques for connection of the capsule bodies are by welding and a mechanical joint. Both techniques are developed in parallel as a technical development item. Our Hot lab division takes charge of a welding technique[(1)], and Irradiation Division I takes charge of a mechanical joint technique using metal O-ring. Some of out-of-pile tests were carried out and both connecting techniques were established. Water flow in the capsule was verified using a mock-up capsule.

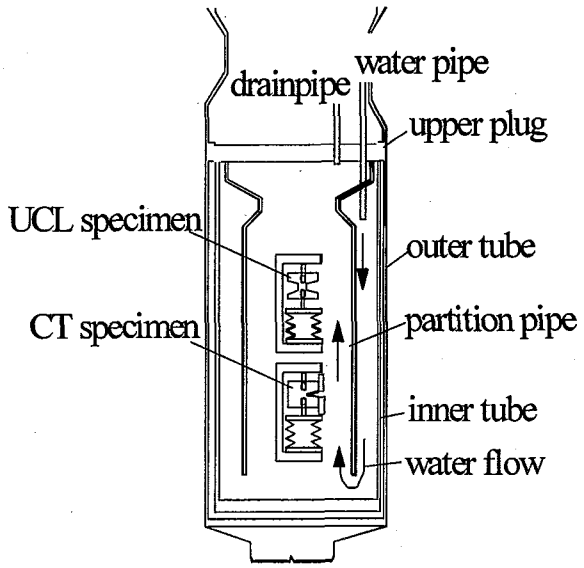

Fig.1 Conceptual structure of capsule.

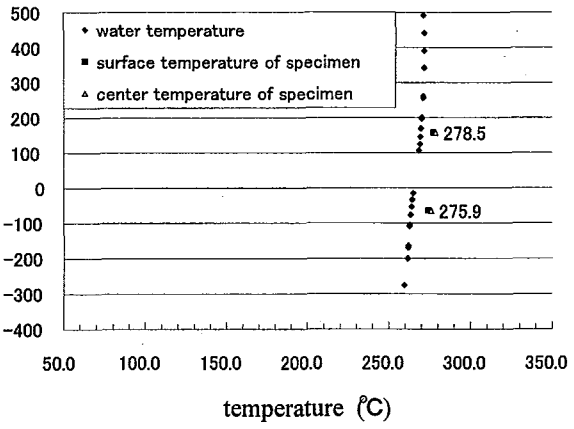

Fig.2-1 Temperature calculation in the capsule for the crack growth test.

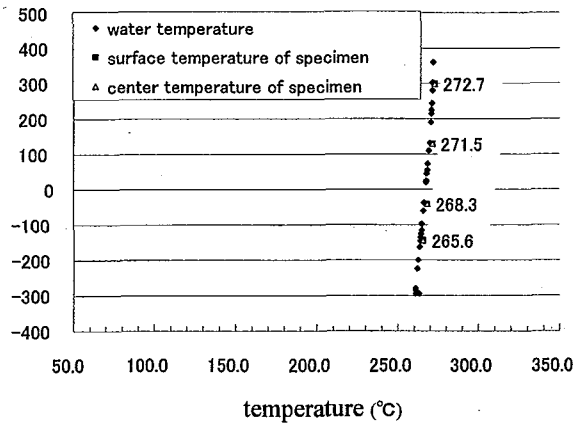

Fig.2-2 Temperature calculation in the capsule for the crack initiation test.

A loading method using metal bellows is adopted for in-pile SCC test at JMTR. The load for specimen must be controlled by a pressure difference between gas inside a bellows and water outside a bellows in the irradiation capsule for IASCC study. Division of Nuclear Energy System takes charge of development of the load control system, and the detection technique for crack initiation and the potential drop method for crack growth measurement were verified on out-of-pile tests.

DEVELOPMENT OF CONNECTION METHODS FOR CAPSULE BODY

Welding method

A remote welding technique was established for stainless steel tubes with 40mm of outer diameter and 1.5mm of thickness in the Hot Lab Division, but welding for outer tube of capsule (type 316 SS tube with 60mm of outer diameter and 4mm of thickness) was very difficult. Therefore capsule body rotation technique was adopted instead of welding torch rotation technique. The outer diameter of welding point was changed to 54mm, and the thickness of the tube was changed from 4mm to 3mm. By changes of size of the capsule, difficulties for remote welding technique could be solved. The welding method of inner and outer tubes by remote handling is shown in **Fig.3**. The detailed paper for remote welding technique is reported in this seminar [1].

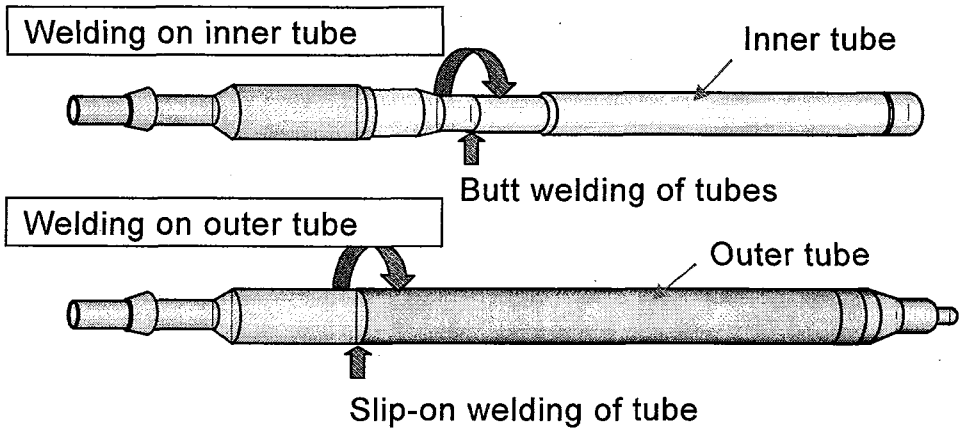

Fig.3 Welding method of inner and outer tubes by remote handling.

Mechanical joint method

For the mechanical joint system using a metal O-ring, the thickness of joint part must be larger than the width of O-ring. Moreover, outer diameter of the capsule was

needed to make less than 68mm for diameter of insert nozzle on the reactor cover, and inner diameter of the inner tube was needed to make 48mm larger of diameter of the partition tube. Therefore, a size of metal O-ring was fixed by inner diameter of the capsule tube and strength of fixing nut in the mock-up test unit. The cross section of the mock-up test unit is shown in **Fig.4-1**.

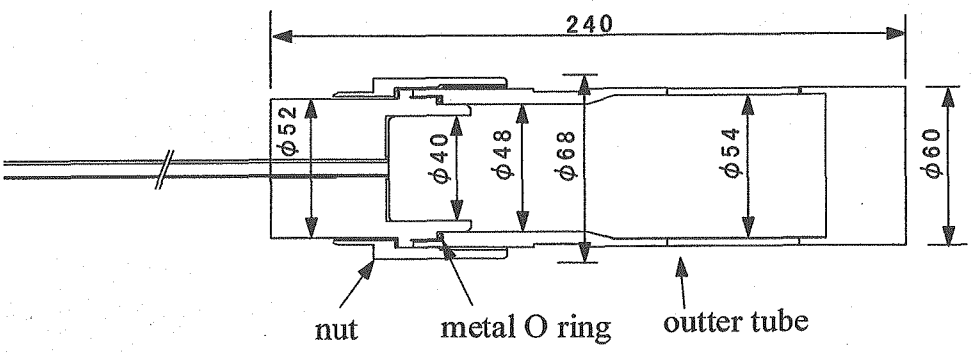

Fig.4-1 Cross section of the mock-up test unit.

The mock-up tests were carried out for the resisting pressure examination of 15MPa, the helium leak examination, the thermal cycle examination, the vibration examination and the drop test, and the structural integrity of this unit was confirmed in these mock-up tests. The resisting pressure examination for the mock-up test is shown in **Fig.4-2**.

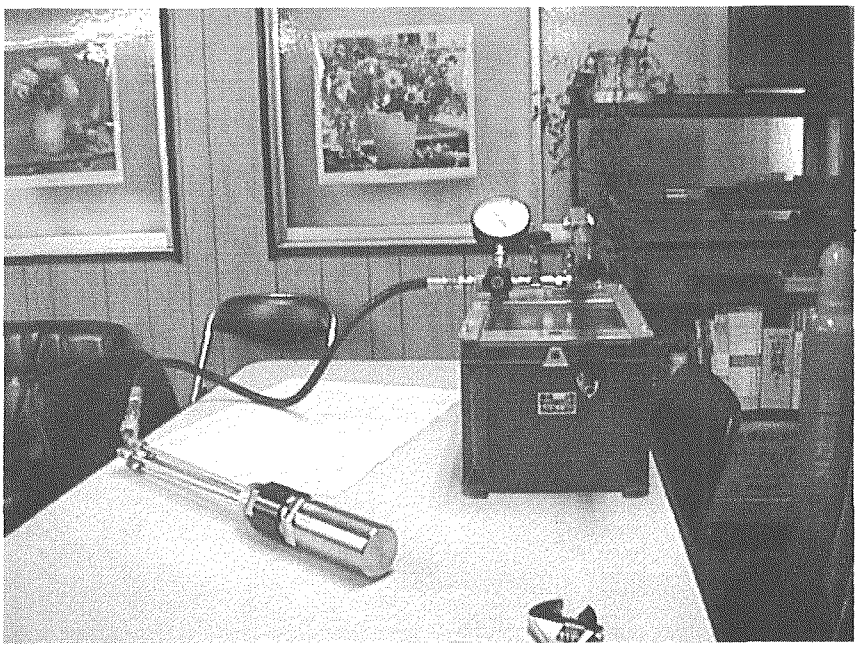

Fig.4-2 Resisting pressure examination for the mock-up test.

On the other hand, there is a problem in the mechanical joint method. A vacuum pipe for controlling vacuum pressure of heat insulation layer between an inner tube and an outer tube cannot be set up to the capsule. Therefore in the case of using mechanical joint method, an inner tube and an outer tube have to be united, and the heat insulation layer must be confined to high vacuum pressure. Because the capsule design is needed high reliability for the first in-pile SCC tests, the remote welding method is decided to adopt in the in-pile SCC capsule.

DEVELOPMENT OF LOAD CONTROL TECHNIQUE BY BELLOWS

Load control method by bellows

The load control system for in-pile SCC tests must be deal with helium gas outside bellows in the capsule. To reduce fluctuation of gas pressure, some capillary tubes with less than 1mm of inner diameter and several meters length are adopted for the load control device. The responsibility for the simulated pressure signal was checked in the first step of out-of-pile tests. At the second step, the responsibility and the durability were confirmed for the pressure of the high temperature water of the loop

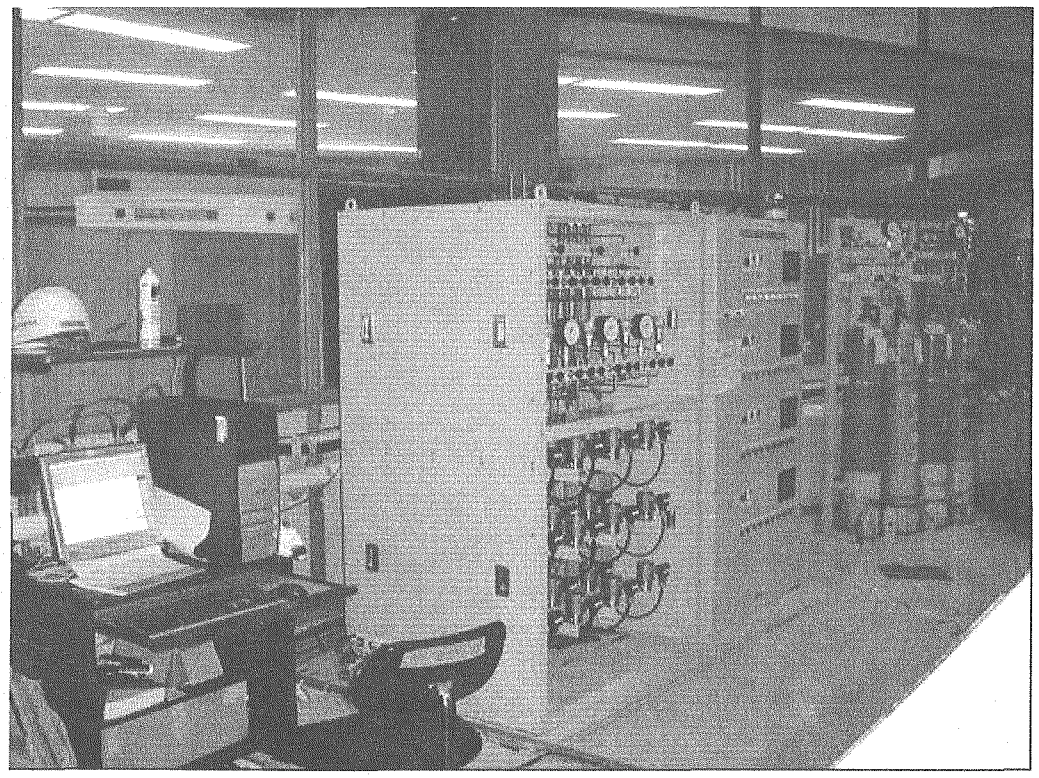

Fig.5 Load control device.

facility at JMTR. Based on these test results, a new load control device for four in-pile test capsules was made to refer the mock-up device, and responsibilities under several pressure conditions were checked using the mock-up capsule. The load control device is shown in **Fig.5**.

In-pile test unit

The design of in-pile test unit must be considered that irradiated specimen can be installed easily in hot cell and it has sufficient strength for applied load during in-pile SCC test. Therefore, the geometry was open-type to install the specimen easily and its strength was verified by 3-dimensional stress analysis. The characteristic of bellows was checked using the relation between pressure difference between inside and outside bellows and applied load. The out-of-pile test was performed using this in-pile test unit and specifications were confirmed on crack growth test and the crack initiation test. Moreover, its normality was checked using a mock-up capsule under the up-and-down pressure and constant pressure conditions at room temperature. The in-pile test unit for the crack growth test and the crack initiation test are shown in **Figs.6-1** and **6-2**, respectively.

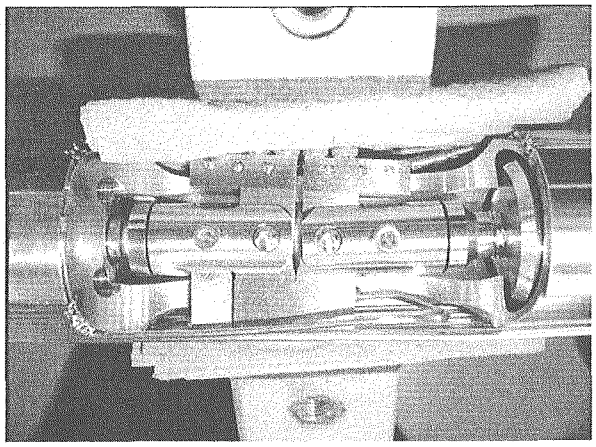

Fig.6-1 In-pile test unit for the crack growth test.

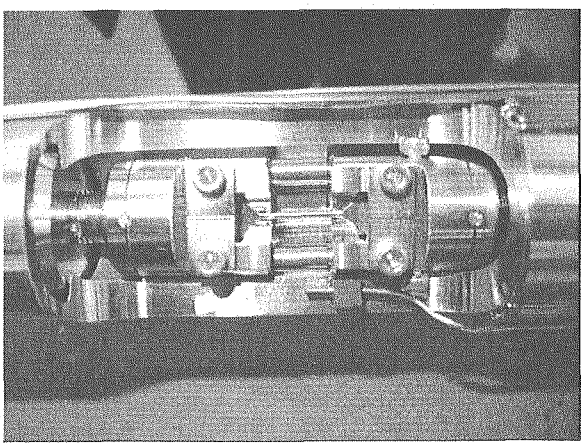

Fig.6-2 In-pile test unit for the crack initiation test.

MOCK-UP TEST OF DEMONSTRATION CAPSULE

Installing techniques of specimens were verified using unirradiated thermally sensitized specimens. Moreover, capsule assembling technique in hot cell and insert technique to JMTR reactor core were confirmed using a demonstration capsule. The schematic diagram of the mock-up capsule is shown in **Fig.7**. To evaluate specimen

temperature during in-pile test exactly, fundamental data were obtained by measuring specimen temperature directly.

In the case of crack growth test[4], the value of potential drop difference increased slightly, it seemed that the crack on the CT specimen grow up during in-pile SCC test (**Fig.8**). In the case of crack initiation test[5], the electric resistance as the rupture signal of the UCL specimen was changed after about 35 hours from loading start (**Fig.9**). The technical prospect of in-pile SCC test could be acquired by the irradiation of the demonstration capsule.

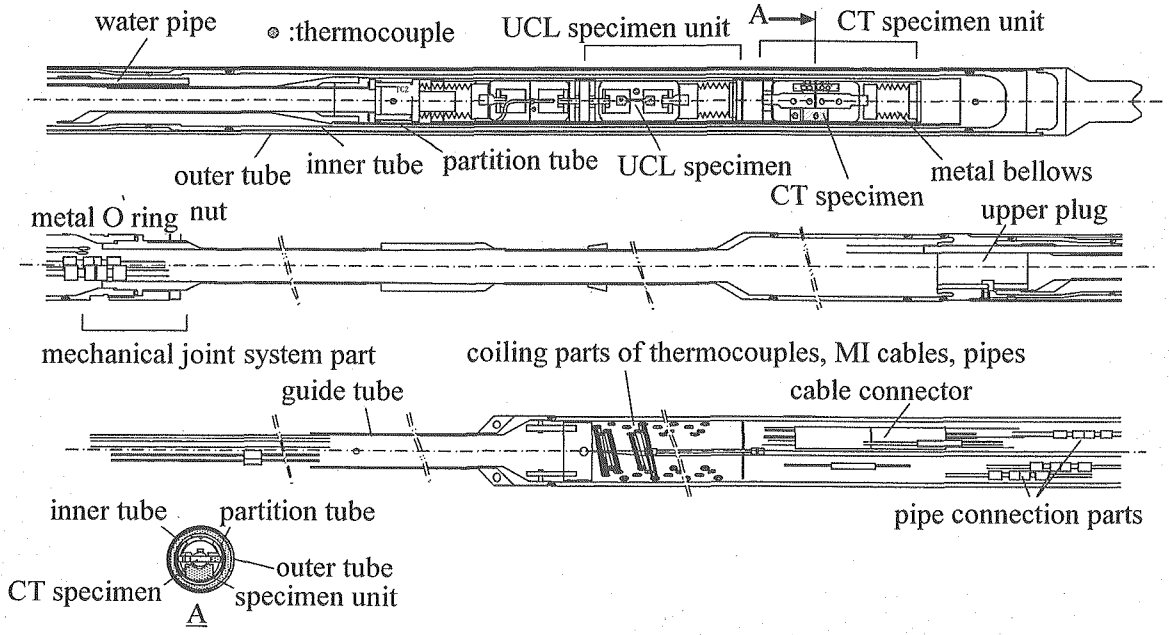

Fig.7 Schematic diagram of mock-up capsule.

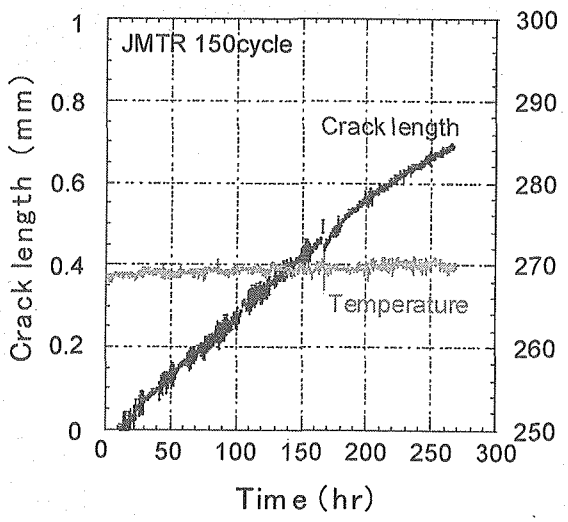

Fig.8 Result of potential drop.

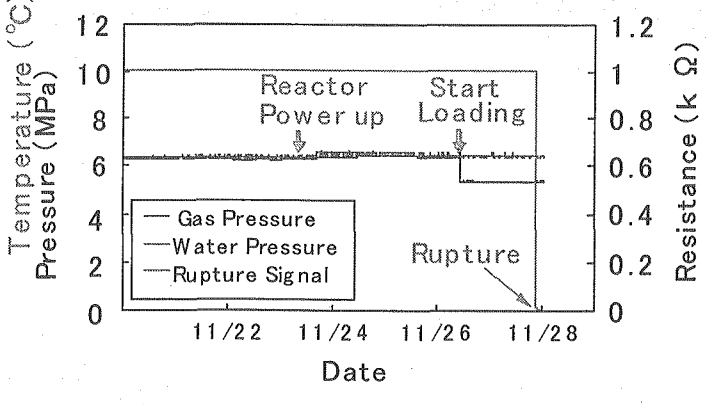

Fig.9 Result of rupture signal.

IN-PILE CAPSULE

Irradiated specimens were installed in the in-pile capsule by remote handling, and inner and outer tubes of the capsule were assembled using the remote welding technique. Then, several cables, water pipes, bellows gas pressure pipes and a guide tube were jointed to capsule bodies on the water canal of Hot Laboratory at JMTR. Four capsules for in-pile SCC tests were completed, and they were inserted in the JMTR reactor core one by one to irradiate from the 155th cycle to 158th cycle or from 157th cycle to 160th. The irradiation temperature is shown in Table 1. The temperature became from 272 degree C to 277 degree C similar to the base irradiation temperature.

In the case of a crack growth test, the signal of potential drop difference increased rapidly from second cycle, and it could not be measured. The potential drop difference curves were revised by the crack of PIE, and its result is going to be presented by another paper.

In the case of crack initiation test, although it was satisfactory to the fracture signal at the beginning, the noise had appeared gradually. Rupture of specimen was occurred at 35 hours from loading start in the demonstration capsule. But in this capsule, contact points in bellows thought to be oxidized by long term irradiation at 270 degree C , and electrical insulation of MI cable might be deceased. The results of rupture time of specimen are verifying at present. Capsules after this will be exchanged enough helium gas in the bellows for the oxidization prevention disposal.

Table 1 Average temperature of CT and UCL specimens for irradiation cycles

Capsule name	Specimen No.	JMTR irradiation cycle					
		155	156	157	158	159	160
00M-9A CT specimen	1	275.8	276.1	276.9	276.8	---	---
	2	272.8	273.6	273.9	273.6	---	---
00M-12A CT specimen	1	---	---	275.8	274.9	274.9	274.7
	2	---	---	274.0	273.7	273.7	273.5
00M-14A UCL specimen	1	274.1	273.8	273.8	273.6	273.2	---
	2	275.4	275.1	275.2	274.9	275.1	---
	3	274.7	274.5	274.6	274.2	274.4	---
	4	273.3	273.7	273.6	273.3	273.5	---
00M-17A UCL specimen	1	274.3	274.2	273.7	273.3	273.0	---
	2	276.1	276.3	276.4	276.1	276.1	---
	3	274.2	275.0	274.9	274.5	274.7	---
	4	272.9	273.7	273.6	273.3	273.4	---

CONCLUSION

The capsule assembly technique by remote handing can be established in this study. Although minor changes of some measuring methods may be necessary, it is considered that in-pile SCC tests are carried out successfully. In future, the in-pile SCC test results will be published, and it is expected that development of the irradiation technology becomes to be advance in JMTR.

ACKNOWLEDGEMENTS

The authors would like to express their appreciate to Mr. Kikuchi and Mechanical Engineering and Electronics Section stuffs of JAEA for the production of the demonstration capsule and the development of the specimen unit.

REFERENCES

(1) K. Kawamata, et al., 2005 JAEA-KAERI Joint Seminar. S2-2 (2005).
(2) H. Ide, et al., JAERI-Tech 2002-079 (2002).
(3) H. Ide, et al., ICONE-11 ICONE11-36106 (2003).
(4) Y. Kaji, et al., ICONE-11 ICONE11-36119(2003).
(5) H. Ugachi, et al., ICONE-11 ICONE11-36106 (2003).

2.2 REMOTE-WELDING TECHNIQUE FOR ASSEMBLING IN-PILE IASCC CAPSULE IN HOT CELL

Kazuo Kawamata [1], Toshimitsu Ishii [2], Yoshiharu Kanazawa [1], Shigemi Iwamatsu [1], Masao Ohmi [1], Michio Shimizu [1], Yoshinori Matsui [2], Hirokazu Ugachi [3], Yoshiyuki Kaji [3], Takashi Tsukada [3] and Jun-ichi Saito [4]

1: JMTR Hot Laboratory Section, Department of JMTR
2: Irradiation Technology Section, Technology Development Department
4: Department of JMTR
Oarai Research and Development Center, Japan Atomic Energy Agency
4002 Narita-cho, Oarai-machi, Higashi-Ibaraki-gun, Ibaraki-ken, 311-1393 Japan
3: Research Group for Corrosion Damage Mechanism, Nuclear Science and Engineering Directorate
Japan Atomic Energy Agency
2-4 Shirakata Shirane, Tokai-mura, Naka-gun, Ibaraki-ken, 319-1195 Japan

ABSTRACT

In order to investigate behavior of the irradiation assisted stress corrosion cracking (IASCC) caused by the simultaneous effects of neutron irradiation and high temperature water environment in such a light water reactor (LWR), it is necessary to perform crack growth tests in an in-pile IASCC capsule irradiated in the Japan Materials Testing Reactor (JMTR). The development of the remote-welding technique is essential for remotely assembling the in-pile IASCC capsule installing the pre-irradiated CT specimens.

This report describes a new remote-welding machine developed for assembling the in-pile IASCC capsule. The remote-welding technique that the capsule tube is rotated light under the fixed torch was applied to the machine for the welding of thick and large-diameter tubes. The assembly work of four in-pile IASCC capsules having pre-irradiated CT specimens in the hot cell was succeeded for performing the crack growth test under the neutron irradiation in JMTR. The irradiation test of two capsules has been already finished in JMTR without problems.

KEYWORDS: IASCC, Remote-assembly work, Remote-welding technique, In-pile IASCC capsule, JMTR Hot Laboratory

INTRODUCTION

For the study of the irradiation assisted stress corrosion cracking (IASCC) occurred to in-core structural materials for light water reactors (LWRs), the slow strain rate tests (SSRTs) and crack growth tests of specimens irradiated in the Japan Materials Testing Reactor (JMTR) have been performed by the post-irradiation examination (PIE) machines installed in the hot cells of the JMTR Hot Laboratory (JMTR HL). Several years ago, SSRTs and crack growth tests using pre-irradiated specimens under the neutron irradiation in JMTR were planed to investigate behavior of IASCC under simultaneous effects of the neutron irradiation, stress and high temperature water environment. Then the development of an assembly technique of an in-pile IASCC capsule is essential for this requirement. Since JMTR HL has an advantage that its No.1 concrete cell is connected with JMTR by a canal pool, assembly works of the boiling water capsule (BOCA)[1] and the coupling capsule[2] was performed for several kinds of re-irradiation tests in JMTR. In JMTR HL, however, there has been no experience that the irradiated CT specimen was remotely installed in the crack growth test unit and the capsule tube with large diameter and thick wall was TIG-welded by the remote manipulation. Therefore, the remote-assembly technique of the in-pile IASCC capsule to perform the crack growth test of pre-irradiated CT specimens in JMTR. Especially, the development of a new remote-welding machine for both inner and outer capsule tubes was essential for JMTR HL to establish the assembly technique of the in-pile IASCC capsule.

This paper especially describes the development of the remote-welding technique for assembling the in-pile IASCC capsule whose test unit is installing pre-irradiated CT specimens for the crack growth test under the neutron irradiation in JMTR.

RE-IRRADIATION TESTS IN JMTR

A schematic of the transportation of irradiated and re-irradiation capsules between JMTR and JMTR HL is shown in **Fig.1**.

JMTR HL associated with JMTR was put into service in 1971 to perform PIEs of nuclear fuels for LWR and structural materials for LWR and a fusion reactor after the irradiation test in JMTR[3].

Usually, the capsules irradiated in JMTR are transferred for dismantling from the reactor to the JMTR HL's No.1 concrete cell through the canal pool of 6 m in depth and 3 m in width. Specially, the remote-assembled capsules installing several kinds of specimens pre-irradiated in JMTR or the other reactors can be easily transferred from the No.1 concrete cell to the reactor through the canal pool for the re-irradiation test in JMTR. Therefore, remote-assembly techniques of BOCA[1] installing the fuel cladding irradiated in the commercial reactor and coupling capsules[2] installing materials irradiated in the

experimental fast reactor have been developed in JMTR HL.

ASSEMBLY WORK OF IN-PILE IASCC CAPSULE

An in-cell assembly work of the in-pile IASCC capsule is illustrated in **Fig.2**. Firstly, in order to carry out the crack growth test under the neutron irradiation in JMTR, two CT specimens pre-irradiated in JMTR are remotely installed in the crack growth test unit of the capsule in the hot cell. After the installation of CT specimens, the unit is covered with an inner capsule tube. The location of a butt joint of inner tubes is TIG-welded for the circumferential direction. Finally, the welded inner tube is also covered with an outer capsule tube, and the location of a butt joint of the outer tube and an upper end plug is also TIG-welded for the circumferential direction. Though JMTR HL had experiences of remote-welding work for the fuel cladding and re-irradiation capsule with the thin and small-diameter tube, there was no experience of the welding work for the thick and large-diameter capsule tube. Therefore, the new remote-welding technique had to be developed for assembling the long and bent in-pile IASCC capsule.

NEW REMOTE-WELDING MACHINE

The remote-welding technique that the welding torch moves along the capsule tube's surface for circumferentially has been already developed in JMTR HL for assembling coupling capsules. Though this technique was applied to the welding for the inner tube of the in-pile IASCC capsule, flaws like craters were observed in the penetration bead on the outside surface of the tube. Therefore, a new remote-welding machine whose torch was fixed over the tube had been manufactured from August 2003 to January 2004. A schematic drawing and a schematic view of the machine are shown in **Fig.3** and **Fig.4**, respectively. In JMTR HL, the remote-welding technique that the capsule tube is rotated light under the fixed torch during welding was particularly needed for the butt joint of the capsule tube with large diameter. The capsule tube from 40 to 65 mm in diameter can be welded by the machine. The rotating speed of the capsule tube during welding can be controlled from 60 to 200 sec/round.

Furthermore, as means to rotate the long and bent capsule tube smoothly, a special rig with a balance weight was mounted on the capsule tube during welding, and the grip made of rubber was applied to the driving wheels of the machine.

WELDING CONDITIONS FOR INNER AND OUTER TUBES

Several kinds of welding conditions for both inner and outer tubes made of type 316L stainless steel for the in-pile IASCC capsule were investigated by the cold mock-up welding tests using the shorter model tubes with same diameter and thickness of each tube.

Before the mock-up welding tests, the mounting position of the special rig with the suitable balance weigh on the long and bent capsule tube was found to rotate it more smoothly.

Fig.5 shows the result of cold mock-up welding test of the model tube with the same diameter and thickness of the inner tube. The most suitable welding conditions were determined from the visual observation on the surface of the penetration bead and the microscopic observation on the sectional view of the penetration bead produced by a lot of mock-up welding tests as follows. An ideal torch gap that is the distance between the tip of torch and the surface of tube was 1.5 mm for the welding of both inner and outer tubes. The tube was rotated two times during TIG-welding. The rotational speed of the inner tube is 109 sec/round in both the first and the second rotations. That of the outer tube is 184 sec/round in both rotations. The welding periods of both rotations for inner and outer tubes were 236 sec and 376 sec, respectively. The welding currents in the first rotation and the second rotation for both tubes were 120 A and 100 A, respectively.

REMOTE-ASSEMBLY WORK OF IN-PILE IASCC CAPSULE

After the cold mock-up tests, the remote-welding machine was temporary set into the No.1 concrete cell for remote-assembly work of the in-pile IASCC capsule. Before the installation of the pre-irradiated CT specimens in the capsule, the mock-up welding tests using sample tubes were performed by the machine to check its performance and to reconfirm the welding conditions in the hot cell. Furthermore, the balance weight was directory mounted on the in-pile IASCC capsule by the in-cell work of staffs, and they check the state of butt joint and torch gap during rotating.

Schematic of remote-assembly works of the in-pile SCC capsule in the hot cell are shown in **Fig.6**. The assembly work to install pre-irradiated specimens in the capsule was started at the end of May 2004. The pre-irradiated CT specimen is fixed in the crack growth test unit as shown in **Fig.6-(a)**. The test unit is covered with the inner tube of 54 mm in outer-diameter and 3 mm in thickness. The location of butt joint between inner tubes is set light under the torch as shown in **Fig.6-(b)**. Inner tube is TIG-welded for circumferential direction as shown in **Fig.6-(c)**. The surface of the weld location was ground remotely by a grinder to remove an oxide film as shown in **Fig.6-(d)**. After the welding of the inner capsule tube, the same welding procedure is applied to the outer capsule tube of 65 mm in outer-diameter and 2 mm in thickness.

INSPECTION AND TRANSPORTATION OF IN-PILE IASCC CAPSULE AFTER ASSEMBLY WORK

The helium leak testing, liquid penetrant testing and visual observation of the in-pile IASCC capsule assembled in the hot cell were remotely performed as the final inspection before the re-irradiation test in JMTR.

Schematic views of the helium leak testing and liquid penetrant testing are shown in **Fig.7**. The helium leak testing was performed to find the presence of flaws through the capsule tube at the welding location. Before the leak testing, the welding location of the capsule was covered with the vinyl sack and the vinyl tube to send helium gas into the sack was set near the welding location. The assembled in-pile IASCC capsule was evacuated up to 10^{-5} Pa by the vacuum system with a helium leak detector. Helium gas was sent around the welding location.

Liquid penetrant testing was carried out to detect surface flaws like cracks at the welding location by flaw indications. The solvent removable fluorescent penetrant was remotely painted using a brush held by manipulator on the capsule tube around the welding location after the welding location was pre-cleaned by cloths containing solvent cleaner as a pre-cleaning. After 15 minutes have passed, the solvent removable fluorescent penetrant was wiped out on the surface of tube by cloths containing solvent cleaner. Furthermore, the aqueous developer was also painted using the brush on the surface. After 15 minutes have passed again, flaw indications were looked for through the cell window.

Schematic views of the transportation of the in-pile IASCC capsule from the No.1 concrete cell to the reactor are shown in **Fig.8**. The in-pile IASCC capsule that is assembled in the No.1 concrete cell is transferred from the No.1 concrete cell to the reactor after the inspections of the capsule in the hot cell.

SUMMARY

In order to carry out the in-pile IASCC growth tests of pre-irradiated materials in JMTR, the new remote-welding machine was developed in JMTR HL.

Firstly, the remote-welding technique, that the capsule tube is rotated light under the fixed torch during welding, was developed for assembling the in-pile IASCC capsule.

Secondly, the bent and long capsule tube can be smoothly rotated during welding by the mounting of the special rig with balance weight on the capsule and the application of the grip made of rubber to the driving wheel of the welding machine.

Thirdly, the welding conditions of inner and outer tubes were obtained through a lot of cold mock-up tests.

Finally, four in-pile IASCC capsules having pre-irradiated CT specimens were remotely assembled in the hot cell for performing crack growth tests under the neutron irradiation in

JMTR. The irradiation test of two in-pile IASCC capsules has been already finished successfully in JMTR.

ACKNOWLEDGEMENTS

Authors would like to acknowledge the support of this work from colleagues in the JMTR HL. The development of the remote-welding technique for in-pile IASCC test was conducted under the cooperative research program with JAPC (Japan Atomic Power Company). They would also like to acknowledge technical advice and support from JAPC.

REFERENCES

(1) J. Saito, et al., "Current status and future prospects of JMTR Hot Laboratory", Proceedings of the 4th KAERI-JAERI joint seminar on PIE technology, KAERI GP-192, (2002)
(2) Y. Matsui, et al., "Irradiation-coupling techniques using JMTR and another facility", J. Nuclear Mater., 283-287 (2000) 997-1000
(3) Department of JMTR, "Annual Report of JMTR FY1997 [April 1, 1997-March 31, 1998]", JAERI-Review 99-005, (1999)

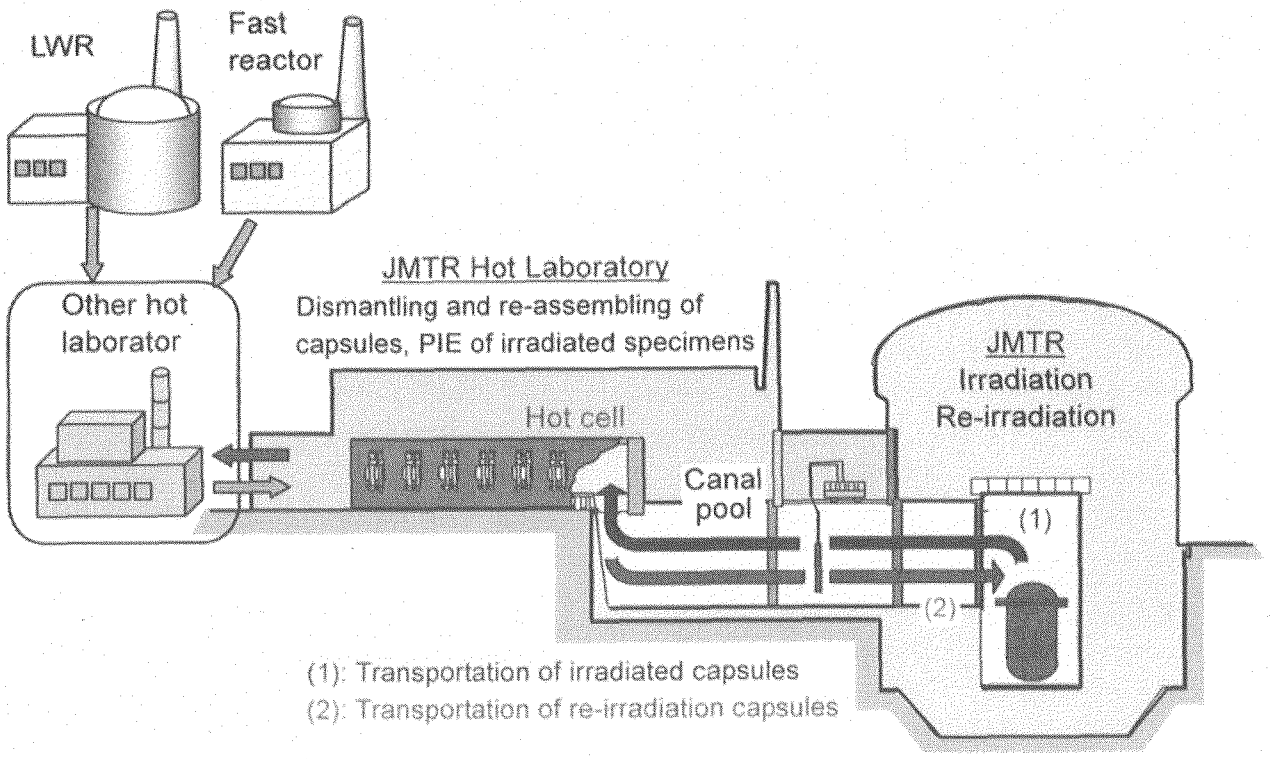

Fig.1 Schematic of transportation of irradiated and re-irradiation capsules between JMTR and JMTR HL through canal poor.

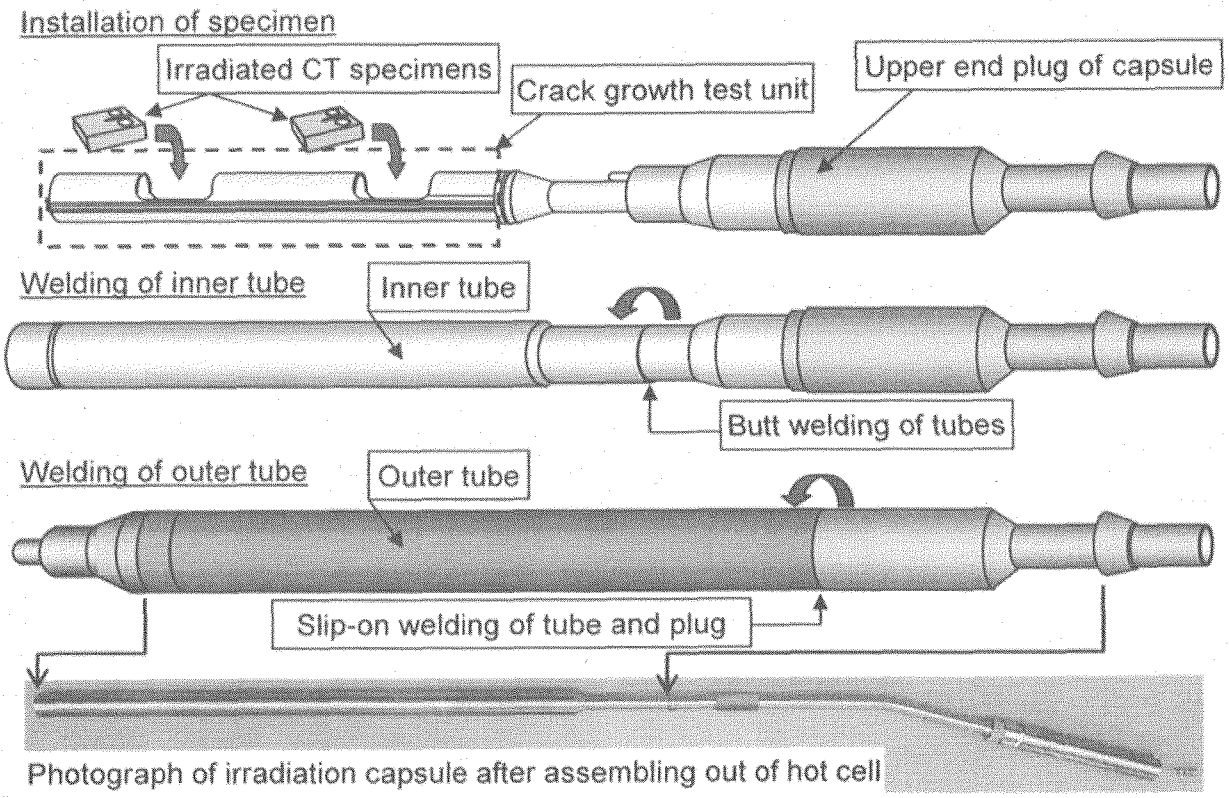

Fig.2 Assembling work of in-pile IASCC capsule.

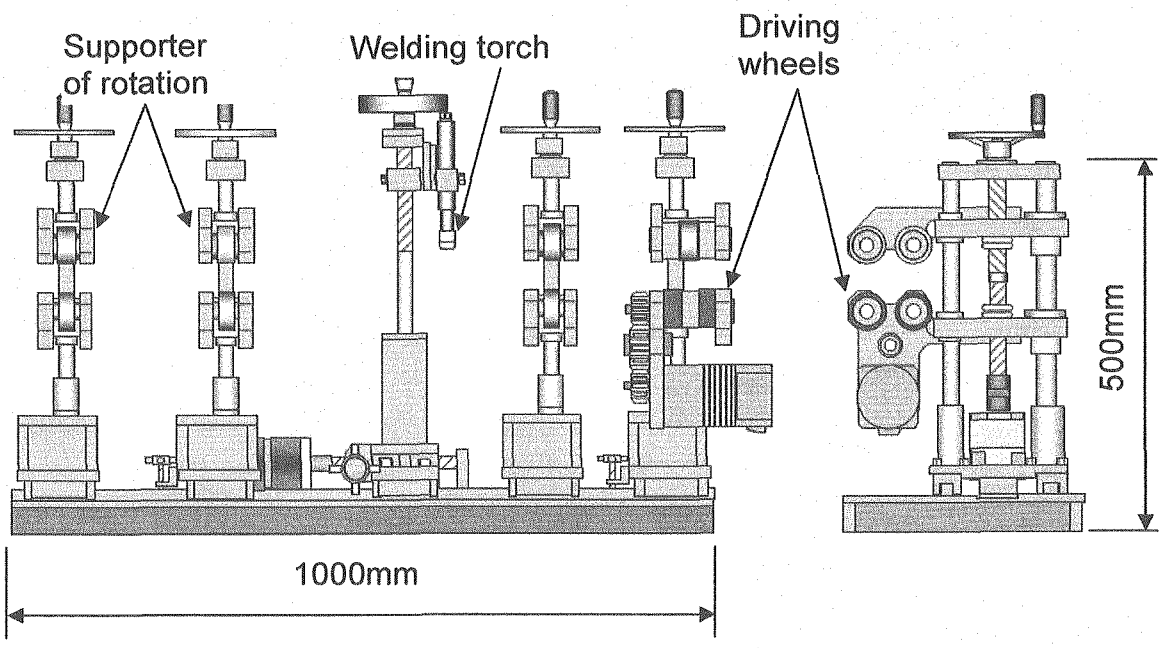

Fig.3 Schematic drawing of welding apparatus.

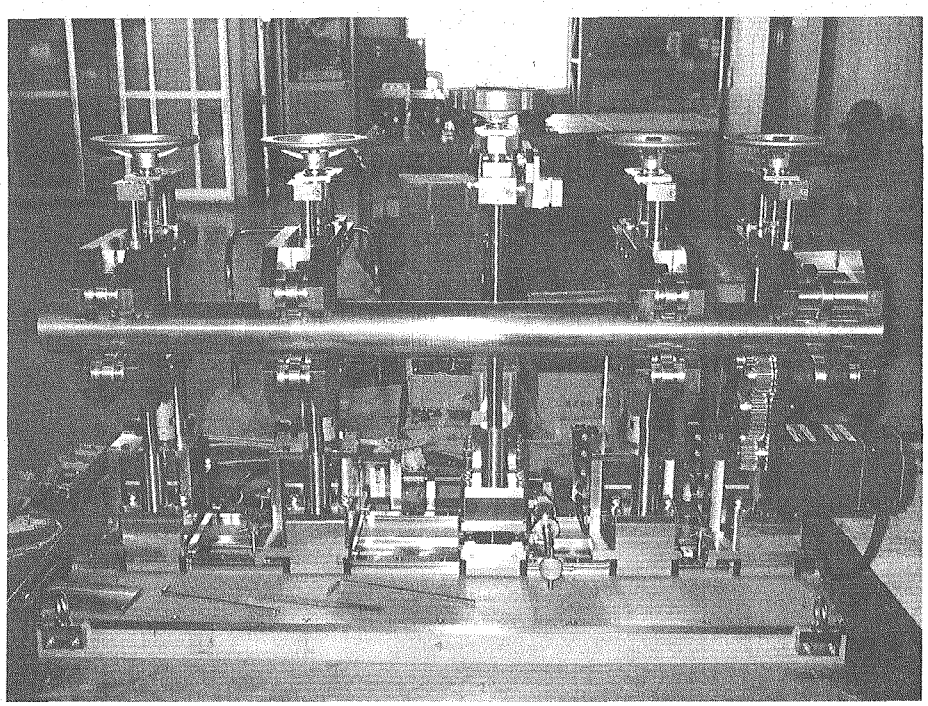

Fig.4 Schematic view of welding apparatus.

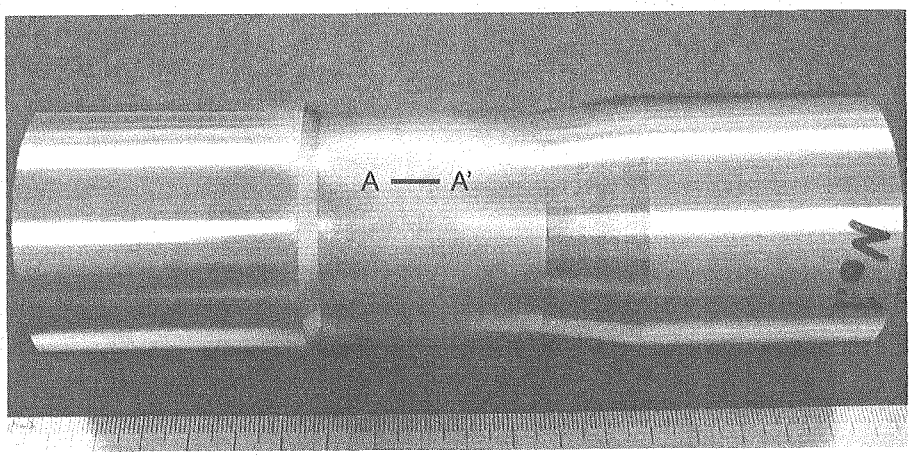

(a) Exterior of weldment surface

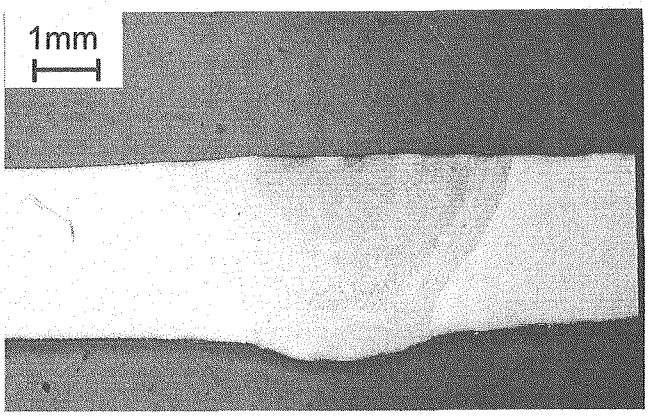

(b) Sectional view of penetration bead (A-A' section)

Fig.5 Result of cold mock-up welding test.

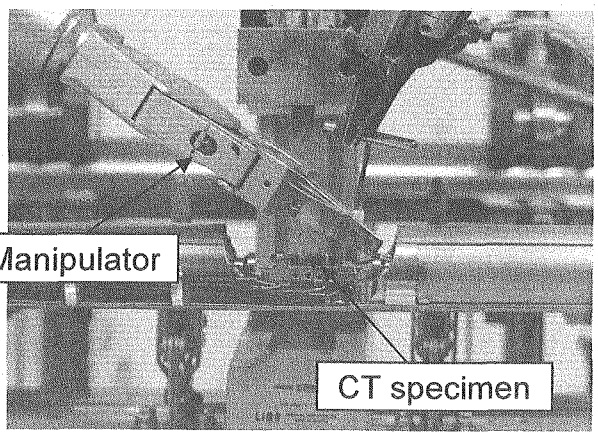

(a) Installation of irradiated specimen

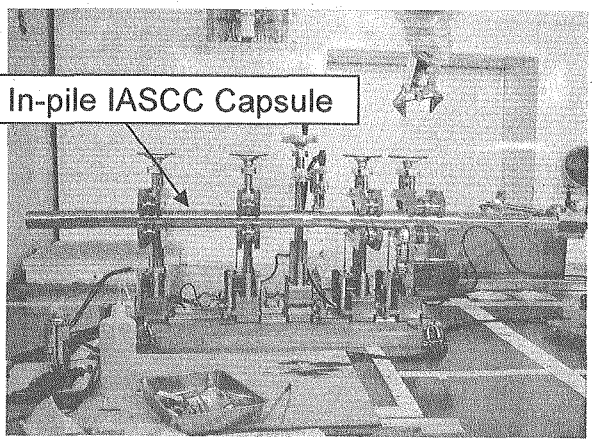

(b) Inner capsule tube setting before welding

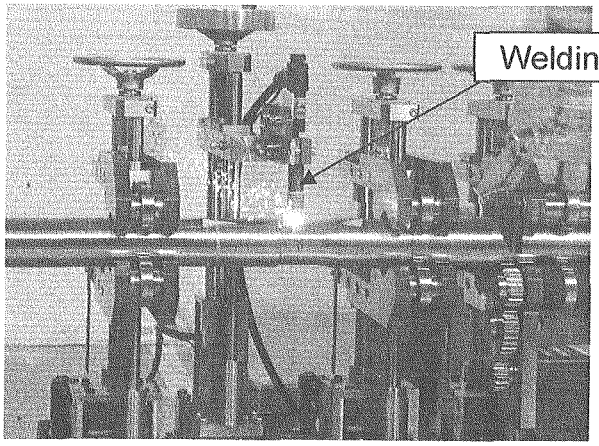

(c) In-cell welding of irradiation capsule

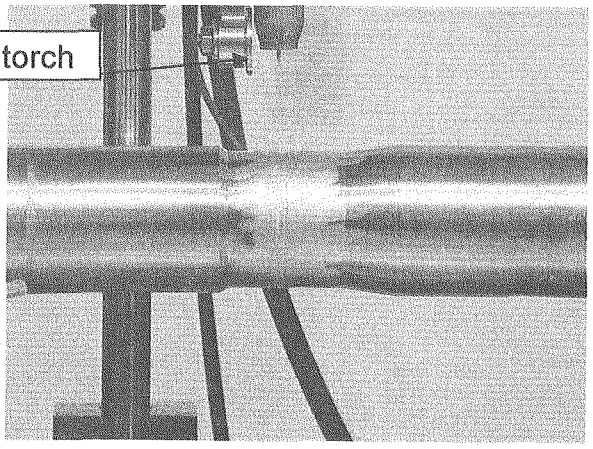

(d) Grinding capsule surface after welding

Fig.6 Assembling works to install pre-irradiated specimens in in-pile IASCC capsule.

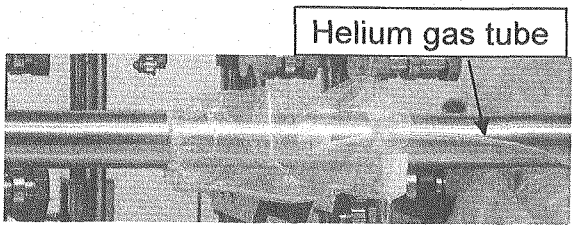

(a) Helium leak testing

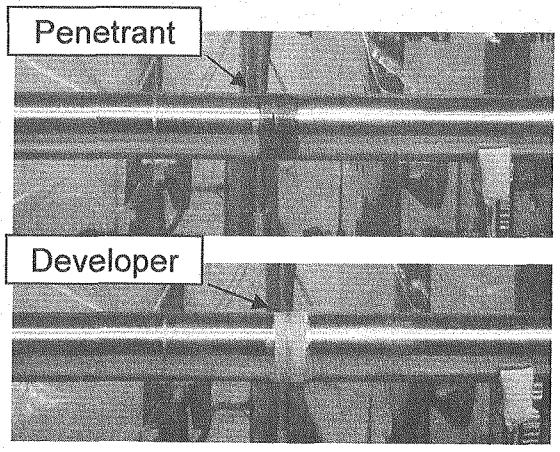

(b) Liquid penetrant testing

Fig.7 Schematic view of inspection of assembled in-pile IASCC capsule in hot cell.

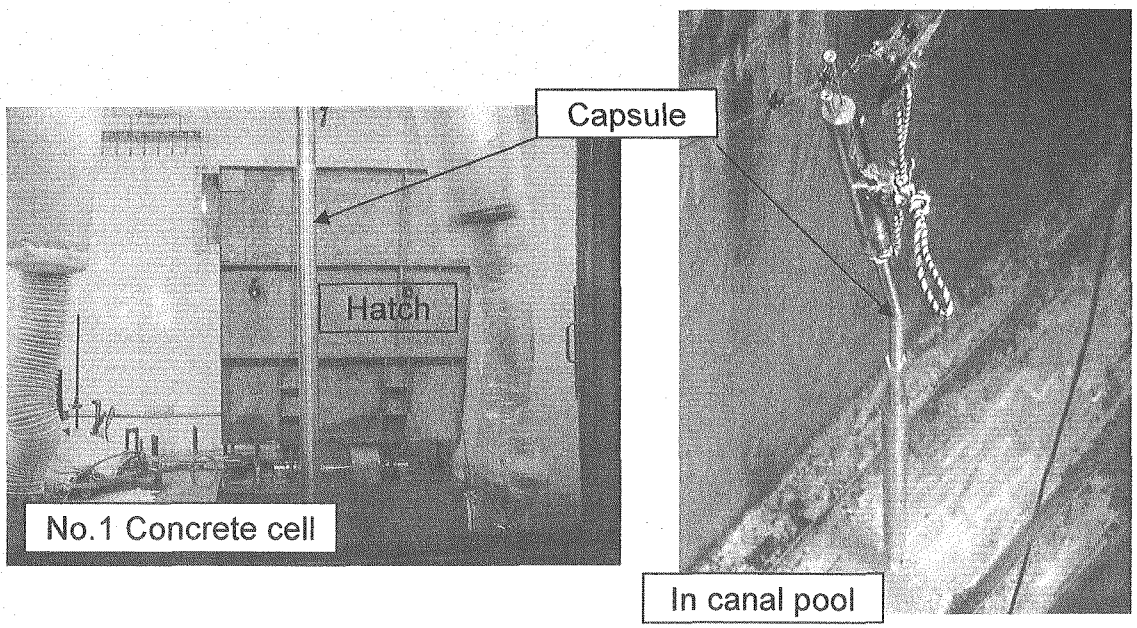

Fig.8 Schematic views of transportation of in-pile IASCC capsule.

2.3 CORE MANAGEMENT AND FAST NEUTRON FIELD CHARACTERIZATION OF JOYO

Yasushi Ohkawachi, Takashi Sekine and Takafumi Aoyama

Fast Reactor Technology Section, Experimental Fast Reactor Department,
O-arai Research and Development Center, Japan Atomic Energy Agency
4002 Narita, O-arai, Ibaraki 311-1393 JAPAN

ABSTRACT

Twenty eight years of operations at the experimental fast reactor JOYO provide a wealth of experience with core management and characterization of fast neutron field. This experience has been applied to several core modifications to upgrade JOYO's irradiation capability. Reactor physics tests and neutron flux measurement results have been used to confirm the accuracy of neutron diffusion theory calculations. These experiences and accumulated data will be useful for the core design in future fast reactors.

KEYWORDS: Experimental fast reactor, JOYO, MK-III, Core management, Fast neutron field, Characterization, Reactor physics test, Reactor dosimetry

INTRODUCTION

The experimental fast reactor JOYO at O-arai Engineering Center of Japan Nuclear Cycle Development Institute attained initial criticality in April 1977 with the MK-I breeder core. The MK-I core was operated at 50 MWt and 75 MWt as the first liquid metal cooled fast reactor in Japan. Through the MK-I operations, basic characteristics of Fast Breeder Reactor (FBR) plant were studied. As an irradiation test bed to develop the fuels and materials for future fast reactors, the JOYO MK-II core achieved the maximum design output of 100 MWt in March 1983. Thirty-five duty cycle operations and several special tests were conducted using the MK-II core by June 2000. JOYO was recently upgraded to the MK-III[1] core for various requirements of irradiation tests. The MK-III core was achieved the initial criticality in July 2003.

In order to predict the core parameters for operation and refueling plan within the design

limitation, the core management code system has been developed. The nuclear calculation was based on diffusion theory and corrected with a bias method. Results from the core physics tests have been used to confirm the accuracy of these predictions. These verifications are also important to conduct various irradiation tests accurately.

The neutron field of JOYO has been characterized by means of reactor dosimetry based on the multiple foil activation method and helium accumulation fluence monitor in addition to nuclear calculations.

This paper describes the method of core management and characterization of fast neutron field developed in JOYO.

SPECIFICATIONS OF JOYO MK-III CORE

Figure 1 shows the core configurations of MK-II and MK-III cores. The fuel region was divided into two regions in the MK-III core to flatten the neutron flux distribution. Two of six control rods were shifted from the 3rd row to the 5th row to provide the loaded positions for the instrumented type irradiation subassemblies in the high flux of fast neutron field.

To reduce neutron dose in the in-vessel fuel storage rack, the outer two layers of radial stainless steel reflectors were replaced by the shielding subassemblies which contain 45% enriched boron carbide. As a result, neutron flux at the in-vessel fuel storage rack in the MK-III core decreased about one third of the MK-II core. **Table 1** compares the major specifications of JOYO MK-II and MK-III cores.

In order to enlarge the high neutron flux irradiation field, the maximum number of driver fuel subassemblies was increased from 67 to 85. The maximum number of irradiation test subassemblies was increased from 9 to 21. The core height was decreased from 55 cm to 50 cm to obtain higher neutron flux with smaller power peaking. With the core modification, the maximum fast neutron flux ($E \geqq 0.1MeV$) was increased from 3.2×10^{15} n/cm^2·s to 4.0×10^{15} n/cm^2·s and the reactor power was consequently increased from 100 MWt to 140 MWt.

REACTOR PHYSICS TEST FOR THE JOYO MK-III START-UP CORE

Performance test[2] was carried out in the experimental fast reactor JOYO for the upgraded MK-III core from July through November 2003. In the test, several neutronics characteristics,

such as the control rod worth, the excess reactivity, the isothermal temperature coefficient and the power coefficient were measured and compared with the calculation.

The Approach to Criticality and Excess Reactivity Measurements

In the approach to criticality test, the MK-III core achieved initial criticality at the control rod bank position of 412.8mm on 14:03 July 2nd, 2003. Because the replacement of the outer two rows of reflector subassemblies with shielding subassemblies reduced the source range monitor to one third at the same reactor power compared with those in the MK-II core, we measured the change of the monitor's response and determined the count rate of "2 x 10^4 cps." as the zero power criticality. Inverse count rate was plotted versus the calculated reactivity insertion, as shown in **Fig.2**.

The isothermal core temperature during the excess reactivity measurement was about 250 degree-C. Based on the measured critical rod bank position and the measured rod worths as described below, the zero power excess reactivity obtained was 2.99 ± 0.09 %Δk/kk'. The measured excess reactivity was within a safety requirement limit.

Calculation

Excess reactivity was predicted by five methods in preparation for the initial MK-III approach to criticality.

• The "MAGI" method was the standard method used for MK-II analyses. The base MAGI calculation uses finite-difference diffusion theory with one mesh per subassembly and 5 cm mesh intervals axially. It uses 7-group homogeneous neutron cross sections based on JENDL-3.2. A difference between the measured and calculated excess reactivity for the last MK-II operational cycle was applied to the base-calculation prediction for the MK-III core as the bias correction factor.

• HESTIA was developed for MK-III core management based on the MAGI. The "HESTIA" method was adopted as the standard method for MK-III core management analyses. Consequently, it was used for the approach to criticality. It features finer detail in space (24 triangles/subassembly and 2.5 cm axial mesh in the fuel) and energy (18 groups for neutron and 7 groups for gamma-ray) to improve calculation accuracy. In other respects, the approach is the same as MAGI.

• The "JUPITER" method applies mesh, transport, heterogeneity and three other corrections to a 6 triangle per subassembly diffusion theory calculation.

• The MCNP code was used to model the reactor components pin by pin, with continuous energy JENDL-3.2 cross sections.

• The "JUPITER Adjusted" method is the same as the "JUPITER" method except the ADJ2000R adjusted cross section set [3] is used instead of the bias correction for the base calculation.

A comparison of the excess reactivity, measured and predicted by the above mentioned calculation methods, is shown in **Fig.3**. The approach described in Ref. (4) was used to derive the uncertainties in the calculated values using the covariance and sensitivity coefficient. All of the calculated values are within two standard deviations from the measured value.

Control Rod Calibrations

All six of the control rods have the same poison-type design. The poison section contains B_4C enriched to 90 % in ^{10}B. The poison section is 650 mm long and the rod can move same distance. As noted above, two of the rods, Numbers 2 and 5, are in Row 5 in the MK-III core. Because of the radial flux and adjoint gradients, these rods worth is about 40 % of the four rods in Row 3. Two methods of the rod calibration are described below.

Inverse Kinetics Method

Measurements

Reference calibrations use the inverse kinetics method with uniform rod bank. The rod being calibrated (measured rod) was moved from 0 mm to 650 mm in steps worth about 8 ¢ each. The example reactivity and power traces during calibration steps are shown in **Fig. 4**. It can be seen that the random error at each calibration step can be significant. However, the effect on the full-travel rod worth is very small.

Calculation

Experimental and calculated full-travel control rod worths from the reference calibrations are compared in **Table 2**. The rod worth uncertainty, in the natural measurement unit, dollars, has an estimated random component of 0.3 % and an estimated systematic component of 1.0 %, which add in quadrature to 1.0 %. Converting to the natural calculation unit, $\Delta k/kk'$, adds the 3 % uncertainty in k_{eff}, for a total uncertainty of 3.2 %.

The base calculation uses transport theory, 7 group cross sections and an XYZ geometry representation of the core in the TRITAC code. The bias factors in the middle column are based on the period measurements and TRITAC calculations for a Row 3 rod and a Row 5 rod in the last MK-II operational cycle. Since the measured worths of control rods in a given reactor row differ by only a few percent, as seen from the experimental worths in **Table 2**, the use of a row-dependent bias is justified. The final (biased) calculated worths are low by 3 % to 4 % for rods in Row 3 but are 1 % from the measured values for rods in Row 5.

Juggling Method

Juggling calibrations are more dynamic measurements, in which exactly critical condition is not required once the calibration begins. This is the routine calibration approach at JOYO for calibrating control rods in the third row. At the beginning, two rods are at 295 mm (poison inserted to 30 mm below the fuel center) and other two rods are at 650 mm (fully withdrawn). These four rods are calibrated over the 295 mm to 650 mm range by alternately moving one rod up and another rod down in steps. The reactivity and power traces during several steps of such a calibration are shown in **Fig. 5**.

The reference and juggling calibration measurement results are compared in **Table 3**. Both measurement results agree within 0.9 %. As the juggling method is performed in a short time, it is practical as a routine control rod calibration procedure and can be used as the alternative for the period method.

Isothermal Temperature Coefficient

Measurements

To begin the isothermal temperature coefficient measurement, a uniform temperature of approximately 250 degree-C was established throughout the primary system (isothermal), and the excess reactivity was determined. Next the reactor power was increased in 20 degree-C steps, measuring excess reactivity at each step, until the primary system reached approximately 350 degree-C. The next day, the reactor temperature was brought back to 250 degree-C by cooling the coolant sodium by the natural air draft in the dump heat exchangers with the temperature decreasing in 20 degree-C steps. The ascending and descending measurements were repeated, providing four measurements of the temperature coefficient.

The measurements results are shown in **Table 4** and **Fig.6**. There is a clear difference between coefficients measured with the temperature increasing and decreasing. This difference is considered to be related with a time lag of control rod drive shaft expansion during the measurements.

Calculation

The calculated isothermal temperature coefficient has two main components, Doppler broadening of neutron cross section resonances, and thermal expansion. The items contributing to thermal expansion include coolant density change, core radial expansion, structural material axial expansion and fuel axial expansion. For the Doppler components calculation, exact perturbation theory was used with neutron flux and adjoint flux obtained by 70 group 3-D diffusion code. The thermal expansion component was obtained by taking the

difference of two k_{eff} at different temperatures. The ratios of the calculated coefficient to the various experimental values are shown in the last column of **Table 4**. The calculation agreed with the measurement. The reactivity effect of each component is shown in **Fig.7**. The largest effect was core radial expansion. It is nearly 40% of all the reactivity which is mainly caused by the radial expansion of the core support plate.

Power Coefficient

During the MK-III performance test, the reactor power was repeatedly increased and decreased, and the burn-up and power dependence of the power coefficient was measured with the same reactor inlet temperature condition. The measurement results are shown in **Fig.8**. The measured power coefficients were negative in all the power range. The absolute value of the power coefficients were decreased, when reactor power increased form 100MWt to 120MWt for the first time. This is considered to be caused by the restructuring of the fuel pellet. Further investigation will be performed to understand the change of the power coefficient. The measured results of November 4th and 8th shown in **Fig.8** became about a half of the ones measured at the low burn-up of the MK-III performance core in October.

Summary of Results

The MK-III design predictions are consistent with the performance test results. Some of the results are summarized in **Table 5**. Most of the C/Es are within 5% of unity. All of the technical safety requirements for JOYO were satisfied.

NEUTRON FIELD CHARACTERIZATION METHOD IN JOYO

The neutron field of the JOYO has been characterized [5] by means of reactor dosimetry based on the foil activation method and helium accumulation fluence monitor in addition to nuclear calculations.

Calculation

In JOYO, core configuration and the number of driver fuel subassembly were changed for each operational cycle with the loading of the irradiation test subassemblies. Therefore, it is essential to evaluate the core physics characteristics, which depend on the core configuration and fuel burn-up.

Figure 9 illustrates the system outline for characterizing JOYOs neutron field. HESTIA was used to calculate the neutron flux distribution and fuel burn-up composition. At the positions

away from the core center, the precise neutron flux distribution and spectrum were calculated using the two-dimensional transport code "DORT". The Monte Carlo code "MCNP" was used to calculate the neutron flux inside the irradiation test subassembly. The neutron source distribution was calculated by HESTIA was used as an input to these calculations. To confirm the accuracy of the calculation, the reactor dosimetry tests using the multiple foil activation method has been conducted. The neutron spectrum was adjusted with the measured reaction rates of irradiated dosimeters using the NEUPAC J-log code.

Two-Dimensional Transport calculation

In the calculation of "DORT" as shown in **Fig.9**, the compositions of each core subassembly and neutron source distribution were calculated by HESTIA and were used as an input to DORT. The MACROJG[6] system computes the 100 energy group macroscopic cross sections using JSSTDL-100 shielding constants set. The transport equation was solved as a fixed source problem.

The XY geometry model was used for the evaluation at the in-core region. In this case, the RZ model was applied to evaluate the axial buckling of DB^2. The neutron flux distribution in the core was obtained by two calculation results, the radial distribution using XY geometry at the core middle plane and the axial distribution using RZ geometry. The RZ geometry calculation region includes the radial carbon shield and concrete pedestal.

The XY-Rθ geometry model was the synthetic calculation method with XY in-core region model and Rθ ex-core region model. The angular neutron flux of the in-core region calculated by XY geometry was used as an input to the Rθ calculation. The XY-Rθ geometry model was used for the evaluation at the in-vessel fuel storage rack. **Figure 10** shows an example of the radial neutron flux distribution in each calculation model of XY, RZ and Rθ.

Monte Carlo Calculation

MCNP was used to evaluate the neutron flux at each fuel pin and specimen within the irradiation test subassemblies. In the MCNP calculation, whole core geometry was simulated using exact three-dimensional modeling of the subassembly. The compositions of each core subassembly and neutron source distribution calculated by HESTIA were used as the same way for DORT. The FSXLIB-J3R2[7] cross section library, which was processed from JENDL-3.2, was used.

Measurement

Neutron Spectrum Adjustment by Foil Activation Method

In order to measure the neutron flux distribution, the multiple foil activation method was

used. Fe, Ni, Cu, Ti, Co, Nb, Sc, Np, ^{235}U and ^{238}U were used as dosimeters to cover the neutron spectrum of which energy ranges from approximately 0.1eV to 20MeV. Measured reaction rates of the dosimeters were used for adjusting the initial guess neutron spectrum.

The reaction rate was determined by analyzing the gamma-ray or X-ray spectra as measured from the irradiated dosimeters. The measurements were performed with a high purity Germanium gamma-ray detector and a Low Energy Photon Spectrometer. Both detectors were calibrated by the standard gamma-ray sources whose energies spanned those of the activated nuclides.

The calculated neutron spectrum was then adjusted by the measured reaction rates using "NEUPAC", the J1 type spectrum unfolding code package. NEUPAC uses the 103-group cross-section set with the error covariances, which are processed from the JENDL dosimetry file based on JENDL-3. **Figure 11** shows an example of the adjusted neutron spectrum at the core center position with a 90% confidence level for each reaction rate.

Neutron Flux Distribution Measurement and Comparison with Calculation

In order to verify the neutron spectrum adjustment by foil activation method, the neutron flux distribution from the core center to ex-vessel irradiation hole was measured in the MK-II core. **Figure 12** shows loaded positions of the irradiation test subassemblies and capsules which contained a set of dosimeter materials. Irradiation test subassemblies were loaded at the core center, the reflector region (9th row) and the in-vessel fuel storage rack. In addition, irradiation capsules were placed in the ex-vessel irradiation hole which was located between the reactor vessel and graphite shield.

Axial positions of the dosimeter sets were from the core center –62.7 cm to 94.2 cm. These test subassemblies were irradiated for 117.1 E.F.P.Ds in the MK-II core from November 1999 to June 2000.

Table 6 shows the comparison of C/E values of reaction rates using the initial guess spectrum and the adjusted value. Using the NEUPAC, the initial guess spectrum was largely improved after the adjustment and the averaged C/E value became approximately 1.03.

The comparison of calculated neutron fluence with measured results was shown in **Table 7**. MCNP was used to calculate in the axial positions of 0 cm and +25.8 cm at the core center, and DORT was used in the axial positions of +62.7 cm and +94.2 cm at the core center and the other irradiation positions. In the axial position of 0 cm at the core center, the C/E value of the total fluence was 1.22. It seems that the local flux distribution inside the irradiation test subassembly with no fuel is not fully predicted by MCNP that needs further investigation. At the axial position of +62.7 cm, the C/E value of the total fluence was 0.87. This axial elevation corresponds to a boundary between the axial stainless steel reflector and fission gas

plenum of the driver fuel. Therefore, the difference is considered due to the neutron streaming effect. At the reflector region, in-vessel storage rack and ex-vessel irradiation hole, calculation showed a fairly good agreement with the measured values.

Helium Accumulation Method

Concerning the evaluation of helium production in the irradiated materials, a helium accumulation fluence monitor (HAFM) has been developed and it was used for fast reactor dosimetry in addition to the activation and fission foils[8]. The HAFM method is a technique to determine the helium production rate in materials by measuring the number of helium atoms, which were produced by helium production reactions such as the (n, α) reaction. The monitor material of HAFM such as boron and beryllium is enclosed in a vanadium capsule to contain helium gas accumulated inside the HAFM. The HAFM is suitable to measure neutron fluence in long-term irradiation tests because the helium has a stable nuclide and is produced by neutron reactions of the HAFM elements, which is not saturated during irradiation and does not decay during and after irradiation. Using HAFM, neutron fluence is obtained by

$$\Phi = - LN(1 - N/N_0) / \sigma_{ave}$$

where Φ : neutron fluence (n/cm^2)

N : number of helium atoms produced (atoms/sample)

N_0 : number of monitor material of HAFM before irradiation(atoms/sample)

σ_{ave} : one group averaged helium production cross section considering self-shielding effect (cm^2).

N is measured by the mass spectrometer, and N_0 is obtained from the monitor material's weight by a microbalance. σ_{ave} is calculated by collapsing the helium production cross section with neutron spectrum at the position where HAFM is irradiated.

This method also has an advantage of directly measuring the helium production in stainless steels used for reactor structural component materials whereas the conventional foil activation method relies on the calculation of the helium production rate using its cross section and the neutron spectrum.

Figure 13 shows the comparison of the measured helium production of enriched boron type HAFM and the calculated one using the adjusted neutron spectrum by NEUPAC. HAFM was irradiated at the same test subassemblies in **Fig.12**. The ratios of calculation to experiment values were 0.96 ~ 1.05 and both were in good agreement within the experimental uncertainty (5 % in standard deviation). This result indicates that the HAFM can be applicable to monitor neutron fluence in fast reactor.

SUMMARY

Core and fuel management techniques for fast reactors have been developed through successful operation of the experimental fast reactor JOYO. The core characteristics and neutron diffusion theory calculations were verified by core physics tests.

To characterize the neutron field of the JOYO, HESTIA, DORT and MCNP codes were used. Calculation accuracy was verified using the multiple foil activation method and HAFM. As a result, it was confirmed that the calculation method with experimental correction in each core region can characterize the JOYO neutron field accurately.

REFERENCES

(1) Y.Maeda et al., "Distinguished Achievements of a Quarter-Century Operation and a Promising Project Named MK-III in JOYO, " Nuclear Technology Vol.150, April.2005, pp.16-36(2005).

(2) T.Aoyama , et al., "Core Performance Tests at Low Power for the JOYO Upgrade to MK-III, " Proc. of the 12th International Conference on Nuclear Engineering, Arlington(2004).

(3) M.Ishikawa, et al., "Development of a Unified Cross-Section Set ADJ2000 Based on Adjustment Technique for Fast Reactor Analysis," Journal of Nuclear Science and Technology, Supplement 2, p.1073-1076 (2002).

(4) T.Takeda, et al., "Prediction Uncertainty Evaluation Methods of Core Performance Parameters in Large Liquid-Metal Fast Breeder Reactors," Nuclear Science and Engineering, 103, p.157-165 (1989).

(5) T.Aoyama , et al., "Characterization of Neutron Field in the Experimental Fast Reactor JOYO for Fuel and Structural material irradiation Test, " Nuclear Engineering and Design pp.21-34, 288(2004).

(6)A.Hasegawa, te al., "JSSTDL-300: The Standard shielding cross section library based on JENDL-3.2," Journal of Nuclear Science and Technology, p.723-727(2000).

(7)K. Kosako et al., "A Continuous Energy Cross Section Library for MCNP Based on JENDL-3.2," JAERI-Data-Code-94-20 (1994).

(8) C.Ito, et al., "Development of Helium Accumulation Fluence Monitor for Fast Reactor Dosimetry," Proc. of the 11th International Symposium on Reactor Dosimetry, ENS/ASTM, Brussels, August 18-23, 2002, pp. 150-159(2002).

Table 1 Major Core Parameters of JOYO MK-II and MK-III

Specification			MK-III Core	MK-II Core
Reactor Thermal Power		(MWt)	140	100
Max. Number of Driver Fuel*			85	67
Equivalent Core Diameter		(cm)	80	73
Core Height		(cm)	50	55
^{235}UEnrichment		(wt%)	18	18
Pu Content: Pu/(Pu+U)		(wt%)	23/30**	30
Fissile Pu Content: (^{239}Pu+^{241}Pu)/(Pu+U)		(wt%)	16/21**	21
Max. Linear Heat Rate of Fuel Pin		(W/cm)	420	400
Max. Burn-up of Fuel(Pin Average)		(GWd/t)	90	75
Total Neutron Flux		(n/cm^2・s)	5.7x10^{15}	4.5x10^{15}
Fast Neutron Flux		(n/cm^2・s)	4.0x10^{15}	3.2x10^{15}
Number of Control Rod	In 3rd Row		4	6
	In 5th Row		2	0
Reflector/Shielding			SUS/B_4C	SUS/SUS
Flow Rate of Primary Sodium		(t/h)	2,700	2,200
Primary Coolant Temperture (Inlet/Outlet)		(oC)	350/500	370/500
Operation Period per Cycle		(day)	60	70

*Includeing "Number of Irradiation Test Fuel"
**Inner Core / Outer Core

Table 2 Reference Rod Calibration Results

Rod	Exp. Worth (%Δk/kk')	Base Calc. (%Δk/kk')	Bias Factor	Biased Calc. (%Δk/kk')	C/E
1	2.09 ±0.07	2.01	1.00	2.01	0.96
2	0.80 ±0.03	0.80	0.98	0.79	0.98
3	2.03 ±0.07	1.97	1.00	1.99	0.97
4	2.08 ±0.07	2.01	1.00	2.01	0.97
5	0.78 ±0.03	0.80	0.98	0.79	1.00
6	2.06 ±0.07	1.97	1.00	1.97	0.96

Table 3 295-to-650 mm Rod Worths from Two Calibration Approaches (%Δk/kk')

Rod	Reference Calibration	Juggling Calibration
1	1.13	1.14
3	1.11	1.12
4	1.13	1.14
6	1.14	1.15

Table 4 Isothermal Temperature Coefficient Results

	Temperature Direction	Isothermal Temp. Coef. (%Δk/kk'/ °C)		C/E
		Exp.	Cal.	
1	ascending	-0.00370	-0.00368	0.995
2	ascending	-0.00375		0.981
3	descending	-0.00386		0.952
4	descending	-0.00385		0.955

Table 5 Summary of Results

Measured Quantity	Calculation Method	C/E
Excess Reactivity	HESTIA – hex-z, fine mesh, 18 group diffusion theory with bias adjustment	1.05
Control Rod Worths	TRITAC – xyz, 7 group transport theory with bias adjustment	0.96 to 1.01
Isothermal Temperature Coefficient	JUPITER – hex-z diffusion theory with mesh, group, heterogeneity and transport corrections.	0.95 to 1.01

Table 6 Comparison of Measured and Calculated Reaction Rates (Core Center)

Reaction	Calculation / Measured	
	Before adjustment	After adjustment
$^{54}Fe(n,p)^{54}Mn$	1.12	1.04
$^{58}Ni(n,p)^{58}Co$	1.10	1.01
$^{63}Cu(n,\alpha)^{60}Co$	1.16	1.03
$^{46}Ti(n,p)^{46}Sc$	1.15	1.03
$^{45}Sc(n,\gamma)^{46}Sc$	1.27	1.04
$^{237}Np(n,f)$	1.38	1.04
$^{235}U(n,f)$	1.20	1.01
average	1.20	1.03

Table 7 Measured Neutron Fluence

Position	Axial Position (cm)	Measured Neutron Fluence (n/cm^2)		Calculation / Measurement	
		Total	E>0.1MeV	Total	E>0.1MeV
Core Center	0	3.28×10^{22}	2.29×10^{22}	1.22	1.31
	+25.8	1.74×10^{22}	1.17×10^{22}	1.20	1.29
	+62.7	2.90×10^{21}	1.10×10^{21}	0.87	0.99
	+94.2	6.78×10^{20}	1.72×10^{20}	1.19	1.36
Reflector Region	0	2.92×10^{21}	9.43×10^{20}	1.11	1.13
In-Vessel Storage Rack	0	7.99×10^{20}	1.55×10^{20}	1.11	1.02
Ex-Vessel Irradiation Hole	0	7.34×10^{18}	1.23×10^{17}	0.98	—

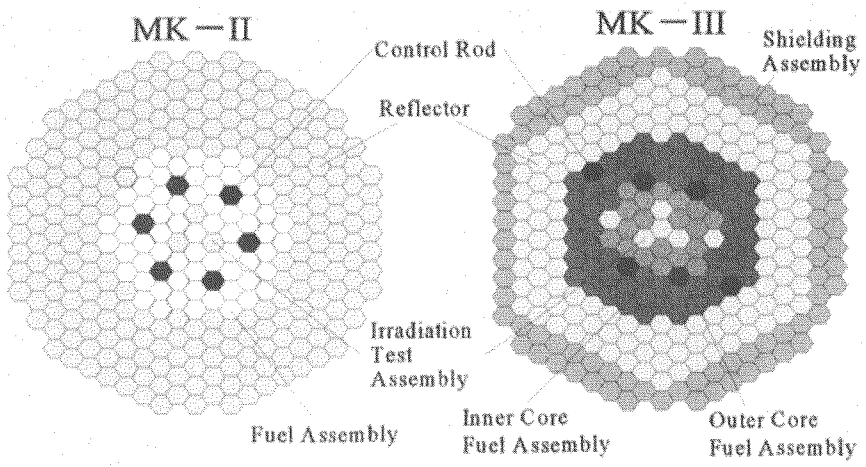

Fig. 1 Core Configurations of the MK-II and MK-III Core.

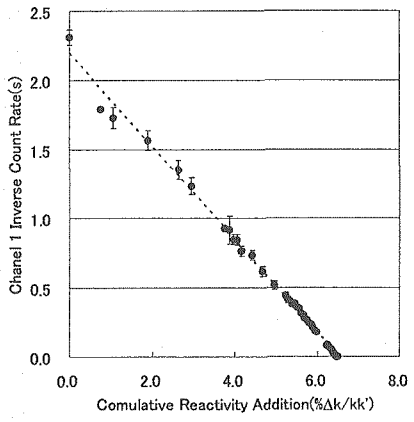

Fig. 2 MK-III Initial Approach to Critical.

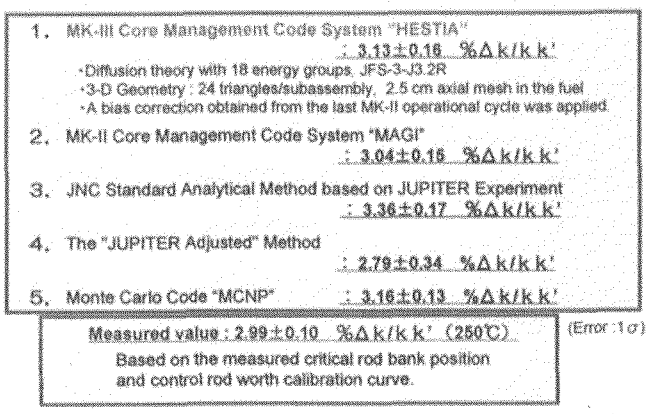

Fig. 3 Measured and Calculated Excess Reactivity.

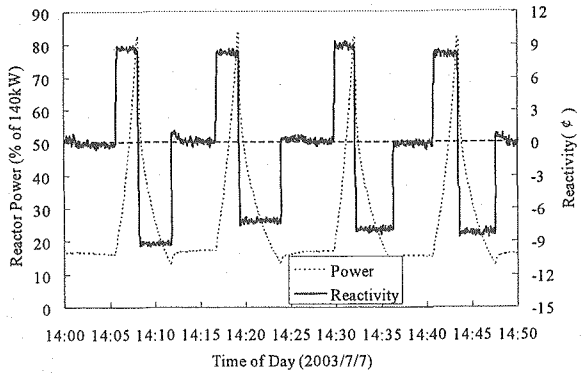

Fig. 4 Reactivity and Power During Part of a Reference-Type Calibration.

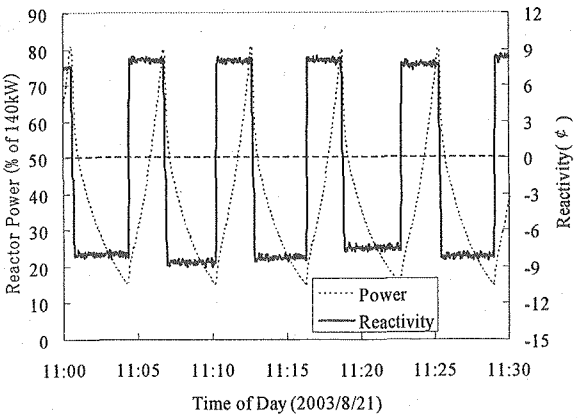

Fig. 5 Reactivity and Power Traces from a Juggling-Type Rod Calibration.

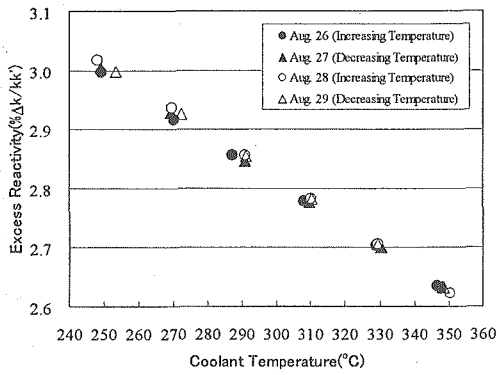

Fig. 6 Isothermal Temperature Coefficient Measurement Data.

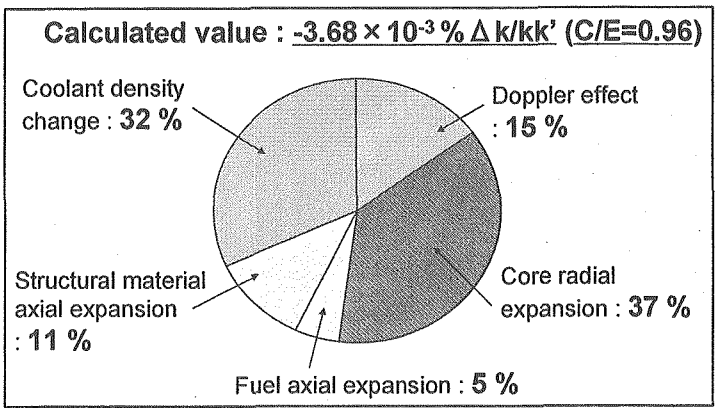

Fig.7 Analysis of Isothermal Temperature Coefficient.

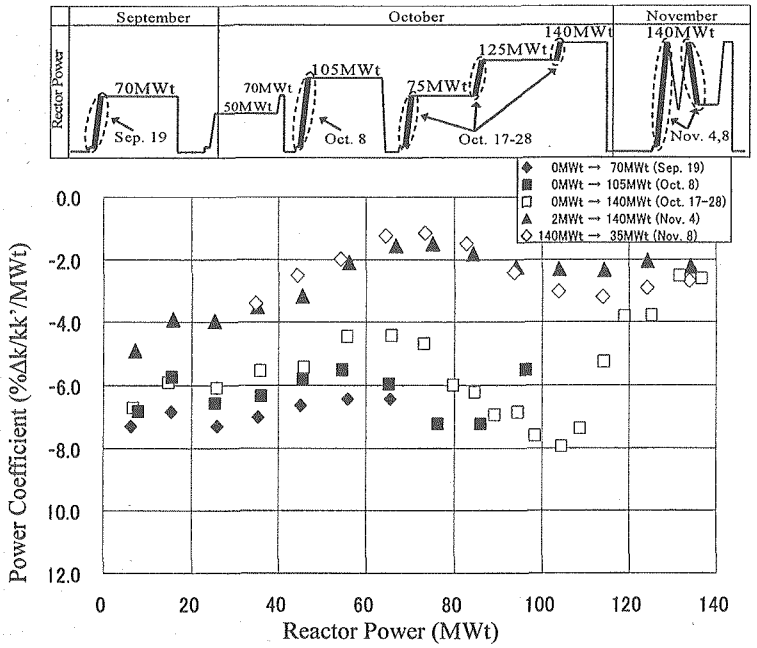

Fig. 8 Power Coefficient Measurements Results.

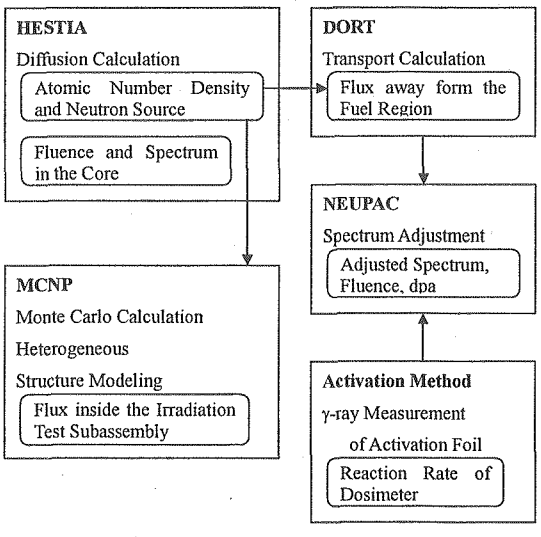

Fig.9 JOYO Neutron Field Evaluation System.

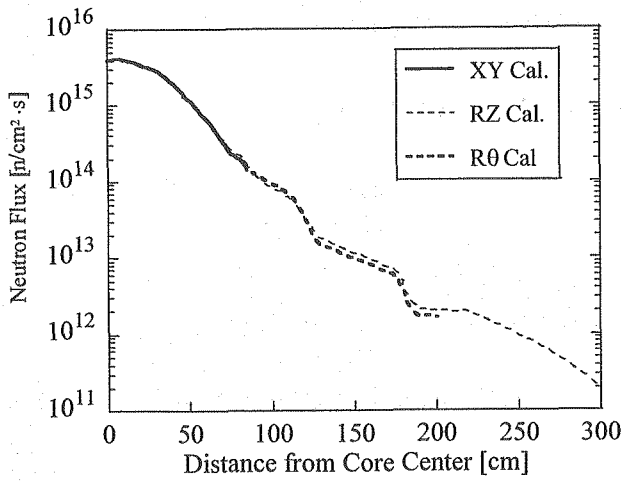

Fig. 10 Radial Flux Distribution by DORT.

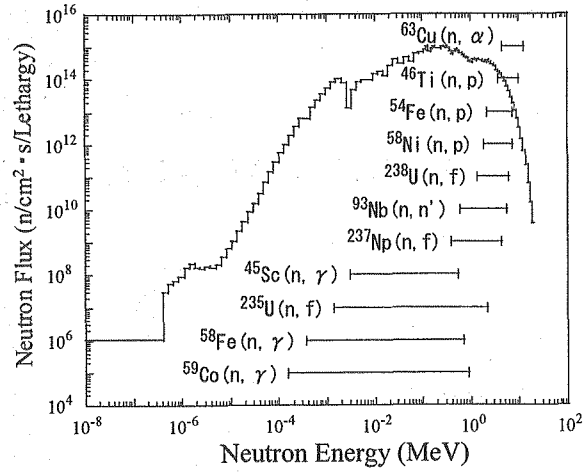

Fig. 11 Neutron Spectrum and 90% Confidence Level of Each Reaction

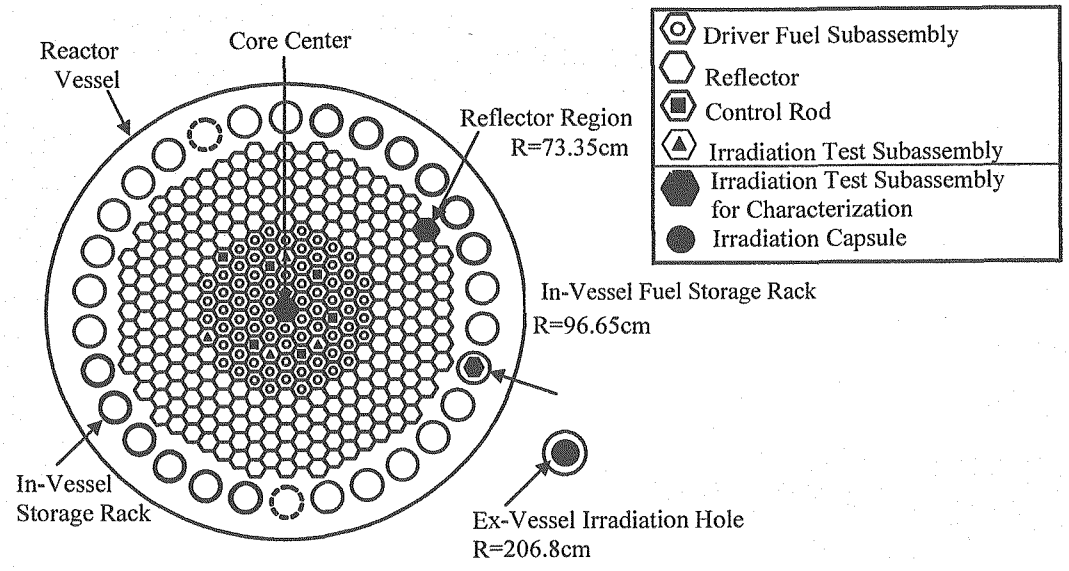

Fig. 12 Irradiation Test Subassemblies and Capsule Position.

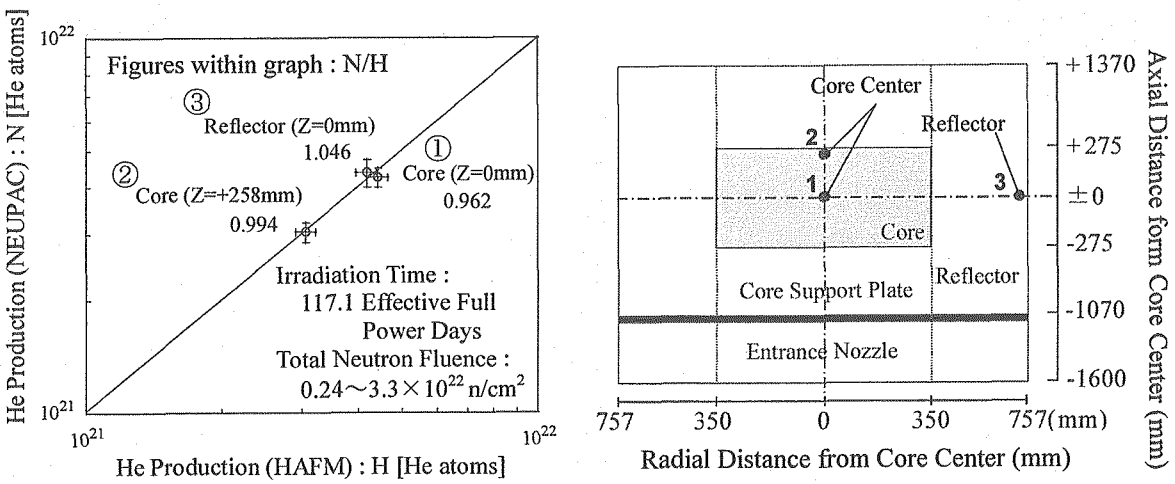

Fig. 13 Comparison of He Production Measurements at JOYO.

2.4 A STUDY ON THE THERMAL ANALYSIS AND STRUCTURAL DESIGN OPTIMIZATION OF A CYLINDRICAL STRUCTURE WITH MULTI SPECIMENS

Young-Shin Lee[1], Young-Jin Choi[2] and Young-Hwan Kang[3]

1: Dept. of Mechanical Design Engineering, Chungnam National University, 220 Kung-Dong, Yuseong, Daejeon, 305-764, Korea, +82-42-825-6531, leeys@cnu.ac.kr
2: Graduate School, Dept. of Mechanical Design Engineering, Chungnam National University, 220 Kung-Dong, Yuseong, Daejeon, 305-764, Korea
3: Korea Atomic Energy Research Institute(KAERI), Korea

ABSTRACT

During the irradiation tests of materials, all the components of a cylindrical structure with multiple specimens act like heat sources due to a high gamma flux. The thermal stress is induced by a temperature difference among the heat sources. In this study, the thermal stress of a cylindrical structure is minimized by using an optimization method regarding the geometric variables. The rectangular and circular shapes of the multi-specimens are investigated. For the thermal analysis of the structure, the finite element method code, ANSYS 8.1 is used. A sub-problem approximation method is used for the structural design optimization.

KEYWORDS: Optimization, Capsule, Thermal Stress

INTRODUCTUON

During a material irradiation test in a research reactor, all the components of a cylindrical structure with multiple specimens act as heat sources due to the γ-flux. Because of the different geometric shapes of the components, different temperature distributions for the heat source and different mechanical characteristics for the temperature are expected. The purpose of this study is to reduce the thermal stress of a cylindrical structure with multiple specimens used for the irradiation test. The optimization analysis of the cylindrical structure is performed by the ANSYS 8.1 program.

FINITE ELEMENT ANALYSIS

Analysis Model

Fig. 1 shows the geometry of the analysis model used in this study. The cylindrical structure is composed of the specimens, specimen holders and outer tube. The coolant

flows to the outside of the outer tube. The coolant temperature of the outer tube is constant. The heat generation density of each component of the cylindrical structure is constant. **Table 1** shows the dimensions of the cylindrical structure with multiple specimens. The material and heat generation of the components are presented in **Table 2**. **Table 3** shows mechanical and thermal properties of the cylindrical structure. In this study, the cylindrical structure has five specimens. **Fig. 2** shows the boundary conditions of the analysis model. Convection is considered for the boundary conditions at the outside of the outer tube. The heat transfer at the gap is by conduction through the gap. To conduct the optimal design for reducing the thermal stress of the cylindrical structure, an object function and limit conditions are formulated as follow;

Minimize: σ_{Max}

Subject to: 300 °C < T_{Max} < 500 °C

Design variable: r_2, r_4, α

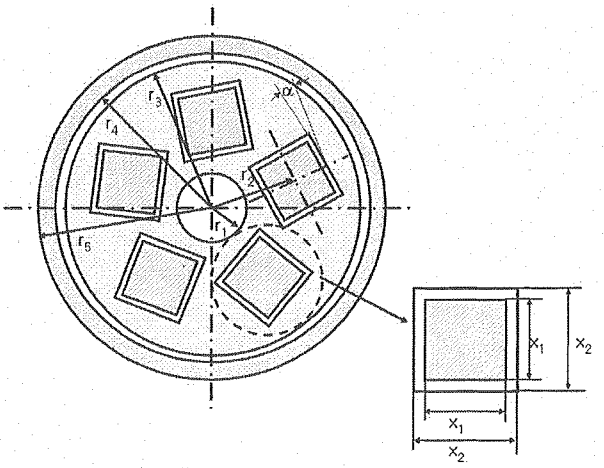

Fig. 1 Analysis model of the cylindrical structure.

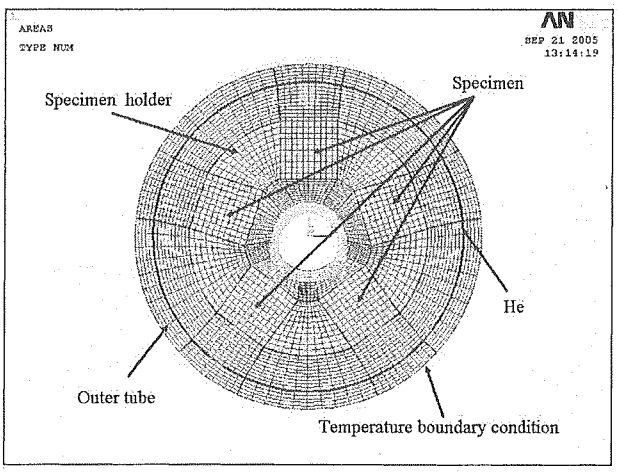

Fig. 2 Boundary temperature conditions of the cylindrical structure with multiple specimens.

Table 1 Dimensions of the cylindrical structure with multiple specimens

Descriptions	Symbol	Dimension (mm)
Inner radius of the center hole	r_1	6.00
Distance from the center of the hole to the center of the specimen	r_2	15.00
Outer radius of the holder	r_3	26.75
Inner radius of the outer tube	r_4	27.00
Outer radius of the outer tube	r_5	30.00

Table 2 Material and heat generation of components

	Material	Heat Generation (MW/m^3)
Specimen	SUS316	30.36
Specimen holder	Aluminum	10.79
Outer Tube	SUS316	30.64

Table 3 Mechanical and thermal properties of components

Property	Material	Temperature					
		50	100	150	200	250	300
Young's modulus (GPa)	SUS316	197.0	193.5	189.2	185.4	181.7	178.2
	Aluminum	67.8	65.6	60.2	55.2	44.6	34.5
Thermal expansion coeff.(W/℃)	SUS316	16.0e-6	16.0e-6	16.0e-6	16.0e-6	16.0e-6	16.0e-6
	Aluminum	23.3e-6	23.8e-6	24.1e-6	24.5e-6	25.0e-6	25.5e-6
Thermal conductivity (W/m · ℃)	SUS316	16.0	16.3	16.7	17.0	17.0	17.0
	Aluminum	204.2	206.3	210.9	215.3	222.7	230.4
	He	15.8e-2	17.3e-2	18.8e-2	20.3e-2	21.8e-2	23.3e-2
Mass density (kg/m^3)	SUS316	8000					
	Aluminum	2710					
Poisson's ratio	SUS316	0.3					
	Aluminum	0.33					

RESULTS AND DISCUSSION

Fig. 3 shows the initial results of the temperature profile of the cylindrical structure with multiple specimens. The highest temperature of the specimens and the lowest temperature of the outer tube are 386.4 °C and 55.3 °C, respectively. Due to the effect of the coolant, the heat flux in the outer direction is smaller than the heat flux of the center direction in the cylindrical structure. Therefore, the highest temperature does not occur in the center of the specimens.

Fig. 4 shows the initial result of the thermal stress of the cylindrical structure with multiple specimens. The maximum thermal stress is 68.5 MPa. The maximum thermal stress at the outer tube occurred by the temperature gradient.

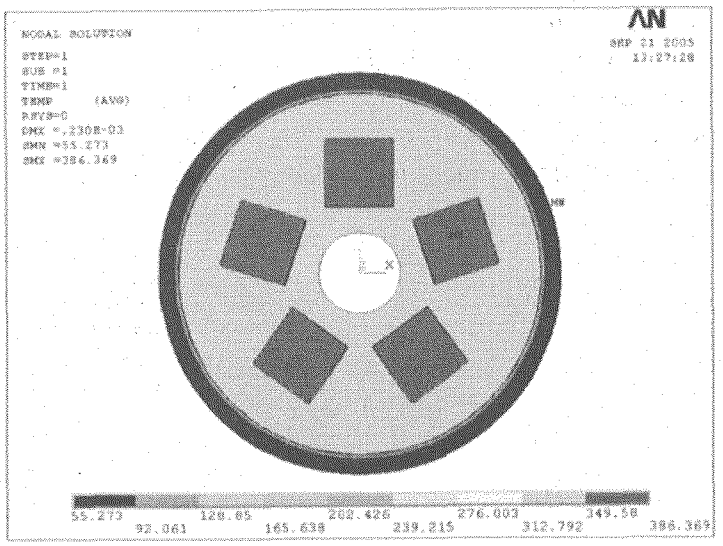

Fig. 3 Initial temperature distribution of the cylindrical structure with multiple specimens.

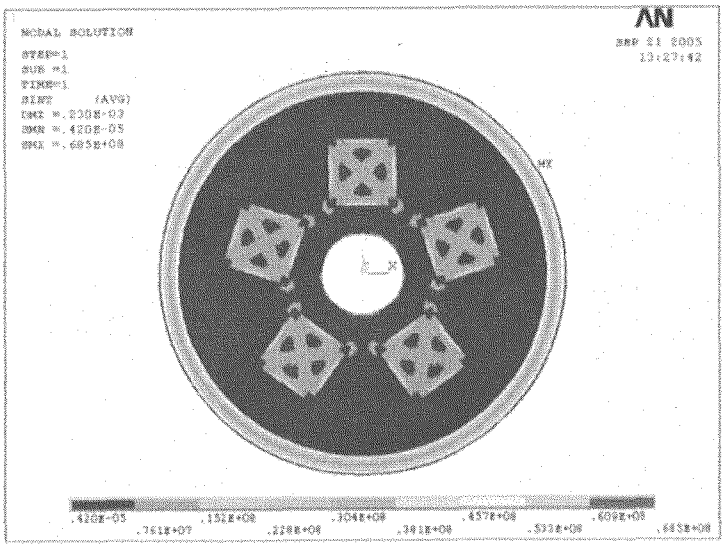

Fig. 4 Initial thermal stress of the cylindrical structure with multiple specimens.

Fig. 5 shows the design variable histories of the cylindrical structure. From the optimal results of the cylindrical structure, the inner radius of the outer tube and the rotation angle of the specimens increase with an optimal number of iterations 9. The rotation angle of the specimens of the cylindrical structure also increase from 0 ° to 5.4 °. The specimens

distance from the center of the cylindrical structure increases from 15.00 mm to 15.72 mm. The inner radius of the outer tube of the cylindrical structure increases from 27.00 mm to 28.00 mm. Due to the expansion of the space between the specimens and the outer tube, the maximum temperature of the cylindrical structure is reduced. And the location of the maximum temperature of the specimens is not in the center of the specimen because of the expansion of the specimens for the cylindrical structure.

Fig. 6 shows the maximum temperature histories and maximum stress of the cylindrical structure. The temperature variation by the r_2 is larger than the temperature variation by r_4 and α. The maximum temperature is affected by r_2.

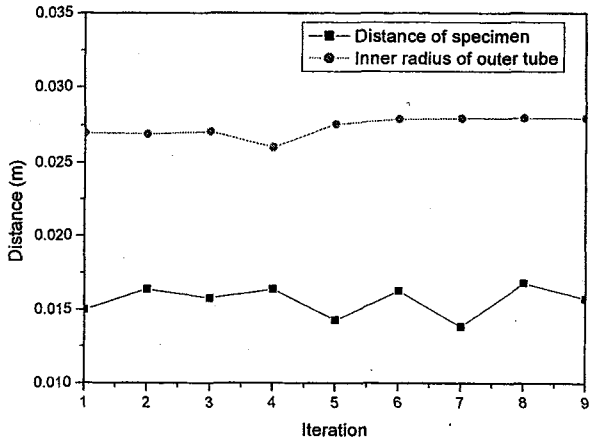

(a) Distance

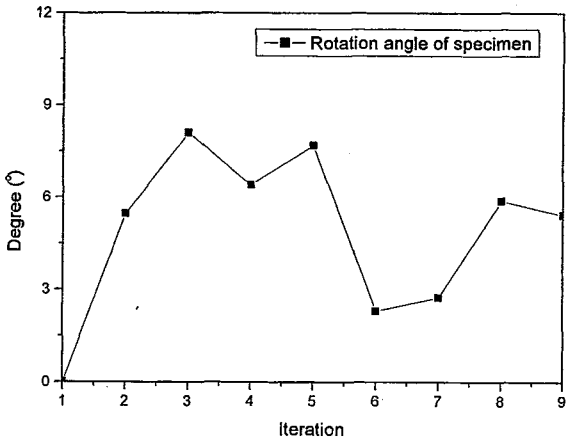

(b) Angle

Fig. 5 Design variable histories of the cylindrical structure.

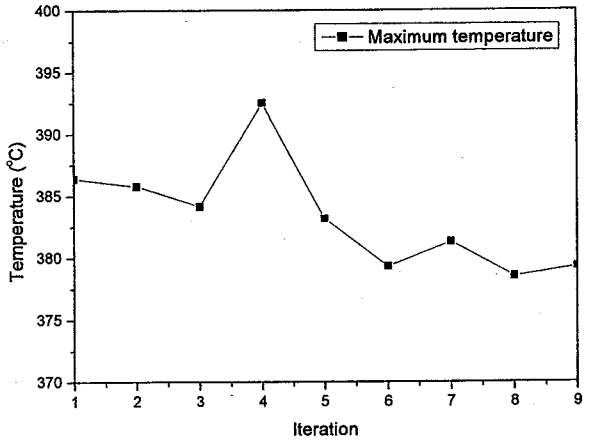

(a) Temperature

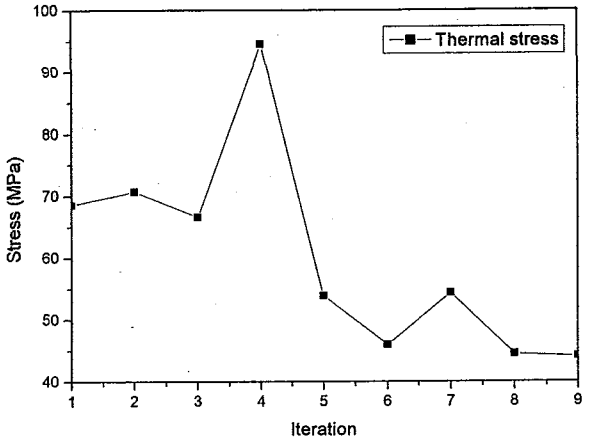

(b) Thermal stress

Fig. 6 Temperature histories and thermal stress histories of the cylindrical structure.

Fig. 7 shows the temperature distribution of the cylindrical structure with the optimized variables. The highest temperature of the specimens and the lowest temperature of the outer tube are 379.3 °C and 54.2 °C, respectively. The maximum temperature of the cylindrical structure is reduced by an increase of the specimens distance from the center of the cylindrical structure. Because of the rapid temperature variation of the cylindrical structure, the location of the maximum temperature of the specimens moves to the center hole.

Fig. 8 shows the thermal stress of the cylindrical structure with the optimized variables. At the outer tube of the cylindrical structure, the maximum thermal stress of 44.1 MPa is obtained along a temperature gradient. The maximum thermal stress at the outer tube decreases from 68.5 MPa to 44.1 MPa. The thermal stress distribution of the specimen holder occurred asymmetrically by the rotation angle of the specimens.

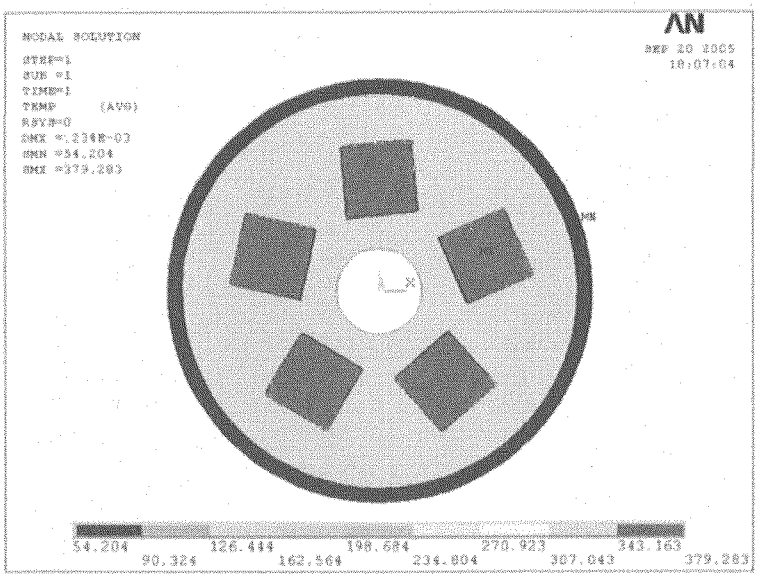

Fig. 7 Temperature distribution of the cylindrical structure with the optimized variables.

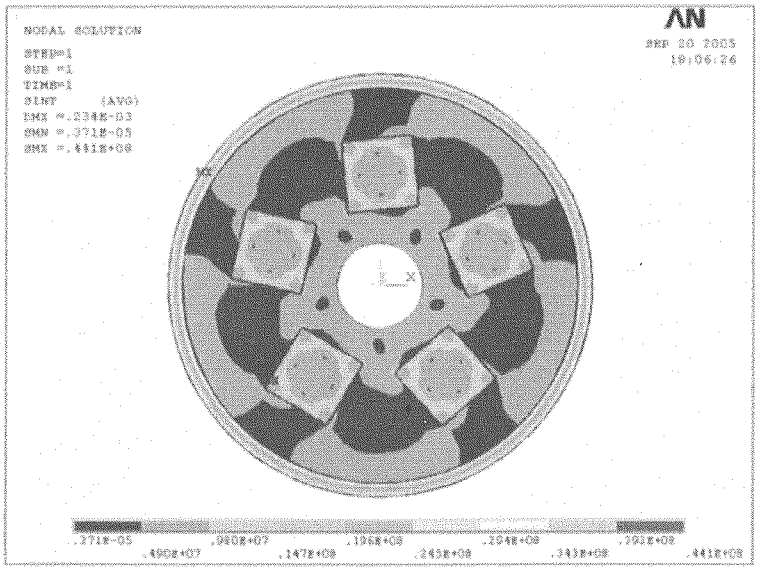

Fig. 8 Thermal stress of the cylindrical structure with the optimized variables.

CONCLUSIONS

The major findings from this study are as follows:

1) The inner radius of the outer tube of the cylindrical structure increases.
2) The location of the specimens moves to the outer tube direction.
3) The temperature variation by r_2 is larger than that of the other design variables.
4) The maximum temperature by an increase of the specimens distance from the center of the cylindrical structure decreases from 386.4 °C to 379.3 °C.
5) The maximum thermal stress by an increase of the specimens distance from the center of the cylindrical structure decreases from 68.4 MPa to 44.1 MPa.

REFERENCES

(1) Y. Harayama and M. Kyoya, 1986, "Analysis of Effect Eccentric Specimens in Pellets on Temperature and Heat Flux Distribution in Specimens", Journal of Nuclear Science and Technology, Vol. 23, No. 2, pp.151~159.
(2) Y. Harayama, H. Someya and T. Hoshiya, 1991, "Effect of Eccentric Pellet on Gap conductance in Specimens", Journal of Nuclear Science and Technology, Vol. 28, No. 10, pp.961~964.
(3) F. Kaminaga, S. Sato and Y. Okamoto, 1991, "Evaluation of Gap Heat Transfer between Boron Carbide Pellet and Cladding in Control Rod of FBR", Journal of Nuclear Science and Technology, Vol. 29, No. 2, pp.121~130.
(4) Y. Harayama, T. Hoshiya, H. Someya, M. Niimi and T. Kobayashi, 1993, "Estimation for Temperature Distribution in a Heat-Generating Cylinder with Multiple Specimens", Journal of Nuclear Science and Technology, Vol. 30, No.4, pp. 291~301.
(5) T. Furukwa, N. Noda and F. Ashida, 1990, "Generalized Thermoelasticity for an Infinite Body with a Circular Cylindrical Specimens", JSME International Journal, Series, Vol. 33, No. 1, pp. 26~32.
(6) Kang, Y. H., Lee, Y. S. and Choi, M. H., 1996, "Thermal and Mechanical Characteristics of Instrumented Capsule for Material Irradiation Test", Proceeding of the 5th Asian Symposium on Research Reactors, Vol.1, pp.328~332.
(7) Lee, Y. S., Choi, M. H., Kang, Y. H. and Shin, D. S., 2002, "A Structure Analysis of the Circular Cylinder with Multi-specimens under Thermal Loading", Nuclear Engineering and Design, Vol. 212, No. 27, pp.273~297.
(8) Choi, Y. J., 2002, "A Study on the Temperature and Thermal Stress of Cylindrical Structure with Multi-Specimens", Chungnam National University, Master Thesis
(9) Yoshihiro, O., Yoshinobu, T. and Osamu, I. 2000, "Optimization of Material Composition of Functionally Graded Plate for Thermal Stress Relaxation using a Genetic Algorithm", Journal of Thermal Stresses, Vol. 23, No. 3, pp.257~271.
(10) Lindgren, L. E., 2001, "Finite Element Modeling and Simulation of Welding Part 1: Increased Complexity", Journal of Thermal Stresses, Vol. 24, No. 7, pp.141~192.

2.5 IRRADIATION TEST PROGRAM OF HANA CLADDINGS IN HALDEN REACTOR

Myung Ho Lee, Jong Hyuk Baek, Jun Hwan Kim and Yong Hwan Jeong

Advanced Alloy Development, Advanced LWR Fuel Div.
Korea Atomic Energy Research Institute
P.O. Box 105, Yuseong, Daejeon, 305-600, KOREA

ABSTRACT

Since1997, KAERI (Korea Atomic Energy Research Institute) had launched an R & D program on the development of the advanced cladding for the high burn-up nuclear fuel. The newly developing claddings were being tested to verify their performances in both of the out-of-pile and in-pile conditions. Halden reactor (HBWR) in Norway was being utilized for the in-pile tests. Two rigs have been irradiated in the HBWR since February 2004, which water chemistry, neutron fluence and thermal hydraulic conditions are similar to those of commercial PWRs. The corrosion behavior of the cladding materials is assessed by means of once-a-year interim inspections, the first of which was performed in November 2004.

KEYWORDS: Halden Reactor, Irradiation Test, Fuel Cladding, HANA Cladding,

INTRODUCTION

The development of advanced zirconium alloys with an improved performance would be a prerequisite to meet the requirements of the high burn-up operation on the nuclear power plant. Since 1997, KAERI has carried out the R&D activities on the development of the advanced cladding for the high burn-up fuel. KAERI had produced the advanced claddings (HANA, High-performance Alloy for Nuclear Application) from the inherent composition and manufacturing process in the international collaborations. Now, the HANA claddings have being demonstrated their good performances from the out-of-pile tests including the corrosion, creep, burst, tensile, microstructures, LOCA, RIA, wear, and so on. In parallel to the out-of-pile performance tests, the *HANA* claddings are being undertaken to evaluate their in-pile properties in Halden reactor (HBWR) in Norway. Two irradiation rigs are devoted to the HANA claddings conducted at the Halden reactor. These tests are consisted of two sorts to the experiment: one is the fuelled cladding sections and the other unfuelled coupons. The two rigs have been irradiated in the HBWR since February 2004 during exposure to water chemistry, fluence and thermal hydraulic conditions similar to those found in commercial PWRs. The corrosion behavior of the test materials (in the form of fuelled tube claddings and/or coupons) is assessed by means of once-a-year interim inspections, the first of which

was performed in November 2004. In this paper, it contains the technologies, conditions, and results on the irradiation tests of the HANA claddings in Halden reactor.

HALDEN RESEARCH REACTOR

Halden Boiling Water Reactor (HBWR)

The Halden Boiling Water Reactor (HBWR) is located in Halden, a coastal town in south-east Norway near to the border to Sweden. The reactor vessel primary circuit system is inside a rock cavern with a net volume of 4500 m^2, as shown in **Fig. 1**. The rock covering is 30~60 m thick. Heat removal circuits are either placed inside the reactor hall or in the reactor entrance tunnel. Control room and service facilities are placed outside the excavation.

The HBWR is a natural circulation boiling heavy water reactor. The maximum power is 25 MW (thermal), and the water temperature is 240°C, corresponding to an operating pressure of 33.3 bar. The heavy water acts as coolant and moderator. A mixture of steam and water flows upwards by natural circulation inside the shroud tubes which surround the fuel rods. And, light water and high pressure loops provide facilities for testing under prototypic BWR and PWR conditions.

Reactor core description

Each driver fuel assembly consists of eight or nine fuel rods with 6 % fuel enrichment and standard fuel pellet diameter. The core consists of about 110~120 fuel assemblies, including the test fuel, in an open hexagonal lattice with a lattice pitch of 130 mm. 30 lattice positions are occupied by control stations. The maximum height of fuel section is 1710 mm, and the core is reflected by heavy water. The central position in the core is occupied by an emergency cooling tube with nozzles, and the positions between eight and fourteen core positions contain pressure flasks for the light water and high pressure test loops.

There are normally 2~3 main shutdowns per year, dictated primarily by the experimental programs, and a few additional cooling downs for special tests. The normal heating and cooling rates are 10°C/h.

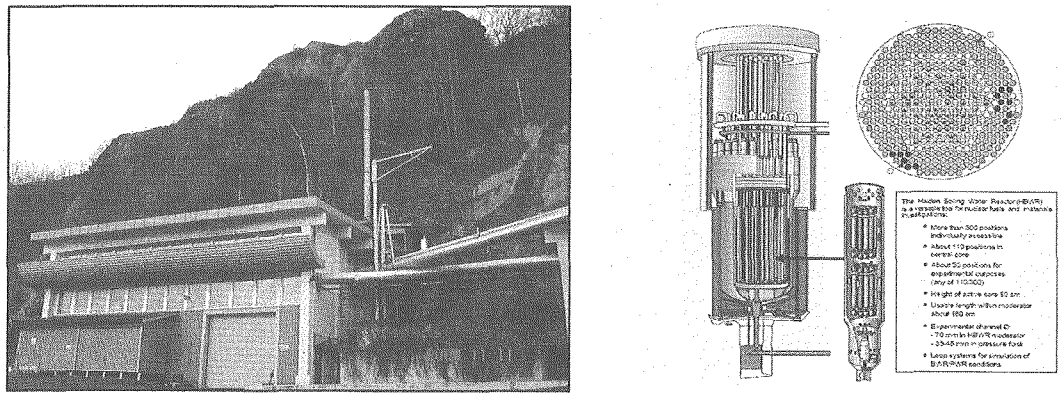

Fig. 1 Halden boiling water reactor (HBWR).

TEST RIG

Test rigs

Two irradiation rigs (IFA-673 and IFA-674) have been used for performing the KAERI advanced cladding corrosion test programme. IFA is an abbreviation for Instrumented Fuel Assembly. FFA-024 and FFA-025, the two pressure flasks to be used for loading of IFA-673 and IFA-674 in the Halden Boiling Water Reactor (HBWR). FFA is an abbreviation for Fuelled Flask Assembly. In other words, FFA indicates a pressure flask surrounded by booster fuel rods.

The irradiation rigs (IFA-673 / 674) with pressure flasks (FFA-024 / 025) are loaded into individual irradiation positions in the HBWR. The mechanical designs of all irradiation positions in the HBWR core are identical. An irradiation position is represented by a separate hole in the reactor lid and a cross-section of the upper part of an irradiation position is shown in **Fig. 2**. All pressure boundary seals (both between the reactor lid and the pressure flask assembly and between the pressure flask assembly and the irradiation rig) are represented by conical sealing surfaces and the mechanical force applied threaded nuts. **Fig. 2** shows the two conical seals, the nuts for applying the mechanical force to the sealing surfaces and other related components.

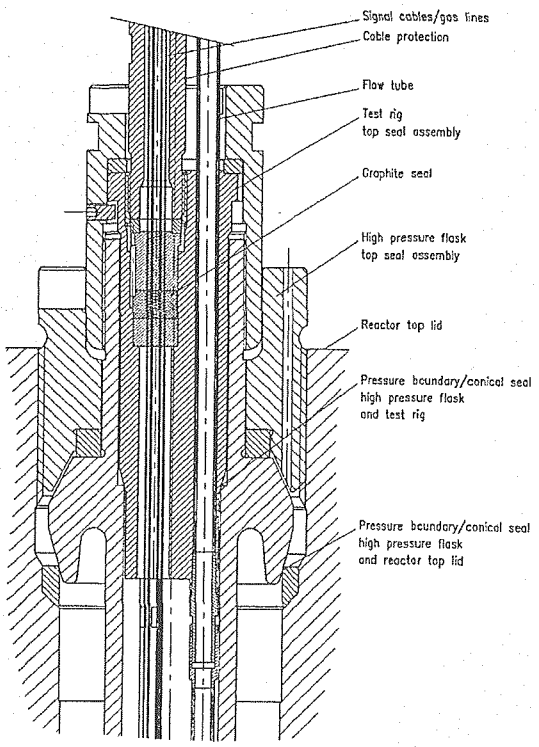

Fig. 2 Outline of a typical irradiation rig with pressure flask.

The overall design of the two irradiation rigs IFA-673 and IFA-674 is shown in **Fig. 3** (IFA-673 is shown, but the two rigs are identical). The irradiation rigs consist of several main components. The upper part of the rigs is the top seal assembly which serves as the main pressure boundary. The manifold assembly routes the coolant water to the test section and

connects the test section to the top seal assembly. The test section contains the test rods and material samples/coupons together with the instrumentation for thermal-hydraulic and neutronic measurements. The bottom cone which represents the lower part of the test section, routes the coolant water through the test section and serves as a guide when the irradiation rigs are loaded into the pressure flask assemblies. The construction materials are stainless steel, Inconel and zirconium alloys for the test section.

The top seal assembly constitutes the upper part of the irradiation rigs and represents the pressure boundary between the environment inside the high pressure loop and the environment outside the reactor pressure vessel. The top seal assembly serves triple functions; one is sealing against the high pressure flask, another is sealing of signal cables coming from the instruments and the other is connecting inlet and outlet flow tubes from the rig to the external loop system. The seal between the top seal assembly and the high pressure flask consists of a conical sealing surface which seals against a conical insert in the high pressure flask (see **Fig. 2**). The top seal assembly is forced against the conical seat in the high pressure flask by means of a threaded nut.

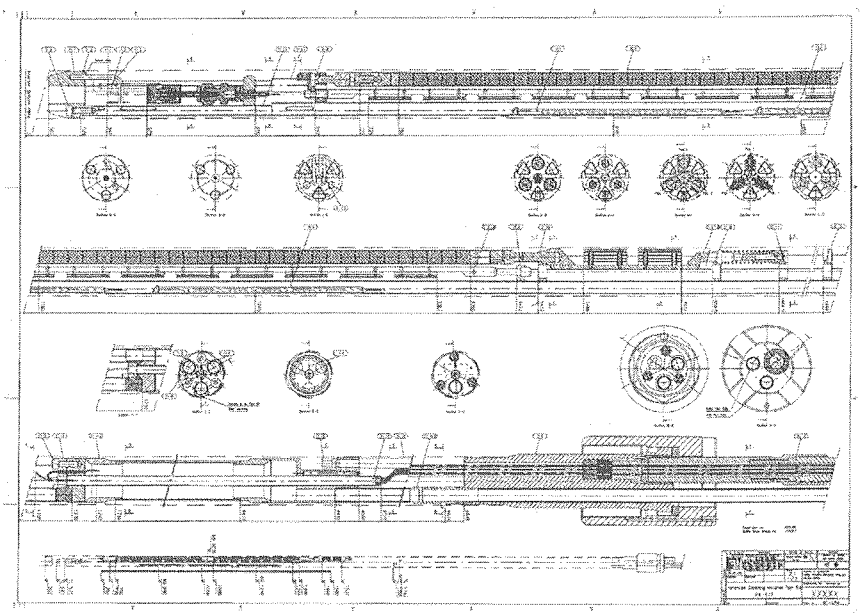

Fig. 3 Irradiation rig assembly of IFA-673.

The seal between the signal cables and the top seal assembly consists of a compressed graphite seal (see **Fig. 2**). The signal cables leaving the irradiation rigs are protected by flexible protection tubes/hoses made from a double braided stainless steel mesh. The flexible cable protections cover/protect the signal cables over the distance from the top seal assembly to the permanent signal cable connections in the reactor hall. The flexible cable protections used on IFA-673 and IFA-674.

The flow tubes in the top seal assembly have a function of the connection between the external loop system and the irradiation rigs. A section of the inlet and outlet flow tubes are welded to the bottom end of the top seal assembly. Above the top seal assembly the inlet and outlet flow tubes are connected to the external loop system with mechanical seals, consisting of conical seals loaded by threaded nuts. The top seal flow tube connectors represents a

standard Halden Project design qualified and used for test rigs which are loaded into the HBWR. The lower end of the inlet flow tube is connected to the upper end of the manifold assembly with a tube extension.

The manifold assembly connects the top seal assembly with two downcomer tubes and a signal cable tube in the test section. Both downcomer tubes and the signal cable tube represent the lower structural part of the rig. The downcomer tubes route the coolant water to the bottom of the rig, where the inlet section is located. The inlet section routes the coolant water through the test section where it is exposed to the test rods and coupons. After the coolant water has passed through the test section, the coolant water is routed into the manifold assembly again (the outlet ports) and leaves the irradiation rig through the top seal assembly. The cable tube first routes the signal cables through the test section into the manifold assembly and then to the top seal assembly.

For temperature monitoring, three inlet coolant thermocouples, one outlet and one downcomer coolant thermocouple is installed in each irradiation rig. System pressure, temperature, flow, and water chemistry are monitored in the outer loop system. Each irradiation rig will also be instrumented with three self-powered neutron detectors (vanadium-type for measuring thermal flux). The thermal flux can be related to fast flux by neutronic calculations which again can be verified by the analysis of fluence monitor wires installed in the test rig. Three different fluence monitor wires is installed in the test rig - iron and nickel wires for measuring fast neutron fluence and cobalt wires for measuring thermal neutron fluence. The fluence monitor wires can be analysed in conjunction with interim inspections. The fluence monitor wires cover the full length of the test section in the irradiation rigs.

Pressure flasks

The pressure flasks serve as the pressure boundary between the environment inside the reactor pressure vessel and environment inside the PWR loop system. The pressure flasks also serve as the main pressure boundary between the environment inside the reactor pressure vessel and the environment outside the reactor pressure vessel. The pressure flasks are made from zirconium alloys, Inconel and different types of stainless steels.

The top seal assembly constitutes the upper part of the pressure flask. The top seal assembly serves double functions; one is to seal against the reactor lid, the other is to serve as the conical seat which seals against a conical sealing surface in the irradiation test rigs (see **Fig. 4**). The seal between the top seal assembly and the reactor lid consists of a conical sealing surface which seals against a conical seat in the reactor lid. The top seal assembly is forced against the conical seat in the reactor lid by means of a threaded nut.

The zirconium alloy pressure tube (representing the test channel) is connected to the top seal assembly by using a co-extruded joint and is the pressure boundary between the PWR loop system and the HBWR moderator. The pressure tube is covered by a thermal insulation tube (forming an insulating steam blanket between the thermal insulating tube and the pressure tube) for reducing the heat losses to the HBWR moderator (which operates at 235 °C) and enables to increase the temperature within the test rigs to typical PWR conditions.

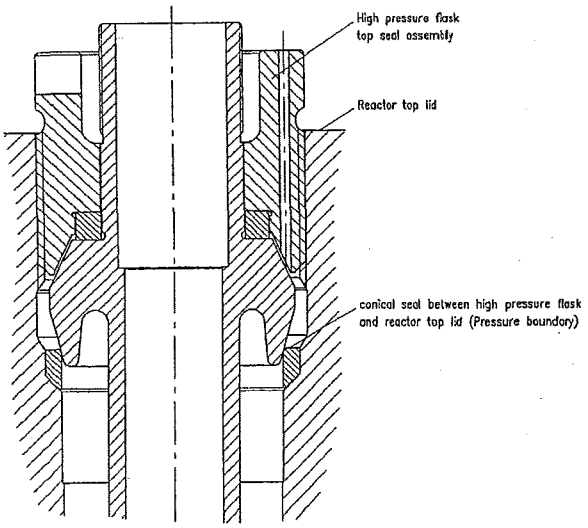

Fig. 4 Outline of a typical pressure flask.

In order to achieve the specified fast neutron flux in the irradiation rigs, the pressure flasks are surrounded by 15 enriched booster fuel rods. The enriched/active length of the booster fuel rods is 800 mm. The booster fuel rods are located outside the thermal insulation tube surrounding the pressure tube, and are contained within a thin walled shroud (representing the outer boundary of the irradiation channel).

The inlet section constitutes the lower end of the pressure flasks and serves double functions; one is guide for the flask assembly into the reactor bottom plate, the other is to serve as the distributor of coolant water (moderator water) into the channel between the shroud and the pressure tube for cooling the booster fuel rods. The inlet section is made in such a way that we can change between forced and natural circulation of the coolant water.

Test specimens

Each of the two irradiation rigs, IFA-673 and IFA-674, will contain three segmented fuel rods (see **Fig. 5**). Each segment will have an enriched fuel length of 300 mm. Further, the two irradiation rigs accommodate 39 coupons at maximum. The coupons are positioned according to the test matrix given in the specifications. A total of 15 coupons can be installed in a central coupon holder located between the fuel rods and a total of 24 coupons can be installed in two clusters just above the fuel rods.

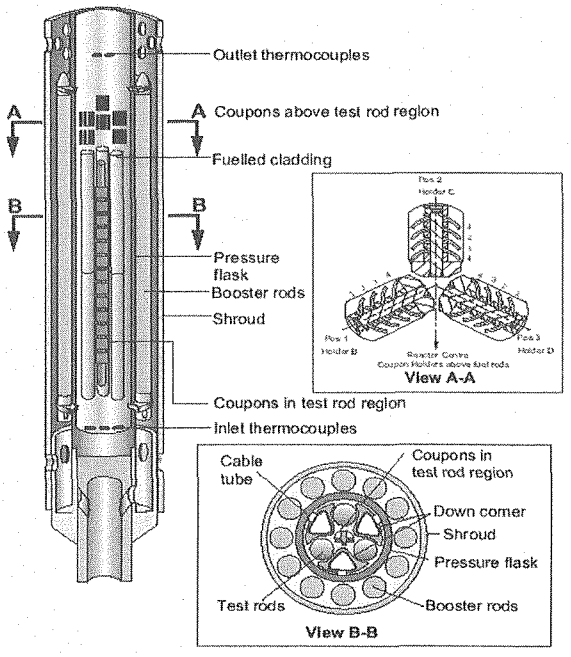

Fig. 5 Schematic view of irradiation rig with test rods and test coupons.

IRRADIATION CONDITIONS

Heat rate

The average linear heat rate has been in the range from 30 to 35 kW/m during most of the irradiation in all the rods.

Neutron flux and fluence

The fast neutron flux levels ($\geq$ 1 MeV) within the fuel rod region ranges from 2.0 to 3.5 x 10^{13} n/cm^2/s. Calculated fast neutron fluence levels at the fuelled section were 0.3 to 0.5 × 10^{21} n/cm^2-s.

Coolant temperature

The coolant temperature measured at the inlet of the test rig was 291°C with about 25°C rise in temperature through the channel.

Coolant pressure and flow rate

The coolant flow rate and pressure have been kept at about 1.68m/s and from 163 to 166 bar, respectively, for the main part of the irradiation. The thermal hydraulic conditions along the axial length of the fuel rods have been calculated from the start-up. The results of these calculations, which are based on the average measured oxide thickness for each segment assuming that the thermal conductivity of zirconium oxide is 0.020 W/cm-K.

Water Chemistry

It is measured the concentrations of lithium (2 ppm) and boron (700 ppm) from the coolant analysis and calculated the pH_{300} (~7.1) in IFA-673 and IFA-674. The hydrogen

content has been maintained at about 2 ppm, and no oxygen has been measured in the coolant.

IRRADIATION RESULTS

Test methods

The interim inspections of IFA-673 and IFA-674 cover the following; photography of cladding segments (both before and after brushing), diameter measurements of fuelled cladding segments, oxide thickness measurements on fuelled cladding segments by means of an eddy current proximity probe (based on an individual calibration for each material type), eddy current measurements on fuelled cladding segments to look for the effects of hydrides and possible cladding defects, and photography and weighing of coupons.

The coupons were ultrasonically cleaned for 10 minutes in de-mineralized water, and then dried for 1 hour at 100°C before weighing on a five-point balance.

Test results of fuel test rods

(1) Corrosion

The oxide thicknesses on the fuel rods range from ~5 μm to ~17 μm depending on alloy and axial position (i.e. heat flux). The average oxide thickness for the highest region of each segment (top of lower segment and bottom of upper segment) is plotted in **Fig. 2** for all alloys. It is seen that, in general, the *HANA* claddings show better corrosion resistance than the two reference alloys (A-cladding and Zry4). All of the *HANA* claddings had an excellent corrosion resistance in the comparison with the references, as shown in **Fig. 6**. The corrosion resistance of some *HANA* claddings was improved by 40~50 % when compared with the reference A-cladding on the basis of the oxide thickness measurements.

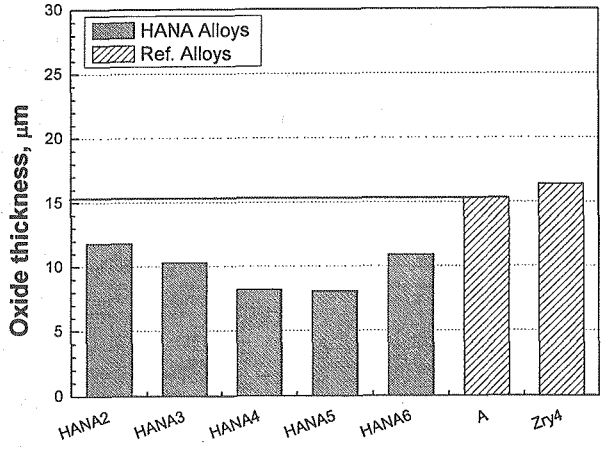

Fig. 6 In-pile oxide thickness of HANA claddings.

(2) Creep

Fig. 7 shows that the creep-downs of the *HANA* claddings were superior to those of the two references (A-Cladding and Zircaloy-4). Especially, the creep resistance of *HANA4* was improved by about 70%, compared with the reference A-cladding.

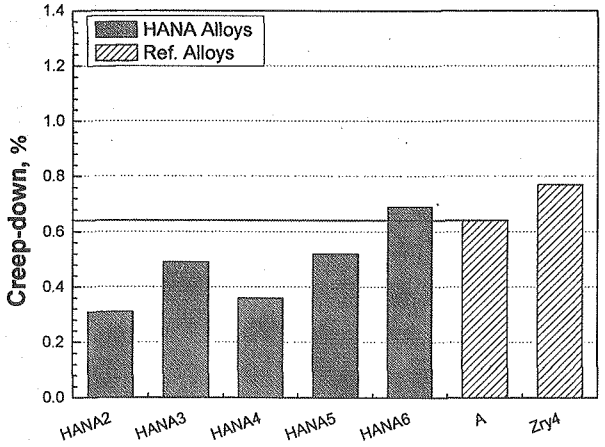

Fig. 7 In-pile creep downs of HANA claddings.

(3) Hydrides and defect
No evidence of clad defects was seen from these scans on any of the fuel rods.

(4) Visual inspection
No irregularities were seen on any of the rods.

Test results of unfuelled corrosion coupons

(1) Corrosion
All coupons showed weight gain in the range 21 mg/dm^2 to 56 mg/dm^2 depending on alloy and axial position. The weight gains of HANA cladding coupons were lower than those of the reference cladding coupons.

(2) Visual inspection
No irregularities were seen on any of the coupons.

CONCLUSIONS

The irradiation rigs IFA-673 and IFA-674 are devoted to the HANA claddings conducted at the Halden Reactor (HBWR) in Norway. This test is consisted of two parts to the experiment: one using fuelled cladding sections and the other using unfuelled coupons. The position of the coupons is in holders both above the test fuel rods and also along the center of the rig. The two rigs IFA-673 and IFA-674 have been irradiated in the HBWR since February 2004 during exposure to water chemistry, neutron fluence and thermal hydraulic conditions similar to those of the commercial PWRs. From the irradiation test, The HANA claddings showed better corrosion and creep resistances than the two reference alloys (A-Cladding and Zircaloy-4). And the weight gains of HANA cladding coupons were lower than those of the reference cladding coupons.

2.6 DEVELOPMENT OF MOX FUEL CONTAINING AMERICIUM -ITS FABRICATION AND CHARACTERIZATION-

Shuhei Miwa, Masahiko Osaka, Hiroshi Yoshimochi and Kenya Tanaka

Alpha-Gamma Section, Fuels and Materials Department,
O-arai Research and Development Center, Japan Atomic Energy Agency
4002 Narita-cho, Oarai-machi, Higashi-Ibaraki-gun, Ibaraki-ken, 311-1393 Japan

Ken Kurosaki and Sinsuke Yamanaka

Department of Nuclear Engineering, Graduate School of Engineering, Osaka University

ABSTRACT

The effect of oxygen potential on the sintering behavior of MOX fuel containing Am, which has high oxygen potential, is investigated by ceramography and metrology. Then, the phase relation of the fabricated Am-MOX is obtained by ceramography, XRD and DTA.

KEYWORDS: MOX fuel, Minor actinides, Americium, Sintering behavior, Phase relation

INTRODUCTION

In reprocessing spent nuclear fuel, the minor actinides (MAs); i.e. neptunium (Np), americium (Am) and curium (Cm), are transferred into the high-level radioactive waste. Included among them are the key nuclides, Np and Am. Since these elements, which are radiologically toxic, have a large generation yield and long half-life. And their impact on the environment through the geological disposal of the high-level waste can not be ignored.

Japan Nuclear Cycle Development Institute (JNC) promotes R&D programs for future nuclear cycle technology based on fast reactors [1]. One of the programs is to establish a technique to separate MAs from the high-level waste and then to transmute them to non-radiotoxic and short-lived nuclides by neutron irradiation. The development of mixed

oxide fuel containing Am (Am-MOX) is one item of this program which is underway.

So far, the fabrication technique of Am-MOX with remote handling has been established [2] by using various apparatuses installed in the hot cell. **Fig. 1** shows their layout in shielded hot cells, which contain an air-tight stainless steel box in it. Several properties such as oxygen potential [3] have also been experimentally determined. Results of these studies showed that only a small amount of Am addition to MOX had significant effects on various properties.

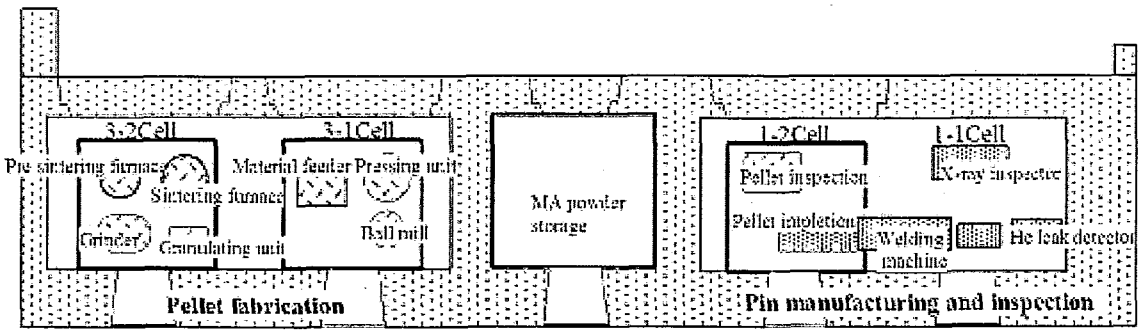

Fig. 1 Layout of in-cell apparatuses used for the Am-MOX fuel pellet fabrication and pin manufacturing.

The oxygen potential of Am-MOX, which is an important property from the viewpoint of fuel design, was found to be extremely high [3], compared to that of MOX. Oxygen potential is known to affect sintering behavior of nuclear fuel. Therefore, it is important to investigate the effect of oxygen potential on the sintering behavior of Am-MOX. In this study, Am-MOX pellets sintered at various oxygen potentials were examined by ceramography and metrology.

The phase relation of Am-MOX solid solution is also an essential prerequisite for evaluating various properties, together with the irradiation behavior of Am-MOX pellet. In this study, therefore, the effects of Am addition up to 5 % to MOX on the phase relation are investigated experimentally. Am-MOX of which the oxygen contents (O/M ratios) are adjusted are examined by XRD, ceramography and DTA.

EXPERIMENTAL

Sintering tests of Am-MOX

Green pellets of Am-MOX were prepared by a conventional powder metallurgical technique.

Known amounts of UO_2, PuO_2 and $(Pu,^{241}Am)O_2$ powders were weighed out using an electronic balance for the preparation of $(U_{0.68}Pu_{0.27}Am_{0.05})O_2$. This was followed by

mixing for 8 h using alumina balls in a ball mill. Organic binder was added to the mixed powder and this was compacted by uni-axial pressing at 400 MPa to get green pellets. The green pellets were heated at 800 °C for 2.5 h in a reducing atmosphere to remove the organic binder [2].

Sintering tests for the green pellets were performed at 1700 °C for 3 h under an Ar atmosphere containing 5 % H_2. Both heating and cooling rates were 200 °C/h. The oxygen potentials of the sintering atmosphere were adjusted by adding moisture to get values of -520 kJ/mol, -390 kJ/mol and -340 kJ/mol at 1700 °C.

The density was obtained from metrological results of the pellets. The microstructural analyses of the sintered Am-MOX pellets were done by cross-sectional ceramography.

Phase relation

Sintered pellets were then thermally treated under Ar/H_2 at different oxygen potentials to adjust the O/M ratios to 1.94, 1.96, 1.97 and 2.00. Phase relation was investigated using X-ray diffractometry (XRD), ceramography, and differential thermal analysis (DTA) for pellets of different O/M ratios.

The XRD patterns of the pellets were obtained by using CuKα radiation. The lattice parameter of Am-MOX was obtained by detailed peak analysis.

RESULTS

Sintering behavior of Am-MOX

Fig. 2 shows the density (percents of theoretical density; %TD) of the sintered Am-MOX pellets as a function of the oxygen potential. The densities of the Am-MOX pellets sintered at -520 kJ/mol, -390 kJ/mol and -340 kJ/mol are 92.3 %TD, 94.0 %TD and 91.1 %TD, respectively. Clearly, the sintered densities are affected by the oxygen potential. The sintered density increases with increase of oxygen potential up to -390 kJ/mol (threshold oxygen potential), then decreases above that potential. This tendency is similar to that observed in the $(U,Gd)O_2$ system [4].

Fig. 3 shows ceramographic images of as-polished surfaces of Am-MOX pellets. For the pellet sintered at -520 kJ/mol, both small and large pores with rough inner surfaces are observed and its grain boundaries are wider than those of other two. This result is similar to that for low O/M ratio=1.97 as mentioned below, and may be attributed to the lowered O/M ratio. Relatively large pores with smooth inner surfaces are distributed in the pellets sintered at -390 kJ/mol and -340 kJ/mol.

Fig. 4 shows the area of total pores, pore radius and pore number density are obtained by image analysis for a detailed discussion of the microstructure. While the pellet sintered at -340 kJ/mol has almost the same number density of pores as the pellet sintered at -390 kJ/mol, it has a larger pore radius and therefore, a larger total area of pores.

This difference in the pore structures can explain the difference in the density of Am-MOX pellets shown in **Fig. 2**.

Am-MOX pellets having high density are obtained by sintering at -390 kJ/mol for these experimental conditions.

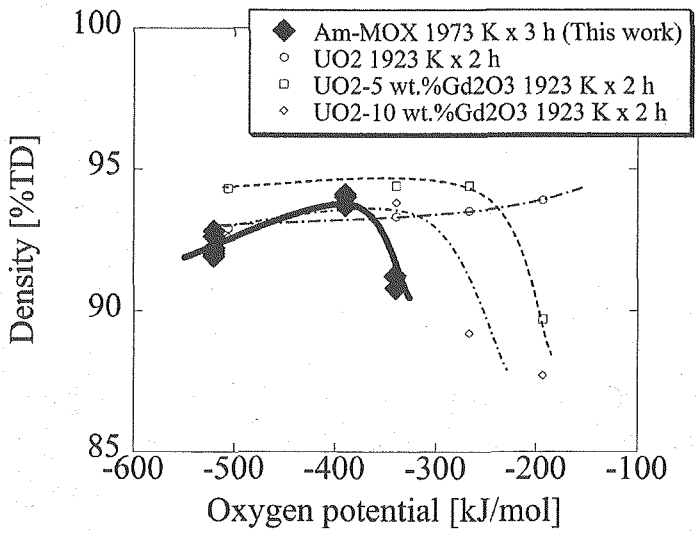

Fig. 2 Dependence of sintered theoretical density of 5% Am-MOX and $(U,Gd)O_2$ [4] on the oxygen potential.

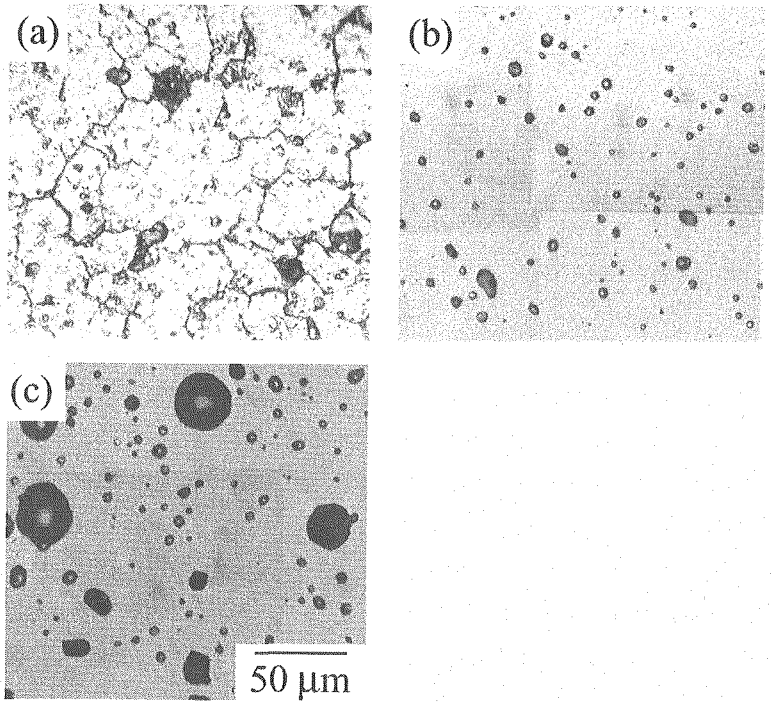

Fig. 3 Ceramographic images for as-polished surface of Am-MOX pellets sintered at (a) -520 kJ/mol, (b) -390 kJ/mol and (c) -340 kJ/mol.

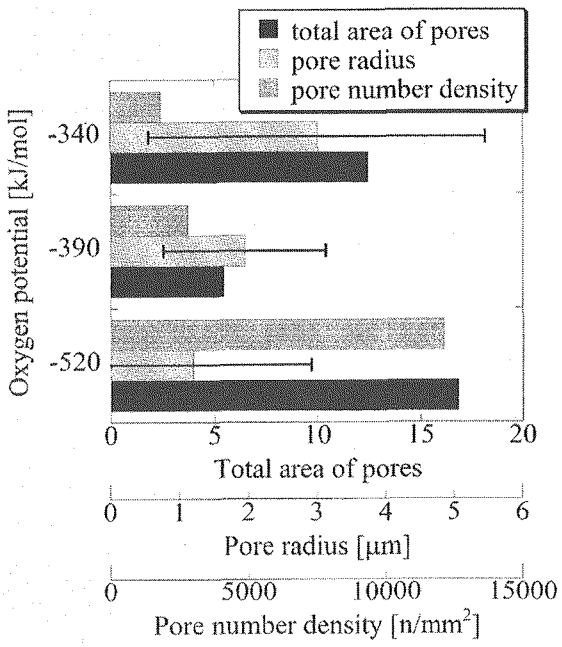

Fig. 4 Pore analysis, total pore areas, pore radius and pore number density.

Phase relation

Am-MOX pellets sintered at -390 kJ/mol were then thermally treated under Ar/H_2 at different oxygen potentials to adjust the O/M ratios to 1.94, 1.96, 1.97 and 2.00.

Fig. 5 shows the X-ray patterns for $(U_{0.66}Pu_{0.29}Am_{0.05})O_{1.97}$ and $(U_{0.66}Pu_{0.29}Am_{0.05})O_{2.00}$. Sharp and separated peaks for $(U_{0.66}Pu_{0.29}Am_{0.05})O_{2.00}$ are observed. The peaks for $(U_{0.66}Pu_{0.29}Am_{0.05})O_{1.97}$ are broader than those for $(U_{0.66}Pu_{0.29}Am_{0.05})O_{2.00}$. This result is attributed to the difference of O/M ratio, i.e., a distortion of the lattice. There were no other peaks than those derived from fcc single phase for $(U_{0.66}Pu_{0.29}Am_{0.05})O_{1.97}$ and $(U_{0.66}Pu_{0.29}Am_{0.05})O_{2.00}$.

Fig. 6 shows the lattice parameter dependence of hypostoichiometric $(U_{0.66}Pu_{0.29}Am_{0.05})O_{2-x}$ on O/M ratio. The lattice parameter increases with decrease of O/M ratio. It is noted that the slope of the line for lattice parameter versus O/M ratio of $(U_{0.66}Pu_{0.29}Am_{0.05})O_{2-x}$ is smaller than that of non Am-containing $(U_{0.7}Pu_{0.3})O_{2-x}$ [(5)]. The reason is not clear at the present, nevertheless it may be caused by a different kinetic aspect of oxidation/reduction for Am-MOX from that of MOX.

Fig. 7 shows ceramographic images of $(U_{0.66}Pu_{0.29}Am_{0.05})O_{2-x}$ with O/M=2.00 (as-etched), 1.99 (as-etched) and 1.97 (as-polished). Structures of $(U_{0.66}Pu_{0.29}Am_{0.05})O_{2-x}$ with O/M=2.00 and 1.99 are homogeneous; there are relatively small pores and homogeneous grain growth. On the other hand, the structure of hypostoichiometric $(U_{0.66}Pu_{0.29}Am_{0.05})O_{1.97}$ is not homogeneous; in particular, grain boundaries are wider despite being as-polished specimens and their surfaces are rougher. In addition, large pores, which were caused by coming off of grains, are observed. This indicates that the grain

boundary of $(U_{0.66}Pu_{0.29}Am_{0.05})O_{2-x}$ was weakened by lowering the O/M ratio.

Fig. 8 plots DTA peak locations observed in the phase diagram of temperature versus O/M ratio of $(U_{0.66}Pu_{0.29}Am_{0.05})O_{2-x}$. Many DTA peaks which showed a phase transition were observed on both raising and lowering the temperature at constant O/M ratios. The DTA peaks are so small that they should by derived not from stable phase transitions but from quasi-stable ones. Since such DTA peaks are not observed for $(U,Pu)O_{2-x}$, these are considered to be caused by the Am addition.

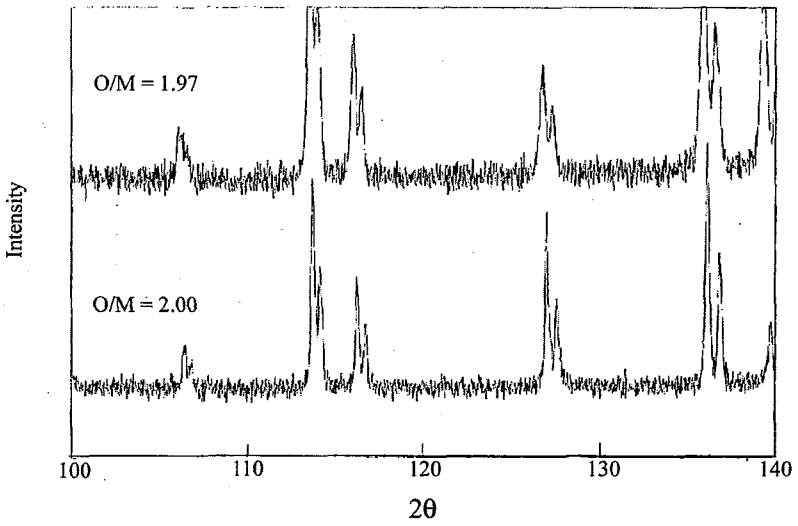

Fig. 5 X-ray patterns for Am-MOX.

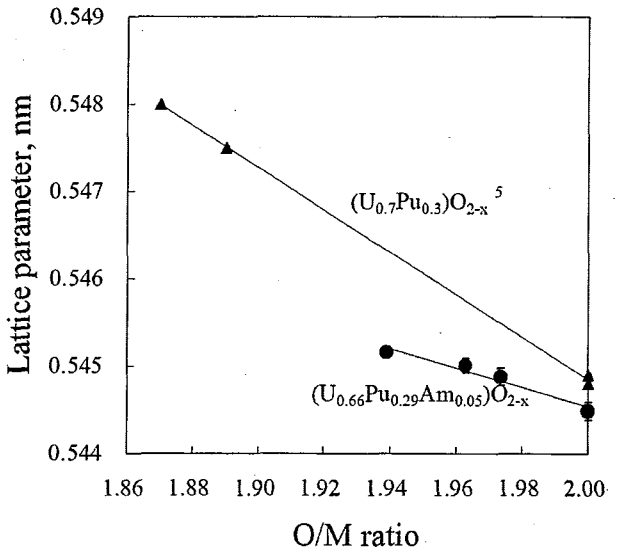

Fig. 6 Dependences of lattice parameter of $(U,Pu,Am)O_{2-x}$ on O/M ratio.

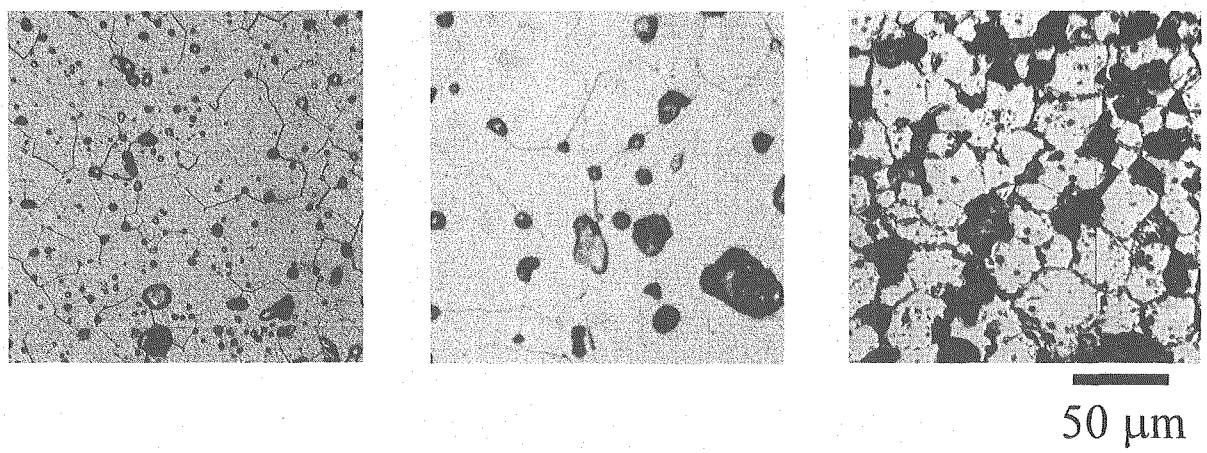

(a) O/M: 2.00 (b) O/M: 1.99 (c) O/M: 1.97

Fig. 7 Ceramographic images of: (a) stoichiometric $(U_{0.66}Pu_{0.29}Am_{0.05})O_{2.00}$, (b) $(U_{0.66}Pu_{0.29}Am_{0.05})O_{1.99}$ and (c) $(U_{0.66}Pu_{0.29}Am_{0.05})O_{1.97}$.

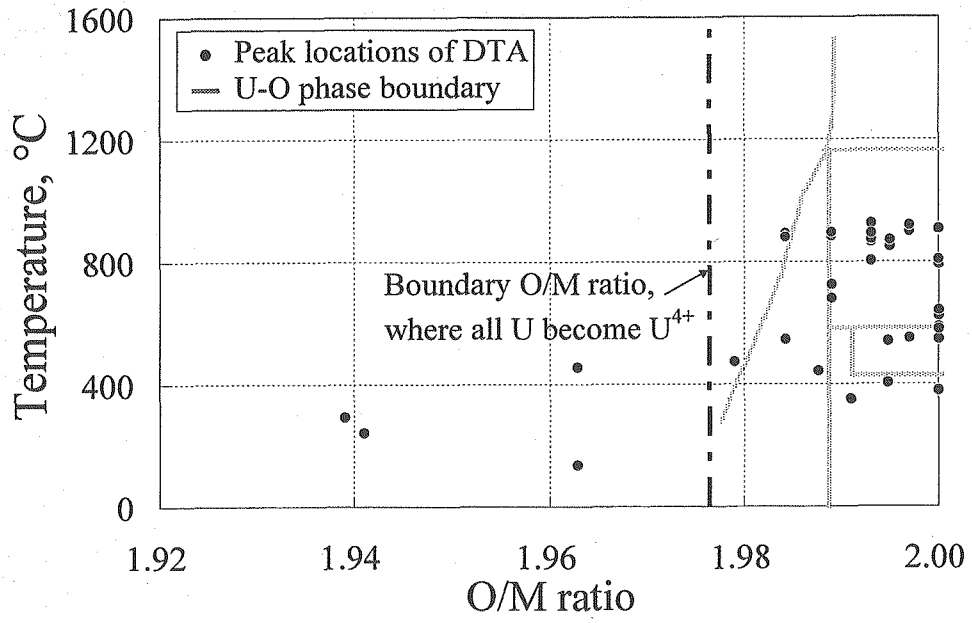

Fig. 8 Peak locations observed in DTA plotted on the phase diagram of temperature versus O/M ratio of $(U_{0.66}Pu_{0.29}Am_{0.05})O_{2-x}$.

DISCUSSION

Effects of oxygen potential on the sintering behavior

The difference in the sintering behavior of Am-MOX pellets is considered to be affected by the difference in the pore structures. Though previous works show the effect of sintering

atmosphere, that is oxygen potential, on the sintering behavior [6,7,8,9], the existence of a threshold oxygen potential which causes lowering of sintering density has not been shown for $UO_{2\pm x}$ and $(U,Pu)O_{2\pm x}$. On the other hand, the lowering of density is observed in $(U,Gd)O_2$ systems, as shown in **Fig. 2**. A mechanism for pore evolution is discussed below by adopting Yuda and Une's [4] hypothesis for $(U,Gd)O_2$ based on the difference in cation diffusivities for different sintering atmospheres, i.e. oxidizing and reducing.

Previous reports have been made on the dependences of sintering behavior of UO_2 [6] and $(U,Pu)O_2$ [7] on oxygen potential. These studies noted that the diffusion coefficients of U and Pu in $UO_{2\pm x}$ and $(U,Pu)O_{2\pm x}$ were higher in the oxidizing atmosphere by 4-5 orders of magnitude at a constant temperature compared to those in the reducing atmosphere. In the present case, U and Pu have relatively high diffusivities at -340 kJ/mol (oxidizing atmosphere), compared to those at -390 kJ/mol (reducing atmosphere) [4,10]. These results are attributed to the variable valences of U and Pu. It was also noted that densification began at a much lower temperature in the oxidizing atmosphere [6,7].

On the other hand, all Am atoms are considered to be in a trivalent state under the experimental conditions as mentioned below. Therefore the diffusivity of Am is unlikely to be dependent on the oxygen potential. The diffusion of Am is, thus, mainly dependent on temperature the same as for Gd, which has only a trivalent state in $(U,Gd)O_2$ solid [4].

In the oxidizing atmosphere, the interdiffusion between U or Pu and Am is considered to take place at relatively high temperature, compared to interdiffusion of the U/U and U/Pu systems. Accordingly, in the final sintering stage, larger pores can be generated by the diffusion of Am into $(U,Pu)O_2$ from the region where $(Pu,Am)O_2$ particles were originally present. On the other hand, in the reducing atmosphere, since interdiffusions of U/U and U/Pu are not enhanced, simultaneous interdiffusion between U, Pu and Am may take place. Consequently, the pores become small due to the further densification in the intermediate and final sintering stages.

Valence state of Am in Am-MOX and Phase relation

To discuss the different aspects of $(U_{0.66}Pu_{0.29}Am_{0.05})O_{2-x}$ from $(U,Pu)O_{2-x}$ as mentioned above, the following hypothesis is adopted: all Am atoms in $(U,Pu,Am)O_{2-x}$ are trivalent and a corresponding number of U atoms are pentavalent to compensate for positive charges caused by the oxygen deficiencies. This hypothesis has been proved to be correct in the $(U_{0.5}Am_{0.5})O_2$ system [11]. In addition, Pu atoms become trivalent below the O/M ratio where all U atoms become tetravalent (boundary O/M ratio). This is expressed by the following formulae:

$$O/M > 2\text{-}z/2 : (U^{5+}_{z-2x}U^{4+}_{1-y-2z+2x}Pu^{4+}_{y}Am^{3+}_{z})O_{2-x} \quad (1)$$

$$O/M < 2\text{-}z/2 : (U^{4+}_{1-y-z}Pu^{4+}_{y-2x+z}Pu^{3+}_{2x-z}Am^{3+}_{z})O_{2-x} \quad (2)$$

In the case of $(U_{0.66}Pu_{0.29}Am_{0.05})O_{2-x}$, the boundary O/M ratio is 1.975.

From this hypothesis, the smaller slope for the dependences of lattice parameter $(U_{0.66}Pu_{0.29}Am_{0.05})O_{2-x}$ (**Fig. 5**) can be caused by the Am valence, which may form a different type of oxide such as pervoskite, $AmUO_4$ [11].

Also the structural change around O/M=1.98 as shown in **Fig. 2** can be explained by the fact that this O/M is close to the boundary O/M ratio, 1.975. Yang et al. [12] showed the structure change occurred at the boundary (O/M=2-y/2) of the U valence transition in $(U_{1-y}Gd_y)O_{2-x}$ systems. Therefore, the structural change of $(U,Pu,Am)O_{2-x}$ is attributed to the transition of cation valence.

Regarding the many DTA peaks as shown in **Fig. 3**, the corresponding U-O phase diagram above O/M=2 is plotted according to the hypothesis. It seems that the plotted phase boundary of the U-O system agrees with the experimentally observed DTA peaks.

From these discussion, it can be concluded that Am was likely to exist as Am^{3+} and a corresponding number of U^{4+} ions were substituted by U^{5+} to preserve electrical neutrality.

SUMMARY

The sintering behavior of MOX fuel containing Am having high oxygen potential was investigated by ceramography and metrology. Then, the phase relation of the fabricated Am-MOX was obtained by ceramography, XRD and DTA. The following results were obtained:

(1) The sintered density of Am-MOX increased with increase of oxygen potential up to -390 kJ/mol (threshold oxygen potential), then decreased above that. This was affected by the difference in the pore structures.

(2) The fcc single phase was obtained for Am-MOX above O/M=1.97.

(3) The lattice parameter increased with decrease of O/M ratio. It was noted that the slope of $(U_{0.66}Pu_{0.29}Am_{0.05})O_{2-x}$ was smaller than that of $(U_{0.7}Pu_{0.3})O_{2-x}$.

(4) The structure of Am-MOX changed around O/M=1.98. Above O/M=1.98, the structure was homogeneous. Below O/M=1.98, the structure was not homogeneous; in particular, grain boundaries were wider and their surfaces were rougher.

(5) It was concluded that Am was likely to exist as Am^{3+} and a corresponding number of U^{4+} ions were substituted by U^{5+} to preserve electrical neutrality. This supported the interpretation of the results of Am addition to $(U,Pu)O_{2-x}$ for sintering behavior and the phase relation.

REFERENCES

(1) K. Aizawa, Prog. Nucl. Energy, 40 (2002) 349.
(2) H. Yoshimochi, M. Nemoto, K. Mondo, S. Koyama and T. Namekawa, J. Nucl. Sci. Technol., 41 (2004) 850.
(3) M. Osaka, I. Sato, T. Namekawa, K. Kurosaki and S. Yamanaka, J. Alloys and Comp. 397 (2005) 110.
(4) R. Yuda and K. Une, J. Nucl. Mater., 178 (1991) 195.
(5) T. L. Markin and R. S. Street, J. Inorg. Nucl. Chem., 29 (1967) 2265.
(6) T. R. G. Kutty, P. V. Hegde, K. B. Khan, U. Basak, S. N. Pillai, A. K. Sengupta, G. C. Jain, S. Majumdar, H. S. Kamath, D. S. C. Purushothem, J. Nucl. Mater., 305 (2002) 159.
(7) T. R. G. Kutty, P. V. Hegde, R. Keswani, K. B. Khan, D. S. C. Purushothem, J. Nucl. Mater., 264 (1999) 10.
(8) Hj. Matzke and T. Sorensen, Nonstoichiometric Oxides, Academic Press, New York, (1981) 156.
(9) Hj. Matzke, J. Chem. Soc. Faraday Trans. 86 (1990) 1243.
(10) Hj. Matzke, J. Nucl. Mater., 114 (1983) 121.
(11) K. Mayer, B. Kanellakopoulos, J. Naegele and L. Koch, J. Alloys Comp., 213/214 (1994) 456.
(12) J. H. Yang, K. S. Kim, K. W. Kang, K. W. Song, Y. H. Jung, J. Nucl. Mater., 340 (2005) 171.

2.7 PIE TECHNIQUE OF LWR FUEL CLADDING FRACTURE TOUGHNESS TEST

Shinya Endo, Koji Usami, Masahito Nakata, Takuji Fukuda*, Masami Numata, Minoru Kizaki and Yasuharu Nishino

Department of Hot Laboratories and Facilities
Nuclear Science Research Institute
Tokai Research and Development Center
Japan Atomic Energy Agency

ABSTRACT

Remote-handling techniques were developed by cooperative research between the Department of Hot Laboratories in the Japan Atomic Energy Research Institute (JAERI) and the Nuclear Fuel Industries Ltd. (NFI) for evaluating the fracture toughness on irradiated LWR fuel cladding. The developed techniques, sample machining by using the electrical discharge machine (EDM), pre-cracking by fatigue tester, sample assembling to the compact tension (CT) shaped test fixture gave a satisfied result for a fracture toughness test developed by NFI. And post-irradiation examination (PIE) using the remote-handling techniques were carried out to evaluate the fracture toughness on BWR spent fuel cladding in the Waste Safety Testing Facility (WASTEF).

KEYWORDS : Remote-handling, Fracture toughness test, Brittle fracture, Fuel Cladding, High burn-up, Post Irradiation Examination

INTRODUCTION

A brittle fracture with a longitudinal crack on fuel cladding has been observed in simulated reactivity-initiated accident (RIA) experiments using high burn-up BWR fuel at the Nuclear Safety Research Reactor (NSRR)[1]. The cause of the brittle fracture seems to be related with hydrogen absorbed in fuel claddings. An embrittlement of fuel claddings caused by the increase of hydrogen absorption severely degrades the mechanical properties of them. However, in case of the fuel claddings, the resistance to crack propagation is

*: Visiting Researcher in 2003 (Currently, Nuclear Fuel Industries Ltd.)

impossible to evaluate quantitatively by the conventional mechanical test in PIE such as burst and tensile tests. In addition, the configuration of fuel cladding is not suitable for a standard fracture toughness test.

New PIE technique, the NFI-type compact tension test that called the NCT method [2] was proposed by NFI. Facture toughness test for fuel cladding by the NCT method has been conducted by un-irradiated fuel cladding in NFI. To apply PIE, several advanced remote-handling techniques, that is to say, sample machining by using the EDM, pre-cracking by fatigue tester, specimen assembling using compact tension (CT) shaped test fixture were developed by cooperative research between the Department of Hot Laboratories in JAERI and NFI.

CLADDING FRACTURE TOUGHNESS TEST BY NCT METHOD

A fracture toughness test is an effective method to evaluate the resistance of crack propagation on brittle materials. A standard test method ASTM-E1820[3] of fracture toughness test is defined about specimen size and configuration, procedure and analysis of results. Although the ASTM-E1820 requires satisfying the plane strain condition during the test, in case of fuel claddings, it is impossible because specimen size and configuration is an arc-shape half tube with less than 1 mm thickness and about 5 mm radius. Fracture toughness test for fuel cladding by the NCT method is non-standard mechanical test. However, the test procedure and toughness evaluation are based on ASTM-E1820. In addition, the NCT method uses an assembled specimen by utilizing the CT shaped fixture that is a special test fixture for the pin-loading tension. J value-like obtained from the NCT method can be evaluated the fracture toughness of spent fuel cladding by burn-up parameter, relatively. Therefore, the NCT method is very useful for estimating the reliability of high burn-up fuel.

A simplified illustration of the half tube sample and test fixture is shown in **Fig.1**.

For spent fuel cladding, the testing procedure of fuel cladding fracture toughness test by The NCT method is as follows (see **Fig.2**).

1. Test part with 15mm length is cut off from the decided position of a spent fuel rod. UO_2 fuel is removed by drilling way. (These steps are performed with conventional PIE technique in the Reactor Fuel Examination Facility. And following advanced techniques are carried out in the WASTEF.)
2. Sample, actual test part is machined by using the EDM from the test part tube.
3. The sample is assembled into the CT shaped test fixture that is a special test fixture.
4. Assembled CT shaped specimen is set up on fatigue tester and applied cyclic load for pre-cracking.
5. Pre-cracked CT shaped specimen is loaded in the tensile testing machine and tested.
6. After the test, pre-crack length is measured by digital optical microscope. And J

value-like, fracture toughness is evaluated on the basis on ASTM E-1820.

The most important things in this method as PIE test technique are to maintain the same conditions during specimen preparation to fracture toughness test for all of samples, of course including cold test. Therefore, remote-handling techniques were developed to apply the NCT method to PIE. In particular, it is important to develop sample machining technique, sample assembling technique for CT shaped specimen and making technique of pre-crack.

REMOTE-HANDLING TECHNIQUES

Sample machining technique

In beginning stage of this work, wire-cut type EDM was chosen and used for the cold sample machining. But there were some problems in the use of this machine in the hot cell, i.e. large space is necessary, and the wire exchange is not so easy. In addition, waste increases because of using a lot of the machine oil. To avoid these problems, the electrode type EDM that was compact design and using a few of oil was developed by cooperative research. It has two-type electrodes, that is, one is disk type rotating electrode, and another one is a plate type fixed electrode. The former is used for grip-section machining by using the width electrode (4mm thickness , 40mm in diameter) and cutting off in two-half by using the narrow one (1mm thickness, 60mm in diameter). And the latter is utilized for starter notch machining. The three kinds of electrodes can be easily exchanged by manipulator. The starter notch machining (i.e.0.2mm width, 0.1mm tip-radius) that is the most important is accomplished with good accuracy by using the plate type electrode, even an arc shape of the notch tip. The EDM installation and three kinds of electrodes are shown in **Fig.3**.

Use of the rotating electrode has the advantage of maintaining the machining accuracy during the long term, that is, for so much sample machining, because the electrode consumption is a little and the lees occurred with the discharge are swept.

These machining are able to carry out by exchanging the three kinds of electrodes, depending on the cutting place. The targeted value of machining accuracy is ± 0.1mm.

Assembling technique of CT shaped specimen

To assemble the machined sample into the CT shaped test fixture, the assembling device was developed. The assembling device has good operationality and reproducibility. The CT shaped test fixture is composed with two pieces for the upper side and lower side, respectively. That is to say, to simulate CT shaped specimen, the machined sample is fixed between the upper and lower sides with four-screws. This is a specimen in the NCT method fracture toughness test. The assembling device consists of the precision stage installed liner guide rails that has X-motion, Z-motion driven and its positioning mechanisms for the

upper and lower fixtures and a torque-controlled wrench for screwing. Remote handling on the assembling device is quite simple and easy for manipulation using HWM-A100 manipulator as shown in **Fig.4**.

The process of assembling technique is as follows.

1. The upper and lower fixtures are put on the Z-motion and X-motion stages, respectively.
2. A sample positioned and placed on the lower fixture is checked by the optical scope. If the fitting is no good, it can be exchanged another one.
3. After that, the lower fixture is moved until under position of the upper fixture. Then both fixtures perfectly are piled at end-limit of the stage
4. And both fixtures are easily clamped by screwing used guide plate and torque-controlled wrench.

Right torque value was decided by mock-up test at out of hot cell. Result of these steps, the sample is assembled as a CT shaped specimen with the best reliability and reproducibility.

Fatigue pre-cracking technique

Pre-cracking to the notch tip of the specimen is performed under load control by using a small capacity fatigue tester. The appropriate cyclic load (max. load 100 N) is obtained from cold test on simulated sample. Furthermore, the fatigue pre-crack length recommended is 1mm from cold test by NFI

It is not so easy to control the length of the pre-crack. Therefore, two techniques are developed to control the pre-crack length. One is in-situ observation of pre-crack growth by CCD camera. Another is the prediction of pre-crack length by elastic compliance technique based on ASTM E1820. The unique technique that is used measurement by CCD camera together with prediction by elastic compliance method is applied to spent fuel cladding. The fatigue pre-cracking system is shown in **Fig.5**.

The in-situ observation technique is very useful for un-irradiated sample. However, its success must be depended on the surface condition, especially roughness. In other words, the technique probably will be useless for high burn up fuel claddings because the surface condition of high burn up fuel claddings is not good by the oxidation and bonding. The problem is able to resolve by applying the elastic compliance technique for the non-standard specimen mentioned above. The elastic compliance technique needs crack opening displacements measured on the load line. The displacements are measured by clip gage. Therefore, the clip gage has the important role in the NCT method fracture toughness test to predict the length of pre-crack. To avoid the handling damage, a clip gage setting device was developed to set up a clip gage on the specimen, because it has very sensitive performance.

Fig 6 shows the clip gage setting device and setting procedure.

In the PIE, calibration technique for the clip gage is very important, because calibration is the best way to check the maintaining the performance required. The calibration also can

be curried out in hot cell by calibrator handling with distinguished technique.

The unique technique of the pre-cracking is as follows.

1. A clip gage is set up on the specimen by using a clip gage-setting device (see **Fig.6**).
2. The specimen with clip gage is set up on the fatigue tester.
3. CCD camera is set up the best position for inner surface observation.
4. Pre-cracking is started with tension-tension cyclic load controlled (max. load 100 N).
5. Operation of the fatigue tester, that is, pre-cracking is stopped at the likely intervals obtained from mock-up test. For example, as shown in **Fig.7**.
6. In the each step, the pre-crack growth is observed carefully and measured by CCD camera system. On the other hand, the pre-crack length predicted is also calculated on the basis on ASTM E-1820 using the elastic compliance data (i.e. slope at the un-loading, $\Delta v / \Delta P$) .
7. By comparing with the both pre-crack lengths, validity of the elastic compliance method is checked. Then an extrapolation point on the pre-crack length versus number of cycles curve decides a cumulative cycle number that will be pre-cracked until an expected length (see **Fig. 7**).
8. When number of cycle reached to the cumulative cycle number predicted, the both pre-crack lengths are compared. If measured value by CCD camera is shorter than an expected length, pre-cracking is carefully continued.

MOCK-UP TEST

Mock-up test was conducted to check and demonstrate the above aforesaid remote-handling techniques. In the mock-up test, much kinds of Zry-2 tube were tested, for example re-crystallized, hydrogen doped, autoclaved, 80% cold-worked and the double treated materials. And result of that, following affairs was found out.

1. In the sample machining technique, the test informed on the electrode life and machining accuracy. Life of the rotating electrode was so long. After machined more than fifty samples, outer shape and accuracy were no changed. Although the diameter of the rotating electrode slightly reduced, it has little effect on the life and machining accuracy. The accuracy is within ± 0.1mm which is targeted value.
2. In assembling technique of CT shaped specimen, the torque value for the screwing was confirmed. In the case of weak clamping power, sliding occurs between CT shaped fixture and test part. Therefore, the appropriate clamping power was determined by cold test. The torque value of 150 Ncm is used for the test.
3. In fatigue pre-cracking technique, pre-cracking using the unique technique was useful for all of materials including the hydrogen concentration of 250ppm. The both techniques show the good relation between predicted pre-crack length and observed length on inner surface, experimentally (see **Fig.7**). In addition, clip gage chosen and

calibrated by the WASTEF has be maintained the integrity after about 3×10^5 cycles corresponding to pre-cracked for 5 samples.

For an elevated temperature test at 300℃, a clip gage was investigated. The clip gage endured to apply the elevated temperature tests at 300℃ during four times. Therefore, the elevated temperature test with a clip gage can be performed.

POST IRRDIATION EXAMINATION

PIE using the remote-handling techniques established in this work was carried out to evaluate the fracture toughness on BWR spent fuel cladding under contract with NFI in national program.

Results of the remote-handling techniques are as follows.

1. In the sample machining technique, the samples were machined as expected, that is, CRUD and oxidation on the surface didn't influence for the EDM machining.
2. In assembling technique of CT shaped specimen, ovality and ridging on the test part didn't influence for the sample assembling with standard size fixtures. Torque decided by mock-up test, 150 Ncm was also appropriate value.
3. In fatigue pre-cracking technique, pre-cracking was achieved by applying the unique techniques mentioned above. As it was hard to observe the pre-cracking by CCD camera, the predicted pre-crack length by the elastic compliance method was useful very much. The average fatigue crack length is 1.02 ± 0.1mm for 5 samples.
4. The fracture toughness test on the BWR spent fuel cladding irradiated in nuclear power plant has been performed at room temperature.

SUMMARY

The remote-handling techniques were developed and established by cooperative research between the Department of Hot Laboratories in JAERI and the NFI for evaluating the fracture toughness on irradiated LWR fuel cladding. These techniques, that is, machining by the EDM, assembling by special devises, pre-cracking using the in-situ observation and elastic compliance method gave a satisfied result for mock-up test of the NCT method fracture toughness test suggested by NFI. Then usefulness on the developed techniques has been adequately confirmed with PIE in the WASTEF on the BWR spent fuel claddings irradiated 3 cycles in nuclear power plant under contract with NFI in national program.

Although established techniques was useful for 3 cycles irradiated sample, we have no experience of the fuel cladding fracture toughness test for more high burn-up fuel, yet. It must be more difficult to achieve the test. However, we believe that experience obtained in

this work probably will resolve the problem as a result of try and error.

ACKNOWLEDGEMENTS

The authors acknowledge to Mr. H. Amano, director of the Department of Hot Laboratories and facilities. The authors would also like to thank to the staffs of Department of Hot Laboratories and facilities for their assistance in performing the experiments.

REFERENCES

(1) T.NAKAMURA, et al, "Failure Thresholds of High Burn-up BWR Fuel Rods under RIA Conditions", J.Nucl.Sci.Technol.,41,37-43(2004)
(2) T.FUKUDA, et al, "Fracture Toughness pf Hydrogen-Absorbed Zircalloy-2 cladding tubes", Proceedings European Nuclear Society TOPFUEL, Wurtzburg, March 2003
(3) ASTM Designation E1820-02, "Standard Test Method for Measurement of Fracture toughness"

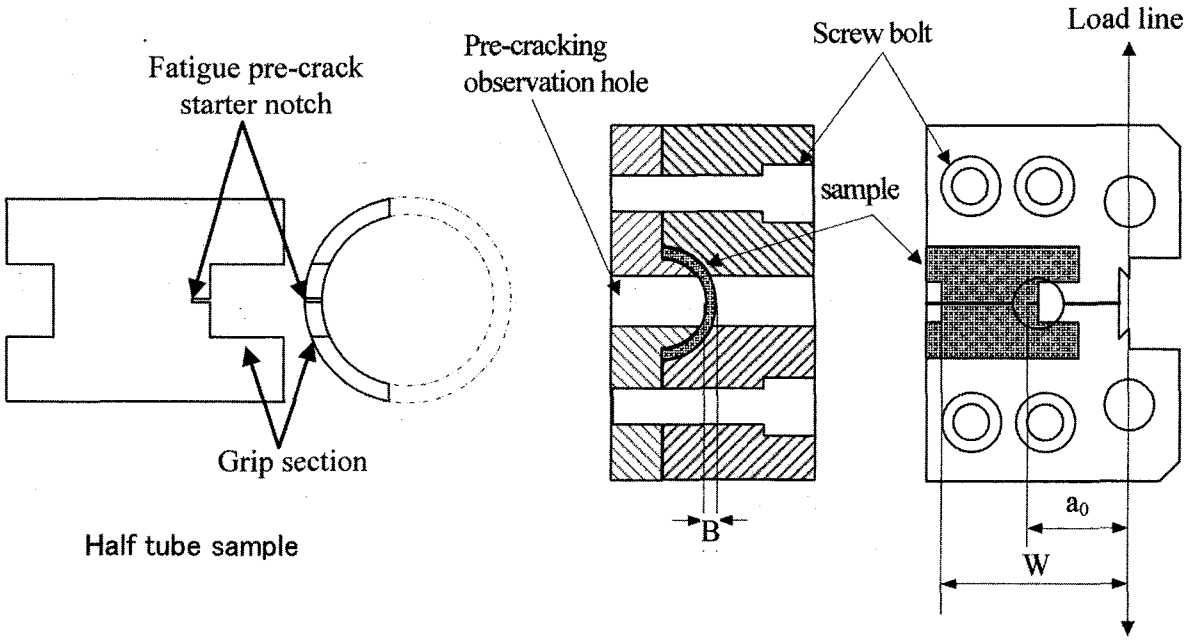

Fig .1 Sample and CT shaped test fixture.

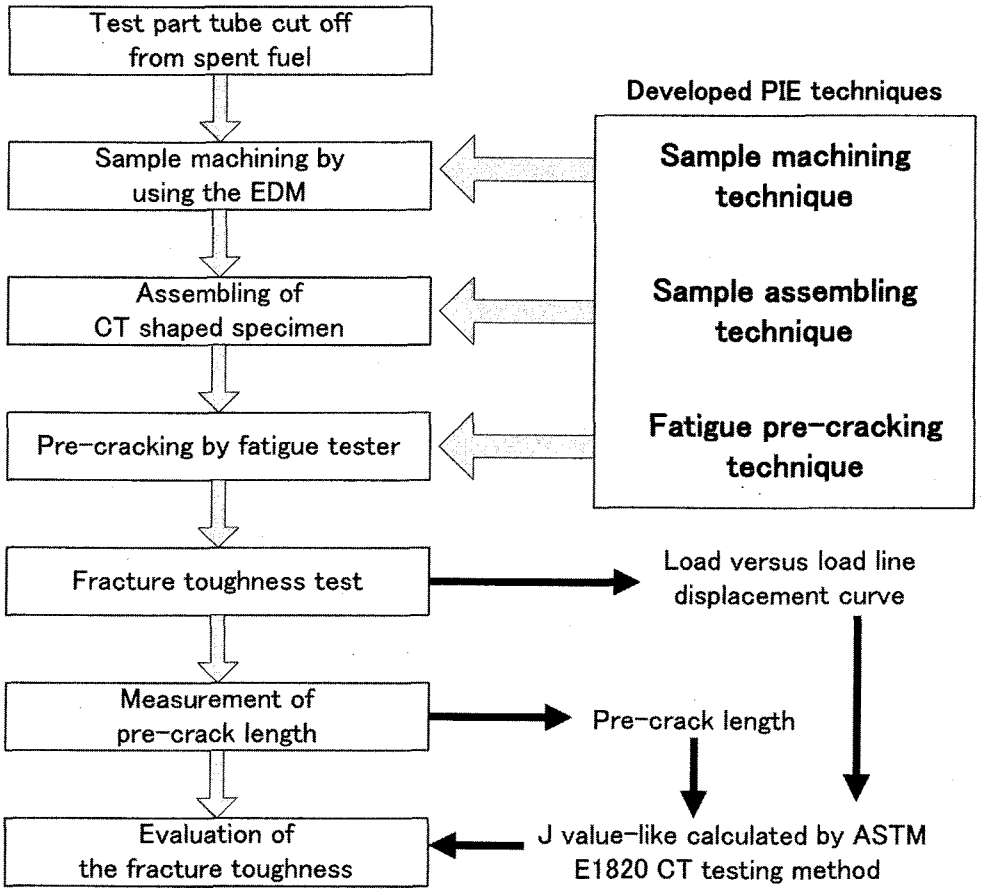

Fig.2 Flow chart of fuel cladding fracture toughness test.

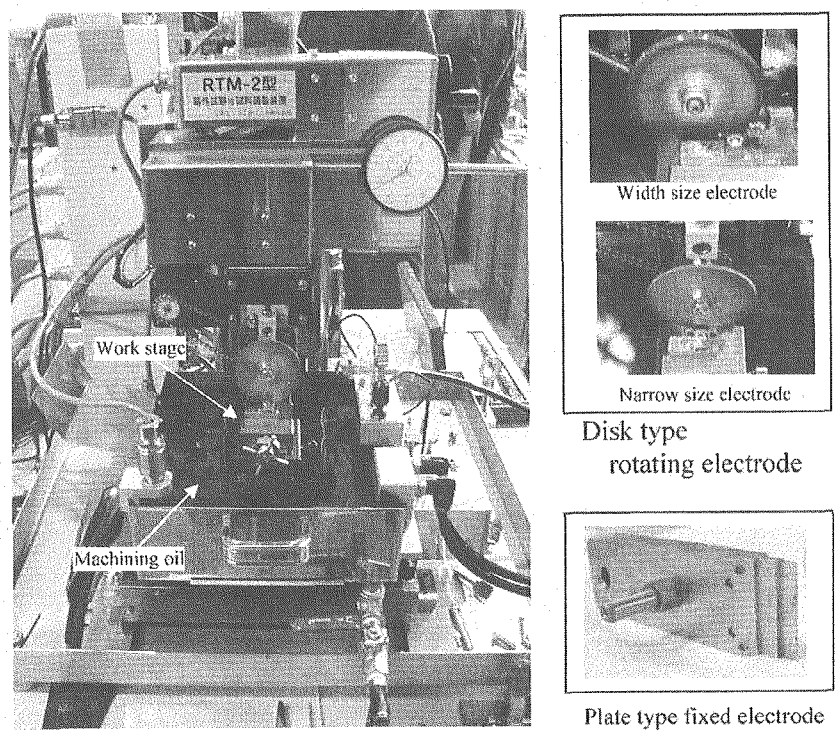

Fig.3 EDM and three kinds of electrodes.

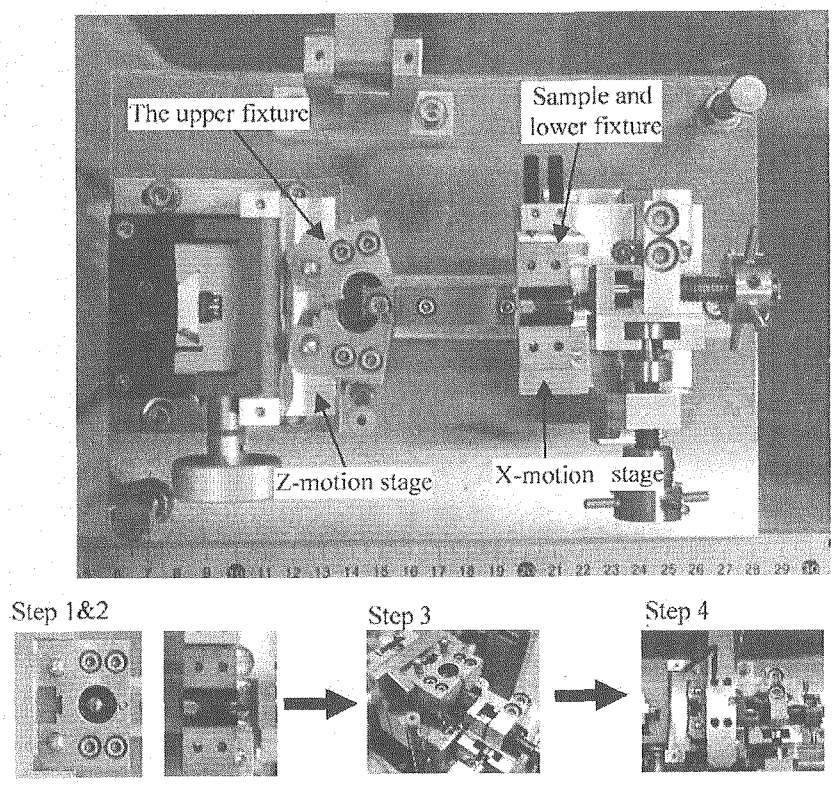

Fig.4 Assembling procedure for CT shaped specimen.

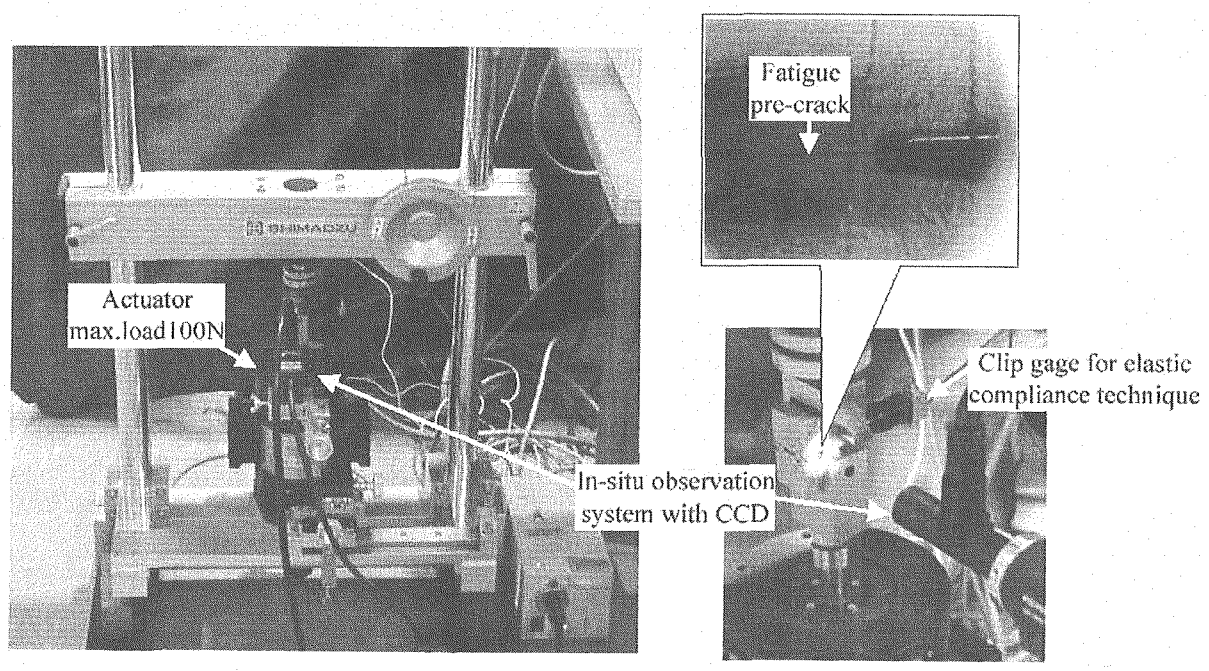

Fig.5 Fatigue pre-cracking system.

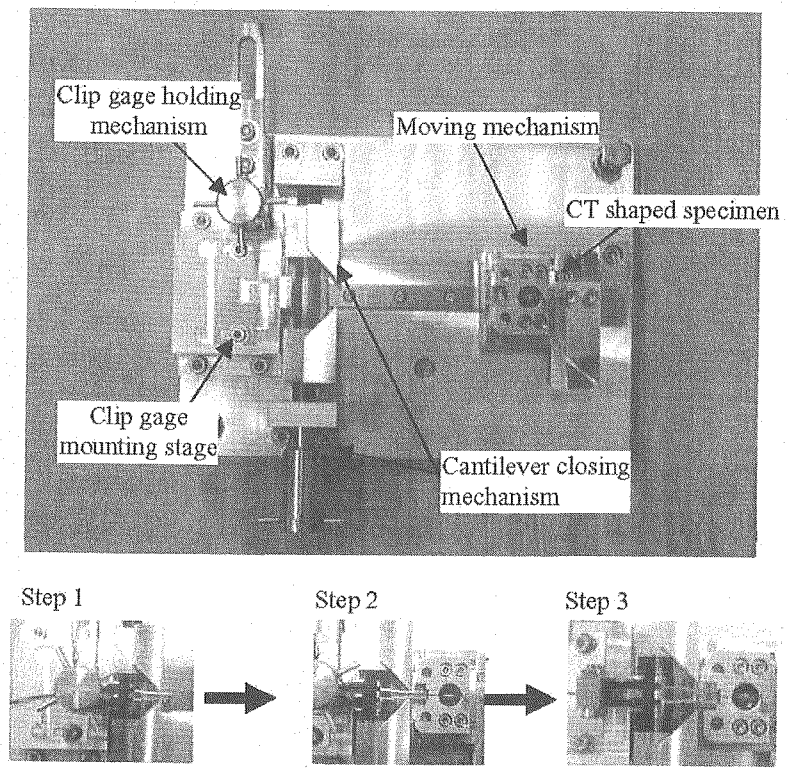

Fig.6 Clip gage setting device and operating step.

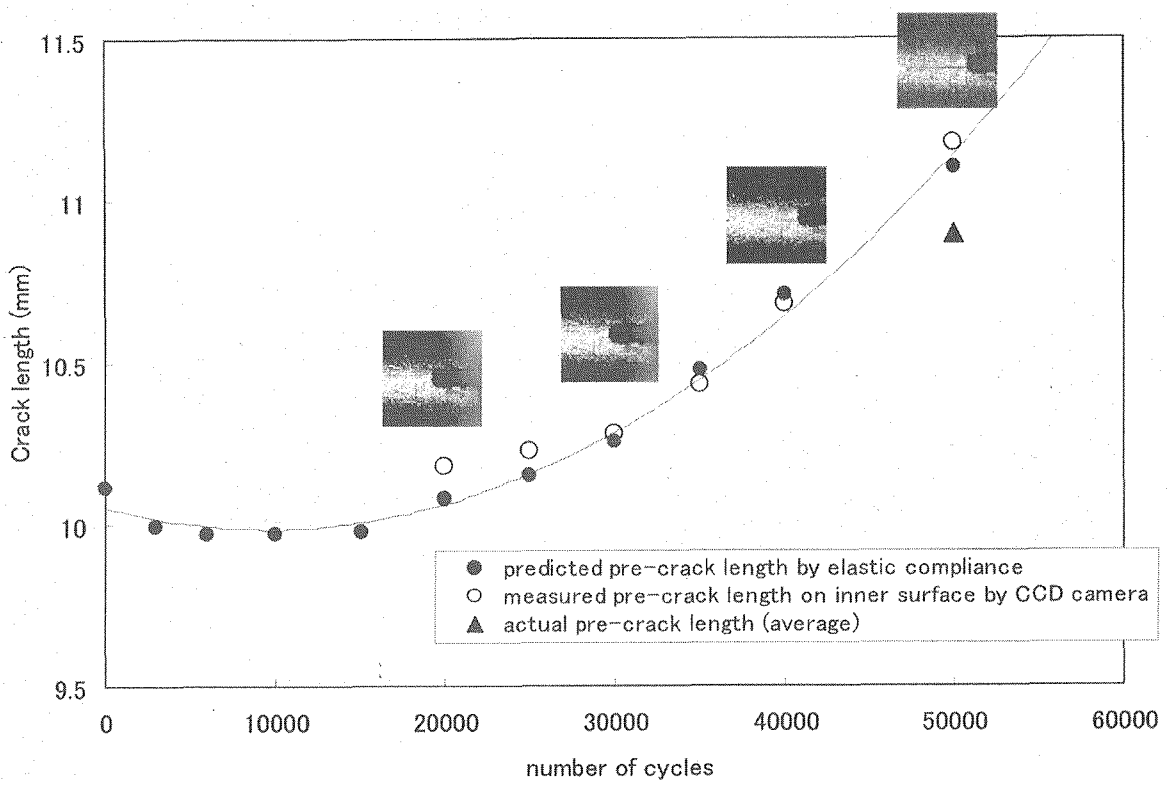

Fig.7 Relationship between number of cycles and crack length.

2.8 DEVELOPMENT OF THE UNDER-WATER BURNUP MEASURING SYSTEM FOR A SPENT PWR FUEL ASSEMBLY

Y.B. Chun, K.J. Park, H.D. Kim, K.J. Jung and S.W. Park

Korea Atomic Energy Research Institute
150 Dukjin-dong, Yusong-gu, Taejon 305-353, Korea

ABSTRACT

The under-water burnup measuring system was developed at KAERI to determine the burnup profile of spent nuclear fuel assembly. It is important to provide useful data for the critical safety analysis and the safeguard of an advanced spent fuel management process. The measuring system consists of the HPGe gamma-ray detector, collimators, down tube and electronic equipment. In this study, the burnup of a spent nuclear fuel assembly discharged from Nuclear Power Plant in Korea was determined and the results were verified by the chemically determined burnup. As a result, nondestructively determined burnup values showed a good agreement with the chemically obtained results within 6 % error. And a cooling system of HPGe detector was modified for solving the problem of LN_2 supply in the pool area.

KEYWORDS: Underwater Examination, Spent Fuel Assembly, Burnup Measurement, Gamma Spectroscopy

INTRODUCTION

Safety analyses of criticality have been performed based on the fresh fuel assumption, which is very conservative since the potential reactivity of the nuclear fuel is substantially reduced after the fuel has been irradiated in the reactor core. This conservative analysis on the criticality safety has an economic disadvantage in storage, transportation, and reprocessing of the spent fuel. Therefore, a reasonable spent fuel management should be propelled to satisfy both the economic benefits and the criticality safety. And so, the concept of taking credit for the reduction in the reactivity of the nuclear fuel due to burnup of the fuel is under

consideration and some countries are presently applying the concept. In connection with the spent fuel management, under-water burnup measuring system was developed at KAERI for the burnup determination of PWR spent fuel assemblies. The system has operated at the unloading pool in the post-irradiation examination facility of KAERI as shown in **Fig.1**. This report describes briefly the design, fabrication and performance test of under-water burnup measuring device, and also the cooling type of HPGe detector adopted in the device.

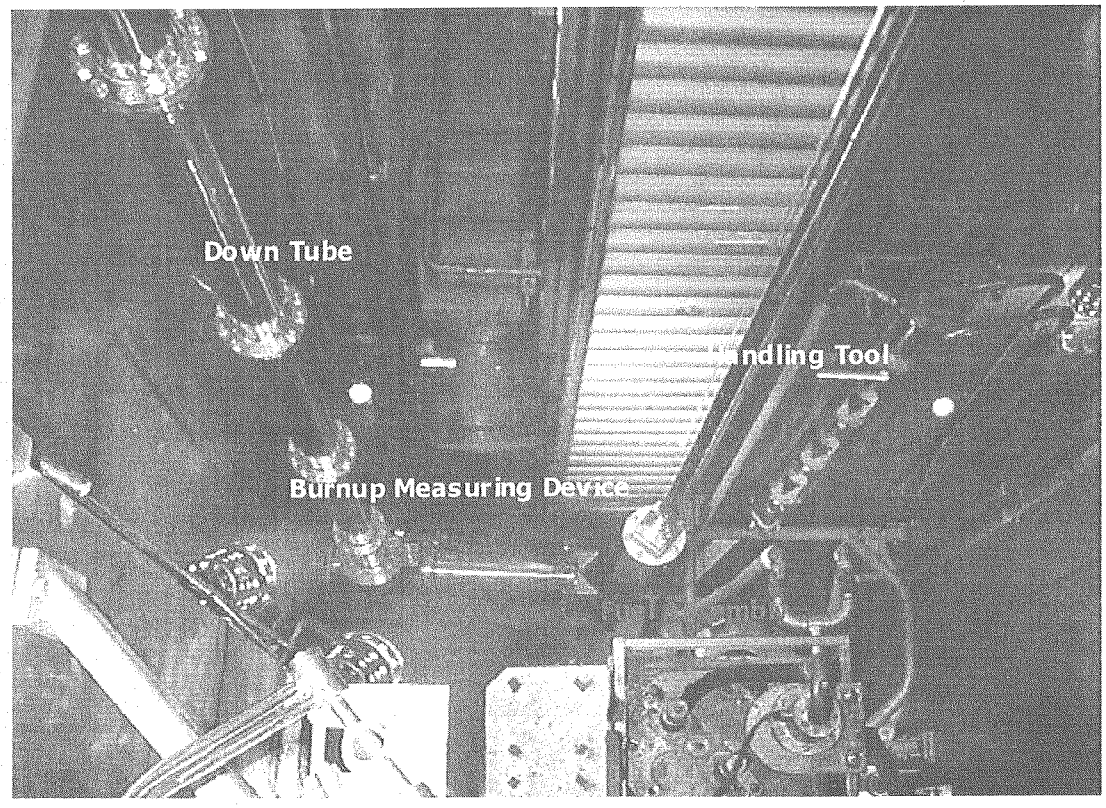

Fig.1 Burnup Measuring Device and Spent Fuel Assembly in the Unloading Pool of PIEF.

DEVELOPMENT OF UNDER-WATER BURNUP MEASURING DEVICE

Design and Fabrication

A device which is able to determine the burnup of a spent fuel assembly in the pool was developed by KAERI as shown in **Fig.2**. This device was designed to be able to measure the gamma activity up to 37 PBq(1,000,000 Ci), and the shielding capability of detector of the device has kept lower than 10 μSv/h at the position of the HPGe detector.[1)] Also, the size of device was determined by considering the dimension of the unloading pool 9401 and the operational height of overhead crane operated at the pool working area of PIEF.

Performance Test

After fabricating the device, the performance tests related in the integrity of detector shield, air leak, collimator alignment and so on, were carried out in an inactive area. After solving the problems occurred in the course of performance tests, the device was installed in the unloading pool of PIEF as shown in **Fig.3**. The performance tests in the active area were carried out for the leak and gamma-ray detectable function.

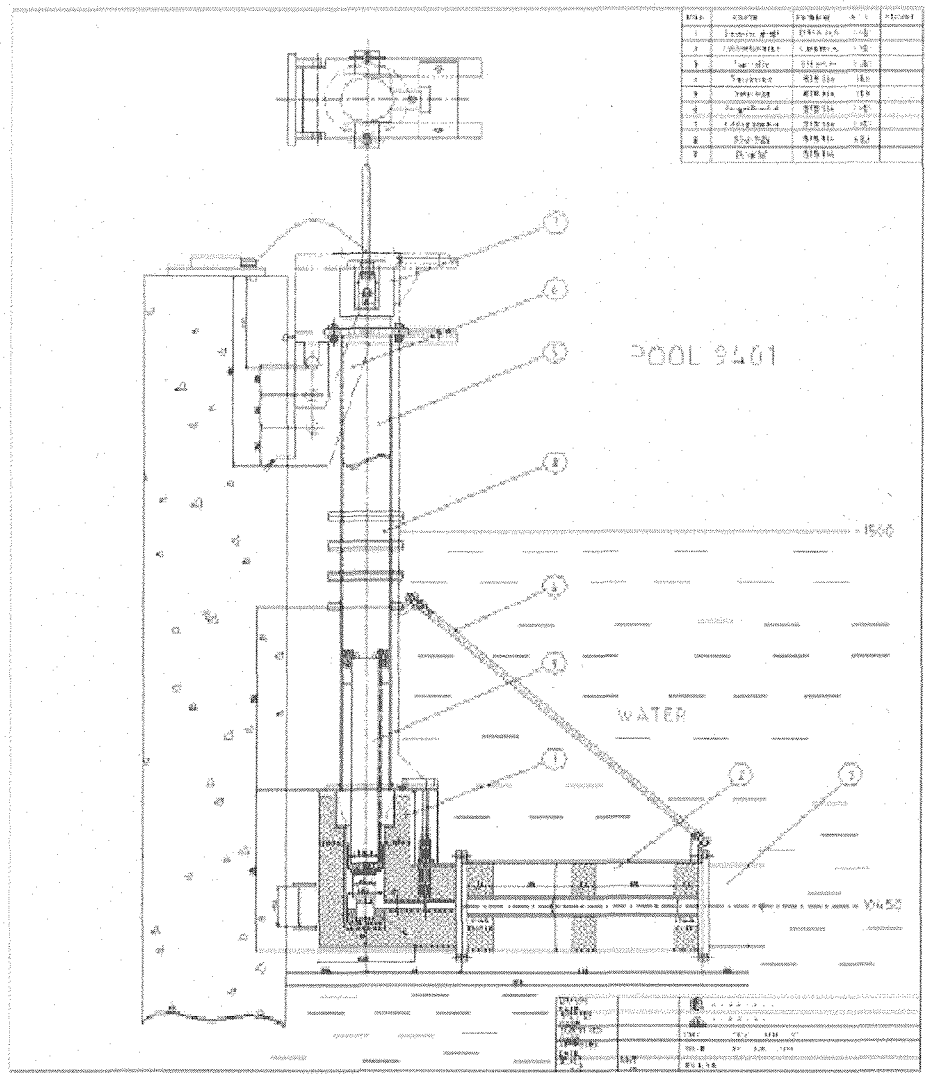

Fig.2 Drawing of Under-Water Burnup Measuring Device for PWR Spent Fuel Assembly.

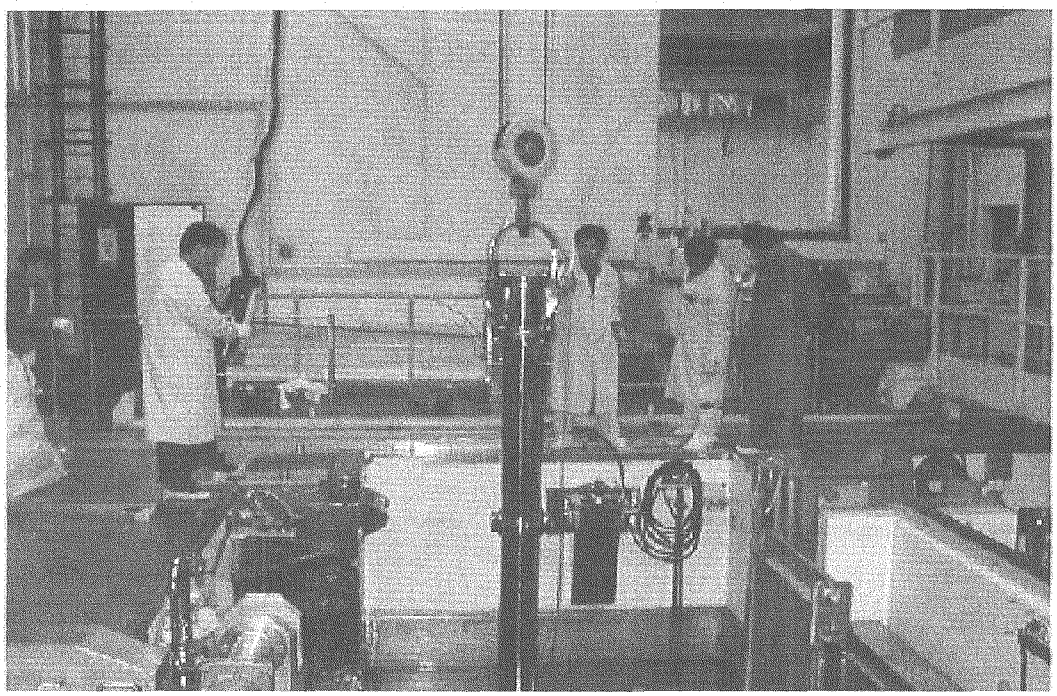

Fig.3 Under-Water Burnup Measuring Device Launching in the Unloading Pool at PIEF.

BURNUP DETERMINATION OF SPENT NUCLEAR FUELS

Experiments

In this experiment, a spent fuel assembly discharged from NPP was selected for the burnup determination. The principle design characteristics of the fuel assembly are given in **Table 1**. E11 fuel rod of the assembly was selected and 3 specimens were taken from the rod for the estimation of the relative axial burnup distribution and the chemical analysis.

Table 1 Characteristics of Examined PWR Spent Fuel Assembly

Fuel Type	Enrichment	Irradiation Reactor	Cycle (Position)	Discharge Burnup	Discharge
14x14 PWR	3.1968 wt%	Kori-1	7(E9), 8(J5), 9(H11)	37,840 MWd/tU	20 Jan.1989

Burnup evaluation tests of the fuel assembly, rod and specimens were carried out by the procedure of the gamma-ray measurement, computer code calculation and chemical analysis as shown in **Fig.4**. The axial burnup distribution and average burnup were determined by the burnup determination algorithm after acquiring the gamma-ray spectrum from the fuel.

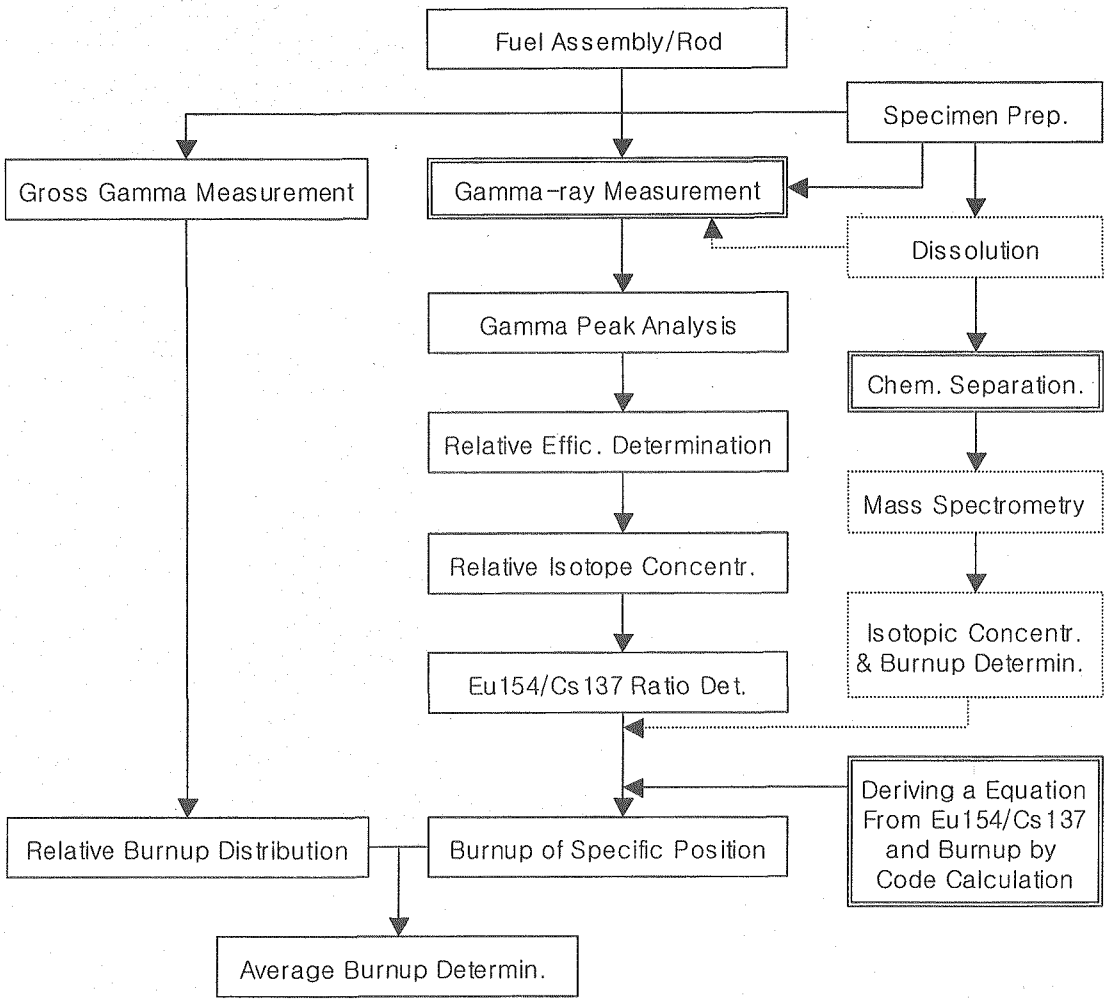

Fig.4 Burnup Determination Procedure for Spent Nuclear Fuels by NDT and DT Method.

Algorithm for Burnup Determination

The burnup determination algorithm employed the combined method of the isotope ratio by gamma-ray spectrometry and the isotope ratio-burnup relation by code calculation. Fission product inventory as function of the burnup was calculated by SCALE-4.4/ORIGEN-S code. For promptness of the burnup determination, the database for the burnup monitor sorted by fuel type, enrichment and cooling time were prepared previously.

Precision

The precision of the measuring system was verified by the chemical method as a reference. It is weakly depending on the fuel types, burnup, and cooling time. Burnup values determined by the combination of gamma-ray measurement and computer code calculation were compared with chemically determined burnup value. As the result, the error bound in the case of the examined spent fuel appeared to be within 6% as shown in **Table 2.**

Table 2 Burnup Values Determined by Gamma-ray Measurement/Code Calculation and Chemical Analysis at the 3 Selected Positions of Fuel Rod E11

Sample	Axial Position	Isotope Ratio (Eu-154/Cs-137)	Burnup(GWd/tU)		Diff.
			NDT	Chem.	
E11-4	346 mm	7.78×10^{-3}	34.9	36.2	3.6 %
E11-7	660 mm	8.28×10^{-3}	38.4	36.2	6.0 %
E11-9	862 mm	8.10×10^{-3}	37.1	39.0	4.8 %

MODIFICATION OF COOLING TYPE

Abnormal Operation of HPGe Detector

The component parts of the burnup measuring system are directly or indirectly affected by the moisture because of the under water installation. During the data acquisition after installing the system in the pool at the first time, an abnormal operation of the system occurred intermittently, and subsequent difficulties with the operation threw the experimenter into confusion. After charging LN_2 in the Dewar and applying the high voltage to HPGe detector, the experimental data were obtained normally the first day, but could not do at all the next day. Although the high voltage was applied, the detection system did not operate any more. The experiment was tried again after several days, and the detection system was normally operated as the first day. But the system did not operate at all the next day as before. This phenomenon was repeatedly continued for a long time. And then, we tried to find out the cause of this phenomenon. First of all, we took necessary actions such as the replacement of MCA, HV supply, UPS supply, first-class grounding, etc. for the electronic equipment. But we did not solve the problems. So it was doubtful whether the HPGe detector itself had a problem, and we moved the detector from the active pool area to the cold laboratory in order to make a diagnosis of problems.

Diagnosis of HPGe detector

HPGe detector (PGT IGC-30185) is a major part of the burnup measuring system, and more expensive than the other parts. It is very difficult to cope instantly with the troublesome situation caused by the careless handling because the detector is not a product in our country. Then we first checked the preamplifier (RG-11B/C) positioned between the detector and LN_2 Dewar before disassembling the detector for the diagnosis. The check of preamplifier was carried out with the multi-tester and oscilloscope based on the troubleshooting guide of Princeton Gamma Technology after charging LN_2 in clod laboratory. As a result of the check, it was identified that the operating function was normal. But the detection system did not

operated at all as before. We finally come to disassemble the preamplifier because we had no idea any more to solve the problem without disassembling the detector and preamplifier. The moment we disassembled it, the cause of problem was apparently found out. It was just the condensed water accumulated on the circuit board of preamplifier.

Cause of Condensed Water Production

The cold rod connected from the LN_2 Dewar to the detector crystal passes through the preamplifier as shown in **Fig.5**. When the semiconductor detector is used in the high humid condition like water pool, moisture around the preamplifier results in the condensed water due to the low temperature of cold rod. In the case of horizontal circuit board position, condensed water accumulates on the board of preamplifier as time goes by. When condensed water is enough to cover the circuit board, the preamplifier seems to have a short circuit. And HV is not applied because the detector has a safety device. Condensed water accumulated on the circuit board disappears completely in 3-4 days by natural evaporation. Since then, the detection system operates normally.

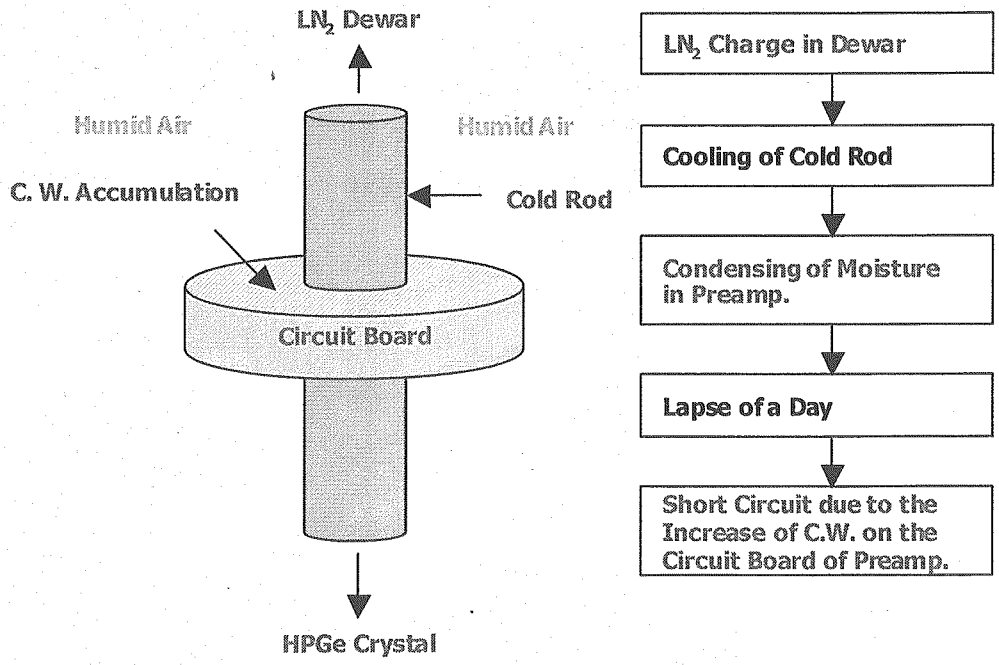

Fig.5 Accumulating Process of Condensed Water on the Circuit Board of Preamplifier.

Alternative Plans and Modification of Cooling Type

To solve the short circuit problem caused by condensed water, the manufacturer of HPGe detector should consider a counter-plan for improving the preamplifier design. Also the use of moisture absorber in the preamplifier is a temporary expedient for extending the experimental

time. We selected the later for the experimental schedule of a set date.

We tried to make a plan for improving the burnup measuring system, because the short circuit was caused by the condensed water and it was difficult to supply LN_2 in the pool. The HPGe detector has frequently to pull out from and insert into the down tube positioned in the unloading pool of 10 m depth level by overhead crane for LN_2 charge. When the detector is pulled out or inserted, it is apt to be damaged by the collision between the detector and the inside wall of down tube. Then, we decided to change the existing LN_2 cooling type into the refrigerant circulation type for the reduction of damage by the collision and the elimination of the LN_2 supply troublesome. The refrigerant circulation cooling type has an advantage of long term cooling function in only once refrigerant charge and the refrigerant do not evaporate in the outside as shown in **Fig.6**. PGT (Princeton Gamma-Tech), the supplier of HPGe detector/LN_2 Dewar, performed the modification of cooling type.

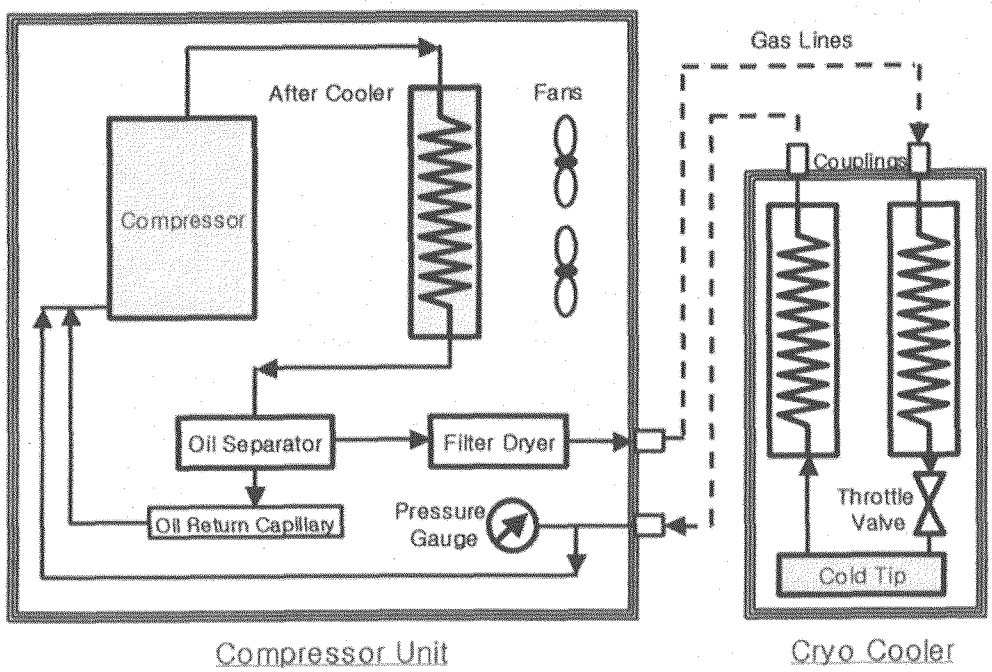

Fig.6 Schematic Description of Cryo Cooler and Compressor Unit for HPGe Detector.

APPLICATION

Nondestructive and under-water measuring techniques developed in this study make it possible to determine easily and accurately the average burnup, cooling time and initial enrichment of the PWR spent fuel in simultaneous manner. The techniques will be applied for the efficient management of spent fuel such as transportation, storage and disposal in the future.

2.9 PERFORMANCE TESTS OF THE I&C SYSTEM (GSF-2002) USING A FUEL CAPSULE MOCKUP

Young Hwan Kang, Sung Jae Park, Do Hee Ahn, Man Soon Cho, Kee Nam Choo and Bong Goo Kim

Korea Atomic Energy Research Institute
150 Deokjin-dong, Yuseong-gu, Daejeon 305-353, Korea
yhkang2@kaeri.re.kr

ABSTRACT

A new I&C system for an irradiation test using an instrumented fuel capsule in the HANARO reactor has been designed and manufactured to provide more qualified data to a fuel developer. In order to ensure that the system fulfills the functional and performance requirements, a series of tests were performed to investigate the thermal response of the capsule mockup connected to the gas mixing system of the new I&C system (GSF-2002) in the cold test loop. Main test parameters are the mass flow rates of 25, 50 and 100 cc/min of the He/Ne gas, a gas pressure of 1 to 3 kg/cm^2, a heater power of 1 to 3.4kW and a few gas mixing ratios of He to Ne. From the out-pile tests, it was confirmed that the new type of I&C system (GSF-2002) would be feasible for a fuel irradiation using a fuel capsule in the HANARO research reactor. Also included in this paper is a description of the system and the test results analysis, as well as comments on the test constraints or limitations.

KEYWORDS: Fuel Capsule, I&C System, Performance Test, Gas Pressure, Gas Flow Rate, Gas Mixing Ratio, HANARO

INTRODUCTION

The currently progressing irradiation programs, which include more than 10 instrumented capsules, are to address the effects of the irradiation temperature, neutron flux/neutron fluence and burn-up.[1~3] Most users want to control their specimen temperature to within a desired temperature range. However, a temperature control of the specimen within an allowable difference can not be obtained easily due to a change of the control rod position of the HANARO reactor by increasing the duration time during an irradiation test. [4]

One of the well known methods for a temperature control is based on the thermal conductivity variation between the inner and outer tube of the capsule, the outside of which is in contact with the reactor primary coolant. The thermal conductivity is varied by changing the composition of the binary gas mixture of He and Ne in the annular thermal insulation space formed between the inner tube and the outer one [5].

In light of the additional growing test needs in HANARO, a new I&C system[6] for an irradiation test using an instrumented fuel capsule in the HANARO reactor has been designed and manufactured to provide more qualified data to a fuel developer. A series of tests were performed to ensure that the I&C system for the fuel irradiation tests fulfills the functional and performance requirements specified for them. An additional purpose of the experiments was to understand the effects of the binary gas mixture, as well as its gas pressure and flow rates.

EXPERIMENTAL

Description of the I&C System(GSF-2002)

The basic design of the system was started at the beginning of 2000. A detailed review of the design concept and an applicable methodology for controlling the temperature of the specimens were accomplished in 2001. Detailed design of the system was completed by 2002. The I&C system(GSF-2002) for the fuel irradiation tests was manufactured and installed for the qualification tests in an engineering laboratory.

The I&C system developed for the user's required tests consists of two major sub-systems: a temperature control system and a fuel failure monitoring system [6]. **Fig. 1** shows the photograph of the I&C system(GSF-2002) for the fuel irradiation tests. The temperature control system controls the surface temperature of the specimens by adjusting the mixing ratio of the gas in an annular gas space. It can control a wide range of specimen temperatures. It will also monitor the process variables and trigger specific alarms or safety functions. In addition, an emergency gas supply system is actuated to supply 100% helium gas to the capsule in the event that the monitored reactor temperature becomes too high, which is the main safety action. The fuel failure monitoring system has a role to detect the fission products in the annulus gap due to a fuel cladding failure in each mini-capsule separately mounted inside the basket.

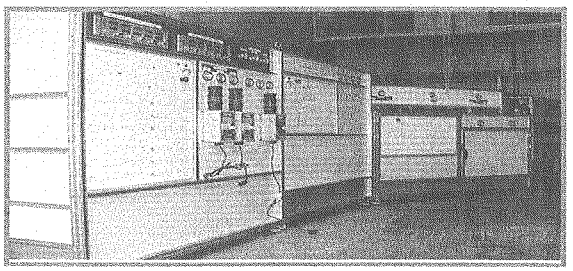

Fig. 1 I&C system for fuel irradiation tests.

Instrumented Capsule Mockup

For the required fuel irradiation test the design concept of the capsule, to be connected to a new I&C system, is created by applying a universal principle (double containment concept) for experiments involving fissile in a research reactor. In this study, a mockup capsule[7] was designed and fabricated to perform the experiments under the HANARO hydraulic conditions. The mini-capsule mockup was instrumented with a thermocouple for monitoring and controlling the cladding surface temperature and a heater of 3.4kW as a simulated heat source. **Fig. 2** is a photograph of the instrumented capsule used.

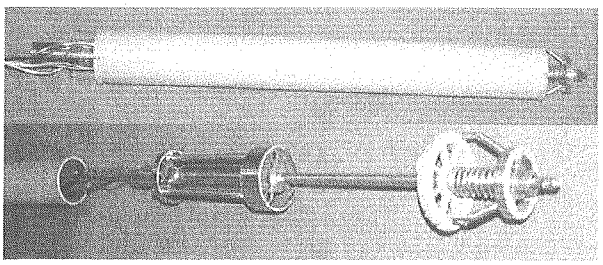

Fig. 2 Photograph of the instrumented capsule mockup.

Performance Test

This performance test which was started in 2004, has two main objectives; namely an attempt to understand the performance of the new I&C system by a comparsion of the previous experimental results[8] with the data obtained from the new system, and a testing to comprehend the time-temperature processing of the mini-capsule we used in this test.

In this study, the capsule mock-up was installed in the test section, equivalent to the cylindrical flux traps of the HANARO, of the single channel test loop. The dimension of a flux trap, which is a fuel irradiation test hole, is 60 mm in inside diameter and approximately 900 mm in height. Water was the working fluid in the test loop. Fluid entered from the bottom of the flow housing and moved upward. The schematic of the assembled test section consists of a variable speed pump, a storage tank, flow control valves, and orifice flow meters etc. During the experiments, the water temperature in the test section

was maintained at 40 °C. The temperature did not rise very high mainly because the flow rate was not controlled by the valve opening rate but by the pump speed. The target fluid temperature for the tests was obtained using the heater installed in the storage tank. The experiments were carried out at a steady state condition. The mass flow rates were measured by the orifice flowmeter. Temperature data for the capsules were obtained from the thermocouples installed in the inside position of the external tube. Main test parameters are the mass flow rates of 25, 50 and 100 cc/min of He/Ne gas, a gas pressure of 1 to 3 kg/cm^2, a heater power of 1 to 3.4kW and a few gas mixing ratios of He to Ne.

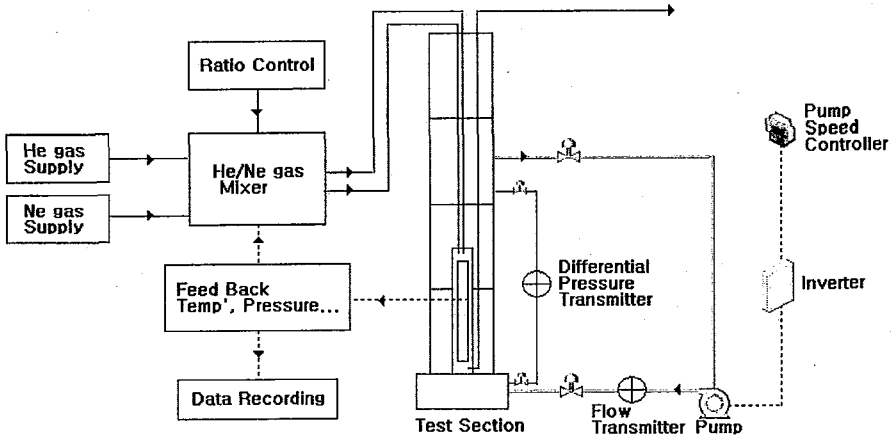

Fig. 3 Schematic diagram of cold test loop and I&C system.

RESULTS AND DISCUSSION

Heat Transfer Coefficient and Temperature Review

The heat transfers in our model are processes that occur in series with each other. Since there is a small radiation component of a heat transfer from the gas to the cylinder wall, two types of heat transfer mechanisms are thought to exist in a steady state heat transfer situation. In a heat transfer resistance modeling, we look for regions which have a relatively large temperature difference, and calculate the heat transfer resistance across each region. It also assumes that the heat transfer is one dimensional across the resistance element. The thermal resistance is defined as the ratio of the temperature difference to the heat transfer.

$$Q=\Delta T/\Sigma R=\Delta T/(R1 + R2 + R3)$$

The object of the experiments was to measure the overall resistance to a heat transfer at different operating conditions and compare these measurements to those predicted by the well-known equations in the literature.

From a consideration of the heat transfer theory, heat transfer coefficients for a cooling

by a forced convection may be setup as functions of the Reynolds number(Re), of the Prandtl number(Pr), and of the non-dimensional ratios of the various important dimensions of the capsule structure. The inner surface temperature of the mini-capsule may be obtained from the following equation.

$Nu=h^* D_h /k=0.023*Re^{0.8}*Pr^{0.3}$, $h=Nu*k/ D_h$

The heat transfer rate can then be calculated by using the input data described in **Table 1**.

Table 1 Input data for analysis of temperature

O.D. of heater(m), r 3	9.40E-03
Length of heater(m), L	1.70E-01
He gap(m)	1.00E-04
I.D. of mini-capsule(m), r2	9.50E-03
O.D. of mini-capsule(m), r2	1.10E-02
Thermal conductivity of STS k(W/m.k)	1.70E+01
Viscosity of He m kg/(m.s)	1.99E-09
Thermal conductivity of He k(W/m.k)	1.52E-01
Viscosity of H2O m kg/(m.s)	5.77E-04
Thermal conductivity of H2O k(W/m.k)	6.40E-01
Velocity of H2O m(kg/s)	1.27E+01
Temperature of H2O(°C)	4.50E+01

Based on the temperature data obtained by a thermocouple placed at the inside of the external tube, the heat resistivity and heat transfer coefficients are compared theoretically. The estimates of the calculated temperatures and the measured temperatures are presented in **Table 2**. Although the measured temperatures are lower when compared to the estimated temperature, the deviation is within a few percentage points. It is seen that the calculated values are in good agreement with the experiments.

Table 2 Surface Temperature of the mini-capsule

Test Condition	Calculated Temperature(°C)	Measured Temperature(°C)
Q=3kW, He=100%, 100cc/min	266.5	260
Q=2kW, He=100%, 100cc/min	192.7	193
Q=1kW, He=100%, 100cc/min	118.8	126

Thermal Response

From this test, as expected, the effects of the mass flow rate of the gas and the gas pressure on the surface temperature of the simulated fuel (hereafter called "fuel") are found to be negligible in the ranges of both the flow rate of 50 and 100 cc/min and the pressure of 1 to 3 kg/cm^2 as shown in **Fig. 4**. This is believed to be due to the poorer heat transfer resulting from a smaller percentage variation of the thermal conductivity with the pressure and flow rates of the gas. The effects of the heater power and the gas mixing ratio of the He/Ne gas on the fuel specimen temperature was found to be altered noticeably and showed a good dependency, indicating that the heat transfer coefficient is very dependent on the heat source and the conductivity of the gas composition. Similarly, the dependency of the gas mixing ratio on the fuel specimen temperature decreases with an increase in the He-to-Ne ratio.

It is concluded that the applied temperature control methodology is feasible to control the surface temperature of the fuel. To comprehend the integrated time-temperature processing of the mini-capsule, a series of tests was implemented by observing the temperature characteristics of the specimen during a heating and a cooling cycle. The heat-balanced surface temperature of the specimen at the above flow rate of 50 cc/min was found to be constant. This experimental data shows that a specimen does not reach a thermally balanced temperature instantaneously and the minimum flow rate of the gas for the effective control of the specimen temperature is above 50 cc/min in **Fig. 5**.

Analysis results also show that the surface temperature increases with an increase of the heater power, however, and the temperature increase per unit power, decreases with an increase of the heater power as shown in **Fig. 6**. By properly setting all three control gains (PID) based on the obtained response times of the capsule, the I&C system could be optimized for an application to the HANARO reactor.

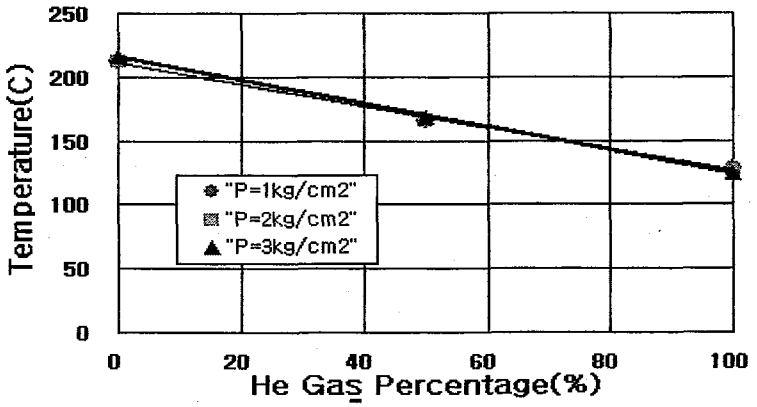

Fig. 4 Effects of the gas mixing ratio and the gas pressure.

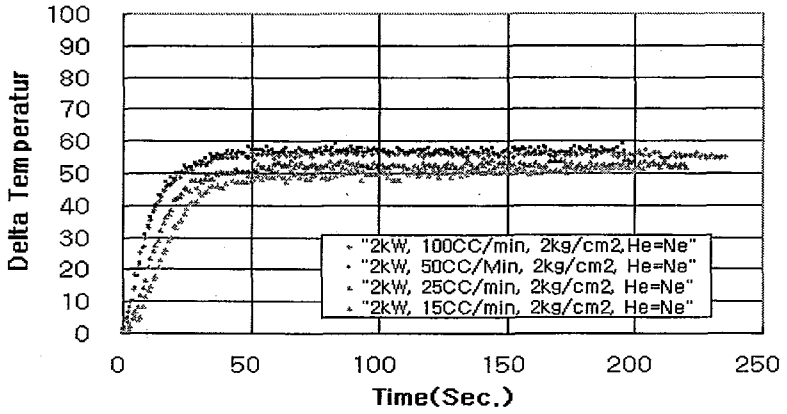

Fig. 5 Effects of the gas flow rate.

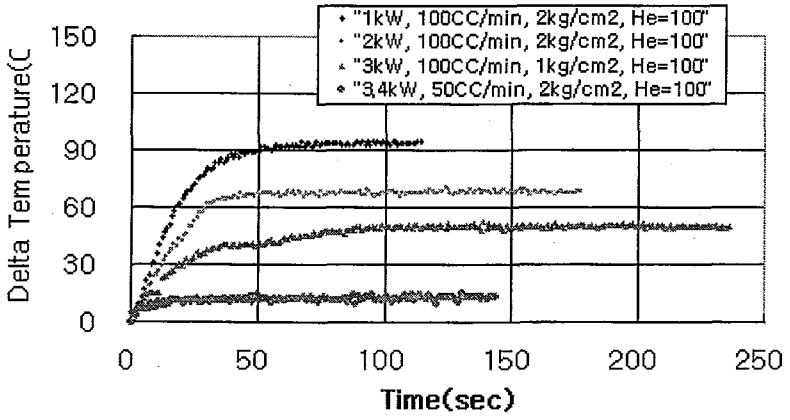

Fig. 6 Effects of the heater power.

CONCLUSION

From the out-pile tests, it was confirmed that the new type of I&C system (GSF-2002) would be feasible for a fuel irradiation using a fuel capsule in the HANARO research reactor. Both the analytical and test data prepared by this study will be used directly for the safety evaluation of the capsule and submitted to the relevant authorities for permission to use the capsule in HANARO.

ACKNOWLEDGEMENTS

The authors would like to express their appreciation to the Ministry of Science and Technology (MOST) of the Republic of Korea and Korea Science and Engineering Foundation (KOSEF) for the support of this work through the mid- and long-term Nuclear R&D Project.

REFERENCES

(1) Y.H. Kang, et al., "Advanced Fuel Irradiation Experiments in the HANARO", 2002 ANES, Miami, U.S.A.(2002)

(2) Y.H. Kang, et al., "Fuel Irradiation Experiments for an advanced PWR fuel development in the HANARO", 2002 Fuel Safety Research Specialist' Meeting, Tokai, Japan (2002).

(3) Y.H. Kang, et al., "Thermal Characteristics of New Concept of Capsule for Fuel Irradiation Test in HANARO", Proceedings of the Korean Nuclear Society Spring Meeting, Suwon, Korea, May 2001.

(4) C.K. Seo, "Preliminary neutronic calculation for the irradiation test of the high burnup fuel" HANARO Internal Memo, HAN-RR-CR-900-00-082. (2000)

(5) W.W. Godsin, et al., "Temperature Control of Fueled Irradiation Capsules by Variable Conductance", GA-1114, 1960.

(6) Y.H. Kang, et al., "Development of New I&C System for Fuel Irradiation Tests", HANARO Workshop 2003, Daejeon, Korea, May 2003.

(7) Y.H. Kang, et al., "Out-pile characteristics of basic designed capsule mockup", Proceedings of the Korean Nuclear Society Spring Meeting, Korea, May 2002.

(8) Kang, Y.H., et al., "Fuel Irradiation Experiments for an advanced PWR fuel development in the HANARO", 2002 Fuel Safety Research Specialist' Meeting, Tokai Japan (2002).

2.10 DEVELOPMENT OF THE INSTRUMENTED CAPSULE FOR NUCLEAR FUEL IRRADIATION TEST AT HANARO

Jae Min Sohn, Jong Myung Oh, Sung Jae Park, Yoon Taeg Shin, Bong Goo Kim, Young Hwan Kang, Hark Rho Kim and Young Jin Kim

HANARO Utilization Technology Development Division
Korea Atomic Energy Research Institute
P.O.Box 105, Yuseong, Daejeon, Korea, 305-353

ABSTRACT

The instrumented capsule for the nuclear fuel irradiation test (hereinafter referred to as "instrumented fuel capsule"), which is crucial for the verification of a nuclear fuel performance and safety, has been developed at HANARO(High-flux Advanced Neutron Application Reactor). The irradiation test of the first instrumented fuel capsule was carried out in March 2003 and the irradiation test of the second instrumented fuel capsule was carried out in April 2004 at HANARO. Through the irradiation tests of the two capsules, the design specifications and safety of the instrumented fuel capsule were successfully verified. In the first instrumented fuel capsule, only the technologies for measuring the center temperature of the nuclear fuel and neutron flux were implemented. In the second instrumented fuel capsule, the technologies for measuring the center temperature of the nuclear fuel, the internal pressure of the fuel rod, the elongation of the nuclear fuel and the neutron flux were implemented. Currently the dual instrumented technologies that allow for two characteristics to be measured simultaneously in one fuel rod, is being developed. The duel instrumented fuel rods have been successfully designed as a part of the technology enhancement program for the instrumented fuel capsule. The instrumented fuel capsule will be utilized for the development of nuclear fuel. The instrumentation technologies for measuring the nuclear fuel characteristics will be applied to the 3-pin FTL(Fuel Test Loop) facility which is currently being developed. And, the duel instrumented technologies will contribute to enhancing the efficiency of the irradiation test using an instrumented fuel capsule at HANARO.

KEYWORDS: Instrumented Fuel Capsule, Nuclear Fuel, Irradiation Test, HANARO, Center Temperature of the Nuclear Fuel, Internal Pressure of the Nuclear Fuel Rod, Elongation of the Nuclear Fuel Pellet, Surface temperature of the Nuclear Fuel, Dual Instrumented Fuel Rods

INTRODUCTION

At KAERI, the irradiation test capsules, which are crucial for the verification of a nuclear fuel performance and safety, have been developed and they are currently being utilized. In May 1998, the non-instrumented fuel capsule was developed to perform the irradiation test of nuclear fuel at HANARO. The non-instrumented fuel capsule is being utilized to develop the DUPIC fuel, research reactor's fuel, advanced PWR fuels etc. and to verify their performance.

The instrumented fuel capsules, as shown in Fig. 1, have also been developed. The first instrumented fuel capsule(02F-11K) was successfully tested from March 14, 2003 to June 1, 2003 for 53.84 EFPD(Effective Full Power Days) and the second instrumented fuel capsule(03F-05K) was tested from April 27, 2004 to October 1, 2004 for 59.5 EFPD in the OR5 experimental vertical hole of HANARO.[1][2][3][4] Through the irradiation tests of the two capsules, the design specifications and safety of the instrumented fuel capsule were verified successfully.

This paper presents the instrumentation technologies for measuring the characteristics of the nuclear fuels during an irradiation test, the irradiation tests of two instrumented fuel capsules and the dual instrumented technologies.

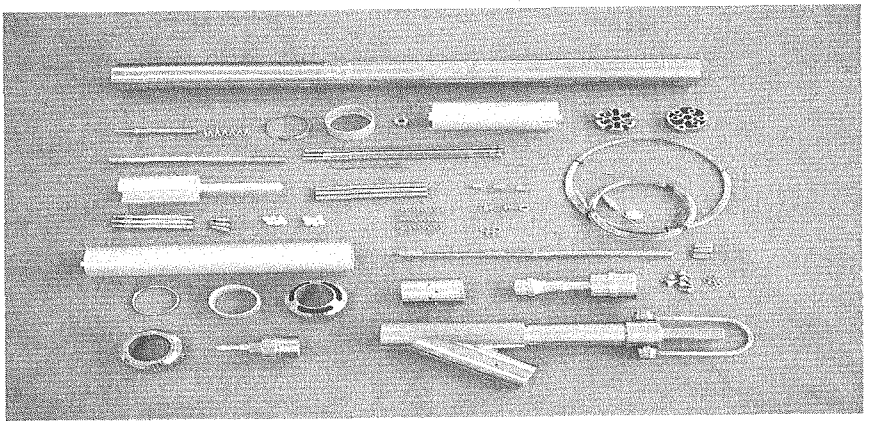

(a) Assemble parts of instrumented fuel capsule

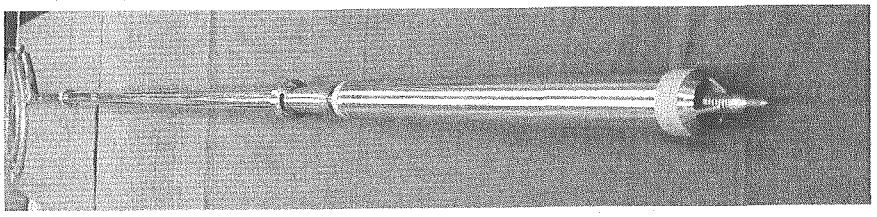

(b) Assembled instrumented fuel capsule

Fig. 1 Instrumented Fuel Capsule

INSTRUMENTATION TECHNOLOGIES

The instrumentation technologies of the nuclear fuel irradiation tests are being used for in-pile behavior studies and for acquiring design specifications of the nuclear fuel. The characteristics of a nuclear fuel that can be measured through irradiation tests are the following; center and surface temperature of the fuel, internal pressure of the fuel rod, elongation of the fuel pellets, elongation of the fuel rod, thickness of the oxidized layer, and the neutron flux etc. In the first instrumented fuel capsule(02F-11K), only the technologies for measuring the center temperature of the nuclear fuel and neutron flux were implemented. In the second instrumented fuel capsule(03F-05K), the technologies for measuring the center temperature of the nuclear fuel, the internal pressure of the fuel rod, the elongation of the nuclear fuel and the neutron flux were implemented.

In the instrumented fuel rods, the C-type thermocouple is used to measure the center temperature of the nuclear fuel, the K-type thermocouple is used to measure the surface temperature of the nuclear fuel, the pressure transducer and the LVDT(Linear Variable Differential Transformer) are used to measure the internal pressure of the fuel rod[5], the elongation detector and the LVDT are used to measure the elongation of the fuel pellets[6], and the SPND(Self-Powered Neutron Detector) with a rhodium emitter is used to measure the neutron flux.[7] Fig. 2 shows three instrumented fuel rods of the 03F-05K instrumented fuel capsule.

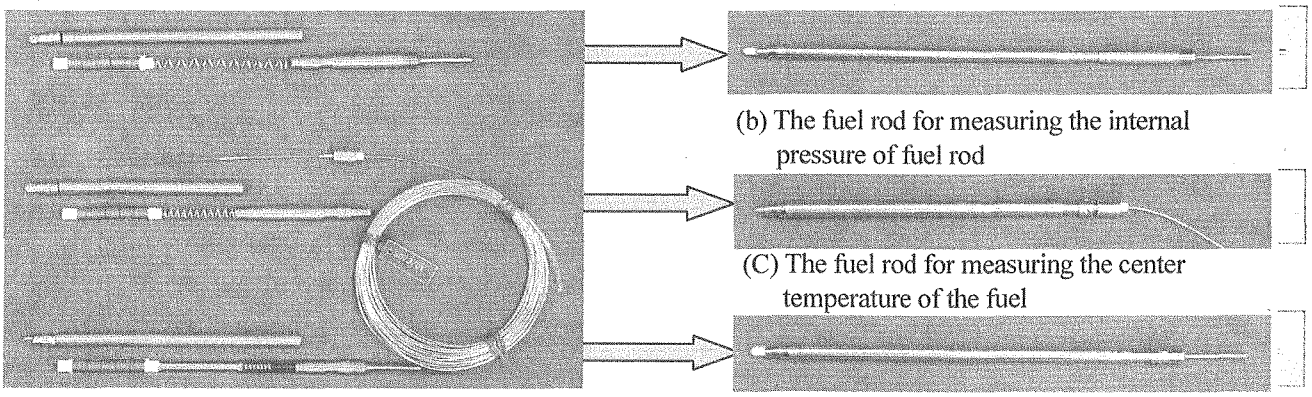

Fig. 2 Instrumented fuel rods of the 03F-05K instrumented fuel capsule

IRRADIATION TESTS OF INSTRUMENTED FUEL CAPSULES

As stated above, the irradiation tests of two instrumented fuel capsules were carried out successfully in the OR5 experimental vertical hole of HANARO, as shown in Fig. 3. Table 1 shows the results of the two irradiation tests using the instrumented fuel capsules(02F-11K & 03F-05K).

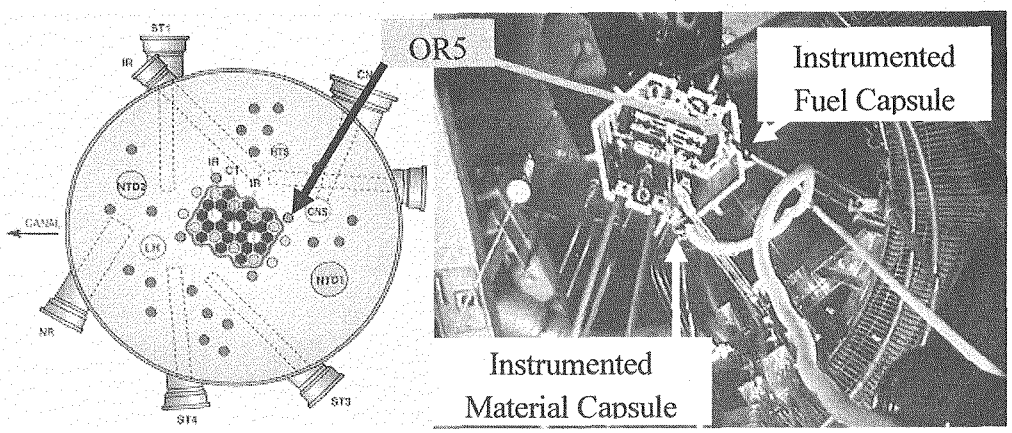

Fig. 3 Instrumented fuel capsule in the OR5 vertical experimental hole of HANARO

Table 1 Results of irradiation tests using the instrumented fuel capsules

Irradiation Test Subjects	02F-11K	03F-05K
HANARO Power (MW)	24	24 ~ 30
Experimental Vertical Hole	OR5	OR5
Maximum Linear Power (kW/m)	53.2	50.1
Average Linear Power (kW/m)	49.2	46.3
Average Burn-up (MWD/MTU)	5,930	5,556
Effective Full Power Days	53.84	59.5
Center Temperature (℃)	1,375	1,316
Irradiation Test Period	2003.3.14 ~ 6.1	2004.4.27 ~ 10.1

During the irradiation test, data for the following measurements was acquired; thermocouple signals for the center temperature of the fuel, LVDT signals for the internal pressure of the fuel rod, LVDT signals for the elongation of the fuel pellets, and the SPNDs' signals for the neutron flux. Data of HANARO's reactor power level(MW) and control rod height(mm) was also acquired. Fig. 4 shows the typical measured data of the 02F-11K instrumented fuel capsule during the 24-1, 2402, 25-1 and 25-2 operation cycles of HANARO. And Fig. 5 shows the typical measured data of the 03F-05K instrumented fuel capsule during the 31-2, 32-1, 32-2 and 33-1 operation cycles of HANARO. This data has been collected over 1-minute interval.

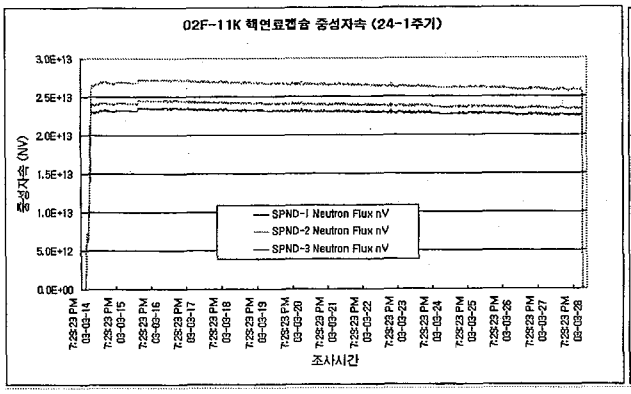

(a) 24-1 operation cycle of HANARO

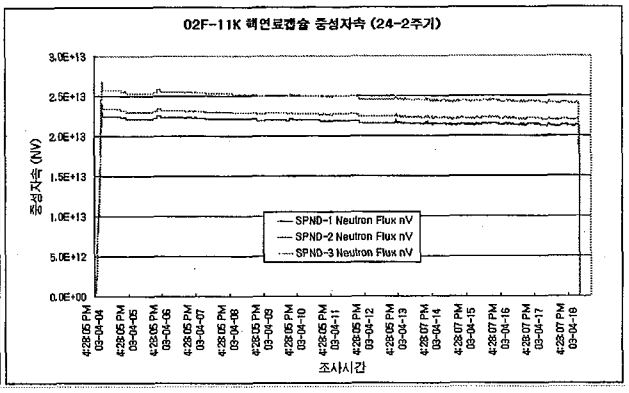

(b) 24-2 operation cycle of HANARO

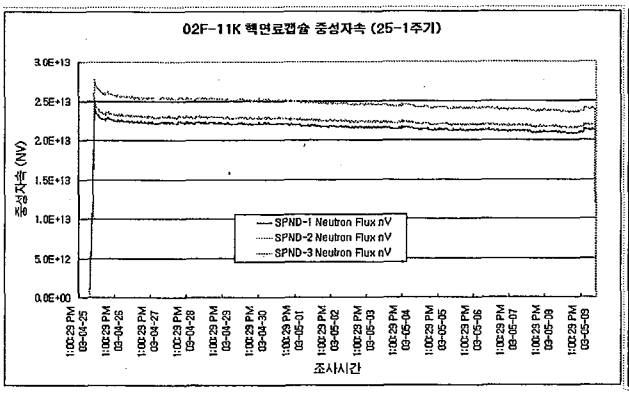

(c) 25-1 operation cycle of HANARO

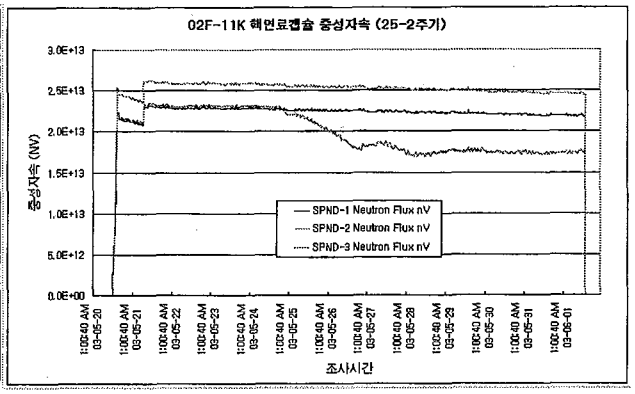

(d) 25-2 operation cycle of HANARO

Fig. 4 Irradiation test data of 02F-11K instrumented fuel capsule

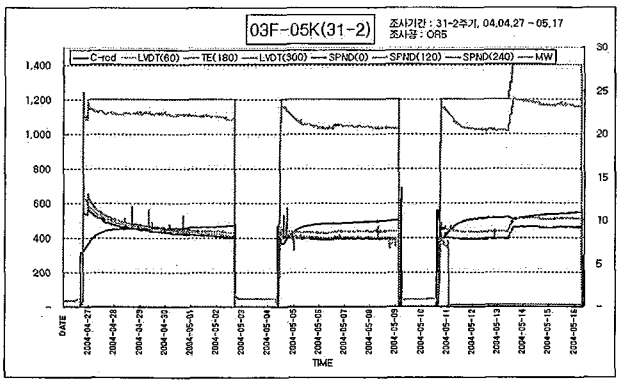

(a) 31-2 operation cycle of HANARO

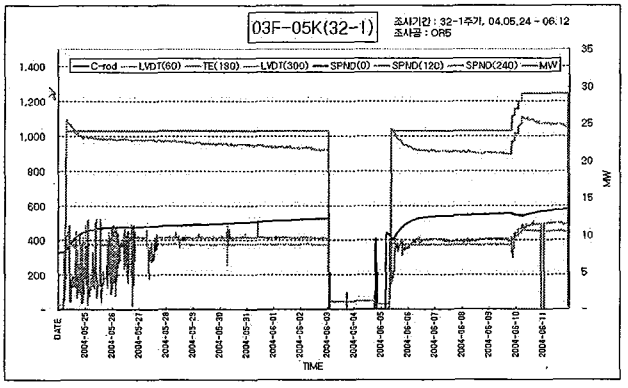

(b) 32-1 operation cycle of HANARO

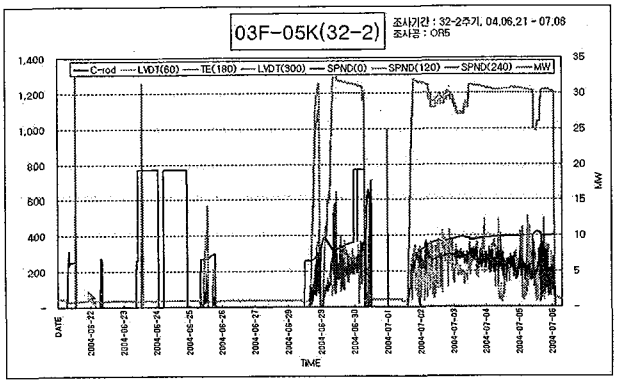

(c) 32-2 operation cycle of HANARO

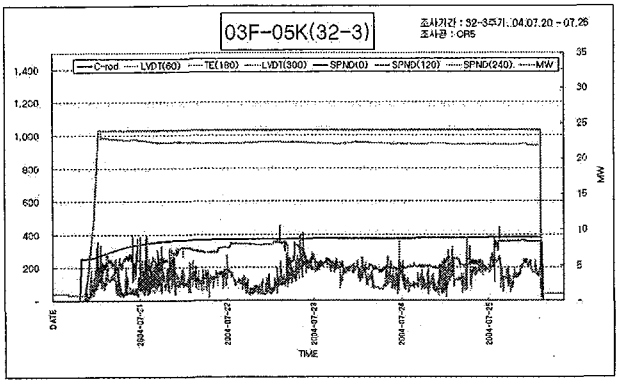

(d) 32-3 operation cycle of HANARO

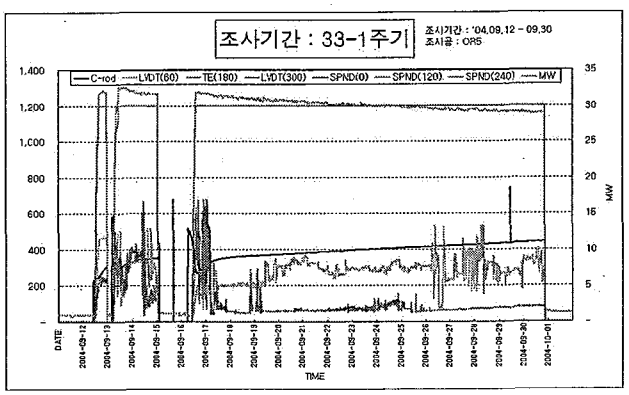

(e) 31-2 operation cycle of HANARO

Fig. 5 Irradiation test data of the 03F-05K instrumented fuel capsule

DUAL INSTRUMENTATION TECHNOLOGIES

The dual instrumented fuel rods have been designed to enhance the efficiency of the irradiation test using an instrumented fuel capsule.[8] There are six different types of dual instrumented fuel rods. The designed dual instrumented fuel rods are shown in Fig. 6. The different functions of these six types are summarized as follows; 1) to measure the center temperature of the nuclear fuel and the internal pressure of the fuel rod, 2) to measure the center temperature of the nuclear fuel and the elongation of the fuel pellet, 3) to measure the surface temperature of the nuclear fuel and the internal pressure of the fuel rod, 4) to measure the surface temperature of the nuclear fuel and the elongation of the fuel pellet, 5) to measure the center and surface temperature of the nuclear fuel, and 6) to measure the center temperature of the nuclear fuel of the upper and lower part.[6] Fig. 7 shows the cross section of the assembled fuel rod for measuring the center and surface temperature of the fuel pellets.

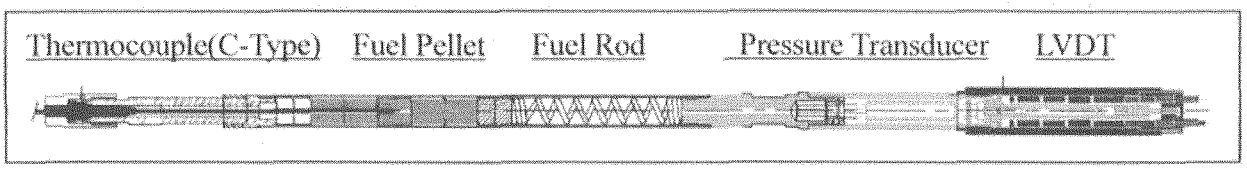

(a) The duel instrumented fuel rod to measure the center temperature of the nuclear fuel and the internal pressure of the fuel rod

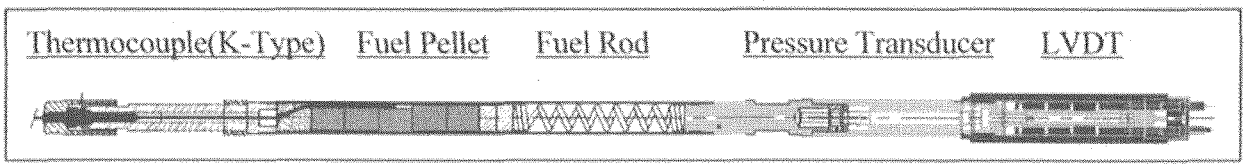

(b) The duel instrumented fuel rod to measure the center temperature e of the nuclear fuel and the elongation of the fuel pellet

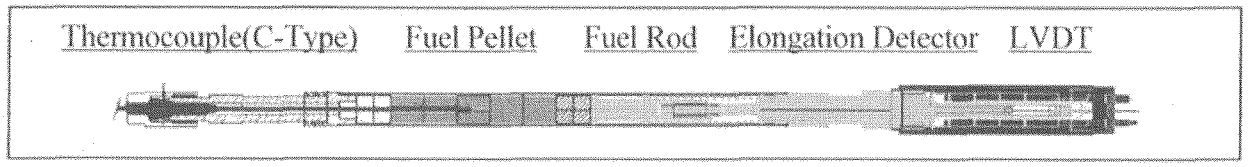

(c) The duel instrumented fuel rod to measure the surface temperature of the nuclear fuel and the internal pressure

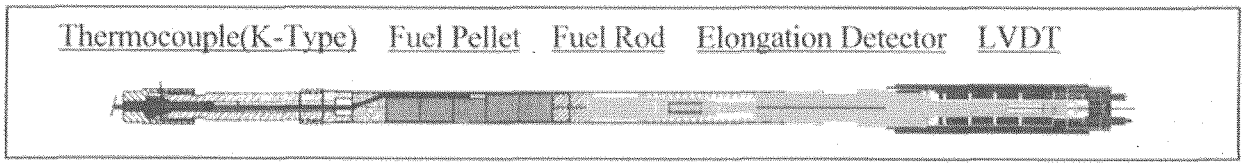

(d) The duel instrumented fuel rod to measure the surface temperature of the nuclear fuel and the elongation of the fuel pellet

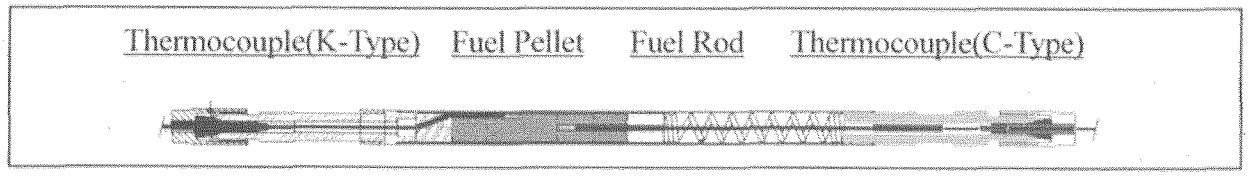

(e) The duel instrumented fuel rod to measure the center and surface temperature of the nuclear fuel

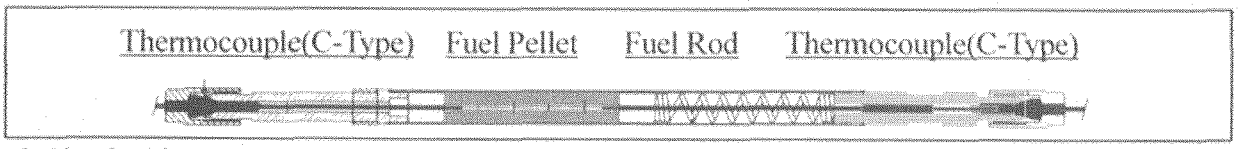

(f) The duel instrumented fuel rod to measure the center temperature of the nuclear fuel of the upper and lower part

Fig. 6 Duel instrumented fuel rods

The 05F-01K instrumented fuel capsule was designed and is being manufactured for a design verification test of the dual instrumented fuel rods. The estimated maximum linear power of the 05F-01K instrumented capsule was calculated at 545.17 W/cm by the MCNP code. By assuming the HANARO fuel assembly is 0 mm, the center of the fuel stacks of the instrumented fuel rods were designed at the relative elevation of -22.5 mm. Fig. 8 shows the relative elevation of the fuel stacks for the three capsules(02F-11K, 03F-05K and 05F-01K).

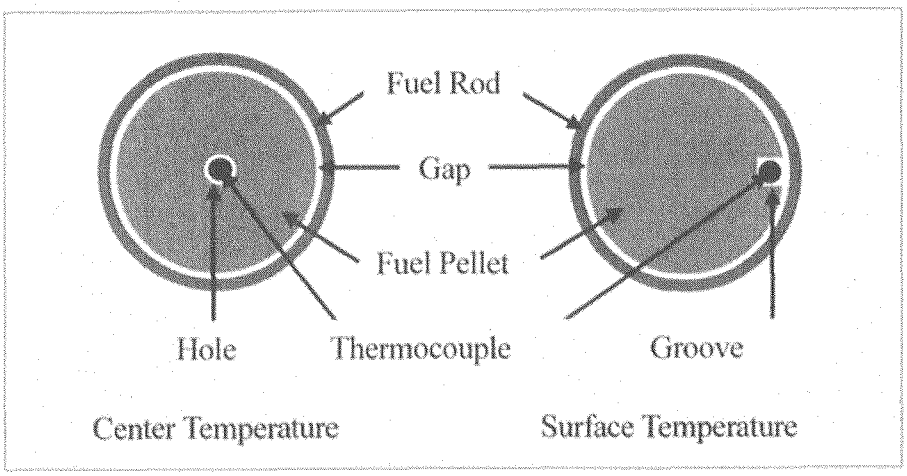

Fig. 7 Cross section of instrumented fuel rod for measuring the temperature of the fuel pellet

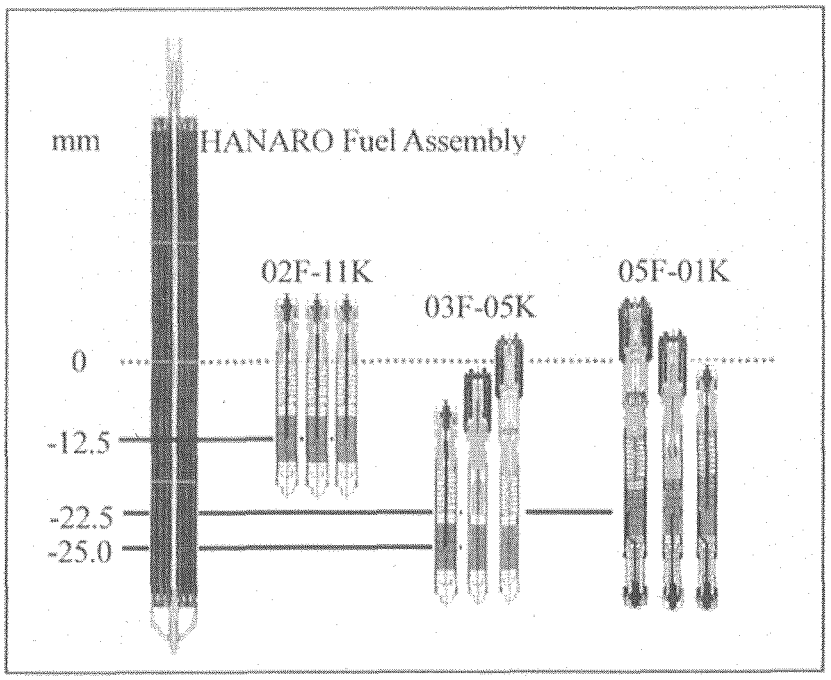

Fig. 8 Elevation of the instrumented fuel rods for irradiation test

In the 05F-01K instrumented fuel capsule, by assuming that the branch direction of the sensor cable protection tube is 0°, the SPNDs have been installed clockwise at 0°, 120°, 240° respectively. And the fuel rod for measuring the internal pressure & the surface temperature of the fuel, the fuel rod for measuring the center & surface temperature of the fuel, and the fuel rod for measuring the elongation of the fuel pellets & the center temperature of the fuel will be installed at 60°, 180°, 300° respectively, as shown in Fig 9. Three SPNDs(Self-Powered Neutron Detectors) will be installed at the same elevation of the stacks of the fuel pellets.

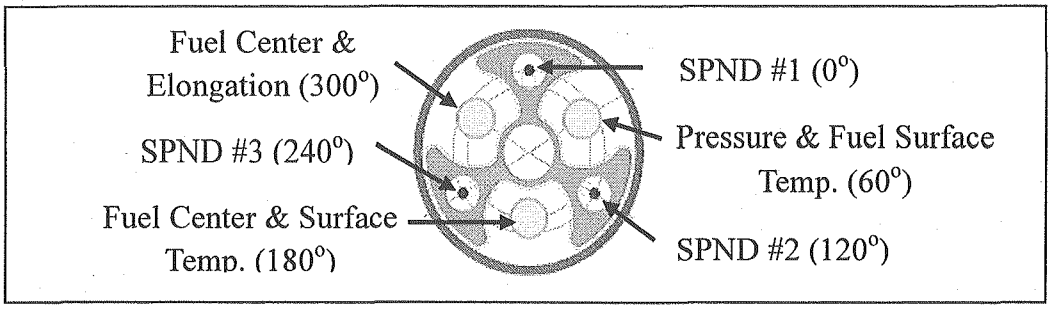

Fig. 9 Arrangement of the instrumented fuel rods & the SPNDs in the 05F-01K instrumented fuel capsule

SUMMARY

The irradiation tests for measuring nuclear characteristics are crucial for the development of a nuclear fuel. Therefore, instrumented fuel capsules have been designed and manufactured for measuring not only the nuclear fuel characteristics such as the center temperature of the fuel using a thermocouple, the internal pressure of the fuel rods using a pressure transducer and a LVDT, and the elongation of the fuel pellets using an elongation detector and a LVDT, but also for the measuring neutron flux using SPNDs. The irradiation test has been successfully performed at the OR5 vertical experimental hole of HANARO, and the nuclear fuel characteristics data has been successfully acquired.

The duel instrumented fuel rods have been successfully designed as a part of the technology enhancement program for the instrumented fuel capsule. The dual instrumented technologies for measuring the nuclear fuel characteristics will contribute to enhancing the efficiency of the irradiation test using an instrumented fuel capsule at HANARO.

The 05F-01K instrumented fuel capsule has been successfully designed and is being manufactured to verify the performance of the dual instrumented fuel rods. The irradiation test of the 05F-01K instrumented fuel capsule will be carried out in the OR5 vertical experimental hole of HANARO at the end of this year.

The instrumented fuel capsules and instrumentation technologies for measuring the nuclear fuel characteristics will be applied to the 3-pin FTL(Fuel Test Loop) facility which

is currently being developed and they will contribute to both national and international nuclear fuel development research.

ACKNOWLEDGEMENTS

This study was supported by Korea Institute of Science & Technology Evaluation and Planning (KISTEP), Korea Science and Engineering Foundation (KOSEF) and Ministry of Science & Technology (MOST), Korean government, through its National Nuclear Technology Program.

REFERENCES

(1) B.G.Kim, "Design and Manufacturing of Instrumented Capsule(02F-11K) for Nuclear Fuel Irradiation in HANARO", KAERI/TR-2408/2003, Korea Atomic Energy Research Institute, 2003

(2) B.G.Kim, "Design Verification Test of Instrumented Capsule(02F-11K) for Nuclear Fuel Irradiation in HANARO", KAERI/TR-2658/2004, Korea Atomic Energy Research Institute, 2004..

(3) B.G.Kim, "Design and Manufacturing of Instrumented Capsule(03F-05K) for Nuclear Fuel Irradiation in HANARO", KAERI/TR-2773/2004, Korea Atomic Energy Research Institute, 2004.

(4) J.M.Sohn, "Irradiation Test of 03F-05K Instrumented Capsule for Nuclear Fuel Irradiation in HANARO", KAERI/TR-3035/2005, Korea Atomic Energy Research Institute, 2005.

(5) J.M.Sohn, "The High Temperature Out-of-Pile Test of LVDT for Internal Pressure Measurement Technology Development of Nuclear Fuel Rod", Korea Nuclear Society, 2002.

(6) J.M.Sohn, "The High Temperature Out-of-Pile Test of LVDT for Elongation Measurement of Fuel Pellet", Korea Nuclear Society, 2003.

(7) J.M.Sohn, "Development of the Measurement Technologies for Nuclear Fuel Characteristics by using the Instrumented Capsule for Nuclear Fuel Irradiation Test at HANARO", International Symposium on Research Reactor and Neutron Science, 2005

(8) J.M.Sohn, "Design of the Dual Instrumented Fuel Rods to Measure the Nuclear Fuel Characteristics during Irradiation Test at HANARO", Korea Nuclear Society, 2004.

2.11 AN INTERNAL HEATING EXPERIMENTAL METHOD FOR IRRADIATED FUEL CLADDING TUBES

Toru Higuchi, Toshio Kubo and Tomoya Yonekawa

Nippon Nuclear Fuel Development Co., Ltd.,
2163 Narita-cho, Oarai-machi, Higashi-Ibaraki-gun,
Ibaraki-ken, 311-1313, Japan

ABSTRACT

A remote controlled device has been developed for an internal heating experimental method in a hot-cell in order to evaluate the behavior of hydrogen and elucidate the formation mechanism of radially oriented hydrides in irradiated fuel cladding tubes. The device enables one to perform internal heating experiments under conditions of up to 300 W/cm with a linear heat rate and 209 MPa hoop stress. Quantitative analysis of the hydrogen content indicates thermal diffusion under the conditions used in this study. The radial orientation of hydrides remarkably appeared in the range from 235 W/cm to 295 W/cm after being constant in the range under 235 W/cm. The hoop stress slightly promoted the radial orientation of hydrides.

KEYWORDS: BWR, Zircaloy-2, fuel cladding tube, ramp test, radially oriented hydride, temperature gradient, hoop stress, internal heating experimental method

INTRODUCTION

Zircaloy-2 has been successfully used as the material for fuel cladding tubes in boiling water reactors (BWRs). The extended fuel burnup and longer operating cycles gradually decrease the ductility of the zircaloy cladding tubes, mainly due to the combined effects of neutron irradiation and hydrogen uptake during service. Furthermore, it was recently reported that some high burnup fuel rods had failed in power ramp tests[(1)], with cracks initiating at radially oriented hydrides in the outer surfaces of the cladding tubes, indicating that the radially oriented hydrides play a key role in the failure mechanism and are a critical issue for high burnup. It is well known that the segregation of radially oriented hydrides is promoted in the presence of a radial temperature gradient, which induces the

diffusion of hydrogen atoms from bulk to periphery of the cladding tubes, and tensile hoop stress, which forms radially oriented hydrides. Although the behavior of hydrogen under temperature gradient has been clarified by experimental and theoretical investigations[2-6], few studies have been performed on the combined effects of temperature gradient and hoop stress on the diffusion of hydrogen and the precipitation of hydride.

In addition, the internal heating experimental method is effective to study the simultaneous effects of a temperature gradient and hoop stress in order to simulate such conditions for a tubular specimen. However, few investigations using this method have been carried out because of the difficulty of performing the experiment. In particular, there has been no investigation on effects on irradiated fuel cladding tubes.

In order to evaluate the behavior of hydrogen and elucidate the formation mechanism of radially oriented hydrides in irradiated fuel cladding tubes under power ramp conditions at high burnup, we have developed a remotely controlled device to perform internal heating experiments in a hot-cell. In addition, preliminary tests on unirradiated materials were carried out to confirm the performance of the device.

EXPERIMENTAL

Development of apparatus

The device for the internal heating experimental method developed for the present study consists of an internal heater, a pump, a thermo-static bath and a cooler as schematically shown in **Fig. 1**. The internal heater of 10 mm∅ diameter is inserted into the tubular specimen of 12.27 mm∅ outside diameter and 10.55 mm∅ inside diameter, and mechanically sealed at both ends using swagelok fittings. The maximum linear heat rate was 300 W/cm. A pump set in the hot-cell pressurizes water with the pressure ranging from 20 MPa to 30 MPa in the specimen, applying hoop stress. Assuming the fuel cladding tube to be a thin-walled tube, the hoop stress σ_θ is estimated by

$$\sigma_\theta = \frac{P_i}{(d_o/d_i)-1} \qquad [1]$$

where P_i is the internal pressure in the case where the effect of thermal stress caused by a temperature gradient is ignored. The internal pressure corresponds to a range from 139 MPa to 209 MPa hoop stress, neglecting the strength of the Zr liner. The specimen is placed in a thermo-static bath filled by liquid alloy (Sn/Bi) in order to control the temperature condition using cooling water. The temperature was measured at the outer surface of the specimen by a chromel-alumel thermocouple. Although it is very difficult to directly measure the temperature of the inner surface T_i, it is theoretically expressed by

$$T_i = T_o + Q' \times \ln\left(\frac{d_o}{2\pi K_c d_i}\right) \quad [2]$$

where T_o is the temperature of the outer surface, Q' the linear heat rate, d_i the inside diameter, d_o the outside diameter and K_c the thermal conductivity. A temperature gradient of 51 °C/mm was attained for a 300 W/cm linear heat rate. The experiment and sample preparation are remotely operated using a manipulator.

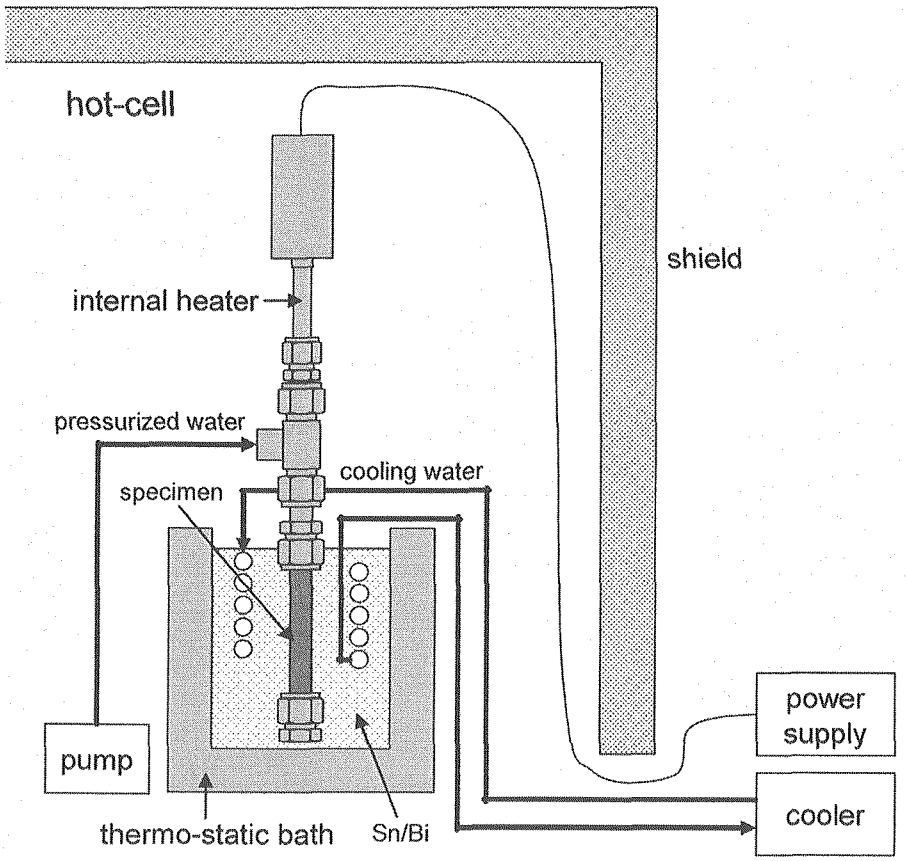

Fig. 1 A schematic drawing of the internal heating experimental device for an irradiated fuel cladding tube in a hot-cell.

Experimental procedure

Unirradiated, recrystallized Zr lined Zircaloy-2 fuel cladding tubes were used in the preliminary tests. Seven specimens of 110 mm length were taken from 4 m long cladding tube. Hydrogen with 120-180 ppm concentration was injected into the specimens by heating in 2 mol/*l* LiOH aqueous solution at 300 °C for 22 hours. Five specimens were used for the internal heating experiments while the others were just heated at 290-300 °C as

a reference. In the internal heating experiments, the specimens were pressurized and heated for 4 hours in the thermo-static bath, controlling the temperature of the outer surface with the ranging from 285 °C to 305 °C. The specimens were taken out of the bath and then rapidly cooled using a fan after the removal of the internal pressurization and heating. The conditions of the experiments are summarized in **Table 1**. The distribution of hydrogen content was measured by secondary ion mass spectrometry (SIMS) analysis of specimens No. 1, 2. The morphology was examined using optical microscopy for the specimens No.3-7. The average hydrogen content was determined by gas analysis.

RESULTS AND DISCUSSION

Fig. 2 shows the distribution of hydrogen content along the radial direction as a function of the distance from the outer surface for the reference (No. 1) and the specimen tested with 300 W/cm linear heat rate and 209 MPa hoop stress (No. 2). The region of about 90 μm thickness from the inner surface corresponds to the Zr liner which absorbs hydrogen revealing a high hydrogen content. The hydrogen content of the specimen examined in the internal heating experiment drastically increased in range less than about 100 μm from the outer surface in contrast to that of the reference which remained almost constant. This result indicated that the hydrogen atoms diffused from the inner region to the outer region in the presence of the temperature gradient and tensile stress.

Table 1 Experimental conditions and average hydrogen content for the specimens used in the study. Samples no.1 and 2 were used for SIMS analysis. Samples no. 3-7 were used for metallographic observations.

Sample No.	linear heat rate [W/cm]	hoop stress [MPa]	average hydrogen content [ppm]
1	0	0	174
2	300	209	187
3	0	0	161
4	235	174	181
5	235	209	161
6	295	174	116
7	295	209	145

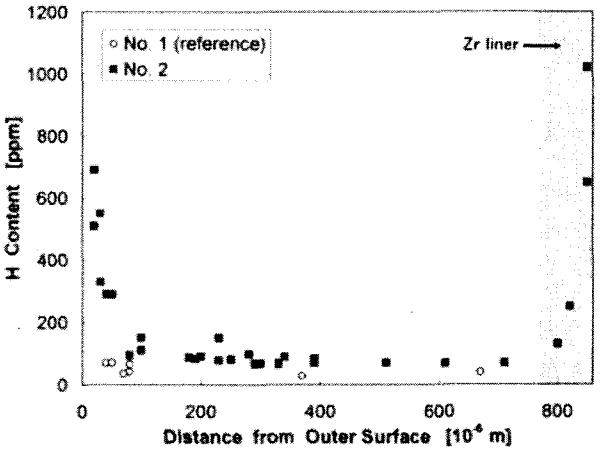

Fig. 2 Distribution of hydrogen along the radial direction for the specimens with (No. 2) and without (No. 1) the internal heating experiment.

Fig. 3 (a) and **(b)** show the metallography of the reference (No. 3) specimen and the specimen tested with 295 W/cm linear heat rate and 209 MPa hoop stress (No. 7), respectively. Hydrides were formed uniformly throughout the specimen and few radially oriented hydrides are observed in **Fig. 3 (a)**. On the other hand, some radial hydrides were observed at the region near the outer surface in **Fig. 3 (b)**. This phenomenon is caused by an increase in hydrogen concentration near the outer surface, as shown in **Fig. 2**.

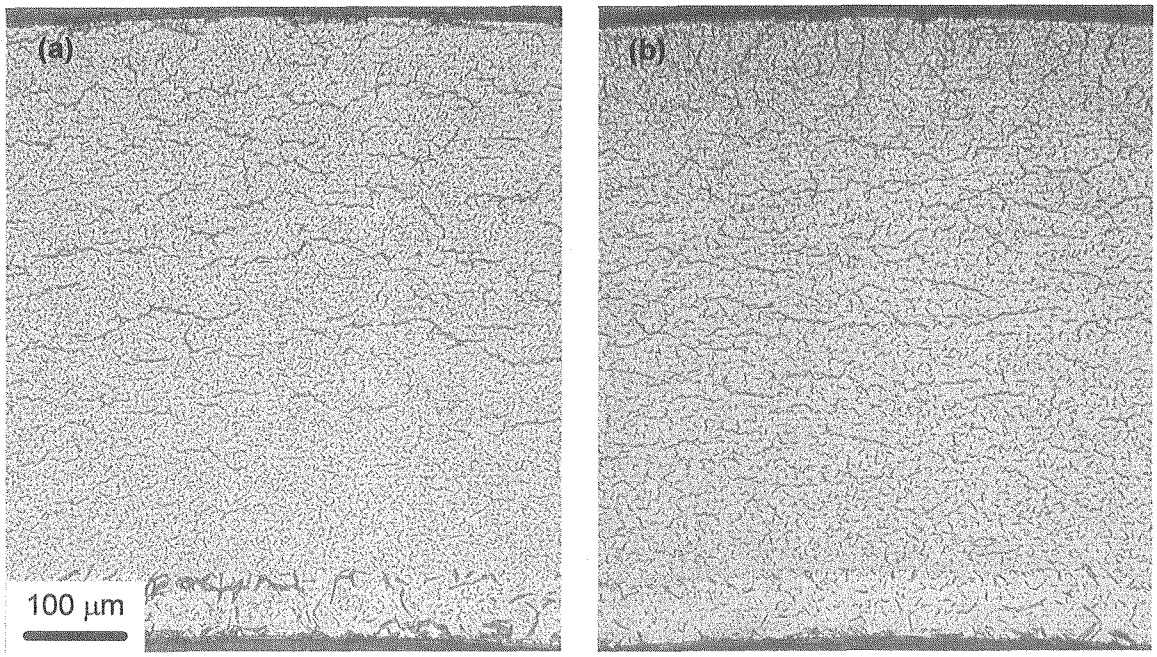

Fig. 3 Metallography of (a) the reference and (b) the specimen tested at 295 W/cm linear heating rate and 209 MPa hoop stress.

Although the value of *Fn*, which is the ratio of radially oriented hydrides to all hydrides, is generally used as the indicator for the orientation of hydrides, it does not take the lengths of the hydrides into account. Hence, a new orientation factor, Θ was defined for the macroscopic orientation of hydrides which is expressed by

$$\Theta = \sin^{-1}\left(\frac{\sum l_i \sin\theta_i}{\sum l_i}\right) \qquad [3]$$

where θ_i and l_i are the angle and length of individual hydrides, respectively, as shown in **Fig.4**, in order to express information on the length. Assuming the hydrides to be straight lines, as shown in **Fig. 5**, their angle and length were measured in the region of about 100 μm from the outer surface in order to observe the phenomena near the outer surface. In this work, we required the hydrides to have a much larger length than width to decide the orientation.

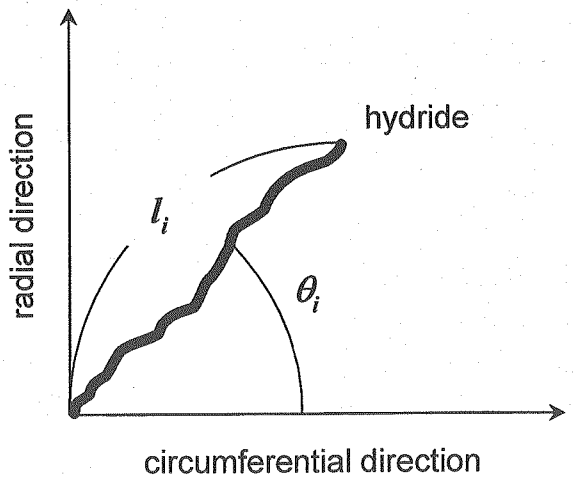

Fig. 4 A schematic diagram showing length and angle of the hydrides.

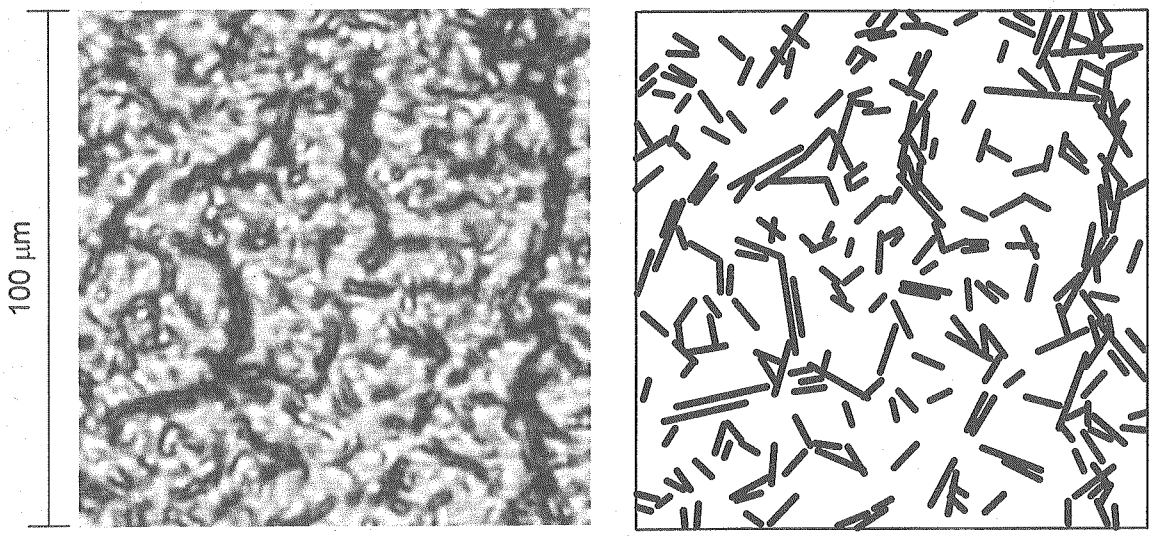

Fig. 5 A measurement method for length and angle of the hydrides by assuming the hydrides to be straight lines.

Fig. 6 shows the macroscopic orientation of the hydrides as a function of the linear heat rate for two different hoop stresses. The reference had a ~30 degrees macroscopic orientation of hydrides which agrees with other report[7]. The radial orientation of hydrides remarkably appeared in the range from 235 W/cm to 295 W/cm after being constant in the range under 235 W/cm. Besides, it was observed that the hoop stress slightly promotes the radial orientation. We assume that the diffusion of hydrogen enlarged radially oriented hydrides after the hoop stress had caused radially nucleation of hydrides. The nuclei are basically liable to grow under the high concentration of solute. In addition, it is likely that

large precipitations have priority to absorb excess solute because of the growing mechanism, implying the size of precipitation drastically depends on concentration of solute. Therefore, it is considered that formation of radially oriented hydride is depends on linear heat rate in this work.

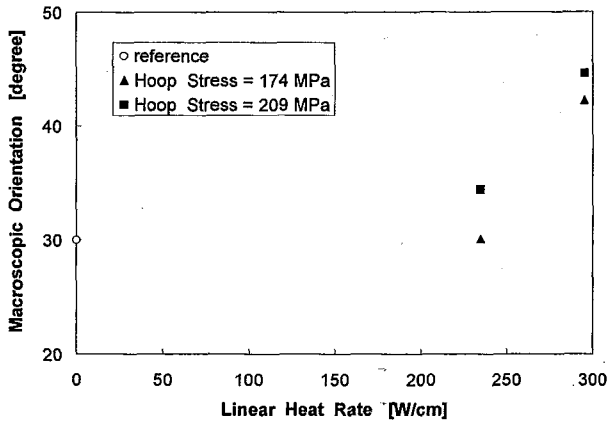

Fig. 6 Macroscopic orientation of the hydrides as a function of linear heating rate for the reference and the specimen tested at 174 and 209 MPa hoop stress.

SUMMARY

A device for an internal heating experiment was developed and preliminary tests were carried out to confirm the performance of the device using unirradiated materials. The salient results of the study are summarized below.

(1) The device developed enables one to perform internal heating experiments under the condition wherein the linear heat rate and hoop stress can rise up to 300 W/cm and 209 MPa, respectively.

(2) Hydrogen thermally diffused under the conditions of this study, causing the consequent increase of hydrogen content near the outer surface.

(3) Preliminary tests were able to reproduce the radially oriented hydrides which were observed in the power ramp test.

(4) The radially oriented hydrides remarkably appeared under the condition of 295 W/cm linear heat rate.

(5) The hoop stress slightly promoted the radial orientation of the hydrides.

REFERENCES

(1) S. Shimada, E. Etoh, H. Hayashi, et al., J. Nucl. Mater., 327,97(2004)
(2) A. Sawatzky, J. Nucl. Mater., 2,321(1960)
(3) A. Sawatzky, Trans. Met. Soc. AIME., 227,917(1963)
(4) H. Maki and M. Sato, J. Nucl. Sci. Thecnol., 12[10], 637(1975)
(5) K. Forsberg and A.R. Massih, J. Nucl. Mater., 172,130(1990)
(6) A.G. Varias and A.R. Massih, J. Nucl. Mater., 279, 273(2000)
(7) K. Sakamoto and M. Nakatsuka, Proceedings of 2005 Water Reactor Fuel Performance Meeting., to be published

2.12 IMPROVED TECHNIQUE OF HYDROGEN CONCENTRATION MEASUREMENT IN FUEL CLADDING BY BACKSCATTERED ELECTRON IMAGE ANALYSIS

Atsushi Onozawa, Akio Harada, Junichi Honda, Ryo Yasuda, Masahito Nakata, Hiroyuki Kanazawa and Yasuharu Nishino

Department of Hot Laboratories and Facilities, Nuclear Science Research Institute
Japan Atomic Energy Agency
2-4 shirakata-shirane, Tokai-mura, Naka-gun, Ibaraki-ken, 319-1195 Japan

ABSTRACT

In the Reactor Fuel Examination Facility (RFEF), a measuring method of hydrogen concentration by backscattered electron image analysis was improved to obtain more local hydrogen concentration data in fuel claddings. The sample preparation and image analysis procedures of this were able to measure hydrogen concentration efficiently and precisely. This paper describes the improved techniques.

KEYWORDS: Hydrogen Concentration Measurement, Backscattered Electron Image, Fuel Cladding, High burn-up, Post Irradiation Examination

INTRODUCTION

For high burn-up fuel, increasing of hydrogen absorption to the fuel cladding is serious problem from the viewpoint of keeping the integrity of fuel cladding. The hydrogen is absorbed to the fuel cladding with the formation of oxide layer during irradiation. The absorbed hydrogen that exceed solid solubility limit precipitates as the hydride phase. Those hydrides tend to precipitate it in the outer circumference side because hydrogen has a characteristic to migrate to the low temperature side, and high concentration of hydride causes the fuel cladding brittleness. Therefore it is important to evaluate hydrogen concentration at local area in claddings to confirm the safety margin of them.

A measurement technique for local area hydrogen concentration using backscattered electron image analysis (BEI method)[1] had been developed by Studsvik Nuclear AB, Sweden.

The BEI method is very useful for the measurement of radial hydrogen concentration profile in fuel claddings. In the RFEF, a sample preparation and image analysis procedures of the BEI method were improved to measure hydrogen concentration efficiently and precisely. In addition, confirmation tests were successfully carried out to apply that improved method for the Post-Irradiation Examinations (PIEs).

OUTLINE OF BEI METHOD

BEIs are taken with SEM, and the hydride area fraction in the BEI is measured by image analysis system. Hydrogen concentration is calculated using formula (1).

$$Wt_H = Wt_\delta \cdot F \left(\frac{\rho_\delta}{\rho_{Zr}(1-F) + \rho_\delta \cdot F} \right) \quad \text{----------} \quad (1)$$

Wt_H = Hydrogen concentration (wt ppm)

Wt_δ = Hydrogen concentration in δ-phase hydride (wt ppm)

F = Measured area fraction of hydride

ρ_δ = Density of δ-phase hydride (5.65g/cm^3)

ρ_{Zr} = Density of α-phase hydride (6.54g/cm^3)

IMPROVEMENTS OF BEI METHOD

To measure the hydrogen concentration using the BEI method, it is necessary to image the hydrides on the observation plane accurately and to measure the hydride area fraction precisely. Polishing techniques for the specimen surface and the image analysis technique for the hydride area fraction measurement are improved for these aims.

Polishing techniques for the observation plane

The local hydrogen concentration can be determined by formula (1) from the hydride area fraction on a target plane. On this method, the concavo-convex surface of the specimen affects the accuracy of the measurement data. The BEI taken on concavo-convex surface shows the excessive hydride area caused by backscattered electron from the hydride on the other multiple planes.

In the usual procedure of sample preparation for metallography, the buff polishings with the diamond abrasive are carried out after the grindings to obtain a mirror-like surface. However, this process is unsuitable to make the flat surface on the cladding with hydrides, because polishing rates are different between the matrix zircaloy and hydride in the cause of their hardness difference. Therefore the diamond abrasive removes the matrix zircaloy mainly, and most of hydrides were remained as protuberant on the observation surface at the end of

the diamond polishing process.

To make the flat surface, alkaline liquid (pH9.8) with oxide abrasive was implemented additionally after the diamond polishing. The specimen surface after these polishing ways is brought to a flat surface which has the maximum roughness of 0.05μm, and it is possible to image the hydrides accurately on the BEI. Schematic drawing of these polishing techniques is shown in **Fig.1**.

Image analysis technique for the hydride area fraction measurement

Figure 2(a) shows typical BEI of a fuel cladding. BEIs are taken as the grayscale images whose gray levels depend on the intensity of backscattered electron from the surface composition, and the hydrides in that grayscale images are observed as black pixels. In usual image analysis, image conversion from grayscale to black-and-white (B/W) is performed according to a random threshold of the brightness, and the area fraction of black pixels in that B/W image is measured as that of the hydride.

However, there are blackish pixels rather than black pixels of the hydrides in BEI, which are pixels of scratches, pits, etc. And the pixels of the matrix zircaloy have the brightness irregularity. If B/W conversion according to a brightness threshold is applied to BEI, all black and blackish pixels including scratches, pits and brightness irregularity are measured as the hydrides pixels. Therefore, it is important for accuracy measurement to distinguish the hydride pixels only from black and blackish pixels.

One of the image analysis techniques, called "Color Gamut Selection (CGS) method", is used to distinguish the hydride pixels only. The CGS method has four steps,

1) Choose one "Criterion pixel" on the center of a random hydride,
2) Select pixels which have about the same brightness as the "Criterion pixel",
3) From those selected pixels at Step 2), Un-select pixels which are not cascaded to the "Criterion pixel".
4) Selected pixels mean the hydride pixels that contain "Criterion pixel" chosen at Step 1).

After applying the CGS method to all hydrides, the selected pixels are estimate to hydrides. **Figure 3** shows schematic drawing of the CGS method. Moreover, the comparison of B/W images converted by brightness threshold and CGS method is shown at **Fig.2(b)**.

The CGS provides good distinction of the hydride pixels from black and blackish pixels, and the hydride area fraction is accurately measured by this method

CONFIRMATION TEST

The confirmation tests have been performed using the un-irradiated zircaloy claddings which have the different hydrogen concentrations to determine the reliability of the improved BEI method. The hydrogen concentration measured by the improved BEI method is compared with that by Hot Vacuum Extraction (HVE) method, which is one of the reliable methods for

the hydrogen concentration measurement.

BEI method is developed to evaluate hydrogen concentrations at local area and HVE method provides the average hydrogen concentration in the specimen. Therefore, to compare these two hydrogen concentrations measured by BEI and HVE method, the confirmation test was carried out with the following examination processes.

[BEI method]

i. Take BEIs from the outer to inner circumference continuously and combine those BEIs
ii. Measure the hydride area fraction of combined BEI and calculate a hydrogen concentration
iii. Perform the same process on four directions, 0°, 90°, 180° and 270°to calculate hydrogen concentrations of each direction
iv. The hydrogen concentration by BEI method is determined with averaging those four measured concentrations

[HVE method]

i. Divide a ring sliced specimen into four pieces
ii. Measure the hydrogen concentration of each divided specimen by HVE apparatus
iii. The hydrogen concentration by HVE method is determined with averaging those four measured concentrations

Simplified graphic representation of this comparing way is shown in **Fig.4**.

Figure 5 shows each measured hydrogen concentrations by the BEI and HVE. These measured concentrations show good agreement from 150ppm to 700ppm. It is said that the improved BEI method can provide the accurate hydrogen concentrations at local area in claddings, that can't be measured by HVE method.

SUMMARY

In BEI method, the polishing techniques for the observation plane and the image analysis technique for the hydride area fraction measurement were improved to measure local hydrogen concentrations at RFEF. In the confirmation test with un-irradiated claddings, the hydrogen concentration measured by the improved BEI method gave good agreement with the results of HVE method from 150ppm to 700ppm. The improved BEI method is very effective to measure the radial hydrogen concentration profiles in fuel claddings. Furthermore, to apply the improved BEI method to PIE, the confirmation tests with claddings of higher hydrogen concentrated, hydrides segregated and irradiated will be performed.

ACKNOWLEDGEMENTS

The HVE measurements and the SEM observations are supported by the Fuel Examination section. The specimens are provided from the Fuel Safety Evaluation Research Group. The authors wish to express their sincere thanks to all of them.

REFERENCES

(1) David I. Schrire and John H. Pearce, "Scanning Electron Microscope Techniques for Studying Zircaloy Corrosion and Hydriding", *Zirconium in the Nuclear Industry: Tenth International Symposium, ASTM STP 1245*

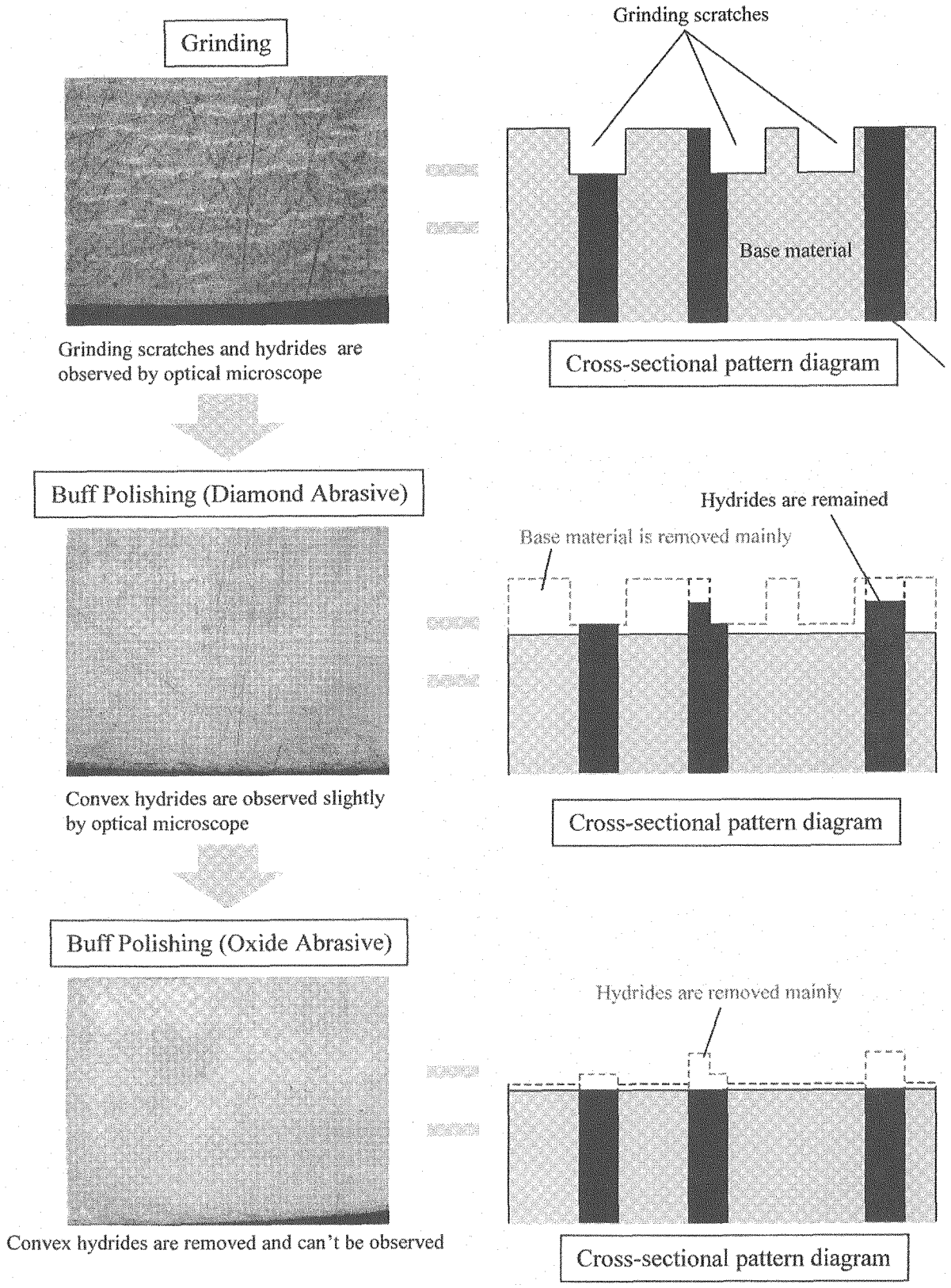

Figure 1 Schematic drawing of Polishing technique for BEI method

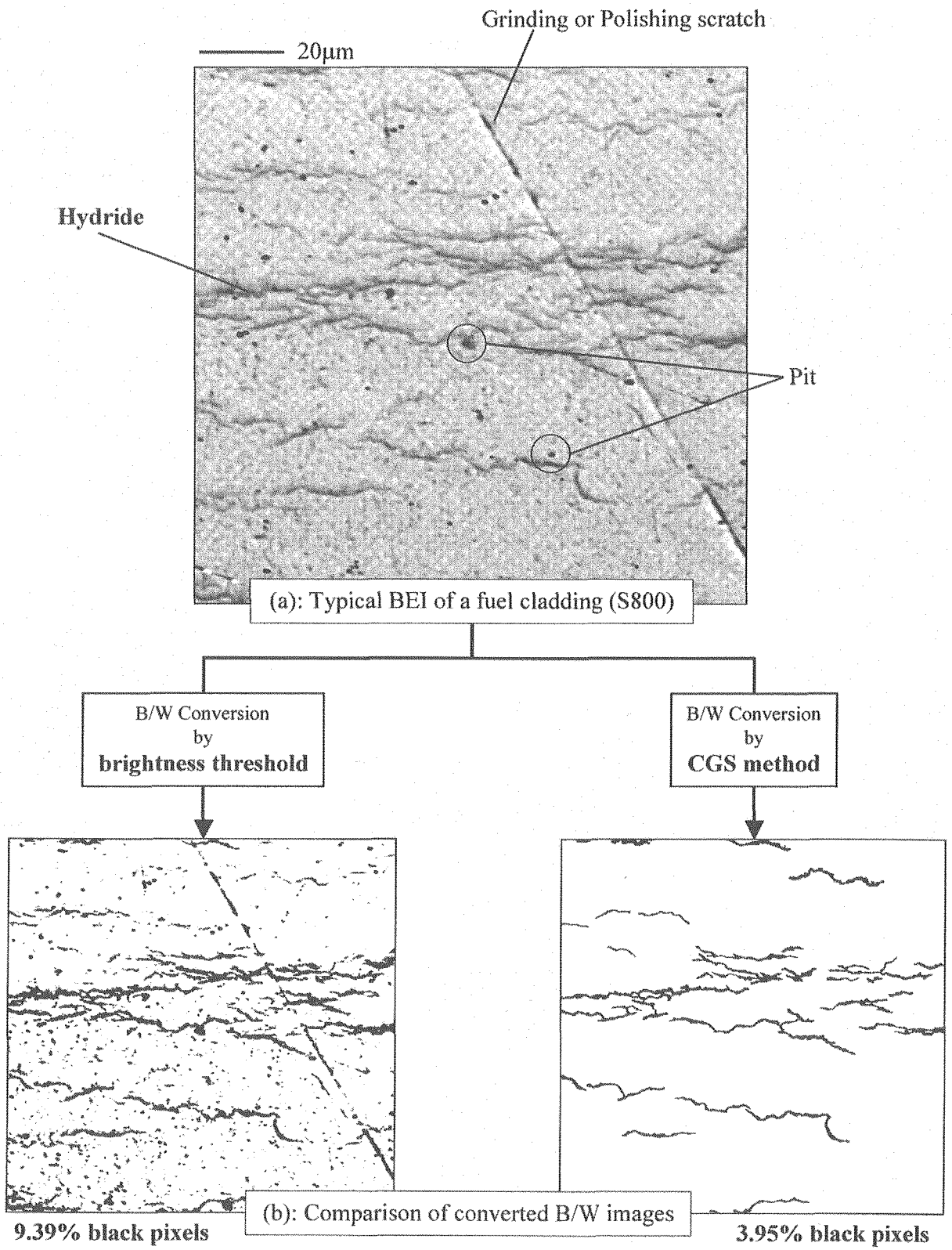

Figure 2 Typical BEI and B/W converted images

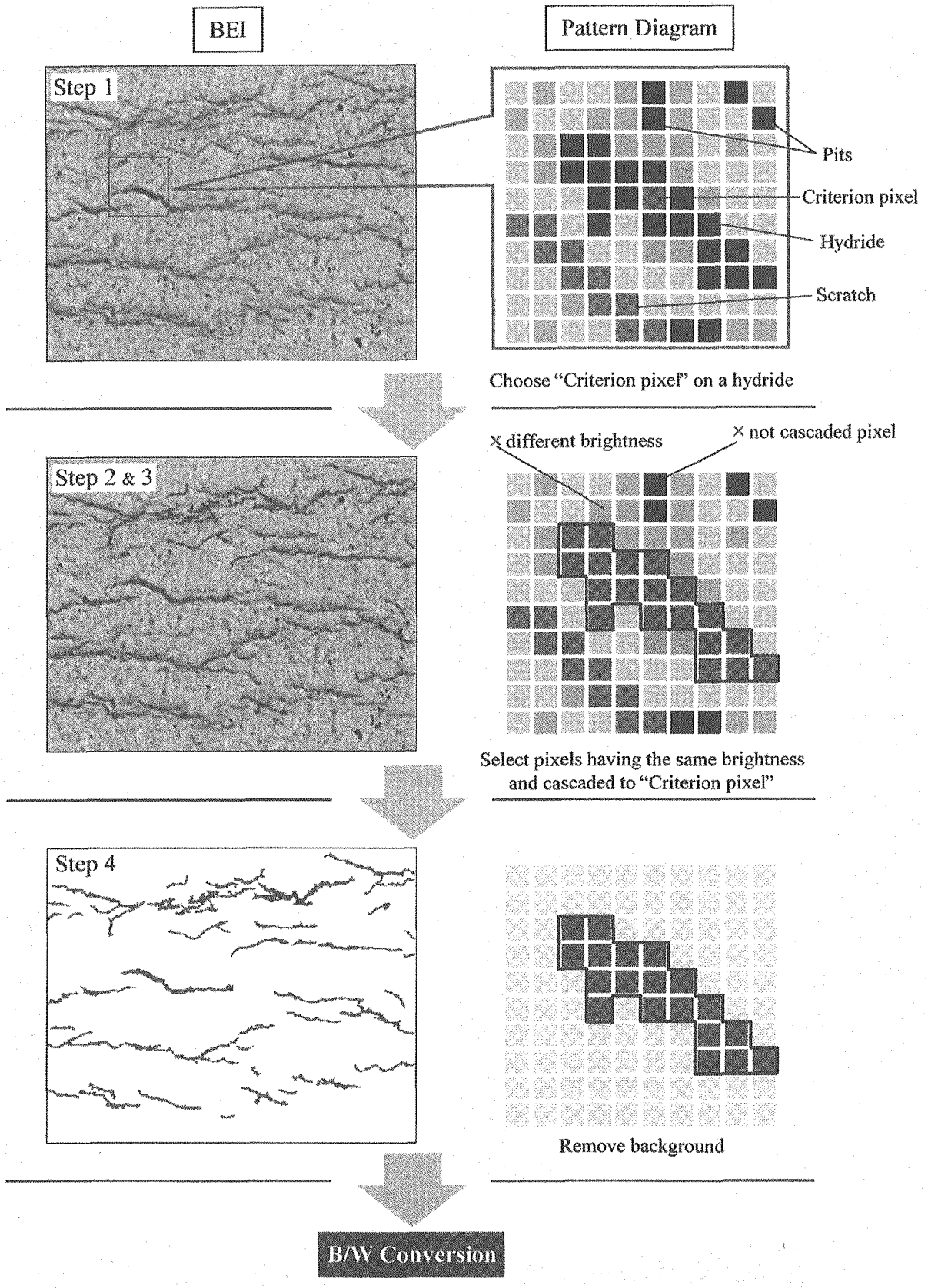

Figure 3 Schematic drawing of Color Gamut Selection Method

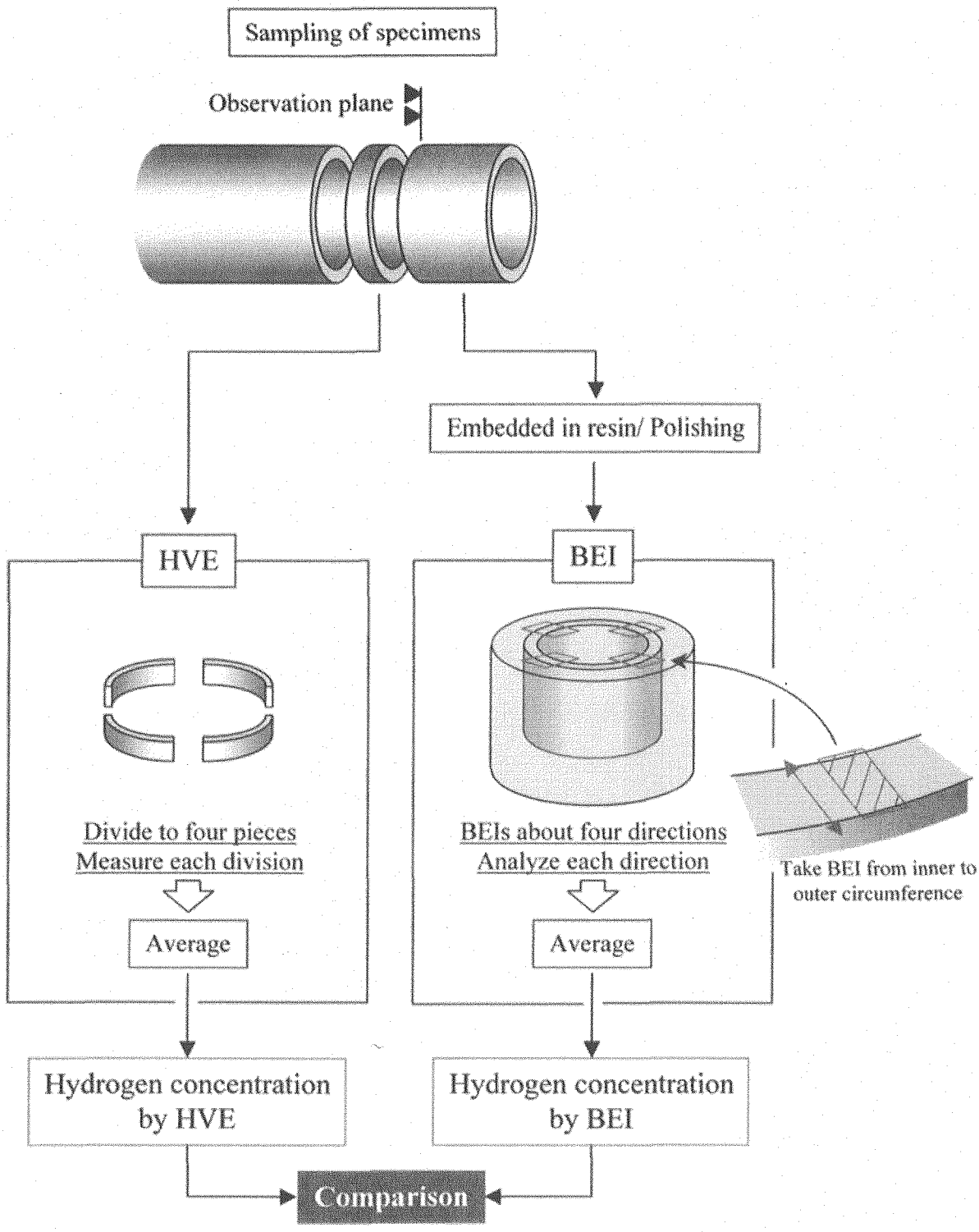

Figure 4 Confirmation test method for improved BEI

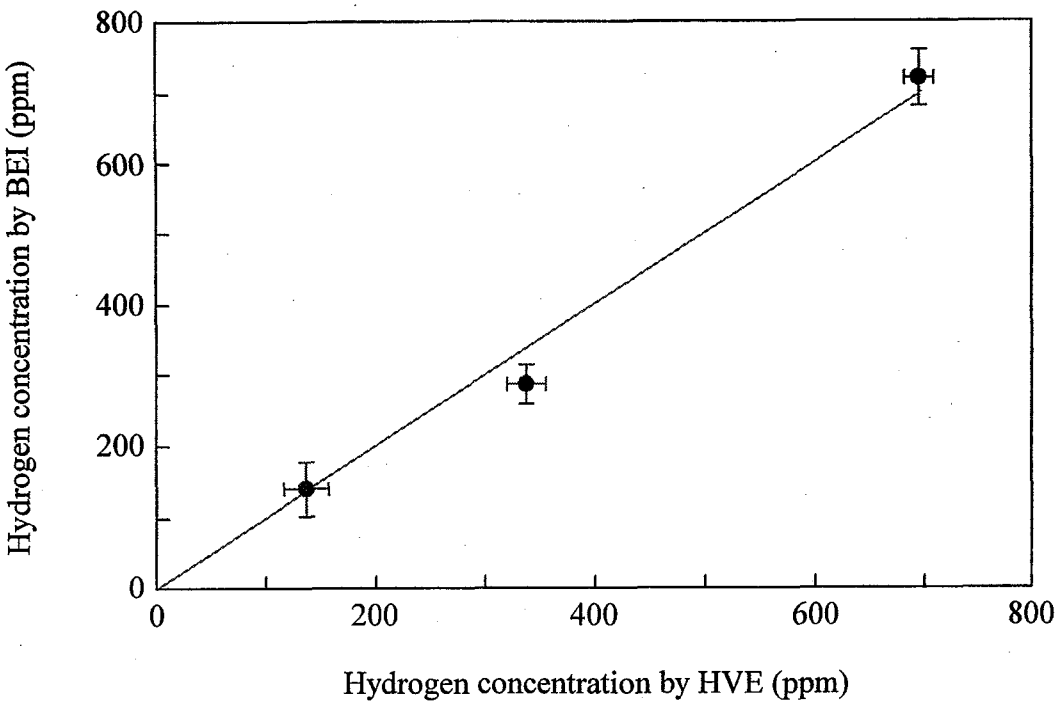

Figure 5 Result of confirmation test

2.13 FRACTURE TOUGHNESS EVALUATION OF FERRITIC STEELS BY MINIATURIZED THREE-POINT BEND SPECIMENS

Hiroaki Kurishita[1], Takuya Yamamoto[2], Takuya Nagasaka[3], Arata Nishimura[3], Takeo Muroga[3] and Shiro Jitsukawa[4]

1: International Research Center for Nuclear Materials Science, IMR, Tohoku University, Oarai, Ibaraki 311-1313, Japan
2: Department of Chemical Engineering, UCSB, Santa Barbara, CA 93106-5080, USA
3: National Institute for Fusion Science, Oroshi, Toki, Gifu-Ken, 509-5292, Japan
4: Radiation Effects and Analyses, Department of Materials Science, Japan Atomic Energy Agency, 2-4 Shirakata, Tokai-Mura, Ibaraki-Ken, 319-1195, Japan

ABSTRACT

From the viewpoint of small specimen test techniques of fracture toughness testing, the three-point bend (3PB) specimens have several advantages over the compact tension (CT) specimens. In order to determine the most effective 3PB specimen geometry for reliable fracture toughness evaluation, elastic-plastic fracture toughness tests by the unloading compliance method at room temperature and plane-strain fracture toughness tests at 77 K were performed for miniaturized 3PB specimens of the Japanese low activation ferritic steels. Effects of specimen size, fatigue pre-cracking and side grooving on the test results were examined. It was found that miniaturized 3PB specimens with dimensions of 3.3 mm in thickness, 5.0 mm in width and 25 mm in length can be used to obtain reliable fracture toughness test results when fatigue pre-cracking and side grooving were appropriately made for the specimens. The obtained values of J_Q at room temperature and K_{IC} at 77 K were approximately 500 kJ/m^2 and 20 MPam$^{1/2}$, respectively.

KEY WORDS: Small Specimen Test Technique, Three-Point Bend Specimen, Elastic-Plastic Fracture Toughness, Plane-Strain Fracture Toughness, Fatigue Precracking, Side Grooving, Two-Parameter Weibull Plot, Low Activation Ferritic Steel

INTRODUCTION

Fracture toughness is a key engineering property of structural materials. The dimensions of the standard size specimens used for fracture toughness testing are as large as 62.5 x 60 x 25 mm for compact tension (CT) and 250 x 50 x 25 mm for 3-point bending (3PB). In order to evaluate the degradation of fracture toughness due to high energy particle irradiations of structural materials, it is necessary to develop small specimen test technologies in fracture toughness testing because of a limited irradiation volume in currently available high flux reactors and future accelerator-based high energy neutron sources such as International Fusion Materials Irradiation Facility, IFMIF [1, 2]. The technology is also required for minimization of the influence of inhomogeneity in flux and temperature distributions during irradiation and the evaluation of fracture toughness for thin wall structures of several millimeters thick, such as the first wall and blanket of fusion reactors.

The previous specimen miniaturization for fracture toughness testing has been mainly concentrated on the CT specimen. This is probably because the load-line displacement can be precisely measured with a clip gage for the CT specimen, but not for the 3PB specimen. However, the 3PB specimen has several advantages over the CT specimen. For instance, the 3PB specimen has a suitable geometry to fully utilize the irradiation volume, easily control test temperatures and coincide with the techniques accumulated so far in miniaturized Charpy impact testing where the specimens with the similar geometry to the miniaturized 3PB specimens have been used. Therefore, it is desirable to develop test techniques for reliable evaluation of fracture toughness using miniaturized 3PB specimens.

In this study miniaturized 3PB specimens with thicknesses 7.0, 5.0 and 3.3 mm of reduced activation ferritic steels were prepared and tested using parameters J and K under the opening mode (Mode I) loading condition. It is shown that miniaturized 3PB specimens with dimensions of 3.3 mm in thickness, 5.0 mm in width and 25 mm in length can be used to obtain reliable fracture toughness test results when fatigue pre-cracking and side grooving are appropriately made for the specimens.

EXPERIMENTAL

Material and specimen

Two kinds of Japanese low activation ferritic steels, JLF-1 [3] and JLF-1-LN (JLF-1 JOYO heats) [4, 5], having the chemical compositions listed in **Table 1** were used. Plates of 30 mm were normalized at 1323 K for 3.6 ks and tempered at 1053 K for 3.6 ks, followed by air cooling and plastic working.

The plates were machined into four types of 3PB specimens shown in **Fig. 1** and **Table 2**. The specimens have two different orientations: a crack extends in parallel or vertical to the

Table 1 Chemical compositions of Japanese low activation ferritic steels, JLF-1 and JLF-1-LN (mass%)

Material	C	Si	Mn	P	S	Cr	W	V	Ta	Ti	B	N
JLF-1	0.10	0.05	0.45	0.003	0.0002	8.85	1.99	0.20	0.080	---	0.0002	0.0231
JLF-1-LN	0.098	0.050	0.50	<0.002	0.0004	8.99	2.00	0.20	0.098	<0.002	0.0001	0.0149

rolling direction, as designated as orientations LT and TL, respectively. A straight-through precrack starter notch terminating in a semi-circle with a radius of 0.06mm and a depth between 0.6 and 3.0 mm depending on specimen width was introduced by spark discharge. For the 3PB specimens with the widths (W) of 10.0 and 5.0 mm, a pair of knife-edges to place a clip gauge was machined on the notched side of each specimen (**Fig. 1(a)**). However, for the 3PB specimens with 3.3 mm in width a clip gauge was seated on an attachable knife-edge cemented to the notched side (**Fig. 1(b)**). Side grooves with depths, 2D, ranging from 0.15B to 0.4B, an angle of 45 degrees and root radius of 0.05 mm were machined to increase the constraint for specimens tested at room temperature because JLF-1 exhibits a high fracture toughness at room temperature [5-7], but not at 77K (D = 0 mm) in most cases.

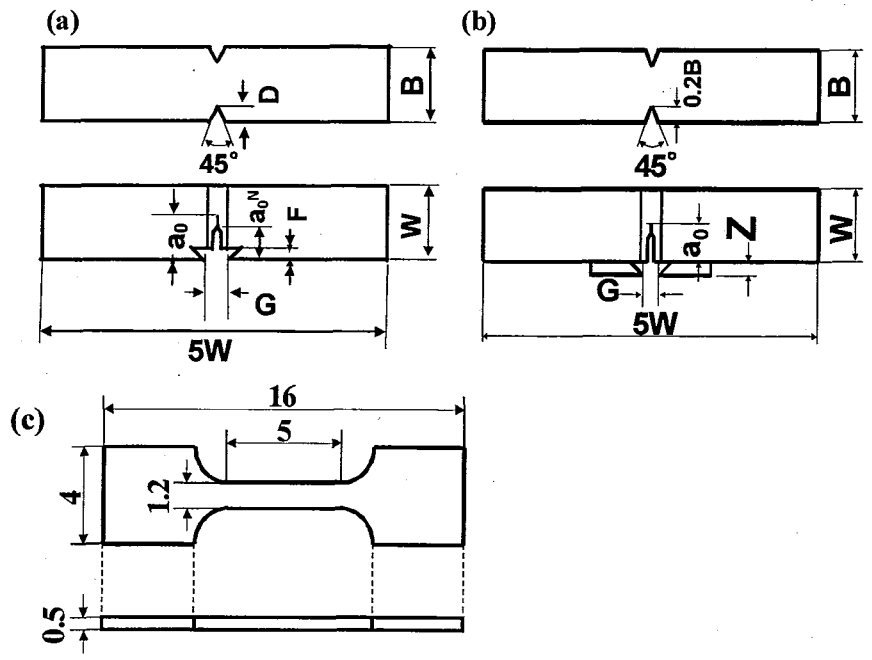

Fig. 1 Configurations of 3PB specimens (a) and (b), and tensile specimen (c). Dimensions in 3PB specimens are shown in table 2.

Table 2 Dimensions of miniaturized 3PB specimens used

Specimen Type	W (mm)	B (mm)	D (mm)	a_0^N (mm)	F (mm)	G (mm)	Z (mm)
1	10.00	7.00	0~1.40	2.50	0.70	2.00	0
2	5.00	5.00	0~1.00	1.20	0.70	2.00	0
3	5.00	3.33	0~0.66	1.20	0.70	2.00	0
4	3.33	3.33	0.66	0.65	0	2.00	1.00

Miniaturized tensile specimens with the orientations LT and TL were also machined. Their geometry and dimensions are shown in **Fig. 1(c)**, the feature being no pin holes to avoid any plastic deformation except the gage section and utilize the two grip regions with approximately 4 mm x 4 mm for material characterization such as hardness measurements and TEM observations after testing. Its shoulder part was hence designed to support the applied load at the curved regions of 1.6R.

Test methods

(1) Fatigue pre-cracking

In order to obtain reliable fracture toughness test results, it is prerequisite to introduce a well-defined fatigue pre-crack for the 3PB specimens. For the introduction one should meet the following requirements.

$$K_{fmax}(3\%) < 0.6(\sigma_{YS1}/\sigma_{YS2})K_Q \quad (1)$$

$$P_f = 0.5Bb_0^2\sigma_Y/S, \quad (2)$$

where $K_{fmax}(3\%)$ is the final 3% of fatigue precrack extension, σ_{YS1} and σ_{YS2} are the 0.2% offset static yield stresses at temperatures where fatigue precracking and fracture toughness testing were conducted, respectively. K_Q is the measured fracture toughness for the specimen and P_f is the applied load during fatigue pre-cracking. B is the specimen thickness and b_0 is the ligament size: $b_0 = W - a_0$, where W is the specimen width and a_0 is the original crack length. σ_Y is the effective yield strength, defined as $\sigma_Y = (\sigma_{YS} + \sigma_{TS})/2$, where σ_{TS} is the ultimate tensile strength and S is the span. Since the value of σ_{YS2} of ferritic steels increases rapidly with decreasing test temperature, the above condition (1) requires very small $K_{fmax}(3\%)$ for specimens used for fracture toughness testing at low temperatures.

In this study, a fatigue testing machine (Shimadzu Servopulser of 50-kN capacity equipped with a 5-kN shear-type load cell) together with 3PB test fixtures with different spans of 40.0, 20.3 and 13.2 mm was used to introduce a well-defined crack. A miniature clip gauge with a working range of 2.0 mm was attached on the 3PB specimen. Fatigue cycling was conducted with a sinusoidal waveform of 20Hz and a ratio of the minimum to maximum fatigue loads of 0.095. The pre-crack extension was estimated by measuring the compliance

Table 3 Typical data of fatigue precracking for miniaturized 3PB specimens tested at 77K for JLF-1 and JLF-1-LN

Material/ Orientation		W (mm)	B (mm)	a_0 (mm)	b_0 (mm)	ΔK_f (MPam$^{1/2}$)	K_{fmax} (MPam$^{1/2}$)	K_{fmax}(3%) (MPam$^{1/2}$)	Cycle Number
JLF-1/LT	1	10.01	7.00	5.57	4.44	5.25	5.82	5.95	828768
JLF-1/LT	2	5.03	4.99	2.92	2.11	5.03	5.58	5.58	555170
JLF-1/LT	3	5.01	3.29	2.77	2.24	5.06	5.65	5.65	599998
JLF-1-/LT	4	3.33	3.32	1.96	1.37	3.95	4.39	4.80	794564
JLF-1-LN/LT	5	5.03	3.32	2.60	2.40	4.73	5.23	5.62	726154
JLF-1-LN/TL	6	5.02	3.31	2.59	2.41	4.63	5.14	5.50	765151

In this study, a fatigue testing machine (Shimadzu Servopulser of 50-kN capacity equipped with a 5-kN shear-type load cell) together with 3PB test fixtures with different spans of 40.0, 20.3 and 13.2 mm was used to introduce a well-defined crack. A miniature clip gauge with a working range of 2.0 mm was attached on the 3PB specimen. Fatigue cycling was conducted with a sinusoidal waveform of 20Hz and a ratio of the minimum to maximum fatigue loads of 0.095. The pre-crack extension was estimated by measuring the compliance of the 3PB specimen with the clip gauge. Once the estimated pre-crack extension reached the aimed value, the fatigue pre-cracking was automatically arrested. For pre-cracking, the stress intensify factor, ΔK, was decreased smoothly to meet the requirements (1) and (2) depending on specimen size, test temperature and notch preparation. The original crack length was controlled between 0.50W and 0.56W and the fatigue precrack length was not less than 1.3 mm. Some typical data on pre-cracking for each type of 3PB specimens are listed in **Table 3**.

(2) Fracture toughness testing

Elastic-plastic fracture toughness tests by the single specimen method at room temperature and plane strain fracture toughness tests at 77 K were conducted in general accordance with the ASTM standards [8, 9] at a cross-head speed of 0.005 mm/s. A program for the unloading compliance method including load frame compliance corrections was used for the 3PB tests. A temperature control bath was designed and a linear variable differential transformer (LVDT) of $\pm$ 2.5 mm was installed on the actuator head for precise measurements of the load-line displacements. The elastic-plastic fracture toughness tested specimens were heat-tinted at 573 K for 1.3 ks and then fractured at 77 K to measure the initial and final crack lengths.

Tensile tests were conducted at room temperature and 77 K at an initial strain rate of 1 x 10^{-3} $s^{-1}$by the above testing machine.

RESULTS AND DISCUSSION

Elastic plastic fracture toughness test results at room temperature

At first, for the largest pre-cracked 3PB specimens (type 1 in **Table 2**) without side groove of JLF-1, elastic-plastic fracture toughness tests by the unloading compliance method were performed at room temperature. As a result, an increase in applied load did not cause any changes in compliance, or no extension of pre-crack, even when the crack opening displacement (COD) reached 2.0 mm that is the maximum measurable by the present miniature clip gauge. Optical observations on the specimen surfaces showed the occurrence of severe branching of pre-crack tips due to severe plastic deformation around the crack tip. This result shows that JLF-1 is a very tough material. Therefore, side grooving was made to increase plastic constraint ahead of the pre-crack tips for the thinnest 3PB specimens (type 3: B = 3.3 mm, W = 5.0 mm) because crack extension becomes difficult as the specimen thickness decreases. For side-grooved specimens with a depth (2D) ranging from 0.15B to 0.4B the crack extension behavior was examined as a function of 2D. An example of the results obtained for the LT orientation of JLF-1-NL is shown in **Figs. 2** and **3**. As 2D increases, the crack extension increases. For 2D = 0.15B and 0.25B which met the ASTM standards recommendation [5], the pre-crack clearly extends. However, appreciable plastic deformation is observed around the crack tips, indicating that plastic constraint caused by 2D = 0.15B and 0.25B is not sufficient. For 2D = 0.30B and 0.40B plastic deformation around the crack tips is much less. In addition, only J integral versus crack extension curves (J - Δa) for 2D = 0.30B and 0.40B satisfied the conditions that the curves intersect with the line of Δa = 2.0 mm and there are 5 and more data points above the line to estimate J_Q. The estimated J_Q values for 2D = 0.30B and those for 2D = 0.40B were almost the same and their difference was in the range of data scattering. Therefore, the value of 2D adopted as side groove depth in this study was 0.30B for JLF-1-NL and 0.40B for JLF-1.

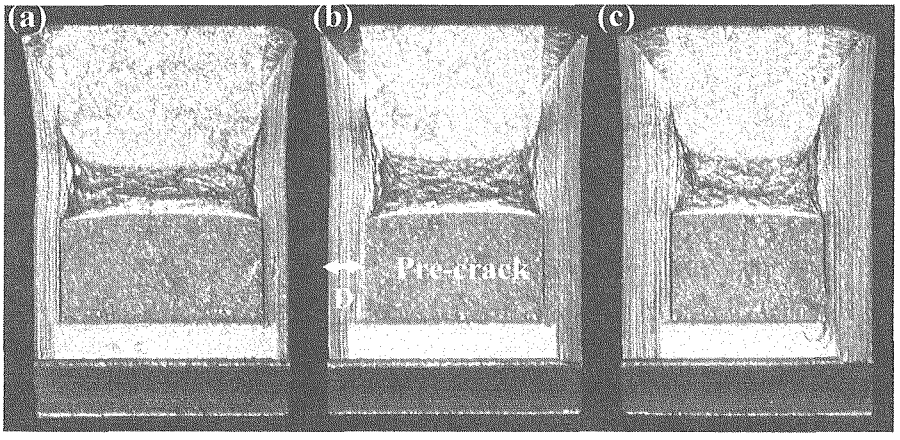

Fig. 2 Fracture surfaces for 3PB specimens (type 3: W = 5.0 mm, B = 3.3 mm) with different depths of side groove.
(a) 2D = 0.20B, (b) 2D = 0.30B, (c) 2D = 0.40B.

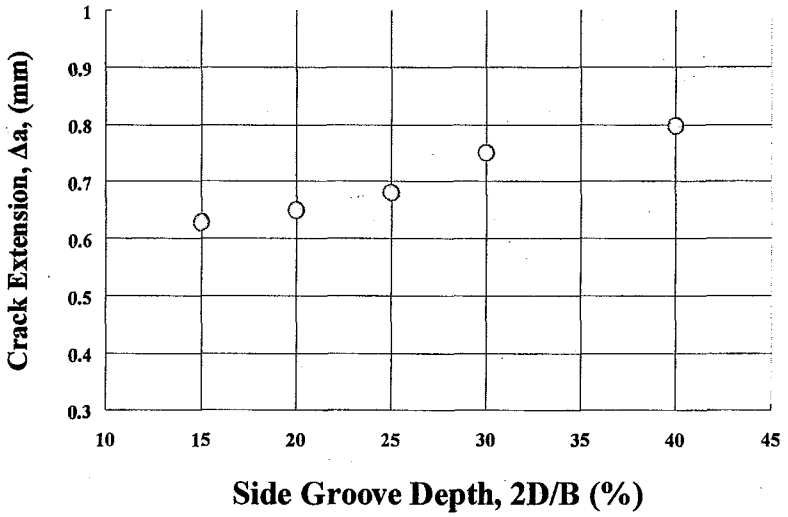

Fig. 3 Crack extension in 3PB specimens (W = 5.0 mm, B = 3.3 mm) as a function of relative side groove depth, 2D/B, for crack opening displacement of 2.0 mm.

Fig. 4 shows typical examples of load versus load line displacement records, J - Δa curves and a fracture surface to determine crack extension for the thinnest specimens of JLF-1-NL (W = 5.0 mm, B = 3.3 mm, 2D = 0.30B). The J_Q values at room temperature for both the LT and TL orientations of JLF-1-LN determined according to the ASTM standards are listed in **Table 4**. In the table B_N is the net specimen thickness, i.e., $B_N = B - 2D$. Since the purpose of this study is to show the reliability of facture toughness values obtained by the miniaturized 3PB specimens, 6 ~ 8 pieces of the specimens of the LT and TL orientations were tested. It is seen from the table that the value of J_Q for LT is in the range of 483~518 kJ/m^2 with an average of 495 kJ/m^2 and that for TL is 469~525 kJ/m^2 with an average of 503 kJ/m^2. No significant data scattering is observed. In order to make reliability analysis, the J_Q values were assumed to obey a two-parameter Weibull distribution. The Weibull distribution functions for the LT and TL orientations are given as

$$F(J_Q) = 1 - \exp\{-(J_Q/495)^{52}\} \quad (3)$$

$$F(J_Q) = 1 - \exp\{-(J_Q/507)^{24}\} \quad (4)$$

respectively. These results may indicate that data variability for both the LT and TL orientations are small and the reliability of the measured J_Q values is high.

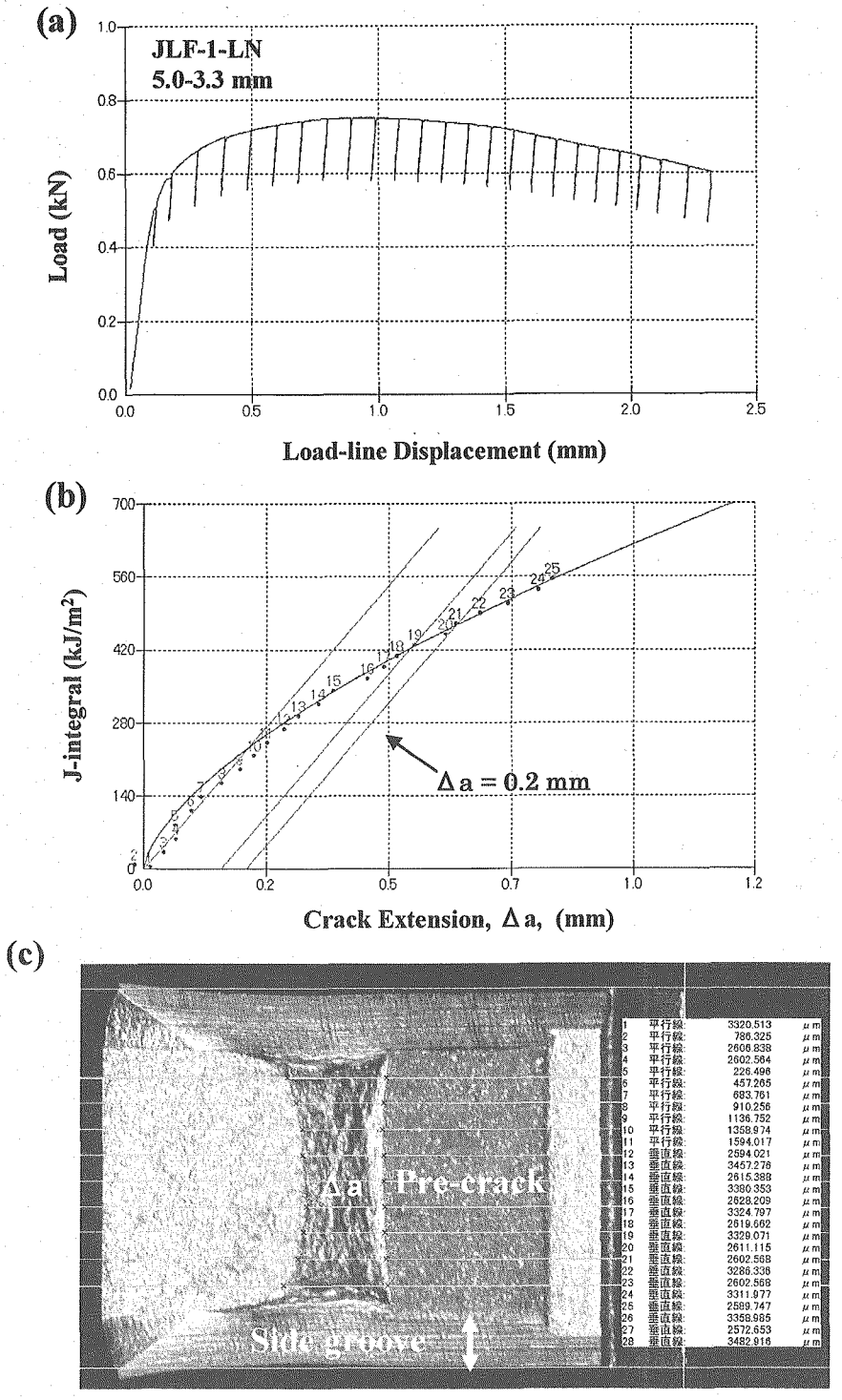

Fig. 4 Records of elastic plastic fracture toughness tests at room temperature for 3PB specimens (W = 5.0 mm, B = 3.3 mm, 2D = 0.30B) of JLF-1-LN.
(a) Load versus load-line displacement curve, (b) J-Δa curve and (c) fracture surface and crack extension measurements.

Table 4 Elastic plastic fracture toughness test results at room temperature for 3PB specimens (W = 5.0 mm, B = 3.3 mm, 2D = 0.30B) with the LT and TL orientations of JLF-1-LN

Orientation-Specimen	W (mm)	B (mm)	B_N (mm)	a_0 (mm)	$a_0 + \Delta a$ (mm)	J_Q (kJ/m^2)
LT-1	5.03	3.32	2.32	2.71	3.43	518
LT-2	5.02	3.33	2.33	2.66	3.41	488
LT-3	5.02	3.32	2.32	2.67	3.45	483
LT-4	5.03	3.32	2.32	2.66	3.42	491
LT-5	5.03	3.31	2.31	2.68	3.47	486
LT-6	5.01	3.32	2.32	2.67	3.42	494
LT-7	5.02	3.32	2.32	2.64	3.39	504
LT-8	5.02	3.31	2.32	2.64	3.41	495
TL-1	5.02	3.30	2.30	2.66	3.42	481
TL-2	5.01	3.30	2.30	2.65	3.40	523
TL-3	5.02	3.32	2.32	2.64	3.43	469
TL-4	5.02	3.30	2.30	2.64	3.39	515
TL-5	5.02	3.30	2.30	2.73	3.50	504
TL-6	5.02	3.32	2.32	2.65	3.40	525

Plane strain fracture toughness test results at 77K

Plane strain fracture toughness test results at 77K showed that the thinnest 3PB specimens without side groove fractured in the elastic range in a brittle manner. Therefore, 3PB specimens without side groove were used for plane strain fracture toughness tests at 77K. For appropriate fatigue pre-cracking the above equations (1) and (2) are for the standard sized specimens, and it is necessary to examine whether or not these equations are still valid for the miniaturized pre-cracked specimens. At first, effects of the $K_{fmax}(3\%)$ values in fatigue pre-cracking on the plane strain fracture toughness test results at 77K were examined for the thinnest 3PB specimens of JLF-1-LN with $K_{fmax}(3\%)$ values in the range of 5 ~14. The results are shown in **Fig. 5.** The values of K_Q decrease with decreasing $K_{fmax}(3\%)$ and tend to saturate a constant value when $K_{fmax}(3\%)$ is 7 or less. Therefore, plane strain fracture toughness tests at 77K were performed for 3PB specimens with $K_{fmax}(3\%)$ of 7 or less. In addition, most of the pre-crack fronts of the tested specimens without side groove are appreciably bent and the difference between the maximum and minimum pre-crack extension was not small enough to satisfy the ASTM standards. Therefore, either of the side surface layers of 3PB specimens was mechanically polished until the difference satisfies the ASTM standards (**Fig. 6**). The test results for the LT and TL orientations of JLF-1 are listed in **Table 5.** The K_Q values determined according to the ASTM standards are in the range of 19.1~22.6 MPam$^{1/2}$ with an average of 20.9 MPam$^{1/2}$ for LT and 19.2~22.8 MPam$^{1/2}$ with an average of

21.6 $MPam^{1/2}$ for TL. As shown later, all of the K_Q values were qualified as K_{IC}. The Weibull distribution functions for the LT and TL orientations are given as

$$F(K_{IC}) = 1 - \exp\{-K_{IC}/21.5)^{15.0}\} \quad (5)$$

$$F(K_{IC}) = 1 - \exp\{-(K_{IC}/21.8)^{21.0}\} \quad (6)$$

respectively. The results indicate that the reliability of measured K_{IC} values is high.

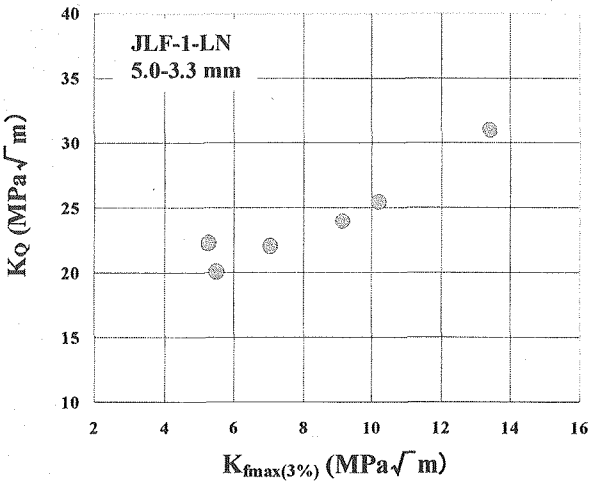

Fig. 5 Effects of $K_{fmax(3\%)}$ in precracking on K_Q values measured at 77K for J LF-1-LN.

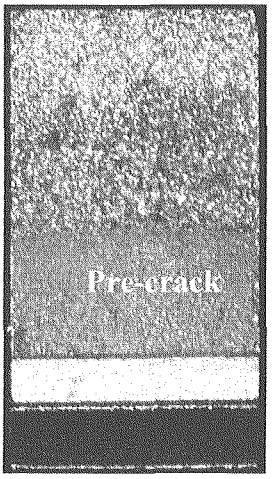

Fig. 6 Fracture surface at 77K.

Table 5 Plane strain fracture toughness test results at 77K for 3PB specimens (W = 5.0 mm, B = 3.3 mm, 2D = 0.30B) with LT and TL orientations of JLF-1-LN

Orientation-Specimen	W (mm)	B (mm)	a_0 (mm)	$K_{fmax(3\%)}$ ($MPam^{1/2}$)	P_Q (kN)	$K_Q = K_{IC}$ ($MPam^{1/2}$)
LT-9	5.03	3.32	2.72	5.64	0.417	21.7
LT-10	5.03	3.32	2.58	5.28	0.477	22.3
LT-11	5.02	3.32	2.55	5.79	0.463	21.2
LT-12	5.02	3.32	2.58	5.38	0.473	22.6
LT-13	5.03	3.32	2.59	5.62	0.398	19.1
LT-14	5.02	3.31	2.57	5.79	0.417	19.9
LT-15	5.03	3.33	2.57	5.44	0.425	20.0
LT-16	5.02	3.04	2.62	5.50	0.374	20.1
TL-8	5.02	3.30	2.56	5.84	0.448	21.3
TL-9	5.02	3.31	2.56	5.49	0.463	21.9
TL-10	5.02	3.32	2.58	5.51	0.446	21.2
TL-11	5.01	2.96	2.63	5.51	0.344	19.2
TL-12	5.02	3.31	2.56	5.41	0.475	22.6
TL-13	5.02	2.72	2.58	5.63	0.390	22.8
TL-14	5.02	2.72	2.64	5.84	0.369	22.4

Table 6 shows fracture toughness values at 77K for differently sized 3PB specimens including the averages for LT and TL in **Table 5**. The measured K_Q values were examined to be consistent with the size and yield strength requirements in K_{IC}: B, $b_0 > 2.5(K_Q/\sigma_{YS})^2$. The tensile test results are listed in **Table 7**. Since all of the measured values satisfied the requirements and the pre-crack front was flat, the measured fracture toughness values were judged to be K_{IC}. The values of K_{IC} lie in the range of 20-22 $MPam^{1/2}$ regardless of specimen size. It should be noted that the results showed that the plane strain fracture toughness can be estimated from the present miniaturized 3PB specimens with several millimeter thickness.

Table 6 Plane strain fracture toughness test results (average) at 77K for differently miniaturized 3PB specimens of JLF-1 and JLF-1-LN

Material/ Orientation	W (mm)	B (mm)	P_Q (kN)	$K_Q = K_{IC}$ ($MPam^{1/2}$)	$0.6(\sigma_{YS1}/\sigma_{YS2})K_Q$ ($MPam^{1/2}$)	$2.5(K_{IC}/\sigma_{YS})^2$ (mm)	B, $b_0 > 2.5(K_{IC}/\sigma_{YS})^2$
JLF-1/LT	10.01	7.00	1.14	21.0	6.01	1.00	○
JLF-1/LT	5.03	5.01	0.51	20.1	5.74	0.91	○
JLF-1/LT	5.01	3.31	0.42	22.4	6.40	1.13	○
JLF-1-/LT	3.32	3.31	0.28	20.6	5.89	0.96	○
JLF-1-LN/LT	5.03	3.32	0.44	20.9	6.34	0.95	○
JLF-1-LN/TL	5.02	3.31	0.46	21.6	6.53	1.03	○

Table 7 Tensile test results at room temperature and 77K for LT and TL orientations of JLF-1 and JLF-1-LN. ε_U is the uniform elongation and ε_T is the total elongation.

Material/ Orientation	Test Temp. (K)	Strain Rate (s^{-1})	σ_{YS} (MPa)	σ_U (MPa)	σ_Y (MPa)	ε_U (%)	ε_T (%)
JLF-1/LT	298	1×10^{-3}	476	623	550	7.97	18.8
JLF-1-/LT	77	1×10^{-3}	1052	1111	1082	4.70	4.70
JLF-1-LN/LT	291	1×10^{-3}	487	599	543	7.76	19.5
JLF-1-LN/LT	77	1×10^{-3}	1061	1085	1074	4.34	4.34
JLF-1-LN/TL	292	1×10^{-3}	470	598	535	7.95	19.0
JLF-1-LN/TL	77	1×10^{-3}	1050	1075	1062	2.72	2.72

CONCLUSIONS

1) Miniaturized 3PB specimens with dimensions of 3.3 mm in thickness, 5.0 mm in width and 25 mm in length can be used to obtain reliable results on both elastic-plastic fracture toughness tests at room temperature and plane-strain fracture toughness tests at 77 K for the Japanese low activation ferritic steels, JLF-1 and JLF-1-LN-1. For the test at room temperature, side grooves with depths of 0.30B~0.40B (B is the specimen thickness) are required to increase the constraint.
2) The elastic plastic fracture toughness values, J_Q, for the LT orientation are in the range of 483～518 kJ/m^2 with an average of 495 kJ/m^2 and those for the TL orientation are 469～525 kJ/m^2 with an average of 503 kJ/m^2. The two-parameter Weibull distribution functions for the LT and TL orientations are given as

$$F(J_Q) = 1 - \exp\{-(J_Q/495)^{52}\} \quad \text{(LT)}$$
$$F(J_Q) = 1 - \exp\{-(J_Q/507)^{24}\} \quad \text{(TL)}$$

3) The plane strain fracture toughness values, K_{IC}, are estimated from miniaturized 3PB specimens with thicknesses of 7.0, 5.0 and 3.3 mm. The values of K_{IC} are 20-22 MPam$^{1/2}$ regardless of specimen size. The two-parameter Weibull distribution functions for K_{IC} of the LT and TL orientations are given as

$$F(K_{IC}) = 1 - \exp\{-K_{IC}/21.5)^{15.0}\} \quad \text{(LT)}$$
$$F(K_{IC}) = 1 - \exp\{-(K_{IC}/21.8)^{21.0}\} \quad \text{(TL)}$$

ACKNOWLEDGEMENTS

The authors would like to express their gratitude to Drs. A. Kimura and R. Kasada for their supply of JLF-1 and JLF-1-LN plates, to Dr. H. Suwarno for his experimental assistance to a part of this work and to Dr. S. Matsuo for his review. The present work was performed as the activity of International Fusion Materials Irradiation Facility Key Element Technology Phase (KEP) supported by National Institute for Fusion Science in Japan, which is greatly appreciated.

REFERENCES

(1) T.Kondo: IFMIF, Its Facility Concept and Technology: J. Nucl. Mater. **258-263**(1998) 47-55.
(2) K.Noda, K.Ehrlich, S.Jitsukawa, A.Moslang and S.Zinkle: J. Nucl. Mater. **258-263** (1998) 97-105.
(3) A.Kohyama, Y.Kohno, K.Asakura and H.Kayano: J. Nucl. Mater. **212-215**(1994) 684-689.

(4) R. Kasada, H. Ono, H. Sakasegawa, T. Hirose, A. Kimura and A. Kohyama, Fus. Sci. Technol., **44** (2003) 145.
(5) H. Ono, R. Kasada and A. Kimura, J. Nucl. Mater. **329-333** (2004) 1117-1121.
(6) A.Nishimura, N.Inoue and T.Muroga: J.Nucl. Mater. **258-263** (1998) 1242-1247.
(7) H. Kurishita, T. Yamamoto, T. Nagasaka, A. Nishimura, T. Muroga and S. Jitsukawa: Mater. Trans., **45** (2004) 936-941.
(8) ASTM E1820-99a, Standard Test Method for Measurement of Fracture Toughness, Annual Book of ASTM Standards, (2000).
(9) ASTM E399-90, Standard Test Method for Plane-Strain Fracture Toughness of Metallic Materials, Annual Book of ASTM Standards, (1990).

2.14 DEVELOPMENT OF A REMOTE-CONTROLLED MAGNETIC FLUX LEAKAGE MEASUREMENT APPARATUS

Y.Nagae, S.Takaya and K.Aoto

Advanced Material Technology Group, Advanced Nuclear System Research and Development Directorate, Japan Atomic Energy Agency
4002 Narita-cho, Oarai-machi, Higashi-Ibaraki-gun, Ibaraki-ken, 311-1393 JAPAN

T.Yoshitake, Y.Abe, T.Hoshiya, Y.Shigeto* and Y.Nakamura

Materials Monitoring Section, Fuels and Materials Department
O-arai Research and Development Center, Japan Atomic Energy Agency
*Inspection Development Co.Ltd
4002 Narita-cho, Oarai-machi, Higashi-Ibaraki-gun, Ibaraki-ken, 311-1393 JAPAN

ABSTRACT

We have recently started investigating that the magnetic property changes in irradiated austenitic stainless steel, to evaluate the aging and degradation of structural materials. A measurement apparatus had been installed in hot cell of Material Monitoring Section (MMS) in Oarai Engineering Center. We will mainly introduce the magnetic measurement apparatus.

KEYWORDS: Magnetic Property, Flux-Gate Sensor, Leakage Magnetic Flux Density, Austenitic Stainless Steel, Degradation, Radiation

INTRODUCTION

Austenitic stainless steels are the main structural materials for the components in fission and fusion reactor. In Fast Breeder Reactor (FBR) plants, these materials consist of structural components such as several kinds of primary and secondary coolant tubes.

Specially, in these radiation environments, how to control and suppress the aging and degradation phenomena of structural materials is the key issue governing the integrity of structural component over 60 years during operation. The changes of tensile and creep properties are related to the degradation in the structural materials. When the material is heavily irradiated, the tensile elongation or creep strength decreases [1-2]. The changes can be due to the radiation defects such as Frank loops.

On the other hand, the issue of irradiation assisted stress corrosion cracking (IASCC) is the major concern on the irradiation degradation phenomena in Light Water Reactor (LWR) plants. Major element effects on SCC susceptibility have already been discussed [3-4]. The occurrence of the degradation in both circumstances can be explained by changes in characteristics.

It is important to estimate the degradation in both reactors. These microstructure changes lead to physical and chemical property change. Therefore it is possible to evaluate the change of microstructure using physical and chemical property nondestructively.

We have concentrated on the physical (magnetic property) phenomena to evaluate the degradation. We will show you the measurement apparatus of magnetic property in hot cell of MMS.

REMOTE-CONTROLLED MAGNETIC MEASUREMENT APPARATUS

A schematic drawing of the remote-controlled magnetic measurement system installed in the hot cell of MMS is shown in **Fig. 1**. The apparatus had been invented to operate easily even in remote field.

MAGNETIC SENSORS USED IN THE APPARATUS

There are several types of magnetic sensor. Major three sensors will be shown in this paper. First one is the Hall sensor, second one is Flux-Gate sensor and last one is Superconducting Quantum Inference Device (SQUID) sensor. The measurement range of magnetic field is shown in **Fig. 2**.

Hall sensor is typical magnetic sensor and utilizes Hall-effect. The measurement range is usually over about 0.5T, which the magnetism of the earth is about 0.5T. Hall sensor with high sensitivity has recently developed. SQUID sensor has higher sensitivity than that of other sensors, but the measurement range is limited. Moreover coolant system of liquid He is necessary for SQUID sensor. We had chosen the Flux-Gate sensor, because of the wide range of magnetic field.

Three Flux-Gate sensors, which each sensor is made in different companies, are equipped

in the system as shown in **Fig 3**. The sensitivity, measurement range and sensor size are different as shown in **Table 1**. The sensor made by Simazu Co. Ltd. [5] (Simazu sensor) highest sensitivity in three sensors, but the maximum magnetic field is 1 Gauss. Though the sensor made by Sumitomo Co. Ltd. [6] (Sumitomo sensor) has lower sensitivity than that of Simazu sensor, the measurement range is wider and about 3 Gauss. The sensor made by MTI is lowest sensitivity. We can measure the magnetic property with wide range magnetic field using these three types of Flux-Gate sensors.

AN EXAMPLE of MAGNETIC MEASUREMENT RESULTS IN IRRADIATED TYPE 304 STAINLESS STEEL

We will show n example of measurement results in **Fig. 4**. Chemical composition in Type 304 stainless steel is shown in **Table 2**. Left graph is for as-received material and right one is for crept specimen after irradiation. Irradiation condition and creep condition is shown in **Table 3**. After magnetization by 0.3T, the magnetic property was measured using Sumitomo sensor. The leakage magnetic flux density of crept material after irradiation is higher than that of as-received material. We checked the operation of the apparatus and confirmed that the results with high resolution were obtained.

SUMMARY

In order to obtain magnetic property data of irradiated materials for the nuclear reactor, we had installed the magnetic leakage flux measurement apparatus in hot cell of MMS. We checked the operation of the apparatus and tried to measure the leakage magnetic flux density. We confirm that the measurement data with high resolution will be obtained for the irradiated materials.

REFERENCES

(1) N. Miyaji, Y. Abe, S. Ukai and S. Onose: Post-irradiation creep rupture properties of FBR grade 316SS structural material, J. Nucl. Mater., Vol.271&272, (1999) p.173.
(2) K. Aoto, Y.Abe, I.Shibahara and Y. Wada: Effect of neutron irradiation on creep properties of FBR grade 316 stainless steel, IAEA-TECDOC-817, (1993) 27.
(3) T. Tsukada, JAERI-Research, 98-007 (1998).
(4) S. M. Breummer, E. P. Simonen, Corrosion, 50, (1994), p.940.
(5) T.Munaka, K.Yoshimi, H.Nakanishi and Y.Yamada, Simazu Hyoron, 53, (1996), 75. (in Japanese)

(6) M.Kawakami and T.Hazama, Sumitomo Tokusyu Kinzoku Technology Report, 14, (2003), 109. (in Japanese)

Table 1 Comparison of Flux-Gate magnetic sensors

	Sumitomo sensor	Simazu sensor	MTI sensor
size	1.0*0.3*0.9mm	3.0*1.0*15mm	7ϕ*24mm
resolution	0.5μm	50nT	10nT
range	-3G-+3G	-1G-+1G	-10G-+10G

Table 2 Chemical composition of material used in this test. (wt%)

C	Si	Mn	P	S	Cr	Ni	Mo	Ti	Al	N	Co	Fe
0.04	0.54	0.77	0.021	0.002	18.4	9.0	0.10	0.01	<0.01	0.04	0.05	Bal.

Table 3 Irradiation and creep conditions of magnetic measurement specimen

T.P. No.	Irradiation conditions					Creep conditions			Ruptured/ Interrupted
	Irrad. Temp. (K)	Fluence (n/m^2)		Dose (dpa)	He content (appm)	Temp. (K)	Stress (MPa)	Testing time (hr)	
		E>0.1MeV	E<0.4MeV						
H9T0BX	810	6.0×10^{26}	1.3×10^{22}	37.5	23	823	187	562	Ruptured

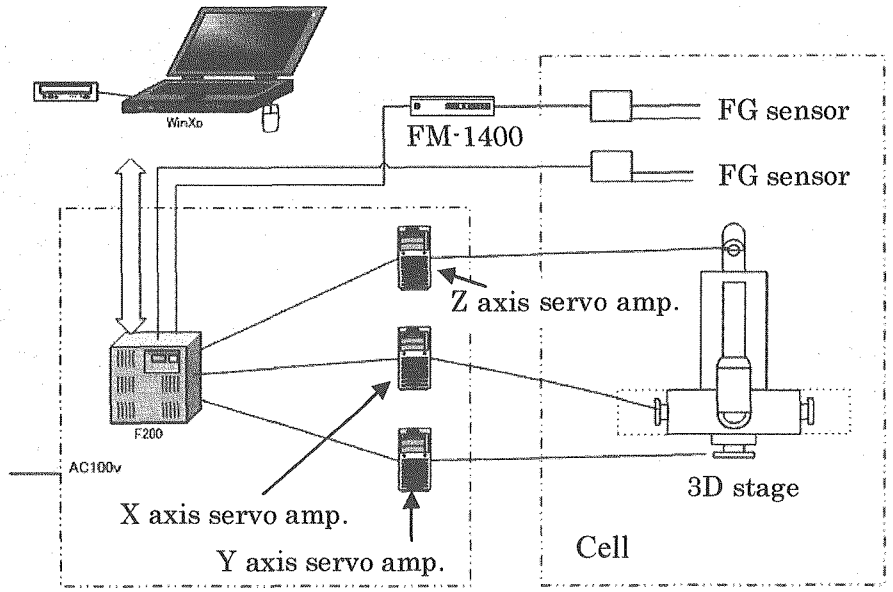

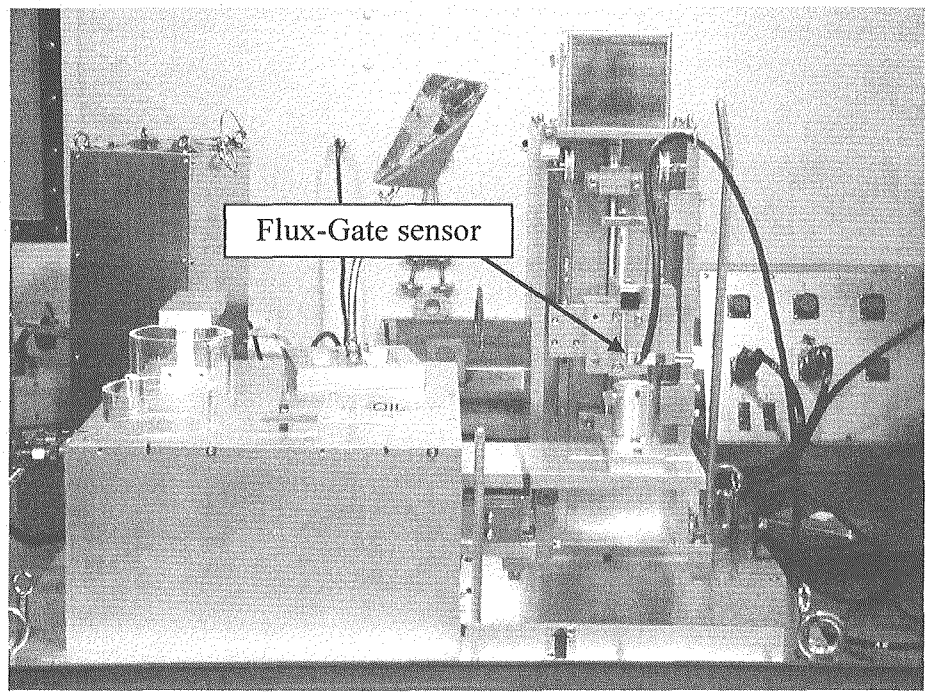

Fig. 1 Schematic drawing of the remote-controlled magnetic measurement apparatus.

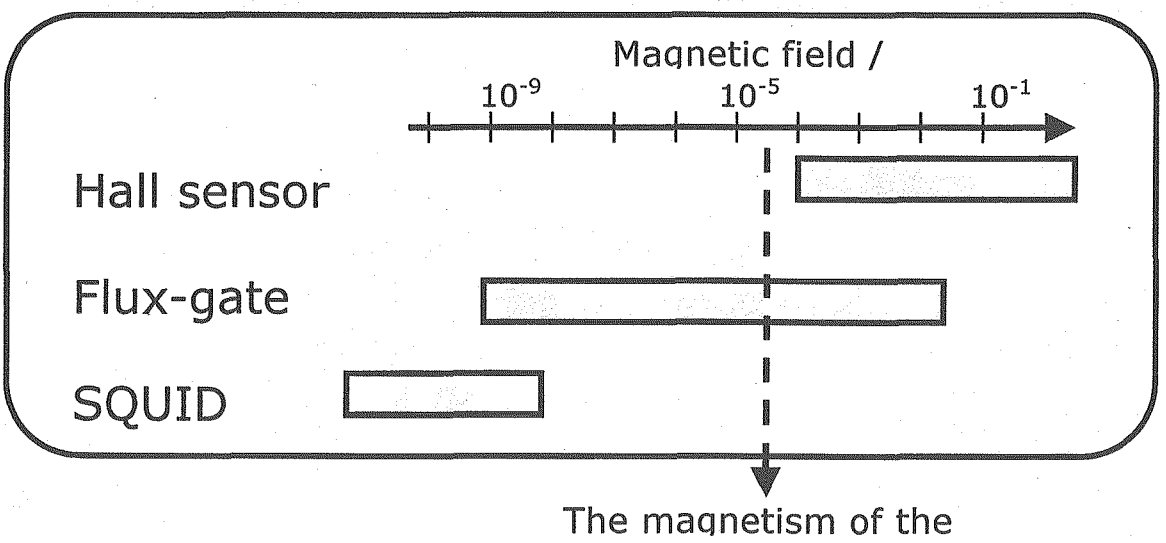

Fig. 2 Measurement range in each magnetic sensor.

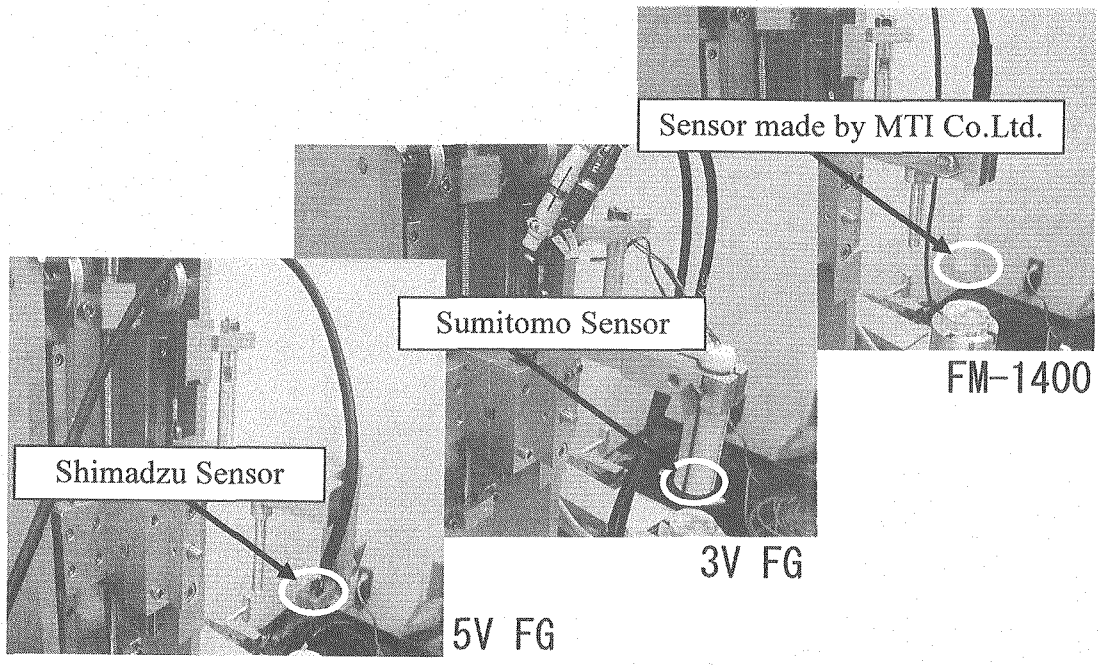

Fig. 3 Three types of Flux-Gate magnetic sensors used in the apparatus.

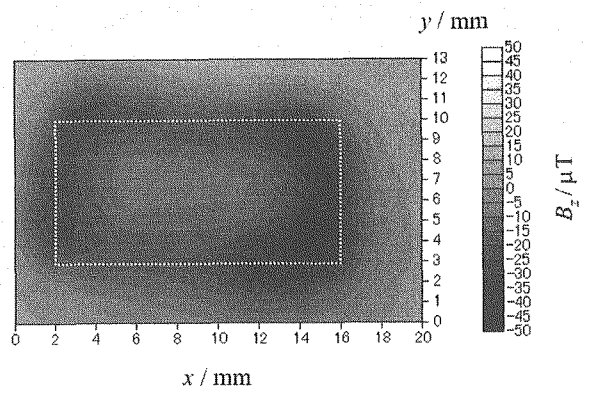

(a) As-received sample

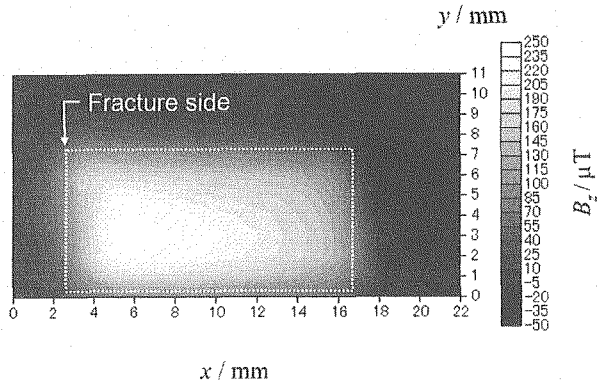

(b) Sample subjected to a creep test after irradiated

Fig. 4 An example of magnetic measurement results.

2.15 DEVELOPMENT OF SGS FOR VARIOUS WASTE DRUMS

Ki-Hong Kim, Young-Gerl Ryu, Kyung-Kil Kwak and Yong-Young Ji

Korea Atomic Energy Research Institute,
150 Duckjin-dong, Yusong-gu, Taejon, 305-600, Korea

ABSTRACT

Radioactive waste assay system was manufactured to measure the individual nuclides' activity in homogeneous and non-homogeneous waste drums and to exclude worker's exposure. After measuring the activities of all individual γ-emitters, our system was programmed to calculate the activities of α, β emitters, automatically and then calculated total activities of drum by utilizing scaling factor(relationship between α, β emitters and Co-60, Cs-137).

In general, SGS(Segmented gamma Scanning system) divided a waste drum into 8 segments vertically, and also 8 sectors in one segment to minimize the error. And SGS can be determined the density of drum by using the several matrix correction methods such as transmission ratio, differential peak absorption and mean density correction, individually or by combination.

However, from the NPPs and other nuclear facilities, various drum (100 ~ 350L) could be generated. To analyze the activities of γ-emitters from various drums, we modified the collimator(horizontal and vertical) and added detector mover to the existing SGS system.

As a results, the measurement error was < 12 % in a short distance(10 segments, Co-60; 47.87μ Ci and Cs-137; 101.16μCi) and was < 25 % in a long distance(8 segments, same sources).

This system can be applied to the drum which TGS system does not analyze drum(for example, high density, high activities and large volume).

KEYWORDS : Waste acceptance criteria, Waste Inventory, Segmented Gamma Scanning, Collimator, Density Correction

INTRODUCTION

To dispose the waste drums, the waste form's integrity and the nuclides' inventories must be assured according to the national and site waste acceptance criteria. Because they might be would gravely affected the performance objectives of disposal site. Our national regulation for the waste inventory related to "Radioactive Waste Acceptance Criteria" requires that the activities of 13

nuclides and gross α must be measured and the 95 % of nuclides incorporated in the drum must be identified.

It is very difficult to measure the radioactivity with accuracy from waste drum, so have a large error. In general the accuracy of TGS (Tomographic Gamma Scanning System) is known below 20 % and that of SGS is below 30 %. The accuracy of TGS is better than that of SGS. But it is sure that TGS has no economic benefit because of the high expensive, the difficult operation, limits in a certain drum (high density, high level) and a long time of measurement.

Therefore to overcome the measurement error and to cover the disadvantage of TGS, we modified the existing SGS system such as an easy control of the distance between detector and drum (possible to change the number of segments of drum) and make the attenuation file similar to the real drum (chemical composition, ratio of waste and matrix, etc.).

The assay system of a radioactive waste drum is complex. To know the individual and total activities in a drum, some technologies (development of system operation program, manufacture of a model drums, communication and interface among various devices, raw waste sampling in situ and radiochemistry, determination of scaling factor, database tool, and so on.) are necessary.

Therefore, we have studied and developed various fields as following bellows;

1) Development of non-destructive assay technique to measure the specific activity from waste drum incorporated various wastes

2) Design of model drum to evaluate the performance of our SGS system

3) Development of the integrated control program and communication protocol for radioactive waste assay system

4) Establishment on the normal and abnormal operation guide of radioactive waste assay system

5) Optimization of the operating condition of SGS system by using a model drum and a standard gamma source

6) Manufacture of marking system on the drum surface of the result

7) Development of the radioactive waste sampling technique and device

8) Development of chemical analysis technique for radioactive wastes

9) Development of scaling factor determination program.

But the objectives of this study are to measure the activities in homogeneous and non-homogeneous radioactive materials by non-destructive method.

This method was explained, clearly and in detail in Ref. 1.

In shortly, Fo and Fx are proportional to the squared distances,

$$\frac{F_o}{F_x} = \frac{S_o^{\,2}}{(S_o + x)^2}$$

The net count rate with an activity Ao at the distance So is,

$$Z_o = \frac{K}{4\pi S_o^{\,2}} Ao$$

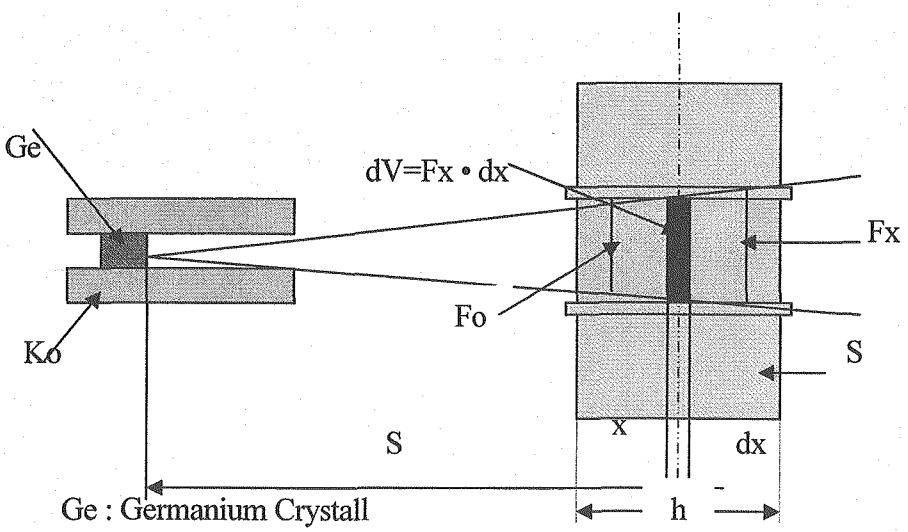

Ge : Germanium Crystall
Ko : Collimator Shielding
S : Radiation Source

Fig. 1 Schematic diagram for the measurement of activity from drum.

The count rate in the dV at a distance (So + x) is,

$$dZ = Fx = \frac{Ke^{-\mu x}}{4\pi(S_o + x)^2} C_A dV$$

Where, CA : the active concentration

μ : the linear attenuation coefficient

And thus,

$$dV = F_x dx = \frac{(S_o + x)^2}{So^2} F_o dx$$

Finally by integration over the depth of the source x, we can get the following equation,

$$Z = \frac{Z_o F_o C_A K_1}{A_o \mu}$$

$K_1 = 1 - e^{-\mu h} \approx 1$ for a large volume

Zo, Fo, Ao : constant(calibration data of the detector system)

Thus if Z is measured, C_A can be calculated.
And also we can get the μ by matrix correction method.

The matrix correction used in this study is given in **Table 1**.

Table 1 Various matrix correction methods

Waste Type	Correction method
	$\varepsilon_c = CF_i \varepsilon_i$ $CF_i = e^{-\mu_i(\rho t)}$ εc : the uncorrected efficiency at energy Ei εi : the corrected efficiency at energy Ei CFi : the correction factor at energy Ei
Homogeneous Drum	1. Average Mean Density Attenuation Correction 2. Transmission Source Correction 3. Differential Peak Attenuation Correction 4. Combined Efficiency Attenuation Correction
Non Homogeneous Drum	1. Non Uniformity Correction Software(NUCS)

EXPERIMENT AND RESULTS

Existing results[2]

Determination of mass attenuation coefficient

To calculate correction factor (CF), we must know the mass attenuation coefficient (μ, cm^2/g) and the calculated sample mass per unit area (g/cm^2). The calculated sample mass per unit area is obtained by three method (**Table 1**). The mass attenuation coefficient depends on the material composition according to the type of waste and the solidification matrix. The mass attenuation coefficient affects small to calculate matrix correction factor.

Thus as shown in **Table 2**, the computer file (mass attenuation file) was prepared according to th e similar materials by considering the main components in waste drums.

Drum Rotation

To minimize the error and to calculate activity emitting from all of surface, drum must be rotated (**Fig. 1**). In addition, to know how much the drum rotation speed affects the measuring result. 8, 9, 10, 11 and 12 rpm are selected as a rotation speed.

As shown in **Table 3**, the 10 rpm was more accurate than other rpms in the blank drum. In the wooden model drum, the same result obtained. The position (5,5) of the model drum means that the former 5 is the hole number and the latter 5 is the segment number.

Table 2 Calculation of Mass Attenuation Coefficient in Various Drums

Drum Type	Main Components in Waste Drum	Pseudo material
Miscellaneous	Vinyl sheet, Protection Cloth, Paper, Wood, others	Polyethylene
Shielded	Glass fiber, Metal, Sand	SiO_2
Spent resin	Cement, Water, Wet Spent Resin	Cement : 63%, Water : 30%, Reins : 7%
Spent Filter	Filter shielded by cement	Cement
Concentrate	Paraffin, Boric waste	Paraffin : 25%, Borate% : 75

Measuring Time

In general, it is desirable to take the measurement time long. but it takes long time to analyze one waste drum. Based on the average 30 minutes to measure one drum, the relation between the measure time and their measured value was investigated, and the result is shown in **Table 4.**

Table 3 Analysis results according to the change of drum rotation speed

Drum Type	Rotaion, Rpm	Co-60, μCi	Cs-137, μCi	
Blank	8	5.3 ± 1.2	4.1 ± 1.4	- Meas. time:100 sec/segment - Std. Source : Co-60:10.5 μCi, Cs-137:10.3 μCi - Source Position : 5, 5
	9	6.3 ± 1.3	6.2 ± 2.5	
	10	8.1 ± 1.6	8.7 ± 3.1	
	11	6.4 ± 1.3	8.5 ± 3.9	
	12	6.6 ± 1.4	6.2 ± 2.7	
Wood (d=0.68)	8	81 ± 21	88 ± 36	- Meas. time : 50 sec/segment - Std. Source : Co-60, 93 μCi, Cs-137, 86 μCi - Source Position : 3, 5
	9	99 ± 22	94 ± 30	
	10	86 ± 21	85 ± 13	
	11	111 ± 24	121 ± 39	
	12	96 ± 20	96 ± 32	

Up to 200 seconds/segment, the results were almost similar and it is possible to take the measuring time as a 100 seconds/segment.

On the other hand, 300 seconds/segment showed much more accuracy in very low-level waste drum. However, it will be take 45 minutes to measure one drum.

However, in this test, we knew that it needs more time to measure the very low-level specific activity

Table 4 Analysis results according to the change of measuring time

Drum Type	Meas. Time(sec)	Co-60, μCi	Cs-137, μCi	
Wood (d=0.68)	50	3.9 ± 1.1	2.7 ± 1.1	Co-60, 10.5 μCi Cs-137, 10.3 μCi
	100	4.0 ± 0.9	3.5 ± 1.4	
	150	4.5 ± 1.0	4.1 ± 1.5	
	200	4.6 ± 1.0	4.4 ± 1.6	
	300	10.0 ± 1.7	10.6 ± 3.8	
Paraffin (d=1.1)	100	11,300 ± 5,600	19,200 ± 17,800	Co-60, 8.7 mCi
	200	11,300 ± 7,500	19,200 ± 23,900	Cs-137, 9.3 mCi

Non Uniformity Correction (NUC)

Non Uniformity Correction (NUC) Method, like a multichannel scaling method, was to developed to apply the correction factor to the standard analysis in the case of non-homogeneous waste drum by Canberra Company.

Table 5 showed the comparison of results applied with NUC and without NUC.

We evaluated NUC changing the position of standard source to take the model drum as a non-homogeneous drum. As shown in **Table 5**, it is desirable to apply NUC to that drum.

Comparison of Matrix Correction Methods

There are three methods to correct the attenuation of the material to measure the specific activity as shown in **Table 1**. These methods were evaluated with some known-density drums.

In the drums (density: < 0.84), the differential peak (DP) is not good method showing large error but the average density and the transmission method were considered good.

In other drums (density : > 1.16), the differential peak(DP) and the average density are better tha n the transmission method due to shielding effect, and also can be considered as a better method in case of high-level drums.

This study's results

Changing the distance

The purpose to change the distance between the detector and the drum is in the measurement of activities from the low-level drum (in spite of density). For this purpose, we added the detector mover and modified the collimator to change the solid angle of an aperture as shown in **Fig. 2, 3.** Therefore, we can divide the number of segment of drum as above 8 segments. We obtained the results from 8(in normal distance range) and 10(in short distance range) segments of one drum (200L) of which density is 0.34 and 1.9 g/cm^3.

Table 5 Analysis Results Applied With and Without Non Uniformity Correction

Source Position	Co-60		Cs-137		
	With	Without	With	Without	
3, 5	0.99	1.25	1.11	1.52	- 100 s/segment - Co-60, 93 μCi Cs-137, 86 μCi
5, 5	1.02	1.68	1.01	1.95	
6, 5	1.05	1.73	1.20	2.32	
7, 5	0.92	1.85	1.00	2.48	
8, 5	1.23	1.87	1.29	2.56	
9, 5	0.88	1.88	1.02	2.76	

o Drum Type : wooden(d=0.68)

o The value means the measured value/the standard value.

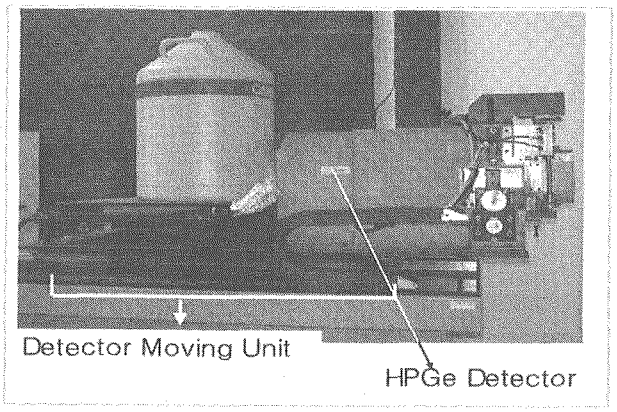

Fig. 2 Photo of detector mover installed in existing system.

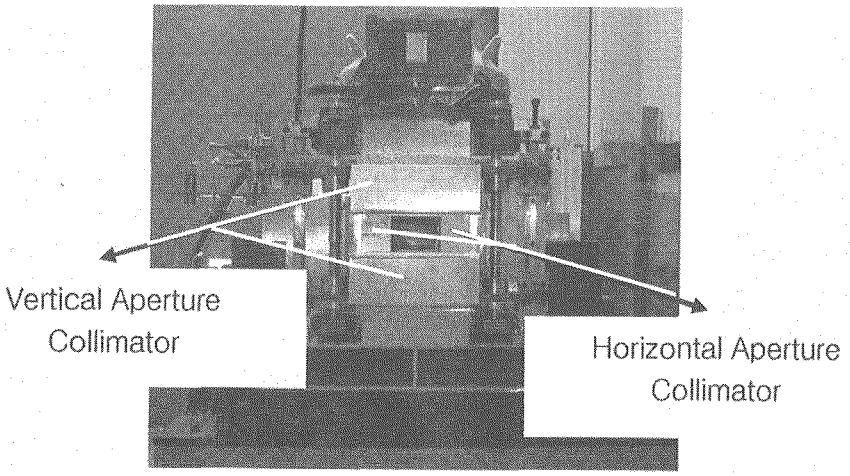

Fig. 3 Photo of the modified collimator.

Table 6 Analysis results measured in a short distance (10 segments)

Drum Type	Meas. Time(sec)	Co-60	Cs-137	
Cork D=0.34	60	52.311 ± 5.378	89.916 ± 16.098	Standard source Co-60, 47.87 μCi Cs-137, 101.16 μCi
	120	52.140 ± 5.136	91.318 ± 15.860	
	180	53.114 ± 5.240	94.145 ± 16.520	
	240	53.676 ± 5.269	93.198 ± 16.380	
	300	52.117 ± 5.121	91.947 ± 16.211	
Sand D=1.9	90	49.827 ± 27.697	103.840 ± 108.690	
	120	50.295 ± 26.985	98.954 ± 99.930	
	180	50.631 ± 27.028	93.840 ± 94.228	
	240	53.230 ± 28.022	101.550 ± 100.610	
	300	49.521 ± 27.776	95.876 ± 94.836	

In **Table 6**, we could know that the activity of Co-60 was measured high, and Cs-137 was measured low compared to that of standard source. Nevertheless, the measurement error was below 12%.

Table 7 Analysis results measured in a short distance (8 segments)

Drum Type	Meas. Time(sec)	Co-60	Cs-137	
Cork D=0.34	60	47.395 ± 5.411	81.897 ± 15.765	Standard source Co-60, 47.87 μCi Cs-137, 101.16 μCi
	120	43.524 ± 4.578	75.812 ± 13.756	
	180	45.617 ± 4.532	78.714 ± 13.693	
	240	44.592 ± 4.430	77.675 ± 13.528	
	300	44.562 ± 4.398	78.064 ± 34.532	
Sand D=1.9	100	41.400 ± 19.592	79.491 ± 70.819	
	120	41.887 ± 19.522	84.233 ± 71.259	
	180	42.524 ± 24.083	85.006 ± 87.268	
	240	42.584 ± 19.229	82.702 ± 68.080	
	300	42.249 ± 22.819	80.287 ± 80.928	

In **Table 7**, we could know that the activity of Co-60 and Cs-137 was measured low compared to that of standard source. The measurement error was below 13.6% for Co-60, 25.1% for Cs-137.

The result obtained from 10 segments was more accuracy than from 8 segments.

If our system could be complemented in detector type (wide, >30%) and mass attenuation, we can say that our system have the performance of TGS. and can be applied to the drum which TGS system does not analyze drum (for example, high density, high activities and large volume).

CONCULSION

An optimum operating conditions of radwaste drum assay system was induced by evaluating the affecting factors (drum's rotation speed, measuring time, source position and methods attenuation correction) on the measurement of activity. In addition, we knew that the measurement error could be depended on the density of drum matrix, the specific activity the measuring time, the position of source (non-homogeneity).

To analyze the activities of γ-emitters from various drums, we modified the collimator (horizontal and vertical) and added detector mover to the existing SGS system.

As a results, the measurement error was below than 12 % in a short distance(10 segments, Co-60; 47.87μCi and Cs-137; 101.16μCi) and was < 25 % in a long distance(8 segments, same sources). Finally, our system could be applied to the drum which TGS system does not analyze drum (for example, high density, high activities and large volume).

REFFERENCE

(1) Peter Filβ, "Specific activity of large-volume sources determined by a collimated external gamma detector," Independent Journal on Energy Systems and radiation, 1989/3

(2) Ki-Hong, Kim, "Development of Segmented Gamma Scanner for 200L Drum," presented in KAERI-JAERI JOINT SEMINAR of 2002

Session 3

Evaluation of Irradiation and PIE Data

Chairs:

【3.1 ~ 3.3】

Sang Bok Ahn (KAERI) and Taiju Shibata (JAEA)

【3.4 ~ 3.10】

Man Soon Cho (KAERI) and Takehiko Nakamura (JAEA)

This is a blank page.

3.1 PIE TECHNOLOGIES FOR THE STUDY OF STRESS CORROSION CRACKING OF REACTOR STRUCTURAL MATERIALS

Hirokazu Ugachi, Jun-ichi Nakano, Yoshiyuki Nemoto, Keietsu Kondo, Yukio Miwa, Yoshiyuki Kaji, TakashiTsukada and Minoru Kizaki

Japan Atomic Energy Agency, Tokai Research and Development Center
2-4 Shirakata Shirane, Tokai-mura, Naka-gun, Ibaraki-ken, 319-1195

Masao Ohmi and Michio Shimizu

Japan Atomic Energy Agency, Department of JMTR, Hot Laboratory Section
3607 Narita-cho, Oarai-machi, Higashi-Ibaraki-gun, Ibaraki-ken, 311-1394 Japan

ABSTRACT

Irradiation assisted stress corrosion cracking (IASCC) is one of the critical concerns when stainless steel components have been in service in the light water reactors (LWRs) for a long period. In general, IASCC can be reproduced on the materials irradiated over a certain threshold fluence level of fast neutron by the post-irradiation examinations (PIEs) at hot laboratories. On the other hand, recently in the Japanese boiling water reactor (BWR) power plants, many incidents of stress corrosion cracking (SCC) of structural material such as the reactor core shrouds and primary loop recirculation (PLR) system piping were reported. In order to investigate the cause of SCC, PIEs at hot laboratories were carried out on the sample material extracted from BWR power plants. SCC studies require various kind of PIE techniques, because the SCC is caused by a complicated synergistic effects of stress and chemical environment on material that suffered degradations by irradiation and/or thermal aging. In this paper, we describe the PIE techniques adopted recently for our SCC studies, especially the crack growth measurement, uniaxial constant load (UCL) tensile test method, in-situ observation during slow strain rate test (SSRT) and several metallurgical test techniques using the field-emission type transmission electron microscopy (FE-TEM), focused ion beam (FIB) processing technique, three Dimensional Atom Probe (3DAP) analysis and atomic force microscopy (AFM).

KEYWORDS: SCC, PIE, LWR, Hot Laboratory, JMTR, WASTEF, IMR, Crack Growth Test, UCL Test, In-situ Observation, FE-TEM, EDS, FIB, 3DAP, AFM

INTRODUCTION

Irradiation assisted stress corrosion cracking (IASCC) of the austenitic stainless caused by the simultaneous effects of neutron irradiation and high temperature water environment has been considered to be one of the major concerns of in-core structural materials not only for the aged LWRs but also for the water-cooled fusion reactor, i.e. the International Thermonuclear Experimental Reactor (ITER). IASCC can be reproduced on the material irradiated over a certain threshold fluence level of fast neutron by the post-irradiation examinations (PIEs) carried out at hot laboratories [(1)]. Through PIEs, we have understood that a primary cause of IASCC is the generation/migration and aggregation of radiation defects and especially the radiation induced segregation (RIS) at grain boundary plays an essential role in IASCC phenomena.

On the other hand, recently in the Japanese boiling water reactor (BWR) power plants, many incidents of stress corrosion cracking (SCC) of structural material of components such as reactor core shrouds and primary loop recirculation (PLR) system piping were reported. In order to investigate the cause of SCC, the material examinations were carried out on the sample material extracted from BWR power plants at hot laboratories, for example, of the Japan Atomic Energy Research Institute (JAERI), the predecessor of the Japan Atomic Energy Agency (JAEA) [(2,3)]. The examinations were PIEs, because the samples were managed as the radio active material or material contaminated by the nuclear fuel.

As described above, the PIE technologies are essential for the studies of SCC of reactor structural materials. And furthermore, SCC studies require various kinds of PIE techniques, because the SCC is caused by complicated synergistic effects of stress and chemical environment on material that suffered degradations by irradiation and/or thermal aging, e.g. the RIS at grain boundaries (GBs). This paper describes testing facilities for PIEs used for our recent SCC studies at the JMTR Hot Laboratory (JMHL), Waste Safety Testing Facility (WASTEF) and Institute for Material Research of Tohoku University (IMR) techniques at these facilities.

FACILITY FOR CRACK GROWTH TEST

In March 2002, a new IASCC growth test machine having with two autoclaves for producing the test condition of high temperature and pressurized water was installed in the

hot cell of JMHL to evaluate the IASCC growth rate by the crack growth tests of irradiated compact tension (CT) specimens under the BWR environmental conditions. A schematic drawing of the SCC growth test machine and a view of autoclave are shown in **Fig.1**. The maximum operational parameters of the facility are as follows; load capacity: 10 kN, temperature: 573 K, pressure: 10 MPa, and flow rate: 1000 little per hour. The test water is circulated in the system by a main pump and a booster pump. The pressure of high temperature water can be controlled by a pressure control valve. The water temperature in the system is controlled by band heaters equipped around autoclaves and pre-heaters installed in the loop system. This test machine has heat exchangers to control the temperature of circulating water economically.

To simulate the normal water chemistry (NWC) and hydrogen water chemistry (HWC) conditions of BWR, the dissolved oxygen (DO) and dissolved hydrogen (DH) concentrations can be controlled in this loop system. The DO and DH concentrations can be controlled within the range of 10ppb - 32ppm and 10ppb – 2ppm, respectively. It is well known that the corrosive environment, determined by hydrogen peroxide (H_2O_2), is much severer than that determined by oxygen with the same effective oxygen concentration designated as the sum of $[O_2]$ and $1/2[H_2O_2]$[4,5]. Therefore, H_2O_2 concentration can be also controlled in this machine. H_2O_2 injection piping line was lined with the poly tetra fluoro ethylene (PTFE) to prevent surface decomposition of H_2O_2. Furthermore, the electrochemical potential (ECP) of specimen can be monitored by the silver/silver chloride (Ag/AgCl) type external reference electrode. A crack growth length is monitored by means of the direct current potential drop (DCPD) method during the test. After SCC growth test, crack length is calibrated by the optical observation of fracture surface of CT specimen using the scanning electron microscope (SEM) installed in a hot cell.

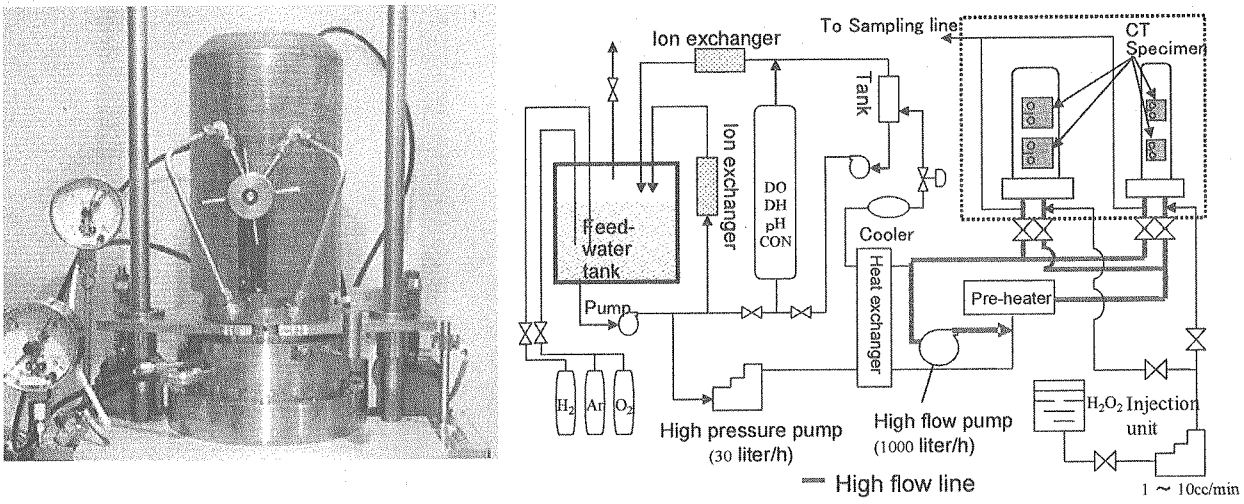

Fig.1 Schematic drawing of IASCC growth test machines and a view of autoclave.

FACILITY FOR UNIAXCIAL CONSTANT LOAD TEST

The uniaxial constant load (UCL) test technique is usually adopted to obtain the data on relationship between the loading stress and time to SCC failure that can be used for the structural design and also for the assessment of SCC initiation time. **Fig. 2** shows a schematic flow diagram of the UCL test facility installed at WASTEF. In order to carry out the SCC tests efficiency using multiple specimens, four autoclaves are equipped with this facility to carry out the SSRT and UCL testing. To obtain a high flow rate condition, a circulation pump (maximum flow rate: $1m^3$/hour) is installed at the water loop system. **Fig.3** shows the view of test facility equipped with four autoclaves. For SCC initiation test, we are using the round bar type tensile specimen with a relatively small diameter of 1.5 mm in gage section, because an immediate rapture of specimen can be expected when SCC initiated on the specimen.

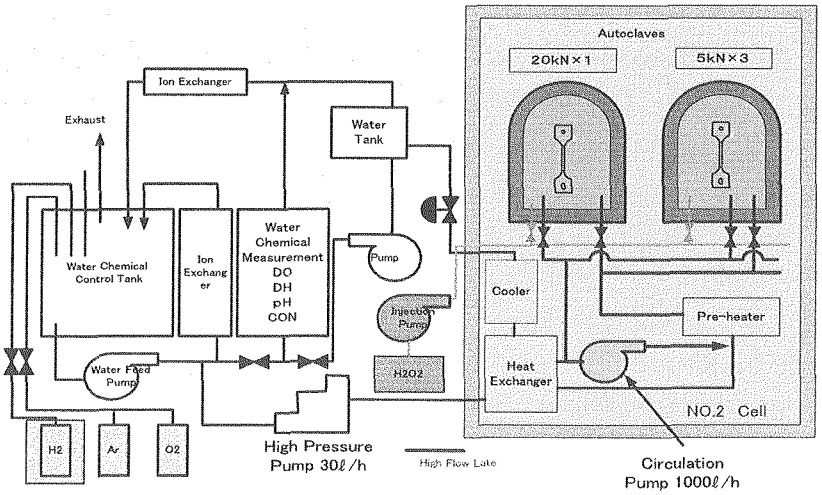

Fig.2 Schematic flow diagram of SCC test facility at WASTEF.

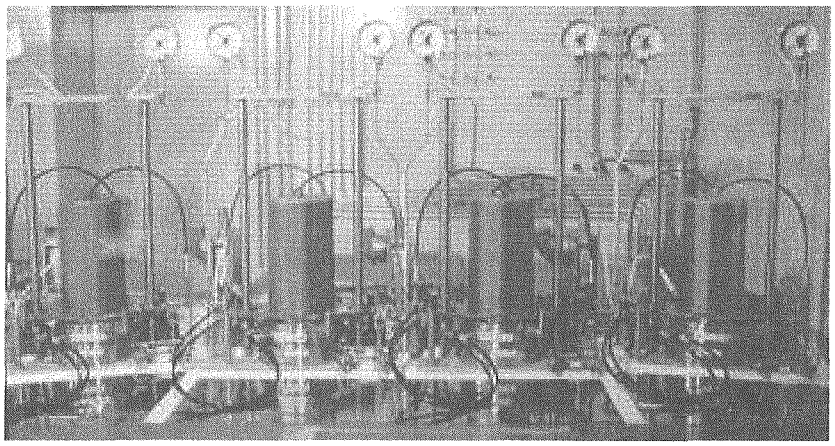

Fig.3 View of the test facility equipped with four autoclaves.

FACILITY FOR IN-SITU OBSERVATION DURING SLOW STRAIN RATE TESTING

Schematic flow diagram of a SSRT facility and its autoclave installed in the hot cell of WASTEF are shown in **Fig. 4** [6,7]. For SSRT in a simulated BWR environment, the maximum operational parameters are designed as follows; temperature: 573 K, pressure: 10 MPa and flow rate: 30 ℓ/h. To simulate NWC and HWC conditions, DO and DH can be controlled within the range of 10 ppb - 32 ppm and 10 ppb - 2.8 ppm, respectively. A special design of this test machine is an equipment of a window for in-situ observation of the specimen during SSRT through the window. The window is made of sapphire glass that is durable in high temperature water.

Fig. 5 shows stress-strain curves obtained using the SSRT facility. To evaluate effects of additional elements, the high purity SSs doped with Si were irradiated to 3.5 x 10^{25} n/m^2 (E>1MeV) in JRR-3. SSRT was conducted in high purity water at 561 K and DO=8ppm. In the case of neutron irradiation to 6.7 x 10^{24} n/m^2 (E>1MeV), more than 20% elongation was observed in the high purity SS with Si [8,9]. Although it was beneficial in delaying the onset of or suppressing the susceptibility to IASCC, the effect of Si disappeared or had saturated at fluence to 3.5 x 10^{25} n/m^2 [10].

Fig. 6 shows a stress-strain curve and images obtained by in-situ observation during SSRT. A type 304 SS specimen was irradiated to 1.0 x 10^{26} n/m^2 (E>1MeV) at 323 K in JMTR. The first crack was introduced from left side on the gage length after maximum stress and propagated with time. The second crack was introduced from right side after the first crack was opened sufficiently. It can be exactly known points of crack initiation and propagation process by in-situ observation during SSRT. For understanding of IASCC behavior, it is useful to combine the analysis of stress-strain curve, in-situ observation and

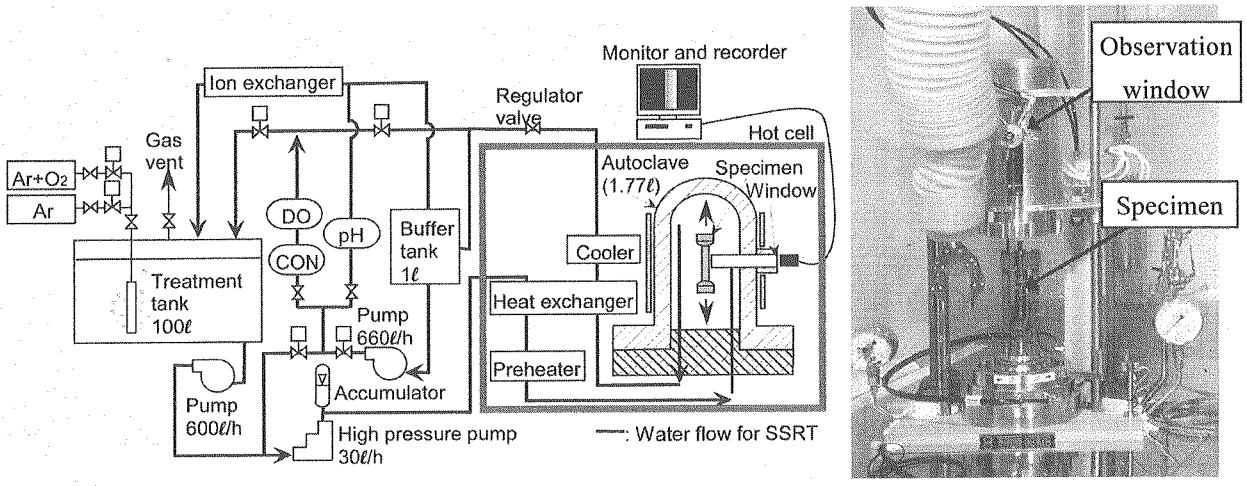

Fig.4 Schematic flow diagram of SSRT facility[6,7].

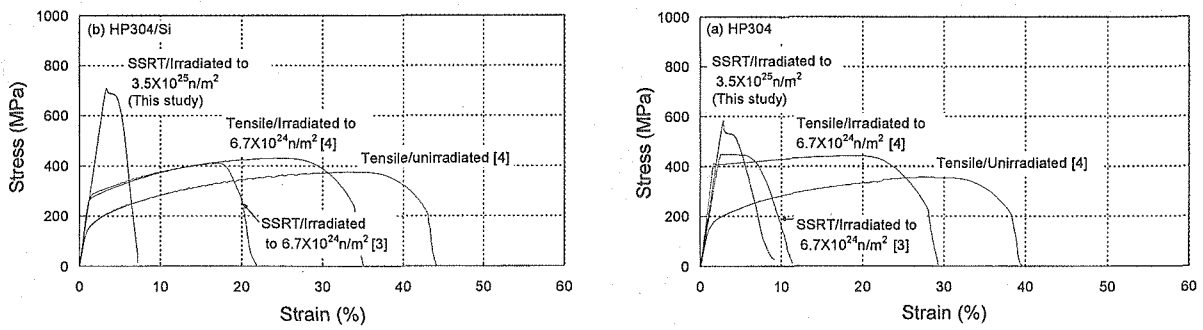

Fig.5 Stress-strain curve and images during SSRT for irradiated material[8-10].

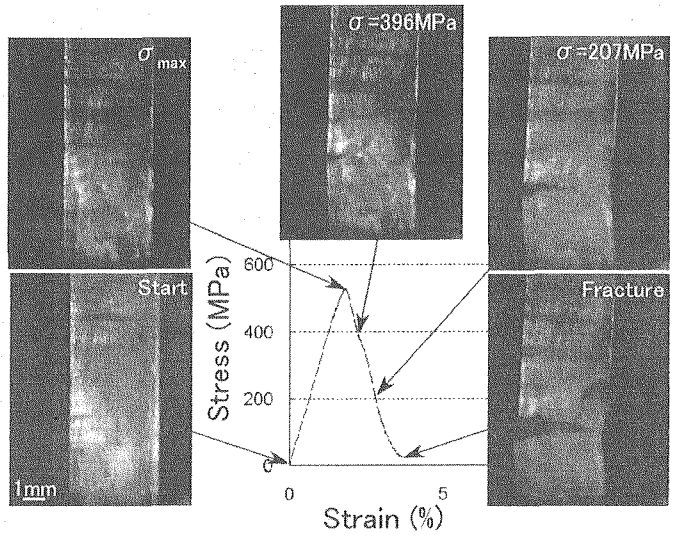

Fig. 6 Stress-strain curve and images during SSRT for irradiated material.

METALLURGICAL EXAMINATIONS

In order to elucidate the IGSCC and IASCC mechanism, it was important to study the chemical and physical properties at/near GBs, because the IGSCC and IASCC propagate along GBs. From a view point of the chemical properties, the corrosion resistance at/near GBs was thought to be one of key factors for the SCC mechanism. The corrosion resistance was attributable to the chemical compositional change at/near GBs that was induced during the fabrication process, aging and irradiation. The chemical compositional change was affected by grain boundary character such as grain boundary energy and coherency. From a view point of physical property, on the other hand, deformation behavior at/near GBs was thought to be one of the key factors. The deformation behavior was attributable to the stress/strain field at crack tip and the slip process at/near GBs. The slip process was affected by the coherency at GBs and the relationship of lattice orientation in grains. Techniques to

study the above subjects were described below.

Field-emission type transmission electron microscope (FE-TEM) and focused ion beam (FIB) processing technique

To study the chemical compositional change at/near GBs, a Hitachi HF-2000 FE-TEM with energy dispersive X-ray spectrometer (EDS) was installed at the WASTEF hot laboratory. An incident beam probe size of the FE-TEM was about 3 nm in diameter. **Fig. 7(a)** shows the chemical compositional profile across a grain boundary of high purity type Fe-18Cr-12Ni alloy irradiated at 543 K to 5.5 dpa in Japan Research Reactor No.3 (JRR-3). Depletion of Cr and enrichment of Ni was observed in a narrow range (~4 nm) adjacent to the grain boundary. In this experiment, FIB micro-sampling technique was used to reduce back-ground X-ray spectra from radio-isotopes such as ^{54}Mn. A micro-sample, ~10 μm x ~10 μm x ~0.2μm, was taken from a conventional TEM sample with a size of ϕ 1~3 mm x t0.2 mm). As seen in **Fig. 7(b)**, the influence of the back ground spectra can be neglected on the micro-sample.

The FIB micro-sampling technique can be also applied to a TEM specimen preparation from any places such as IGSCC fracture surface. The micro-sampling technique is enable us to observe and identify the oxides in cracks and the dislocation structure near cracks and also to estimate the water chemistry in cracks and the deformation behavior near cracks. **Fig. 8** shows the oxide films developed in oxygenated waters containing either 200ppb or 36ppm dissolved oxygen [(11)]. The developed oxide films were affected by the concentration of dissolved oxygen.

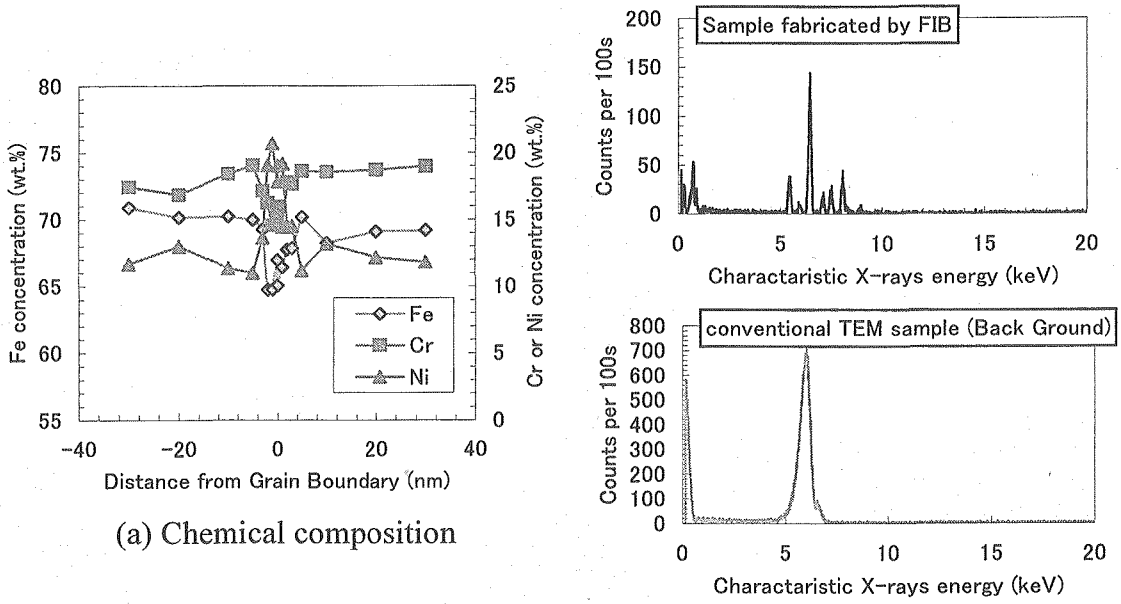

(a) Chemical composition

(b) EDS spectrums

Fig. 7 Chemical composition profile across GB of high purity Fe-18Cr-12Ni alloy irradiated at 543 K to 5.5 dpa.

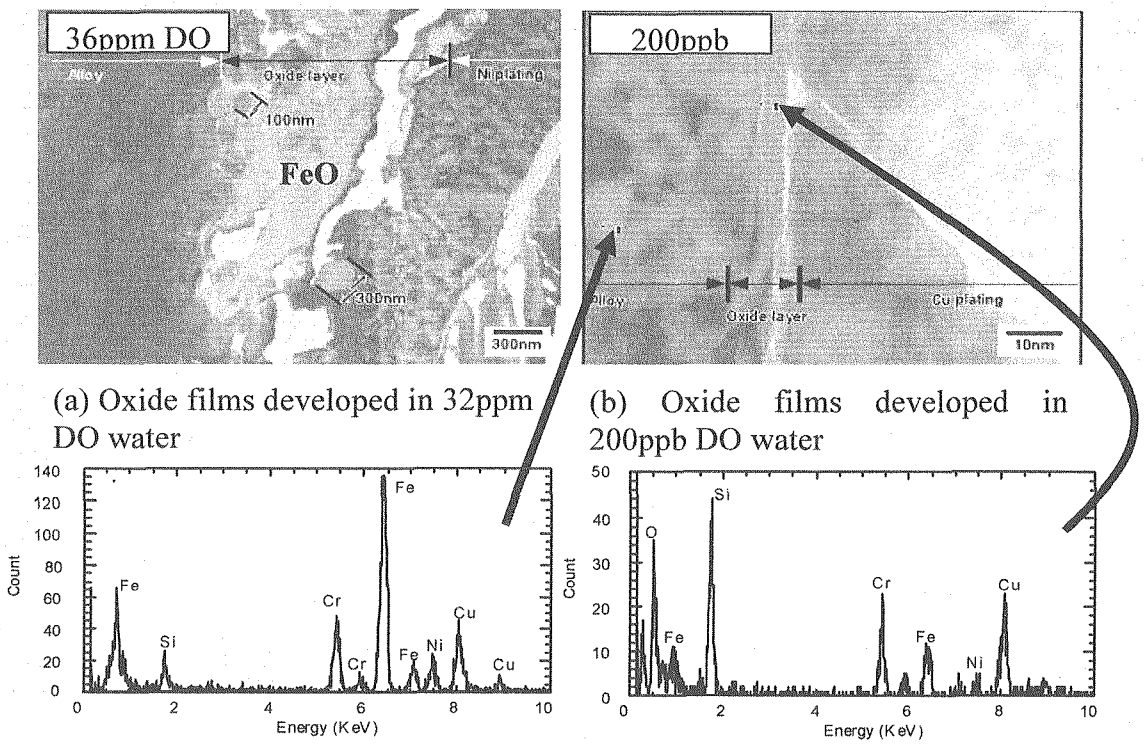

(a) Oxide films developed in 32ppm DO water

(b) Oxide films developed in 200ppb DO water

(c) EDX spectrum of alloy matrix in

(d) EDX spectrum of oxide film in (b)

Peak of Cu was originated from sample holder.

Fig. 8 Microstructure and micro composition of oxide films developed on SUS304 in oxygenated water at 561 K[11].

Three dimensional atom probe (3DAP)

The 3DAP is the analytical instrument which provides the highest spatial resolution among the various micro-analytical techniques which are used in the material science [12-15]. Therefore, it is expected to obtain more detailed information about the solute distribution due to segregation, precipitation and clustering in matrix or at grain boundaries.

In a 3DAP, the field evaporation that is achieved by applying high voltage pulses to a specimen tip is used to remove individual atoms from the surface. A position sensitive detector is used for measurement of both flight time (to identify atomic species) and impact position (which enables the original position of each atom on the specimen surface to be recorded). Thus, the atom distributions can be reconstructed in a three-dimensional real space. The 3DAP has a depth resolution of a single atomic layer and sub nanometer (~0.2 nm) lateral resolution. Another advantage of 3DAP techniques is their quantitatively. Under proper experimental conditions, concentrations of elements are reliable and directly proportional to the number of atoms collected from the specimen.

It is necessary to prepare the needle-shaped specimens for 3DAP analysis in the form of a needle with an apex radius of curvature of 10-100 nm, to achieve the field evaporation.

For most materials, specimens were prepared by electrochemically polishing fine wires cut from bulk materials. For analyzing the region of interest such as a grain boundary, specimen preparation using Focus Ion Beam (FIB) milling technique is available, because it enables to produce a specimen with a desired micro-structural feature in the apex region.

For the mechanistic understanding of IGSCC of low carbon austenitic stainless steel, the 3DAP analyses on the material, type 316L stainless steel, extracted from a core shroud of Japanese BWR were conducted at the Institute for Material Research of Tohoku University (IMR) [16]. **Fig. 9** shows atom maps of solute elements of shroud material near grain boundary. Enrichment of Mo, Si is seen in 3D atom map, and the width of the enriched area is about 2 nm across a grain boundary. Analyses of the concentration profile near grain boundary obtained from 3DAP dataset results in the random distribution of Cr and Mn, enrichment of Si, Mo. Further analyses are necessary to discuss the relation between this results and a mechanism of SCC propagation.

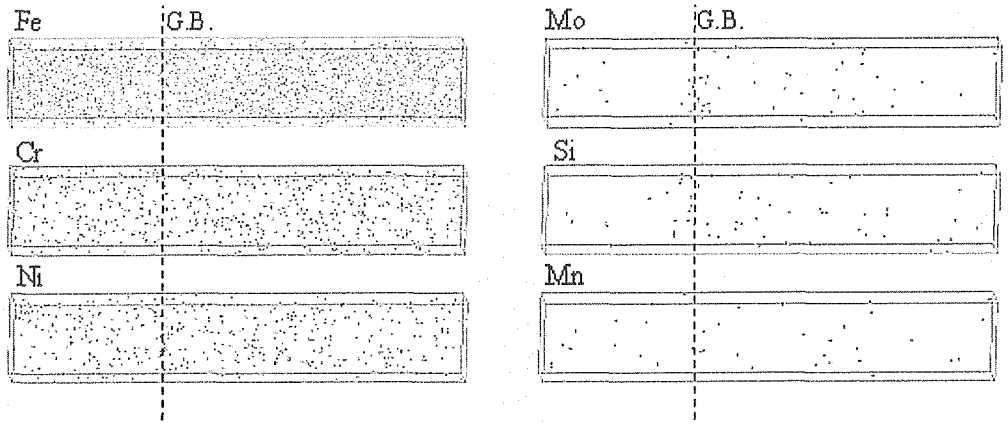

Fig. 9 3DAP atom map of solute elements of shroud material near grain boundary (volume is about 1.4×3.5×19 nm^3)[16].

Electrochemical corrosion testing and atomic force microscope (AFM) evaluation technologies

We developed an electrochemical corrosion testing equipment for the irradiated specimens [17]. The Electrolyte cell (**Fig.10(a)**) was designed for easy handling by manipulators. A capacity of the cell was kept to a minimum for reduction of radioactive liquid waste but enough for reliable corrosion tests. The electrodes equipped on the cell is connected to the potentiostat placed outside of the hot-cell by cables with 5 meters long, so corrosion testing can be operated by remote control.

The micro-corrosion measurement apparatus (**Fig.10(b)**) was developed for the evaluation of surface topography on the irradiated specimens after corrosion test [17]. This apparatus was assembled from an atomic force microscope (AFM), optical microscope, remote controllable stage system and remote controllable cantilever exchanging system. The specimen holder of the stage system was designed so that a specimen can be installed easily by manipulators. The remote controllable stage system was designed to shift a specimen

precisely between the positions of the optical microscope and AFM, so the same area on a specimen can be observed by the optical microscope and the AFM. The remote controllable cantilever exchanging system was developed because the worn cantilever needs to be renewed in hot-cell after several evaluations.

Corrosion behavior of a stainless steel specimen taken from nearest portion of SCC on BWR core shroud was studied with the usage of these remote controllable equipments [18]. An illustration of cross section of the BWR core shroud with SCC is shown in **Fig.11**. An optical microscope image and AFM topographies of the specimen cross section after corrosion test are also presented in **Fig.11**. **Fig.11(a)** shows the AFM topography on the area close to the core shroud surface, and **Fig.11(b)** shows the matrix area. On **Fig.11(a)**, slip lines were preferentially corroded. These slip lines were observed only on **Fig11(a)**, so it is considered that these slip lines were introduced by surface fabrication on the core shroud. This result suggests that preferential corrosion on the slip lines on the surface layer of the core shroud would be one of the reasons to cause trans-granular type SCC.

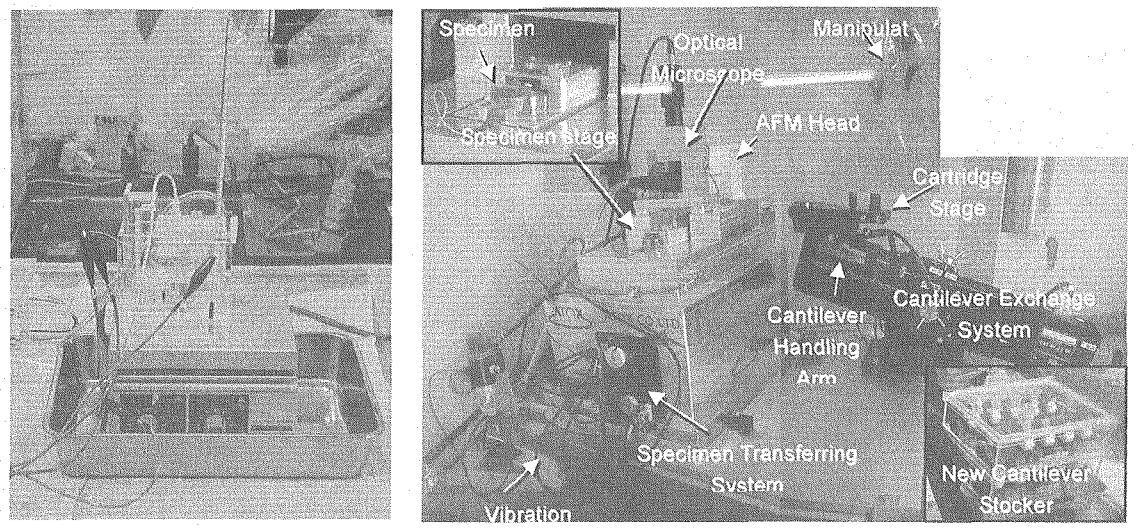

Fig.10 (a) Electrolyte cell for electrochemical corrosion testing in hot-cell [17],
(b) Remote-controlled micro-corrosion measurement apparatus in hot-cell[17]

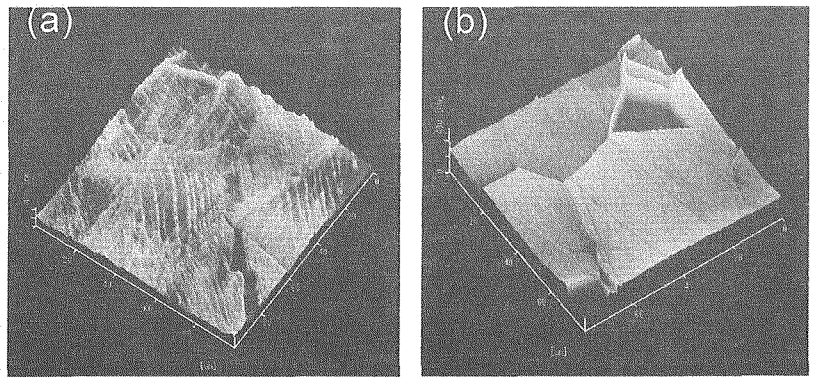

Fig.11 AFM topography observed after corrosion test on the cross sectional area of the core shroud specimen[18]. (a) Hardened layer near the surface. (b) Matrix layer.

Electron back-scattered diffraction pattern (EBSP) technique

Deformation ability of GBs and grains on both sides of the GBs was dependent on structural parameters such as the coherency of atoms at GBs, the GB energy, the relationship between lattice orientation of the grains and the relationship between slip direction and applied force. The GB energy may influence on driving force for precipitation and segregation at GBs. These structural parameters were sometimes related to GB characters such as coincidence site lattice (CSL). In order to study the effect of GB characters on IGSCC and IASCC, we installed the orientation imaging microscopy (OIM) based on an electron back-scattered diffraction pattern (EBSP) technique in a hot cell at JMHL. EBSP technique was used to determine the orientation of the grains of cracked samples [16].

Plastic strain distribution was evaluated around IGSCC tip by means of a new EBSP technique to evaluate the change in misorientation in grains. **Fig.12** shows the branched IGSCC and the plastic strain distribution map at crack tip[19]. IGSCC was formed in the CT specimen of sensitized SUS304 stainless steel after constant load test at 561K in oxygenated water. The explicitly deformed area around crack tip spread to a size of about one grain (a few 100 μm). The deformed area was also spread heterogeneously and seemed to be limited to the grains on both sides of the crack. It was speculated that the IGSCC might be affected by the locally-developed plastic deformation. In mechanical testing to study IGSCC and IASCC, test techniques based on the linear elastic fracture mechanics (LEFM) were usually used because of the applicability of test results to life prediction of components. The LEFM uses the elastic strain field as a parameter. The elastic strain field widely spreads over a few mm away from the crack tip. Therefore, we try to correlate the effects of locally-developed plastic deformation to the LEFM.

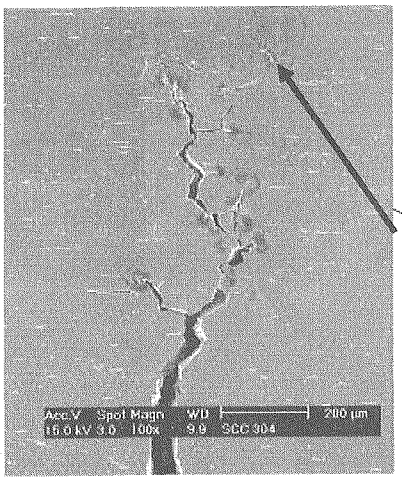

(a) Branched IGSCC crack

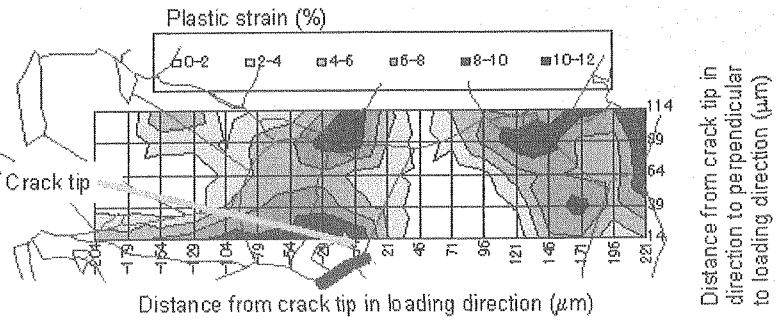

(b) Plastic strain distribution around IGSCC tip. Red line indicates the grain boundaries.

Fig.12 Locally-developed plastic strain field around IGSCC tip[19].

COCLUDING REMARKS

In this report, we described the several test techniques that had been adopted in our recent SCC studies. Those are the PIE techniques for crack growth measurement, UCL tensile test, in-situ observation during SSRT test and several metallurgical examinations using FE-TEM, EDS, FIB, 3DAP and AFM for microscopic evaluation of the chemical and physical properties at/near grain boundaries of structural materials. There are still many unknown factors on the IASCC and other SCC phenomena. For the mechanistic understanding and development of countermeasures against SCC of reactor structural materials, we have to eagerly make the further improvement or upgrade of present PIE techniques and also the introducing of up-to-date techniques into the PIE field.

REFERENCES

(1) Y. Kaji, T. Tsukada, H. Tsuji, and H. Nakajima, Proc. of 9th Int. Symp. Environmental Degradation of Materials in Nuclear Power Systems – Water Reactors, pp 987-994 (1999).
(2) The Working Team for Examination Operation of Samples from Core Shroud at Fukushima Dai-ni Unit-3, JAERI-Tech 2004-044 (2004) (in Japanese).
(3) The Working Team for Examination Operation of Samples from Primary Loop Recirculation Piping at Onagawa Unit-1, JAERI-Tech 2004-003 (2004) (in Japanese).
(4) Y. Wada, A. Watanabe, M. Tachibana, N. Uetake, S. Uchida and K. Ishigure, J. Nucl. Sci. Tech., 37 (2000) 901-921.
(5) S. Uchida, T. Satoh, J. Sugama, N. Yamashiro, Y. Morishima, T. Hirose, T. Miyazawa, Y. Satoh, K. Iinuma, Y. Wada and M. Tachibana, J. Nucl. Sci. Tech., 42 (2005) 66-74.
(6) J. Nakano, H. Ugachi, T. Tsukada and H. Tsuji, Proceedings of 11th International Conference on Nuclear Engineering, ICONE11-36145 (2003).
(7) J. Nakano, T. Tsukada, H. Tsuji, S. Terakado, T. Kohya and S. Endo, JAERI-Tech 2003-092 (2004). (in Japanese)
(8) T. Tsukada, Y. Miwa and H. Nakajima: Proc. 7th Int. Symp. Environmental Degradation of Materials in Nuclear Power Systems - Water Reactors (1995) p. 1009.
(9) T. Tsukada, JAERI-Research 98-007, (JAERI, 1998). (in Japanese)
(10) J. Nakano, Y. Miwa, T. Kohya and T. Tsukada, J. Nucl. Mater., 329-333, (2004) 643-647.
(11) Y. Nemoto, Y. Miwa, M. Kikuchi, Y. Kaji, T. Tsukada and H. Tsuji, J. Nucl. Sci. Tech., 39 (2002) 996-1001.
(12) M.K. Miller, "Atom probe tomography,", Kluwer Academic / Plenum Publishers, (2000)
(13) K. Hono, Prog. Mater. Sci. 47 (2002) 621

(14) D.L. Larson, A.K. Petford-Long, Y.Q Ma, A. Cerezo, Acta mater. 52 (2004) 2847-2862
(15) P. Auger, P. Pareige, S. welzel, J-C. Van Duysen, J.Nucl.Mater. 280 (2000) 331
(16) Y. Miwa, Y. Nemoto, K. Kondo, Y. Kaji, T. Tsukada, Y. Nagai, M. Hasegawa, T. Ookubo, K. Hono, Proc. 52nd Japan Conf. on Materials and Environments, JSCE (2005) 189-192 (in Japanese).
(17) F.Ueno, Y. Nagae, Y. Nemoto, Y. Miwa, S. Takaya, T. Hoshiya, T. Tsukada, K. Aoto, T. Ishii, M. Ohmi, M. Shimizu, Y. Abe, T. Yoshitake, Y. Nakamura, T. Yamashita, JAERI-Research 2005-023, JNC TY9400 2005-013 (in Japanese).
(18) Y. Nemoto, J. Nakano, F. Ueno, K. Kondo, Y. Yukio, M. Ohmi, T. Tsukada, Proceedings of the 52nd Japan Conference on Materials and Environments, JSCE (2005) 197-200 (in Japanese).
(19) Y. Kaji, Y. Miwa, T. Tsukada, M. Hayakawa, N. Nagashima, S. Matsuoka, JAERI-Research 2005-029 (2005) (in Japanese).

3.2 PREDICTION OF DELAYED HYDRIDE CRACK VELOCITY IN THE IRRADIATED ZR-2.5NB CANDU PRESSURE TUBE MATERIALS

Sangbok Ahn, Wanho Oh, Yanghong Jung, Dosik Kim, Yongsun Choo, Kwonpyo Hong

Korea Atomic Energy Research Institute, Irradiated Material Examination Facilty
P.O. Box-105, Yusong, Daejon, Korea, 305-353

Kangsu Kim, Youngsuk Kim

Korea Atomic Energy Research Institute, CANDU Pressure Tube Development Team
P.O. Box-105, Yusong, Daejon, Korea, 305-353

ABSTRACT

Delayed hydride cracking (DHC) is an important factor to restrict the operation life of pressure tube in CANDU reactor. In this paper DHC behaviors for the pressure tube materials from commercial reactor are reviewed on the effect of neutron irradiation experimentally, and the prediction method of the DHC velocity (DHCV) for the irradiated tube materials is proposed based on the test results of the unirradiated ones. Specimens from the unirradiated and the irradiated tubes, which various amounts of hydrogen is charged through diffusing process, are tested under constant loading condition.

The hydride crack grows steadily after incubation time to accumulate hydrogen to crack front, and DHCV's in the irradiated are 4~6 times faster than those of the unirradiated with about 50 kJ in activation energy. According to the irradiation fluence the DHCV has the tendency to be remarkably increased at the initial stages up to $1x10^{25}$ n/m^2 (E>1MeV) and saturated with the increase of fluence.

The crack velocity in the irradiated can be well predicted from the tensile and DHCV test results for the unirradiated, introducing the acceleration factors according to the yield strength and dissolved hydrogen content due to the neutron irradiation. The DHCV acceleration factor for the yield strength has a tendency to decrease and that for the hydrogen content to increase according to temperature, the proposed equation predict the velocity with 0.12 in standard deviation amount and 95% in coefficient of correlation for the irradiated.

KEYWORDS: Zr-2.5Nb, Pressure Tube, Neutron Irradiation, Compact Tension, Hydrogen, Delayed Hydride Cracking Velocity, Acceleration Factor

INTRODUCTION

The pressure tube material with Zr-2.5 wt% Nb alloy has long been used for the primary heat transport system in CANDU (Canadian deuterium uranium) nuclear reactors. This material, despite of good mechanical properties and low neutron absorption, have the susceptibility of a fracture mechanism called delayed hydride cracking. In 1970s many tubes during operation has been removed observing of cracking from DHC phenomena, and extensive research has been conducted in this area. DHC has been generally reported that is an intermittent crack propagation process, and it is caused by the dissolution of the hydride in the far-field stress regions diffusion into the stress-concentrated region when the hydrogen concentration exceeds the terminal solid solubility. The hydrides are accumulated and fracture occurs when the fracture condition is satisfied, and the initiated crack grows until the crack is stopped by the ductile matrix.

It is reported that material parameters effecting DHC are mainly texture [1], microstructure [2], yield stress [3], hydrogen solubility [4]. Neutron irradiation effects on these factors and is inferred to change DHC behaviors. DHC studies for the irradiated tube materials have been limited from the difficulty of specimen preparation and test technique. In this paper DHCV tests are performed for the operated pressure tube, and reviewed on the effect of neutron irradiation experimentally. Based on test results the prediction method of the DHCV introducing the acceleration factors, which consider the yield strength and the amount of the hydrogen solubility in the irradiation tube, are proposed and verified

EXPERIMENTAL PROCEDURE

Material and Specimen

Pressure tube in CANDU reactors are made from Zr-2.5Nb alloy by hot extrusion of hollow billets followed by 25% cold work. The pressure tube is about 6 m long and have an inside diameter of 103 mm and wall thickness 4.2 mm.

The materials used in this experiment come from the unirradiated tube, and the irradiated tube that were removed from the commercial CANDU reactor. The irradiated tube has an amount of 6.8~8.9 x 1025 n/m2 (E>1MeV) in neutron fluences, which are from the coolant inlet part, outlet to middle during over 10 years operation. The specimens are directly cut from various parts and positions as **Fig. 1**, has a shape of 17mm curved compact tension (CCT) in **Fig. 2**.

The specimens are charged with hydrogen for various amounts of 30, 50, 60 ppm in the unirradiated and 50 ppm in the irradiated using an electro-chemical diffusion method. The CCT specimen is hydrided in 0.1 mol sulfuric acid at 90°C for 30 hours to form a solid hydride layer on the surface. The diffusion process annealed at designated temperature is performed to obtain the solubility of hydrogen in whole specimen referring the report, and measure the amount of solubility with chemical method.

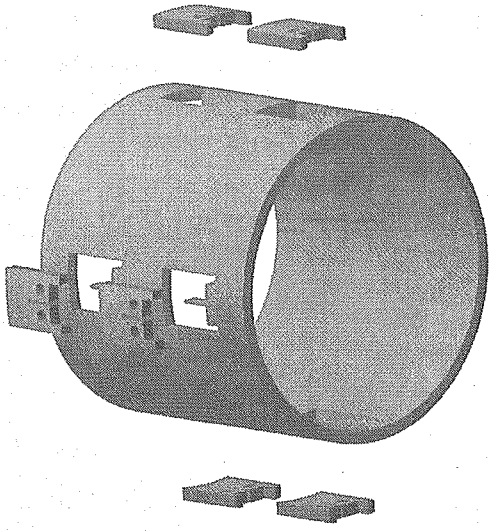

Fig. 1 Positions of specimens in the operated tube.

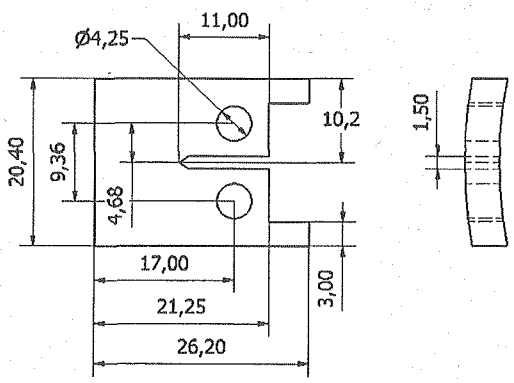

Fig. 2 Configuration of 17mm CCT specimen.

Experimental Techniques

All specimen preparation and test procedure for the irradiated are performed in hot cell. Specimens are pre-cracked to about 1.7mm (a/w = 0.1) with the value of 0.1 in a load ratio (R), 5Hz in a loading cycle while ΔK decreasing with 12~10 MPa•$m^{1/2}$. After pre-cracking at dynamic universal testing machine (UTM), DHC test is performed using static UTM equipped with tubular heating furnace to control with ± 2°C in precision for the test temperature in **Fig. 3**. A static universal testing machine, direct current potential drop device, temperature control furnace, and data acquisition system are set up in hot cell area to perform DHCV test. The input current lines at DCPD system are screwed to the each edge of specimen and the dropped voltage lines are spot welded to the area of crack mouth. After mounting the specimen to jig the thermal heat-up, homogenization and cool-down are started on the thermal route as shown in **Fig. 4**. Some specimens are repeatedly tested with different lower temperature. The load is applied and the dropped voltage measured after holding the test temperature during 2 hours following cool-down step. The applied load is determined in the compliance with ASTM E 399 by 13~15 MPa·$m^{1/2}$ based on the specimen size. To measure crack increment the input current to the specimen is 6 Ampere and the

dropped voltages are 2~3 mV, which is varied with the test temperature and crack length. During test the crack increment amount is forecasted with the equation $\Delta a/W = (1.1\sim1.2)\cdot\Delta V/Vo$ that was determined from the calibration test. After advancing the expected crack length the test is finished and the specimen is heat-tinted during 1 hour in the temperature of 250℃. The crack length is measured on the fractured surface with x20 in magnification using the high-scope system.

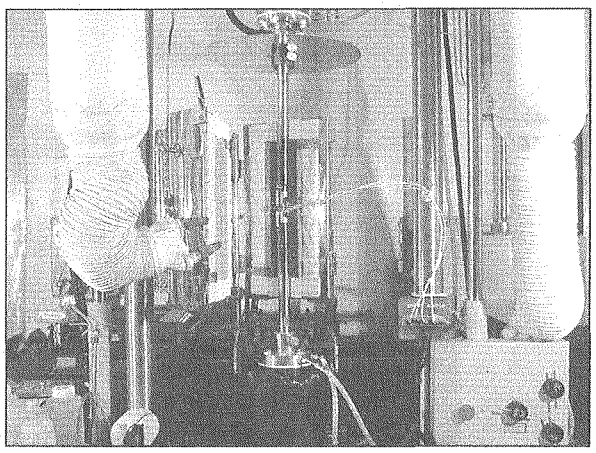

Fig. 3 Shape of DHCV test equipment in hot cell.

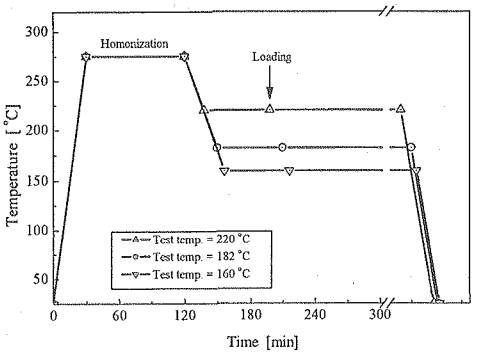

Fig. 4 Thermal history and loading point for DHCV test.

RESULTS AND DISCUSSION

Behaviors of DHC Growth

A whole typical fractured surface for step-I, II, III test shows in **Fig. 5**. In figure the DHC crack grows uniformly in each step. **Fig. 6** shows the typical variation of load, load line displacement (LLD) and dropped voltage according to time. In figure the dropped voltage start to increase behind applying load, so called incubation time. This phenomenon is guessed to be time for hydrogen to accumulate crack tip and formation a hydride. The incubation time in the irradiated specimen is shorter than it in the unirradiated ones. After a dropped voltage start to be changed, it increases uniformly with time. This means that the DHC advances with invariable velocity after the crack being initiated. **Fig. 7** shows the logarithm DHCV plot for the irradiated and the unirradiated specimens according to the inverse of the absolute test temperature. As expected the DHCV in both materials increased exponentially with proportional to the temperature and the velocity in the irradiated one was faster 4~6 times than in the unirradiated one. According to Simpson and Pulse [5, 6]

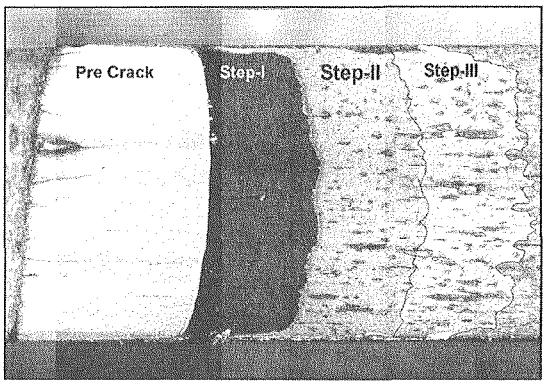

Fig. 5 Typical load-load line displacement-dropped voltage variations during test.

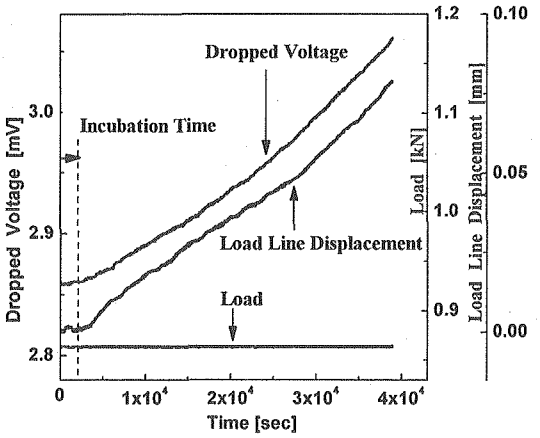

Fig. 6 Typical load, load line displacement displacement- dropped voltage variations during test.

the DHCV can be expressed in the form of the thermal activation energy proposed by Arrenhenius. From the least square linear fit in **Fig. 2** the velocity equation likes as $V= 5.1x10^{-3}$ exp(-47,933/RT) for the unirradiated materials, $V= 3.9x10^{-2}$ exp(-50,514/RT) for the irradiated ones. From the slope linear fit, the activation energy of DHCV was determined to be about 48 kJ/mol and 50.5 kJ/mol for the unirradiated and the irradiated materials respectively.

To investigate the DHCV variation with an irradiation amount, these tests and Sagat's results [7] are shown in **Fig. 8**, which divided into fluences according to the operating position. From the figure the DHCV has a trend to increase rapidly at the initial stage of irradiation up to ($\sim 1x10^{25}$ n/m^2) and saturate to constant value the accumulation of neutron irradiation amount.

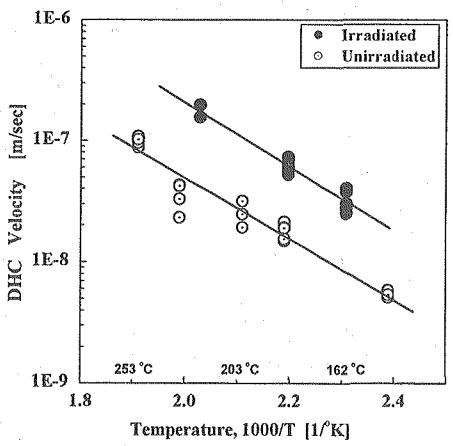

Fig. 7 Temperature dependence of the DHCV in the irradiated and the unirradiated pressure tube materials.

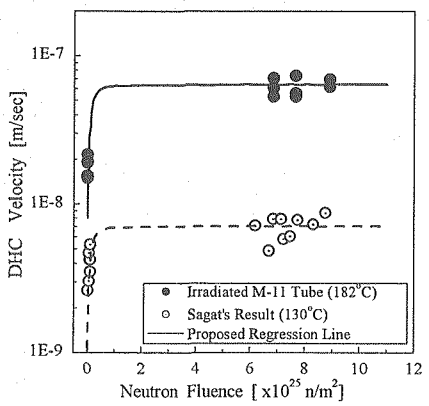

Fig. 8 DHCV variation trend accrording to neutron fluences.

Prediction Model of DHCV for the irradiated

Puls proposed the following equation for DHCV considering the hydrogen concentration in far field stress (E_L) and it in crack tip region(E_l), respectively.[6]

$$DHCV(V_d) = f(L,l)\, D_H\, (E_L - E_l) \qquad (1)$$

Values in Eq(1) express as the following Eq. (2-a,b,c),

$$E_L = C_H \exp(Q_{heat} / RT) \exp(w_t^a(L)/RT) \quad (heating) \qquad (2a)$$

$$E_L = C_H \exp(Q_{cool} / RT) \exp(w_t^a(L)/RT) \quad (cooling) \qquad (2b)$$

$$E_l = C_H \exp(Q_{cool} / RT) \exp(w_t^a(l)/RT) \quad (cooling) \qquad (2c)$$

where w_t^a is the molal interaction energy due to hydride formation, $Q_{heat} = w_{el,p}^{inc} - w_p^{inc}$, and $Q_{cool} = w_{el,p}^{inc} + w_p^{inc}$. Also $w_{el,p}^{inc}$ is the remaining elastic accommodation energy, w_p^{inc} is the molal plastic accommodation energy and C_H the stress-free terminal solid solubility for hydride. In Eq. (1), D_H is the diffusion coefficient of hydrogen in zirconium and $f(L,l)$ is a function of location L, l with conversion factors. Eq. (1) was derived from a hydrogen diffusion equation which described the diffusion of hydrogen from a far-field stress region (L) to a stress concentration region (l). Basically the DHCV is governed by the diffusion coefficient of hydrogen (D_H) and by the terminal solid solubility (C_H) which is related to the dissolution and precipitation of hydrides. It is an important point that DH and CH determine the main temperature dependence of the DHCV. We assume that the temperature dependence of the DHCV is originated from D_H and C_H and that the effect of the yield stress can be separated as an independent function. Therefore, the Puls' DHC model, based on this assumption, can be reformed to Eq. (3) as follows;

$$V_d = A C_H\, D_H\, f(\sigma_{ys}) \qquad (3)$$

where A is a constant, and $f(\sigma_{ys})$ is a function of yield stress.

The form of Eq. (3) is proposed to evaluate the effect of yield stress on the DHCV as an independent function. In the Puls' model, the effect of yield stress is accounted for through the interaction energy of crack tip hydride with the locally applied stress.

In the viewpoints of neutron irradiation, it increased the strength, hydrogen dissolubility [4], and the decomposition content of β-zirconium in Zr-2.5Nb materials. The higher yield strength makes the larger stress gradient at crack front, therefore more hydrogen are accumulated to crack front. Accumulation of hydrogen to crack front make a crack to grow faster than the unirradiated. Higher hydrogen dissolubility in the irradiated also helps a crack to be faster. It is reported that the diffusion speed for hydrogen in the β-zirconium is about second order times faster than in the α-zirconium, and the content of β-

zirconium is increased. In the case of a small cracked area the diffusion speed difference is supposed to be an insignificant affection on the DHCV. Therefore DHCV in the irradiated tube materials ($V_{ir.r.}$) can be comprehensively determined as the following Eq. (4) from it in the unirradiated ($V_{un.}$) considering the material strength and hydrogen solubility etc..

$$V_{irr.} = A \cdot F_{ys} \cdot F_{hs} \cdot V_{un.} \quad (4)$$

Where A is a constant, F_{ys} and F_{hs} are the DHCV acceleration factor for the increased yield strength and the increased hydrogen solubility by neutron irradiation.

Evaluation of acceleration factor by the yield strength

Fig. 9 shows the results of DHCV according to yield strength from the tensile and DHC test results for the irradiated and the unirradiated under 200 °C. The yield strength in the unirradiated are changed by the process of heat treatment. DHCV can be assumed to have a linear exponential relationship between yield strength in figure. Using this relationship and the difference amount of yield strength from the irradiated and the unirradiated, we can calculate the DHCV acceleration factor for the yield strength increase in **Fig. 10**. **Table 1** shows the F_{ys} in various test temperature.

Evaluation of acceleration factor for the dissolved hydrogen content

The effect of irradiation in materials is to trap hydrogen at the irradiation damage sites, and this trapped hydrogen is not available to contribute to the hydride precipitation and dissolution processes [9]. Increasing matrix strength in the irradiated materials should make hydride precipitation less favorable because both elastic and plastic deformation are required to accommodate the substantial local volume change There is a considerable amount of data on hydrogen trapping hydrogen Irradiation defects have roles to prevent hydrogen to diffuse in materials diffusion [9].

These approaches are used to assess the change in solubility due to the irradiation materials. Kearns, Puls, and newly Mcminn reported the terminal solubility solution (TSS) for hydrogen with temperature in unirradiated, and irradiated zirconium base materials [10,6,4]. According to their reports the dissolved hydrogen content in the irradiated Zr-2.5Nb tube materials is 3~8 ppm higher than it in the unirradiated for the same temperature condition in **Fig. 11**. DHCV acceleration factor (F_{hs}) induced by the dissolved hydrogen content can be calculated that DHCV corresponding temperature to the increased dissolved hydrogen content in the unirradiated compares to it to the original temperature. Finally F_{hs} is decided after accounting the F_{ys} portion induced by temperature increase. **Fig. 12** shows the acceleration factor by the dissolved hydrogen content increase in the test temperature, which are calculated **Table 2**.

While the acceleration factor for yield strength has a trend to decrease with temperature increase, it for dissolved hydrogen content has a trend to increase with temperature. An yield strength is generally decrease with temperature and the stress

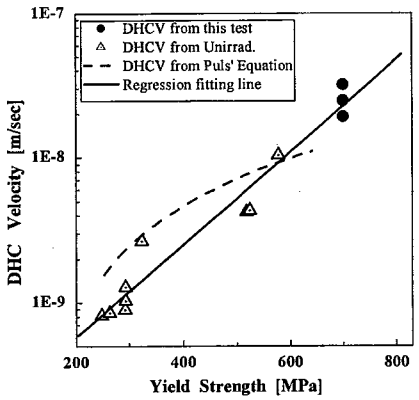

Fig. 9 DHCV variation according to yield strength at 200 °C.

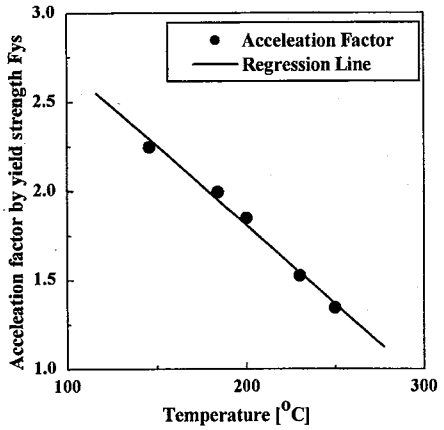

Fig. 10 Acceleration factor by yield strength variation according to temperature.

Table 1 DHCV acceleration factor for yield strength increase with temperature

Temperature [oC]	Yield Strength		Difference of YS [MPa]	Acceleration Factor (Fys)
	Unirradiated	Irradiated		
146	723.3	834.3	110	2.25
184	704.5	798.1	93.5	1.99
200	699.5	783.5	84.0	1.85
230	686.7	744.5	57.8	1.53
250	674.8	715.3	40.5	1.34

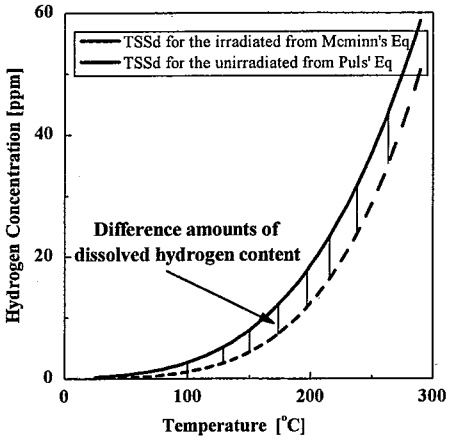

Fig. 11 Dissolved hydrogen content variation according to temperature.

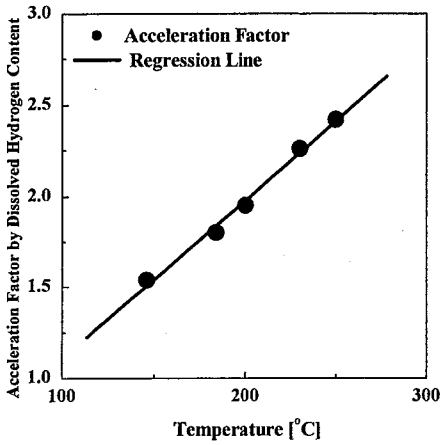

Fig. 12 Acceleration factor variation by dissolved hydrogen content.

Table 2 DHCV acceleration factor by the dissolved hydrogen content increase

Temp. [oC]	Dissolved Hydrogen Content (Cd), [ppm]		Difference (ΔCd)	Corresponding Temp. [oC]	DHCV Acceleration (Fhs x Fys)	Fys	Fhs
	Unirrad.	Irrad.					
146	4.02	7.41	3.39	137.7	1.39	0.90	1.54
184	9.16	14.51	5.35	204.5	1.68	0.93	1.81
200	12.45	18.66	6.21	222.9	1.82	0.93	1.96
230	21.02	28.61	7.59	249.6	2.08	0.92	2.26
250	28.82	37.02	8.8	267.0	2.21	0.91	2.43

gradient in the crack front comes smaller than in low temperature. Therefore this comes that the effect to velocity acceleration comes smaller as the temperature is higher. On the other hand the higher temperature makes the more difference amount in dissolved hydrogen content between the irradiated and the unirradiated.

Verification of test data

Fig. 13 shows the predicted regression line for DHCV in the irradiated from using Eq (4) the unirradiated. In figure the predicted line scaled to only F_{ys} is far from, and inconsistency of trend with temperature change for test data in the irradiated tube. Finally the regression line scaled to F_{hs} multiplied to F_{ys} is well agree to it for the test data in the irradiated. The proposed equation predicts the tested data with 0.12 in standard deviation amount and 95% in coefficient of correlation for the irradiated. Therefore we can easily use Eq. (4) to estimate the DHCV from the test data for the irradiated and the tensile test for the irradiated during the operation of pressure tube.

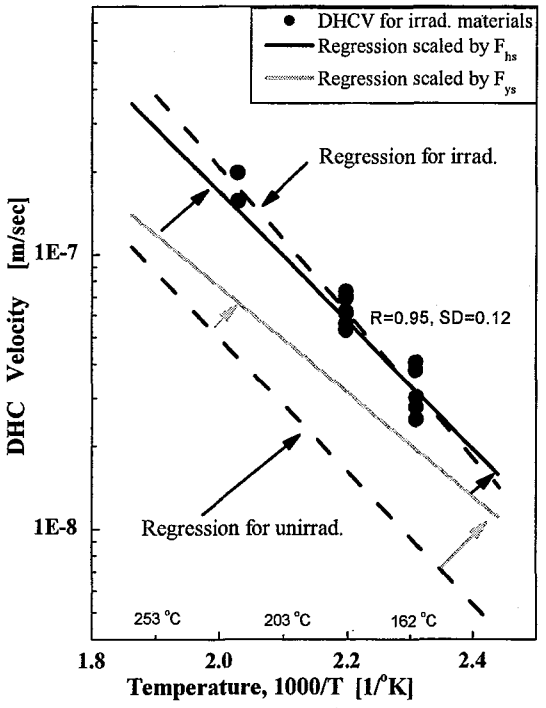

Fig. 13 Prediction of DHCV for the irrad. materials from the unirrad. Ones considering acceleration factors.

SUMMARY

Using the pressure tube materials operated in the commercial CANDU reactor, the behaviors and the prediction model of the delayed hydride cracking velocity for the irradiated materials were reviewed on the point of the effect of neutron irradiation. The DHCV equation of the irradiated materials, which introduce the acceleration factors for the yield strength and the dissolved hydrogen content, is proposed. Using the test data the proposed equation is verified, and the predicted data are well agreed with the test data. The proposed equation can be well used to predicting the DHCV for the operated tube in CANDU reactor.

REFERENCES

(1) Colemann, C. E., Zirconium in the Nuclear Industry, 5th Int. Symp., ASTM STP-754, pp. 393-411, 1982.
(2) Amouzouvi, K. F., Clegg, L. J., Metall. Trans. A, 18A, pp. 1687-1697, 1987
(3) Shek, G. K., Graham, D. B., Zirconium Nuclear Industry 8th Int. Symp., ASTM STP 1023, pp. 89-109, 1989
(4) Mcminn, A., Darby, E. C. and Schofield, J. S., Zirconium Nuclear Industry: 12th Int. Symp., ASTM STP 1354, pp. 173-195, 2000.
(5) Nutall, R., Pulse, M. P., and Simpson, L. A., Metall. Trans. A, 18A, pp. 1553-1562, 1987.
(6) Pulse, M. P., Metall. Trans. A, 21A, pp. 2905-2917, 1990.
(7) Sagat, S., Colemann, S. E., Griffith, M., and Willkins, B. J. S., Zirconium Nuclear Industry 12th Int. Symp., ASTM STP 1245, pp. 35-61, 1994.
(8) Morikawa, H., GKSS Report 81/E/8, GKSS-Forschungszentrum Geesthacht GmbH, 1981.
(9) Lewis, M. B., Journal of Nuclear Materials, Vol. 125, pp. 152-159, 1984.
(10) Kearns, J. J., Journal of Nuclear Materials, Vol. 22, pp. 292-303, 1967.

3.3 SUPERPLASTIC CHARACTERISTICS AND MICROSTRUCTURE OF NEUTRON IRRADIATED 3Y-TZP

Taiju Shibata[1+], Yoshinobu Motohashi[2], Masahiro Ishihara[3], Shinichi Baba[3] and Kazuhiro Sawa[3]

1: Japan Atomic Energy Agency, High Temperature Fuel & Material Group, Nuclear Applied Heat Technology Division
4002 Narita-cho, Oarai-machi, Higashi-Ibaraki-gun, Ibaraki-ken, 311-1393 Japan
+ Studying at Graduate School of Ibaraki University, Japan

2: Research Center for Superplasticity, Faculty of Engineering, Ibaraki University, Hitachi, Ibaraki, 316-8511, Japan

3: Japan Atomic Energy Agency, Japan

ABSTRACT

Fast neutrons (energy > 1.6×10^{-13} J) were irradiated to 3Y-TZP specimens, typical superplastic ceramics, at the fluence of 2.5×10^{24} and 4.3×10^{24} m^{-2} at JMTR of JAEA. The Vickers hardness with indentation load of 4.9 and 9.8 N at room temperature was seemed to be slightly increased by the irradiation. Through the superplastic tensile tests in a temperature range from 1623 to 1773 K with initial strain rates of 5.0×10^{-4} and 1.0×10^{-3} s^{-1}, it was found that the superplastic flow stress is decreased with increasing the neutron fluence. The microstructural features of the fractured specimens were observed by a SEM. It implies that the grain boundary microstructure of the irradiated specimens would be changed by annealing in the superplastic tests at elevated temperatures. It is quite probable that the irradiation-induced vacancy clusters might play an important role to weaken the grain boundary cohesion which may be an important factor to determine the superplastic properties, and hence they would decrease the superplastic flow stress.

KEYWORDS: superplasticity, 3Y-TZP, ceramics, neutron, irradiation, HTGR, hardness, stress, microstructure, SEM

INTRODUCTION

Superplastic ceramics show very high ductility at elevated temperatures[1]. It is probable to form them into net or near-net shapes by means of plastic working as is done for metallic materials[2]. Fine-grained tetragonal zirconia polycrystals containing 3 mol% yttria (3Y-TZP) is a typical superplastic ceramics. Many studies have been carried out on the superplasticity and mechanical properties for 3Y-TZP. Grain boundary sliding and its accommodation processes are believed to be a main superplastic deformation mechanism[3].

High Temperature Gas-cooled Reactors (HTGRs) have received much attention, since they can supply high-temperature helium gas of about 1000 ^{0}C at the reactor outlet and they have inherent safety features due to the large heat capacity of the reactor core[4]. To increase the outlet gas temperature is one of the key technologies to enhance reactor performance. Application of ceramic materials with excellent thermal stability are expected to advance the HTGR performance.

The superplastic ceramics are attractive for the application to the HTGR core in which structural components are used under severe conditions of high temperatures and radiations. However, there have been only a few studies so far concerning irradiation effects on the superplasticity and mechanical properties of them[5-9]. In our neutron irradiation study on 3Y-TZP at a maximum fast neutron fluence of 4.3×10^{24} m^{-2} [8], it has been shown that the elongation to fracture of the irradiated specimens, pulled under superplastic condition, was fairly decreased. The apparent activation energies for the superplastic flows of the irradiated specimens were quite high compared with un-irradiated one. We have pointed out a possible cause that the neutron irradiation would change the grain and grain-boundary microstructures of 3Y-TZP. In this paper, some neutron irradiation effects on hardness at room temperature and the superplastic properties at elevated temperatures are described with relation to its grain microstructures.

EXPERIMENTAL

The experiments were carried out following the study flow shown in **Fig.1**. A fine-grained 3Y-TZP with initial average grain size of 0.39 μm, whose chemical composition is listed in **Table 1**, was used in this study. Flat type tensile specimens with the gauge part of $3^{w}x2^{t}x10^{L}$ mm^3 were prepared for superplastic tensile tests. The each specimen has holes of 5 mm in diameter at its grip ends to attach to the tension machine by pins.

The fast neutron irradiation (energy > 1.6×10^{-13} J) to the specimens was carried out at the Japan Materials Testing Reactor (JMTR) in Japan Atomic Energy Agency (JAEA). The specimens were installed in an irradiation basket with graphite holders in helium gas atmosphere. The irradiation temperature was evaluated about 873 K. Two groups of

irradiated specimens were prepared, namely, the one subjected to the fast neutron fluence of $2.5x10^{24}$ m^{-2} (hereafter referred to as Lightly irradiated) and another subjected to $4.3x10^{24}$ m^{-2} (hereafter Heavily irradiated). After the irradiation, specimens were handled by manipulators at the hot cells of hot laboratory of JMTR. Vickers hardness was measured at room temperature with indentation load of 4.9 and 9.8 N. Superplastic tensile tests were carried out with initial strain rates of $5.0x10^{-4}$ and $1.0x10^{-3}$ s^{-1} in a temperature range from 1623 to 1773 K in the air. The stresses and strains during the tests were measured and evaluated from the load cell and cross-head movement of the tension machine. The superplastically pulled specimens were bent to fracture and their microstructural features of the fracture surfaces were observed by a scanning electron microscope(SEM) in the hot cell.

RESULTS AND DISCUSSION

Vickers hardness

The Vickers hardness of the specimens was measured for the un-irradiated and irradiated specimens. The hardness was measured at ten different points for each specimen with indentation load of 4.9 and 9.8 N at room temperature. The measured hardness is shown in **Table 2**. **Fig. 2** shows the mean hardness in relation to the neutron fluence. For the standard deviation of the measured data, it was difficult to find significant irradiation effects. The mean values at the both indentation loads are seemed to be slightly increased with increasing the neutron fluence. The neutron fluence used in this experiment would not be sufficient to cause significant irradiation-induced hardening and brittleness in the specimen. That is to say, the irradiation damage was not so severe to degrade the mechanical property of 3Y-TZP at room temperature.

Superplastic behavior

The flow stresses of the superplastic tensile test, evaluated as the true stresses at the true tensile strain of 0.1, were listed in **Table 3**. The stress decreases with increasing the neutron fluence. As well known, for metallic materials deformed at low temperatures, neutron irradiation generally increases the stress and decreases the elongation to fracture[10]. In our superplastic tests, the irradiated 3Y-TZP showed a bit different behavior from those mentioned above. Although the irradiation is not sufficient to degrade mechanical properties of 3Y-TZP at room temperature, the superplastic characteristics at the elevated temperatures are seemed to be affected by the irradiation. Since the superplastic tensile tests were carried out at very high temperatures, the irradiation damages, atomic displacements and so on, would be recovered to some extent due to annealing effect. The grain boundary microstructures, which may strongly affect the superplastic characteristics, would be changed through the annealing recovery process during the superplastic deformations. It is

therefore quite probable that the microstructural changes would the decrease the flow stress the irradiated specimens.

Microstructural characteristics

After the superplastic deformation to the engineering strain of 1.0 at 1673 K, the fracture surface of the specimens was observed by SEM. The microstructures are shown in **Fig. 3(a)**, **(b)** and **(c)** for the un-irradiated, Lightly and Heavily irradiated cases, respectively. We can see in **Fig. 3 (a)** the typical inter- and intra- granular fracture features. On the other hand, it is difficult to find such clear features in **Fig. 3 (b)** and **(c)**. It indicated that the grain boundary microstructures of irradiated specimens would be changed by superplastic deformation at elevated temperatures. Moreover, at specimen surface, we had found more cavities in the irradiated specimens than in the un-irradiated one[9]. It implies that the neutron irradiation has weakened the grain boundary cohesion, which may be a crucial factor to determine the superplastic properties [11-13]. The irradiation-induced vacancies would be gathered to make vacancy clusters at the grain boundaries during the superplastic deformation at the elevated temperatures. It is probable that the vacancy clusters would play an important role to weaken the grain boundary cohesion and hence decrease the superplastic flow stress.

The segregation and nuclear transmutation due to the neutron irradiation[8] would also be associated with the changes in the superplastic properties. Further investigations are necessary to clarify the irradiation effects on superplasticity in ceramics.

SUMMARY

The neutron irradiation effects on the Vickers hardness and superplastic characteristics of 3Y-TZP ceramics were examined. The fast neutrons (energy > 1.6×10^{-13} J) were irradiated to 3Y-TZP specimens at the maximum fluence of 4.3×10^{24} m^{-2} at JMTR of JAEA. The Vickers hardness at room temperature was seemed to be slightly increased by the irradiation. Through the superplastic tensile tests in a temperature range from 1623 to 1773 K with initial strain rates of 5.0×10^{-4} and 1.0×10^{-3} s^{-1}, it was found that the superplastic flow stress is decreased with increasing the neutron fluence. The microstructural features of the fractured specimens were observed by the SEM. It implies that the grain boundary microstructure of the irradiated specimens would be changed by annealing in the superplastic tests at elevated temperatures. It is quite probable that the neutron irradiation weakened the grain boundary cohesion. The irradiation-induced vacancy clusters might play an important role for the weakening and hence they would decrease the superplastic flow stress.

ACKNOWLEDGEMENTS

The authors would like to thank the staff members of the JMTR in JAEA for their technical assistance for the neutron irradiation tests and post irradiation examinations.

REFERENCES

(1) Wakai, F., Sakaguchi, S., Matsuno, Y., Adv. Ceram. Mater. 1 (1986) 259.
(2) For example, Motohashi, Y., Shinsozai 4(1993)33 [in Japanese].
(3) Jiménez-Melendo, M., Domínguez-Rodríguez, A., Bravo-León, A., J. Am. Ceram. Soc. 81(1998)2761.
(4) Shiozawa, S., Fujikawa, S., Iyoku, T., Kunitomi, K., Tachibana, Y., Nucl. Eng. Des., 233(2004)401.
(5) Motohashi, Y., Kobayashi, T., Harjo, S., Sakuma, T., Shibata, T., Ishihara, M., Baba, S., Hoshiya, T., Nucl. Instrum. and Methods B 206(2003)144.
(6) Shibata, T., Ishihara, M., Motohashi, Y., Baba, S., Hoshiya, T., Kobayashi, T., Harjo, S., Sakuma, T., Nucl. Instrum. and Methods B 206(2003)139.
(7) Shibata, T., Ishihara, M., Motohashi,Y., Baba, S., Sakuma, T., Hoshiya, T., Mater. Sci. Forum 426-432(2003) 2813.
(8) Shibata, T., Ishihara, M., Motohashi, M., Ito, T., Baba, S., Kikuchi, M., Mater. Trans., 45(2004)2580.
(9) Shibata, T., Motohashi, M., Ishihara, M., Sawa, K., Baba, S., Ito, T., Sumita, J., Proc. of M&P2005, SUP-08, Seattle, USA(2005.6)
(10) For example, Higgy, H. R., Hammad, F. H., J. Nucl. Mater. 55(1975)177.
(11) Thavorniti, P., Ikuhara, Y., Sakuma, T., J.Am.Ceram.Soc. 81(1998) 2927.
(12) Kuwabara, A., Yokota, S., Ikuhara, Y., Sakuma, T., Mater. Trans. 43 (2002) 2468.
(13) Harjo, S., Saroun, J., Motohashi, Y., Kojima, N., Ryukthin, V., Strunz, P., Baron, M., Loidl, R., Mater.Trans., 45 (2004) 824.

Table 1 Chemical composition of 3Y-TZP

Y_2O_3	Al_2O_3	SiO_2	Fe_2O_3	Na_2O	Hf	ZrO_2
5.15±0.2	0.15-0.35	<0.02	<0.01	<0.04	1.7	bal.

(in mass %)

Table 2 Vickers hardness of 3Y-TZP specimens; (a) indentation load of 9.8 N, (b) 4.9 N

	(a) Load: 9.8N		(b) Load: 4.9N	
	Av.	Std.	Av.	Std.
Un-irradiated	1334	14.8	1345	17.1
Lightly irradiated	1342	13.5	1354	12.1
Heavily irradiated	1340	5.7	1356	24.9

Table 3 Superplastic flow stress at true strain of 0.1 for Un-irradiated and Lightly and Heavily irradiated specimens

Temperature / K	Initial strain rate / s-1	Flow stress /MPa		
		Un-irradiated	Lightly	Heavily
1623	5.0E-04	NA	50	44
	1.0E-03	NA	-	NA
1773	5.0E-04	41	26	24
	1.0E-03	57	51	32
1723	5.0E-04	18	12	11
	1.0E-03	NA	24	22

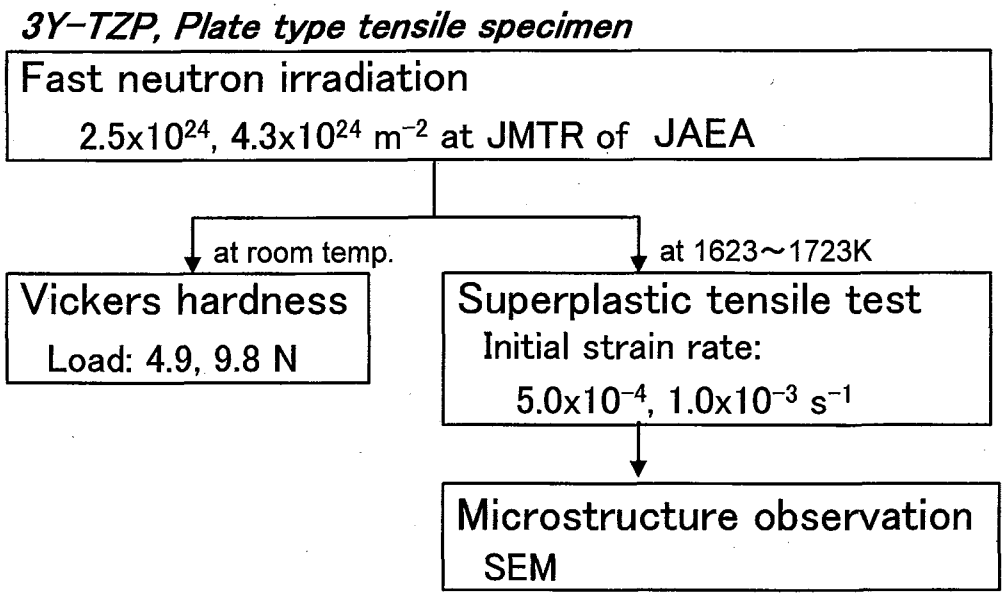

Fig. 1 Experimental study flow.

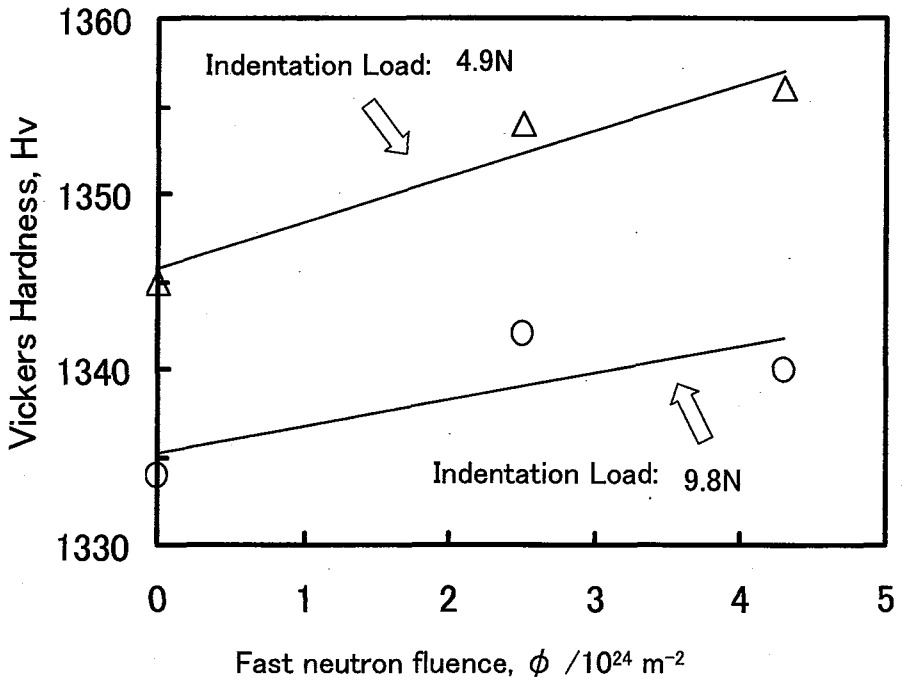

Fig. 2 Mean Vickers hardness in relation to neutron fluence.

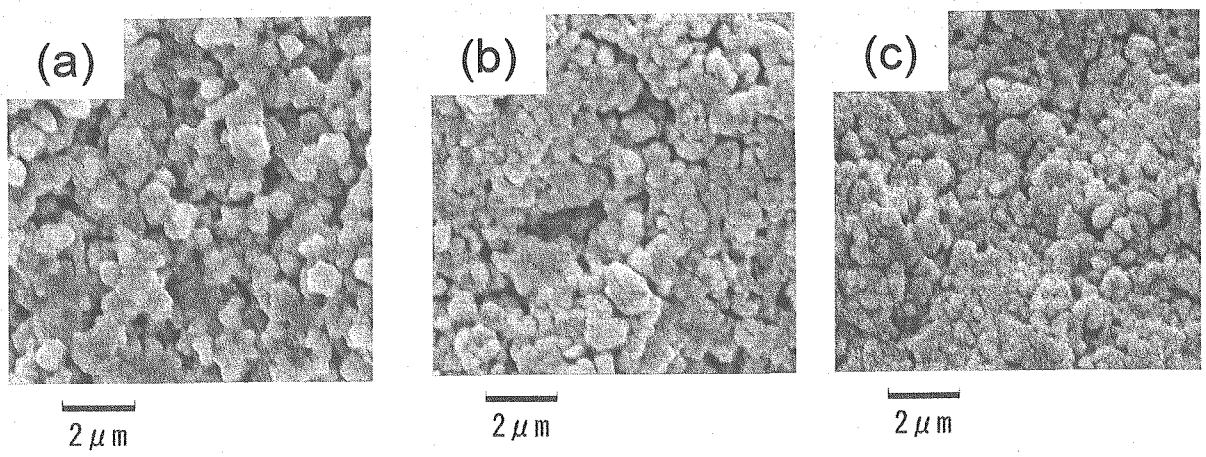

Fig. 3 Fractured surface microstructure after superplastic deformation; (a) Un-irradiated, (b) Lightly and (c) Heavily irradiated.

3.4 INTEGRATED SAFETY RESEARCH PROGRAM OF HIGH BURNUP LWR FUELS

Takehiko Nakamura, Tomoyuki, Sugiyama, Jinichi Nakamura
Fumihisa Nagase and Toyoshi Fuketa

Japan Atomic Energy Agency, Nuclear Safety Research Center,
Fuel Safety Research Group
2-4 Shirakata Shirane, Tokai-mura, Naka-gun, Ibaraki-ken, 319-1195 Japan

ABSTRACT

In order to obtain fuel performance and integrity data important for the safety evaluation of high burnup UO_2 and mixed oxide (MOX) fuel rods for light water reactors (LWRs), new series of irradiation tests utilizing the Japan Materials Testing Reactor (JMTR), Nuclear Safety Research Reactor (NSRR) and hot laboratories are being proposed. Upgraded JMTR loops for the fuel bundle irradiation under well controlled environment simulating the LWR water condition and single rod capsules for power and flow transients will be prepared in the program. Combination of the JMTR tests with simulated reactivity initiated accident (RIA) tests in the NSRR and loss of coolant accident (LOCA) tests in hot laboratories would serve as the integrated fuel safety research on the advanced UO_2 and MOX fuels at burnups exceeding current license limits, covering from the normal to accident conditions.

KEYWORDS: Fuel failure, high burnup fuel, JMTR, NSRR, accident conditions, abnormal transients

INTRODUCTION

Burnup extension of light water reactor fuels has been progressing worldwide to minimize amount of the spent fuels and to achieve more economical operation. Development of new cladding alloy with higher corrosion resistance and modified fuel pellets to minimize fission gas release during the operation is progressing step by step for the purpose. Utilization of mixed oxide (MOX) fuels in light water reactors (LWRs) is being licensed for numbers of pressurized water reactors (PWRs) and boiling water reactors (BWRs) in Japan. The licensed burnup limits for the MOX fuels, however, are lower than those for UO_2 fuels. Therefore, the burnup extension of MOX fuels equivalent to those of UO_2 fuels is desirable for more flexible fuel management, long-term and economic operation. Usage of MOX fuels with higher plutonium content would also be considered for the burnup extension.

In order to make credible safety assessment and to assure the safety operation for these changes, safety evaluation models and criteria need to be modified basing on the reliable data base. New series of irradiation tests utilizing the Japan Materials Testing Reactor (JMTR)[1], Nuclear Safety Research Reactor (NSRR)[2] and hot laboratories are being proposed to provide the reliable data base for the subjects at the Japan Atomic Energy Agency (JAEA), a new organization consisting of the former Japan Atomic Energy Research Institute (JAERI) and the former Japan Nuclear Fuel Cycle Development Corporation (JNC). Upgraded JMTR loops for the fuel bundle irradiation under well controlled environment simulating the LWR water condition and single rod capsules for power and flow transients will be prepared in the program.

OUTLINE OF THE INTEGRATED FUEL SAFETY RESEARCH

A systematic fuel safety research for RIA and LOCA has been conducted in the NSRR and hot laboratories using high burnup fuels irradiated in Japanese LWRs and those from abroad. Their results have been used for safety assessments of high burnup fuels and for establishing safety evaluation guidelines. Another program is being started to refurbish the aged JMTR and to install upgraded normal irradiation loops and transient test capsules. The upgraded JMTR loops for the fuel bundle irradiation would provide on-line measurement and post-test data on fuel behavior under well controlled environment simulating the LWR water conditions. The facility would be able to simulate the new water chemistry, e.g. noble metal and hydrogen addition, and also provide higher burnup UO_2 and MOX fuels for RIA and LOCA tests. Capability of the transient capsules for single rod tests would be extended to cover flow and boiling transients, in addition to the power rumps in the program. Combination of the JMTR tests with simulated reactivity

initiated accident (RIA) tests[3, 4, 5] in the NSRR and loss of coolant accident (LOCA) tests[6, 7] in hot laboratories would serve as the integrated fuel safety research on the advanced UO_2 and MOX fuels at burnups exceeding current license limits, covering from the normal to accident conditions.

NORMAL CONDITION TEST

Irradiation loops for fuel rods in bundle configuration up to 4x4 are being prepared for the normal condition tests in the JMTR. Schematic configuration of the PWR and BWR loops are illustrated in **Fig. 1**. The loops will be installed side by side in the outer part of the JMTR core, as illustrated in **Fig. 2**. Installation works will go in parallel to the refurbishment works of the control rod driving system and secondary cooling system of the JMTR. In the loops, cooling conditions of PWRs and BWRs, including new water chemistry, e.g. noble metal and hydrogen addition, will be carefully simulated, in order to examine influences of the water conditions on the fuel performance. Performance data of modified fuel rods at extended fuel burnups for model development and safety analyses will be obtained from online measurement of fuel temperature, rod internal pressure, etc. and from detailed post test examinations. High burnup fuel samples for transient, RIA and LOCA tests would also be supplied from the normal condition tests. A feasibility study and preliminary designing will be started in year 2006 by sponsorship from Nuclear and Industrial Safety Agency (NISA) of Ministry of Economy, Trade and Industry (METI). Refurbishment of the aged JMTR and installation of the upgraded irradiation loops will be finished in about 6 years after the current operation of the JMTR for material aging study ends in June 2006. Expected rough schedule of the refurbishment and test loop installation in the JMTR is shown in **Fig. 3**.

ABNORMAL TRANSIENT TEST

Power ramp tests of BWR UO_2 fuels has been conducted in the JMTR using BOiling CApsules (BOCAs)[8]. Schematic configuration of the BOCA capsule is illustrated in **Fig. 4**. Capability of the test capsule is going to be extended for flow transients to cover boiling transitions and for PWR cooling conditions. The new transient tests would provide failure criteria of UO_2 and MOX fuels with modified design and materials at high burnups under abnormal transient conditions. The transient tests would also provide fuel performance data at extended burnups for model development and safety analyses from online measurement of fuel and cladding temperature, rod internal pressure, etc. and from detailed post test examinations. Peak linear heat rates would be about 60 kW/m in the tests.

In the latest power ramp tests of BWR fuel rods at burnup of about 60 kWd/kg, longitudinal split failure occurred at relatively low heat rates of about 43kW/m[9]. Investigation on this type of failure associated with hydride behavior under high tensile loading condition is one of the key issues to be studied. Fuel integrity study under cooling conditions with boiling transition is another key to be studied to extend operational limits of the fuels. The integrated transient tests in the JMTR would provide important information on the inter-related thermo-mechanical phenomena of the fuel pellet and the cladding.

REACTIVITY INITIATED ACCIDENT TEST

Nuclear Safety Research Reactor (NSRR) is a modified TRIGA-ACPR (Annular Core Pulse Reactor) of which features the large RIA simulating pulse power capability allowing the 10% enriched fuel to be heated by nuclear fission to above the melting temperature; and large (22 cm in diameter) dry irradiation space located in the center of the reactor core which can accommodate a sizable experiment. About 1,200 RIA tests have been performed by using pulse-irradiation capability of the NSRR, in order to evaluate the thresholds, modes, and consequences of fuel rod failure in terms of fuel enthalpy, fuel burnup, coolant conditions, and fuel design. About 70 tests with irradiated fuel have been conducted since year 1989, the fuel burnups ranges are shown in **Fig. 5**. The tests coved the burnup ranges up to 79 MWd/kg for UO_2 fuel rods and up to 30 MWd/kg for MOX fuel rods. Varieties of fuel design for PWR fuels, including 14x14, 17x17 with cladding of Zircaloy-4, low tin Zircaloy-4, ZIRLO™, MDA and NDA, and for BWR fuels, including 7x7, 8x8 with cladding of Zircaloy-2 with or without Zr liner, have been tested in the RIA study. Four additional RIA tests on European PWR/MOX (59 MWd/kg) and BWR/MOX (45 MWd/kg) fuels are scheduled in about two years, in addition to the current limited data base up to 30 MWd/kg on those from Advanced Thermal Reactor (ATR) "Fugen"[9].

In the study, characteristic cladding failure by pellet cladding mechanical interaction (PCMI) was observed in high burnup PWR and BWR fuel tests, in cases considerable cladding embrittlement occurred due to oxidation/hydriding and irradiation. The cladding failure leads the fuel fragmentation and dispersion, causing mechanical energy generated by the fuel/coolant interaction. Therefore, it is quite important for the safety evaluation of high burnup fuels to clarify the criteria of the failure and significance of the phenomena.

Room temperature test

Double container type test capsules have been used for pulse irradiation of the irradiated fuel rods in the NSRR. The outer capsule is a sealed container of 130 mm in inner diameter and 1,250 mm in height, and the inner capsule is a sealed pressure vessel of 120 mm in inner diameter and 680 mm in height. The outer and inner capsules are illustrated in **Fig. 6**. Assembling and disassembling works of the capsule have to be conducted by

the remote handling, as well as the structural strength. The capsule contains an instrumented test fuel rod, as shown in **Fig. 7**, with stagnant water at atmospheric pressure and ambient temperature. The cooling condition corresponds roughly to the cold start-up conditions of BWRs. Because the cladding failure by the PCMI occurs at quite early stage, in the order of ms, of the short RIA transients, coolant flow condition has the secondary importance on the failure behavior.

High temperature test

The cold start-up RIAs do not occur in PWRs, because the water is heated before the nuclear start-up. Ductility or toughness of the embrittled high burnup fuel cladding could be recovered to some extent at the higher temperatures for the hot stand-by conditions of PWRs. Therefore, pulse irradiation tests at high temperature are being realized with a new high temperature test capsules, as illustrated in **Fig. 8**, in order to minimize possible excess safety margins in the criteria obtained from the cold tests. The coolant water in the high temperature capsule could be electrically heated to about 280 ℃ prior to the pulse irradiation, in order to simulate hot stand-by conditions. The system pressure in the capsule is limited to about 7 MPa. The importance of the pressure, however, is believed to be limited from the above mentioned view points. The instrumentation in the capsule is limited to thermocouples for water and cladding temperature, static and dynamic pressure sensors for water and gas atmosphere in the capsule.

Separate effect test

Magnitude of the destructive driving force on the fuel cladding by fission gases accumulated in the pellets could be enhanced with the progress of the burnup. The burnup effects could become significant non-linearly with formation of high burnup structure (HBS), so called the rim structure. In the context, Fission Gas Dynamics (FGD) tests[10] is being defined as a collaboration program with French IRSN (Institut de Radioprotection et de Sûreté Nucléaire) in order to investigate a role of fission gas in rod deformation, cladding failure and fuel fragmentation in an RIA. Configuration of the test arrangement is illustrated in **Fig. 9**. Dynamic fission gas pressure loading and permeability of the gas through the fuel stack in the cladding will be investigated with sliced and segmented fuels with highly precise pressure measurement. High burnup fuel disks irradiated in the Halden IFA 655 is considered as one of candidate specimens in order to clarify the effects of the high burnup rim structure on the behavior.

LOSS OF COOLANT ACCIDENT TEST

Maintaining the coolable geometry of the reactor core is essentially important to limit the consequence of the LOCA, after the emergency core cooling system (ECCS) water is

injected and subsequent quenching takes place during the LOCA transients. In order to examine the fuel rod sustainability after the heavy oxidation during the LOCA transient, the integral thermal shock tests are currently performed with high burnup PWR fuel claddings in hot laboratories[11]. Two PWR fuel rods with low-Sn (1.3wt%) Zircaloy-4, irradiated to about 39 and 44 MWd/kg (rod average), were examined in the study. The outer diameter and thickness, as-fabricated, are 9.50 and 0.57 mm, respectively. The fuel rod was cut into 190 mm segments and defueled for the tests. Alumina pellets were loaded into the fuel cladding to simulate heat capacity of UO_2 pellets. The rods were pressurized to about 5 MPa with Ar gas at room temperature.

Schematic of the integral thermal shock test apparatus for the LOCA is illustrated in **Fig.10**. The apparatus is consisted with an Instron-type tensile testing machine, a quartz reaction tube, an infrared image furnace with four tungsten-halogen lamps, a steam generator, and a water supply system for flooding. The test rod was subjected to the LOCA conditions including oxidation at high temperature and quench by flowing water inside the quartz reaction tube. By fixing the top end of the test rod, it enables to axially restrain the test rod and measure load changes. An example of typical temperature history during the LOCA test is shown **Fig. 11**. The rod is heated up at a rate of 10 K/s in steam flow of about 36 mg/s, sufficiently high to oxidize cladding tubes without steam starvation. The rod is isothermally oxidized at temperatures from 1430 to 1470 K and for 120 to 500 s, after it ballooned and ruptured at about 1050 to 1100 K during the heat up. Test temperature is monitored and controlled by four Pt-Pt/13%Rh thermocouples spot-welded on the outer surface of the cladding. The rod is cooled in the steam flow to about 970 K and is finally quenched with water flooding from the bottom. The average cooling rate is about 20 to 5 K/s.

SUMMARY

Research on fuel performance under accident conditions, i.e. on reactivity initiated accidents (RIAs) and loss of coolant accidents (LOCAs), has been conducted successfully on high burnup UO_2 and mixed oxide (MOX) fuel rods using Nuclear Safety Research Reactor (NSRR) and hot laboratories. The RIA study is going to be extended to cover high temperature conditions and to clarify influence of fission gases in separate effect tests. In addition, new series of irradiation tests utilizing the Japan Materials Testing Reactor (JMTR) is in preparation stage to extend the research on the normal conditions and abnormal transient conditions. The upgraded JMTR loops for the fuel bundle irradiation under well controlled environment simulating the LWR water condition and single rod capsules for power and flow transients will be prepared in the program. Outlines of the program and the facilities are presented in this paper. Combination of the JMTR tests with simulated RIA tests in the NSRR and LOCA tests in hot laboratories would serve as the

integrated fuel safety research on the advanced UO_2 and MOX fuels at burnups exceeding current license limits, covering from the normal to accident conditions.

REFERENCES

(1) M. Kanno, S. Sakurai, K. Honma, H. Sagawa and C. Nakazaki, "Impruvement of Irradiation Facilities Performance in JMTR," Proc. 6th Asian Symposium on Research reactors, March 29-31, 1999, Mito, Japan, JAERI-Conf 99-006, (1999).

(2) T. Fuketa, T. Sugiyama, H. Sasajima and F. Nagase, "NSRR RIA-simulating Experiments on High Burnup LWR Fuels", No. 1106, Proc. Water Reactor Fuel Performance Meeting, Oct. 3-6, Kyoto, Japan, CD-ROM, (2005).

(3) T. Fuketa, H. Sasajima and T. Sugiyama, "Behavior of High Burnup PWR Fuels with Low-Tin Zircaloy-4 Cladding Under Reactivity-Initiated-Accident Conditions", Nucl. Technol., Vol.133, No.1, pp.50-62, (2001).

(4) T. Nakamura, K. Kusagaya, T. Fuketa and H. Uetsuka, "High Burnup BWR Fuel Behavior under Simulated Reactivity-Initiated Accident Conditions", Nucl. Technol., Vol.138, pp.246-259, (2002).

(5) T. Sugiyama, T. Fuketa, M. Ozawa and F. Nagase, "RIA-simulating Experiments on High Burnup PWR Fuel Rods with Advanced Cladding Alloys", Proc. Int. Top. Mtg. on Light Water Reactor Fuel Performance, Sep. 19-22, Orlando, Florida, U.S.A., CD-ROM, (2004).

(6) F. Nagase and T. Fuketa, "Behavior of Pre-hydrided Zircaloy-4 Cladding under Simulated LOCA Conditions," J. Nucl. Sci. Technol., Vol.42, No.2, 209, (2005).

(7) T. Fuketa, F. Nagase and T. Sugiyama, "RIA- and LOCA- simulating experiments on high burnup LWR fuels," Proc. IAEA Technical Mtg. on Fuel Behavior Modeling under Normal, Transient and Accident Conditions and High Burnups, Sep. 2005, Kendal, UK.

(8) J. Nakamura, M. Shimizu, Y.Endo, H. Nabeya, K. Ichise, J. Saito, K. Ohshima and H. Uetsuka, "Re-irradiation Tests of Spent Fuel at JMTR by Means of Re-instrumentation Technique," Proc. 3rd JAERI-KAERI Joint Seminar on PIE Technology, March 25-26, 1999, JAERI-Conf. 99-009 (1999).

(9) H. Sasajima, T. Fuketa, T. Nakamura, J. Nakamura and K. Kikuchi, "Behavior of Irradiated ATR/MOX Fuel under Reactivity Initiated Accident Conditions," J. Nucl. Sci. Technol. 37, 5, 455-464, (2000).

(10) F. Lemoine, "High Burn-up Fuel Behavior Related to Fission Gas Effects under Reactivity Initiated Accidents (RIA) conditions", F. Lemoine, J. Nucl. Mater., 248, 238-248, (1997).

(11) F. Nagase and T. Fuketa, "Embrittlement and fracture behavior of pre-hydrided cladding under LOCA conditions," Paper No. 1102, Proc. International Conf. on Water Reactor Fuel Performance, Oct. 3-6, 2005, Kyoto.

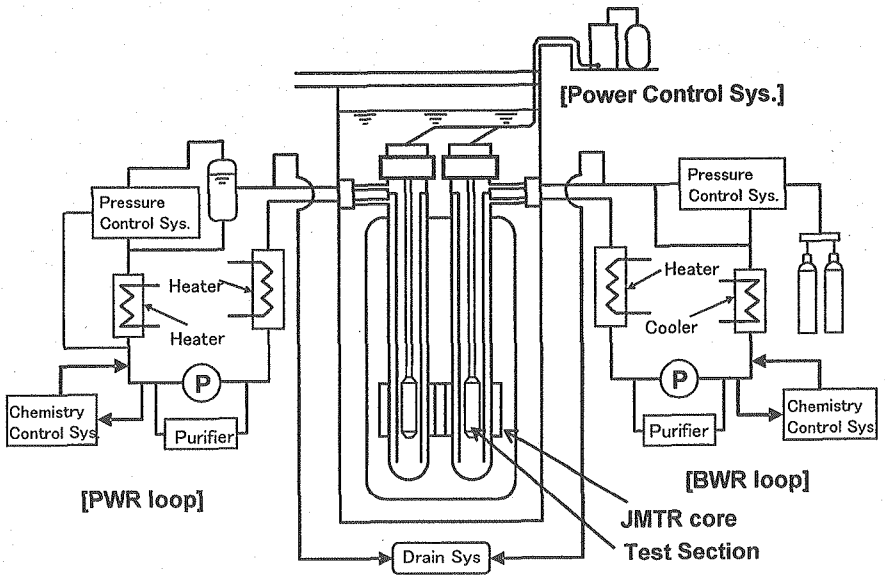

Fig. 1 Schematic configuration of JMTR loops for normal irradiation test.

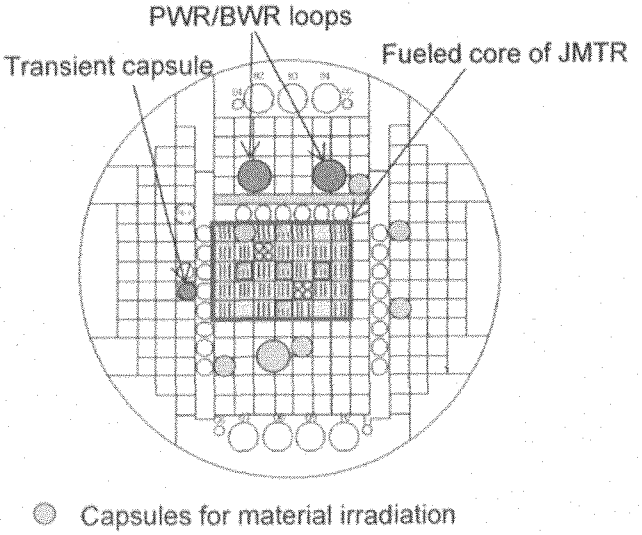

Fig. 2 Expected core arrangement of JMTR for fuel and material irradiation tests.

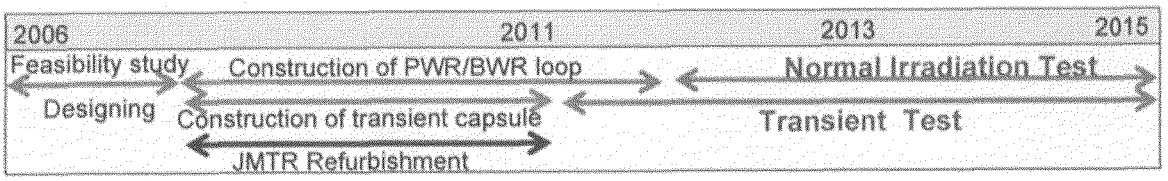

Fig. 3 Expected time schedule for refurbishment of JMTR and installation of test rigs.

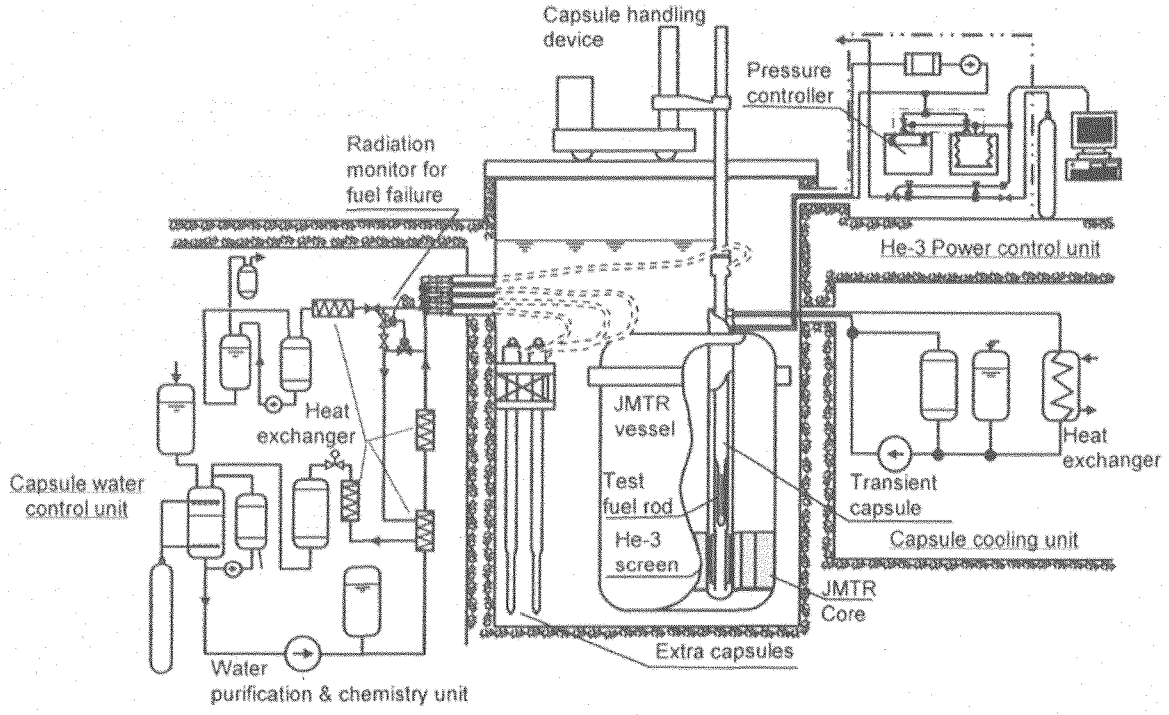

Fig. 4 Schematic configuration of transient test capsule in JMTR.

Test fuels	Fuel burnup (MWd/kg) 10 20 30 40 50 60 70	Number of tests
PWR (14x14, 17x17)		29
BWR (7x7, 8x8)		16
ATR/MOX		6
JMTR pre-irradiated		22

Fig.5 Burnup range of test fuels for RIA tests in NSRR.

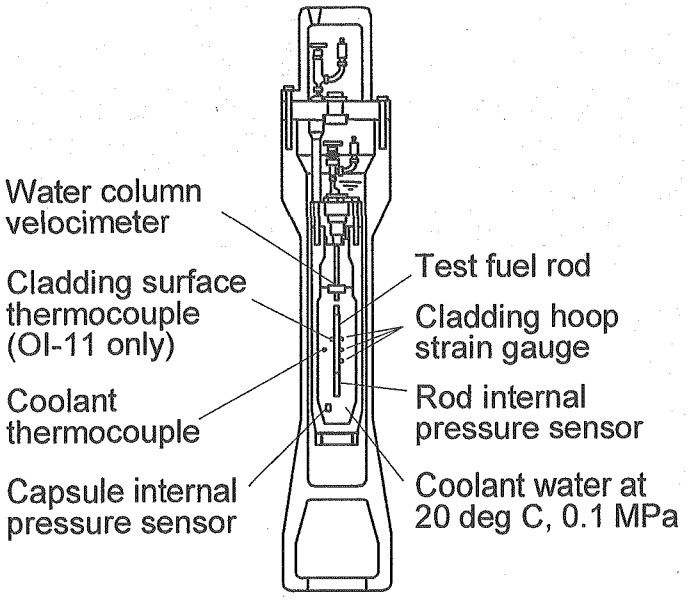

Fig.6 NSRR test capsule for room temperature conditions.

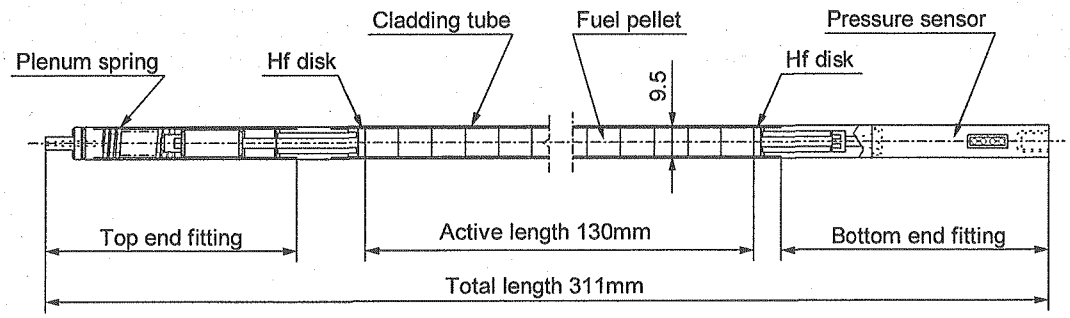

Fig.7 Design of test fuel rod for NSRR RIA tests (17x17 PWR fuel).

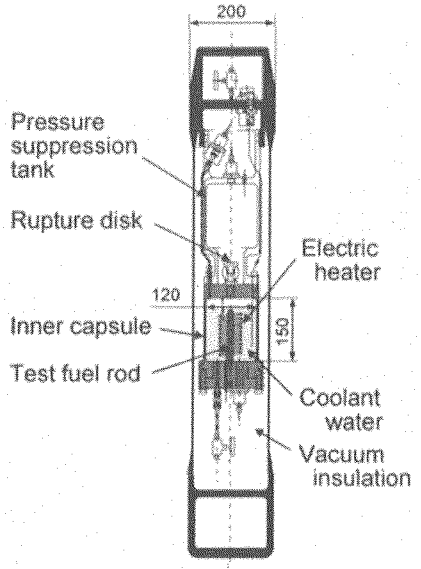

Fig.8 NSRR test capsule for high temperature conditions.

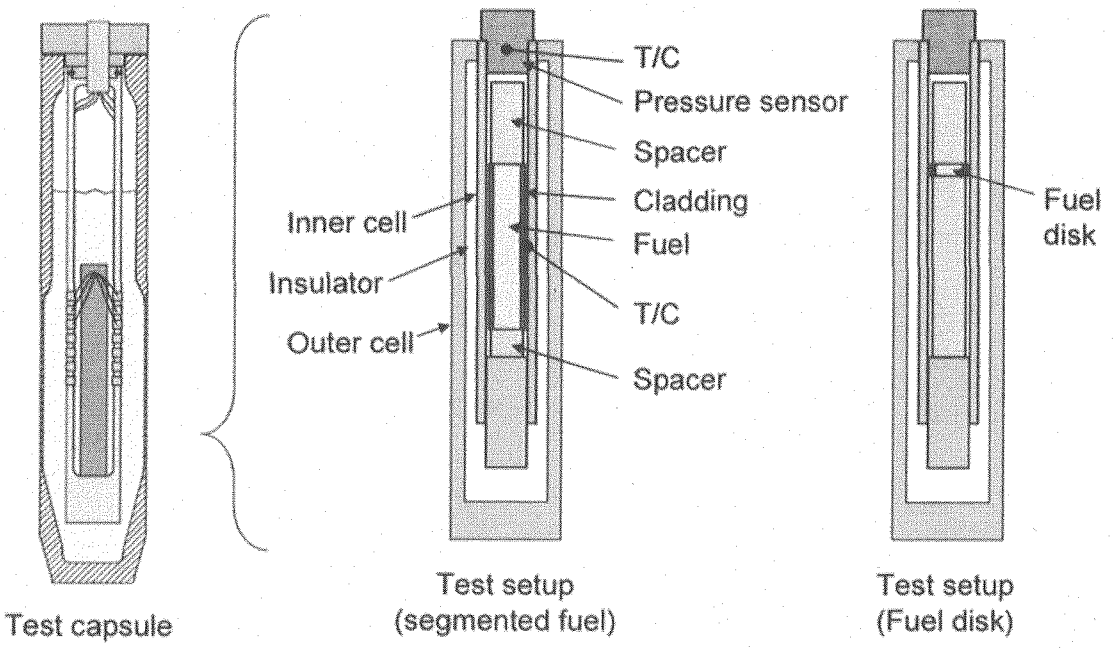

Fig. 9 Configuration of Fission Gas Dynamics test arrangement.

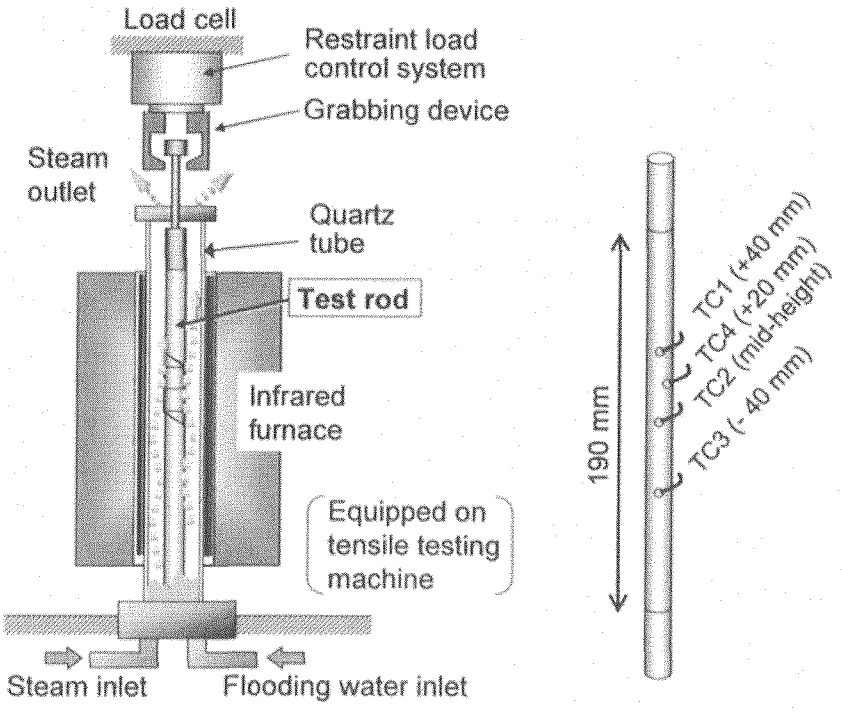

Fig.10 Schematic of test apparatus of LOCA test and thermocouple positions.

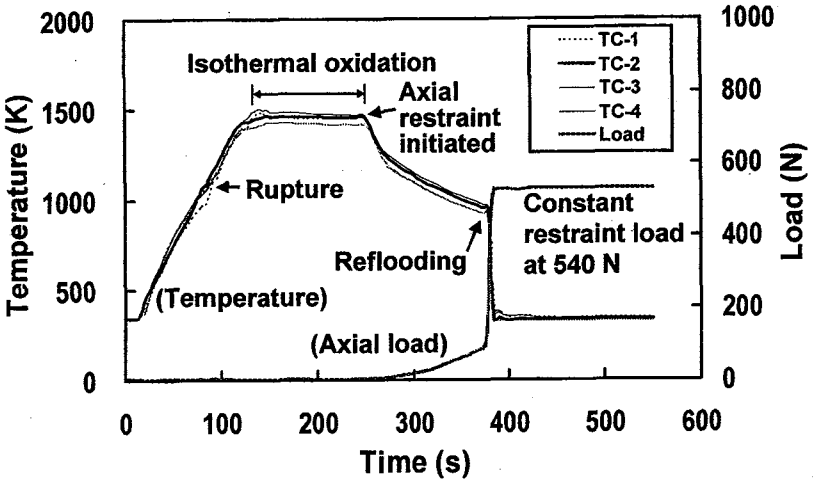

Fig.11 Example of temperature and axial load changes during LOCA test.

3.5 Xe-DIFFUSION COEFFICIENT IN PURE URANIA AND SIMULATED BURNUP URANIA FUEL PELLETS

Kwangheon Park[1], Dongsoo Lee[1], Heemoon Kim[2], Bong Goo Kim[2], Yong Sun Choo[2],Keon Sik Kim[2], Kun Woo Song[2], Kwon Pyo Hong[2], Kichan Song[2], Kwonho Kang[2], Young Hwan Kang[2] and Hojin Ryu[2]

1: Dept. of Nuclear Engineering, Kyunghee University
Seochon-1, Kiheong, Yongin, Kyunggi, 449-701, Rep. of Korea
kpark@khu.ac.kr

2: Korea Atomic Energy Research Institute
150 Ducjin, Yusung, Daijeon, 350-353, Rep. of Korea

ABSTRACT

Xe Diffusion coefficients (Xe-133) in urania and simulated burnup fuel (simfuel) pellets were measured by post irradiation annealing tests. Specimens were powders and pellet cubes. The weight of each cube (2x2x2 mm^3) was about 100mg. Burnup of 0.1 MWd/t-U for each specimen was obtained after irradiation and post irradiation annealing tests were performed at temperatures between 1400 and 1600°C continuously. Diffusion coefficients were obtained by measuring the gamma activity of Xe-133 accumulated in the liquid nitrogen trap with time. Measured diffusion coefficients were compared with those of uranium dioxide (UO_2), mixed thorium-uranium dioxide [$(Th,U)O_2$]. Diffusion coefficients of simfuels are similar to those in the polycrystalline UO_2 at the experimental temperatures with lower activation energy.

INTRODUCTION

Fission gas release modeling is one of important parts in the fuel performance analysis. The diffusion coefficients of the fission gases in the uranium dioxide (UO_2) based fuels used in light water reactors are required in building up a fission gas release model. The diffusion coefficients are a function of temperature, burnup, and stoichiometry. Diffusion coefficient

data from a number of experiments with UO_2 fuel have been published[1]-[2]. The lattice diffusion coefficients measured out-of-pile are mostly dependent on temperature and oxygen potential. The in-pile effects are related to irradiation induced traps such as bubble creation in the matrix. Turnbull and Lewis have suggested diffusion coefficient models that consist of three terms - intrinsic, non-stoichiometric, and irradiation induced effects[7].

Highly-irradiated fuels contain lots of fission products. Generally, the diffusion of fission gases through the solid matrix depends on the defect structure of the solid. The fission products can change the defect structure of the fuel, and may affect the diffusion processes of fission gases. However, the effects of these fission products on the diffusion of fission gases have not been fully analyzed in detail. Therefore, the purpose of this research was to obtain Xe-133 lattice diffusion coefficients in simulated high-burnup fuel (simfuel). We compare those data with diffusion coefficients of UO_2 and $(Th,U)O_2$ fuel.

EXPERIMENTS

The polycrystalline simfuels were made by mixing simulated fission products (13 elements) with the UO_2, and by sintering at high temperatures. Then they were cut into 2x2x2 mm ($8mm^3$) cubes. The theoretical densities of simfuels were 97%. Two types of pellets simulating the burnup of 27,500 and 55,000 MWD/MTU were prepared. The pellet of 27,500 MWD/MTU contains metallic precipitates, while that of 55,000 MWD/MTU contains solid solution only. The properties of specimens in this study are shown in **Table 1**. We allocate an index for each type of specimens such as 'SU' for single-grained UO_2, 'PU' for polycrystalline UO_2, 'PT' for polycrystalline $(Th,U)O_2$, and 'PS' for polycrystalline simfuel.

Table 1 Properties of urania and simfuel specimens used for experiments

Specimens	Type	Density	Grain size
Single UO_2 Powder (SU)	powder	95%	23±2 μm
Single UO_2 Polycrystal (PU)	Cubes $(2\times2\times2)mm^3$	95%	8.1±0.5 μm
Polycrystalline Simfuel (PS)		95%	10.1±1 μm
Polycrystalline Simfuel (MS)		97%	10.5±2 μm

*PS : 55,000 MWD/MTU without metallic precipitates; MS : 27,300 MWD/MTU with metallic precipitates.

Each fuel specimen was contained in a sealed quartz tube, placed into a double-layered aluminum capsule for thermal safety during irradiation, and was irradiated in the HANARO research reactor up to a burnup of 0.1 MWd/t-U. After irradiation, the specimen was cooled for 10~11 days to reduce the irradiation exposure. We used about 300mg of fuel for each irradiation and annealing test. The sketch of the experimental apparatus is shown in **Fig. 1**. It has two sections: the annealing furnace and the trap systems. The specimens were loaded into this furnace with a motorized device. An oxygen sensor was installed at the top of the furnace to measure the oxygen potential of the ambient gas.

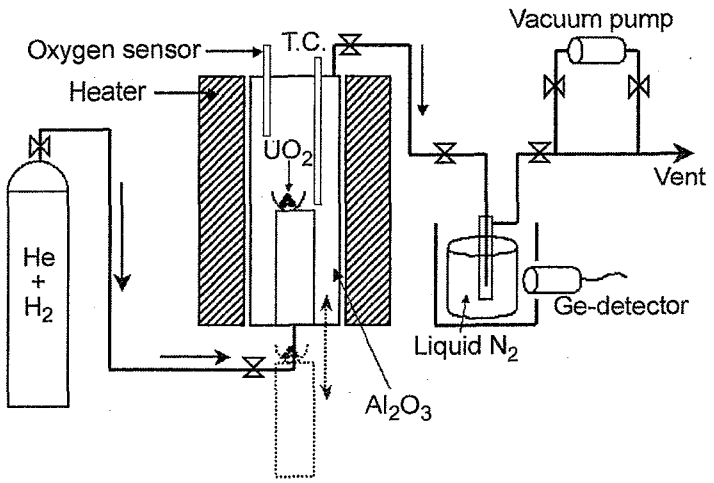

Fig. 1. Schematic of the annealing apparatus.

The trap system was designed to trap the released gases, such as Kr, Xe, and I. The trap material was granular activated carbon inside the trap glass casing, and this glass equipment was placed into liquid nitrogen and surrounded by a lead casing. Liquid nitrogen was used as a cryogenic agent in order to convert the Xe-133 gas to a solid. A Ge detector was installed through a hole in the lead casing of the trap system and measured the gamma rays from the trapped fission gases. Helium gas flowed through the system to transport the released fission gases into the trap system. The helium was mixed with hydrogen in order to control the oxygen potential of the gas and, therefore, the stoichiometry of the specimen. The flow rate of the helium was fixed at 100 ml per minute during the annealing tests.

RESULTS AND DISCUSSION

The fraction of the fission gases released from a given specimen was obtained from the measurements of both the total amount of fission gases remaining in the specimen and the

amount collected in the trap. To obtain the total amount of fission gases in the specimen, we put the specimen in a measurement apparatus of absolute gamma-ray activities, and measured the absolute activities of Xe-133, I-132 and La-140 in the specimen before the annealing experiment. Since the peak energy of Xe-133 (81 keV) is located in a low energy region where the background noise is relatively high, the measured activity of Xe-133 is not accurate enough to be used as a total amount. Hence, the amount of Xe-133 in the specimen was calculated from the exact burnup of the specimen that was obtained from the absolute activities of I-132 and La-140. ORIGEN-II was used for the calculation of the burnup and that of Xe-133 amount. The released amount of X-133 in the liquid nitrogen trap was measured directly by the Ge-detector, where the absolute activity was obtained from a calibration using reference sources (Ba-133, Cs-137) in the trap geometry. The annealing temperature was not fixed throughout the experiment, but changed step-wise to a fixed value during the experiment. Burst release behavior was observed at the change of each temperature.

We used Booth's model[8] to determine the diffusion coefficients of the fission gases from the fractions released from the specimens with respect to time. The solution of the released fraction, f, during the stepwise change of temperature in the post annealing tests can be obtained from Eq. (1).

$$f^2 = \frac{36}{\pi}\frac{Dt}{a^2} = \frac{36}{\pi}D't \qquad (1)$$

where a is the radius used in Booth's model, D is the diffusion coefficient, and D' is empirical diffusion coefficient.

Matzke[9] introduced a plot of the square fraction (f^2) with time to give a more straightened slope at each temperature rather than a plot of 'f' with $t^{1/2}$. Une[10] performed post-annealing experiments with stepwise changing temperatures, and obtained reasonably good diffusion coefficients. We obtained our diffusion coefficients based on the slopes in the plots of f^2 versus t. **Table 2** shows the Xe-133 diffusion coefficients of the specimens used in the experiments, based on the slope analysis. We neglected the burst behavior part that appeared at the temperature change. All diffusion coefficients contain about 20% error that comes from the slope-value determination.

Fig. 2 shows the empirical diffusion coefficients (D') of simfuels and those of other polycrystalline specimens that have been measured by the authors. The diffusion coefficients of simfuels (PS1,MS1) are very close to those of UO_2 fuel. Presence of metallic precipitates (MS1) in the fuel seems to reduce the diffusion coefficients down to the half values of those of solid-solution simfuel (PS1). The amount of simulated fission- products added to fuel is small (ca. 6%) even in the simfuel of high burnup, which may be the reason why the diffusion

coefficients of simfuels are not quite different from those of UO_2 fuel. The valence of some of soluble fission products (Y, La, Nd) added to the fuel is 3+, which is expected to increase oxygen vacancies. This extrinsic defect structure may lower the activation energy of diffusion coefficients of simfuels.

Table 2 Diffusion coefficients of Xe in all specimens

Specimen notation	Oxygen potential (UO_{2+x})	Empirical Diffusion coefficient ($D'=D/a^2$ [1/sec])				Activation Energy** (kJ/mol)
		1400 °C	1500 °C		1600 °C	
PU1	-370kJ/mol ($x<10^{-3}$)	3.31×10^{-12}	1.15×10^{-11}		3.5×10^{-11}	307
PU2	-250kJ/mol ($x=0.01$)	3.77×10^{-11}	8.59×10^{-11}		2.50×10^{-10}	245
PS1	-370kJ/mol ($x<10^{-3}$)	1400 °C	1467 °C	1534 °C	1600 °C	185
		6.69×10^{-12}	1.09×10^{-11}	1.99×10^{-11}	2.66×10^{-11}	
MS1	-370kJ/mol ($x<10^{-3}$)	4.36×10^{-12}	7.57×10^{-12}	1.13×10^{-11}	1.35×10^{-11}	148
SU1*	-370kJ/mol ($x<10^{-3}$)	1.43×10^{-19}	4.05×10^{-19}		1.44×10^{-18}	300
SU2*	-110kJ/mol ($x=0.1$)	8.30×10^{-18}	2.61×10^{-17}		1.47×10^{-16}	372

*The diffusion coefficients of SU1 and SU2 were obtained based on the measured grain size (23μm), and the units are 'm^2/sec.' ** Values contain about 20% error.

Killeen and Turnbull[4] assumed that xenon migrated by uranium vacancies, so they employed a uranium vacancy concentration model based on the models of Lidiard[11] and Sharp[12] in their interpretation of their measured diffusion coefficients. However, Matzke[13] proposed a mechanism of xenon diffusion via neutral tri-vacancies. This proposition was deduced from doping experiments in which the diffusion rate of the xenon was not different in the undoped and the doped UO_2. This implies that xenon does not migrate via uranium vacancies only. Whatever interpretation is correct, the diffusion of fission gases is considered to be strongly related to the concentration of cation vacancies in the fuel.

The major point defects in the urania fuel are anion Frenkel pairs, and mostly oxygen interstitials in hyperstoichiometric fuel. The cation vacancies are in equilibrium with the oxygen vacancies forming Schottky defect pairs. With an increasing hyperstoichiometry of the fuel, the oxygen vacancy concentration decreases due to the anion Frenkel defect equilibrium, resulting in an increase in the cation vacancy concentration from the Schottky defect equilibrium. This increase of cation vacancies enhances the diffusion of the fission gases in the hyperstoichiometric fuel. In the case of simfuels, soluble fission products, especially trivalent ions, can make oxygen and cation vacancies in the matrix extrinsically. This seems the reason why the simfuels have lower activation energies of diffusion coefficient than UO_2 fuels.

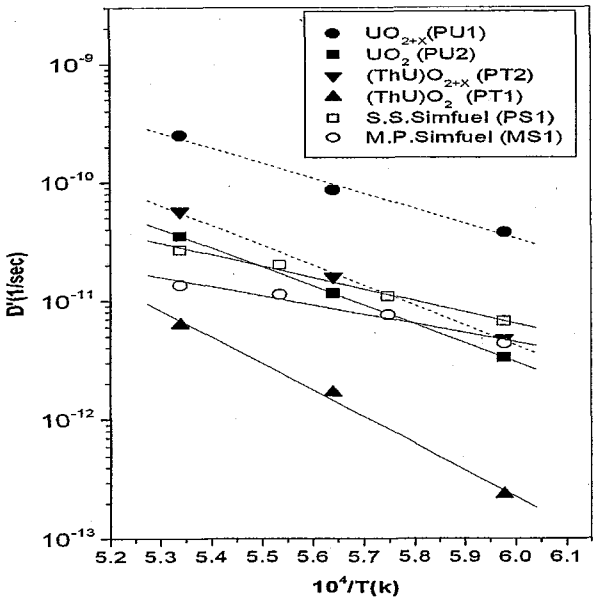

Fig. 2. Empirical diffusion coefficients of polycrystalline specimens.

CONCLUSIONS

The diffusion coefficients of Xe-133 in simfuel have been measured. The diffusion coefficient was obtained from the Xe-133 release fraction for each specimen during annealing tests. The $(Th,U)O_2$ fuel has one-order of magnitude lower Xe-133 diffusion coefficients than the UO_2 fuel. Simfuels have the similar diffusion coefficients of Xe-133 to those of UO_2 fuel. However, the activation energy in simfuels is much lower than that in UO_2 fuel. The extrinsically formed oxygen vacancies by trivalent fission products may explain the lower activation energy.

ACKNOWLEDGMENTS

This work was supported by the Ministry of Science and Technology of the Republic of Korea under the Long- and Mid-term development of Nuclear Energy.

REFERNCES

(1) M.A.Mansouri, D.R.Olander, "Fission product release from trace irradiated UO2+X", J. Nicl. Mater., 254, 22 (1998)

(2) K. Une, I. Tanabe, and M. Oguma, "Effects of Additives and The Oxygen Potential on The Fission Gas Diffusion in UO2 Fuel.", J. Nucl. Mater., 150, 93 (1987)

(3) J. R. MacEwan and W. H. Stevens, "Xenon diffusion in UO2", J. Nucl. Mater., 11, 77 (1964)

(4) J. C. Killeen, J. A. Turnbull, "An experimental and theoretical treatment of the release of Kr-85 from hyperstoichiometric uranium dioxide.", Proc. Sym. on chemical reactivity of oxide fuel and fission product release, Berkeley, UK (1987)

(5) Hj. Matzke, Radiation Effects, "Radiation enhanced diffusion in UO2 and (U, Pu)O2", 75, 317 (1983)

(6) J. A. Turnbull, C. A. Friskney, J. R. Findlay, F. A. Johnson, A. J. Walter, "The diffusion coefficients of gaseous and volatile species during the irradiation of uranium dioxides.", J. Nucl. Mater., 107, 168 (1982)

(7) B. J. Lewis, B. Szpunar, "Modelling of Fuel Oxidation Behavior in Operationg Deffective Fuel Rods", Proc. Sym, on Fission Gas Behavior in Water Reactor Fuels, Cadarache, France (2000) 293-310

(8) A. H. Booth, "A Method of Calculating Fission Gas Diffusion from UO2 Fuel and Its Application to The x-2-f Loop Test.", CRDC-721 (1957)

(9) Hj. Matzke, Radiation Effects, "Gas release mechanisms in UO2-A critical review.", 53, 219 (1980)

(10) S. Kashibe and K. Une, "Effect of additives (Cr2O3, Al2O3, SiO2, MgO) on diffusional release of Xe-133 from UO2 fuels.", J. Nucl. Mater., 254, 234 (1998)

(11) A. B. Lidiard, "Self-diffusion of uranium in UO2.", J. Nucl. Mater., 16, 106 (1966)

(12) J. V. Sharp, "Radiation enhanced diffusion", AERE Report No.6267 (1969)

(13) Hj. Matzke, "Diffusion in Doped UO2.", Nuclear Applications, 2, 131 (1966)

3.6 CHARACTERIZATION OF FISSION PRODUCTS OF IRRADIATED SIMFUEL

Yang-Hong Jung, Byung-Ok Yoo, Hee-Mon Kim, Yong-Sun Choo, Kwon-Pyo Hong and In-Ha Jung

Korea Atomic Energy Research Institute
150, Dukjin-Dong, Yuseong-gu, Daejeon, 305-353, Korea

ABSTRACT

Fission products of SIMFUEL (SIMulated nuclear FUEL), irradiated in the HANARO research reactor with a 61 kW/m maximum linear power and 1,770 MWd/MTU average burn-up, were characterized by EPMA(Electron Probe Micro-Analyzer). In order to obtain an accurate characterization, the analysis results by EPMA of fresh simulated fuel containing the fission products as chemicals were compared with that of a wet chemical analysis. The metallic precipitates observed at the center of the un-irradiated SIMFUEL were about 1 ㎛ in size and their major components by EPMA were Mo-53.89 at.%, Ru-37.40 at.%, and Pd+Rh-8.71 at.%. The established procedure for the un-irradiated SIMFUEL was applied to the irradiated SIMFUEL. Observed size of the metallic precipitates were 2~2.5 ㎛ and their compositions were Mo-47.34 at.%, Ru-46 at.%, and Pd+Rh-6.65 at.% The uncommon things from this experiment are a special treatment for improving the conductivity was attempted for the specimen and the conditions of on exact irradiation of an electron beam to a small metallic precipitate were suggested.

KEYWORDS: EPMA, Fission Products, SIMFUEL, Metallic Precipitates, Specimen Preparation, Perovskite Phase.

INTRODUCTION

More than 30 fission products are generated from UO_2 fuel during irradiation in a reactor. The composition of the fission products are mainly determined by fissionable materials, critical power, neutron energy, irradiation period and cooling time[(1)].

Since a high radiation prohibits the irradiated fuel from direct examinations, such as measuring the concentration of the fission products, evaluation of the fuel performance, the

thermal and mechanical properties, simulated fuels have been used frequently instead[2].

Experimentally, simulated spent fuels are fabricated by adding chemicals into UO_2 powder to as much as their burn-up production rate. Experimental data of the fuel property, fission gas release, grain growth, etc. for them are used for characterizing the fuel behavior in a reactor and the fuel performance.

Fission products existing in the spent fuel can be group as follows[3];

(a) Elements dissolved in a matrix : Sr, Zr, Nb, Y, La, Ce, Pr, Nd, Pm, Sm

(b) Metallic precipitates : Mo, Tc, Ru, Rh, Pd, Ag, Cd, In, Sb, Te

(c) Oxide precipitates : Ba, Zr, Nb, Mo, Rb, Cs, Te

(d) Volatile elements : Kr, Xe, Br, I

Metallic precipitates in the fission products affects the fuel's electric and thermal conductivities, and a large quantity of them changes the fuel performance especially for high burn-up fuels, therefore, characterizing the metallic precipitates in a post irradiation examination is very important. In this paper, a characterization procedure and a manner for improving the measurement accuracy by EPMA were established with a well informed simulated fuel which was applied to characterizing the fission products and metallic precipitates of the SIMFUEL irradiated at HANARO.

EXPERIMENTAL PROCEDURE

Specimen Preparation

(1) Un-irradiated SIMFUEL

SIMFUEL was fabricated by adding 14 representative chemicals which originated from the ORIGEN code, which corresponds to a 35,000 MWd/MTU burn-up in a PWR. **Table 1** shows its concentrations. To fabricate SIMFUEL, about 400 g of mixed powder of a 3.2 % slightly enriched uranium and natural uranium were milled at a dry attrite with 150 rpm for 15 min, which was replicated 5 times.

Particle size of raw powder was the 3.28 ㎛, which was decreased to 1.68 ㎛ after 1 cycle and showed 0.5 ㎛ after 5 cycles. Particle size was further decreased after repeating the steps. To reduce the friction between the surface of the palletizing die and the pellet, Zn separate dis-solved in benzene was spread on to the surface of the die. Palletizing was carried out at a pressure of about 1.65 t/cm^2, and sintered at a 1,800 ℃ at reduction condition(H_2 100 %) for 10 hours.

Fig.1 shows the metallic precipitates of 1~1.5 ㎛ and they are shown as a white spot in the image of secondary electron. They were extracted as metal or oxide precipitates during the sintering from the added chemicals in the UO_2 powder.

Table 1 Composition of SIMFUEL (wt%)

Element	g/kg U	Element	g/kg U
Zr	0.606	Pr	0.158
Mo	0.606	Nd	0.571
Ru	0.375	Sm	0.120
Pd	0.221	Rb	0.533
Ba	0.323	Sr	0.103
La	0.173	Y	0.068
Ce	0.360	Rh	0.062

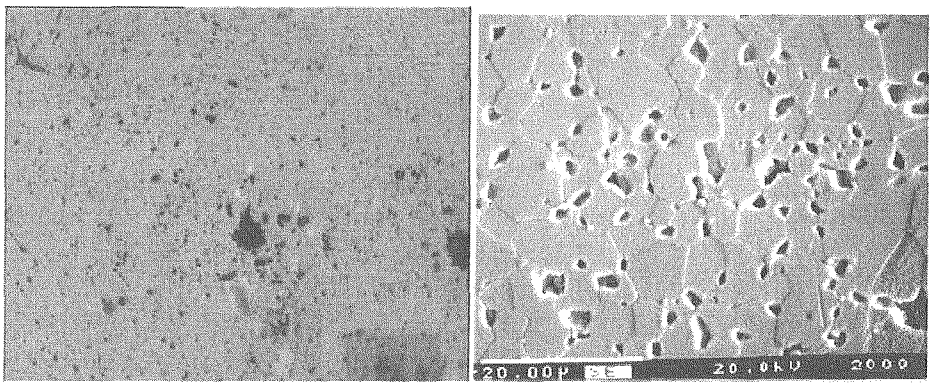

(a) (b)

Fig. 1 Cross section of optical image(x.400)(a) and a SEM image (b).

(2) Irradiated SIMFUEL

A specimen of SIMFUEL fabricated in the hot cell with spent PWR fuel was irradiated at HANARO to as much as a 1,770 MWd/MTU burn-up with the condition of a 61 kW/m maximum linear power and 53 kW/m average linear power. The irradiation rig (**Fig. 2(a)**) retaining the SIMFUEL was fabricated with Al-6061 and it was 960 mm in length, 56 mm in diameter and 3.0 kg in weight. The cladding tube was fabricated with Zr-4 with a 0.66 mm in thickness, 10.08 mm in inner diameter and 199 mm in length. The dimension of the sintered pellet was 10 mm in length, 10.6 mm in diameter and a 10.07 cm^3/g theoretical density. After irradiation at HANARO, a specimen for observing the microstructure was extracted with a 5 mm in thickness using a diamond wheel at a position 100 mm from the top of the cladding tube.

(3) Specimen preparation of the irradiated SIMFUEL

To characterize the concentration of the fission products from the irradiated SIMFUEL, the radiation activity of a specimen is required to be below 37x10GBq for protecting the operator and damage to the EPMA. Although the specimen size has to be minimized, its volume could be managed by the manipulator in a hot cell. After cutting the specimen to a manageable size by the manipulator, the specimen was hot mounted with conducting resin at 150 ℃ and 0.6 Mpa. Too thin a specimen is liable to be broken during the hot mount, so its thickness was cut to be about 5 mm at first. And finally, a specimen of 2.5 x 5 x 1.5 mm^3 (WxLxD) was fabricated by repeating the mounting and cutting several times for decreasing the radiation with a manipulator. After polishing the specimen, it was etched by an immersion method.

The solution was a mixed acid of 163 ml of demi-water, 72 ml of nitric acid, 1 ml of hydrogen fluoride and 3.4 g of citric acid. Etching was accomplished for 40 to 45 seconds at room temperature. Electric conductivity of the oxide fuel is generally as low as $3x10^{-1}$~ $4x10^{-8}$/ohm.cm[4] so that a charging caused by a short of the electron dissipation disturbs the observation of the specimen by the secondary electron or the analyzing of the elements. Conventionally, vapor deposition has been applied to the surface of the specimen to improve the conductivity, but in this experiment silver paint (Leistsilver 2000 silver paint, TED PELLA, INC.) was partially coated on to the hot mounted specimen.

This is a convenient way to abort a charging without doing dangerous and hard work in a hot cell[5]. Silver paint can penetrate into the inside of the specimen by a capillary active phenomenon, which is believed to be a conductor against the irradiated electrons on the specimen[6]. To enhance the electric conductivity, sufficient enough silver paint was spread on to the surface of the specimen, and then it was put it in a vacuum chamber for a deep penetration for about 30 min. Completed specimen was installed in the chamber of the EPMA which is shielded with lead brick by using a transportation cart and tong, as shown in **Fig. 2(e)** and **(f)**.

EPMA(Electron Probe Micro-Analyzer)

EPMA(Electron Probe Micro-Analyzer, SX-50R, CAMECA, Paris, France) used in this experiment can treat a irradiated nuclear fuel by a special shielding of the specimen holder and is specifically shielded with lead and tungsten to permit the analysis of an irradiated nuclear fuel. The maximum radiation activity in this EPMA is allowed to be below to 37x10GBq. The EPMA of Nd, Mo, Ru, Rh and Pd was carried out at an electron acceleration potential of 20 kV and a beam current of 20 nA.

La, Nd and Mo were analyzed using the $L\alpha_1$ X-ray line and a PET(Pentaerythritol Tetrakis) diffracting crystal in the WDS-1. The others were analyzed using the $L\alpha_1$ X-ray line and a PET(Pentaerythritol Tetrakis) diffracting crystal in the WDS-2. But Pu and Am were excluded because of an absent of standards. It is absolutely recommended that the electron beam is radiated exactly at the center of the precipitate and perpendicular against

the electron beam for characterizing the small metallic precipitates. At the same time, even a tiny vibration should be excluded during the measurement. For this, the stage motor was turned off during the measurement and the electron beam was radiated in a fixed mode with a 1 μm beam size.

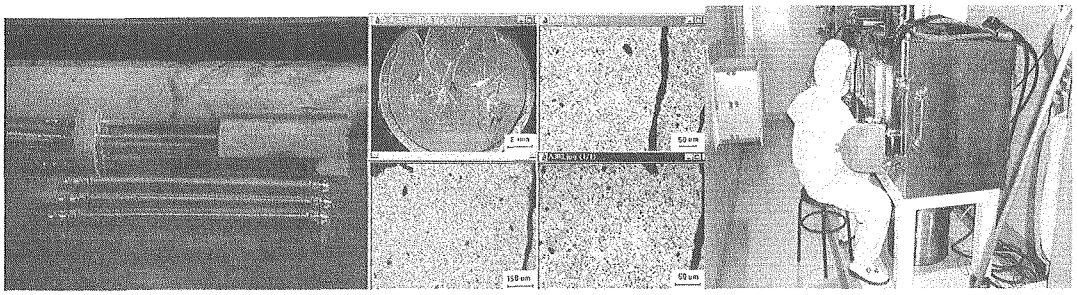

(a) (b) (c)

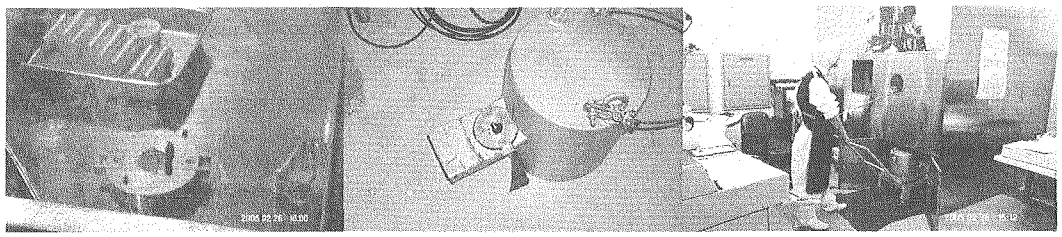

(d) (e) (f)

Fig. 2 Specimen preparation and mounting to the EPMA.
(a) Dismantled rig and fuel elements,
(b) metallographic of the irradiated SIMFUEL,
(c) specimen preparation in a glove box,
(d) mounted specimen in a specimen holder,
(e) lead cask for transferring the specimen,
(f) mounting the specimen to EPMA.

RESULTS AND DISCUSSION

Analysis of the un-irradiated Simulate Fuel

(1) Metal Precipitates

To compare the results of the analysis by the EPMA, a wet chemical analysis was carried out[7]. **Table 2** shows these results[8]. Column (a) in **Table 2** presents the result of the wet chemical analysis. They agreed well with the initial concentration of the added chemicals as well as the results by the EPMA of column (b) in **Table 2**. The EPMA measurement is carried out by scanning the small area with a TV mode at a magnification of 20,000.

In the case of the fix mode, error can occur from eliminating the precipitates extracted at the grain boundaries or the vacancies, so a large area was scanned. After the set up of the characterizing conditions such as applying the voltage and current, characterizing by the EPMA was accomplished for the metallic precipitates of the SIMFUEL.

Table 2 Compare of the concentrations between wet chemical analysis and EPMA analysis (wt.%)

Chemical elements	Chemical analysis, (a)	EPMA analysis, (b)	Concen. of ppt. (c)	Chemical elements	Chemical analysis, (a)	EPMA analysis, (b)	Concen. of ppt. (c)
$Zr(ZrO_2)$	0.397	0.367	0.108	$Ce(CeO_2)$	0.233	0.278	0.035
$Mo(MoO_3)$	0.449	0.392	**49.521**	$Nd(Nd_2O_3)$	0.480	0.476	0.055
$Ru(RuO_2)$	0.239	0.269	**32.153**	Sr(SrO)	0.076	0.084	-
Pd(PdO)	0.028	0.187	**3.682**	$Y(Y_2O_3)$	0.050	0.052	-
$Ba(BaCO_3$	0.203	0.218	-	$Rh(Rh_2O_3)$	0.073	0.049	**3.232**
$La(La_2O_3)$	0.155	0.143	0.09	U			11.48

Column (c) in **Table 2** shows these results. The concentrations of the components of the metallic precipitates such as Mo, Ru, Rh and Pd are relatively lower than those of the oxide precipitates such as Ba, Zr and Mo in **Table 2**, which is suggested that the metallic precipitates are produced less than the oxides.

Fig. 3 shows the metallic precipitates(a) and the result of the quantitative analysis of the metallic precipitate(b) with 10 points. The concentrations were Mo-49.512 wt%, Ru-32.153 wt%, Pd-3.682 wt%, Rh-3.232 wt% and U-11.48 wt% respectively and measurement point #6 in (b) is suspected to be the center of the precipitate.

Representing them in an atomic percent by excluding the uranium, they were Mo-53.89 at.%, Ru-37.40 at.% and Pd+Rh-8.71 at.%. From this, the metallic precipitates in the un-irradiated SIMFUEL seems to have a hexagonal structure of the ε-phase[9, 10].

(2) Perovskite phase

Barium and zirconium may produce a barium-zirconate type of Perovskite during irradiation according to the peripheral oxygen potential. Those size are known to be smaller than 0.1 ㎛ in diameter and evenly spread out in the whole of the fuel[11-13]. Perovskite was also observed in this specimen as showing in **Fig. 4(a)**. **Fig. 4(b)** represents the concentration of the barium of the Perovskite. Sometimes, Perovskite were observed in a cluster with a few ㎛ in diameter, which is a group of small Perovskite. This cluster of Perovskite was observed as a whitish gray on the image of the secondary electron, which was observed at the grain boundaries as well as the intra grains of the specimen. Major

constituents of the Perovskite were Ba, Zr and O, and their concentrations were Ba-18.96 at.%, Zr-17.27 at.% and O-60.17 at.%. The ratio of these elements in chemical formula corresponds to $BaZrO_3$ of the Perovskite according to other papers[14]. From the power diffraction files[12], pure Perovskite of $BaZrO_3$ is cubic with a 0.419 nm in lattice parameter.

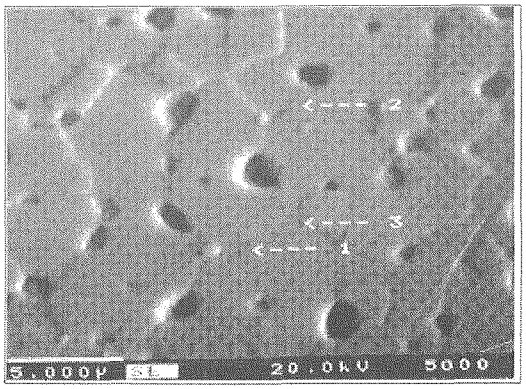

(a)

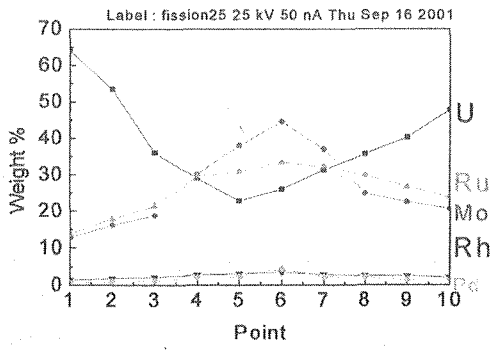

(b)

Fig.3 Metallic precipitates in the un-irradiated SIMFUEL(a) and its concentration(b).

Table 3 Concentration of the Perovskite in SIMFUEL

element	concen. wt %	normal. at %	compound	concen. wt %
Ba	43.114	**18.96**	BaO	48.136
Mo	0.108	0.07	MoO_3	0.163
U	8.962	2.27	UO_2	10.167
Zr	26.234	**17.37**	ZrO_2	35.436
O	15.937	**60.17**		
total	96.515			96.515

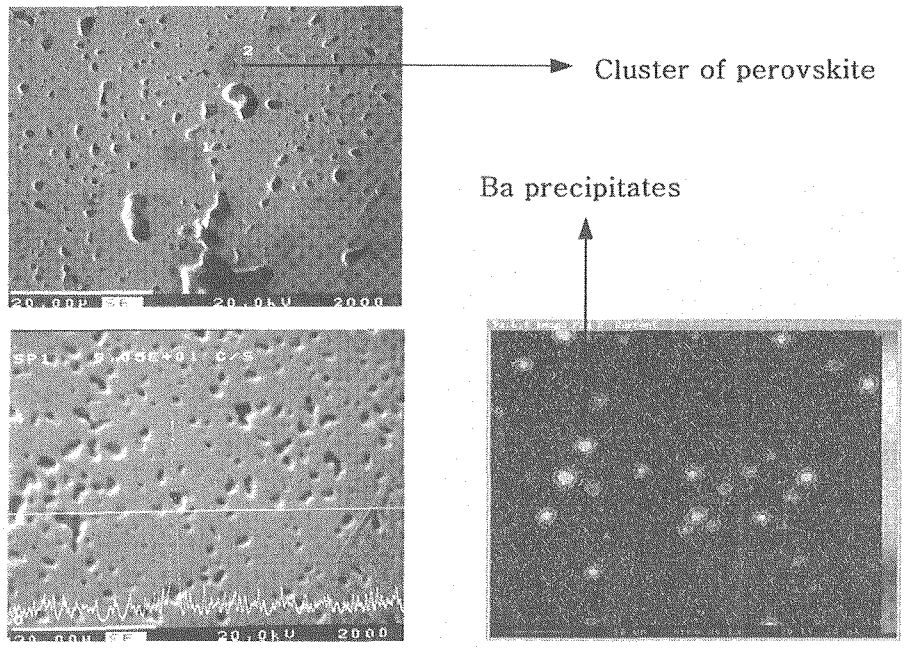

Fig. 4. Cluster of perovskite (a), Ba trace(b) and image map of Ba(C).

Analysis of the irradiated SIMFUEL

(1) The microstructure by an optical microscope and SEM

Fig. 5 shows the results of the post irradiation examination of SIMFUEL irradiated at HANARO, and (a) shows the cross section observed by an optical microscope (TELATOM III, LAICA, Austria). **Fig. 5(b)** is the metallic precipitate at the grain boundary at the position of $r/r_0 \approx 0$. While the size of the precipitates observed in the un-irradiated SIMFUEL were 1~1.5 ㎛, those of SIMFUEL were 2~2.5 ㎛ in diameter. This is believed to be initially produced by the precipitates during the sintering were they are grown by combining with the newly produced fission products during irradiation.

Metallic precipitates were observed at the grain boundaries as well as the intra grains. Compositions between the precipitates observed at grain boundaries and intra grains were no different from each other. But, they were observed differently along the position of the radius in the fuel. Metallic precipitates were generally composed of Mo, Ru, Rh and Pd, and the ratio of those elements one shown in **Fig. 5(c)**. Namely, the concentrations of Mo and Ru tend to decrease when the r/r_0 is increased. The reason for this phenomenon is supposed to be the peripheral oxygen concentration. These two elements are likely to be oxides when the concentration of oxygen is high.

Fig. 5(d) shows the concentration profile of the Mo dissolved in the fuel matrix, the trend represents that the concentration of Mo at fuel surface is higher than that of center. Neutrons are generally more absorbed at the fuel surface, which results in a higher fission

rate. Therefore, a higher oxygen concentration is maintained at the fuel surface due to the liberated oxygen from the UO_2 during a nuclear fission. The reason of low concentration of Mo in the precipitate at the fuel surface is that Mo is likely to be oxides of MoO_2 at higher oxygen concentration. And, Ru is also known to have the same characteristic. This results in lower concentrations of Mo and Ru in the precipitates.

Fig. 5(e) shows the concentration profile of fission products characterized by EPMA. The measurement was accomplished for 5,000 μm by every 200 μm from center of the fuel to the fuel surface with a 1 μm beam size using the same procedure SIMFUEL. High concentrations of Mo and Ru at #14 and #22 are responsible for metallic precipitates.

(2) Perovskite

Perovskite of barium-zirconate could not be observed in the irradiated SIMFUEL which described in 3.1.2 for un-irradiated SIMFUEL. No references were found on the behavior of Perovskite during irradiation. We also could not observe the Perovskite in this specimen.

(3) Characterization of metallic precipitates

Fig. 6 shows metallic precipitates in the irradiated SIMFUEL and their concentration profile. **Fig. 6(b)** shows the quantitative analysis result of metallic precipitate about at 2.5 μm with a beam size of 1 μm by every 0.5 μm. Measured point #3 does not contained uranium, so this point may stand for a typical concentration of the metallic precipitates of irradiated SIMFUEL. **Table 4** shows the concentrations of precipitates both at grain boundary and intra grain. There was no difference among the adjacent ones as shown in **Table 4**. But their concentrations are presented somewhat differently according to their position in the radius direction, similar to SIMFUEL as described in 3.2.1.

Concentrations of the metallic precipitates in **Table 4** are Mo-47.34 at.%, Ru-46 at.% and Pd+Rh-6.65 at.% in atomic percent. This ratio corresponds to tetragonal structure of ε-phase shows **Fig. 7** [9, 10].

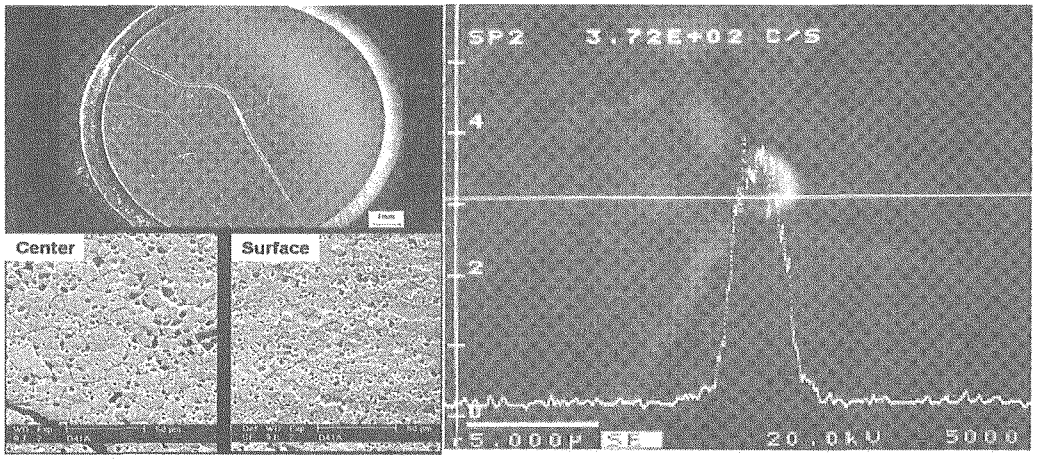

(a) (b)

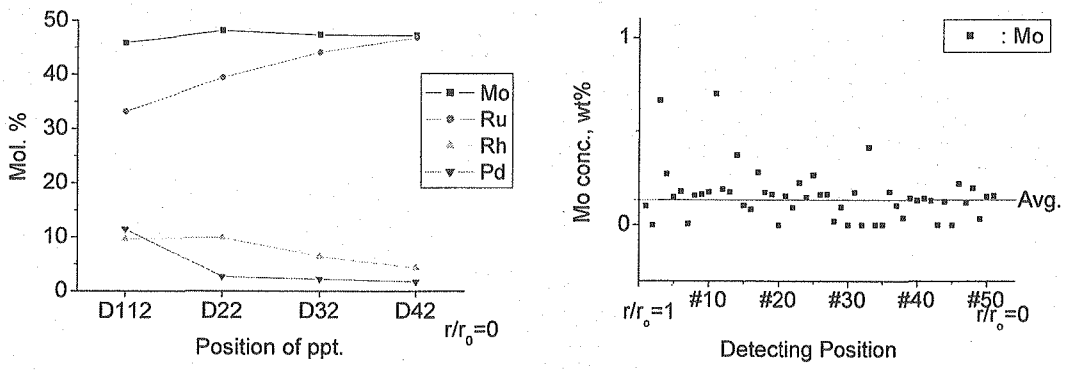

(c) (d)

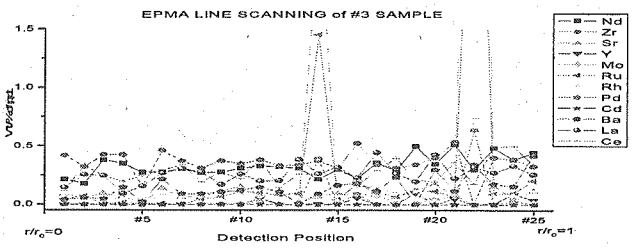

(e)

Fig. 5 Results of post irradiation examination of SIMFUEL.
(a) Cross section of SIMFUEL fuel by optical microscope,
(b) metallic precipitate on grain boundary and trace of concentration of Mo,
(c) concentration profile of the precipitates along the radius of the fuel,
(d) concentration profile of Mo along the radius of the fuel,
(e) concentration profile of fission products along the radius of the fuel.

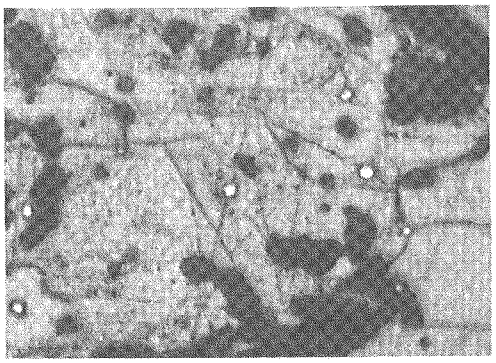

(a)

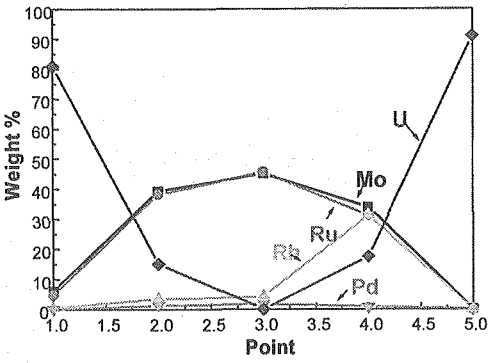

(b)

Fig. 6 Metallic precipitates in the irradiated SIMFUEL(x2,000)(a) and their concentrations(b).

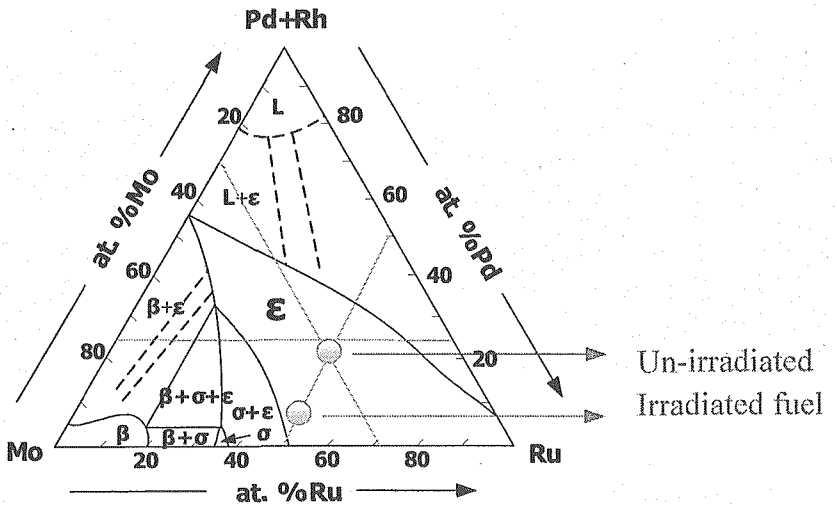

Fig. 7 Section of Mo-Ru-Pd phase diagram at 1,700 ℃.

Table 4 Concentrations of precipitates on grain boundaries and intra grains (wt.%)

element	intra grain	grain boundary
Mo	45.000	42.490
Ru	45.590	45.210
Rh	4.239	4.246
Pd	1.675	1.806
U	0	1.319
Total	96.634	95.172

SUMMARY

Fission products of SIMFUEL were characterized by EPMA. It was irradiated at HANARO at the conditions of a 61 kW/m maximum linear power, 53 kW/m average linear power and a 1,770 MWd/MTU average burn-up. To establish the procedure of an accurate measurement by EPMA, the measurement was accomplished with SIMFUEL which was fabricated with chemicals instead of fission products. Those results were also compared with the results of a wet chemical analysis. The size of metallic precipitate of the un-irradiated SIMFUEL was about 1 ㎛, and their concentrations were 49.512 wt% of Mo, 32.153 wt% of Ru, 3.682 wt% of Pd and 3.232 wt% of Rh. Perovskite from the oxide composite of barium and zirconium were observed in SIMFUEL, and they were composed of 18.96 at.% of Ba, 7.27 at.% of Zn and 60.17 at.% of O. The chemical formula of it was corresponded to $BaZrO_3$.

The size of the metallic precipitates in the irradiated SIMFUEL was observed at 2~2.5 ㎛ in diameter, and they appeared to be 47.34 at.% of Mo, 46 at.% of Ru and 6.65 at.% of Pd+Ph.

REFERENCES

(1) P.G.Lucata, BJ.Palmer, Hj.Matzke, D.S.Hartwig, "Preparation and Character of SIMFUEL" Proc. Int. Conf. on CANDU Fuel, CNS, Toronto (1989) 132.

(2) P.G. Luctuta, R.A. Verrall, Hj. Matzke and B.J. Palmer.,"Micro structural Features of SIMFUEL", J. Nucl. Mater. 178 (1991) 48.

(3) KLEYKAMP H.,"The Chemical State of the Fission Products in Oxide Fuels:, J.Nucl.Mater.,131 (1985) 221-246.

(4) J.Belle. Uranium Dioxide : Properties and Application,USAEC(1961)

(5) Y.H. Jung, B.O. Yoo. Y.S. Choo, K.P. Hong., "Irradiated U_3Si Fuel EPMA Quantitative", KAERI/MR-353 (2000) 154.

(6) Y.H. Jung, K. P. Hong, D.G. Park, S.B. Ahn., "EPMA Analysis of non-coated UO_2 pellet", KAERI/TR-2579, KAERI (2003) 143.

(7) M. S. Yang. J.J. Park, H.S. Park, K.K. Bae, J.S.Lee, I.H. Jung., 11th pacific basin Nuclear Conference, Penbrooke, Canada (1998) 87.

(8) IN-Ha Jung. K.C. Song, K.H. Kang, B.O. Yoo, Y.H. Jung, H.S. Park M.S. Yang,. "Characterization of Irradiated SIMFUEL", Metals and Materials International, 7 (2001) 514.

(9) H.KLEYKAMP "Constitution and Thermodynamics of the Mo-Ru-Pd Systems",J.Nucl.Mater.167 (1989) 49-63.

(10) P.G. Luctuta, R.A. Verrall, Hj. Matzke and B.J. Palmer.,"Micro structural Features of SIMFUEL", J. Nucl. Mater. 178 (1991) 53.
(11) T. Muromura, T. Adachi, H. Takeishi. Z.Yoshida, T. Yamamoto and K. Ueno. J. Nucl. Mater. 151 (1988) 318.
(12) SARI C., WALKER C.T., SCHUMACHER G., "Sdlubility and Migration of Fission Product Barium in Oxide Fuel" J.Nucl.Mater., 79 (1979) 255-259.
(13) KOIZUMI M., SATOH M., NORO K.. "Phase Study on Solid Fission Products, Ba,Sr, and Zr in Oxide Fuel", J.Nucl.Mater.51 (1974) 90-94.
(14) Powder Diffraction Files, Inorganic materials, JCPOS, Inter. Center for Diffraction Data, Penn., Vol. 6, Card No.-139, Barium Zirconium Oxide BaZrO3.

3.7 TWO-STEP TWO-STAGE FISSION GAS RELEASE MODEL

Yong-soo Kim

Nuclear Engineering Dept., Hanyang university
Seoul 133-791, Korea
T: 82-2-2290—0467, F: 82-2-2281-5131, E: yongskim@hanyang.ac.kr

Chan-bock Lee

KAERI (Korea Atomic Energy Research Institute)
Taejon 305-353, Korea

ABSTRACT

Based on the recent theoretical model, two-step two-stage model is developed which incorporates two stage diffusion processes, grain lattice and grain boundary diffusion, coupled with the two step burn-up factor in the low and high burn-up regime. FRAPCON-3 code and its in-pile data sets have been used for the benchmarking and validation of this model. Results reveals that its prediction is in better agreement with the experimental measurements than that by any model contained in the FRAPCON-3 code such as ANS 5.4, modified ANS5.4, and Forsberg-Massih model over whole burn-up range up to 70,000 MWd/MTU.

KEYWORDS: Fission Gas Release, High Burn-up, Grain Boundary Diffusion

INTRODUCTION

Since the LWR operation mode changed from annual to extended/high burn-up fuel cycles in the late 1980s, more attention has been paid to fission gas release phenomena [1–7]. There have been reports that fractional fission gas release is even accelerating with increasing burn-

up. Therefore, for the development of high performance fuels, fission gas release is considered a potential design-limiting factor because of its crucial influence on the thermo-mechanical behavior of the current LWR fuel rods in heavy duty applications.

Uranium dioxide fuel pellets are a polycrystalline ceramic material consisting of many small grains. Fission gas atoms generated by fission reactions start to volumetrically diffuse onto grain boundaries and, on reaching there, continuously diffuse along the boundaries until they release to the open space in the fuel rod. The grain boundary is believed to have a significant role in the release, as do inter- and intra-fission gas bubbles, especially in high burn-up fuels. Excellent works on the grain-boundary-related fission gas release have been reported by several authors [8-13].

Nevertheless, analytical approaches to the gas transport in the two regions of the operating fuels, grain lattice and grain boundary, have not been successful and the current understanding of the role of the grain boundary and its related phenomena is still ambiguous. A diffusion model to describe the physical processes of the fission gas release in UO_2 fuel was first proposed by Booth [14]. In that model, fuel is treated as an assembly of uniform spheres with a single equivalent radius along with the perfect sink boundary condition. With the accumulation of in-pile experience, however, it has been revealed that gas–gas interactions lead to the formation of gas-filled intra-granular bubbles during the diffusion process when fuel burn-up increases. In addition, the perfect sink assumption does not conform to the micro-graphical examination results that gas atoms accumulate continuously in the grain boundaries, mostly causing the formation of inter-granular bubbles. It has also been found that fission fragments resolve the bubbles into the near-grain boundary region during reactor operation, and this augments the concentration of fission gas atoms in the grain boundary. The intra- and inter-granular bubbles, especially in high burn-up fuels, are schematically shown in **Figure 1**.

In actuality, the precipitation of gas atoms in the bubbles and their resolution into the lattice complicate the analysis of fission gas release phenomena. Several mechanistic models have been proposed to take the non-zero grain boundary concentration into consideration [15-18]. Speight proposed a method to determine the grain boundary concentration [15], and Turnbull derived the analytic solution for the non-zero constant boundary concentration case [16]. Forsberg and Massih considered the time-dependent grain boundary condition and treated it numerically with the assumption that fission gas atoms release completely when the grain boundary concentration exceeds a certain saturated value and then accumulate again [18].

Recently a theoretical two-stage model was proposed which mechanistically depicts the release process of fission gas atoms through the diffusion in the two regions, grain lattice and

grain boundary [19]. The model directly solves two simultaneous time-dependent balance equations for fission gas atoms in the grain lattice and grain boundary with the time-dependent grain boundary condition, coupled with bubble trapping and resolution. With the relative diffusivity ratio α incorporated into a time-dependent surface boundary condition of the third kind, it successfully explains the role and the effect of the grain boundary in terms of a new dimensionless parameter $a/(\alpha+a)$, a so-called two-stage parameter.

Based on the model, therefore, two-step two-stage model is developed which incorporates two stage diffusion processes, grain lattice and grain boundary diffusion, coupled with the two step burn-up factor in the low and high burn-up regime. The burn-up factor mechanistically describes the inter-granular high burn-up behavior in terms of activation energy change for the grain boundary diffusion of fission gas atoms.

DEVELOPMENT OF THE MODEL

Two-Stage Model

With the accumulation of in-pile experience it has been revealed that fission gas atom–atom interactions lead to the formation of gas-filled intra-granular bubbles in the grain lattice during the diffusion process when fuel burn-up increases. In addition, apart from the perfect sink boundary condition, fission gas atoms accumulate continuously in the grain boundaries, mostly causing the formation of inter-granular bubbles and fission fragments resolve the bubbles into the near-grain boundary region during reactor operation, and this augments the concentration of fission gas atoms in the grain boundary. The intra- and inter-granular bubbles, especially in high burn-up fuels, are schematically shown in **Figure 1**.

In the model, coupled with the bubble trap and the bubble resolution, fission gas transport is broken down into the two principal processes: the effective grain lattice diffusion, and the effective grain boundary diffusion. **Figure 2** schematically shows the fundamental processes of the current two-stage model with the assumption that a grain has an ideal tetrakaidecahedron structure and fission gas bubbles at the grain edges are linked together to form grain edge tunnels that are finally connected to the open space inside the fuel rod. This means that, after the fission gases volumetrically diffuse through the grain lattice and reach the grain boundaries, they continuously surface-diffuse again along the grain boundaries and release on arrival at the edge tunnels of grain surfaces.

Therefore, the governing equation for the effective grain lattice diffusion is then:

$$\frac{\partial C_v}{\partial t} = \beta + \frac{1}{R^2}\frac{\partial}{\partial R}\left(D_v^{eff} R^2 \frac{\partial C_v}{\partial R}\right) \quad (1)$$

with the initial condition $C_v(R,0) = 0$, and boundary conditions $C_v(0,t) =$ finite and $C_v(a,t) = \overline{C}_{gb}(t)$. In the equation, C_v is the volumetric fission gas concentration within the grain, β is the fission gas generation rate, and a is the equivalent radius of the grain. The lattice diffusion term in the RHS of Equation (1) is expressed in spherical coordinates because the polyhedral grain is treated as an equivalent sphere in this analysis. Note that the surface boundary condition is the time-dependent average grain boundary concentration that is to be solved simultaneously. D_v^{eff} is defined as $D_v^{eff} = (b/b+g)D_{trap}^{in-pile}$ that was proposed by Speight for the application of Booth concept to the high burn-up cases [15].

Now, the fission gas atom concentration in the grain boundary is expressed as:

$$\delta\frac{\partial C_{gb}}{\partial t} = \delta\frac{1}{r}\frac{\partial}{\partial r}\left(D_{gb}^{eff} r \frac{\partial C_{gb}}{\partial r}\right) - 2D_v^{eff}\left(\frac{\partial C_v}{\partial R}\right)_{R=a} \quad (2)$$

subject to the initial condition $C_{gb}(r,0) = 0$, and the boundary conditions $C_{gb}(0,t) =$ finite and $C_{gb}(s,t) = 0$. In Equation (2), C_{gb} is the fission gas concentration in the grain boundary, δ is the grain boundary thickness, and s is the equivalent radius of the grain surface. The effective grain boundary diffusion coefficient D_{gb}^{eff} can be defined similarly to D_v^{eff} in Equation (1), because qualitatively inter-granular bubbles can also trap the inter-granularly diffusing gas atoms and the bubbles can be resolved into the boundary region by the fission fragments. The two principal fission gas transports, D_v^{eff} and D_{gb}^{eff}, are schematically shown in **Figures 1** and **2**.

Most nuclear power plants are operated in the steady state with the designed constant power, although the linear heat generation rate and the temperature profile inside a fuel rod differ from rod to rod and change slowly with fuel burn-up. In such states without rapid power ramp or drop, it can be postulated that there is no sudden accumulation or depletion of fission gas atoms in the grain boundary. That is, all the fission gas atoms reaching the grain boundaries diffuse towards the grain edges and eventually leak out to the open space in the

fuel rod, maintaining a constant grain boundary concentration. In this case, the leakage rate out of the grain surface becomes equal to the arrival rate at the grain surface.

That is,

$$\delta D_{gb}^{eff} \left.\frac{\partial C_{gb}}{\partial r}\right|_{r=s} \cong s D_v^{eff} \left.\frac{\partial C_v}{\partial R}\right|_{R=a} \tag{3}$$

This relation turns equation (2) representing the balance of the fission gas atoms in the grain boundary into the following boundary condition without any significant loss of analytical foundation:

$$\alpha \left.\frac{\partial C_v}{\partial R}\right|_{R=a} - C_v(a,t) = 0 \tag{4}$$

where $\alpha = \frac{2}{\delta\beta_1^2}\frac{D_v^{eff}}{D_{gb}^{eff}}$

Then, according to the following definition, the fractional fission gas release is finally obtained:

$$F \cong \frac{4}{\sqrt{\pi}}\left(\frac{a}{\alpha+a}\right)^2\left(\frac{D_v^{eff}t}{a^2}\right)^{1/2} - \frac{3}{2}\left(\frac{a}{\alpha+a}\right)\left(\frac{D_v^{eff}t}{a^2}\right) \tag{5}$$

As seen in the equation, multiples of the two-stage parameter, $a/(\alpha+a)$, appear in each term of the simple Booth solution, factorizing it with the new dimensionless property. This result clearly shows that the current two-stage mathematical model reduces to the simple Booth single-stage model when $\alpha = 0$, i.e., when grain boundary diffusivity is infinite, which corresponds to the perfect surface sink condition. Suppression of the fractional fission gas release as a function of α based on the two-stage parameter is shown in **Figure 3**.

Two-Step Two-Stage Model

The successful depiction of two-stage model on the high burn-up behaviors leads to the development of current two-step two-stage model.

Basically α is D_v^{eff}/D_{gb}^{eff} with the unit of centimeter since δ is on the order of 10^{-8} cm, β_1 is 2.405/s where s is the equivalent radius of a grain surface which is on the order of 10^{-4} cm, and thus $2/\delta\beta_1^2$ is close to unity. Thus, the ratio of diffusivities α is rewritten in the following way:

$$\alpha \cong \frac{D_v^{\ eff}}{D_{gb}^{\ eff}} = \frac{D_{v0}e^{-Q_v/RT}}{D_{gb0}e^{-Q_{gb}/RT}} = \alpha_0 e^{-(Q_v-Q_{gb})/RT} = \alpha_0 e^{-Q_v\left(1-\frac{Q_{gb}}{Q_v}\right)/RT}$$

Then, burn-up factor f_{Bu} is introduced in the following way:

$$\alpha = \alpha_0 e^{-f_{Bu}Q_v/RT} \tag{6}$$

where $f_{Bu} = 1 - Q_{gb}/Q_v$.

Finally, the fractional release of fission gas atoms is obtained as:

$$F = \frac{4}{\sqrt{\pi}}\left(\frac{1}{1+\alpha' e^{-f_{Bu}Q_v/RT}}\right)^2 \left\{\left(\frac{D_0}{a^2}\right)\exp\left(\frac{-Q_v}{RT}\right)t\right\}^{\frac{1}{2}} \tag{7}$$

where $\alpha' = \alpha_0/a$

In the low burn-up regime, trapping of fission gas atoms in the grain boundary plays significant role in the activated release process, which means that the activation energy Q_{gb} for the grain boundary diffusion is fully employed. The trapping suppresses the fission gas release. In the high burn-up regime especially when it exceeds the threshold burn-up, however, the inter-linkage of inter-granular bubbles begins to mobilize the trapped fission gas atoms in the grain boundaries and thus increases the grain boundary diffusivity. The more bubbles interlink and the inter-linkage connects each other to the open space, the more freely the trapped atoms are released. Fundamentally the enhancement of this grain boundary diffusivity is achieved mostly by activation energy decrease since the inter-linkage lowers the activation energy Q_{gb} for the activated grain boundary diffusion process.

Therefore, the burn-up factor f_{Bu} is treated step-wisely in this two-step two-stage model, depending on the fuel burn-up. Until the burn-up reaches the threshold value it remains zero since Q_{gb} stays close to Q_v, never exceeding, in the low burn-up regime. On the other hand, it begins to increase linearly up to the unity in high burn-up regime because Q_{gb} linearly decreases down to zero at the ultimate high burn-up.

MODEL VALIDATION AND DISCUSSION

For the derivation of constituent parameters and the validation of the model FRAPCON-3 code and its in-pile measurement data sets are used [20].

First, ten data sets that are all distributed by the FRAPCON-3 code authority are chosen for the derivation of best fitting parameters of the model. The reason for the choice is to take publicly accepted standard data sets in order to avoid unnecessary errors or deviation. In addition, it is because the ten sets cover whole burn-up range. In this best fitting analysis, 25,000 MWd/MTU is taken for the threshold burn-up as recommended in modified ANS5.4 model. Finally derived best-fit parameters are as follows:

$$\alpha' = 1.06$$
$$f_{Bu} = Max(0, Bu - 25000)/72000$$
$$(D_0/a^2) = 0.018 \text{ /sec}$$
$$Q = 188.16 \text{ kJ/mol}$$

As seen in **Table 1**, all of these parameters are in the comparable ranges with those of other popular models. Particularly, the activation energy of fission gas atoms diffusion is very close to that of modified ANS5.4 model. The ultimate burn-up at which the grain boundary diffusion becomes non-activated with zero activation energy can be assumed based on the in-pile experience but in this study it is analyzed with best fitting techniques. It turns out to be 97,000 MWd/MTU in this analysis.

Then, the model predictions are checked against the same data sets for its validation with those best-fit parameters and compared with those by other popular models, especially contained in FRAPCON-3 code. As shown in **Figure 4** and **Figure 5**, over whole burn-up range up to 70,000 MWd/MTU its prediction is in much better agreement with the experimental measurements than that by any model in the FRAPCON-3 code such as ANS 5.4, modified ANS5.4, and Forsberg - Massih model except one measurements data set. As pointed out by other authors, the experimental measurements (TVO-1) seem to be high compared to the power profile. All other mechanistic models also predict quite lower fraction than the measurement. The plot of $F_{predited} - F_{measured}$ in **Figure 5** clearly demonstrates that current two-step two-stage model predicts the fractional release most closely to the in-pile measurements.

It is noticeable that current model prediction is still in good agreement with the measurements in the high burn-up regime while those of other models go wrong. It is easily

understood when the burn-up factors of the models are compared and reviewed. **Figure 6** shows the comparison: as fuel burn-up goes up the two-step burn-up factor of the current model saturates to the unity but all others increase exponentially which is quite wrong, physically and mechanistically. In fact, the burn-up and temperature dependent two-step burn-up factor is mechanistically derived but others are empirically correlated with intermediate burn-up in-pile data.

CONCLUSIONS

Based on the recent theoretical model, two-step two-stage model is developed with the incorporation of step-wisely divided burn-up factor in the low and high burn-up regime. In the model the two-step factor is introduced to the two-stage parameter of the two-stage model in order to simulate the decreasing activation energy for the fission gas atoms diffusion through the grain boundary with fuel burn-up increase. For the derivation of the factor it is reasonably assumed that activation energy for grain boundary diffusion is identical to that for grain lattice diffusion in the low burn-up regime and begins to decrease linearly down to zero as fuel burn-up exceeds a threshold burn-up. According to the in-pile experiences the threshold and ultimate burn-ups for the non-activated grain boundary transport are determined to be 25,000 MWd/MTU and 97,000 MWd/MTU, respectively.

FRAPCON-3 code and its in-pile measurement data sets are used for the derivation of constituent parameters in the model and its validation. Only the data sets that are distributed by the FRAPCON-3 code authority are chosen and the deviation of current model prediction from the measurement is examined. The total number of the data sets is ten and current model predictions with the derived best fitting parameters are compared with those from the popular fission gas models contained in FRAPCON-3 code.

Results reveals that over whole burn-up range up to 70,000 MWd/MTU its prediction is in much better agreement with the experimental measurements than that by any model in the FRAPCON-3 code such as ANS 5.4, modified ANS5.4, and Forsberg - Massih model. This excellent agreement may confirm that two-step burn-up factor and two-stage parameter introduced to this model are based on sound mechanistic foundation.

REFERENCES

(1) R. Manzel and M. Coquerelle, Proc. ANS Int. Topical Meeting on LWR Fuel Performance, Portland, Oregon, USA, March 2-6, 1997, p. 463.
(2) J.O. Barher, M.E. Cunningham, M.D. Freshley, and D.D. Lanning, Nucl. Tech., 102 (1993) 210.
(3) K. Une, K. Nogita, S. Kashibe, and M. Imamura, J. Nucl. Mater., 188 (1992) 65.
(4) C.C. Dollins and M. Jursich, J. Nucl. Mater., 105 (1982) 269.
(5) S. Bremier, C.T. Walker, and R. Manzel, Proc. Int. Seminar on Fission Gas Behavior in Water Reactor Fuels, Cadarache, France, Sept. 26-29, 2000.
(6) M. Tourasse, M. Boidron, and B. Pasquet, J. Nucl. Mater., 188 (1992) 49.
(7) M.E. Cunningham, M.D. Freshley, and D.D. Lanning, J. Nucl. Mater., 200 (1993) 24.
(8) D.R. Olander and P. Van Uffelen, J. Nucl. Mater., 288 (2001) 137.
(9) F. Lemoine, J. Papin, J.M. Frizonnet, B. Cuzalis, and H. Rigot, Proc. Int. Seminar on Fission Gas Behavior in Water Reactor Fuels, Cadarache, France, Sept. 26-29, 2000.
(10) M. Paraschiv and A. Paraschiv, J. Nucl. Mater., 185 (1991) 182.
(11) D.R. Olander, in I.J. Hastings (Ed), Advances in ceramics, vol. 17, The American Ceramic Society, Columbus, Ohio, 1986, p.271.
(12) M.V. Speight and J.A. Turnbull, J. Nucl. Mater., 68 (1977) 244.
(13) J.A. Turnbull and C.A. Friskney, J. Nucl. Mater., 58 (1975) 31.
(14) A.H. Booth, AECL Report CRDC-721 (1957).
(15) M.V. Speight, Nucl. Sci. Eng., 37 (1969) 180.
(16) J.A. Turnbull, J. Nucl. Mater., 50 (1974) 62.
(17) R.J. White and M.O. Tucker, J. Nucl. Mater., 113 (1983) 1.
(18) K. Forsberg and A.R. Massih, J. Nucl. Mater., 127 (1985) 141.
(19) Y. Kim, J. Nucl. Mater., 326 (2004) 97.
(20) NUREG/CR-6534, PNNL-11513 (1997).

Table 1 Comparison of current two-step two-stage model (Kim & Lee model) parameters with those used in the popular FRAPCON-3 code models

FGR models	Activation energy	D_0 / a^2	Burn-up factor	Resolution, parameter $b\lambda$
ANS 5.4	72,300 cal/mol	0.61/sec	$100^{Bu/28000}$	N/A
modified ANS 5.4	49,700 cal/mol	22.1×10^{-4}/sec	$100^{Max(Bu-25000)/21000}$	N/A
Forsberg & Massih	45,470 cal/mol	8.56×10^{-3}/sec	N/A	1.84×10^{-14}
modified Forsberg & Massih	57,742 cal/mol	8.56×10^{-3}/sec	$100^{Max(Bu-21000)/35000}$	1.47×10^{-12}
Two- step two-stage model (Kim & Lee model)	44,906 cal/mol	0.018/sec	$\left(\frac{1}{1+\alpha' e^{-f_{Bu}Q/RT}}\right)^4$ where, $\alpha'=1.06$ $f_{Bu} = \mathrm{Max}(0, Bu-25000)/72000$	N/A

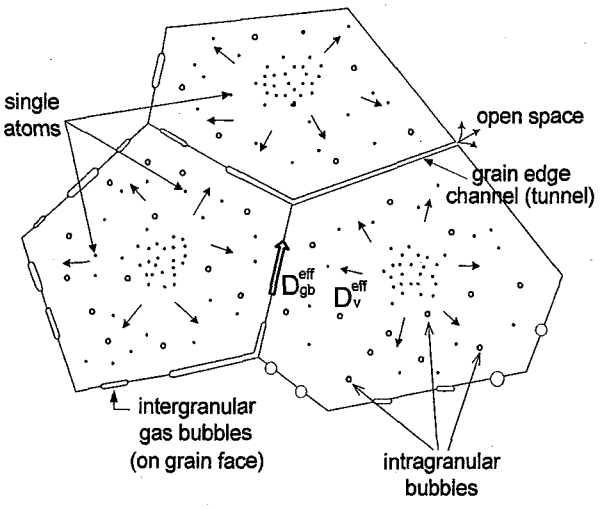

Figure 1. Typical cross-sectional view of a high burn-up fuel.

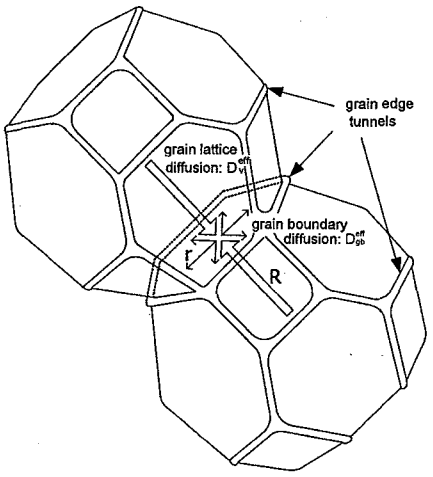

Figure 2. A schematic of two principal diffusion processes in the current two-stage two-step model (Kim & Lee model) with grain lattice diffusion D_v^{eff} and grain boundary diffusion D_{gb}^{eff}

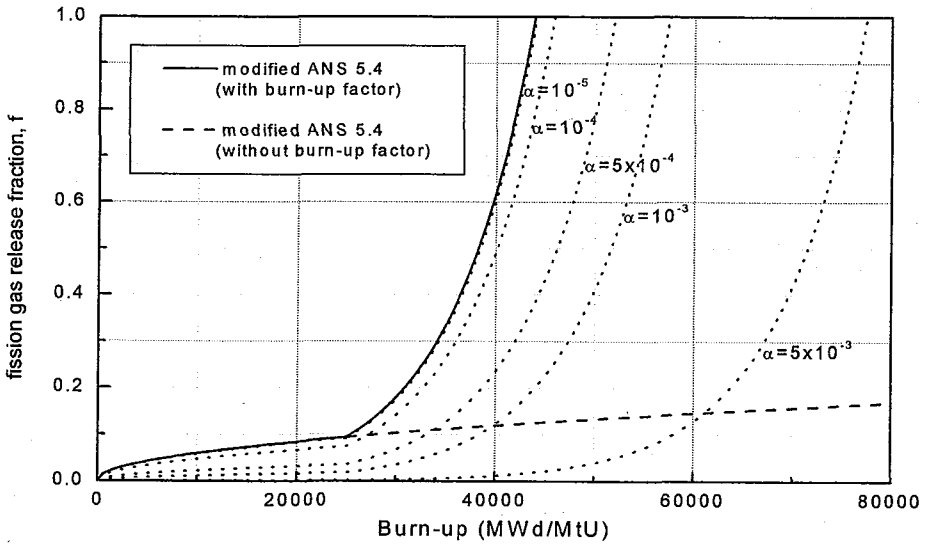

Figure 3. Suppression of the fractional fission gas release as a function of α based on the two-stage parameter. Comparison is made against the modified ANS5.4 model with burn-up enhancement factor, $100^{\mathrm{Max}(0,\mathrm{Bu}-25{,}000)/21{,}000}$.

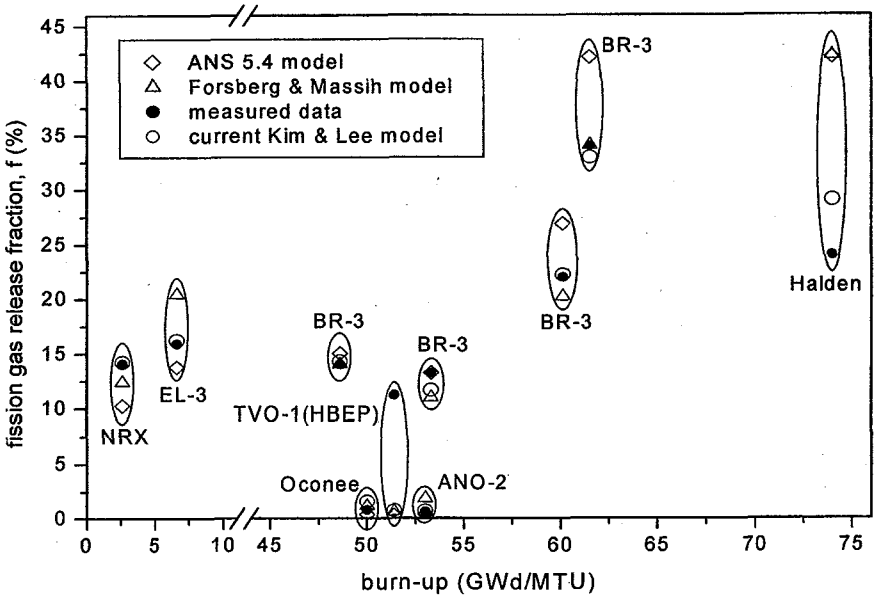

Figure 4. Results of current two- step two-stage model (Kim & Lee model) prediction and their comparison using the same in-pile data sets used for FRAPCON model validation.

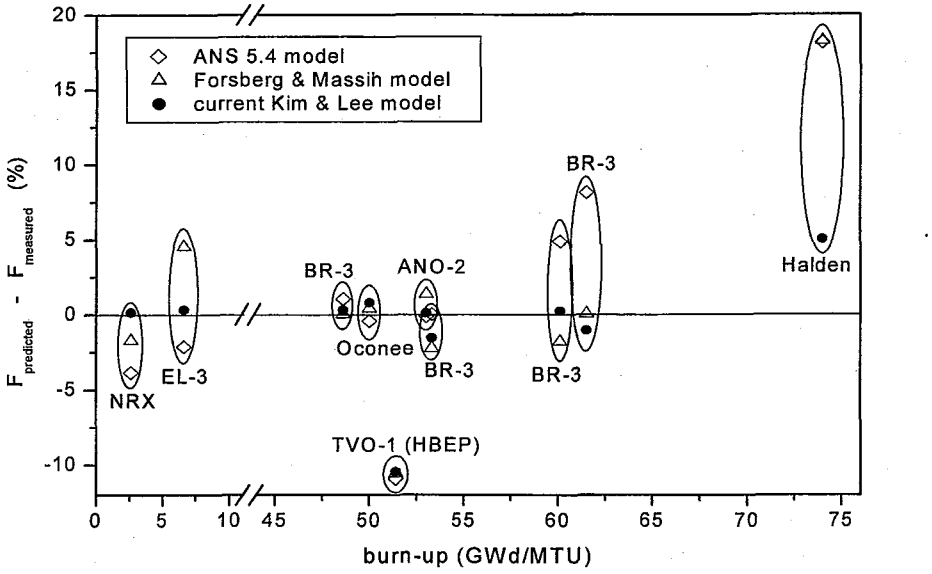

Figure 5. Comparison with the popular FRAPCON models in terms of $F_{predited} - F_{measured}$.

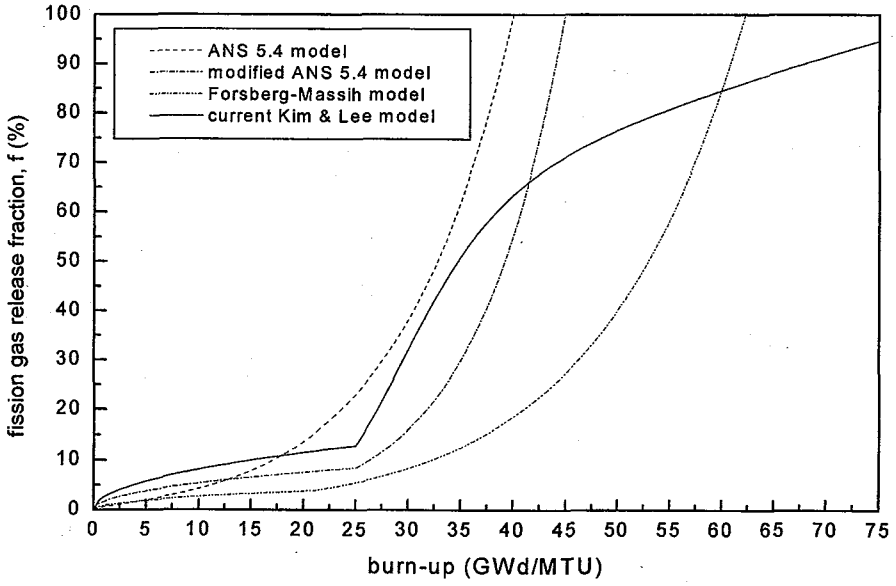

Figure 6. Graphical comparison of burn-up factor derived in the current two-step two-stage model (Kim & Lee model) with those used in the popular FRAPCON models.

3.8 IRRADIATION TEST FOR A CREEP CAPSULE WITH A SINGLE SPECIMEN

Man Soon Cho, Myung Hwan Choi, Kee Nam Choo, Cheol Gyo Seo, and Bong Goo Kim

HANARO Utilization Technology Development Division
Korea Atomic Energy Research Institute
150 Deokjin-dong, Yuseong-gu, Daejeon 305-353, Korea

ABSTRACT

A creep capsule was irradiated at the IR2 test hole of the HANARO 34-1 operation cycle in 2004. As a creep test was performed in the in-core test hole of HANARO, a safety review during the irradiation test had been performed for the reactivity change, the structural integrity of the capsule and the temperature prediction. During the analysis, the reactivity effect satisfied the limiting conditions for HANARO and the structural integrity was confirmed for the normal and abnormal test conditions. By a thermal analysis at a 24 MW_{th} HANARO power, the specimen temperature was analyzed and the temperature requirement for the irradiation test could be satisfied by a control of the internal He pressure and the heater power. During the irradiation test, the temperature of the specimen was 650±5 °C over the whole irradiation period. The measured temperature of the components showed differences of not more than 50 °C when compared with the design values and this indicates the error range to be within 10% when compared with the design values. It is expected that the results presented here will be utilized in the design and manufacturing of creep capsules with multiple specimens in the future.

KEYWORDS : Creep Capsule, Nuclear Analysis, Structural Integrity, Thermal Analysis, Irradiation Test , Displacement, LVDT

INTRODUCTION

A creep capsule is useful and important for the study of the changes of a nuclear material or its fuel properties during an irradiation test in HANARO. A creep capsule(02S-08K), which was aimed at confirming the design characteristics and the structural integrity,

was manufactured and irradiated at the IR2 test hole in November, 2004. To review its safety for an irradiation test, the reactivity effect in HANARO was analyzed and the stress and temperatures on the capsule were estimated. In the abnormal operating condition during the test of the capsule, the effect exerted on the capsule's outer body by a leakage or breakage of the stress loading unit equipped in the capsule was analyzed. During the irradiation test, the temperature of the components and the displacement of the specimen were measured and analyzed.

NUCLEAR ANALYSIS

The creep capsule was irradiated at the IR2 test hole for the HANARO 34-1 cycle, which was operated for 18 days. The reactivity effect, the neutron flux and the heating rate caused by loading the capsule into the test hole were estimated. The capsule model used for an estimation of the data in the core is as in **Fig. 1**.

In this estimation, a capsule half breakage was assumed such that half of the capsule was lost for an irradiation test. The reactivity worth is no more than -2.1 mk if the Ir rig was placed in the IR2 test hole instead of the capsule. This indicates that the reactivity effect is not so great. As a result, the reactivity effect by loading, unloading and a breakage of an experimental object does not exceed +12.5 mk as specified in the "HANARO operation technical specification[1]".

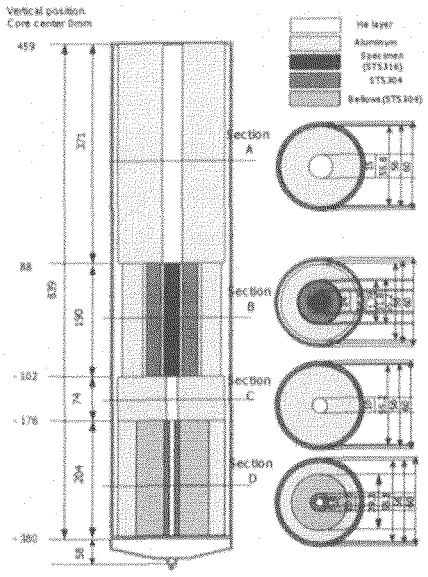

Fig. 1 Model for the nuclear/thermal calculation of the creep capsule(02S-08K).

STRUCTURAL INTEGRITY

The structural integrity analysis for the capsule's outer tube was performed. The critical buckling stress[2] of the outer tube is calculated as 15.52 MPa, and this value is higher than the buckling stress (3P) due to the applied coolant pressure (P= 0.4 MPa). The combined stresses (primary membrane + secondary thermal) on the outer tube are 78.16 and 96.06 MPa for a 24 and 30 MW_{th}, HANARO power, respectively. **Table 1** represents the results of the stress analysis and the strength evaluation based on the ASME code requirements. These results meet the allowable stress value, 344.76 MPa for the combined stresses.

Table 1 Stress in the capsule's outer tube (unit : MPa)

Item		Calculation Stress	Allowable Stress	Code requirement
P_{cr}		1.2	15.52	$P_{cr} > 3P^*$
P_m		4.36	114.92	$P_m < S_m$
24MW	P_m+P_e	78.16	344.76	$P_m+P_e < 3S_m$
30MW	P_m+P_e	96.06	344.76	$P_m+P_e < 3S_m$

* Coolant pressure (P=0.4 MPa)

During the irradiation test, some abnormal accidents can be assumed by a damage or breakage of the bellows in the stress loading unit in the capsule because it works normally at a high pressure of 30~40 kgf/cm^2. For this case, a stress analysis was performed to confirm the structural integrity of the capsule's outer tube. The design pressure (p) is assumed to be 50 kgf/cm^2 and the hoop stress of the capsule's outer tube can be calculated by the following equation

$$\sigma_h = \frac{pr}{t} \quad (1)$$

Where, r and t are the radius(30mm) and the thickness(2mm) of the capsule, respectively. The hoop stress using Eq. (1) due to the abnormal internal pressure[3] is calculated as 73.5 MPa, which is less than the allowable stress(114.92 MPa) of the outer tube material (STS316LN). As a result, the structural integrity of the capsule is ensured even if an abnormal pressure increase has occurred.

THERMAL ANALYSIS

During the irradiation test, the required temperature of the specimen is 600 °C(±10%)[4]. The heating rate by neutron and gamma on the components of the capsule loaded in the IR2 was calculated for the position from 250 to 550mm of the control rods expected in the 34-1

cycle of the HANARO operation. The heating rates on the internal structure and the outer tube according to the positions of the control rods are shown in **Fig. 2** and **Fig. 3**.

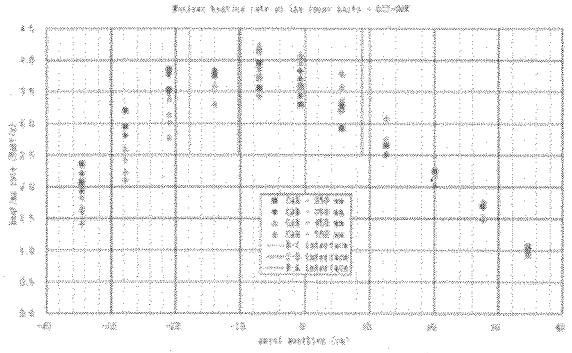

Fig. 2 Heating rate at the internal structure according to the position of the control rods.

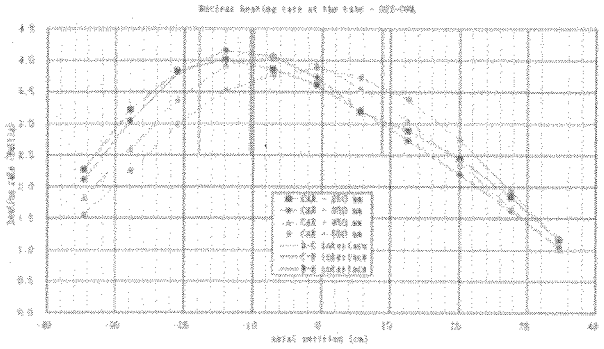

Fig. 3 Heating rate at the outer tube according to the position of the control rods.

The maximum heating rate is expected to be 4.23 W/g at the specimen when the control rods are at a height of 450 mm. The range of the fluctuation for the heating rate at the specimen is not so big depending on positions of the control rods. The model for the cross section of the capsule for the temperature calculation is shown in **Fig. 4**.

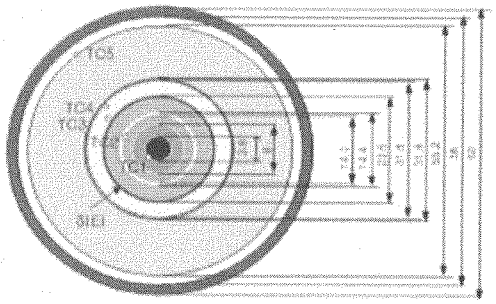

Fig. 4 Model for the temperature calculation of the specimen section.

Temperatures at the vertical positions

Temperatures calculated at various vertical positions of the capsule are calculated as in **Table 2**. These will be compared with the temperatures measured on the capsule parts.

Table 2 Temperatures at the vertical positions of the capsule

	Parts	Temperature (°C)	
		0.6K(~70torr)	1K(1atm)
Section A	LVDT	113	87
Section B	Specimen	664	544
Section C	Thermal media	184	106
Section D	Bellows outer tube	449	439

Temperature distribution around the specimen

The estimated temperature distribution at a 24 MW_{th} of HANARO power is shown in **Table 3**. The specimen temperature can be controlled from 664 °C to 544 °C by a change of the internal He pressure in the capsule. Therefore, the requirement for the specimen temperature is satisfied. At a 30 MW_{th} HANARO power, the specimen temperature is estimated to be from 745 °C to 614 °C. This range is a little higher than the required temperature 600 °C(±10%).

Table 3 Temperature distribution (IR2, control rod 450mm)

Parts	24MW	
	0.6K (~70torr)	1K (1atm)
Specimen	664	544
Heater	499	415
Connector	438	357
Thermal media	365	307
Outer tube	44	44

Temperature limit of a specimen during an irradiation test

The test temperature of the specimen was decided on as 600 °C based on the creep test temperature at the outpile for the STS316LN material. The specimen does not melt even though the temperature on the specimen becomes 600 °C or above. To set the limit of the temperature for an irradiation, it is desirable to consider the temperature of the Al thermal media rather than the specimen. The temperature of the specimen has nothing to do with the safety of the capsule as far as it is not higher than its melting temperature of 1,450 °C[5]. Therefore, the upper limit of the test temperature had to be set at the value that the

temperature of the Al(TC-5) would be 600 °C, when the temperature of the Al thermal media is less than its melting temperature[6].

IRRADIATION TEST

The results for the irradiation test

The temperatures of the capsule components and the displacement at the specimen were measured through the irradiation test. The data on the temperatures, pressure, displacement etc. are as in **Fig. 5**. The target temperature of the specimen in this capsule was 600 °C (±10%). As a result of the irradiation, the temperature of the specimen was 650±5 °C over the whole irradiation period. The irradiation test was performed at this temperature by a gamma heating without using a heater. The stress on the specimen was started at 150MPa first to Dec. 10 and then it was increased to180MPa for the last 3 days to Dec. 12. An abnormal signal in the displacement occurred for the first few days of the irradiation. The signal of the LVDT was started at +10mm in the beginning and was increased to +15mm with a temperature rise by the power increase of HANARO, and then it disappeared. The period that the signal disappeared was 5 days. And then, the function of the LVDT was recovered at Dec. 3 and the signal for the displacement was generated normally.

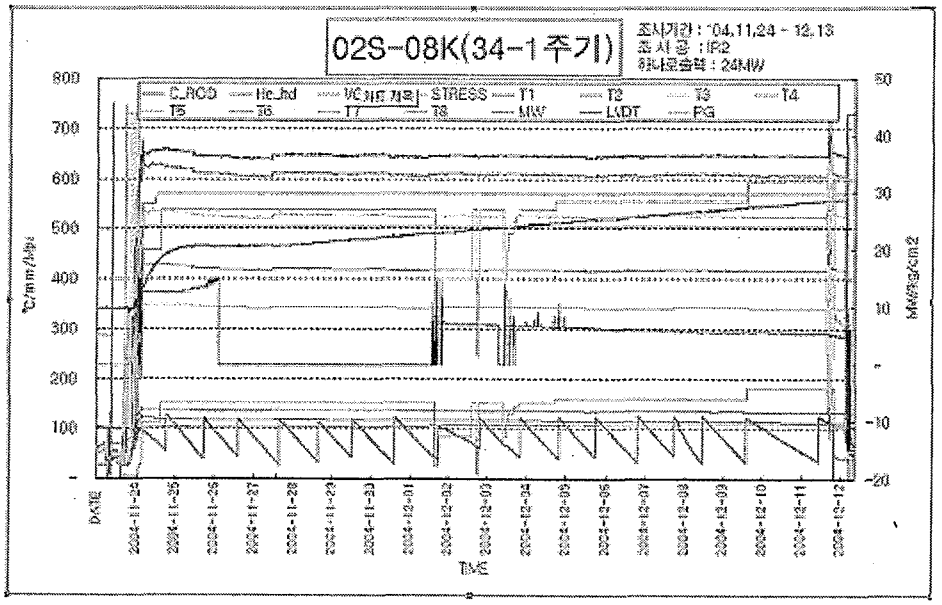

Fig. 5 The results for the irradiation test of the 02S-08K capsule.

(1) The internal temperature of the capsule

The temperatures measured with the change of the HANARO power and the vacuum condition during the irradiation test are as in **Table 4**. The irradiation test of the 02S-08K capsule was performed in the IR2 hole, the temperatures in **Table 4** were measured during

the process of the HANARO power rise. The control rod was located at 340~440mm at this time. When the power of HANARO is 23 MW, the temperature of the specimen increases from 634 °C at the vacuum pressure of 400 torr to 659 °C at the vacuum pressure of 200 torr. During the irradiation test, the average temperature of the specimen over the whole irradiation period was 650±5 °C.

Table 4 Temperature distribution at sections of the specimen (°C)

	* Irradiation hole : IR2, Heater power=0, control rod 340~440 mm measured during the normal operation of HANARO										
Thermo-couple	HANARO power(MW)	5		10		15		23		24	
	Vacuum(torr)	80	730	80	730	80	730	200	400	80	730
TC-1	Specimen	279	227	462	354	586	463	659	634	757	639
TC-2	Spacer2	272	223	449	345	556	453	638	618	704	599
TC-3	Heater rod Outside	237	195	387	297	475	387	539	523	606	518
TC-4	Connector Outside	202	169	323	249	387	321	430	420	469	411
TC-5	Al thermal media Outside	166	141	263	208	308	263	344	340	369	335
TC-6	Connection part between specimen and bellows	68	59	100	86	120	107	138	134	147	129
TC-7	Thermal media of bellows	62	53	89	76	107	95	124	119	125	109
TC-8	Thermal media of LVDT	50	44	73	58	87	73	101	97	125	108

To investigate the temperatures depending on the degree of vacuum, the temperatures of the capsule components were measured by changing the degree of vacuum inside the capsule at 24MW. The degree of vacuum can reach up to 80 torr in the present capsule control unit, and so the temperatures were measured at a vacuum of 80~730 torr. The temperature changes depending on the degree of vacuum are shown in **Table 5** and **Fig. 6**. A drastic change of temperature was not shown in the data when the vacuum is descending from 570 to 80 torr. The part showing the drastic change of temperature depending on the degree of vacuum seems to appear at a vacuum lower than 80 torr.

Table 5 Temperature distribution depending on the vacuum at 24MW of a HANARO power

	* Irradiation hole : IR2, Heater power=0, measured during the normal operation of HANARO control rod 556 mm												
Thermo-couple	Vacuum (torr)	80	90	100	120	130	150	200	250	300	400	500	570
TC-1	Specimen	757	746	739	727	723	711	692	678	667	655	649	644
TC-2	Spacer	704	694	687	679	675	664	647	635	625	614	609	605
TC-3	Heater	606	598	592	584	580	572	558	547	539	539	526	522
TC-4	Connector	469	464	460	455	453	446	438	431	425	420	418	416
TC-5	Al thermal media	369	366	364	361	360	356	351	348	345	342	342	340

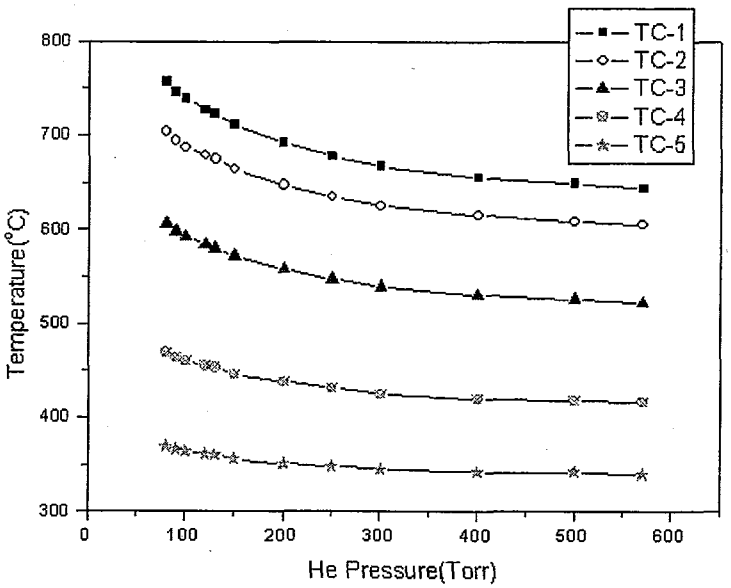

Fig. 6 Changes of the temperatures depending on the vacuum (24MW).

(2) The displacement of the specimen

The signal of the LVDT during the irradiation test is shown in **Fig. 7** with the data of the temperature and the stress. The LVDT installed in this capsule is able to measure a displacement in the range of ±15mm. The signal of a displacement disappeared in the first few days during the irradiation test as shown in **Fig. 7**. However, after that, the signal shows a tension of 2mm from +7.1mm to +5.1mm in the direction of the stress[7]. The centerline in **Fig. 7** is the line of the displacement in the LVDT, and this indicates that its signal disappeared for about 5 days.

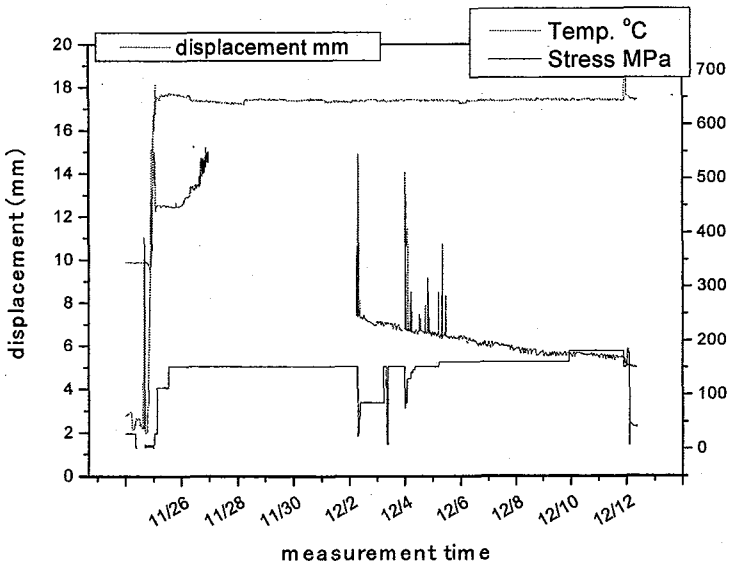

Fig. 7 The irradiation history for the displacement, temperature and stress (02S-08K).

The analysis of the results

(1) The estimation of the temperatures depending on the reactor power

The temperatures in the HANARO power higher than 24MW can be estimated by using the measured temperature shown in **Fig. 8**. The function obtained by a graph fitting using the temperature data measured depending on the HANARO power for the specimen as in **Fig. 8** is

$$Y = 90.573 + 28.6624\,X - 0.24953\,X^2 \qquad (2)$$

where X is the power of HANARO and Y is the temperature of the specimen.

The temperature of the specimen calculated at a 30MW power using this function is 726 °C. This estimated temperature of the specimen becomes the design criteria of a specimen when the creep capsule is irradiated at a 30MW power of HANARO. The temperature of 726 °C is too high for the temperature of a specimen in the creep test. The temperature of a specimen in the irradiation test of the creep capsule is normally 550~600 °C. In the next creep test for the 03S-07K, the creep capsule will be irradiated at a 30MW power of HANARO, and the target temperature of the specimen is 550 °C. Therefore, it is necessary to reduce the size of the gap to lower the temperature of the specimen to 550 °C.

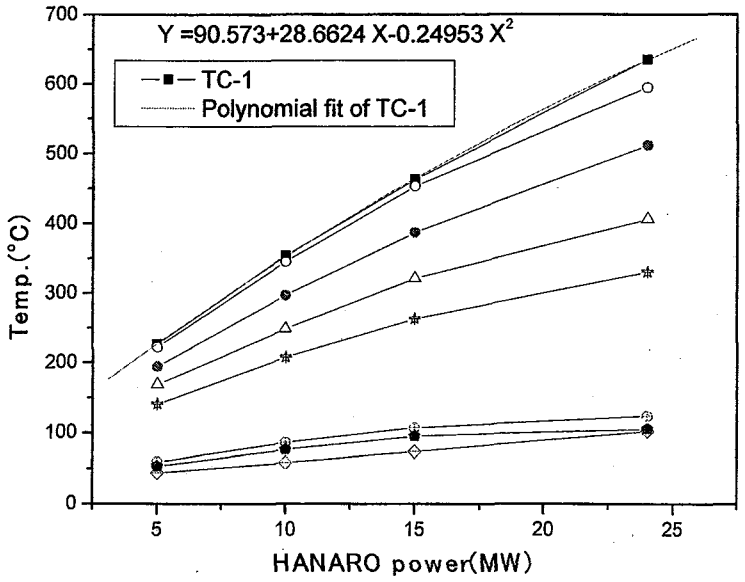

Fig. 8 Temperature changes of the components according to the HANARO power.

(2) Comparison between the design and measured temperature

Fig. 9 shows the design and the measured temperatures for the specimen and the components of the 02S-08K creep capsule. For the temperature of the specimen, the measured value shows an error of 12.2~14.8% depending on the degree of vacuum when compared with the design temperature. The temperature calculated before the irradiation test was estimated as lower than 100 °C when compared with the measured one.

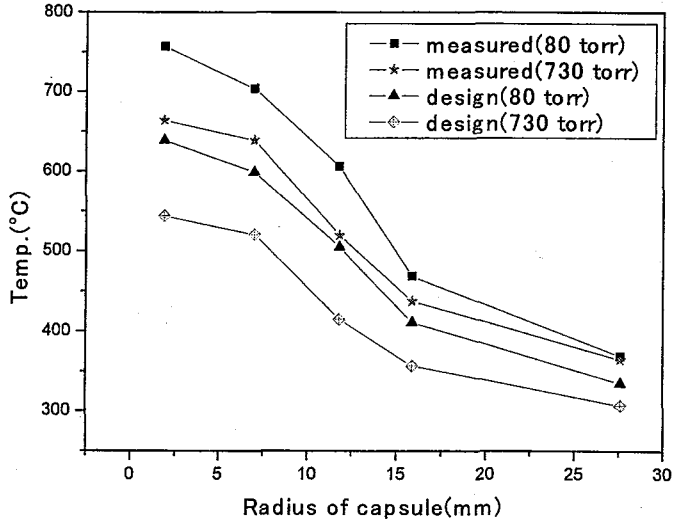

Fig. 9 Design and measured temperatures of the specimen.

The gap between the thermal media and the outer tube, which was established for controlling the temperature of the specimen, is 0.4mm. This shows that there is an error of 25 °C per 0.1mm gap between the design and measured temperature.

(3) Creep rate

To obtain the creep rate using the result of the measurement for the displacement during the irradiation test, the creep strain was estimated for the period where the stress of 150MPa was imposed, and the graph for the creep strain vs. time is shown in **Fig. 10**. The average temperature of the specimen during this period is 650 °C, the deviation is in the range of ±5 °C. As a result for the displacement, there was a little disturbance in the early stage of the displacement signal, however the general trend of the displacement shows a tension in the direction of the stress as expected. The whole time period of the irradiation test is 432hours, which corresponds to 28 EFPD(Effective Full Power Day), and the time period where the stress of 150MPa was imposed was 160 hours. During the period of the irradiation test, a rupture did not occur by a creep tension. The creep rate($d\varepsilon/dt$) is measured to be $9.5 \times 10^{-8} s^{-1}$.

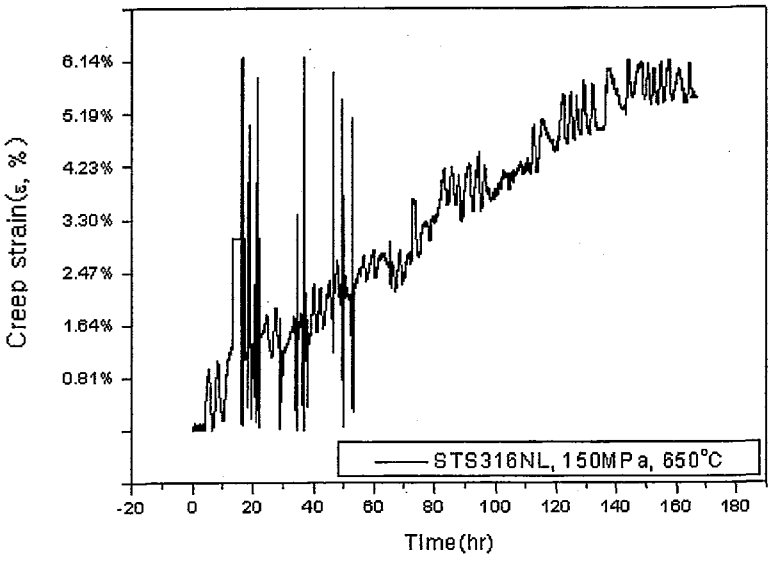

Fig. 10 Creep curve on the in-pile test at 650 °C.

CONCLUSIONS

In the design of the creep capsule(02S-08K), the reactivity effect was +6.2mk and this satisfies the limit condition(+12.5mk) in HANARO. And the structural integrity of the capsule was confirmed in the normal and abnormal test condition. By a thermal analysis at a 24 MW_{th} HANARO power, the specimen temperature was in the range of 544~664 °C and the temperature requirement for the irradiation test of the specimen can be satisfied by a

control of the internal He pressure and the heater power. In the irradiation test, the temperature of the specimen was 650±5 °C over the whole irradiation period without using a heater. As for a strain, there is some disturbance for the signal of the LVDT, but the LVDT shows the general trend of the creep strain well, which was expanded in the direction of the stress by 2mm. The measured temperature of the specimen was estimated at no less than 100 °C when compared with the design value and this is shown to be in the error range of 12.2~14.8% of the design value. It is expected that the results presented here will be utilized in the design and manufacturing of creep capsules with 2 or 4 specimens in the future.

ACKNOWLEDGEMENTS

This study was supported by Korea Science and Engineering Foundation(KOSEF) and Ministry of Science & Technology (MOST), Korean government through its National Nuclear Technology Program.

REFERENCES

(1) HANARO operation technical specification, KM-042-RZ-K002, p. 36, 1996. 7
(2) ASME Boiler and Pressure Vessel Code, Section III, Div. 1, Subsection NB, 1989 edition
(3) S.H. Crandall, N.C. Dahl and T.J. Lardner, An Introduction to the Mechanics of Solids, MacGraw-Hill, Inc.. 1978.
(4) M. S. Cho, Irradiation Test Plan and Safety Analysis of Creep Capsule(02S-08K) for In-core Irradiation Test in HANARO, KAERI/TR-2790/2004, 2004. 7
(5) ASM Specialty Handbook Series- Stainless Steel, ASM International, 1994
(6) Metal Handbook 8th edition, Vol. 1 Properties and Selection, American Society for Metals
(7) M. S. Cho, Review of the LVDT signal during the irradiation test of 02S-08K creep capsule, KAERI internal memo, HAN-IC-CR-04-36, 2004. 12

3.9 THERMAL ANALYSIS OF AN INSTRUMENTED CAPSULE USING AN ANSYS PROGRAM

Myoung Hwan Choi, Kee Nam Choo, Young Hwan Kang, Man Soon Cho Jae Min Sohn and Bong Goo Kim

HANARO Utilization Technology Development Division
Korea Atomic Energy Research Institute
150 Deokjin-dong, Yuseong-gu, Daejeon 305-353, Korea

ABSTRACT

An instrumented capsule has been used for an irradiation test of various nuclear materials in the research reactor, HANARO. To obtain the design data of the instrumented capsule, a thermal analysis is performed using a finite element analysis program, ANSYS. The 2-dimensional model for a cross section of the capsule including the specimens is generated, and a gamma-heating rate of the materials for the HANARO power of 24 or 30MW is considered as an input force. The effect of the gap size and the control rod position on the temperature of the specimens or other components is discussed. From the analysis it is found that the gap between the thermal media and the external tube has a significant effect on the temperature of the specimen. In the case of the material capsule, the maximum temperature for the reactor power of 24MW is 255 °C for an irradiation test and 257 °C for a FE analysis at the center stage of the capsule in the axial direction. It is expected that the analysis models using an ANSYS program will be useful in designing the instrumented capsules for an irradiation test and estimating the test results.

KEYWORDS: Instrumented Capsule, Irradiation Test, ANSYS Program, Temperature Thermal Analysis, Heat Generation Density, HANARO

INTRODUCTION

HANARO is one of the world's most powerful multipurpose research reactors. This reactor provides a variety of irradiation tests that benefit from the exceptionally high neutron flux available. The main activities of the capsule development and utilization programs are focused on in-reactor material tests, new and advanced fuel research and

development, safety-related research and development for nuclear reactor materials and components, and basic research. Now, capsules have been developed and they are being utilized for the irradiation test of materials and nuclear fuel in HANARO[(1)].

Especially, the instrumented capsule for material irradiation tests has an important role in the integrity evaluation of reactor core materials and the development of new materials. The material capsule called 02M-02K was designed and manufactured to evaluate the fracture toughness of the irradiated RPV materials in 2003. The capsule was irradiated in the CT test hole of HANARO at a 24 MW thermal output at 290±10 °C up to a fast neutron fluence of 0.64×10^{20} n/cm^2 (E>1.0MeV) for about 6 days[(2)]. Also, to obtain the creep characteristics of nuclear materials during an irradiation, the development of an advanced capsule with 4 specimens called 04M-23K is under way [(3)].

As a part of the analysis for the irradiation test and the preliminary design, a comparison of the temperatures by the irradiation test and an analysis is necessary to verify the design data and to estimate the reliability of the model using a finite element (FE) analysis program, ANSYS[(4)]. Thus, in this study for the 02M-02K capsule the modeling and thermal analysis are carried out, and the analysis results are compared with those of the irradiation tests. The results between the two methods show a good agreement, and we can confirm the reliability of the FE model. In order to obtain the basic data for the design of a capsule with 4 specimens, a preliminary thermal analysis for the 04M-23K capsule is also performed. The two-dimensional (2D) model and the three-dimensional (3D) model are generated in the FE analysis. The influence of the control rod position and the gap between the components on the temperature of the capsule is investigated.

CAPSULE MODEL

Fig. 1 shows the geometrical shape of the instrumented capsules which consists of the bottom structure, the mainbody, the protection tube and the guide tube etc.. The rod tip of the bottom structure is assembled with a receptacle in the reactor core, and the protection and guide tube play the guide part role of various lines such as the thermocouples, micro-heaters and helium supply tubes up to the control unit system on the reactor outside. The mainbody is a major part of the capsule in which specimens, measuring devices and various components are installed, and it includes the external tube of a cylindrical shell with 60 mm in external diameter, 2.0 mm in thickness and 870 mm in length.

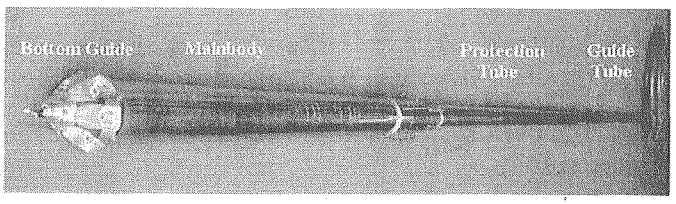

Fig. 1 Shape of the instrumented capsule for an irradiation tests.

Fig. 2 shows the schematic view of the cross section with the specimen. The thermal media is a cylinder with four rectangular specimen holes (**Fig. 2a**) and is used for fixing the test specimens. The thermal media of 114mm consists of 5 stages in the axial direction, and the insulators made of alumina between the medias are placed to prevent the heat from transferring between the stages and to control the temperature of each stage independently. The thermocouples are installed on the top and bottom edges of the specimen inserted in hole #3. The gap between the thermal media and the specimens is designed as 0.1 mm, and that between the media and the tube is 0.105~0.33 mm, which is designed to effectively control the temperature of each stage. **Fig. 2b** shows the cross section of the specimen part for the 04S-23K capsule. This section consists of four main parts; two modules, a thermal media, an external tube, and helium gaps, and one module includes the specimens, spacers, connectors and heater rods. The specimen and the external tube made of STS 316 are 1.5mm and 60mm in diameter, respectively. The gap between the components in the analysis is considered as parameters in the range of 0.05~0.2mm.

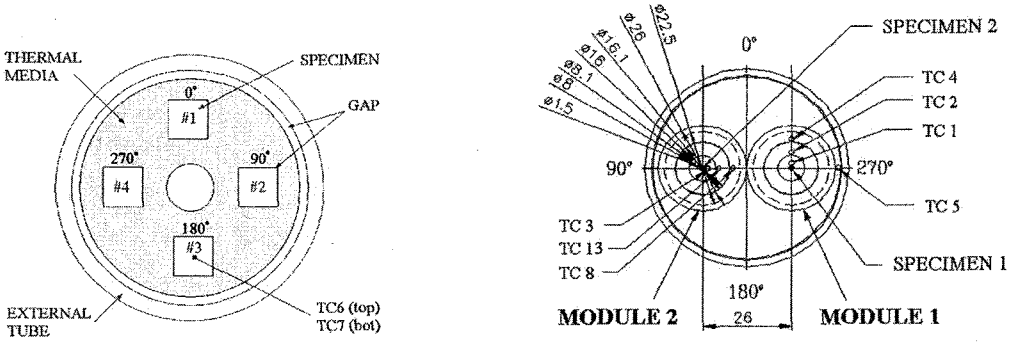

(a) 02M-02K (b) 04S-23K

Fig. 2 Schematic view of the cross section with the specimen.

FINITE ELEMENT ANALYSIS

Modeling

For the thermal analysis of the 02M-02K capsule, two FE models are generated using an ANSYS program. One is the 2D model of a quarter section with two specimens and one center hole as shown in **Fig. 3a**. This model consists of four parts such as specimens (SA508), helium gaps, the thermal media (Al1050) and the external tube (STS 316L). Another (**Fig. 3b**) is the 3D model to obtain the temperature distribution in the axial direction. For the thermal media region of 114 mm in length, an eighth sectional model in the circumferential direction is generated. **Fig. 4** shows a quarter 2D model of the cross-section with the specimen for the 04S-23K capsule. There are many gaps between the components, and they will play an important role in the temperature of the capsule.

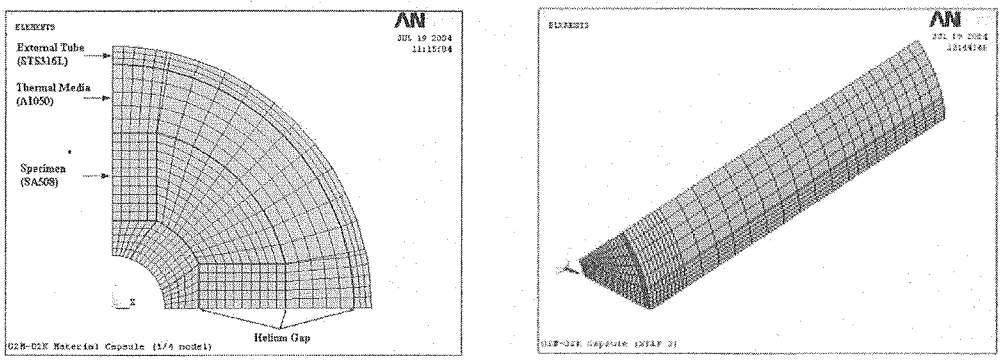

(a) 2D model (b) 3D model

Fig. 3 Finite element model of the 02M-02K capsule.

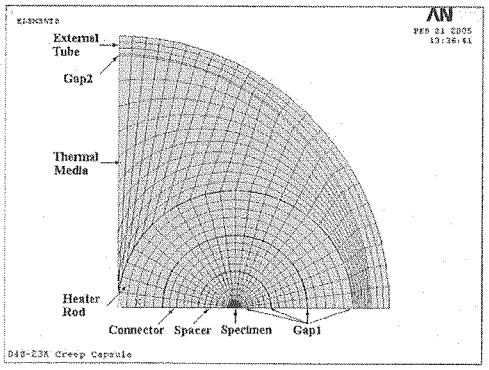

Fig. 4 Finite element model of the 04M-23K capsule.

In the FE model the micro heaters for controlling the temperature of the specimens are neglected. Since the helium gap space in the capsule is small, only the heat conduction can be considered as a heat transmission, thus ignoring the convection and the radiation in the gap space[5].

Force and boundary conditions

The temperature of a cooling water in the reactor in-core is about 40 °C, and the heat transfer coefficient at the outer surface of the external tube is 30.3×10^3 W/m^2 °C, which is experimentally determined[6]. The above two conditions are considered as boundary conditions, and the symmetric conditions are also applied for the symmetric axes of the models. In the reactor in-core, all the materials of the capsule work as a heat source due to a gamma ray irradiation by varying the axial position. The heat generation density of the capsule materials used as an input force is listed in **Table 1**. Also the properties such as a thermal conductivity and a thermal expansion coefficient with the time are used in the thermal analysis.

Table 1 Heat generation density (W/m^3) for the thermal analysis of the capsule

Control Rod (mm)	y-coord.* (cm)	Specimen (SA508)	Specimen (SA508)	Components (STS304)	Media (Al1050)	Tube (STS 316L)
		Material Cap. (24MW)				
430	2.65	3.434E+07			1.073E+07	3.576E+07
430	-7.35	3.730E+07			1.163E+07	3.888E+07
		Creep Cap. (30MW)				
350	-17.7		3.962E+07	3.939E+07	1.280E+07	3.916E+07
450	-17.7		3.588E+07	3.619E+07	1.188E+07	3.588E+07
550	-17.7		3.276E+07	3.214E+07	1.045E+07	3.182E+07

* : Y-coordinate indicates the position of modeled in the reactor in-core

RESULTS AND DISCUSSION

Material capsule (02M-02K)

Table 2 presents the measured and calculated temperature of the capsule specimens at a 24 MW power. The maximum calculated temperature is 263.9 °C at the TC7 position, and shows a 3% higher value than that of the irradiation test. The temperature difference between the top and the bottom of the specimen by the irradiation tests is 1 °C. This means the specimen can maintain a uniform temperature during the irradiation test. For the five stages of the capsule, the temperature distribution has a similar trend because of the same arrangement of the specimens at each stage, although the results for the other stages except for stage 3 are not describe here.

Fig. 5a shows the temperature distribution for the TC6 position of stage 3, and (b) presents that in the radial direction at θ = 0 position. The maximum is 257.1 °C at the rectangular specimen because this stage has the highest gamma heating rate, and the temperature of the thermal media is varied in the 200~215 °C range. The temperature is rapidly decreased at the gap. Especially the effect of the gap between the thermal media and the external tube is larger than that between the specimen and the thermal media, and it has an important influence on the control of the temperature of the specimen using a helium pressure.

Table 2 Comparison of the specimen temperature at 24 MW power

Stage	y-coord. (cm)	Thermocouple	Measured	Calculated (ANSYS)	Error*
3	2.65	TC6 (top)	255	257.1	-0.8
	-7.35	TC7 (bot)	256	263.9	-3.0

* Error = (Measured-Calculated)/Measured×100(%)

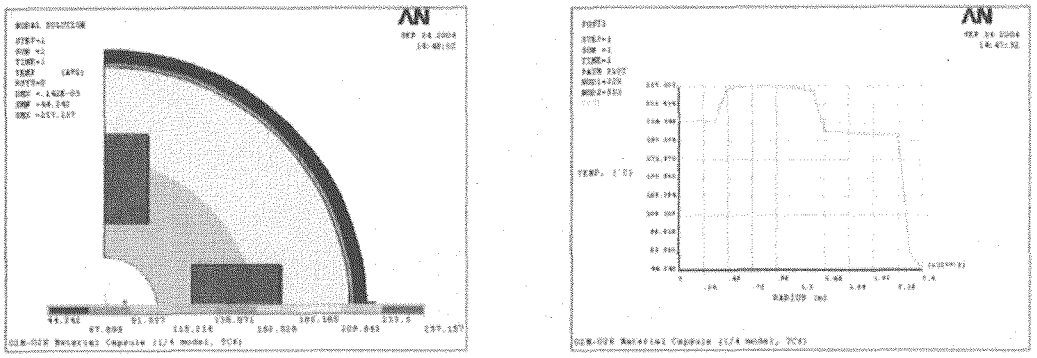

(a) Temperature distribution (b) Temperature profile in the radial direction

Fig. 5 Temperature distribution of the 02M-02K capsule at the TC6 position of stage 3.

Fig. 6 shows the temperature distribution of the specimen and the capsule of stage 3 using a 3D model. Similar to the results using a 2D model, the highest temperature occurs at the specimen, and the thermal media has a temperature of about 200 °C. Also we can confirm a large variation of the temperature at the gap. **Fig. 6b** shows the detailed temperature of the specimen. The maximum value is 264.9 °C at the bottom of the specimen center, and the minimum is 251 °C at the corner, which can increase the heat transfer due to the decreased gap size. In this case the temperature difference of the top and the bottom along the center of the specimen in the axial direction is very small at 3.4 °C, although these values vary with the gap size and the gamma flux.

The 3D analysis results agreed with the 2D results to within 5 °C for the section with the thermocouple. It is found that the FE model using the 2D and the 3D elements shows nearly the same temperature. The analysis results also show a good agreement with those of the irradiation test, and they mean that the analysis model simulates the measured temperature well. From these results we are sure that the specimens of the 02M-02K material capsule have been irradiated in a similar environment without a large variation of the temperature in the axial and radial direction.

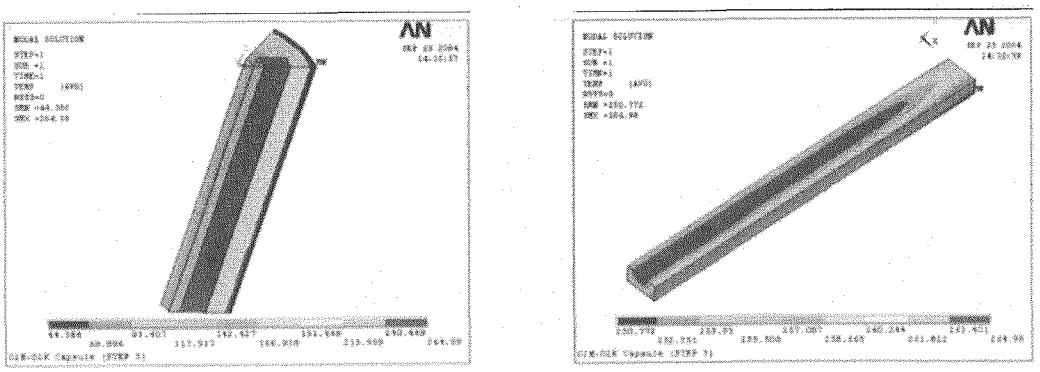

(a) Temperature distribution (b) Temperature distribution of the specimen

Fig. 6 Temperature of the stage 3 specimen using a 3D model.

Creep capsule (04S-23K)

The preliminary thermal analysis to obtain the basic data for the detailed design of the 04S-23K creep capsule is performed. This capsule will be irradiated in the IR hole at a 30 MW power. **Table 3** presents the temperatures of the specimen with the control rod position and the gap size. In this case, the temperature increases according to the increment of the level of the control rod in the reactor. The reason is because the heat generation density of the materials is decreased with the increased elevation of the control rod. The gap size between the thermal media and the external tube has a larger influence than the control rod position on the temperature. It is found that the effect of Gap2 is more sensitive than Gap1 on the temperature of the specimen and the components. When the gap2 size is increased to 0.05mm, the temperature increases by about 60°C.

Table 3 Temperature (°C) of the specimen with the position of the control rod

Gap2 size (mm)	Control Rod Position (mm)		
	350	450	550
0.05	403	378	345
0.10	468	439	402
0.15	530	497	454
0.20	589	553	504

For the Gap2 size of 0.1mm and the control rod position of 450mm, the temperature distribution of the capsule is shown in **Fig. 7a**. The maximum is 439°C and it occurs at the specimen located in the center of the module. The temperature of the thermal media made of pure aluminum is 240~320°C which is below its melting temperature, 660°C. Also this figure shows that the temperature is varied depending on the circular gaps between the components like the material capsule.

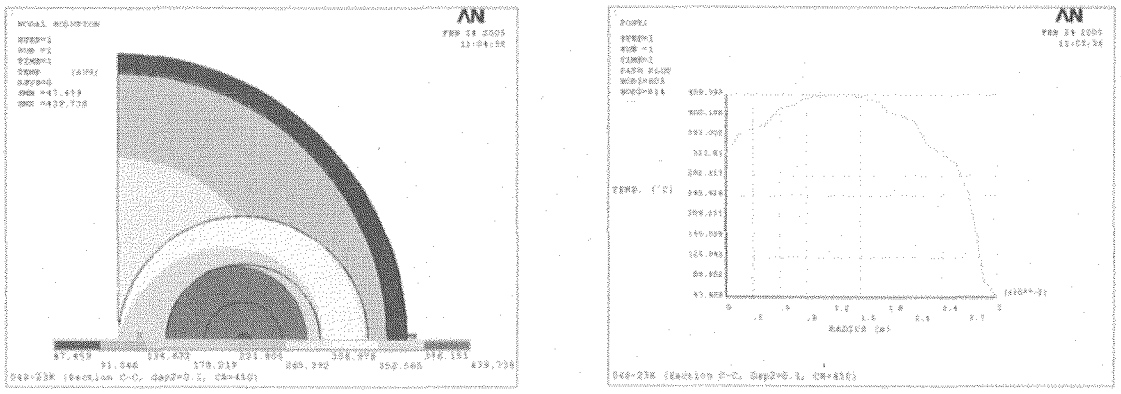

(a) Temperature distribution (b) Temperature profile in the radial direction

Fig. 7 Temperature distribution of the 04M-23K capsule.

Fig. 7b presents the temperature profile for the section of the specimen part at $\theta = 0$ in the radial direction. The temperature of the module including the specimen and the other components is distributed in the range of 300~440°C, and the temperature decrement due to the 0.05mm gap (Gap1) between the components is small. But similar to the material capsule, the gap (Gap2) that exists between the thermal media and the external tube has a significant effect on the temperature. This is because the helium gas filling the gap plays a thermal resistance role with a low thermal conductivity.

CONCLUSIONS

1) For the HANARO power of 24 MW, the measured and calculated temperatures of the 02M-02K capsule specimens at stage 3 (TC6) are 255 and 257°C, respectively. The analysis results show a slightly higher temperature than the measured one. But the temperature between the two methods has a good agreement with each other, and we can confirm the reliability of the FE model for the thermal analysis of the capsule.
2) The FE model using the 2D and the 3D elements has nearly the same results showing a difference within 5 °C at the section with the thermocouple.
3) From the preliminary thermal analysis of the 04S-23K capsule, the temperature of the specimen in the case of the 30MW and the gap size of 0.1mm is 468~402°C for a control rod position of 350~550 mm. When the gap size is increased to 0.05mm, the temperature is increased by about 60°C. The temperature of the thermal media is lower than the aluminum's melting one.
4) The important factor which influences on the temperature of the specimen is the helium gap, and we think that the design of a creep capsule to meet the target temperature is possible by means of a control of the gap size and a positioning of the specimen at the reactor in-core in the axial direction.

ACKNOWLEDGEMENTS

This study was supported by Korea Science and Engineering Foundation (KOSEF) and Ministry of Science & Technology (MOST), Korean government, through its National Nuclear Technology Program.

REFERENCES

(1) Y.H. Kang et al., Capsule Development and Utilization for Material Irradiation Tests. KAERI/RR–2360/03 (2003) KAERI.
(2) K.N. Choo et al., Design, Fabrication and Test Report on HANARO Instrumented Capsule(02M-02K) for the Evaluation of Fracture Toughness of Irradiation RPV Materials. KAERI/TR-2596/2003 (2003) KAERI.
(3) M.S. Song, Y. Choi, M.S. Cho, B.G. Kim and Y.H. Kang, Multi-Channel Mechanical Test Machine for HANARO (I). *2004 KNS Autumn Meeting,* 979~980 (2004).
(4) ANSYS IP Inc., ANSYS User's manual Ver. 9.0. (2005) ANSYS IP Inc..
(5) Y.S. Lee, M.H. Choi, Y.H. Kang and D.S. Shin, Nucl. Eng. and Des.. Vol.212, No.1-3, 273-279 (2002).
(6) Y.S. Lee, M.H. Choi and Y.H. Kang, Nucl. Eng. and Des.. Vol.205, No.1-2, 205-212 (2001).

3.10 WATER CHEMISTRY OF THE JMTR IASCC IRRADIATION LOOP SYSTEM

Satoshi Hanawa[1], Jin Oogiyanagi[2], Yuichiro Mori[2] and Junichi Saito[2]

1: Technology Development Department
2: Department of JMTR
Japan Atomic Energy Agency
4002 Narita-cho, Oarai-machi, Higashi-Ibaraki-gun, Ibaraki-ken, 311-1393 Japan

Takashi Tsukada

Nuclear Science and Energy Directorate
Japan Atomic Energy Agency
2-4 Shirakata Shirane, Tokai-mura, Naka-gun, Ibaraki-ken, 319-1195 Japan

ABSTRACT

Irradiation assisted stress corrosion cracking (IASCC) is recognized as an important degradation issue of the core-internal material for aged Boiling Water Reactors (BWRs). Therefore, irradiation loop system has been developed and installed in the Japan Materials Testing Reactor to perform the IASCC irradiation test. In the IASCC irradiation test, water chemistry of irradiation field is one of the most important key parameters because it affects initiation and propagation of cracks. This paper summarizes the measurement and evaluation method of water chemistry of IASCC irradiation loop system.

KEYWORDS: JMTR, IASCC, Irradiation loop system, Water chemistry

INTRODUCTION

Irradiation Assisted Stress Corrosion Cracking (IASCC) is one of the significant issues relevant to the aging degradation of LWR vessel internals. Japan Atomic Energy Agency (JAEA) is, therefore, conducting a corporative research program with the Japan Atomic Power Company to study in-core IASCC behavior under boiling water reactor (BWR) conditions using the irradiation loop system installed in the Japan Materials Testing Reactor

(JMTR). The irradiation loop system consists of the water control unit (WCU) and saturated temperature capsules (SATCAPs)[1,2].

In the IASCC irradiation test, water chemistry such as dissolved oxygen (DO), dissolved hydrogen (DH), hydrogen peroxide (H_2O_2) contents is one of the most important parameter as same as neutron/gamma fluence or stress condition because they govern the corrosive environment of test specimens. Therefore, the water chemistry of irradiation loop system is controlled or monitored. In viewpoint of advanced IASCC irradiation experiment, it is essential to assess the water chemistry nearby the irradiated specimens in SATCAPs under irradiation condition. Accordingly, the water radiolysis code for the irradiation loop system (WRAC-JM) is developed based on the water radiolysis in a crevice code (WRAC)[3].

In this paper, the measurement and evaluation method of the water chemistry of IASCC irradiation loop system is summarized and the water radiolysis code which evaluates water chemistry around the irradiation field is reported.

OVERVIEW OF THE IRRADIATION LOOP SYSTEM

A schematic diagram of the irradiation loop system is shown in **Fig. 1**. The irradiation loop system consists of the WCU and SATCAPs. Major specifications of the WCU are shown in **Table 1**. The WCU supplies high temperature and high pressure water to simulate BWR's water condition. In the water conditioning tank, DO and DH is controlled by bubbling of mixed gas of oxygen-helium, hydrogen-helium or pure helium. Two of the three main pumps usually operate to prevent loss of flow from the safety point of view. To reduce fluctuation of flow rate, the main pump of three plungers is employed and a surge tank of forty litters is installed at outlet of the main pumps. At the downstream of the regenerative heat exchanger, feeding water line is divided into five paths to the capsules. Headers and coolers of the high capacity are employed to maintain the temperature of feeding water because 100% of flow rate should be cooled for purification and then heated again for temperature control of specimens. Instrumentation for on-line monitoring is provided and batch sampling can also be done for water chemistry analysis.

Schematically drawn cross section of a SATCAP is shown in **Fig. 2**. A SATCAP contains several types of irradiation specimens such as CT specimens, UCL specimens and so on. Temperature of test specimens can be controlled by the saturation temperature of feeding water. By controlling the water pressure, temperature of all specimens in a SATCAP can be controlled within the range from 538K to 575K during irradiation experiments.

WATER CHEMISTRY OF THE IRRADIATION LOOP SYSTEM

Measurement of water chemistry

In order to evaluate water chemistry variables of the irradiation loop, DO, DH, H_2O_2, conductivity and pH are measured by online monitoring or batch sampling. At the outlet of the water conditioning tank, the water chemistry is monitored not only for evaluation but also to control DO or DH. In addition, outlet water as well as inlet water of the in-pile section is measured by selecting selection valves as shown in **Fig. 1** to evaluate the water chemistry of in-pile region. In viewpoint of corrosion phenomenon on SCC, it is well known that DO, DH and H_2O_2 are important parameters because oxygen and H_2O_2 increase the electrochemical corrosion potential (ECP), whereas hydrogen decrease the ECP. DO and DH are measured by polarographic type sensors (TOA denpa Co.Ltd.), and these are installed in the WCU for online monitoring. Wide range of DO or DH (few ppb ~ ppm) with reliable measurement is available with these sensors. On the other hand, detection method for H_2O_2 is quite different from others. For understanding the behavior of H_2O_2, high detection level of sub-ppb is required. One of the most promising methods for detection is chemical photoluminescence, using luminol as a chemical phosphor. In order to detect H_2O_2 by the chemical photoluminescence procedure, the flow injection type H_2O_2 detection method[4] is employed in the irradiation loop system. A schematic diagram of this method is shown in **Fig. 3**. The mixed reagent is consisted of luminol, Co^{2+}, and buffer solution. The carrier water is supplied continuously into a mixing joint. The mixed reagent and carrier water are fed into the mixing joint with the same flow rate. 20μl of sample water are fed into the mixing joint by rotating the injection valve. H_2O_2 in the sample water reacts with the luminol on passing into the flow cell. The luminous intensity is measured by the chemiluminescence analyzer CLA-2100 (Tohoku Electronic Industrial Co.,Ltd.).

Water chemistry of the irradiation loop system

Water chemistry change during the reactor operation is shown in **Fig. 4**. In this operation mode, DO of feeding water was controlled at 170ppb with the variation range of less than 10ppb. From this figure the water chemistry of inlet water maintained the constant value, therefore it can be said stable irradiation experiments are available with the irradiation loop system. DO and DH of the outlet water increased with the time elapse at the beginning of irradiation, and then values were saturated at the constant value. These changes at the beginning of irradiation are thought to be caused by oxidation of surface of test specimens.

Change of H_2O_2 during the reactor power up is shown in **Table 2**. Due to decomposition of water in the SATCAP, H_2O_2 was generated and increased with increasing the reactor power. Moreover, generated H_2O_2 was accumulated in the water conditioning tank then the concentration of H_2O_2 at the inlet increased. But it is well known that H_2O_2 is decomposed easily at higher temperature, therefore the H_2O_2 was decreased by the reactor

full power operation condition and the concentration became few ppb.

WATER RADIOLYSIS CODE

In order to evaluate the water chemistry in SATCAPs, the WRAC-JM code is developed based on the WRAC code. In the WRAC-JM code, direct generation of radiolytic species due to radiation energy deposition in the water, secondary generation and disappearance caused by their interaction, interaction with the SATCAP surface are introduced. The basic equations are shown in Eqs.(1),

$$\partial C_i^k / \partial t = g_i^\gamma Q^{gk} + g_i^n Q^{nk} + \sum k_{mn}^i C_m^k C_n^k - C_i^k \sum k_{is} C_s^k + \sum k_{mn}^{wi} C_m^k C_n^k - C_i^k \sum k_{is}^{wk} C_s^k + C_i^{k-1} G_{in}^k / V^k - C_i^{k-1} G_{out}^k / V^k \quad (1)$$

where C_i:concentration, g:g value, γ:γ ray, n:neutron, Q:energy absorption rate, k:reaction constant and k^w:reaction constant with surface. The first and second terms of right side are direct generation of radiolytic species by γ ray and neutron. The third and forth terms are secondary generation and disappearance by their interaction. The fifth and sixth terms are generation and disappearance with surface. The seventh and eighth terms are connection with adjacent nodes. Main components in the irradiation loop system were modeled into several nodes as shown in **Fig. 5**. Contents of oxygen, hydrogen, H_2O_2 and other radicals can be calculated in the order of water flow. The SATCAP was also modeled into several nodes in connection with the structure and fluence distribution. In this study, distributions of oxygen, hydrogen and H_2O_2 in the SATCAP as well as the WCU were calculated using the WRAC-JM. **Fig. 6** shows an example of the water chemistry distributions obtained by the WRAC-JM. In this calculation, initial conditions of DO, DH and H_2O_2 at the water conditioning tank was 170ppb, 2ppb and 10ppb, respectively. By passing through the heater, concentration of H_2O_2 decreases whereas DO increases because of thermal decomposition of H_2O_2. Inside of the irradiation field, the water chemistry changes extremely due to water radiolysis by neutron or gamma-ray. Especially, concentration of H_2O_2 increases up to 175ppb, and after passing through the irradiation field it reduces extremely because of thermal decomposition. From this analysis code, précised water chemistry at optional point can be evaluated. In other words, important information for IASCC irradiation tests can be obtained by this analysis code.

CONCLUDING REMARKS

Irradiation loop system which simulates BWRs core condition was installed in the JMTR.

The irradiation loop system consists of the WCU and SATCAPs. Water chemistry such as DO, DH, H_2O_2, conductivity and pH are measured the inlet water as well as the outlet water of the irradiation field.

The water radiolysis code has developed to evaluate the water chemistry of irradiation field. Important information for IASCC irradiation tests can be obtained by this analysis code.

REFERENCES

(1) Y.Matsui, , M. Niimi, T. Hoshiya, T. Tsukada and H. Tsuji, Journal of Nuclear Materials, 258-263 (1998) 378.
(2) H.Ide, Y.Matsui, Y.Itabasi, Y.Komori,Y.Nagao, JAERI-Tech 2002-079 (2002).
(3) Tomonori SATOH, Yoshiyuki SATOH and Shunsuke UCHIDA, Journal of Nuclear Science and Technology, Vol. 40 (2003), No. 5, pp.334-342
(4) N.Yamashiro, S.Uchida, Y.Satoh, Y.Morishima, H.Yokoyama, T.Satoh, J.Sugama and R.Yamada, Journal of Nuclear Science andTechnology, vol.41, No.9, pp.890-897 (2004)

Table 1 Major specifications of the WCU

Capacity	**5 Capsules** **Max. Temperature 593K** **Max. Pressure 10MPa** **Max. Flow Rate 0.2m^3/h/capsule**
Temp. of Specimens	**561K $^{+14K}_{-23K}$ for all specimens**
Water Chemistry	
Conductivity	**< 10μS/m**
Impurities	**SO_4^{2-} < 5ppm** **Fe, Cr < 10ppb**
Dissolved Oxygen	**controllable between 10 - 200ppb**
Dissolved Hydrogen	**controllable below 1ppm**

Table 2 Change of H_2O_2 during the reactor power up

Reactor power (MW)		10	30	40	50
H_2O_2 (ppb)	Inlet	11	24	51	68
	Outlet	50	76	75	80

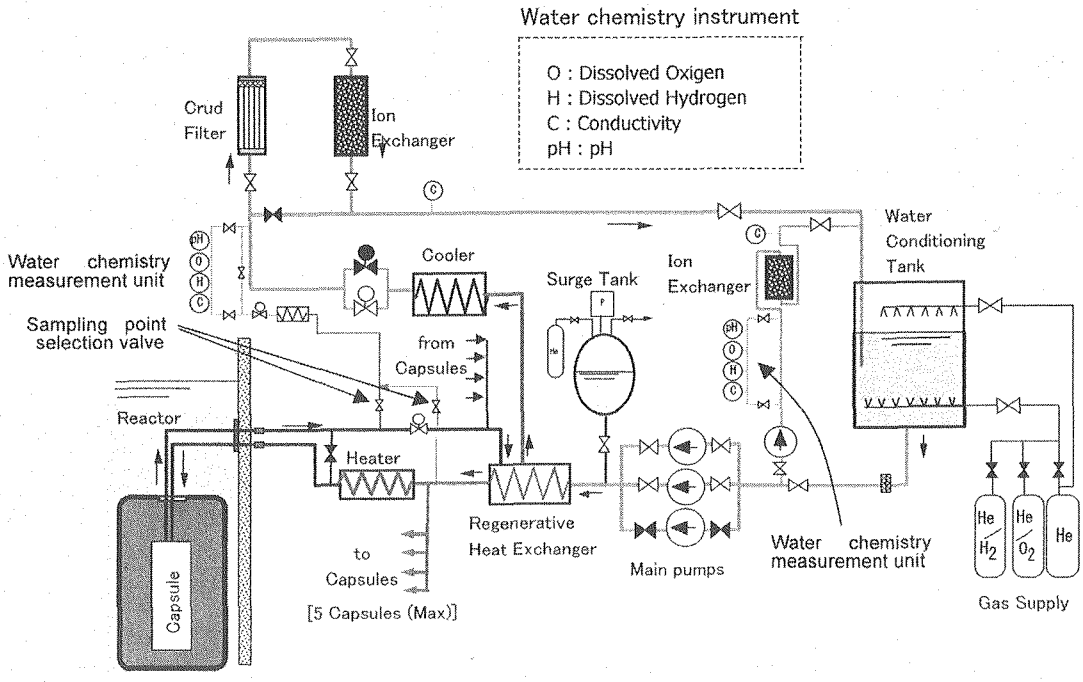

Fig. 1 A schematic diagram of the irradiation loop system.

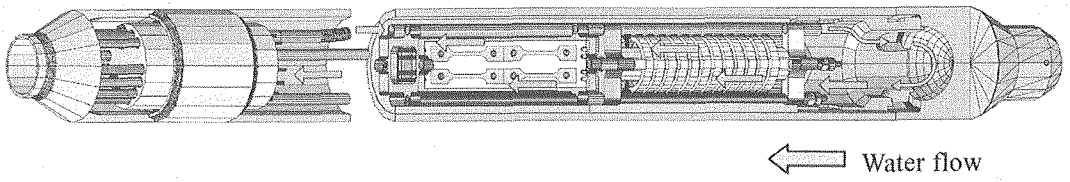

Fig. 2 A schematic diagram of a SATCAP.

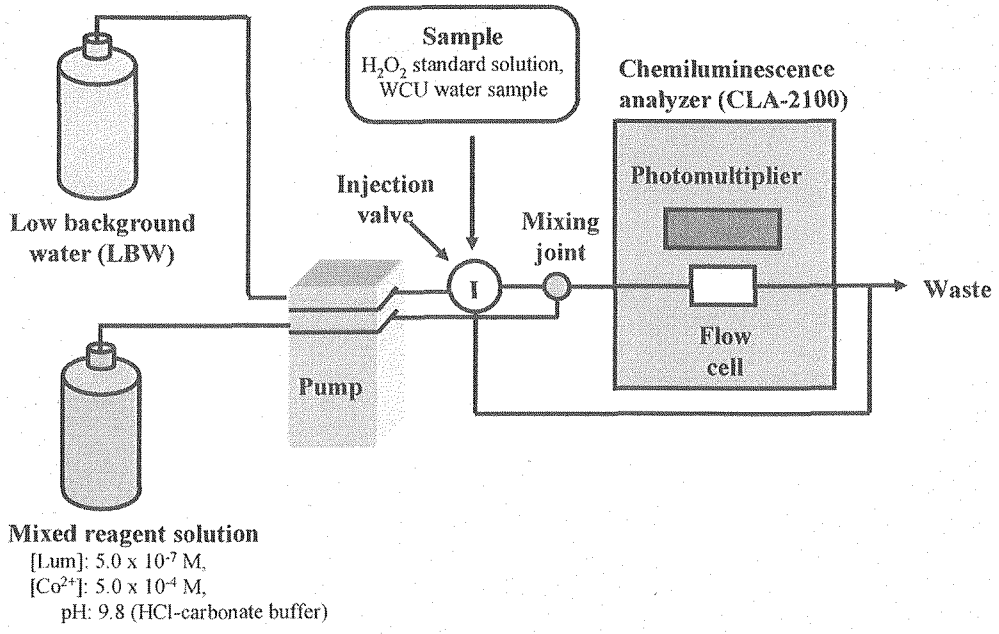

Fig. 3 Apparatus for determination of H_2O_2.

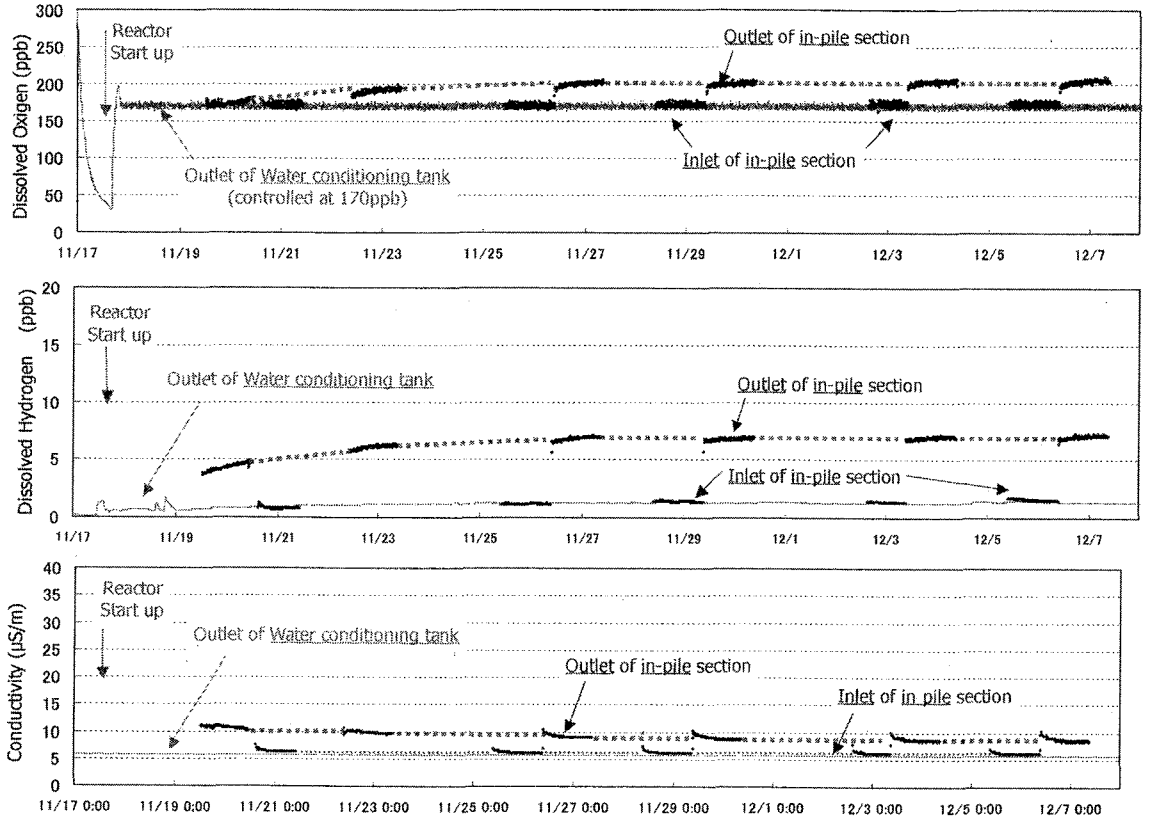

Fig. 4 Water chemistry change during the reactor operation.

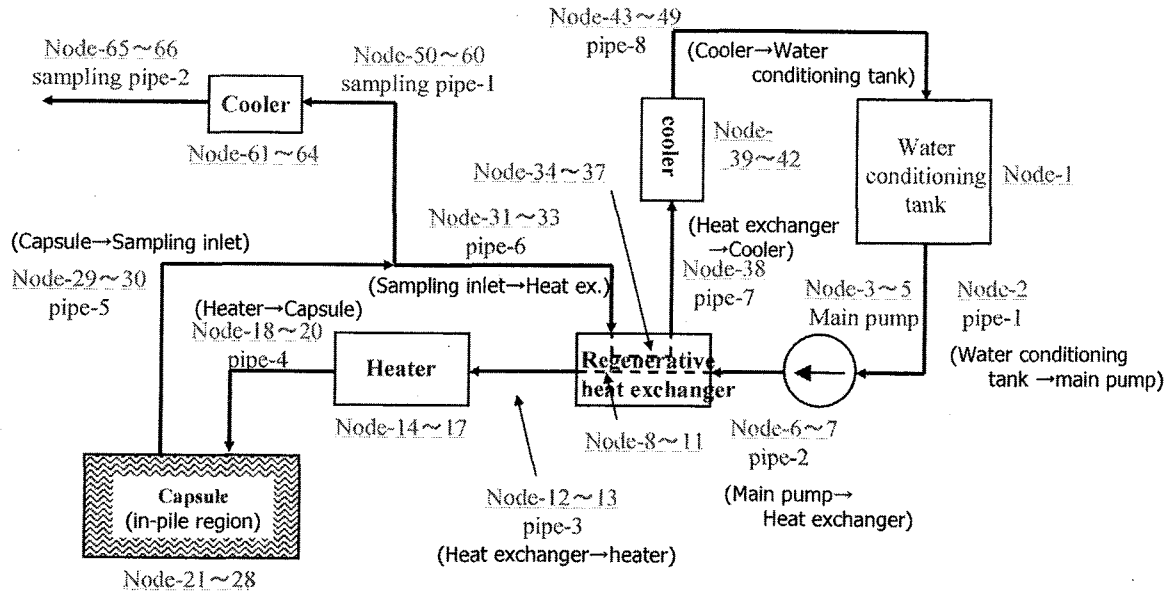

Fig. 5 Modeling of the irradiation loop system.

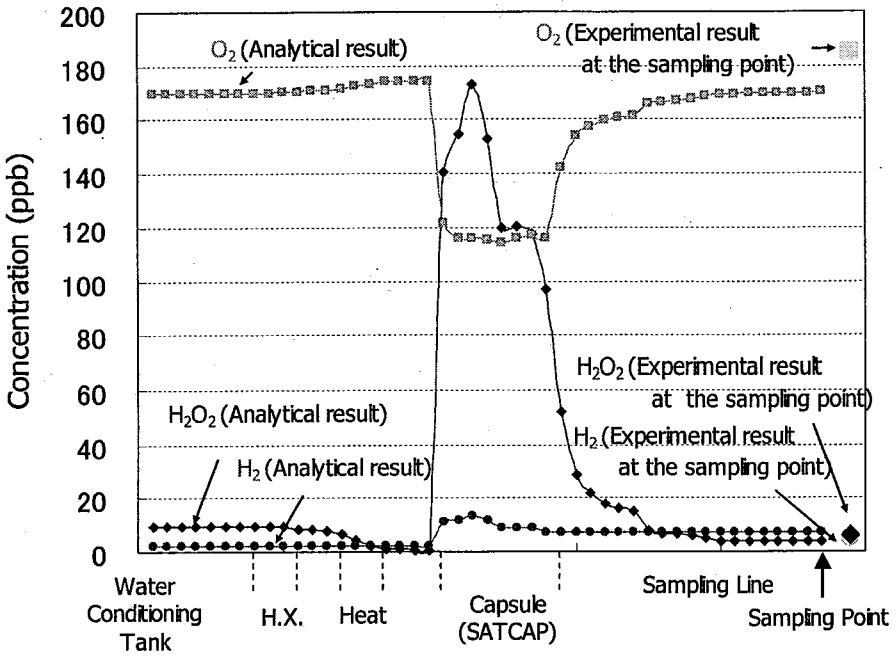

Fig. 6 Water chemistry distributions obtained by the WRAC-JM.

Closing Address

by
Young Hwan Kang
Cooperative Program Coordinator
Principal Researcher, HANARO Utilization Technology Development Division
Korea Atomic Energy Research Institute

Good afternoon, Director General Dr. Takashi Nagata, Deputy Director General Dr. Teruo Nakajima, Director Dr. Yusaku Wada, and Distinguished Delegates, Ladies and Gentlemen.

It is my pleasure to make this closing address as one of the Korean participants at this seminar. I would first like to say that this seminar has succeeded with help of each participant based on the close cooperation between JAEA and KAERI. Also, I would like to express our appreciation for the warm hospitality of you and your Institute.

As you know, the 1st joint seminar between JAEA and KAERI began in 1992 as one of the cooperative research programs based on the advanced irradiation and PIE technology since the late 1980s. Looking back over the past 10 years, this meeting has acted as a technical information exchanger of the on-going programs between KAERI and JAEA. Now, we have entered into a new vital phase such as joining several user groups together for the effective utilization of the HANARO and JMTR reactor as well as PIE facilities.

While we have been here, there have been several issues that have occupied our time from which I hope progress in the fields of the irradiation and PIE technologies will be made. These include: 1. Current Status and future program on the irradiation test and PIE; 2. Operation experiences of the irradiation test and PIE facility; 3. Development of the irradiation and PIE technologies; and 4. Evaluation of the irradiation and PIE data. From the joint seminar, both sides have recognized that there is a need for continued meetings in the fields of the irradiation and PIE technologies between KAERI and JAEA. Additionally, I hope that the recommendations obtained from the meeting of the cooperative program coordinators will be given the required attention.

From these few issues mentioned above, this meeting has clearly been very successful and could be of critical importance to the future of both sides.

Mr. Chairman, on behalf of the President of KAERI, Dr. Chang Gyu Park, please convey our deep felt appreciation and thanks to the President of JAEA for hosting us. We have already discussed about the next Joint seminar during this meeting and decided to open the next joint seminar in the Fall of 2008 in Korea. I hope that each of us will meet again in Korea with innovative results from our researchers and be ever more focused on "current world issues" like the programs of the VHTR development.

Thank you and have a pleasant afternoon.

Closing Address

by
Teruo Nakajima
Deputy Director General, Oarai Research and Development Center
Japan Atomic Energy Agency

First of all, it is my grate pleasure to give participants the closing address.

We have now come to the end of the seminar. Many contributions were made during this seminar for further development in the field of irradiation test and PIE with having totally 100 participants. I hope all of you are satisfied with the seminar, and also enjoyed friendly communications and being stayed in Oarai.

I wish to express our sincere gratitude to all participants for their contributions to this seminar, and I would like to thank members of the organizing committee for their assistance to precede the seminar smoothly.

Finally, on behalf of JAEA, I appreciate fourteen-Korean specialists in irradiation and PIE technologies participate in this seminar. And, I hope a lot of Japanese specialist in this field will also be able to visit KAERI and to participate in the next joint seminar. We look forward to seeing many of you again in next joint seminar at KAERI.

Now, this brings 2005 JAEA-KAERI joint seminar on advanced irradiation and PIE technology in JAEA to a close.

Thank you.

Appendix A

COMMITTEE

Executive Committee
Chairman: Motoji Niimi
Vice Chairmen: Jun-ichi Saito, Hideaki Nabeya
Secretariat: Toshimitsu Ishii, Yoshinori Matsui, Jin Ohgiyanagi

Member in charge of general affairs

Shinya Abe (Head)	Jingo Ohtaka	Tatsuya Iida
Kazuki Hayakawa	Takao Komuro	Shoko Kimura
Masaru Kanno	Takayuki Yamaura	Minako Abe
Tomoko Abe		

Member in charge of planning

Yoshinori Matsui (Head)	Satoshi Hanawa	Jin Ohgiyanagi
Kazuo Kawamata	Shin-ichi Koyama	Kozo Katsuyama
Akira Shibata	Hiroshi Ide	Masahito Nakata

Member in charge of meeting room arrangement

Masao Ohmi (Head)	Shizuo Sozawa	Fumiki Takada
Yoshiaki Kato	Takashi Saito	Noriyuki Takemoto
Tomonori Soga	Masaya Yamamoto	Wataru Itagaki
Naoyuki Ishihara		

Member in charge of compilation of proceedings

Toshimitsu Ishii (Head)	Jin Ohgiyanagi

Number of presentations for 2005 JAEA-KAERI Joint Seminar on Advanced Irradiation and PIE Technologies

Nation	Organization	Number of presentations	
Japan	Japan Atomic Energy Agency (JAEA)	14	19
	Tohoku University	2	
	Nippon Nuclear Fuel Development Co., Ltd. (NFD)	2	
	Nuclear Development Corporation (NDC)	1	
Korea	Korea Atomic Energy Research Institute (KAERI)	13	16
	Chungnam National University	1	
	Kyunghee University	1	
	Hanyang University	1	
		Total	35

Number of participants for 2005 JAEA-KAERI Joint Seminar on Advanced Irradiation and PIE Technologies

Organization		Number of participants		
JAEA	Oarai R&D Center	73	97	104
	Tokai R&D Center	24		
Tohoku University		2		
NFD		3		
NDC		1		
Oarai Town (Mayer)		1		
KAERI		11		14
Chungnam National University		1		
Kyunghee University		1		
Hanyang University		1		
		Total		118

Appendix B

Schedule of 2005 JAEA-KAERI Joint Seminar on Advanced Irradiation and PIE Technologies

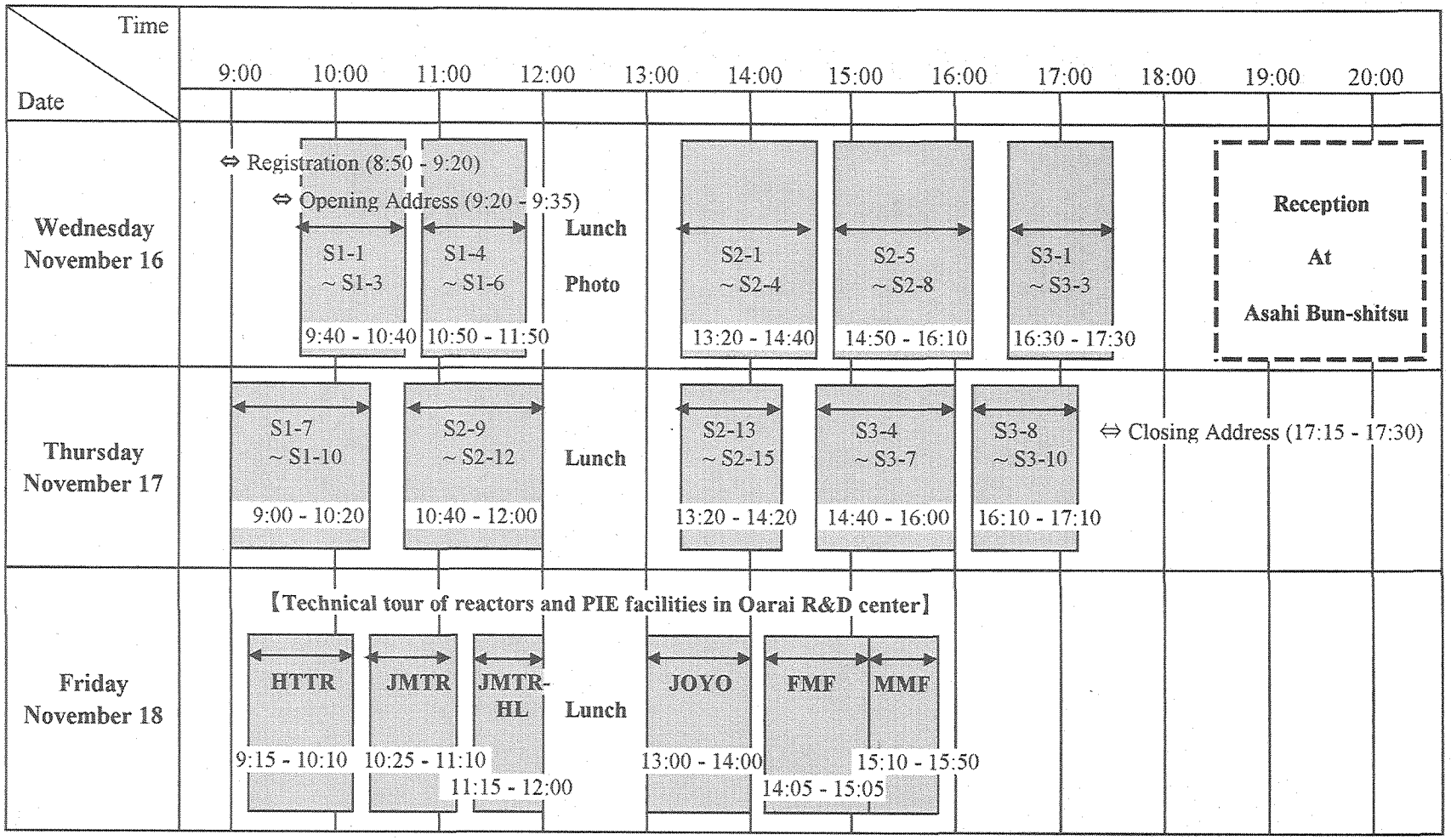

JAEA-Conf 2006-003

Appendix C

2005 JAEA-KAERI Joint Seminar on Advanced Irradiation and PIE Technologies

Program

Wednesday, November 16, At F-Cerveaux in JAEA Oarai R&D Center

[Opening address, & Welcome message (9:20~9:35)]

[Chairperson: Y. Wada (Director, Technology Development Department, JAEA)]

+ Dr. T. Nagata (Director General, Oarai Research and Development Center, JAEA)

+ Dr. K-P. Hong (Director, Nuclear Fuel Cycle Examination Division, KAERI)

+ Mr. T. Kotani (Mayor, Oarai Town)

[Session 1 Current status and future program on irradiation test and PIE (9:40~11:50)]

[Chairperson: K-P. Hong (KAERI) and T. Ishii (JAEA)]

S1-1 Status of the material capsule irradiation and the development of the new capsule technology in HANARO
K-N. Choo, Y-H. Kang, M-H. Choi, M-S. Cho, B-G. Kim (KAERI)

S1-2 Current status of irradiation facilities in JRR-3 and JRR-4
N. Hori, S. Wada, F. Sasajima, T. Kusunoki (JAEA)

S1-3 Introduction of the experimental fast reactor JOYO
K. Matsuba, H. Kawahara, T. Aoyama (JAEA)

Coffee break (10:40~10:50)

S1-4 Current status of nuclear fuel cycle examination facilities in KAERI
K-P. Hong, S-W. Park (KAERI)

S1-5 Current activities in development of PIE techniques in JMTR Hot Laboratory
T. Ishii, M. Ohmi, M. Shimizu, Y. Kaji, F. Ueno (JAEA)

S1-6 PIE activities in NFD hot laboratory
M. Kodama, M. Hirai, N. Sakaguchi (NFD)

Lunch (11:50~13:20)

[Session 2 Development of irradiation and PIE technologies (13:20~16:10)]

[Chairperson: Y-B. Chun (KAERI) and Y. Matsui (JAEA)]

S2-1 Development of in-pile capsule for IASCC study at JMTR
Y. Matsui, S. Hanawa, H. Ide, M. Tobita, J. Hosokawa, Y. Onuma, K. Kawamata, Y. Kanazawa, S. Iwamatsu, H. Ugachi, T. Tsukada, J. Saito (JAEA)

S2-2 Remote-welding technique for assembling in-pile IASCC capsule in hot cell
K. Kawamata, T. Ishii, Y. Kanazawa, S. Iwamatsu, M. Ohmi, M. Shimizu, Y. Matsui, H. Ugachi, Y. Kaji, T. Tsukada, J. Saito (JAEA)

S2-3 Core management and fast neutron field characterization of JOYO
Y. Ohkawachi, T. Sekine, T. Aoyama (JAEA)

S2-4 A study on the thermal analysis and structural design optimization of a cylindrical structure with multi specimens
Y-S. Lee[1], Y-J. Choi[1], Y-H. Kang[2] (1: Chungnam National Univ., 2: KAERI)

Coffee break (14:40~14:50)

S2-5 Irradiation test program of HANA claddings in HALDEN reactor
M-H. Lee, J-H. Baek, J-H. Kim, Y-H. Jeong (KAERI)

S2-6 Development of MOX fuel containing americium
-Its fabrication and characterization-
S. Miwa, M. Osaka, H. Yoshimochi, K. Tanaka, K. Kurosaki, S. Yamanaka (JAEA)

S2-7 PIE technique of LWR fuel cladding fracture toughness test
S. Endo, K. Usami, M. Nakata, T. Fukuda, M. Numata, M. Kizaki, Y. Nishino (JAEA)

S2-8 Development of the under-water burnup measuring system for a spent PWR fuel assembly
Y-B. Chun, K-J. Park, H-D. Kim, K-J. Jung, S-W. Park (KAERI)

Coffee break (16:10~16:30)

[Session 3 Evaluation of irradiation and PIE data (16:30~17:30)]

[Chairperson: S-B. Ahn (KAERI) and T. Shibata (JAEA)]

S3-1 PIE technologies for the study of stress corrosion cracking of reactor structural materials
H. Ugachi, J. Nakano, Y. Nemoto, K. Kondo, Y. Miwa, Y. Kaji, T. Tsukada, M. Kizaki, M. Ohmi, M. Shimizu (JAEA)

S3-2 Prediction of delayed hydride crack velocity in the irradiated Zr-2.5Nb CANDU pressure tube materials
S-B. Ahn, W-H. Oh, Y-H. Jung, D-S. Kim, Y-S. Choo, K-S. Kim, Y-S. Kim, K-P. Hong (KAERI)

S3-3 Superplastic characteristics and microstructure of neutron irradiated 3Y-TZP
T. Shibata[1], Y. Motohashi[2], M. Ishihara[1], S. Baba[1], K. Sawa[1] (1: JAEA, 2: Ibaraki Univ.)

[Reception at Asahi Bun-shitsu (18:30~20:30)]

[Toastmaster: Toshimitsu Ishii]

Thursday, November 17, At F-Cerveaux in JAEA Oarai R&D Center

[Session 1 Current status and future program on irradiation test and PIE (9:00~10:20)]

[Chairperson: D-K. Min (KAERI) and T. Shikama (Tohoku Univ.)]

S1-7 The Oarai branch of IMR, Tohoku university as open facility for university researchers utilizing fission reactors
T. Shikama (Tohoku Univ.)

S1-8 PIE results and new techniques applied for 55 GWd/t high burnup fuel of PWR
T. Tsuda[1], Y. Yamaguchi[1], Y. Shinohara[1], M. Sugano[1], Y. Kosaka[1], Y. Takeda[1], T. Kitagawa[2]
(1: NDC, 2: MHI)

S1-9 Post-irradiation examination of high burnup PWR fuel
D-K. Min, Y-B. Chun, E-P. Lee, H-G. Lee, H-S. Seo, S-H. Eom, H-M. Kwon (KAERI)

S1-10 Recent chemistry work for the burnup measurement in KAERI
J-G. Kim, K-S. Joe, J-S. Kim, Y-S. Jeon, B-C. Song, S-H. Han (KAERI)

Coffee break (10:20~10:40)

[Session 2 Development of irradiation and PIE technologies (10:40~14:20)]

[Chairperson: Y-H. Kang (KAERI) and H. Kurishita (Tohoku Univ.)]

S2-9 Performance tests of the I&C system (GSF-2002) using a fuel capsule mockup
Y-H. Kang, S-J. Park, D-H. Ahn, M-S. Cho, K-N. Choo, B-G. Kim (KAERI)

S2-10 Development of the instrumented capsule for nuclear fuel irradiation test at HANARO
J-M. Sohn, J-M. Oh, S-J. Park, Y-T. Shin, B-G. Kim, Y-H. Kang, H-R. Kim, Y-J. Kim (KAERI)

S2-11 An internal heating experimental method for irradiated fuel cladding tubes
T. Higuchi, T. Kubo, T. Yonekawa (NFD)

S2-12 Improved technique of hydrogen concentration measurement in fuel cladding by backscattered electron image analysis
A. Onozawa, A. Harada, J. Honda, R. Yasuda, M. Nakata, H. Kanazawa, Y. Nishino (JAEA)

Lunch (12:00~13:20)

S2-13 Fracture toughness evaluation of ferritic steels by miniaturized three-point bend specimens
H. Kurishita[1], T. Yamamoto[2], T. Nagasaka[3], A. Nishimura[3], T. Muroga[3], S. Jitsukawa[4]
(1: Tohoku Univ., 2: UCSB, 3: NIFS, 4: JAEA)

S2-14 Development of a remote-controlled magnetic flux leakage measurement apparatus
Y. Nagae[1], S. Takaya[1], K. Aoto[1], T. Yoshitake[1], Y. Abe[1], T. Hoshiya[1], Y. Shigeto[2], Y. Nakamura[1]
(1: JAEA., 2: Inspection Development Co. Ltd)

S2-15 Development of SGS for various waste drums
K-H. Kim, Y-G. Ryu, K-K. Kwak, Y-Y. Ji (KAERI)

Coffee break (14:20~14:40)

[Session 3 Evaluation of irradiation and PIE data (14:40~17:10)]

[Chairperson: M-S. Cho (KAERI) and T. Nakamura (JAEA)]

S3-4 Integrated safety research program of high burnup LWR fuels
T. Nakamura, T. Sugiyama, J. Nakamura, F. Nagase, T. Fuketa (JAEA)

S3-5 Xe diffusion coefficient in pure urania and simulated burnup urania fuel pellets
K. Park[1], D. Lee[1], H. Kim[2], B-G. Kim[2], Y-S. Choo[2], K-S. Kim[2], K-W. Song[2], K-P. Hong[2], K. Song[2], K. Kang[2], Y-H. Kang[2], H. Ryu[2] (1: Kyunghee Univ., 2: KAERI)

S3-6 Characterization of fission products of irradiated SIMFUEL
Y-H. Jung, B-O. Yoo, H-M. Kim, Y-S. Choo, K-P. Hong, I-H. Jung (KAERI)

S3-7 Two-step two-stage fission gas release model
Y-S. Kim[1], C-B. Lee[2] (1: Hanyang Univ., 2: KAERI)

Coffee break (16:00~16:10)

S3-8 Irradiation test for a creep capsule with a single specimen
M-S. Cho, M-H. Choi, K-N. Choo, C-G. Seo, B-G. Kim (KAERI)

S3-9 Thermal analysis of an instrumented capsule using an ANSYS program
M-H. Choi, K-N. Choo, Y-H. Kang, M-S. Cho, J-M. Sohn, B-G. Kim (KAERI)

S3-10 Water chemistry of the JMTR IASCC irradiation loop system
S. Hanawa, J. Oogiyanagi, Y. Mori, J. Saito, T. Tsukada (JAEA)

[Closing Address (17:15~17:30)]

[Chairperson: Y. Wada (Director, Technology Development Department, JAEA)]

Closing Addresses

+ Dr. Y-H. Kang (Principal Researcher, Hanaro Utilization Technology Development Division, KAERI)
+ Mr. T. Nakajima (Deputy Director General, Oarai Research and Development Center, JAEA)

Friday, November 18

[Technical tour of reactors and PIE facilities in Oarai Research and Development Center (9:15~15:50)]
Attendants: T. Ishii, S. Hanawa and J. Ohgiyanagi

HTTR (Reactor)	9:15～10:10 (55 min)
JMTR (Reactor)	10:25～11:10 (45 min)
JMTR-HL (PIE Facility)	11:15～12:00 (45 min)

Lunch time **12:00～13:00**

JOYO (Reactor)	13:00～14:00 (60 min)
FMF (PIE Facility)	14:05～15:05 (60 min)
MMF (PIE Facility)	15:10～15:50 (40 min)

This is a blank page.

国際単位系（SI）

表１．SI 基本単位

基本量	SI 基本単位	
	名称	記号
長さ	メートル	m
質量	キログラム	kg
時間	秒	s
電流	アンペア	A
熱力学温度	ケルビン	K
物質量	モル	mol
光度	カンデラ	cd

表２．基本単位を用いて表されるSI組立単位の例

組立量	SI 基本単位	
	名称	記号
面積	平方メートル	m^2
体積	立法メートル	m^3
速さ，速度	メートル毎秒	m/s
加速度	メートル毎秒毎秒	m/s^2
波数	毎メートル	m^{-1}
密度（質量密度）	キログラム毎立法メートル	kg/m^3
質量体積（比体積）	立法メートル毎キログラム	m^3/kg
電流密度	アンペア毎平方メートル	A/m^2
磁界の強さ	アンペア毎メートル	A/m
（物質量の）濃度	モル毎立方メートル	mol/m^3
輝度	カンデラ毎平方メートル	cd/m^2
屈折率	（数の）1	1

表５．SI 接頭語

乗数	接頭語	記号	乗数	接頭語	記号
10^{24}	ヨタ	Y	10^{-1}	デシ	d
10^{21}	ゼタ	Z	10^{-2}	センチ	c
10^{18}	エクサ	E	10^{-3}	ミリ	m
10^{15}	ペタ	P	10^{-6}	マイクロ	μ
10^{12}	テラ	T	10^{-9}	ナノ	n
10^{9}	ギガ	G	10^{-12}	ピコ	p
10^{6}	メガ	M	10^{-15}	フェムト	f
10^{3}	キロ	k	10^{-18}	アト	a
10^{2}	ヘクト	h	10^{-21}	ゼプト	z
10^{1}	デカ	da	10^{-24}	ヨクト	y

表３．固有の名称とその独自の記号で表されるSI組立単位

組立量	SI 組立単位			
	名称	記号	他のSI単位による表し方	SI基本単位による表し方
平面角	ラジアン(a)	rad		$m \cdot m^{-1}=1$(b)
立体角	ステラジアン(a)	sr(c)		$m^2 \cdot m^{-2}=1$(b)
周波数	ヘルツ	Hz		s^{-1}
力	ニュートン	N		$m \cdot kg \cdot s^{-2}$
圧力，応力	パスカル	Pa	N/m^2	$m^{-1} \cdot kg \cdot s^{-2}$
エネルギー，仕事，熱量	ジュール	J	$N \cdot m$	$m^2 \cdot kg \cdot s^{-2}$
工率，放射束	ワット	W	J/s	$m^2 \cdot kg \cdot s^{-3}$
電荷，電気量	クーロン	C		$s \cdot A$
電位差（電圧），起電力	ボルト	V	W/A	$m^2 \cdot kg \cdot s^{-3} \cdot A^{-1}$
静電容量	ファラド	F	C/V	$m^{-2} \cdot kg^{-1} \cdot s^4 \cdot A^2$
電気抵抗	オーム	Ω	V/A	$m^2 \cdot kg \cdot s^{-3} \cdot A^{-2}$
コンダクタンス	ジーメンス	S	A/V	$m^{-2} \cdot kg^{-1} \cdot s^3 \cdot A^2$
磁束	ウエーバ	Wb	$V \cdot s$	$m^2 \cdot kg \cdot s^{-2} \cdot A^{-1}$
磁束密度	テスラ	T	Wb/m^2	$kg \cdot s^{-2} \cdot A^{-1}$
インダクタンス	ヘンリー	H	Wb/A	$m^2 \cdot kg \cdot s^{-2} \cdot A^{-2}$
セルシウス温度	セルシウス度(d)	℃		K
光束	ルーメン	lm	$cd \cdot sr$(c)	$m^2 \cdot m^{-2} \cdot cd=cd$
照度	ルクス	lx	lm/m^2	$m^2 \cdot m^{-4} \cdot cd=m^{-2} \cdot cd$
（放射性核種の）放射能	ベクレル	Bq		s^{-1}
吸収線量，質量エネルギー分与，カーマ	グレイ	Gy	J/kg	$m^2 \cdot s^{-2}$
線量当量，周辺線量当量，方向性線量当量，個人線量当量，組織線量当	シーベルト	Sv	J/kg	$m^2 \cdot s^{-2}$

(a) ラジアン及びステラジアンの使用は、同じ次元であっても異なった性質をもった量を区別するときの組立単位の表し方として利点がある。組立単位を形作るときのいくつかの用例は表４に示されている。
(b) 実際には、使用する時には記号rad及びsrが用いられるが、習慣として組立単位としての記号“１”は明示されない。
(c) 測光学では、ステラジアンの名称と記号srを単位の表し方の中にそのまま維持している。
(d) この単位は、例としてミリセルシウス度m℃のようにSI接頭語を伴って用いても良い。

表４．単位の中に固有の名称とその独自の記号を含むSI組立単位の例

組立量	SI 組立単位		
	名称	記号	SI 基本単位による表し方
粘度	パスカル秒	Pa・s	$m^{-1} \cdot kg \cdot s^{-1}$
力のモーメント	ニュートンメートル	N・m	$m^2 \cdot kg \cdot s^{-2}$
表面張力	ニュートン毎メートル	N/m	$kg \cdot s^{-2}$
角速度	ラジアン毎秒	rad/s	$m \cdot m^{-1} \cdot s^{-1}=s^{-1}$
角加速度	ラジアン毎平方秒	rad/s^2	$m \cdot m^{-1} \cdot s^{-2}=s^{-2}$
熱流密度，放射照度	ワット毎平方メートル	W/m^2	$kg \cdot s^{-3}$
熱容量，エントロピー	ジュール毎ケルビン	J/K	$m^2 \cdot kg \cdot s^{-2} \cdot K^{-1}$
質量熱容量（比熱容量），質量エントロピー	ジュール毎キログラム毎ケルビン	J/(kg・K)	$m^2 \cdot s^{-2} \cdot K^{-1}$
質量エネルギー（比エネルギー）	ジュール毎キログラム	J/kg	$m^2 \cdot s^{-2} \cdot K^{-1}$
熱伝導率	ワット毎メートル毎ケルビン	W/(m・K)	$m \cdot kg \cdot s^{-3} \cdot K^{-1}$
体積エネルギー	ジュール毎立方メートル	J/m^3	$m^{-1} \cdot kg \cdot s^{-2}$
電界の強さ	ボルト毎メートル	V/m	$m \cdot kg \cdot s^{-3} \cdot A^{-1}$
体積電荷	クーロン毎立方メートル	C/m^3	$m^{-3} \cdot s \cdot A$
電気変位	クーロン毎平方メートル	C/m^2	$m^{-2} \cdot s \cdot A$
誘電率	ファラド毎メートル	F/m	$m^{-3} \cdot kg^{-1} \cdot s^4 \cdot A^2$
透磁率	ヘンリー毎メートル	H/m	$m \cdot kg \cdot s^{-2} \cdot A^{-2}$
モルエネルギー	ジュール毎モル	J/mol	$m^2 \cdot kg \cdot s^{-2} \cdot mol^{-1}$
モルエントロピー，モル熱容量	ジュール毎モル毎ケルビン	J/(mol・K)	$m^2 \cdot kg \cdot s^{-2} \cdot K^{-1} \cdot mol^{-1}$
照射線量（X線及びγ線）	クーロン毎キログラム	C/kg	$kg^{-1} \cdot s \cdot A$
吸収線量率	グレイ毎秒	Gy/s	$m^2 \cdot s^{-3}$
放射強度	ワット毎ステラジアン	W/sr	$m^4 \cdot m^{-2} \cdot kg \cdot s^{-3}=m^2 \cdot kg \cdot s^{-3}$
放射輝度	ワット毎平方メートル毎ステラジアン	$W/(m^2 \cdot sr)$	$m^2 \cdot m^{-2} \cdot kg \cdot s^{-3}=kg \cdot s^{-3}$

表６．国際単位系と併用されるが国際単位系に属さない単位

名称	記号	SI 単位による値
分	min	1 min=60s
時	h	1h =60 min=3600 s
日	d	1 d=24 h=86400 s
度	°	1° =(π/180) rad
分	’	1’ =(1/60)° =(π/10800) rad
秒	”	1” =(1/60)’ =(π/648000) rad
リットル	l、L	1l=1 $dm^3=10^{-3}m^3$
トン	t	$1t=10^3$ kg
ネーパ	Np	1Np=1
ベル	B	1B=(1/2)ln10(Np)

表７．国際単位系と併用されこれに属さない単位で SI単位で表される数値が実験的に得られるもの

名称	記号	SI 単位であらわされる数値
電子ボルト	eV	$1eV=1.60217733(49) \times 10^{-19}J$
統一原子質量単位	u	$1u=1.6605402(10) \times 10^{-27}kg$
天文単位	ua	$1ua=1.49597870691(30) \times 10^{11}m$

表８．国際単位系に属さないが国際単位系と 併用されるその他の単位

名称	記号	SI 単位であらわされる数値
海里		1海里=1852m
ノット		1ノット=1海里毎時=(1852/3600)m/s
アール	a	1 a=1 $dam^2=10^2m^2$
ヘクタール	ha	1 ha=1 $hm^2=10^4m^2$
バール	bar	1 bar=0.1MPa=100kPa=1000hPa=10^5Pa
オングストローム	Å	1 Å=0.1nm=10^{-10}m
バーン	b	1 b=100$fm^2=10^{-28}m^2$

表９．固有の名称を含むCGS組立単位

名称	記号	SI 単位であらわされる数値
エルグ	erg	1 erg=10^{-7} J
ダイン	dyn	1 dyn=10^{-5}N
ポアズ	P	1 P=1 dyn・s/cm^2=0.1Pa・s
ストークス	St	1 St =1$cm^2/s=10^{-4}m^2/s$
ガウス	G	1 G ^10^{-4}T
エルステッド	Oe	1 Oe ^(1000/4π)A/m
マクスウェル	Mx	1 Mx ^10^{-8}Wb
スチルブ	sb	1 sb =1$cd/cm^2=10^4cd/m^2$
ホト	ph	1 ph=10^4lx
ガル	Gal	1 Gal =1$cm/s^2=10^{-2}m/s^2$

表10．国際単位に属さないその他の単位の例

名称	記号	SI 単位であらわされる数値
キュリー	Ci	1 Ci=3.7×10^{10}Bq
レントゲン	R	1 R = 2.58×10^{-4}C/kg
ラド	rad	1 rad=1cGy=10^{-2}Gy
レム	rem	1 rem=1 cSv=10^{-2}Sv
X線単位		1X unit=1.002×10^{-4}nm
ガンマ	γ	1γ=1 nT=10^{-9}T
ジャンスキー	Jy	1 Jy=$10^{-26}W \cdot m^{-2} \cdot Hz^{-1}$
フェルミ		1 fermi=1 fm=10^{-15}m
メートル系カラット		1 metric carat = 200 mg = 2×10^{-4}kg
トル	Torr	1 Torr = (101 325/760) Pa
標準大気圧	atm	1 atm = 101 325 Pa
カロリー	cal	
ミクロン	μ	1 μ =1μm=10^{-6}m

（第７版，1998年改訂）

2005 JAEA-KAERI
Joint Seminar on Advanced Irradiation and PIE Technologies

어서 오십시오

일본 원자력연구개발기구 에

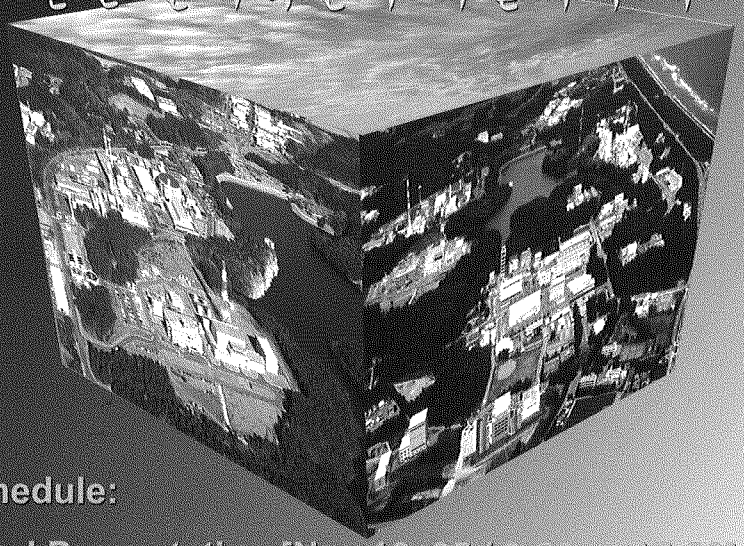

Schedule:

Oral Presentation [Nov.16, 05 / 9:20 ~ 17:30]

Oral Presentation [Nov.17, 05 / 9:00 ~ 17:30]

Technical tour [Nov.18, 05 / 9:15 ~ 15:50]

Venue: Japan Atomic Energy Agency

Oarai Research & Development Center

F-Cerveaux